The Dissertation Committee for Mohammad Reza Mohammad Reza Beygi Certifies that this is the approved version of the following dissertation:

Development of Compositional Three-phase Relative Permeability and Hysteresis Models and Their Application to EOR Processes

Committee:

Mojdeh Delshad, Supervisor

Mary F. Wheeler, Co-Supervisor

Gary A. Pope

Kamy Sepehrnoori

Kishore K. Mohanty

Todd Arbogast

Development of Compositional Three-phase Relative Permeability and Hysteresis Models and Their Application to EOR Processes

by

Mohammad Reza Mohammad Reza Beygi, B.Sc.; M.Sc.

Dissertation

Presented to the Faculty of the Graduate School of

The University of Texas at Austin

in Partial Fulfillment

of the Requirements

for the Degree of

Doctor of Philosophy

The University of Texas at Austin

December 2016

In The Name of God, The Most Gracious, The Most Merciful

"*All Nature is but art, unknown to thee;*

All chance, direction, which thou canst not see;

All discord, harmony not understood;

All partial evil, universal good;

And, spite of pride, in erring reason's spite,

*One truth is clear, whatever is, is right.***"**

An Essay on Man: Epistle I, Alexander Pope

Dedication To

To my parents and brothers,

To my beloved wife,

To my lovely daughter Nikki Naz

and

To all those who committed to real peace in this World

Acknowledgements

This dissertation arose from years of research during my graduate studies at The University of Texas at Austin. I would like to thank all those who inspired and helped me throughout this journey and shaped my dissertation.

I would like to express my sincere thanks to my supervisors Dr. Mojdeh Delshad and Dr. Mary F. Wheeler for their consistent guidance, support, and encouragement throughout my Ph.D. studies. I am very grateful for the constant communication with Dr. Gary A. Pope and his contributions to my professional accomplishments. I am indebted to Dr. Kamy Sepehrnoori for his endless helps in my personal and professional career without that I could not finish my studies. I would also like to appreciate other Ph.D. committee members, Dr. Kishore K. Mohanty, and Dr. Todd Arbogast, who have further enriched this dissertation with their ideas, feedbacks, and comments. My special gratitude goes to Dr. Abodljalil Varavei, Dr. Gergina Pencheva, Dr. Gurpreet Singh, and Dr. Ben Ganis for their helps during the simulation work.

I would like to fully acknowledge the staff of the Center for Subsurface Modeling at the Institute for Computational Engineering and Sciences (ICES), Connie Baxter and Caitlyn Dambro, for always being so helpful, patient, and friendly. Also, I fully appreciate the staff of the Department of Petroleum and Geosystems Engineering including Frankie Hart, Amy D. Stewart, Tim Guinn, and Joanna Castillo.

I do wish to acknowledge indebtedness to the authors of resources that I cited. Also, I sincerely appreciate the technical discussions with Dr. Fredrik Saaf and Dr. Steve S. Shi, Shell, Houston, and Dr. Amos Ben-Zvi and Dr. Subodh Gupta, Cenovus Energy, Calgary.

I am indebted to many of my friends and colleagues who made my time in Austin so rewarding. Specifically, I would like to thank Dr. Mohammad Lotfollahi, Dr. Hamidreza

Lashgari, Dr. Reza Tavakoli, Dr. Morteza Elahi Naraghi, Dr. Ali Naderi-Beni, Dr. Abolghasem Kazemi Nia, Dr. Ali Goudarzi, Dr. Mohammad Mirzaei, Dr. Saeid Enayatpour, Dr. Salar Mesdaghinia, Dr. Seyyed Abolfazl Hosseini, Dr. Behzad Eftekhari, Dr. Ashwin Venkatraman, Dr. Tameem Almani, Mojtaba Ghasemi Doroh, Venkateswaran S. Pudugramam, Mohsen Babazadeh, Hamidreza Mashayekh, Sajjad Sadeghi Neshat, Alireza Sanaei, Ali Abouie, Mahmood Shakiba, as well as many more who I may have failed to mention.

This research is entirely supported by the DOE-NETL under two research contracts. I gratefully acknowledge the financial support from the DOE-NETL during my school years.

Finally, I would like to thank my family for their unconditional love and support: my parents, my brothers, my wife, and my daughter who made innumerable sacrifices for me. Words fail me to express my indebtedness to my lovely wife. I will always be indebted to her for unselfishly letting her intelligence, ambitions, and passions collide with mine.

Mohammad Reza Beygi

Dec 2016

Development of Compositional Three-phase Relative Permeability and Hysteresis Models and Their Application to EOR Processes

Mohammad Reza Mohammad Reza Beygi, Ph.D.

The University of Texas at Austin, 2016

Supervisors: Mojdeh Delshad

Mary F. Wheeler

Enhanced oil recovery (EOR) techniques have the potential to improve hydrocarbon recovery and project economics substantially. Characterizing fluid displacement and the relevant multiphase flow properties are essential to modeling EOR processes to reliably forecast the performance and economics. The spatial-temporal distribution of fluids spans a broad spectrum of composition and saturation spaces. In addition, a fundamental understanding of characteristic parameters of interphase mass-transfer in various EOR applications is crucial to capture and model fluid displacement. Relative permeability is a critical characteristic petrophysical property for modeling fluid displacement in porous media. Also, hysteresis phenomena govern physics of fluid flow in many subsurface applications such as multicyclic EOR processes, geological CO_2 sequestration, and natural gas storage. Capillary trapping is the essence of hysteresis to trap fluids.

In this research, we developed a high-fidelity computational tool for integrating compositional three-phase relative permeability and hysteresis to assist in accurate modeling of multicycle and compositional EOR methods. This viable tool can be implemented into general-purpose reservoir simulators to model field-scale projects. It consists of an integrated compositionally-consistent three-phase relative permeability and

three-phase hysteresis models.

The developed three-phase relative permeability model is valid on entire saturation and composition spaces, is simple with one free parameter for each phase, and is versatile for all phases and wettability states. The general model is saturation-path dependent and adopts a linear saturation-weighted interpolation scheme for calculation of relative permeability parameters.

For the compositional relative permeability modeling, we developed a general framework applicable to hydrocarbon and non-hydrocarbon phases. The developed framework provides a pragmatic approach for adding the direct impact of composition, pressure, and temperature and is independent of the conventional phase-labeling method. The proposed framework unifies thermodynamics, petrophysics, and geochemistry to enhanced relative permeability modeling. Relative permeability parameters are calculated based on a mapping scheme of current-state bulk and interphase Gibbs free energy onto corresponding initial-state values. We applied the developed framework to modeling low-salinity waterflood and complex fluid displacement of near-critical fluids.

The three-phase hysteresis model provides a general and straightforward approach for calculation of capillary trapping in multicyclic processes. The developed hysteresis model provides a set of cycle-dependent relative permeability curves and applies to any three-phase relative permeability model by incorporating the free-saturation concept.

We implemented the developed toolbox into two in-house compositional reservoir simulators (i.e., IPARS and UT-DOECO2). Several synthetic field cases are discussed to validate the implemented models conceptually. Using the enhanced simulators, we demonstrated accurate modeling of multiphase fluid displacement and trapping in EOR processes such as water-alternate-gas injection scheme, low-tension gas flood (i.e., foam), and carbon capture, utilization, and storage (CCUS).

Table of Contents

List of Tables

List of Figures

Chapter 1: **Introduction**

This chapter presents the problem statement and describes the primary objectives of the research. The dissertation chapters are also briefly summarized.

1.1 PROBLEM STATEMENT

Enhanced oil recovery (EOR) techniques have successfully been employed to increase hydrocarbon recovery and project economics. There are critical challenges in reservoir modeling and forecasting since fluid flow spans over a wide range of composition and saturation in addition to complicated multiphase flow and interphase compositional mass transfers. Moreover, cyclic processes, such as water- or surfactant-alternative-gas injection are routinely used in gas EOR methods to improve sweep efficiency. The alternative saturation path will result in irreversibility in relative permeability and capillary pressure data. Thus, in modeling EOR it is essential to have robust, predictive, and accurate algorithms that can treat composition and saturation spaces.

Relative permeability is a critical characteristic petrophysical property for modeling fluid displacement in porous media. Because multiphase relative permeability measurements are incomplete and not physically obtainable, it is a common practice to apply correlations or upscaled models based on pore-scale modeling to provide the required input relative permeability data. Since the latter case of upscaling multiphase flow processes is currently poorly understood and developed, we focus on the development of compositional models. In the development of these models, it is, therefore, imperative to develop viable relative permeability functions which can capture the essential features of fluid displacement of multiphase flow, multi-cyclic processes, and processes with compositional variations and different rock wettability states.

Currently, to the best of my knowledge, there are a lack of relative permeability models that are general, robust, and simple in the sense of realistic reservoir simulation to cover the pertained multiphase fluid configuration in porous media. Moreover, similar remarks apply to the current hysteresis models in multiphase flow.

1.2 RESEARCH OBJECTIVES AND ACCOMPLISHMENTS

The objective of this dissertation is to develop a high-fidelity computational tool for integrating compositional relative permeability and hysteresis to assist in accurate modeling of multicycle and compositional EOR methods. This viable tool will apply to reservoir rocks with varying degrees of wettability and can be directly implemented into numerical reservoir simulators to model field-scale projects. Here, modeling of the direct compositional effect will permit an accurate characterization of fluid displacements.

To accomplish this objective, we developed a toolbox consisting of an integrated compositionally-consistent multiphase relative permeability and multiphase hysteretic models. The input parameters to the toolbox vary from core-scale laboratory measurements to pore-scale rock and fluid properties depending on the selected process, the required accuracy, and the computational cost. The required core-scale, averaged, two-phase relative permeability parameters may be measured experimentally via specific core analysis (SCAL) or evaluated from a coupled digital rock and fluid analysis model. The toolbox delivers multiphase relative permeability values based on compositional effects, hysteresis, applied forces on fluids, fluid-displacement history and covers the full saturation and composition spaces.

1.3 BRIEF DESCRIPTION OF CHAPTERS

In **Chapter 2**, we review the fundamentals of multiphase flow in porous media. We focus on EOR processes involved in an intensive compositional exchange, relative permeability measurement and modeling, hysteresis effect, capillary trapping and remobilization.

In **Chapter 3** a description of the impacting parameters on relative permeability is provided. A review of the expected features of a reliable three-phase relative permeability followed by a discussion on the limitations of the current three-phase relative permeability models is included. The general, compositional, three-phase relative permeability model (UTKR3P model) developed in this research along with its optional features is discussed. Finally, we review the key features this general relative permeability models.

Chapter 4 discusses the impacting parameters on capillary trapping and describes the limitations of the current two- and three-phase hysteresis models as applied to relative permeability models. It then introduces the developed multiphase hysteresis model (UTHYST model) and describes the key features of this general hysteresis model replicating the cycle-dependent relative permeability.

Chapter 5 describes the methodology by which the compositional effects may directly incorporated into relative permeability models (UTPGE framework). It is essential for compositional processes like gas-based EOR and processes in which aqueous phase involves in a significant interphase mass transfer. Without losing the generality of approach, we then present case studies of the application of the developed framework in both processes— the near-miscible displacement and the modified salinity waterflood.

In **Chapter 6**, we illustrate the capability of the developed three-phase relative permeability and hysteresis models as implemented into the IPARS and UT-DOECO2 reservoir simulators to more accurately model complex EOR processes and CO_2 storage. These methods require accurate modeling of relative permeability, hysteresis, and compositional effects and span a broad range of saturation/composition space. They include water-alternate-gas injection scheme in miscible and immiscible modes in mixed-wet rock and low-tension gasflood in low permeability heterogeneous reservoir.

Chapter 7 presents the summary of the dissertation and the concluding remarks. We propose recommendation for more accurate multiphase flow modeling and an integrated approach from pore-scale to field-scale.

In **Appendix A** the terminology of the common parameters in petroleum literature is explained as have been used in this dissertation in an alphabetical order. In **Appendix B**, a discussion of foam flow and modeling in porous media is provided. We thoroughly discuss the complex task of electrolyte solution modeling as required in modeling of composition-dependent aqueous phase in **Appendix C**. This Appendix includes a compilation of electrolyte modeling approaches followed by the Debye-Hückel theory in **Appendix D**. **Appendix E** and **Appendix F**

address the analytical derivative of the UTKR3P and UTHYST models. For the compositionally consistent relative permeability modeling, we described two methods of estimating the reference state Gibbs free energy of electrolyte solutions in **Appendix G** and **Appendix H**. In **Appendix I**, we provide the ideal gas heat capacity and entropy modeling and the pertinent parameters for hydrocarbon components as required for the molar Gibbs free energy modeling. A discussion of the implementation of the developed three-phase relative permeability and hysteresis models in the in-house IPARS and UT-DOECO2 simulators are provided in **Appendix J** and **Appendix K**, respectively. In **Appendix L**, we review the developed framework for modeling low-tension gas flood in the UT-DOECO2 simulator.

Chapter 2: **Background and Literature Review**

This chapter provides a literature review of EOR processes involved with multiphase flow. These processes include compositional demanding activities and gas-mobility-control techniques applicable to various rock wettabilities. We focus mainly on applications where the commonly used relative permeability models draw an incomplete picture of the physical behavior of multiphase and multicomponent displacement.

2.1 **BACKGROUND**

Enhanced oil recovery techniques have played a substantial role in increasing hydrocarbon recovery from the natural resources than primary and secondary production mechanisms. The global incremental contribution of EOR activities represents more than 3 million barrels of oil per day (MMBOPD). This represents about 3% of world oil production.

The gas-based EOR method is a mature and effective method in increasing the hydrocarbon recovery from natural resources. Half of the global incremental oil recovery is attributed to the gas (solvent) injection with an ever increasing rate (51% of total 2.93 MMBOPD as of 2010, **Schulte (2005)**). As shown in **Figure 2-1**, this trend in the United States has continued to grow during 1994-2014 where the gas-based EOR accounted for 60% of the total EOR production in 2014, viz., 470 MBOPD out of 778 MBOPD. In the same period, the role of CO_2-flooding, one of the gas-EOR methods for both miscible and immiscible modes, increased about 47% corresponding to more than 70% of the total incremental oil recovery by gas-EOR methods in 2014. Kuuskraa et al. (**2011**) predicted that the practiced and possible CO_2-EOR together could provide 137 billion barrels (Bbbl) of additional technically recoverable domestic oil with a CO_2 storage capacity equal to 45 billion metric tons. As of 2014, the practiced CO_2-EOR activities include miscible and immiscible CO_2 projects distributed among 110 projects. The next-generation CO_2-EOR will include miscible CO_2-EOR in a harsh environment, near-miscible CO_2, and residual oil zones (ROZ).

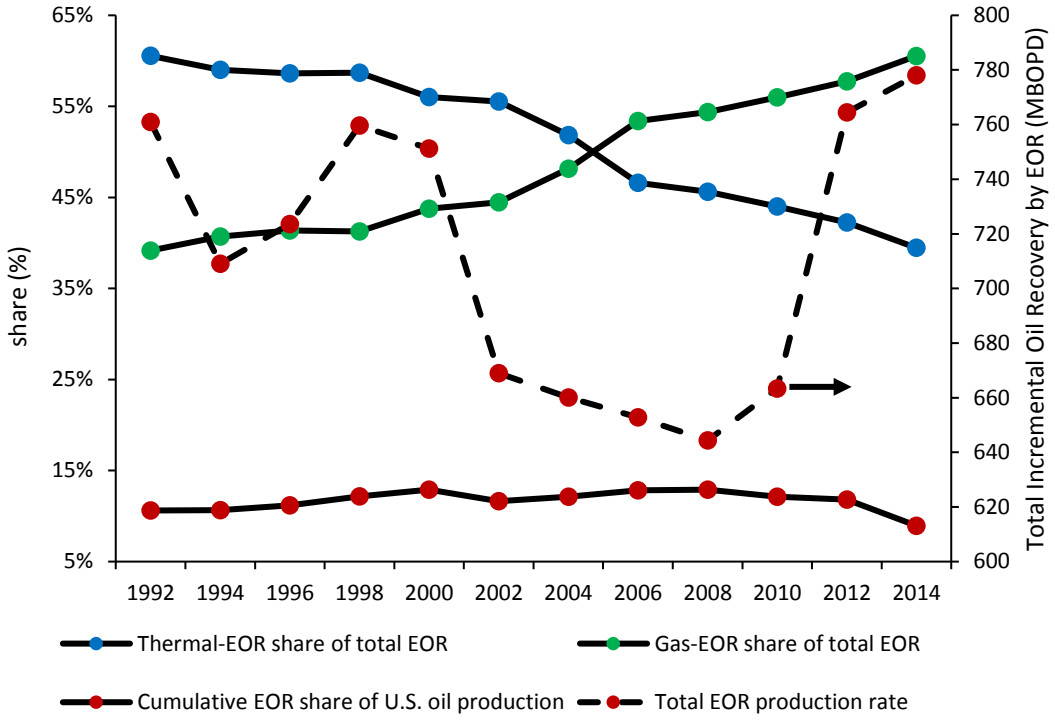

Figure 2-1: The U.S. thermal- and gas-based EOR share and total EOR share of oil production rate (Data: OGJ (**2014**) and EIA (**2016**))

The key role of the EOR methods in securing demanding hydrocarbon production necessitates an accurate modeling of the related processes and displacements.

2.2 MULTIPHASE FLOW MODELING IN POROUS MEDIA

Multiphase flow (i.e., the simultaneous presence of three- or higher number of phases) arises in multiple energy and environmental subsurface applications in porous media: geothermal energy, soil remediation, and EOR among others. Multiphase flow exists both at micro-scale (pore) and macro-scale (Darcy) in EOR applications (i.e., thermal-, chemical-, and solvent-EOR technique). Also, primary oil and gas production mechanisms involve multiphase flow. For example, water flood in solution-gas/gas-cap drive reservoir and hydrocarbon production below its saturation pressure, e.g., gas-condensate and volatile oil reservoirs. Furthermore, multiphase flow both in EOR and primary production mechanisms may encounter considerable interphase mass-exchange, e.g., surfactant flood, miscible gas flood, and modified salinity waterflood as reviewed in **Compositional demanding processes**.

Accurate treatment of fluid mobility is a fundamental aspect of multiphase modeling. Relative permeability is the primary parameter of phase mobility (see **Mobility/conformance control** in Appendix A). These concepts shed light as critical facets of accurate representation of relative permeability particularly for multiphase flow and processes including demanding mass-transfer among phases.

In the following two sections (**Compositional demanding processes** and **Gas mobility control techniques for gas-EOR methods**) we review two categories of applications in which accurate relative permeability modeling remains the keystone of obtaining predictive modeling of fluid displacement in porous media.

2.3 COMPOSITIONAL DEMANDING PROCESSES

A fundamental understanding of characteristic parameters of compositional variation of hydrocarbon and non-hydrocarbon phases and their impact on fluid mobility is essential to capture and model fluid displacement in the subsurface applications. The pronounced interphase mass transfer and variation in phase composition may eventually lead to the appearance/disappearance of both hydrocarbon and non-hydrocarbon phases, e.g., miscibility at gas-injection processes above the minimum miscibility pressure/enrichment condition.

There have been several attempts to enhance the modeling of these processes involving intensive intra- and inter-phase mass exchange. Some of the fundamental aspects of these processes are still overlooked. The direct compositional effect together with the pressure and temperature effects on relative permeability are partiallly introduced in reservoir simulation. They have been employed via the interface phenomena (i.e., capillary-desaturation curve and interfacial tension) (see **Impacting parameters on relative permeability** in Chapter 3), and their direct effect is often ignored in relative permeability/capillary pressure modeling.

In the following section, we briefly describe two physical domains where the fluids experience substantial variation in their composition due to the extensive interphase compositional exchange. We also review the critical role of accurate relative permeability modeling in the

computational domain.

2.3.1 **Aqueous phase**

Aqueous phase is ubiquitous in subsurface resources and requires particular attention in modeling intensive mass-transfer processes. The interactions of this phase with solid rock, liquid and gaseous hydrocarbon and non-hydrocarbon phases may affect the overall performance of a diverse range of fluid displacement. The subsurface displacements and their specific interactions with the aqueous phase include, but are not limited to, (**i**) geothermal applications, (**ii**) soil processes, (**iii**) wettability alteration in modified-salinity water flood, (**iv**) CO_2 dissolution trapping and salt-out effect in CO_2-sequestration, (**v**) gas mobility reduction in foam-assisted mobility control technique with salt concentration, (**vi**) generating water-in-oil or oil-in-water emulsions in chemical EOR, (**vii**) wettability alteration due to asphaltene precipitation/deposition, and (**viii**) rock dissolution/precipitation in aqueous phase, e.g., in modified-salinity waterflood and steam injection.

The aqueous phase and the associated complications in modeling its behavior and interactions with other phases are discussed in detail in **Appendix C.** In the following, we briefly review a promising EOR method in which the compositional variation of aqueous phase impacts oil recovery and the key aspects of precise relative permeability modeling.

Modified-salinity waterflood

Water chemistry impacts the recovery factor of a waterflood (**Morrow & Buckley, 2011**; **Sharma & Filoco, 2000**; **Yildiz et al., 1999**). By modifying the injected water salinity (modified salinity, smart waterflood, or low-salinity waterflood), waterflood may provide a cost-effective method to decrease residual oil saturation to water, to delay breakthrough and enhance displacement stability, and to improve oil recovery from sandstone and carbonate reservoirs in secondary and tertiary flood modes.

Both successes and failures have been reported for the modified-salinity in laboratory and field applications. The successful field-scale tests (**Lager et al., 2008a**, **2008b**; **McGuire et al.,**

2005; **Seccombe et al., 2010**; **Webb et al., 2004**; **Webb et al., 2005**; **Yousef et al., 2012**) showed significant decrease in residual oil saturation to water and an averaged incremental oil recovery of 14% (**Lager et al., 2007**). On the other hand, examples of laboratory and pilot tests exhibited no or minor impact on oil recovery due to advanced waterflood (**Pu et al., 2008**; **Rivet et al., 2010**; **Skrettingland et al., 2010**; **Thyne & Pubudu, 2011**; **Zeinijahromi et al., 2015**). For low-salinity waterflood, the degree of the required water salinity dilution in laboratory and field-scale tests varies between 4-200 fold (diluting to the TDS range of 1000-5000 ppm) (**Jerauld et al., 2008**; **Tang & Morrow, 1999**) including a threshold salinity value from which low-salinity effect starts (**Cissokho et al., 2009**; **Webb et al., 2004**).

Although the required conditions of a successful low-salinity waterflood is still subject to debate, researchers mainly consider the following variables: (**i**) rock lithology particularly its clay content, (**ii**) oil composition particularly the surface active polar components, e.g., carboxylic material, (**iii**) divalent (or trivalent) ions (i.e., Ca^{2+}, Mg^{2+}, and SO_4^{2-} (or BO_3^{3-} and PO_4^{3-})), (**iv**) connate water saturation, and (**v**) the elevated temperature, e.g., to enhance surface reactivity of controlling ions. The key variables impacting the smart waterflood are not unique for sandstone and carbonate rocks. Although the wettability alteration is a common mechanism between sandstone and carbonate rock, the underlying impacting factors on their wettability alteration are not identical. In the sandstone rocks, it is believed that the low-salinity effect expands the electric double-layer when clay is present. In carbonate rocks, however, calcite dissolution and sorption of organic oil components are the primary reasons of wettability alteration (**Hiorth et al., 2010**; **Lee et al., 2010**). Divalent ions demonstrated unpredictable responds in carbonates compared to sandstones. For low salinity effect, the primary impacting divalent in carbonate rocks is poorly understood. While some investigators take either Mg^{2+}, Ca^{2+}, or SO_4^{2-} as the determining ions, some others conclude that a particular combination of these divalent ions, e.g., Ca^{2+} and either Mg^{2+} or SO_4^{2-} are effective. More interestingly, Gupta et al. (**2011**) introduced trivalent ions (i.e., borate and phosphate), as controlling aqueous components rather than conventional divalent cations and observed a positive effect for the low-salinity waterflood.

The interacting mechanisms of low-salinity waterflood is a complex and not well developed subject. The interphase interactions among the injecting water, connate water, rock solids, and oil are complicated due to severe mass-exchange and reactive transport characteristic of a multiphase and multicomponent system. Four fundamental mechanisms of the water-salinity effect have been proposed based on the laboratory experiments and field observations. The primary mechanism impacting fluid displacement by smart waterflood involves altering the rock wettability toward the water-wet state through geochemical reactions. Many mechanisms of wettability alteration due to the low-salinity effect including multi-ionic exchange, pH variation through cation exchange and carbonate mineral dissolution effects, and fine migrations have been stipulated (**RezaeiDoust et al., 2009**). Nonetheless, the underlying facts of wettability alteration by the low-salinity waterflood effect is still unresolved. Second mechanism involves decreasing the water-oil interfacial tension (IFT) (**McGuire et al., 2005**). In contrary, some experiments have shown substantial oil recovery due to the low-salinity waterflood effect without a noticeable change in IFT value, e.g., 1-6 units, far from the conventional ultra-low IFT values (<0.001 mN/m) (**Al-Harrasi et al., 2012**; **Yousef et al., 2010**). Third mechanism is surface reaction, e.g., calcite dissolution in carbonate rocks, particularly for the carbonate rocks (**Gupta et al., 2011**; **Hiorth et al., 2010**). The final mechanism is fine migration due to the release of clay fragments (**Tang & Morrow, 1999**). The migrated fines not only facilitate the wettability alteration but more importantly they elevate the sweep efficiency through the microscopic pore-throat blockage and diverting the flow to the unswept area similar to the cross-linked polymer/gel or polymer flood; nonetheless, the detrimental plugging effect is also plausible.

Several models have been proposed to describe the water salinity effect on oil recovery. They mainly attempt to modify the water and oil relative permeability curves from their conventional ones with salinity (i.e., when a transmission occurs from high to low salinity). To model current-state relative permeability, many of these models modify relative permeabilities based on an interpolation scheme between high- and low-salinity waterflood curves as described below:

$$k_r = \theta\omega^{HS}(S^*) + (1-\theta)\omega^{LS}(S^*), \qquad \textbf{Eq. 2-1}$$

where HS and LS refer to either high- and low-salinity conditions or oil- and water-wet conditions, respectively, and θ denotes the weighting controlling parameter. The ω parameter denotes either relative permeability parameters, e.g. endpoint relative permeability or curvature, or relative permeability curve, or residual oil saturation. **Table 2-1** describes some of the low-salinity models and lists the impacting variable (ω) and the proposed weighting term (θ).

Table 2-1: Impacted parameter (ω) and primary controlling parameter of θ term in **Eq. 2-1**

Reference	ω parameter	$\theta = f(\downarrow)$
Jerauld *et al.* (**2008**)	Residual oil saturation	Total dissolved solids
Omekeh *et al.* (**2012**)	Relative permeability	Divalent ion desorption
Dang *et al.* (**2013**)	Relative permeability	Ionic-exchange capacity of clays
Carbonate: Al-Shalabi (**2014**)	Relative permeability	Contact angle
Sandstone: Korrani (**2014**)	Relative permeability	Total ionic strength
Carbonate: Korrani (**2014**)	Relative permeability	Calcite content

2.3.2 Hydrocarbon phase in *complex* fluids

Here, the term complex refers to a broad range of fluids: (**i**) near-critical fluids, (**ii**) fluids involved in miscible and near-miscible displacements, (**iii**) fluids in compositional-grading reservoirs, (**iv**) wax and asphaltene precipitation, and (**v**) operationally contaminated reservoir fluids.

From a subsurface thermodynamic perspective, the gas-EOR techniques consist of miscible, immiscible, and near-miscible injection schemes. The near-miscible displacement involves mass-transfer among two immiscible fluids close to their critical point. It denotes a region between the immiscible and miscible in a phase diagram occurring when two fluids exchange considerable mass in contact with each other and develop incomplete miscibility at a specified pressure and temperature. At least one of the fluids is the resident fluid in the reservoir, and the other represents an injecting solvent. These fluids can be either in liquid or gas states: liquid-liquid or liquid-gas equilibria in the near-miscible front.

Near-miscible displacement occurs in several oil recovery processes: (**i)** gas-condensate and volatile-oil fluids near their saturation pressure, (**ii)** gas injection, e.g., natural gas (mainly

methane), ethane, LPG, CO_2, and flue gas, at the enrichment/pressure slightly below minimum-miscibility-enrichment/pressure, and **(iii)** multi-contact-miscible displacement in gas-injection process. Mass transfer along with pressure and temperature may change bulk phase and/or interface composition. Fundamental understanding of these parameters and their impact on relative permeability is required to adequately capture the behavior of displacement of miscible and near-miscible fluids.

A great body of evidence states that relative permeability curves approach straight lines, and the residual saturations decrease to zero as miscibility approaches, viz., the maximum conductance of fluid in porous media. The reduction of IFT between two immiscible fluids and the increase in superficial velocity as interphase mass exchange increases, led the investigators (**Blom et al., 2000**; **Pope et al., 2000**) to employ the capillary/trapping number as a controlling parameter of the behavior of near-miscible front (see **Impacting parameters on relative permeability** in Chapter 3). In general, however, phase identification based on fluid density avoids proper and consistent labeling of fluids at the near-miscible front (see **Fluid composition**). This inconsistent phase labeling is called phase flipping issue in numerical reservoir simulation and results in incorrect phase relative permeability estimation and, in turn, leads to the numerical convergence issues (**Jerauld, 1997b**; **Yuan & Pope, 2012**).

2.4 GAS MOBILITY CONTROL TECHNIQUES FOR GAS-EOR METHODS

Unfavorable mobility ratio between the injected gas and resident hydrocarbons reduces the efficiency of gas-injection processes (see **Mobility/conformance control** in appendix A). To increase sweep efficiency of solvent injection, one requires to reduce the adverse effects of gravity override and viscous fingering stemming from the natural characteristics of gas (low density and viscosity values). For example, direct gas thickening techniques like polymer and small-molecule thickeners have the potential to increase gas viscosity. Although the successful viscosifiers enhance the light-alkane viscosity by up to three orders of magnitude, the published thickeners are scarce for the non-hydrocarbon gases such as CO_2 in super-critical or gas state (**Enick et al., 2012**).

Alternatively, modification of the gas relative permeability allows the introduction of the state-of-the-art mobility/conformance techniques including water-alternate-gas (WAG) injection scheme, simultaneous water and gas injection, polymer assisted WAG, and foam. The cost-effective WAG scheme and its variants have successfully been implemented to increase oil recovery. Compared to continuous gas injection mode, WAG injection is a viable technique for controlling both miscible and immiscible processes by increasing the gas utilization factor (see **Gas utilization factor** in Appendix A). The WAG process depends on rock wettability, injecting gas physical properties, half-cycle slug size, WAG ratio, injection start-up, and well-pattern among others (**Christensen et al., 2001**). Although the type of the injection gas is arbitrary and is dependent on availability, approximately half of the known field-scale WAG processes used CO_2 for either miscible, or immiscible, or multi-contact miscible modes followed by light-hydrocarbon gases (**Christensen et al., 2001**). Since the 1950s, several WAG schemes with different WAG ratios has been proposed. For instance, rather than applying a constant WAG ratio the tapered WAG design is used where the dry gas is injected in the first cycle followed by both water and gas in the next cycles as the WAG ratio increases. The tapered WAG is a widely accepted method to increase incremental oil recovery. Unfortunately, the desired level of stable displacement cannot fully be achieved with the conventional WAG approach. Foam called foam-WAG (FWAG) may assist in enhancing the sweep efficiency. Clearly, the application of WAG (or FWAG) results in more complicated multiphase flow behavior than continuous gas injection.

2.4.1 Foam assisted gas mobility/conformance control

Foam is a dispersion of gas bubbles within a continuous liquid phase and is stabilized by a surfactant solution (**Bikerman, 1973**). It can drastically decrease the mobility of flowing gas through a porous medium (**Fried, 1961**) by a factor of several hundred folds. Controlling gas mobility, foam may assist in lowering gas overriding and fingering and provide a higher sweep efficiency. Consequently, foam improves poor sweep efficiency arising from reservoir heterogeneity and channeling, gravity override, and viscous instability. As a conformance

controlling agent, foam can block high permeability streaks and divert gas to lower-permeability zones that otherwise have been bypassed.

In **Appendix B**, a review of foam creation and decay mechanisms, followed by foam transport in porous media are provided. Both the theoretical and empirical models of foam flow are discussed.

2.4.2 Low-tension gas-flood

Low-tension-gas EOR method is a gas-chemical hybrid technique to increase oil production rate and/or oil recovery efficiency. Surfactant flooding can recover all or fraction of the waterflood residual oil by forming a microemulsion at a reduced IFT between the oleic and aqueous phases. A secondary injecting fluid may displace and produce the remobilized oil. Conventionally, a surfactant flood is coupled with a polymer slug (i.e., water including a polymer). Depending on the rock and fluid conditions, the polymer may be injected ahead or behind the surfactant as an adsorption-reductant agent or the conformance control agent, respectively.

Due to technical or economic considerations, e.g. injecting polymer to very low permeability reservoirs, gas may substitute chasing water in the surfactant-polymer flood. The injected gas then plays two roles: (**i**) displacement of the mobilized oil and (**ii**) the improved oil recovery due to increased mass transfer with in-situ hydrocarbons. In addition, a form of gas conformance/mobility agents like foam (see **Mobility/conformance control** in Appendix A) may be required.

Hybrid gas-chemical flood (i.e., low-tension gas flood) requires two surfactants. One surfactant lowers the water-oil IFT and mobilize residual oil. The second surfactant controls gas mobility by generating an in-situ foam. Currently, the broad applications of low-tension-gas flooding are limited due to technical difficulties. The current issues include the heterogeneity and uncertainties involved in reservoir characterization together with the lack of understanding of the process. Also, a predictive reservoir simulator to mechanistically model the process is required. Three hybrid gas-chemical models have been proposed: (**i**) Moncorgé *et al*. (**2012**) presented a

framework aimed at the integration of an improved recovery process for black-oil and equilibrium phase distribution ratio models. (**ii**) Trouillaud *et al*. (**2014**) simulated the effect of pressure and oil composition on microemulsion phase behavior by coupling a gas/oil/water phase behavior model with a microemulsion phase behavior model. (**iii**) Lotfollahi *et al*. (**2015**) developed a hybrid black-oil/surfactant reservoir simulator to model chemical EOR processes with gas.

2.5 RELATIVE PERMEABILITY

In this section, we discuss the laboratory and modeling techniques for relative permeability. Firstly, we depict the typical behavior of relative permeability based upon rock wettability and saturation history followed by isoperm behavior at different wettability states. Next, we address measurement and models vital to estimate relative permeability including both pore- and core-scale approaches.

2.5.1 General observations

Relative permeability for each flowing phase depends on several parameters (see **Impacting parameters on relative permeability** in Chapter 3). Conventionally, relative permeability of each phase is expressed based on saturation, the state of wetting state and saturation history. In the following, we briefly review some of the observations for different wetting conditions

There is a general agreement that in strong wettability conditions, the wetting and non-wetting phase relative permeability depends only on the wetting and non-wetting phase saturations, respectively. The intermediate-wetting phase relative permeability depends on the saturation of two phases and is impacted by the presence of an immobile wetting phase. In an extensive study of Prudhoe Bay intermediate-wet sandstones, Jerauld (**1997b**) observed the direct impact of the initial water saturation on oil relative permeability. Kalaydjian et al. (**1995**) conducted measurements on the water-wet samples and confirmed that both the spreading coefficient and the presence of connate water impact oil relative permeability.

For the oil-wet Tensleep sandstone and Grayburg carbonate samples, Schneider and Owens (**1970**) recognized that in the absence of a water film the water relative permeability decreased by

increasing gas entrapment. The water relative permeability decreased during secondary drainage compared to that of a waterflood at a given water saturation. Even the small residual oil saturation values following a miscible flood drastically reduced the water relative permeability. Baker (**1995**) reported gas-flood experiments on the oil-wet samples from the Tensleep formation and confirmed that initial-residual water saturations are highly interrelated. DiCarlo et al. (**2000**) aged water-wet sand to measure three-phase gravity drainage on the oil-wet sand and showed that water relative permeability for oil-wet sand is similar to oil relative permeability for water-wet sand. Based on the results of a capillary-bundle model by van Dijke et al. (**2001**), gas is always a non-wetting phase to oil and leads to a hysteretic behavior and gas entrapment during oil floods. DiCarlo et al. (**2000**) demonstrated that gas relative permeability in an oil-wet sand is smaller than in a water-wet sand and concluded that gas is not necessarily the non-wetting phase. Vizika and Lombard (**1996**) showed that within a three-phase gas drainage in oil-wet sands, the gas relative permeability did not change both for spreading and non-spreading oil.

For the intermediate-wet state, water, oil, and gas may all show hysteresis. The initial-residual saturation dependency may exist for all phases. Jerauld (**1997b**) found systematic differences between water relative permeability during waterfloods and miscible water alternating gas (WAG) floods in Prudhoe Bay intermediate-wet sandstone. Oak (**1991**) treated water-wet Berea sandstone to make it intermediate wet and found a slight dependency of water relative permeability on the saturations of the other two phases implying water entrapment in non-water wet rocks.

2.5.2 **Isoperms**

It is a common practice to plot isoperms (i.e., contours of constant three-phase relative permeability) in a ternary saturation diagram where each apex represents 100% phase saturation. The experimentally measured relative permeabilities plotted as an isoperm have shown different curvature depending on the impacting parameters on multiphase relative permeability (see **Impacting parameters on relative permeability** in Chapter 3). Researchers have reported three types of isoperm curvatures — straight line, convex, and concave — in the direction of 100% phase saturation (see diagrams in **Figure 2-2**).

The curvature of isoperms directly influences the hydrocarbon recovery and storage capacity in porous media. For instance, keeping all other criteria constant, a set of concave oil-isoperms pointing outward from the oil vertex will result in higher oil recovery than that of convex oil-isoperms. This is due to the fact that convex isoperms require higher phase saturation to obtain the designated relative permeability compared with the concave isoperms. Moreover, the isoperm of zero gas relative permeability may play a pronounced effect on gas inventory capacity in a reservoir. A concave gas-zero-isoperm pointing toward the gas apex indicates that gas trapping is initiated at lower saturations than that of a convex isoperm.

In general, the higher curvature of isoperms implies the stronger dependency of phase relative permeability on the saturation of other phases. Comparing a convex and a straight-line for phase-X isoperm reveals that the former requires higher phase-X saturation than that the latter one; moreover, it infers the negative impact of saturation of other phases on mobility compared to that of two-phase flow. Contrary, the concave isoperm expresses the higher mobility. A straight line isoperm parallel to the baseline of that phase implies that relative permeability is independent of saturation of other phases. **Table 2-2** summarizes experimentally measured isoperms and the associated curvature using consolidated and unconsolidated rock materials. **Figure 2-2** shows the water, oil, and gas isoperms measured at different wettability conditions for variety of saturation histories (**Oak, 1989**; **1991; 1992**). It shows that the trend in curvature of the isoperms is not

straightforward particularly for the intermediate-wetting fluid. Oil isoperm curvature is scattered and concave toward the oil vertex. The oil isoperms, however, flatten as the rock wettability becomes more oil-wet and scatter in the data decreases. The effect of other phases on relative permeability contributes to the data scattering. Besides, **Figure 2-2** depicts that the phase isoperm curvature varies not only with the rock wettability but also with the saturation history. It is due to the fact that as the saturation history varies the fluid configuration and residual saturation varies accordingly.

There have been debates on whether isoperms are straight lines or have a curvature (concave or convex in the direction of 100% phase saturation) (**Dietricht & Bonder, 1976**; **Oak, 1989**, **1990**). Nevertheless, there is no consensus on the prediction of curvature of isoperms under the widely recognized wettability conditions. Quite undeservedly, although several multiphase relative permeability measurements exists in the literature as listed in **Table 2-2**, they do not span a broad range of saturation space. In that the saturation history varies widely during the field applications, the limited number and inconsistent data impose uncertainty in the prediction of the characteristic behavior of phase isoperm.

Yet, it seems fair to assert that for the conventional primary waterflood and gasflood applications the most wetting fluid shows the less dependency on the saturation of the other fluids (i.e., linear isoperm is expected). Also, the isoperms of the most non-wetting fluid, e.g., gas in the water-wet state, shows a linear response confirming that the phase saturation is the primary impacting parameter particularly at the higher phase-saturation region. The prediction of low saturation region and the intermediate-wetting state is not trivial. As a result, during the project lifetime, one may expect that the phase isoperm curvature varies as the saturation history and/or the rock wettability is altered. Only a few three-phase relative permeability models have the essential flexibility to alter the shape of isoperms (**Fayers et al., 2000**; **Beygi et al., 2015**).

Table 2-2: Behavior of isoperms on some of the published three-phase relative permeability measurements

Reference	Material	Wettability	Saturation Direction [a]	Isoperms [b,c]		
				Water	Oil	Gas
Leverett and Lewis (**1941**)	Sandpack	Water-wet	N.A.	Linear	Convex	Convex
Reid (**1956**)	Sandpack	Water-wet	N.A.	Concave	Convex	Concave
Corey (**1956**)	Berea sandstone	Water-wet	DDI	Linear	Concave	Linear
Snell (**1962**)	Sandpack	Water-wet	N.A.	Concave	Convex	Convex
Donaldson (**1966**) [d]	Berea sandstone	Water-wet	DDI	Concave	Concave	Concave (high Sg); Convex (low Sg)
	Arbuckle limestone	Water-wet	DDI	Linear	Concave	Concave
Sarem (**1966**)	Berea sandstone	Water-wet	DDI	Linear	Linear	Linear
Saraf and Fatt (**1967**)	Boise sandstone	Water-wet	DDI	N.A.	Convex	Linear
Guckert (**1968**)	Berea sandstone	Water-wet	DDI	Linear	Convex	Concave
Saraf et al. (**1982**)	Berea sandstone	Water-wet	DDI	Linear	Concave	Linear
Parmeswar et al. (**1988**)	Berea sandstone	Water-wet	N.A.	Linear	Concave	Concave
Maloney et al. (**1990**)	Berea sandstone [e]	Water-wet	N.A.	Linear	Slightly concave	Linear
	Bentheimer sandstone [e]	Water-wet	N.A.	Linear	Concave	Linear (at high Sg); Slightly Concave (at low Sg)
Oak (**1990**)	Berea sandstone	Water-wet	pDDI, IID, IDI, DID, sDDI & DII	Linear	Concave [f]	Linear
Oak (**1991**)	Berea sandstone	Intermediate-wet [g]	pDDI & IID	Slightly Convex	Concave	Linear
Oak (**1992**)	Tensleep sandstone	Oil-wet	pDDI & sDDI	Slightly Convex	Linear	Linear

Table 2-2 (cont'd): Behavior of isoperms on some of the published three-phase relative permeability measurements

Reference	Material	Wettability	Saturation Direction [a]	Isoperms [b,c]		
				Water	Oil	Gas
Jerauld (**1997b**)	Prudhoe Bay sandstone	Mixed-wet	XDX, IDC [h]	Linear (at high So) Concave (at low So)	Linear (at water-mobile region) Concave (at water-immobile region)	N.A.
Petersen Jr et al. (**2008**)	Statfjord sandstone	Mixed-wet	pDDI, sDDI, IID,	Convex (for IID) Convex (for DDI at low S_w) Concave (for DDI at high S_w)	Convex (for IID at low S_o) Concave (for IID at high S_o) Convex (for DDI)	Linear-concave (for IID) Linear-convex (for DDI)
Weifeng et al. (**2012**)	Sandstone outcrop	Water-wet	DDI & IID	Linear	Concave	Convex
	Sandstone outcrop	Weakly oil-wet	DDI & IID	Convex	Convex	Convex

[a] Terminology of saturation direction (see **Saturation history** in Appendix A), p: primary, s: secondary

[b] Isoperm curvature toward phase vertex (100% phase saturation). The isoperm concave toward the phase base is equivalent to that of convex toward the phase apex (vertex) in the ternary saturation diagram.

[c] N.A.: not available or measured.

[d] Questionable results (**Oak, 1989**).

[e] These samples have different pore aspect-ratio; Berea has higher level of microporosity resulting in lower k_{rw} at all saturation levels, higher k_{ro} at higher oil saturation, and higher flowing gas level than those of Bentheimer sandstone.

[f] Oil-isoperms are very scattered in the ternary saturation diagram.

[g] Not measured but implied based on the interpretation of the relative permeability values.

[h] Waterflood, gasflood, and waterflood in the presence of trapped gas.

[I] Data are hard to extract exact shape of isoperm.

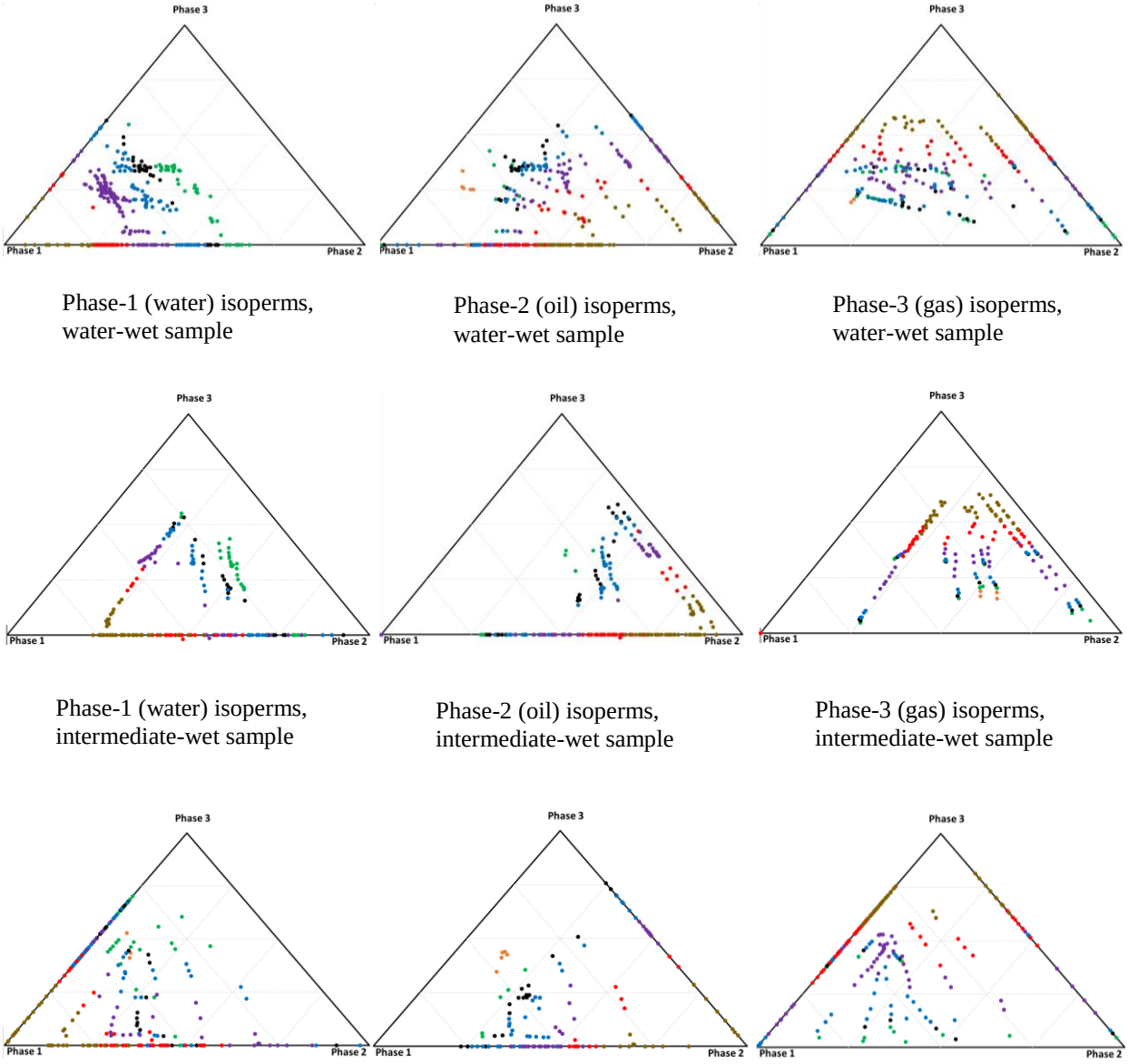

Figure 2-2: Experimentally measured isoperms (k_r^{exp}) for several saturation histories in two- and three-phase flow for samples with different wettability conditions (**Oak**, **1989**; **1991**; **1992**)

2.5.3 **Relative permeability measurement**

Two techniques to measure relative permeability initiate from the scale of the measurement. The core-scale measurement techniques are the conventional methods. The pore-scale techniques, on the other hand, involve the microscopic-level measurement obtained from the pore and fluid structure images through the mathematical methods. The pore-scale relative permeability results must be upscaled for the practical scales of interests. In the following, we briefly review both approaches.

Core-scale relative permeability measurement

Laboratory relative permeability methods include the centrifuge, steady-state, and unsteady-state methods (**Mohanty & Miller, 1991**; **Skauge et al., 1997**). The centrifuge method allows measuring the displaced-phase relative permeability down to the very small mobility value (**Hagoort, 1990**). Nevertheless, one cannot measure gas relative permeability via the centrifuge method even though the extension of the Hagoort method (**1990**) mitigated the other drawbacks of this technique (**van Spronsen, 1982**). In addition, the centrifuge method suffers from the simplifying assumptions that do not hold in particular set of displacement condition.

The unsteady state method and its variants including the JBN-type procedures (**Johnson et al., 1959**) and the gravity-drainage techniques have become a popular method primarily due to the acceptable speed of obtaining the desired data (**Dehghanpour, 2011**; **Kianinejad et al., 2016**; **Mohanty & Miller, 1991**). They provide relative permeability directly from the in-situ saturation profile along with the Darcy equation.

Both unsteady-state and centrifuge methods involve several inherent simplifying assumptions in their mathematical formulations. These assumptions applied to the material-balance techniques contributes to uncertain results. Applying the saturation and relative permeability values estimated from these methods to the field-scale may then become questionable: the field-scale fluid displacement does not replicate the predicted behavior and assumptions of unsteady-state methods.

The steady-state method provides more accurate results for multiphase relative permeability than the dynamic and centrifuge methods. It covers a broader range of saturation space and suffers less from the sample heterogeneities and is practiced with many investigators in the early development of the measurement techniques (**Corey et al., 1956**; **Delshad et al., 1987**; **Leverett & Lewis, 1941**; **Reid, 1956**; **Saraf et al., 1982**; **Snell, 1962**). Nonetheless, the required time for achieving the capillary equilibrium on the order of weeks to months limits its application. Besides, steady-state measurements are technically difficult experiments. Instead today, the approximate and technically simpler methods but less time-consuming are the primary option for relative permeability measurement in the laboratory. A representative relative permeability measurement method must replicate the reservoir conditions including pressure, temperature, fluids, fluid-fluid interaction, rock, and the geomechanical parameters, e.g. net confining stress. Except for modern laboratory measurements (cf. **Wang et al., 2008**), published relative permeability measuring techniques generally do not completely describe their methodology and apparatus and fail to provide all of the required conditions.

Each method replicates a particular fluid displacement in porous media and generally relative permeability curves are not-unique. It then necessitates choosing a particular measurement technique imitating the anticipated fluid displacement and the effective forces on the fluids in reservoir applications. In other words, each section of a field-scale process may require a different set of relative permeability curves in the reservoir simulator (**Singh et al., 2001**). For instance, the viscous-dominated gasflood particularly near miscible fronts requires that the relative permeability curves be obtained from unsteady-state method. This dynamic displacement approach involves high flow rate injection schemes to satisfy the required conditions of the Rapoport and Leas number (**Lake et al., 2014**) that the capillary end-effect does not affect the displacement. The centrifuge technique is preferable when a low-saturation region is the primary target of an EOR process.

To mitigate the incomplete representation of actual fluid movement in the field, a practiced approach is to couple the measurement techniques: a coupled steady- and unsteady-state method

or a coupled unsteady-state and centrifuge method. Both approaches expand the saturation range of displacements in field practices (**Shafer et al., 1990**).

Pore-scale multiphase relative permeability measurement

Emerging advances in technology have accelerated computational rock physics during the last two decades. This evolutionary method consists of 3D imaging of rock samples at the desired/available scale, image processing (segmentation) to discriminate pore space from rock solids and minerals, and numerical simulation conditioned to experiments. The deduced *digital rock* assists in a viable representation of rock microstructure.

Digital rock physics has grown rapidly due to the advent of imaging, computing technologies, and image processing techniques. For example, high spatial and temporal resolutions of 3D images of pore space — to <1 μm and sub-second respectively — have been employed to image pore-scale displacements and to measure real-time pore-scale properties. The high resolution 3D images have been captured by advanced imaging scanners such as non-destructive and non-invasive X-ray micro computed tomography (μ-CT) (or Nano computed tomography for ultra-low permeability samples) and synchrotron (**Arns, et al., 2005b**; **Coker et al., 1996**; **Flannery et al., 1987**; **Hazlett, 1995**; **Ketcham & Carlson, 2001**; **Wildenschild & Sheppard, 2013**). Also, other emerging technologies such as confocal microscopy, e.g., laser scanning fluorescence microscopy, and super-resolution fluorescence microscopy (**Huang et al., 2009**) are conceivable in near future.

Rather than direct 3D imaging, the construction of complex core structure has also flourished by state-of-the-art techniques in stochastic or object-based reconstruction procedures. At first, one requires 2D petrographical thin section images extracted from scanning electron microporosity (SEM) generating submicron scale images. Then, by applying an optimization approach, the reconstruction techniques result in 3D representative rock samples by integrating images and obtained data for example porosity, grain size distribution, clay and cement content (**Bryant et al., 1993a**; **Bryant et al., 1993b**; **Bryant & Blunt, 1994**; **Coles et al., 1998**; **Pilotti,**

2000; **Øren & Bakke, 2002**; **Arns et al., 2002**; **Al-Kharusi & Blunt, 2007**; **Berg et al., 2013**; **Jiang et al., 2013**; **Naraghi et al., 2016**). Nevertheless, even by providing a detailed analysis of 2D thin sections, reconstructing complex pore structures based on currently applied reconstruction methods are problematic. These complexities include, but not limited to, microporosity, clays, and long-range connectivity of pore space.

Finally, high-performance parallel computing such as multi-core Central Processing Unit (CPU) architecture and Graphics Processing Unit (GPU) have rendered data acquisition, processing, and visualizing of computationally intensive pore-scale data emanating from pore-level images. For example, **De Prisco et al. (2012)** applied a domain decomposition method to simulate a matrix of 500×500×1000 voxel (1 voxel of a tomogram or image represents volume element equivalent to a pixel in the 2D element) in parallel with 50 GPUs. They generated a 2048^3 voxel telegram with 128 CPUs in approximately 4 hours.

Providing the desired flow experiment, both the spatial and temporal saturation distribution are accessible through the digitized rock. Once a 3D voxel representation of the porous medium and its embedded fluid(s) are constructed, one shall validate them against laboratory experiments in conventional and special core analysis or 2D micromodels (Scheven (**2005**); Blunt et al. (**2013**) and references therein).

In pore-scale modeling, the parameter estimation, e.g., multiphase relative permeability, is accomplished based on a multiphase flow simulation in pore-level via either direct pore-level models or extracted 3D pore-network models. Direct pore-level modeling on the constructed 3D image is more fundamental and more computation demanding than pore-network in comparison with direct counterpart, pore-network models may not fully capture behavior of a heterogeneous system due to their principal simplifying and averaging assumptions.

Further, one may categorize pore-scale modeling into quasi-static and dynamic approaches for both direct pore-level and pore-network methods (**Blunt et al., 2002**; **Jackson et al., 2005; Blunt et al., 2013**). Quasi-static methods entail a mechanistic approach in which the coupled viscous-capillary fluid displacement is decomposed into a capillary-dominated model followed by

a viscous-dominated model. The former reproduces spatial saturation distribution while the latter captures hydraulic connectivity of flowing continuous phase(s) in porous media.

The widely applied quasi-static methods have several drawbacks compared to their dynamic counterparts. **(i)** They lack discontinuous fluid flow modeling — large-cluster ganglia modeling. As a result, all mass-transfer associated with displacing fluids and displaced ganglia are erroneously withdrawn from these models. **(ii)** In quasi-static formulation, the pore topology is matched against a macroscopic averaged and measured capillary pressure and imposed over the whole porous media like the Darcy-scale modeling. **(iii)** All viscous dominated displacements are excluded from quasi-static modeling.

On the other hand, the dynamic approach is computationally expensive due to the governing equations, e.g., tracking the menisci motion and including a local capillary pressure. But, the dynamic methods model the dynamic processes with considerable viscous effects more accurately. For example, a more physically consistent relative permeability model can be obtained for processes in which intra-phase mass-transfer dominates, hysteresis exists, wettability-alters, interfacial-tension reduces, or layer-drainage displacement dominates (**Nguyen et al., 2005**; **Joekar-Niasar et al., 2010**; **Idowu & Blunt, 2010**; **Hammond, 2012**; **Joekar-Niasar & Hassanizadeh, 2012**; **Raeini et al., 2014**).

Pore-level direct modeling

Based on an extension of the review by Meakin and Tartakovsky (**2009**) and Blunt et al. (**2013**), three general direct pore-level approach and their variants for modeling multiphase flow in a digital rock are discernable: (**i**) the conventional Eulerian grid-based computational fluid dynamics methods coupled with a proper interface/fluid/particle tracking or capturing methods like front-tracking methods (**Tryggvason et al., 2001**), level-set function (**Sussman et al., 1994**; **Osher & Fedkiw, 2001**; **Prodanovic & Bryant, 2006**), volume of fluid (**Hirt & Nichols, 1981**; **Scardovelli & Zaleski, 1999**; **Ubbink & Issa, 1999**; **Raeini et al., 2012**;), and unique scalar field (phase field) (**Jacqmin, 1999**; **Badalassi et al., 2003**; **Mikelic et al., 2015**); (**ii**) the particle-based methods in a

meshless Lagrangian framework like the dissipative particle dynamics, smoothed particle hydrodynamics (**Tartakovsky & Meakin, 2005**; **Gouet-Kaplan et al., 2009**), the off-lattice Monte Carlo methods, and the lattice gas/Boltzmann (**Chen & Doolen, 1998**; **Wolf-Gladrow, 2000**) methods like color-gradient model (**Grunau et al., 1993**; **Gunstensen & Rothman, 1993**; **Liu et al., 2012**) and the pseudo-potential model (**Shan & Chen, 1994**); and (**iii**) the energy-based methods such as the density functional model (**Inamuro et al., 2000**; **Demianov & Dinariev, 2011**).

Lattice Boltzmann is a simple, computationally efficient, and flexible method to circumvent traditional deficiencies of Eulerian grid-based methods in order to solve the Navier-Stokes equations. The Eulerian grid-based methods, e.g., finite difference, finite element, and finite volume, treat particles as a continuum and treat conservation mass, momentum, and energy laws as representative control volumes. The evolving statistical-based lattice Boltzmann method, however, takes benefit from introducing the fictitious mesoscopic particles moving in a discrete lattice while conversing mass and momentum by local collisions (**Wagner, 2008**). Consequently, lattice Boltzmann based models are promising for modeling multiphase fluid displacement modeling in a digital rock: they are computationally less expensive than molecular-dynamic based models and do not require the discretization of partial differential equations as the conventional approach with coupled Eulerian grid-based methods and computation fluid dynamic. Yet, the lattice Boltzmann methods suffer from an integrated, consistent, and comprehensive thermodynamic approach leading to the incomplete modeling of phase transition and surface phenomena. Furthermore, upscaling the application of lattice Boltzmann on the continuum-scale with various degrees of large-scale heterogeneities is cumbersome.

Pore network modeling

Aside from direct pore-level modeling, one may prefer to upscale the detailed constructed digital rock several length scales (i.e., >3 order of magnitude), and extract a large-scale pore-network model from the original 3D image. Despite reducing considerable embedded details from the

digital rock, this upscaling procedure may provide for modeling microscopic-scale fluid displacement in porous media mainly due to computational limitations.

Pore network modeling in porous media pioneered by Fatt (**1956**) introduced the statistical physics of fluid flow. Here, it is assumed that an extracted rock topology from the digital rock represent porous media in which pores connected by narrow throats in a 3D lattice (**Blunt et al., 2002**). A full spectrum of network models has been developed to model multiphase fluid displacement through different physical processes. Initially, pore network approaches applied a simplified representation of physical porous media and later Percolation theory (**Larson et al., 1981**) and population balance equations (**Payatakes et al., 1980**) enhanced pore-network models in predicting the core-scale properties based on pore-network results. Recently, pore-network modeling has included detailed description of rock geometry and topology, general wettability and wettability alteration during the fluid displacement, and the underlying mechanism of multiphase flow in porous media, e.g., multiple displacement, coupled capillary and viscous flow, film flow (**Bakke & Øren, 1997**; **Mani & Mohanty, 1998**; **Øren et al., 1998**; **Lerdahl et al., 2000**; **Patzek, 2001**; **Piri & Blunt, 2005**; **van Dijke et al., 2006**).

Pore-network platform is a viable tool for building and understanding of the complicated multiphase flow in a complex rock structure. The pore-network models are useful in deriving macroscale properties including multiphase relative permeability and in reproducing macroscopic results from laboratory experiments. Moreover, they are computationally efficient compared to other pore-level approaches. Consequently, there is a growing interest in pore-network modeling. Nevertheless, as will be discussed, the latter currently has limited applicability for modeling complex rock structure, fluid distribution, and fluid interface(s) due to its inherent simplifying assumptions.

2.5.4 Three-phase relative permeability modeling approaches

To accomplish the complicated task of modeling Darcy scale relative permeability, several methods have been considered. Although some of the developed methods accurately replicate fluid

displacement processes and assist in providing fundamental understanding of underlying fluid movement mechanisms, they have limited field-scale applicability. Some other methods have been developed that focus on specific experiments or on simplifying assumptions by which the applicability of these models are severely reduced at larger spatial scales. These compromises have made the multiphase relative permeability modeling an unresolved subject in reservoir characterization.

Pore-scale relative permeability modeling

Several researchers have calculated multiphase relative permeability calculations from pore-scale modeling/measurements (**Øren et al., 1998**; **Blunt et al., 2002**; **Suicmez et al., 2008**; **De Prisco et al., 2012**; **Ramstad et al., 2012**; **Natarajan et al., 2014**). A representative relative permeability can be obtained from a detailed analysis of pore-scale pore structure, fluid distribution, fluid configuration, and fluid displacement. In addition, the relative permeabilities need to be upscaled to a large scale. One solution is to tabulate each phase relative permeability in a three-dimensional table, viz., saturation of two phases, as input to the simulator. During a simulation, each grid-block has an associated phase relative permeability based on saturations. This methodology, however, is questionable because the fluid configuration and distribution together with grid wettability are not necessarily identical to those conditions by which the pore-scale modeling was accomplished. As a result, this option cannot represent the physical behavior of fluid flow in porous media.

Alternatively, one may consider coupling dynamic pore-scale relative permeability with a reservoir simulator. This methodology referred to self-consistent three-phase modeling (**Blunt et al., 2002**) represents the physical behavior of fluid displacement accurately as relative permeability is evaluated from pore-scale events. Initially, the network model computes relative permeability based on a fluid configuration within each grid-block; the saturation distribution, then, is re-evaluated using a conventional simulator. The saturation path is checked against the initial input values in the pore-network model. If the saturation paths are not identical, the overall pattern is recomputed until a user-defined tolerance is reached. This dynamic hybrid modeling is based on

domain-decomposition such as locally mass conservative mortar methods (**Toselli & Widlund, 2005**; **Arbogast et al., 2007**; **Balhoff et al., 2008**; **Mehmani & Balhoff, 2014**; **Ganis et al., 2014**).

This multi-scale and multi-physics modeling approach is promising and results in a more detailed representation of fluid flow at several spatial scales. Undeservedly, it is yet quite resource-intensive and computationally expensive for practical field applications: (**i**) it requires spatially pore-scale modeling in each time-level together with Darcy-scale flow modeling; (**ii**) the pore model must be generated separately for each grid block based on locally available digital rock physics which, in turn, is very time-consuming; (**iii**) computational structures still suffer from storing, processing, interpretation, and visualization of computationally-intensive data emanating from multi-scale multi-physics approaches. Yet, the advent of extreme-scale (X-scale) computation is expected to flourish rendering large volumes of data emanating from the field-related applications that require computational power that is current not available.

Thus, other conceivable and versatile approaches must be considered for practical field-scale applications and will be reviewed further.

Current limitations of pore-scale measurements and modeling

The digital rock physics has the potential to characterize reservoirs specifically for estimating relative permeability. The level of detailed information contained in a digital rock is valuable and quantitatively characterizes pore structure for the typical fluid displacements in heterogeneous rocks.

Yet, the 3D digital rocks through the direct measurement are still limited and suffers uncertainty in accurate pore geometry and topology characterization. For example, **(i)** as the level of heterogeneity of the pore geometry and topology increases, constructing a reliable digital rock is still a challenging task for carbonate rocks and/or microporosity. The extensive sub-resolution microporosity contribution in carbonate rocks makes the pore-solid mineral identification a tedious task (**Arns et al., 2005**; **Wildenschild & Sheppard, 2013**). Poor reliability of carbonate digital rock arises due to small-scale heterogeneities in these sediments which results in a wide (bi- or tri-

modal) pore size distribution ranging from sub-micron to meters (**Moctezuma et al., 2003**; **Arns et al., 2005**). **(ii)** A reliable representation of the pore structure and fluid(s) is challenging and requires an appropriate multiscale approach particularly when the history of fluid distribution is required. In other words, the trade-off between sample size and voxel size must be accounted for (**Jiang et al., 2013**).

Both direct pore-scale modeling and pore-network modeling currently suffer from several deficiencies. Pore-network models have restricted predictive capability compared to the direct pore-level modeling approach. This is due to the inherently simplified physics of the pore-network models required to represent complex pore geometry. Finally, there is no robust and integrated tool currently available to fully capture the appropriate mechanisms and to determine the detailed description of macroscopic properties for multiphase flow in porous media (**Blunt, 2001**; **Blunt et al., 2013**).

Both the pore-scale modeling approaches yield relative permeability values at pore-scale. Both require a multiscale approach — from pore to core to field. When using this integrated approach evaluating the temporal and spatial relative permeability values is computation demanding task. It is therefore necessary to apply Darcy-scale parameters. These macroscale parameters are utilized in lieu of the pore-scale parameters and are less computationally expensive. This leads to the use of three-phase correlations incorporating Darcy-scale parameters like porosity, permeability, saturation, and macroscopic averaged parameters such as interfacial tension, rock wettability, and capillary number among others.

Finally, the spatial and temporal distribution of the rock wettability and contact angles as the key impacting parameters on the fluid displacement cannot be captured a priori as required for a pore-scale measurement.

Core-scale relative permeability modeling

A conventional approach in the absence of measured three-phase relative permeability data is to calculate three-phase relative permeability using measured two-phase relative permeabilities of

water/oil and gas/oil. To develop a relative permeability model based on a core-scale approach, one may rely only on observations and develop an empirical correlation for the core scale. This widely applied method is reliable for a very specific displacement conditions tested in the laboratory. Nevertheless, application to a different set of conditions occurring in field-scale remains questionable, particularly for multiscale heterogeneities arising in rock, fluid, and rock-fluid.

Alternatively, one can develop a three-phase relative permeability model based on an integrated pore- and core-scale observations. Here, the developed tool treats parameters of both length scales and honors microscopic results of particular fluid displacement. This results in a more robust representative of fluid displacement than correlations in a field-scale process. Nonetheless, the level of reproducing physical processes depends on the degree by which the pore-level fluid displacement mechanisms and their relevant parameters are incorporated in the model.

There are above thirty multiphase relative permeability models developed based upon different mathematical approaches in which only a few are industry standards. **Table 2-3** provides a chronological list of some of the three-phase relative permeability models and demonstrates that saturation-averaged interpolation method is a common choice in more recent models in lieu of other models of capillary, statistical, and fractal models.

Other relative permeability models not listed in **Table 2-3** are either developed for two-phase flow with limited applicability to three-phase flow or are based on purely mathematical functions. The latter has additional flexible features and includes basis spline (B-spline) and spline-derivative functions (Kulkarni et al. (**1998**) and references therein). In general, these piecewise polynomial functions honor monotonicity of interpolated function at points with higher-order curvature. Nonetheless, they may impose several discontinuities in relative permeability or in its derivative curves. Besides, their formulations require several parameters (**Fincham & Ferreol, 1998**; **Lomeland et al., 2005**). Hence, these purely mathematical formulations are not generally practical.

Table 2-3: Chronological list of some of the three-phase relative permeability models

Model	Basis of model	Wettability	Phase Applicability	Composition Dependency		Main Feature
				N_c *or* N_T	*Composition Consistency*	
Corey et al. (**1956**)	*C.P+B*	*W*	*3P*	NO	NO	Requires k_{rog} at a specified S_w to reproduce all of the k_{ro}^{3P} and k_{rg}^{3P}; $k_{ro} \propto R_H$; Fluid flows in the separate channels with no fluid-fluid interaction
Wyllie and Gardner (**1958**)	*P.S.D*	*W*	oil & gas	NO	NO	Water as part of the rock matrix
Naar and Wygal (**1961**)	*C.P+R*	*W*	*3P*	NO	NO	3-phase imbibition assuming $CS^* = 1/P_C^2$ where C =constant; Adding trapping gas mechanism; S_{wir} is the only adjusting parameter
Land (**1968**)	*C.P+B*	*W*	*3P*	NO	NO	Imbibition 2- and 3- phase KR based on Corey model (**1956**) and modified Naar and Wygal model (**1961**); Defining '*free saturation*'
Stone I (**1970**) and Stone II (**1973**)	*C.F*	*W*	*3P*	NO	NO	Oil blockage by water and gas; k_{rw} and k_{rg} depend on their *sat* Stone I: $k_{ro} \propto f_1(S_w).f_2(S_g).f_3(S_{or}^{3P}, S_{wc})$; Stone II: S_{or}^{3P} does not appear explicitly; $k_{rw} + k_{ro} + k_{rg} \propto f_4(S_w).f_5(S_g)$ (assumption: segregated flow); Stone II model requires four 2-phase KR as opposed to only 2 for stone I model
Modified Stone I (Hirasaki) and Modified Stone II Dietrich and Bondor (**1976**)	*C.F*	*W*	*3P*	NO	NO	**Hirasaki:** Representing all model 2-phase permeabilities relative to k_{ocw} **Dietrich and Bondor:** Renormalizing Stone II model to represent k_{rwo} and k_{rgo} based on combination of KR to oil at S_{wc} and absolute permeability.
Pope and Nelson (**1978**)	*C.F.*	*ALL*	3P	YES	NO	Adding the flexibility to the Corey formulation to adjust the end-point relative permeability parameter as the capillary-desaturation effect occurs.
Modified Stone I and Stone II (**Aziz & Settari, 1979**)	*C.F*	*W*	oil	NO	NO	Smooth reduction to 2-phase data due to added normalized *sat.*
Parmeaswar and (**Parmeswar & Maerefat, 1986**)	*Empirical*	-	*3P*	NO	NO	A power-law function of normalized saturation for all phases; Not reliable for extrapolating the saturation range out of the measured window
Parker and Lenhard (**1987**)	*C.P + Pc-S*	*W*	oil	NO	NO	Based on van Genuchten's Pc-S model and Mualem's hydraulic conductivity model (**Mualem, 1976**); Does not require 2-Phase KR data; $k_{ro} \propto R_H^2$
Alemań and Slattery (**1988**)	*C.F*	*W*	oil	NO	NO	Using a statistical structure model in local volume-averaged method; requires four 2P KR and reduces to Stone I model **(1970)** if k_{row} or k_{rog} is linear function of *sat.*
Baker 1 (**1987**) and Baker 2 (**1988**)	*S.A*	*W*	oil	NO	NO	**1:** Interpolation between 2-phase KR values to find 3-phase oil *KR* based on segregated assumption of water and gas **2:** 'Linear isoperm' by specifying equal KR on ternary saturation diagram.

Table 2-3 (cont'd): Chronological list of some of the three-phase relative permeability models

Model	Basis of model	Wettability	Phase Applicability	Composition Dependency		Main Feature
				N_c or N_T	Composition Consistency	
Delshad and Pope (**1989**)	*S.A*	*W*	oil	NO	NO	2-phase *KR* does not appear explicitly
Modified Stone I (**Kokal & Maini, 1990**)	*C.F*	*W*	oil	NO	NO	Improved modified Stone I (**Aziz & Settari, 1979**) by adding one more normalizing factor
Modified Stone I (**Hustad & Holt, 1992**)	*C.F*	*W*	oil	NO	NO	$k_{ro} \propto \beta_{SI} k_{row} k_{rog}$ where , $\beta_{SI} = f(S_o, S_g, S_{wir}, ROS, n_{HH})$, $0 \leq \beta_{SI} \leq 1$
Dria et al. (**1993**)	*C.P+B*	*W*	*4P*	NO	NO	Extension of Corey's et al. model (**1956**) for *4P* flow based on residual *sat.*
Robinson and Slattery (**1994**)	*C.F*	*W*	oil	NO	NO	Adding hysteresis and S_{or} to Alemań and Slattery (**1988**) model
Goodyear and Townsley (**1995**) **(Balbinski et al., 1999)**	*Pc-S*	*W*	oil	NO	NO	Extension of Brooks-Corey method (**1966**); $k_{ro} \propto k_{rog}^{f} . k_{row}^{1-f}$ and may reduce to Corey form
Bradford et al. (**1997**)	*C.P+B*	*FW*	*W & oil*	NO	NO	Adding the impact of wettability on Burdine model; gas is non-wetting phase
Jerauld (**1997b**)	*P.L*	*int.*	*3P*	YES	*Par*	Inherent hysteresis; $k_{rwo}^{D} \neq k_{rwo}^{I}$; k_{rw}^{3P}: S.A of k_{rwh} and k_{rhw} which in turn are based on S.A of oil and gas phase parameters using f_h; $k_{rog} = f(S_g, S_{org})$; $k_{row} = f(S_w, S_w^{min}, S_{otw})$; $k_{ro}^{3P} = f(k_{roo}, k_{rog}, k_{rhw})$; $k_{rg}^{2P} = f(S_g, S_{gt}, S_{gr})$; $k_{rg}^{3P} = f(k_{rgg}, k_{rgo}, k_{rhw})$; k_{ro}^{3P} and k_{rg}^{3P} are general form of Stone I
Moulu 1 (**1997**) and Moulu 2 (**1999**)	*F.R*	*ALL*	*3P*	NO	NO	Extension of Vizika et al. model (**1993**); 3P in each fractal pore; each phase *sat.* calculated as the relative area occupied; KR calculated by Poiseuille-type flow $k_{rw} = f(S_w, S_{wi}, \mathrm{f})$; $k_{ro} = f(S_L, S_w, S_{or}, \mathrm{f}, k_{ro}^{2P})$; $k_{rg} = f(S_L, \mathrm{f}, k_{rg}^{max})$
DiCarlo et al. (**2000**)	*L.D*	*W+ int.*	oil	NO	NO	$k_{ro} \propto S_o^2$ at $S_o < S_{orw}$. Does not require 2-Phase KR data
Modified Baker (**Blunt, 2000**)	*S.A*	*ALL*	*3P*	YES	*Den*	General Baker (**1988**) model based on layer drainage model; Inherent hysteresis
Modified Baker (**Fayers et al., 2000**)	*S.A*	*ALL*	*3P*	YES	*Den*	Introducing *sat.* rescaling: $S_o^{ri} = r_i S_o + (1 - r_i)(1 - S_{wc})$; $r_i = \frac{1 - S_{ori} - S_{wc}}{1 - S_{om} - S_{wc}}$ $k_{roi} = f(S_{ori})$; $k_{ro}^{3p} = (1 - \psi) k_{row} + \psi k_{rog}$; $k_{ri}^{3p} = S_{oj} k_{rio} + (1 - S_{oj}) k_{rij}$ where $i \neq j,\ i, j = w, g$; $S_{ow} = S_o / (S_o + S_w - S_{wc})$, $S_{og} = S_o / (S_o + S_g)$
Van Dijke et al. (**2001**)	*P.L*	*ALL+ F.W*	*3P*	NO	NO	Determination of saturation-dependencies of KR in 3P flow (process-based approach); Applicable to both spreading and non-spreading oil layer

Table 2-3 (cont'd): Chronological list of some of the three-phase relative permeability models

Model	Basis of model	Wettability	Phase Applicability	Composition Dependency		Main Feature
				N_c or N_T	Composition Consistency	
Skjæveland and co workers (**2002**; **2000**)	*C.P+ B*	*ALL*	*3P*	NO	NO	Introduction of a *Pc* function applicable to a broad range of wettability conditions. Phase *KR* is then calculated based on a *Pc*-weighted averaging between the limiting *KR* expressions depending on the wettability state.
Lomeland et al. (**2005**)	*E*	*mixed*	*3× 2P*	NO	NO	An analytical 3-parameter formulation so-called LET correlation. Applicable to any 2-phase fluid pair but not intended for 3-phase flow.
Hustad & Hansen (**1996**); Hustad (**2002**); Hustad & Browning (**2010**)	*S.A*	*ALL*	*3P*	YES	NO	2-Phase process-dependent normalized *sat*. to look up 2-phase *KR* values and estimate three-phase *KR* based on *S.A* between 2-phase residual *sat.*; Inherent hysteresis
Chavent an co-workers (**2008**);(**2009**);(**2010**)	*T.D.*	*ALL*	*3P*	NO	NO	A partial differential equation- total differential interpolation algorithm applies two-phase flow measurements and global pressure formulation. This reduces the number of functions from three 2-phase *KR*s to two global mobility and global *Pc* functions.
Shahverdi and Sohrabi (**2012**)	*S.A*	*ALL*	*3P*	NO	NO	Independent impact of 2-phase *KR* on 3-phase *KR*; each phase in contact with 2 other phases in 3-phase fluid distribution
Yuan and Pope (**2012**)	*T.H*	*ALL*	*3P*	YES	*GFE*	Adding compositional consistency to any 3-phase *KR* model
UTKR3P (**Beygi et al., 2013**)	*P.S.A*	*ALL*	*3P*	YES	*GFE*	$F_{k_{rJ}} \propto F_{k_{rJL}} + F_{k_{rJM}}$(F: *KR* parameters); Inherent hysteresis (*sat.* path dependence) but another hysteresis method can be added

Abbreviations: 3P**: Water/oil/gas or water/oil/microemulsion; ***4P: Water and three-hydrocarbons (oil, gas, 2nd liquid hydrocarbon in CO_2-oil mixing at low temperature and reservoir pressures (**Khan et al., 1992**; **Mohanty et al., 1995**); ***ALL***: Water-wet, mixed-wet, and oil-wet; ***B***: Burdine pore-size distribution model based on tortuous bundle of parallel capillary tubes (**Burdine, 1953**); ***C.A***: Capillary tubes; ***C.F***: channel flow theory (= probability-based model) considering at most one mobile fluid in any flow channel; ***Den.***: Density; ***E***: Empirical; ***F.R***: Fractal pore; ***F.W***: Fractional wet; ***GFE***: Molar Gibbs free energy; ***Int.***: Intermediate-wet; ***KR***: Relative permeability; ***L.D***: Layer Drainage; ***NAPL***: Light-non-aqueous-phase liquid; ***Par.***: Parachor-weighted molar density; N_c or N_T: Capillary or Trapping number dependency; ***Pc***: Capillary pressure; ***Pc-S***: Capillary pressure-saturation; ***P.L***: Pore-level mechanisms interpretation; ***P.S.A***: Parameter-level saturation-averaged interpolation scheme*;* ***P.S.D***: Pore size distribution; ***R***: Random interconnection of straight capillaries; ***S.A***: Saturation-averaged interpolation scheme; ***Sat.***: Saturation; ***T.D***: Total differential; ***T.H***: Intensive thermodynamic properties, e.g., molar Gibbs free energy (*GFE*); ***W***: Water

2.6 HYSTERESIS

Hysteresis represents a history-dependent phenomenon. It has remarkable implications in a broad spectrum of natural, anthropological, and social events. Example in climate research include, (**i**) the dynamics of ocean circulation-pattern shows hysteresis effect as the fresh-water strength varies (i.e., maintaining ample negative freshwater flux (evaporation-precipitation) are presenting bifurcation as a buoyancy input into the global ocean circulation system) (**Dijkstra & Weijer, 2005**); besides, (**ii**) marine ice-sheet dynamics exhibit discrete equilibrium profiles under the variation of temperature (**Schoof, 2007**). In biology, (**iii**) the DNA denaturation (melting) process under the pressure- and thermal-driven stimuli lead to a delayed structural response primarily contributed to the hysteresis in the form of an internal dissipative coupling in the energy landscape (**Hernández-Lemus et al., 2012**); moreover, (**iv**) it is postulated that hysteresis effect is in charge of bi-stable system in unfolding-refolding processes or in aggregation-association events in proteins (**Zhuang et al., 1996**; **Wales, 2010**). In economics, the hysteresis hypothesis postulates that (**v**) fluctuations in the labor market influence the natural rate of unemployment and leads to the high rate of unemployment even a long time after the recession (**Blanchard & Summers, 1986**). Among other fields of science and engineering, examples of hysteresis in mechanical, chemical, and material engineering include (**vi**) elastic hysteresis of material deformation within loading/unloading process in mechanics, (**vii**) capillary condensation hysteresis of gas adsorption upon variation of temperature and potential in mesoporous materials with pore size of 2-50 nm (**Hunter, 2001**), (**viii**) magnetization hysteresis in ferromagnetic materials, e.g., iron, as applied in magnetic hard disks and credit cards (**Hummel, 1985**; **Dixit et al., 1999**) mechanistic and hysteretic behavior of liquid supercooling and glass reheating processes (**Debenedetti & Stillinger, 2001**), (**ix**) phase transition and voltage hysteresis obtained during the charging-discharging process of lithium-ion batteries (**Dreyer et al., 2010**), (**x**) rate-independent hysteresis

in stress-strain relations of shape memory alloys (**Puglisi & Truskinovsky, 2002**), and (**xi**) unlike behavior of transition from a stationary solution to chaos and the opposite direction for heat convection in porous media.

2.6.1 Hysteresis in porous media

Hysteresis has a pronounced effect on field-performance prediction and project economy for (**i**) hydrocarbon recovery from transition zones, (**ii**) geological carbon storage, and (**iii**) projects imposing several variations in saturation history. (**Larsen & Skauge, 1998**; **Element et al., 2003**; **Flett et al., 2004**; **Righi et al., 2004**; **Masalmeh et al., 2007**; **Spiteri et al., 2008**; **Masalmeh & Wei, 2010**). The latter include multicyclic injection strategies like gas mobility control techniques, near critical fluids, and miscible/near-miscible displacement among others. Hysteresis impacts several parameters including, but are not limited to, hydrocarbon recovery factor, depletion rate, gas inventory content, e.g., capillary trapping in CO_2 sequestration in underground storage sites. It may also impose operational challenges like well injectivity in multicycle processes.

To date, in the study of fluid flow in porous media, investigators have found four characteristic properties showing irreversible and memory-dependent behavior. These macroscale properties include (**i**) relative permeability, (**ii**) capillary pressure, (**iii**) electrical resistivity and (**iv**) foam generation and flow (**Osoba et al., 1951**; **Geffen et al., 1951**; **Killins et al., 1953**; **Land, 1968**; **Longeron et al., 1989**; **Knight, 1991**; **Beygi et al., 2015**; **Lotfollahi et al., 2016**). In this dissertation, we review two- and three-phase hysteresis in relative permeability.

2.6.2 Hysteresis in relative permeability

Relative permeability is saturation-history dependent (see **Saturation history** in Appendix A). Hysteresis may induce a significant discrepancy between phase relative permeability in the increasing and decreasing phase saturation processes. This trend of irreversibility increases as the number of in-situ phases increases.

Depending on the wettability state, there are numerous laboratory and field tests in which water, oil, or gas phase exhibited variation in their relative permeability at the identical phase saturation but at different saturation histories. In two phase flow, hysteresis contributes primarily to the variation of phase relative permeability when the saturation direction of one phase changes (Honarpour et al. (**1986**) and references therein). In multiphase flow, the hysteresis effect is more complicated as the degree of saturation trajectories increases compared to two-phase. The hysteresis effect in multiphase flow is also more pronounced for the less wetting phases.

The saturation-history dependent hysteresis effect results in scanning curves in relative permeability-saturation space. It is due to the fact that depending on the saturation reversal point, the total amount of phase trapping differs (see **Capillary trapping**). In that phase relative permeability depends on the free saturation (see **Saturation** in appendix A), the consolidated and unconsolidated samples show different behaviors of irreversibility.

When comparing the non-wetting fluid relative permeability in the increasing and decreasing saturation processes at a designated saturation value, the pore structure also impacts the level of the hysteresis effect. The consolidated rocks commonly depict a decreased relative permeability in the decreasing saturation process related to the elevated phase trapping in the decreasing saturation process. The unconsolidated samples, however, have shown an increased relative permeability value in the decreasing saturation section compared to the increasing saturation process (**Naar et al., 1962**; **Batychy & McCaffery, 1978**). It shows not only the phase trapping but also the amount of physical dendritic fraction affects the hysteresis phenomenon (**Larsen & Skauge, 1998**).

Cl*osed-loop* hysteresis is the conventional logic postulated for several variations of phase saturation direction in two-phase flow (**Braun & Holland, 1995**). For the relative permeability modeling, the curves of an increasing saturation suite originate on the bounding decreasing saturation curve and move toward a representative end-point relative permeability located at the

residual saturation of the other phase. The suite of scanning curves in the decreasing saturation process originates on the bounding increasing saturation curve and move toward the phase immobile saturation.

The multiphase experimental results, however, have not supported the closed-loop presumption for the less wetting phase involved in a multicycle process. Many laboratory and field tests reveal that the gas relative permeability decreases when during cyclic injection, e.g., huff-n-puff, double-displacement, and WAG injection. This conclusion was made based on laboratory relative permeability measurements or inferred from the abnormal increase of pressure in wellbore areas close to injection wells (**Hawkins & Bouchard, 1989**; **Skauge & Larsen, 1994**; **Larsen & Skauge, 1998**; **Egermann et al., 2000**; **Shahverdi et al., 2011**). Also, the residual oil saturation decreased as the cyclic injection continued confirming that the residual gas saturation increases by increasing the alternate injection of water and gas (see **Gas trapping effect on oil trapping**). Skauge and Larsen (**1994**) conduced WAG injection tests under broad wettablity conditions and observed that residual oil saturation decreased as the injection cycle number increased. The water and gas relative permeaiblity also showed irrevesible loops in increasing and decreasing saturation processes. Later, Larsen and Skauge (**1998**) coined the *cycle-dependent* relative permeability concept. Several investigators reported cycle-dependent hysteresis in laboratory and field measurements of relative permeability and capillary pressure at different wettability conditions.

2.6.3 Hysteresis modeling in relative permeability

There are numerous empirical models to capture the impact of saturation history on relative permeability and/or on capillary pressure. **Table 2-4** lists some of the available two- and three-phase hysteresis models. A standard feature proposed by two-phase hysteresis models is the assumption of reversibility of relative permeability curves where the primary decreasing saturation curve is representative of any subsequent saturation increasing processes. This assumption draws

an incomplete picture of the irreversible behavior in multicycle/multiphase processes. Three-phase hysteresis models, however, predict the cycle-dependent relative permeability curves where each cycle has a designated set of curves for the increasing and decreasing phase saturation processes. These models predict an irreversible hysteresis behavior imposed by the saturation-path dependency.

It is observed that the reduction in gas relative permeability within each WAG cycle at the same saturation leading to the lower well injectivity. Larsen and Skauge (**1998**) published an empirical model based on their immiscible- and miscible-WAG experiments. Their model relaxes the assumption of the reversibility of scanning curves resulting in a cycle-dependent relative permeability model for the gas phase. They also proposed a three-phase water relative permeability model for water-wet media based on the saturation-averaged interpolation scheme between the primary and secondary waterflood relative permeabilities.

For the oil-wet media, the water entrapment by gas is only considered in the Egermann three-phase hysteresis model (**Egermann et al., 2000**). Oil relative permeability in the subsequent WAG cycles increases because the trapped oil saturation decreases with a higher likelihood of the simultaneous water and gas trapping.

2.6.4 Hysteresis mechanisms

The controlling mechanism of multiphase hysteresis is an unresolved subject in the petroleum engineering literature. We review three pore-scale principles proposed to describe the observed irreversibility in the capillary-pressure and relative permeability curves: (**i**) contact-angle hysteresis, (**ii**) wettability alteration (see **Rock wettability** in Appendix A), and (**iii**) free saturation (see **Saturation** in Appendix A).

The contact-angle hysteresis (see **Contact-angle hysteresis** in Appendix A) induces a broad set of plausible fluid configurations in the sequential pore-filling processes. As described in

Appendix A, fluid configuration and spreading significantly vary with the contact angles of different fluid pairs. The digital rock imaging also revealed that contact angle varies the fluid morphology in capillary trapping (see **Capillary trapping**). It delineates the impact of contact-angle hysteresis on fluid morphology, trapping, and hysteresis. Besides, it demonstrates that as contact angle varies from increasing to decreasing saturation processes, it results in different fluid configurations leading to a fluid layer or trapping depending on the pore geometry.

Braun and Holland (**1995**) performed water-oil steady-state and pseudo-steady-state relative permeability measurements on outcrop rock samples and observed a reversible hysteresis loop for oil relative permeability in several saturation directions. They interpreted the reversible scanning curves based on the interface pinning concept (**Kovscek et al., 1993**) and proposed a linkage between the hysteresis pattern in relative permeability and contact angle hysteresis. In contrary, Masalmeh (**2001**) stated that although contact angle hysteresis has a profound effect on capillary pressure hysteresis, it hardly affects the relative permeability hysteresis.

Table 2-4: Chronological list of some of the hysteresis models

Hysteresis Models	Applicable to			Wetta-bility	Main Feature
	Water	Oil	Gas		
Two-Phase Hysteresis (Saturation direction dependent):					
Land (**1971**)	NO	NO	YES	Water	$k_{rj}^{Dec}(S_j) = k_{rj}^{Inc}(S_{jf}), S_{jf} = f(L_j, S_{jr}), S_j = S_{jf} + S_{jt}$; Requires ε to be used in Corey-type equation to calculate imbibition *KR*
Killough (**1976**)	NO	NO	YES	Water	Calls for bounding drainage and imbibition curves; requires λ parameter to calculate imbibition KR; $k_{rj}^{Dec}(S_j) \propto k_{rj}^{PD}(S_j^{norm}).k_{rj}^{PI}(S_j)/k_{rj}^{PI}(S_j^{max})$;
Carlson (**1981**)	YES	YES	YES	Water	Needs a bounding drainage curve and one point on an imbibition curve to produce imbibition curves; Parallel imbibition scanning curves
Fayers and Matthews (**1984**)	NO	YES	NO	ALL	Oleic phase hysteresis when hysteresis is also applied to gaseous phase
Beattie et al. (**1991**)	YES	YES	NO	Water	Defining $k_{rw}^* = \frac{k_{rw}}{(k_{rw})_{ro}}$, $S_w^* = \frac{S_w - (S_w)_{ir}}{(S_w)_{ro} - (S_w)_{ir}}$, and $K = \frac{k_{rwi}^* - k_{rw}^*}{k_{rwi}^* - k_{rwd}^*}$ Assuming a specified saturation dependent form: $K = \alpha_{Be} + \beta_{Be}(1 - S_w^*)^n$ and estimating scanning curves for oil and water relative permeability
Plohr et al. (**2002**)	NO	NO	YES	Water	Defined the fractional flow function variable to record the flow history and track the scanning curves
Delshad et al. (**2003**)	YES	YES	NO	Mixed	Main drainage *Pc* and relative permeability, Brooks-Corey function scanning curve *Pc*, modified van Genuchten function (**1980**), relative permeability prediction by integrating a pore-distribution model.
Masalmeh et al. (**2007**)	YES	YES	NO	ALL	Developed a coupled and parameterized-level KR-PC model for the dynamic modeling of capillary transition zone
Three-Phase Hysteresis (Saturation direction dependent ➔ cycle-dependent relative permeability):					
Parker and Lenhard (**1987**)	YES	YES	YES	ALL	Applying a *KR*-saturation-*Pc* model using 1) 2P wetting-fluid saturation-capillary head pair for primary increasing and decreasing processes, 2) three parameters to define saturation paths
Larsen and Skauge (**1998**)	YES	NO	YES	Water	Water: gas-saturation-interpolation-scheme between 2P (water-oil) and 3P (water-oil-trapped gas) water relative permeability. Gas: $(k_{rg}^{Inc})_n = k_{rg}^{Inc}[S_g; S_w; (S_w^I)_n]$, $k_{rj}^{Dec}(S_j) = k_{rj}^{Inc}(S_{jf})$
Egermann et al. (**2000**)	YES	YES	YES	ALL	Application of fractal theory, Land formulation, and defining the trapping and untrapping coefficients. Different Land coefficient at different cycles
UTHYST (**Beygi et al., 2013**)	YES	YES	YES	ALL	Monotonically increasing trapped saturation but including capillary-desaturation effect at high trapping numbers; Dynamic Land coefficient

***** ALL: Water/Intermediate/Oil wettability condition*; KR*: Relative permeability; *Pc:* Capillary pressure

2.7 CAPILLARY TRAPPING

Phase trapping is a crucial element of accurate multiphase flow modeling particularly for several EOR and geological CO_2 storage applications. The former includes the processes aiming to attain the lowest hydrocarbon trapping. The latter contributes to maximizing the capillary trapping as a key element of a successful CO_2 sequestration. In this dissertation we focus on the capillary trapping among other trapping mechanisms. Further, we apply the trapping and residual terminology interchangeably. To avoid redundancy, we drop the term capillary except otherwise noted (see **Saturation** in Appendix A for the various trapping mechanisms in EOR and sequestration processes).

As noted (see **Low saturation region** in Chapter 3), the primary objective of many EOR activities is to mobilize and produce the trapped hydrocarbon saturation. In CO_2 sequestration, among the contributing mechanisms, researchers have identified that capillary trapping has a significant role in short and medium time frame of planned activities. These delineate the importance of accurate modeling of fluid trapping by different means to fully investigate the displacement efficiency of the emerging EOR techniques.

Sequential pore-space filling process is an indispensable characteristic of fluid displacement in the typical subsurface applications. As fluid experiences a decreasing saturation sequence, it may eventually become discontinuous. The isolated fluid may still migrate in porous media with other displacing fluids or ultimately become immobile and entrapped in porous media where it achieves a capillary equilibrium with a local minimum of surface area to volume (**Morrow, 1970**).

For a fluid configuration at equilibrium and under the pseudo-steady state conditions where fluid interface does not affect flow, the sequential process depends on the rock structure, buffering capacity of the adjacent pore network, and rock-fluid interactions. Therefore, it is entirely possible

that both wetting and non-wetting fluids show non-unique behaviors for a designated saturation when rock-fluid interactions vary.

In extreme wettability conditions, the wetting fluid remains as a continuous bulk distributed over the porous medium irrespective of saturation history. The advancing and receding wetting films formed by increasing and decreasing saturation processes are stable leading to a hydraulically continuous wetting phase even at very low saturations (**Dullien et al., 1989**) — minimal wetting-fluid trapping. This behavior can be contributed to the fluid configuration and topology: the non-wetting phase trapping causes the wetting phase to flow in larger pores than it would otherwise have done in the absence of non-wetting disconnections. In that the level and distribution of the wetting-phase trapping are relatively low, we focus on the non-wetting trapping as a crucial and demanding parameter in subsurface flow modeling.

Within a sequential process where the saturation history of phases varies, the non-wetting fluid may invade the rock pores. It then increases the non-wetting fluid saturation and in turn results in an augmented capillary pressure. If the applied phase potential is greater than the capillary pressure at the pore-throat, the non-wetting fluid spontaneously invades that pore-throat size and the adjoining pore-bodies via the Haines jump (**Haines, 1930**) and drains the wetting phase(s). The invading non-wetting phase passes through the pores does not entrap as its saturation increases. Depending on the saturation history, however, the governing pore-level mechanisms alter the fluid configuration in a porous medium. Accordingly, as the saturation direction switches, the non-wetting fluid either passes through the pore bodies or eventually loses its continuity in the narrow pore constrictions when a capillary equilibrium is established (**Morrow, 1970**).

In the following, we investigate two- and three-phase non-wetting phase trapping in porous media and the pertinent observations. Next, we discuss the possible remedies to remobilize the trapped phase(s). Finally, we discuss the modeling techniques to estimate trapping in multiphase flow.

2.7.1 Multiphase capillary trapping

Two- and three-phase trapping depend on several fluid and rock properties and fluid-rock interaction (**Stegemeier, 1977**). For a sequential process, the variations of the saturation direction and trajectory leads to the altered fluid topology and configuration which, in turn, affect phase trapping. Besides, the wettability and fluid spreading parameters significantly alter the fluid cluster size, morphology, and distribution (**Iglauer et al., 2016**). Inasmuch as the fluid areal-distribution level and volumetric configuration differ for two- and three-phase flow, in general, one may expect to observe a non-unique phase trapping.

The level and mechanism by which the non-wetting phase is trapped inclusively depend on rock and fluid interactions and the applied forces on fluids (**Stegemeier, 1977**). These features include rock wettability, balance of fluid-pair interfacial tensions, fluid composition, fluid topology — fluid connectivity and configuration — and pore structure, viz., geometry and topology (**Salathiel, 1973**; **Pathak et al., 1982**; **Jerauld, 1997a**; **Suzanne et al., 2003**; **Iglauer et al., 2012**; **Pentland et al., 2012**; **Herring et al., 2013**). The applied forces constitute of capillary, viscous, and buoyancy forces. From a microscopic perspective and under a regular water- or immiscible gas-flood conditions, the capillary forces control the displacement of fluids and phase trapping in porous media.

The underlying physical mechanisms of phase trapping particularly for multiphase flow, however, is still unsettled. Theoretically, one can derive the governing mechanisms of fluid flow and trapping via fluid interfacial jumps assuming the stability of fluid interfaces (**Dullien, 1992**). Yet, the underlying principles are not trivial in multiphase flow because several fluid configurations and morphology may exist when characteristic parameter of multiphase trapping vary. They include but are not limited to saturation history variation, wettability variation, and rock-fluid interaction variation.

Researchers have proposed intrinsic principles to describe trapping and ganglia movement

in multiphase flow but have not yet achieved consensus. They have identified or postulated three mechanisms competing for the phase trapping: (**i**) pore-doublet, (**ii**) snap-off (or choke-off), and (**iii**) double- or multi-displacement (**Stegemeier, 1977**; **Suicmez et al., 2008**; **Amaechi et al., 2014**; **Helland & Jettestuen, 2014**). From a pore-scale perspective and for a multiphase flow, both the continuous fluid and the discontinuous clusters may contribute in the overall fluid displacement (**Fenwick & Blunt, 1988**). This double-displacement principle is contrary to that of two-phase flow in which only a continuous fluid could participate in fluid displacement (**Suicmez et al., 2008**).

In subsurface applications with a dynamic fluid properties and configuration more than one mechanism is often operative. Besides, although not all of the proposed mechanism coexist for a particular fluid configuration and displacement, the proposed mechanisms may become interrelated. For instance, one does not anticipate observing a piston-like displacement when a continuous fluid layer exists in porous media, e.g., gas displacement when oil layer exists. The snap-off of fluids by water will contribute on the trapping of both oil and gas phases. Alternatively, the snap-off mechanism may assist or suppress the double-displacement in multiphase trapping (**Suicmez et al., 2008**). This internal competition among several recognized mechanisms has several implications for multiphase trapping including a dynamic fluid configuration and curvature. More importantly, it reveals that multiphase trapping is quite complicated in intermediate/mixed wettabilities and in low saturation region.

The proposed mechanisms are based on the pore-scale observations which cannot appropriately get upscaled for core- and field-scale applications. Although these mechanisms and their associated results are widely applied in fluid flow modeling at the field scale, there is no rigorous connectivity as a bridge between the length scales of interest.

Next, we summarize the main observations of multiphase trapping inducing a pronounced effect on the performance of multiphase subsurface processes like the gas-based EOR, CO_2

sequestration/EOR in the depleted oil reservoirs and gas storage activities.

Initial-trapping saturation behavior

Among other parameters that impact phase trapping, the maximum phase saturation attained in the increasing saturation process (S_j^{max}) is the widely accepted and applied parameter in several empirical trapped models. Pore geometry and topology impacts the trapping behavior. For example, as the rock heterogeneity increases, the trapping increases. Both the moderately homogenous sandstones with inter-granular porosity and highly heterogeneous carbonate rocks however show an increasing level of phase trapping as the initial saturation increases (**Irwin & Batycky, 1997**; **Stegemeier, 1977**). This behavior is more pronounced in the lower maximum saturation region where trapping shows a linear relation with the maximum saturation.

Following the experimental results of initial-trapped saturation relation reported by several investigators (**Holmgren & Morse, 1951**; **Kyte et al., 1956**; **Naar & Wygal, 1961**; **Crowell et al., 1966**), Land (**1968**; **1971**) developed a phenomenological relationship to estimate the trapped non-wetting saturation. Afterward, various adaptations of his approach have been widely used. Ma and Youngren (**1994**) generalized the Land correlation to account for sharp level-off of the trapped saturation at high initial saturations:

$$S_{jt}^{*} = \frac{S_j^{*max}}{1 + a\left(S_j^{*max}\right)^{d}}, \qquad \textbf{Eq. 2-2}$$

where a and d are empirically derived constants and superscript '*' denotes the effective saturation (see **Saturation** in Appendix A). Further, two other models based on laboratory and pore-network results have been proposed which do not match the Land's results. Aissaoui (**1983**) decomposed the initial trapping behavior into two parts: a linear region where trapping monotonically increases as initial saturation increases followed by a constant trapping where further initial saturation results in an invariant phase trapping. Spiteri et al. (**2008**) developed a quadratic relationship to capture

non-monotonic behavior of non-water-wet samples in their network models. **Table 2-5** summarizes different models used to estimate trapped saturation.

Table 2-5: Initial-trapped saturation models

Model	Fluid and Rock System	Trapping Formulation
Land (**1968**)	gas/oil in consolidated sandstone	In **Eq. 2-2**: $a = L_j = \frac{1}{S_{jt}^{*max}} - \frac{1}{S_j^{*max}}$, $d = 1$
Carlson (**1971**)	Conceptual extension of Land's eq. assuming parallel scanning curves	$S_{jt} = S_{jt}^{max} - \Delta S_j$ ΔS_j is shift in scanning waterflood curves
Jerauld (**1997b**)	gas/oil and gas/water in consolidated mixed-wet sandstone	In **Eq. 2-2:** $a = L_j = \frac{1}{S_{jt}^{*max}} - 1$, $d = \frac{\beta_j}{L_j}$ and $0 \le \beta_j \le 1$
Aissaoui (**1983**) and modified Kleppe et al. (**1997**)	gas/water in consolidated sandstone	if $S_j^{max} < S_j^{cr}$: $S_{jt} = \frac{S_j^{max}}{S_j^{cr}} S_{jt}^{max}$; else $S_{jt} = S_{jt}^{max}$
Spiteri et al. (**2008**)	pore-network model	$S_{jt} = \lambda S_j^{max} - \kappa\left(S_j^{max}\right)^2 \quad 0 \le \lambda \le 1, \kappa \ge 0$

We conclude that except for the parabola shape of the Spiteri et al.'s (**2008**) correlation, the trapped saturation monotonically increases at higher initial saturations attained in the saturation increasing process at least at low and moderate initial saturations. Some investigators stated that the hyperbolic laws (i.e., Land or its modified formulations, cannot represent the trapping behavior within their experiments). Two-phase pore-network model results showed that the Land equation does not capture the trend of initial-trapped saturation for high initial saturation in non-water-wet rocks (**Spiteri et al., 2008**). Pentland et al. (**2010**) measured trapped oil as a function of its original saturation in unconsolidated sandpacks. Their results were in agreement with the Aissaoui (**1983**) trapping model. Suzanne et al. (**Suzanne et al., 2003**) examined two-phase initial-trapped gas saturation for a large set of sandstone samples and concluded that the piecewise linear model (i.e., the model of Aissaoui (**1983**)) represents the initial-trapped gas saturation relationship in shaly sandstone rock. They stated that the trapped gas saturation plateau corresponding to the high initial gas saturation is due to the microporosity in which gas does not trap. Studies on sandstone and conglomerates samples with a broad range of grain sizes showed the impact of microporosity on

trapped gas saturation (**Jerauld, 1997a**).

Non-wetting phase(s) trapping

Researchers have reported that the simultaneous trapping of non-wetting fluids in three-phase flow is approximately equal to or higher than individual phase trapping in two-phase flow. Amaechi et al. (**2014**) found an approximately constant cumulative oil and gas trapping in sand pack experiments. Jerauld (**1997b**) showed that for the mixed-wet Prudhoe Bay reservoir cores, cumulative trapped oil and gas increases with two-phase residual oil saturation to water.

The individual phase trapping is more complicated when two fluids compete for the same pore space. One may expect that the level of residual oil (or water) saturation impacts gas isolation when oil (or water) and gas target the same pore sizes. However, for the mixed/intermediate wettability conditions, the complicated fluid configuration induces uncertainties in the prediction of the actual non-wetting phase trapping. In a comparison between two- and three-phase trapping, researchers reported invariant gas trapping when fluid configuration and flow change in porous media. For example, Jerauld (**1997b**) reported a relatively insensitive gas trapping in the presence of oil for the mixed-wet Prudhoe Bay reservoir. Maloney and Zornes (**2003**) performed oil and brine floods using the carbonate cores with a live oil at reservoir conditions and observed an invariant gas trapping in two- and three-phase flow.

For the oil phase, however, several researchers have reported a lower level of trapping in three-phase than in two-phase displacements. Core-scale measurements revealed that three-phase oil trapping significantly reduces in three-phase flow over that in two-phase waterfloods (see references in **Table 2-6**) (cf. **Kralik et al., 2000**; **Al Mansoori et al., 2009**). The rock wettability preference is a controlling parameter on the level of oil trapping reduction in the presence of free gas. For the unconsolidated rocks, however, Al-Mansoori et al. (**2009**) reported an invariant oil trapping in the presence of the trapped gas in the unconsolidated sand packs experiments. For the

oil-wet samples, Kralik et al. (**2000**) observed that after waterflood tests and in the presence of trapped gas, the oil trapping was essentially the same. However, the water relative permeability suppressed in the presence of trapped gas in their non-water-wet media.

Phase trapping models will be reviewed in **Modeling three-phase trapping**. Here, we report on the experimentally measured trapped oil at different wettability conditions when trapped gas exists. **Table 2-6** lists the coefficient reduction factor (a_w) in the Fayer's model (**1989**) (as listed in **Table 2-7**) from experimentally measured three-phase trapped oil in the presence of trapped gas at the different wettability conditions. **Table 2-6** implies that one may expect that gas trapping may not affect oil trapping in the less water-wet samples.

Table 2-6: Value of parameter a_w in Fayer's model (**1989**) from measured S_{or}^{3P} and S_{gr}^{3P} (see **Table 2-7**)

Reference	Porous Material	Water-Wet	Mixed-Wet
Holmgren and Morse (**1951**)	Nellie Bly sandstone	0.6	N.A.
Kyte et al. (**1956**)	Torpedo Sandstone and Dri-Filmed Alundum	0.4	N.A.
Schneider and Owens (**1970**)	Limestone	0.45	N.A.
Fayers (**1989**)	Literature review of water-wet samples	0.5	N.A.
Oak et al. (**1990**) and (**Oak, 1991**)	Berea sandstone	0.71	0.67
Kortekaas and van Poelgest (**1991**)	Consolidated samples from North Sea reservoirs	0.65	N.A.
Larsen and Skauge (**1998**)	Sandstone	0.3 - 0.5[a]	0.9 - 1.1[a]
Unpublished data compiled by Kralik et al. (**2000**)	Sandstone	0.59 ± 0.09	0.45 ± 0.08
Egermann et al. (**2000**)	Fontainebleau Sandstone	0.45	N.A.
Iglauer et al. (**2013**)	Clashach Sandstone	0.65 [b] and 1.07 [c]	N.A.
Amaechi et al. (**1995**)	Sandpack	0.42	N.A.

[a] saturation-history dependent

[b] for gas EOR in a virgin oil reservoir

[c] for gas EOR in a water-flooded oil reservoir

Modeling three-phase trapping

We summarize some of the published three-phase residual saturation models in **Table 2-7**. **Table**

2-7 demonstrates that the proposed models are primarily applicable to the oil phase except for the general multiphase residual model of Yuan and Pope (**2012**). The Fayers' model and its variants (**1984**; **1989**) are the accepted models to relate the oil and gas trapping at different wettability conditions (as discussed in **Non-wetting phase(s) trapping**). Larsen and Skauge (**1998**) generalized the Fayer's model (**1989**) simply by replacing S_{orw} with $S_{or}^{3P,S_{gr}=0}$; this more generalized term has a broad applications and can directly be extracted from the zero gas-isoperms data within two- or three-phase experiments in which no gas trapping has occurred.

Table 2-7: Three-phase residual saturation correlations

Model	Rock Wettability	Phase Applicability	Residual Saturation Correlation
Fayers and Matthews (**1984**)	Water	Oil	$S_{or}^{3P} = \chi S_{orw} + (1-\chi) S_{org}$ where $\chi = 1 - \frac{S_g}{1-S_{wc}-S_{org}}$
Alemań (**1986**)	All	Oil	$S_{or}^{3P} = \left(\frac{S_w - S_{wc}}{1-S_{wc}-S_{orw}}\right)^{\alpha_{Al}} S_{orw} + (1-\chi)^{\beta_{Al}} S_{org}$ where $\chi = 1 - \frac{S_g}{1-S_{wc}-S_{org}}$
Fayers and coworkers (**1989**; **1984**); Larsen and Skauge (**1998**)	All	Oil	$S_{or}^{3P} = S_{orw} - a_w S_{gr}^{3P}$ or $S_{or}^{3P} = S_{or}^{3P,S_{gr}=0} - a_w S_{gr}^{3P}$ $0 \le a_w \le 1$
Fayers et al. (**1939**)	Mixed	Oil	$S_{or}^{3P} = \psi S_{org} + (1-\psi) S_{orw} + S_g \frac{S_w - S_{wc}}{\beta_F S_{orw} - \psi S_{gt}}$ where $\psi = \frac{S_g}{1-S_{wc}-S_o}$
Yuan and Pope (**2012**)	All	Water/Oil/Gas	$S_{jr}^{3P} = \min\left[S_j, S_{jr}^{2P}\left(1 - b_j S_k S_l\right)\right]$ where j =1, 2, and 3 and $j \neq k \neq l$

Trapped cluster morphology

The cluster morphology and distribution impacts the boundary between the microscopic and continuum domains as represented by the REV definition. The morphology of clusters of the trapped phase varies significantly with fluid-fluid interaction (contact angle), wettability, and the applied forces (viscous, capillary, and gravitational forces) (**Stegemeier, 1977**; **Blunt et al., 2013**; **Georgiadis et al., 2013**). As Stegemeier (**1977**) noted and the more recent experimental micro-

computed-tomography (see **Pore-scale relative permeability modeling**) confirmed (**Iglauer et al., 2012**; **Pentland et al., 2012**; **Blunt et al., 2013**; **Georgiadis et al., 2013**; **Iglauer et al., 2016**), the trapped cluster length and volume size distribution is not restricted to a single pore and may span several pores, e.g., 1-10^6 μm^3.

The cluster size distribution follows a power-law distribution at least for the smaller cluster sizes (approximately up to 100 μm^3). These results are on a par with the predicted results of the percolation theory: the invasion percolation theory predicts the terminal point –at which fluid becomes disconnected – corresponding to a percolation threshold (**Blunt & Scher, 1995**) and that the cumulative cluster distribution of size s follows a power-law behavior (i.e., $N(s) \propto s^{-\tau}$). At low capillary number ($N_c \cong 10^{-5} - 10^{-6}$) conditions, the percolation theory predicts a constant value for the Fisher (decay) exponent ($\tau = 2.189 \pm 0.002$) (**Lorenz & Ziff, 1998**). The above experimental results revealed that the decay exponent τ varies with fluid type, wettability, and fluid configuration (saturation history and number of phases) and, for the cluster volume, lies in the range of 0.7-2.12.

The cluster size distribution, however, sharply deviates from the power-law prediction for the larger cluster sizes. Nonetheless, the truncations associated with the resolution of the current imaging techniques may contribute to the deviation from and the underestimation of sizes by the power-law model for the large cluster size.

2.8 TRAPPED PHASE MOBILIZATION

Trapped phase can be released either by preferably changing the balance of viscous, gravitational, and capillary forces or by changing the relative volume of phases in porous media (**Stegemeier, 1977**). The former refers to the widely reported *capillary-desaturation* effect in which trapping (or capillary) number (see **Capillary and trapping number** in Appendix A) controls the reduction in residual phase saturation (**Abrams & Prausnitz, 1975**; **Stegemeier, 1977**; **Delshad et al., 1987**; **Alemań & Slattery, 1988**; **Harouaka et al., 2014**). Lowering the residual oil saturation using a surfactant at concentrations above the critical micelle concentration (CMC) is an example of the capillary-desaturation effect (**Rivet et al., 2010**) where the IFT between oleic and aqueous phases is lowered to ultra-low value (<0.001).

The capillary desaturation effect depends on the rock wettability, displacing-displaced fluid pair, pore structure, and pore-filling sequence. Stegemeier (**1977**) found a critical capillary number of approximately 10^{-5}. Humphry et al. (**2013**) examined rock samples with less water-wet condition and found that as the wettability approaches toward more oil-wetness, the S_{orw} decreases passing a minimum value at the intermediate-wet state. Further, the critical capillary number for the water (displacing)-oil (displaced) pair is higher for the more oil-wet sample at least one order of magnitude. These observations are consistent with the general understanding of the more oil-wet rocks in which the rock affinity keeps the oil ganglia in-place by higher local capillary forces on the trapped oil.

The change in phase relative volume mechanism addresses the critical role of the interphase mass transfer resulting in phase trapping reduction. At a small trapping number, the trapped phase remobilization pertaining to the interphase mass transfer occurs when two mechanisms predominate in fluid displacement: **(i)** when trapped and discontinuous phase dissolves into the displacing phase, e.g., solution of trapped volatile oil into displacing gas or solution of trapped

gaseous CO_2 into a displacing aqueous or oleic phase; **(ii)** when the displaced fluid volume increases and exceeds the maximum immobile saturation and restarts flowing in porous medium, e.g., swelling of trapped oil by preferentially partitioning of displacing gas component(s) into the trapped oleic phase. Both mass–transfer dominated mechanisms may occur at low capillary/trapping number.

Chapter 3: **Three-Phase Relative Permeability Modeling (UTKR3P Model)**

The goal of this chapter is to introduce and validate the three-phase relative permeability model referred to as UTKR3P developed in this research. First, we review the key parameters that affect relative permeability. We then discuss the features of the UTKR3P model.

3.1 IMPACTING PARAMETERS ON RELATIVE PERMEABILITY

Based on an extension of Marle's (**1981**) explanation, numerous pore- and core-scale parameters affect relative permeability: saturation, rock wettability, pore structure, fluid properties, and applied forces on the characteristic length-scale among others. Pore structure parameters include pore size, geometry, and topology. Fluid properties include spreading, fluid topology, configuration, interfacial tension, and composition. Other parameters such as temperature, pressure, and fluid viscosity might impact relative permeability. The empirical correlations, however, only implicitly include their impacts.

In this chapter, we explicitly state key parameters or dependent parameters according to the comprehensive review of models in which the developers focused on a particular set of parameters. For example, (**i**) phase saturation is an averaging core-scale property which can be computed from the pore and fluid properties, e.g., a fluid configuration in a particular pore network. (**ii**) Interfacial tension depends on the composition of fluids. (**iii**) Fluid spreading is computed based on fluid-pair interfacial tensions. (**iv**) The applied forces, viz., capillary, viscous, and buoyancy forces are a function of rock, fluid, and rock-fluid interaction parameters. In the following, we review some of the micro- and macro-scale parameters impacting relative permeability.

3.1.1 Phase saturation

Relative permeability dependency on phase saturation in either two- or three-phase flow is well-

established (**Honarpour et al., 1986**). Besides, relative permeability in many EOR applications exhibits a dependency on both saturation history and the saturation region as discussed in more detail in this chapter.

3.1.1.1 Saturation history

Multiphase relative permeability is saturation history dependent: both saturation direction and saturation path impact relative permeability (see **Saturation history** in Appendix A). Per discussions on **Hysteresis** in Chapter 2 and **Saturation direction**, the well-defined saturation direction, at least in two-phase flow, has a pronounced effect on relative permeability and ultimately hydrocarbon recovery. Saturation-path terminology has been applied to address the impact of saturation trajectory for a specified saturation direction.

The impacting parameters on saturation history include starting- and ending-point saturation of a specified saturation trajectory and saturation path between them. As a result, relative permeability model must be able to capture this phenomenal path- and direction-dependency over the entire saturation space.

Saturation direction

In two-phase flow, there is only two possible saturation direction (ID or DI as defined in **Saturation history** in Appendix A). In three-phase flow, there are up to twelve saturation directions (see **Saturation direction** in Appendix A). Although it is unlikely to observe all the possible saturation directions within a designated fluid displacement, it is likely to encounter several saturation directions, particularly within multicycle processes. In that saturation direction contributes to level of phase trapping, for a fixed phase saturation, phase relative permeability varies depending on the process and the overall saturation direction. Hysteretic relative permeability models capture the effect of saturation direction in multiphase flow. As discussed in **Chapter 4**, several observations of bi-directional and multi-directional experiments underpin the

impact of saturation direction in phase relative permeability. The level of relation between saturation direction and relative permeability is a function of rock wettability, pore-filling sequence, and spreading coefficient.

Saturation path

Relative permeability and overall performance of a process vary when fluid flow experiences a non-unique saturation path (see **Saturation history** in Appendix A). This lends credence to the idea that saturation path and saturation direction may be the reasons for dependency of displacement efficiency on initial saturation as reported by several investigators. Note that the dependency of relative permeability on initial overall saturation is one of the implications of the general saturation path terminology.

Jerauld (**1997b**; **1997c**) reported the impact of initial water saturation on gasflood performance in the mixed-wet Prudhoe Bay reservoirs. The author contributed this phenomenon to the wettability change as the initial water saturation varies by depth. Alizadeh and Piri (**2014**) measured the effect of saturation path on gas relative permeability for water-wet Bentheimer sandstone cores. They observed that gas relative permeability was strongly dependent on saturation path. These investigators, however, reported an invariable oil relative permeability with saturation history and contributed it to the narrow pore size distribution of the core samples. Other researchers noticed that for a fixed oil saturation in the same porous media, oil relative permeability varied up to one order-of-magnitude as overall saturation path changed (**Oak, 1990**, **1991**, **1992**; **Baker, 1995**; **Eleri et al., 1995**; **Kianinejad et al., 2015**).

3.1.1.2 Saturation region

Multiphase flow in porous media may lead to spanning a full spectrum of saturation space including extreme saturation values. Providing a representative relative permeability model is essential for the extreme saturation values. In the following, we review extreme saturation values

encountered in many subsurface processes and their associated relative permeability data.

Low saturation region

Low phase saturation values are desirable for many subsurface applications. (**i**) EOR/IOR methods aim to minimize oil residual saturation. For example, lowering the waterflood residual oil saturation to ultra-low values by solvent injection, WAG process, and the chemical flood is the primary target of chemical-EOR processes. Besides, (**ii**) the extensively trapped oil in ROZ and transition zones (TZ) is the focus of emerging solvent-based EOR techniques, e.g., CO_2-EOR (see **ROZ/TZ** in Appendix A). Moreover, (**iii**) field operators expect to maximize gas immobilization (residual) within underground gas injection processes. For instance, maximizing gas utilization factor in CO_2 sequestration and natural gas storage applications is necessary to efficiently store anthropological or abundant fluids, respectively, in underground saline aquifers, stranded hydrocarbon reservoirs, or gas caps for a predefined short or long time-frame.

Several laboratory and field results for a designed rock wettability state and fluid configuration have reported continuous oleic phase down to S_o=0.001 (**Zhou & Blunt, 1997**). Blunt (**2000**) listed 15 published experimental three-phase results targeted very low oil saturation region (i.e., below the waterflood residual oil saturation). He concluded that in 60% of the experiments, oil relative permeability for a spreading oil in the non-oil-wet rock and the presence of gas has a characteristic quadratic form, viz., layer drainage flow unlike those of some other investigators (cf. **Singh et al., 2001**). Singh et al. (**2001**) analyzed two different set of water-wet samples with spreading oil by applying the centrifuge and gasflood (unsteady-state) methods. They did not observe oil relative permeability proportional to S_o^2.

The spreading coefficient together with rock wettability are critical parameters in the characteristic behavior of thin film layers in porous media (see **Fluid configuration in multiphase flow: layering vs. trapping** in Appendix A). In Appendix A, we investigated the possibility of layer drainage as rock wettability and equilibrium spreading coefficient vary. The conducted

analytical study has implications on the complicated task of modeling phase trapping and existence of a continuous fluid layer. The existence of a stable film layer is particularly important for pore scale heterogeneous media with varying degree of pore structure and wettability. We demonstrated that how rock wettability and IFTs intervene the existence of a stable layer-drainage for pore structures with varying degree of pore angles. As a result, one cannot a priori presume the layer-drainage flow and apply the quadratic correlation between relative permeability and saturation for heterogeneous or less water-wet rocks or all fluid combinations. **Figure 3-1** represents a compilation of oil relative permeability measured data for samples with various wettabilities preferences at positive or negative oil spreading coefficients (**Oak, 1990**, **1991**; **Vizika & Lombard, 1996**; **DiCarlo et al., 2000**; **Alizadeh & Piri, 2014**; **Kianinejad et al., 2016**). **Figure 3-1** demonstrates the possibility of the layer drainage mechanism at low oil saturation below the residual oil saturation to water where oil relative permeability lies on a quadratic fitting line. It is particularly valid for spreading oil systems based on the measured oil spreading coefficients. The level of quadratic oil relative permeability decreases considerably for mixed- and oil-wet rocks. Water did not show layer-drainage regime in the studied non-water-wet datasets (viz., **Figure 3-1** just addresses the oil-layer flow).

High saturation region

Modeling the high-saturation is challenging especially for the non-wetting phase. Here, a reversed S-shape relative permeability curve with *zero slopes* at maximum non-wetting saturation was reported (**Adamson, 1960**; **Jerauld, 1997b**; **Lomeland et al., 2005**). Jerauld (**1997b**) investigated the gas relative permeability for the mixed-wet reservoir of Prudhoe Bay and noticed that the slope of the relative permeability curve continuously decreased as gas saturation is increased (**Figure 3-2**). He contributed this phenomenon to the pores in which the non-wetting phase enters as its saturation increases (i.e., larger pores followed by successively smaller ones). As pore size decreased, its contribution to the relative permeability diminished. Lomeland et al. (**2005**)

performed two-phase experiments using the mixed-wet core samples of the Norwegian Continental Shelf rock at reservoir condition and observed an inverse *S*-shape oil relative permeability curve. They developed a three-parameter two-phase relative permeability model.

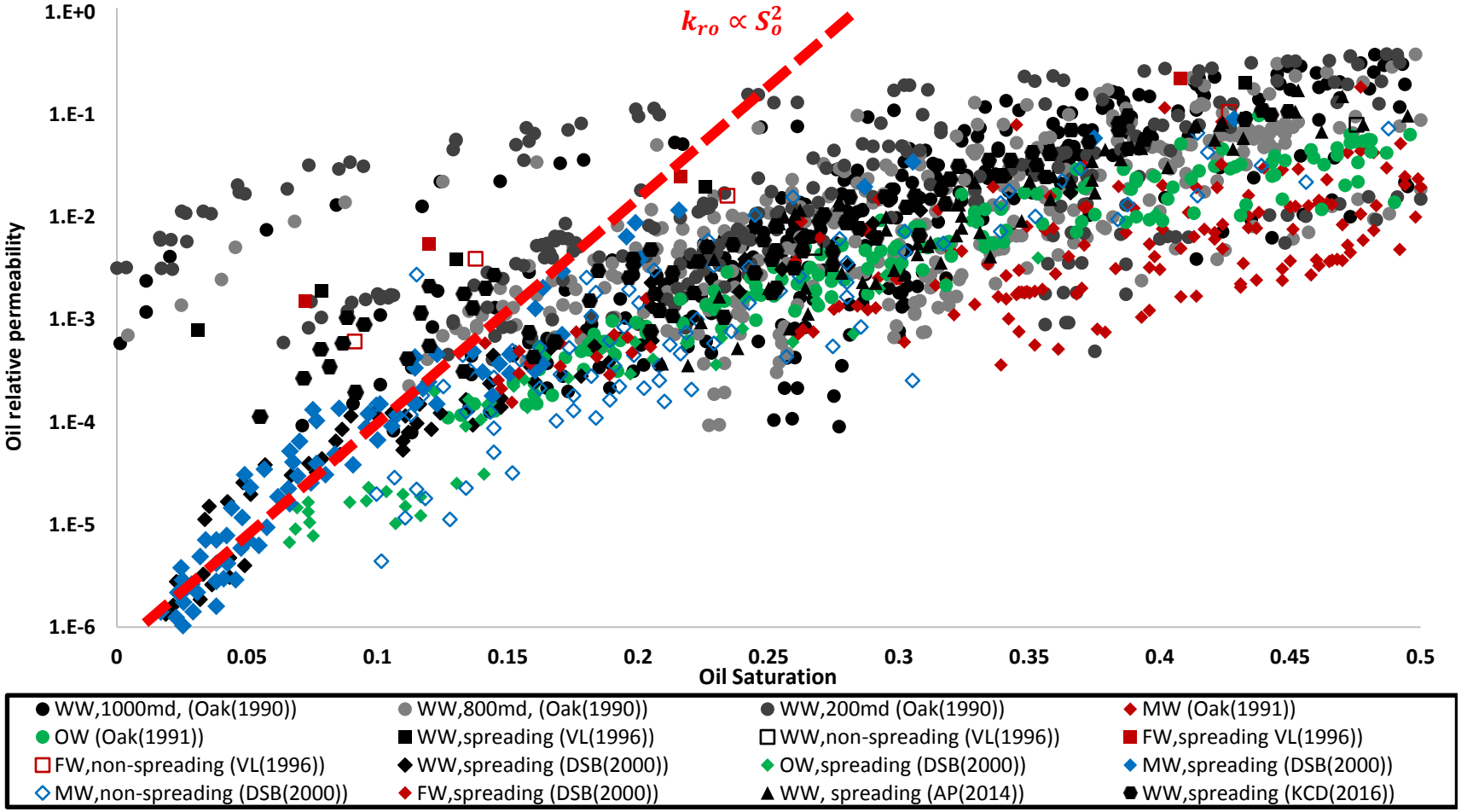

Figure 3-1: Oil relative permeability at low saturation region for selected data with various wettabilities. Oak (**1990**; **1991**): circles, Vizika and Lombard (**1996**): squares, Dicarlo et al. (**2000**): diamonds, Alizadeh and Piri (**2014**): triangles, and Kianinejad et al. (**2016**): hexagonal. Rock wettabilities of samples include water-wet (black and gray), mixed-wet (blue), fractional-wet (**Fredenslund et al., 1975**), and oil-wet (**Greenberg & Møller, 1989**). Open symbols denote a positive oil spreading coefficient, and closed symbols indicate a negative oil spreading factor. Red dashed line represents a quadratic fit at low oil saturation region ($S_o<S_{orw}$).

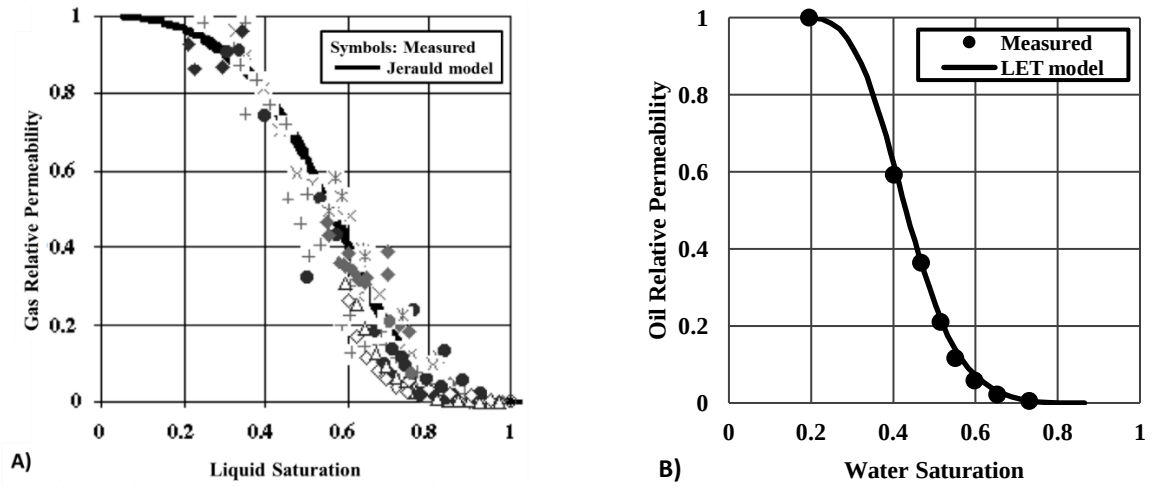

Figure 3-2: Inverted s-shape behavior of oil and gas relative permeability curves on two mixed-wet rocks at high saturation region: **A**) Gas relative permeability for Prudhoe Bay (**Jerauld, 1997b**); **B**) Oil relative permeability for Norwegian Continental Shelf (**Lomeland et al., 2005**).

3.1.2 Rock wettability and fluid spreading

Pore-scale wettability (see **Rock wettability** in Appendix A) coupled with rock wettability plays a pivotal role in multiphase displacement and oil recovery. Owens and Archer (**1971**) studied the effective oil permeability in two-phase flow for a range of wetting condition in the fired Torpedo cores. They observed that rock-wetting preference has a significant effect on oil-water relative permeability. Jerauld (**1997c**) confirmed the variation in water and oil relative permeability with depth where the rock wettability changes from more oil-wet preference toward more water-wet as samples taken higher on Prudhoe Bay structure with lower initial water saturation to lower on the structure with higher initial water saturation. Based upon the pore-network modeling results, the wettability alteration may be due to a clustering process where different intermediate-wet states are resolved into mixed-wet and fractional-wet states (**Dixit et al., 1999**). The fluid films located in the corners of the pores may also alter the intra-pore wetting within a given pore geometry (**Hui & Blunt, 2000**). Vizika and Lombard (**1996**) showed that within three-phase gas drainage in oil-wet sands, gas relative permeability does not change both for spreading and non-spreading oil. DiCarlo et al. (2000) showed that gas relative permeability in an oil-wet sand is smaller than in a

water-wet sand and concluded that gas is not necessarily the non-wetting phase.

In addition, fluid spreading (see **Fluid spreading** in Appendix A) impacts relative permeability. In the study of gas-assisted mobilization of residual oil to water in water-wet displacements, Øren et al. (**1992**) showed that displacement efficiency depends on the sign of the oil/water spreading coefficient: non-negative spreading coefficient resulted in higher oil recovery. Later, Øren and Pinczewski (**1994**) conducted tertiary immiscible gasflood under quasi-static conditions for the oil-wet displacement under positive or negative spreading coefficient. They showed that oil recovery is the highest for the oil-wet state with positive spreading coefficients and is the lowest for water-wet and negative spreading conditions. For water- and oil- wet conditions, the intermediate phase is displaced by a double-displacement mechanism: a gas/oil displacement (first drainage event) followed by a water/oil displacement (second drainage event) where the reconnection and mobilization of the oil drops happens.

3.1.3 Pore structure

Pore structure is a microscopic property and plays a vital role in multiphase fluid displacement and relative permeability. It impacts relative permeability directly and indirectly. Researchers have identified direct impact of pore-structure properties on relative permeability keeping other parameters relatively constant. In addition, the pore structure affects other macroscopic parameters in relative permeability models such as saturation and trapping.

Pore structure properties include pore size, geometry, and topology. This simple statement has several implications making the complete assessment of all impacting parameter on relative permeability an intricate task. In the following section, we briefly address rock mechanics which may strongly affect relative permeability. Next, we review constituting elements of pore structure.

Rock mechanics

We focus on geomechanical and geochemical parameters of the rock mechanics that affect fluid

displacement by impacting pore structure. Mechanical effects are rarely considered in relative permeability measurement and modeling (cf. **Maloney & Brinkmeyer, 1992**). However, geomechanical effects lead to varying the pore confining pressure which, in turn, alters pore/throat size and their distribution in subsurface applications. Consequently, a *geomechanical-dependent* relative permeability is expected.

In addition, the geochemical reactions may change the pore structure and cause variation in rock porosity and wettability which can alter relative permeability data. For example, during the long-time geological carbon storage, CO_2 mineralization (see **Trapped saturation** in Appendix A) continuously evolves the local pore structure. The CO_2 precipitation then may contribute to well injectivity impairment due to changed relative permeability. Currently, the measurement of variation in relative permeability induced by precipitation of CO_2 is challenging. Jiang and Tsuji (**2014**) investigated numerical simulation based on a coupled flow and reactive transport model using the lattice Boltzmann approach. They concluded that variation of the rock microstructure adversely impacted the relative permeability of non-wetting phase, particularly for small wetting saturations.

Quite undeservedly, the impact of geochemical reactions on the geomechanical behavior of porous media is commonly overlooked. Again, like the geochemical effect, it is still not common to implement a *geochemical-dependent* relative permeability model in reservoir simulation studies. Indeed, one of the underlying assumptions of relative permeability models is to exclude possible chemical reactions.

Pore geometry

Relative permeability depends on the pore geometry (see **Pore geometry** in Appendix A) (**Morgan & Gordon, 1970**; **Jerauld & Salter, 1990**; **Dernaika et al., 2013**). The micro-scale properties of pore geometry directly affect macroscopic reservoir properties and relative permeability particularly for water-wet states (**Wardlaw, 1982**).

Pore size

As pore size decrease (finer-grain size) (see **Pore size** in Appendix A), rock specific surface area (i.e., the rock wetted area per unit bulk volume) increases. In that fluid velocity is zero at the surface during fluid flow, this is reflected in less tendency for fluid flow in porous media. As a result, the larger the pore sizes, the lower connate water saturation, and the higher pore-space for multiphase flow is predictable. It implies that the larger pore sizes induce a higher end-point relative permeability and potentially a larger area of the spanned saturation space (**Morgan & Gordon, 1970**; **Wardlaw, 1982**).

Pore network topology

Pore network structure affects fluid flow in porous media by the degree of network connectivity subjecting to network topology (see **Pore structure** in Appendix A). Both mean and distribution of coordination number may impact relative permeability and residual saturation. Further, the coordination number distribution may affect relative permeability from a network modeling perspective.

Based on a 3D network model, Jerauld and Salter (**1990**) concluded that network properties including relative permeabilities for a Voronoi network with broad distribution of coordination number matched those of a lattice network with identical mean coordination number but a narrow distribution of coordination number. This results contrasts with the conclusions of Arns et al. (**2004**) who found that computed relative permeabilities by regular or stochastic models were not in agreement with those of the rock network. The researchers generated network models from tomographic images of Fontainebleau sandstone (**Lindquist et al., 2000**) and compared drainage relative permeability curves derived from the images with those of calculated for the equivalent network model. The discrepancy between relative permeabilities states that even when identical geometric properties, pore and throat sizes, are implemented in the model but a fixed mean coordination number is applied in the model, the relative permeability and residual saturations

differed significantly. Nevertheless, honoring the full coordination number distribution of the rock network, the investigators could reproduce relative permeability values in agreement with those of the sandstone rock network. Pore aspect ratio could also impact phase relative permeability through the phase trapping (discussed in Chapter 4).

3.1.4 Interacting forces

The buoyancy, capillary, and viscous forces act on both displacing and displace fluids. These interacting fluids are not collinear and can be generalized as one group (i.e., trapping number) (see **Capillary and trapping number** in Appendix A). Trapping number consists of the viscous, gravitational, and capillary effects. The relative permeability parameters can be modeled based on a comparative approach between two extreme values of trapping number (see **Trapping number effect**). The direct impacting parameters include fluid density, fluid potential, rock permeability, and interfacial tension. The trapping number also include implicitly added parameters such as temperature, interface composition between two immiscible fluids. However, the defined trapping number does not contain wettability and spreading effects on relative permeability. Moreover, it does not represent direct compositional effects on relative permeability.

3.1.5 Permeability

Empirical relative permeability models generally add absolute permeability implicitly to their formulation. Since the permeability is directly proportional to pore/throat size distribution, it is a valid assumption to consider its impact through other parameters that represent the pore/throat size and distribution of rock. Lower-permeability rocks often have broader pore-size distribution and poor sorting. This results in lower displacement efficiency: higher capillary pressure exponent and higher liquid relative permeability exponent.

Researcher have quantified scale-dependent relative permeability particularly due to the heterogeneity effect (**Honarpour & Saad, 1994**; **Honarpour et al., 1995**; **Jones et al., 1995**). It

highlights the significance effect of permeability distribution in pore-scale with smaller correlation length than the upscaled reservoir simulation elements. In addition, conventionally, the core-scale laboratory measurements are conducted include 1D experiments. Application of the derived relative permeability for field scale variation is, therefore, questionable. Even if the change in permeability is considered in full scale (i.e., a second-order tensor) is applied to the simulator, the relative permeability from 1D experiments does not necessarily replicate the actual fluid displacement in a 3D anisotropic porous media.

3.1.6 **Fluid composition**

Relative permeability is a function of phase(s) saturation as well as phase composition. Phase composition affects fluid distribution in a porous medium through IFT and spreading coefficient. For a designated saturation, phase composition impacts the interplay of gravitational, viscous, and capillary forces through the interfacial phenomena and its associated parameter (i.e., interfacial tension). It delineates the dependency of relative permeability on the ratio of effective forces on the displaced fluid. IFT is viewed as the *indirect* introduction of compositional effects on relative permeability.

Besides, the direct impact of fluid composition and phase behavior on relative permeability is more pronounced for fluids with a higher interphase mass exchange (see **Compositional demanding processes**). The oil and gas phases approach a single hydrocarbon phase in the near-miscible displacements and for the near-critical fluids. Consequently, the densities of fluids approach a unique value and that applying phase identification based on a reference fluid density may fail for either of these phases. Here, incorrect phase labeling (i.e., phase flipping) is possible and causes a discontinuity in relative permeability curve at that time step (**Jerauld, 1997b**; **Yuan & Pope, 2012**). This behavior is not supported with physical behavior of the fluid above. As phase flipping occurs, it leads to convergence issues in compositional reservoir simulation. More

precisely, density-based phase identification is not a general and valid methodology for the near-critical fluid flow modeling. As a result, phase identification and conventional relative permeability models may fail for such conditions.

Furthermore, each relative permeability function must be mathematically continuous as phases appear/disappear both for practical physical applications and to achieve mathematical convergence and numerical instabilities. Quite undeservedly, the *direct* compositional effect has been neglected in several multiphase flow approaches.

These lend credence to the idea that thermodynamics can facilitate the estimation of compositional-dependent relative permeabilities. There have been few attempts to generate relative permeabilities directly from the thermodynamics. Nonetheless, the proposed routines are generally too complicated for purposes of general field-scale compositional modeling. For instance, Papatzacos and Skjæveland (**1987b**) presented a two-phase one-component flow model by assuming a stabilized flow type. The proposed model requires capillary pressure, the equation of state (EOS), and an adjusting parameter proportional to the width of the transition region between phases.

Alternatively, one may develop the constitutive laws for compositional flow rather than applying an extension of Darcy's law. Several approaches have been attempted to more accurately represent a thermodynamically-consistent behavior of the multiphase/multicomponent fluid flowing in porous media. These phenomenological approaches include mixture theory (**Bowen, 1982**) and the homogenization-theory-based methods. The latter may be categorized as (**i**) the weight-function methods from non-equilibrium thermodynamics (**Matheron, 1965**; **Marle, 1982**; **Kalaydjian, 1987**) and (**ii**) the pore-averaging methods based upon the representative elementary volume (REV) concept (**Hassanizadeh & Gray, 1990**; **Gray & Miller, 2005**; **Nordbotten et al., 2008**; **Niessner & Hassanizadeh, 2009**).

The pore-averaging methods, for instance, define the averaging microscale quantities at a

REV regarding the microscopic ones (**Hassanizadeh & Gray, 1990**). The volume averaging methods bridge the length-scales of interest and cover a broad range of quantities including macroscopic thermodynamic properties, e.g., mass density, entropy, internal energy, interfacial velocities and curvatures, contact angle, and macroscale pressure and gravity potential among others. Providing a representative REV, this physically-based method may result in the thermodynamically consistent results particularly when the impact of saturation gradient on relative permeability is considerable, e.g., moving front in an immiscible gas injection project. Based on a mere thermodynamic approach, Hassanizadeh and Gray (**1990**) derived the Darcy velocity for two-phase flow, and that capillary pressure depends on the Helmholtz free energy variation with saturation. They then concluded that relative permeability depends on the saturation gradient; the Helmholtz free energy is saturation-gradient-dependent which in turn is non-negligible in unsteady-state fluid flow.

The required constitutive relationship in pore-averaging methods requires the solution of mass, momentum, and energy in pore-scale followed by a volume-averaged pore-scale conservation equation for the macro scale. One must then formulate the entropy production at an equilibrium condition and obtain its absolute minimum (**Niessner et al., 2011**). This implies that although these methods could represent the underlying mechanisms of the multiphase flow in porous media more accurately than the commonly applied practices, they currently have limiting applicability in the field-scale modeling; they are expensive both from laboratory measurement and computation point of view. Moreover, the representative REV for each reservoir section at the pore-level scale must be available for this method.

To apply the conventional approaches for the compositional-dependent flow, researchers have resorted to adding the secondary parameters to the relative permeability term of the Darcy's law. Jerauld (**1997b**) proposed a gas-like parameter after the Parachor-weighted molar density of immiscible oil, gas, and current condition. Hustad and Holt (**1992**) related the endpoint saturation

to the ratio of IFT under the present state of an immiscible state and also scaled the two-phase relative permeabilities. Masalmeh and Wei (**2010**) proposed linear and logarithmic interpolation schemes for the IFT-dependent relative permeability to integrate compositional effects and hysteresis in relative permeability modeling.

Direct phase composition along with pressure and temperature effects can also be added by introducing an appropriate thermodynamic property to the relative permeability model. That is a continuous and compositionally consistent relative permeability function (**Yuan & Pope, 2012**; **Beygi et al., 2015**). This methodology provides both the compositional effect and facilitates modeling the likely effects of pressure and temperature on relative permeability. To avoid any discontinuities in the relative permeability function, Yuan and Pope (**2012**) indicated that relative permeability must be a function of intensive thermodynamic properties that are continuous at local thermodynamic equilibrium. They proposed the molar Gibbs Free Energy (GFE) of each phase available from flash calculations in compositional simulations. Among different thermodynamic properties, GFE was selected in that it directly matches the local equilibrium requirement in compositional simulation (i.e., constant pressure and temperature at each time level). This model applies a GFE-averaged interpolation scheme for relative permeability parameters. It is noteworthy that this method is inherently *relative*: it relates the reference and current states of each phase. In other words, one requires at least two sets of measured data at the extreme conditions of the anticipated process confirming no extrapolations occur within the saturation nor the compositional space. This method requires relative permeability functions that can be interchangeably used for all phases. It alleviates labeling the phases as water/oil/gas, resolves the phase-flipping issue due to the incorrect phase labeling, and results in continuous relative permeability curves.

In addition, even though the relative permeability functions are continuous, the modeling errors lead to discontinuities in the calculated relative permeabilities. As a result, the compositional effects must be added to the relative permeability model to mitigate the modeling errors. Note that

we do not point the realm of physical discontinuities due to intensive mass transfer or mechanical issues as they naturally happen and must be handled in the numerical simulation in a rigorous fashion.

3.1.7 Secondary properties

Several other physical rock/fluid properties can impact relative permeability. They include but are not limited to, fluid viscosity, fluid density, pressure, and temperature. The empirical correlations only implicitly include their dependence. For example, fluid viscosity and density can be coupled in the viscous and buoyancy terms of trapping number, respectively. Temperature and pressure impact fluid physical properties and composition. If compositional effects are included in relative permeability models, it is required to establish the formulations for the pressure-temperature dependency. Pressure term can also affect the geomechanical parameters and, in turn, pore structure.

3.2 RECOMMENDED FEATURES OF A NEW THREE-PHASE RELATIVE PERMEABILITY MODEL

A reliable three-phase relative permeability model should have the following characteristics to be applicable in reservoir simulators for field-scale studies in different rocks, fluids, and recovery processes:

1. **Validity**: the functional form of the model must be robust and capture the essential fluid displacement in saturation space and for a full range of rock wettabilities:

1.1. *Spanning saturation space*: The model must capture multiphase fluid flow behavior over the full saturation and composition spectrums. During reservoir modeling, phase saturation (or composition) could approach to the extreme regions of the associated space. It includes the extremely low/high saturation and processes involved in a great interphase mass exchange. This confirms that the relative permeability model reconciles the entire experimental and field observations.

1.2. *Robustness*: the model must mathematically be continuous for any saturation combination without facing singularities or discontinuities either in the functional form of the formulation or its derivatives. Balbinski et al. (**1999**) showed that the three-phase relative permeability models having implied residual saturation result in an inconsistent set of relative permeability and unphysical results. Nevertheless, there are some physically supported discontinuities which cannot be avoided, e.g., when one phase disappears/appears due to mass transfer with the other phases.

2. **Simplicity**: it should be mathematically simple to be practically applicable in compositional reservoir simulators. Equations with a minimum of parameters have advantages over tables. Equations can be used to fill in gaps in the experimental data and to smooth the experimental data. For the complex three-phase flow with hysteresis depending on interfacial tension, wettability, and composition, many tables would be required to represent the entire range of relative permeability. Thus, there would never be sufficient experimental data to construct such tables accurately. An excellent analytical model will be consistent with physically correct limits among other advantages over tables. Besides, among a diverse set of three-phase model, the ones with a minimum of parameters have advantages over complex models. The more complex mathematical functions are computationally more expensive and add a limited accuracy to the predictions.

3. **Versatility**: the desired model should be representative of phase behavior without changing the formulation neither for different phases nor the rock wettability condition:

3.1. Phases: one general formulation should apply to three phases. This is desirable when the fundamental state of the fluid is not available, and the identification number of each phase together with its thermodynamic characteristics are the only available parameters for relative

permeability modeling. Here, we require the compositionally-consistent models. Another advantage of the versatile models is the ease of implementation into the reservoir simulators. This results in a less computational cost and coding/debugging efforts.

3.2. *Rock wettability*: A reliable model should be flexible in selecting the rock wettability state without implementing redundant task to adjust the model. The rock wettability option is particularly of interest for the intermediate wet states.

3.3 LIMITATIONS OF CURRENT THREE-PHASE RELATIVE PERMEABILITY MODELS

Relative permeability models are expected to capture the fundamental mechanisms of multiphase flow in porous media and honor the associated impacting parameters on relative permeability. Among impacting parameters on relative permeability, some parameters are deduced from microscopic observations which have not rigorously been upscaled to macro-scale applications as required by Darcy's law. Those microscopic parameters impede the direct implementation of microscopic parameters as necessary for the modeling of a larger length-scale bearing the complicated heterogeneity as introduced at the core- and field-scale applications. Further, it inherently leads to the limiting applicability of the empirical three-phase relative permeability models.

Several investigators have identified various limitations of classical three-phase relative permeability models (**Fayers & Matthews, 1984**; **Delshad et al., 1987**; **Baker, 1988**; **Oak, 1991**; **Hustad & Holt, 1992**; **Skjæveland & Kleppe, 1992**; **Balbinski et al., 1999**; **Pejic & Maini, 2003**; **Spiteri & Juanes, 2006**; **Ahmadloo et al., 2009**). In the following, we review general drawbacks of the popular multiphase relative permeability models:

1) **Rock wettability**: **Table 2-3** shows that approximately 60% of independent three-phase relative permeability models are proposed for the water-wet rocks. As discussed in **Appendix A**, however, there are several petroleum-bearing rocks with a non-strongly-water-wet

preference. The wettability state then impedes the models to estimate the multiphase relative permeability accurately only because their wettability affinity is not on par with the theoretical or experimental backgrounds of the available models.

Commonly, a questionable approach to tackling this limitation of the popular relative permeability models is to keep the as-is relative permeability formulation and change the wetting-phase label in the model to switch water- and oil-wet conditions. Besides, Stone proposed extension methods to oil-wet rocks. Blunt (**2000**) discussed limitations of approaches above. Even if the proposed methodology is valid for both the strong wettability conditions, its application leads to the erroneous results for the intermediate wet state.

2) **Fluid configuration**: there are empirical correlations routinely applied based on an assumed fluid configuration and pore occupancy that are difficult to generalize to another fluid configuration. As described in **Appendix A**, fluid configuration and flow in porous media may delineate regions outside of the assumed fluid configurations in the relative permeability models. Consequently, there are areas in the saturation space where the commonly used three-phase relative permeability models fail to replicate their physical behavior. The extreme values of phase saturation are the primary source of uncertainty in modeling fluid mobility.

The low-saturation region cannot adequately be represented by the available three-phase relative permeability models. Balbinski et al. (**1999**) and Pejic and Maini (**2003**) demonstrated the shortcomings of Stone I and Stone II models and their variations to match two sets of three-phase experimental results. They showed that at saturations near residual oil saturation (S_{orm}), Stone models gives $k_{ro} \propto S_o - S_{orm}$. The results of Stone I and II models are not supported with many experimental data at this low oil saturation below the waterflood residual oil saturation (S_{orw}).

The high saturation value region for a non-wetting phase, e.g., gas phase in mixed-wet rocks, results in continuously decreasing the slope of phase relative permeability (see **High**

saturation region). Currently, except for the multiphase relative permeability models of Jerauld (**1997b**) and Lomeland et al. (**2005**), the commonly used three-phase relative permeability formulations do not replicate this S-shape behavior of phase relative permeability.

3) **Residual saturation**: One of the shortcomings of widely used three-phase relative permeability models to predict the actual behavior in three-phase flow initiates from the incorrect residual saturation prediction. The dynamic behavior of residual saturation in multiphase flow results in primarily variable residual saturation far from initial two-phase measured residual saturation. Balbinski et al. (**1999**) and Blunt (**2000**) investigated the impact of residual oil saturation on the Stone I relative permeability model and the implied residual oil saturation by Stone II model. They realized that there is an inconsistency in the choice of residual oil saturation for the Stone I model. The Stone II formulation results in mathematically singular function of residual oil saturation regarding angular variable 'ψ' (i.e., indicating the balance of water and gas saturations) near the two-phase residual oil saturation. This leads to non-monotonic variation and over-prediction of three-phase residual oil saturation from the Stone II model. Consequently, Stone I and Stone II models may either overestimate or underestimate the oil relative permeability when oil saturation is small.

4) **Model Robustness**: relative permeability function must mathematically be continuous for any saturation combination without facing singularities or discontinuities either in the functional form of the formulation or its derivatives. Balbinski et al. (**1999**) showed that the three-phase relative permeability models having implied residual saturation result in an inconsistent set of relative permeability and unphysical results. Note that there are some physically supported discontinuities which cannot be avoided. For example, when one phase disappears/appears due to mass transfer with the other phases it inherently introduces

discontinuous behavior of phase mobility.

3.4 PREMISES OF UTKR3P MODEL

Based on the studied laboratory/field experimental results, the following are the premises of developing a parameterized-level relative permeability model:

1. Three-phase relative permeability parameters including endpoint relative permeability and curvature quantities do not exceed those of two-phase parameters.
2. Two-phase fluid pair relative permeability parameters are not unique. For example, two-phase end-point relative permeability when flowing with water can be different than that of oil-gas flow.
3. Saturation history (direction and trajectory) affects relative permeability. Regarding the saturation direction, the free saturation is calculated as the difference between the current state total saturation and trapped saturation. Free saturation represents the current state saturation both for increasing and decreasing phase saturation processes.
4. Residual saturation is not unique. It depends on the saturation trajectory, composition, and rock wettability. Three-phase residual saturations can take either higher or lower values than the two-phase flow values.
5. Both phase and interface compositions can affect relative permeability. The direct compositional effects represent the variation of phase or interface composition on relative permeability.
6. Relative permeability curves show either a power-law or an inverse S-shape. The functional form of relative permeabilities remains continuous in saturation and composition spaces.

3.5 UTKR3P MODEL

The general form of relative permeability is based on an extension of the formalism that Jerauld

(**1997b**) used for gas phase modeling. For phase 'j' flowing with phases 'm' and 'l', relative permeability is given by:

$$k_{rj} = k_{rj}^{0} \frac{(1+C_{2j})\bar{S}_j^{C_{1j}}}{1+C_{2j}\bar{S}_j^{C_{1j}\left(1+\frac{1}{C_{2j}}\right)}}, \qquad j\text{= phase 1, 2, or 3,} \qquad \textbf{Eq. 3-1}$$

where normalized saturation is defined as,

$$\bar{S}_j = \frac{S_j^f}{1-\sum_{i=1}^{3} S_{ir}^{3P}}. \qquad \textbf{Eq. 3-2}$$

Here, S_j^f denotes free saturation defined as the difference between phase j total saturation and trapped saturation $\left(S_j^f = S_j - S_{jt}\right)$. Trapped saturation ($S_{jt}$), in turn, is estimated from a hysteresis model, e.g., Carlson (**1981**) or UTHYST model (**Beygi et al., 2015**), and will be discussed in Chapter 4. The denominator of normalized saturation (**Eq. 3-2**) contains three-phase residual saturations (S_{ir}^{3P}). Three-phase parameters (F_j) (i.e., phase endpoint relative permeability (k_{rj}^0) and curvatures (C_{1j} and C_{2j})) are estimated using a linear saturation-weighted interpolation between two-phase parameters as follows:

$$F_j = \frac{S_m^* F_{jm} + S_l^* F_{jl}}{S_m^* + S_l^*}, \qquad \textbf{Eq. 3-3}$$

where F_{jm} and F_{jl} are two-phase pair parameters (k_{rji}^0, C_{1ji}, or C_{2ji} and i=m or l). Supercript '$*$' shows effective saturation (see **Effective saturation** in Appendix A). Adopting a zero minimum saturation in the defintion of effective saturation ($S_i^* = S_i - S_{ic}$), does not change the general form of the UTKR3P model. A zero minimum saturation is discernable when this parameter either is not experimentally measured.

Eq. 3-1 is general and generates either an S-shape (double-curvature: C_{1j} and C_{2j}) or

Corey-type (one curvature (power-law): C_{1j}, where C_{2j}=0) relative permeability curves. At small saturations, the equation approaches Corey-type behavior leading to good agreement with experimental results. The existence of a continuous oil layer, for example, in intermediate-wet states can be modeled effectively using the proposed approach. At high saturations, the second term in the denominator of **Eq. 3-1** dominates and dampens the sharp increase in relative permeability. The power exponent of the second term in the denominator of **Eq. 3-1** is chosen to be the maximum acceptable value resulting in a non-negative slope of the relative permeability curve. We provide the analytical derivative of the UTKR3P model in **Appendix E**.

3.5.1 Three-phase residual saturation

Multiphase residual saturation (S_{ir}^{3P}) is estimated using a modified correlation proposed by Yuan and Pope (**2012**). We have modified the definition of saturation from the original model to implement the effective saturation. For phase 'j', the three-phase residual saturation is defined as:

$$S_{jr}^{3P} = \min\{S_j, S_{jr}^{2P}\left(1 - b_j S_m^* S_l^*\right)\}, \quad m \neq j \neq l \qquad \textbf{Eq. 3-4}$$

where S_{jr}^{2P} is the two-phase reisdual saturation (see **Two-phase residual saturation**) and b_j is the only fitting parameter of the UTKR3P model. This residual saturation model is subject to two-phase residual saturations, rock wettability, fluid composition, and pore-filling sequence. The model is general and applicable to all phases. The conditional format of the equation confirms that the calculated residual saturation does not exceed the total saturation for each phase.

3.5.1.1 Three-phase residual saturation parameter (b)

The fitting parameter b in **Eq. 3-4** depends on rock wettability and phase composition and directly impacts relative permeabilities of all phases. The b parameter is the only free parameter per phase in the UTKR3P model. It can be evaluated based upon experimental results of residual saturation measurements. Alternatively, one may obtain this parameter from a history matching of field/lab results as commonly applied in numerical simulation where zero isoperm results in residual

saturation.

As discussed in **Isoperm** section in Chapter 2, phase relative permeability contours adopt different curvatures in ternary saturation diagram. The presented residual saturation model can capture the variation of isoperm curvature as the *b* parameter varies. In **Figure 3-3**, we show the selected phase-2 isoperms ($k_{r2} = 10^{-4}, 10^{-3}, 10^{-2}, 0.1, 0.2, \dots, 0.9, 1.0$) in the ternary saturation plot where each apex shows the maximum phase saturation ($S_i = 1, i = 1{:}3$). We assume a capillary-dominated process ($N_t = 10^{-8}$) and select the following variables and values for two-phase flow (**Table 3-1**).

Table 3-1: Two-phase parameters and critical saturation

Property	Value
Phase-1 residuals ($\boldsymbol{S_{1r2} = S_{1r3}}$)	0.195
Phase-2 residuals ($\boldsymbol{S_{2r1} = S_{2r3}}$)	0.250
Phase-3 residuals ($\boldsymbol{S_{3r1} = S_{3r2}}$)	0.200
Phase-2 end-points ($\boldsymbol{k^0_{r21} = k^0_{r23}}$)	1.0
Phase-2 1st curvature ($\boldsymbol{C_{121} = C_{123}}$)	6.0
Phase-2 2nd curvature ($\boldsymbol{C_{221} = C_{223}}$)	0.0
Critical saturation ($\boldsymbol{S_{1c} = S_{2c} = S_{3c}}$)	0.0

Next, we investigate the sensitivity of isoperms on the non-unique set of *b* parameter for the fluid parameters. **Figure 3-3** compares phase-3 isoperms ($k_{r3} = 10^{-4},\ 0.01, 0.1, 0.5, \text{and } 0.9$) when b_2 is different than that of the other two phases ($b_1 = b_3 = 3, b_2 = -3$). It reflects the sensitivity of phase-2 isoperms on $b_1, b_2, and\ b_3$ parameters and that the pronounced effect of *b* on overall predictions of the UTKR3P model. A positive b_2 value results in convex phase-2 isoperms toward its vertex particularly for higher relative permeability values (see **Figure 3-3C** and **-F**). As b_2 decreases to zero (i.e., an identical two- and three-phase residual saturation), the close-to-zero isoperms flatten (see **Figure 3-3B** and **-D**). A negative value of b_2 results in concave phase-2 isoperms when viewed from the 100% phase-2 saturation apex (see **Figure 3-3A** and **-E**). In addition, the b_1 and b_3 parameters have pronounced effects on the higher-value isoperms (compare **Figure 3-3C** with **–F**, **B** with **–D**, and **A** with **–E**).

3.5.1.2 Two-phase residual saturation

Two-phase residual saturation $\left(S_{jr}^{2P}\right)$ in **Eq. 3-4** is assumed either as the minimum of measured two-phase residual saturations $\left(\min\left(S_{jrm}, S_{jrl}\right)\right)$ or estimated based on a linear saturation-weighted interpolation between measured two-phase residual saturations (use **Eq. 3-3**). In either case, one requires to correct the two-phase residual saturations for the compositional effects due to the capillary-desaturation effect (use **Eq. 3-6**).

3.5.2 Compositional effects on UTKR3P model

We incorporate compositional effects in two ways: indirectly through the trapping number dependency (**Pope et al., 2000**) and directly through an improved compositionally-consistent method based on the model proposed by Yuan and Pope (**2012**).

3.5.2.1 Trapping number effect

In routine laboratory conditions, the reported relative permeability values are based on a capillary-dominated flow at a microscopic level. We apply the trapping number (see **Capillary and trapping number** in Appendix A) to illustrate the combined effect of the interaction forces on mobilization of trapped fluid. Two-phase parameters denoted as Q_{ji} represent any of the UTKR3P model's parameters of $k_{rji}^{0}, C_{1ji},$ or C_{2ji}. These parameters are modeled based on a capillary-desaturation approach. This method is a relative approach where two sets of experimentally measured parameters are required at low (L) and high (H) trapping numbers:

$$Q_{ji} = Q_{ji}^{L} + (1 - \theta_i)\left(Q_{ji}^{H} - Q_{ji}^{L}\right), \text{ i} = \text{phase m or l.} \qquad \textbf{Eq. 3-5}$$

Two-phase residual saturation is correlated with trapping number by the following equation:

$$S_{jri} = S_{jri}^{H} + \theta_j\left(S_{jri}^{L} - S_{jri}^{H}\right), \quad \text{i} = \text{phase m or l.} \qquad \textbf{Eq. 3-6}$$

Here, the term θ is the trapping coefficient and is a function of trapping number (N_T). Note that trapping coefficients in **Eq. 3-5** and **Eq. 3-6** are associated with phases *i* and *j,* respectively. For phase j the trapping number coefficient is calculated by,

$$\theta_j = \frac{1}{1 + T_j N_{T_j}^{\tau_j}}, \qquad \textbf{Eq. 3-7}$$

where the trapping number parameters T_j and τ_j are obtained by fitting the residual-saturation data for phase *j* displace by phase *i*.

3.5.2.2 Compositional consistency

The direct compositional effects can be added as additional option to the UTKR3P model. We discuss the description of the methodology in **Chapter 5**.

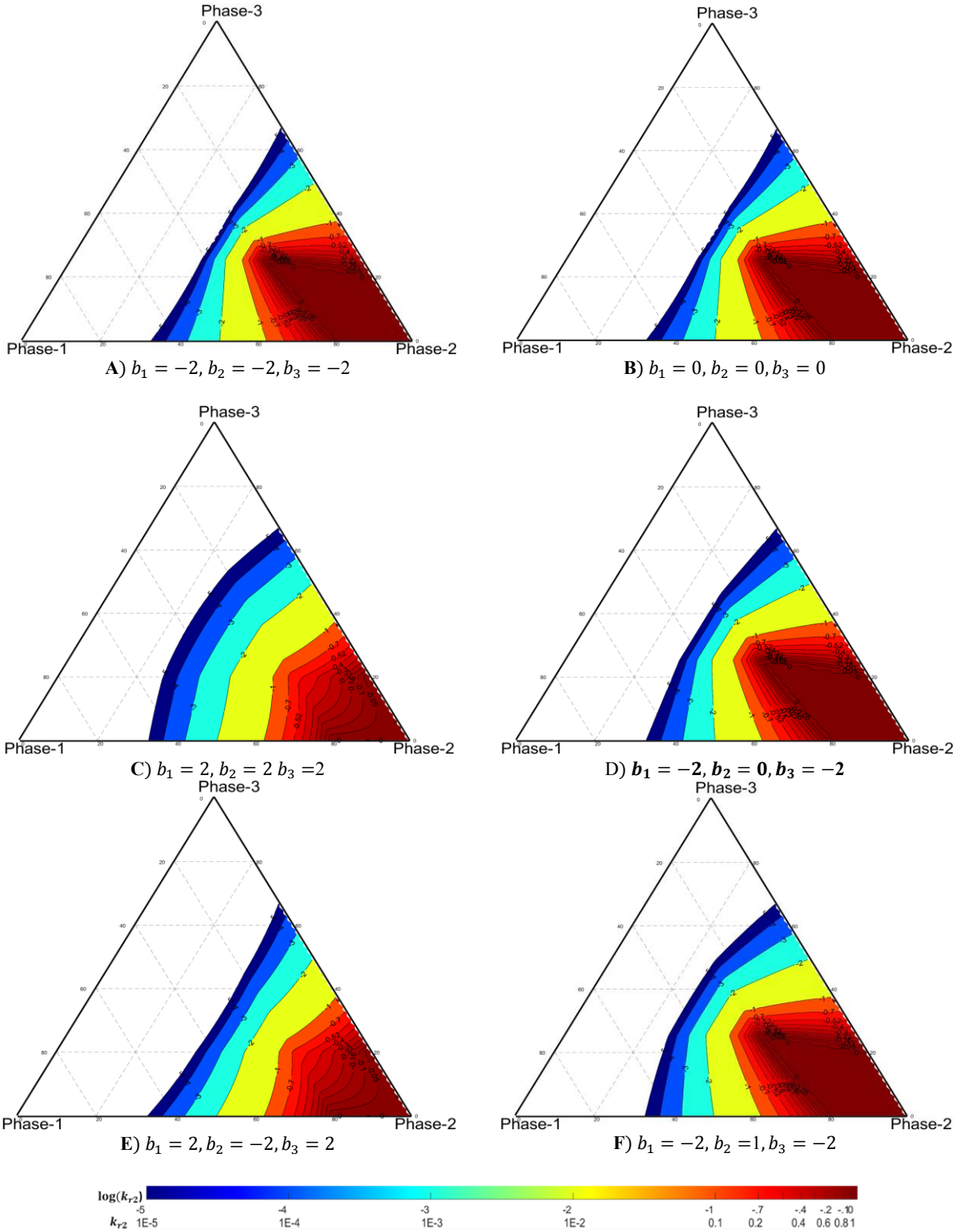

Figure 3-3: Effect of *b* parameter (**Eq. 3-4**) on curvature of phase-2 isoperms

3.6 EVALUATION OF b PARAMETER

We proceed the following procedure to evaluate the b parameter when multiphase experimental results are available. We plot the residual saturation and zero isoperm in ternary saturation and follow a curve fitting process. For the oil phase, for example, **Table 3-2** lists the Oak results (**Oak, 1990**, **1991**, **1992**) and the measured data to estimate the b_o parameter (see **Eq. 3-4**). Here, the measured two-phase residual saturations and zero oil-isoperm (k_{ro}=0) over the saturation space are input data.

To quantify the effectiveness of the residual saturation model compared to the measured three-phase data, we use the standard error of estimate (SEE) as,

$$SEE_j = \sqrt{\frac{\sum n_j \left(k_{rj}^{exp} - k_{rj}^{cal}\right)^2}{N}}, \qquad \textbf{Eq. 3-8}$$

where the superscripts $calc$ and exp denote calculated and measured relative permeability, respectively, and N is number of experimental data points for each phase. Using a MATLAB code, we adjust the b_o parameter in calculation of k_{ro}^{cal} to match the measured data ($k_{ro}^{exp} = 0$). **Figure 3-4** depicts the calculated parameters for the studied samples.

Table 3-2: Estimated b_o parameters for samples with different wettability conditions (Oak data (**1990**, **1991**, **1992**))

Sample no.	Wettability	Permeability (md)	No. of data points (k_{ro}=0)	S_{orw}	S_{org}	b_o	SEE
S-6	water	200	31	0.373	0.259	3.46	0.0191
S-13	water	1000	92	0.294	0.285	3.12	0.022
S-15	Intermediate	1010	72	0.235	0.292	1.14	0.0212
S-16	Intermediate	310	23	0.386	0.298	0.02	0.0251
S-19	Oil	208	39	0.16	0.106	1.48	0.0281
S-20	Oil	126	37	0.157	0.116	1.05	0.0156

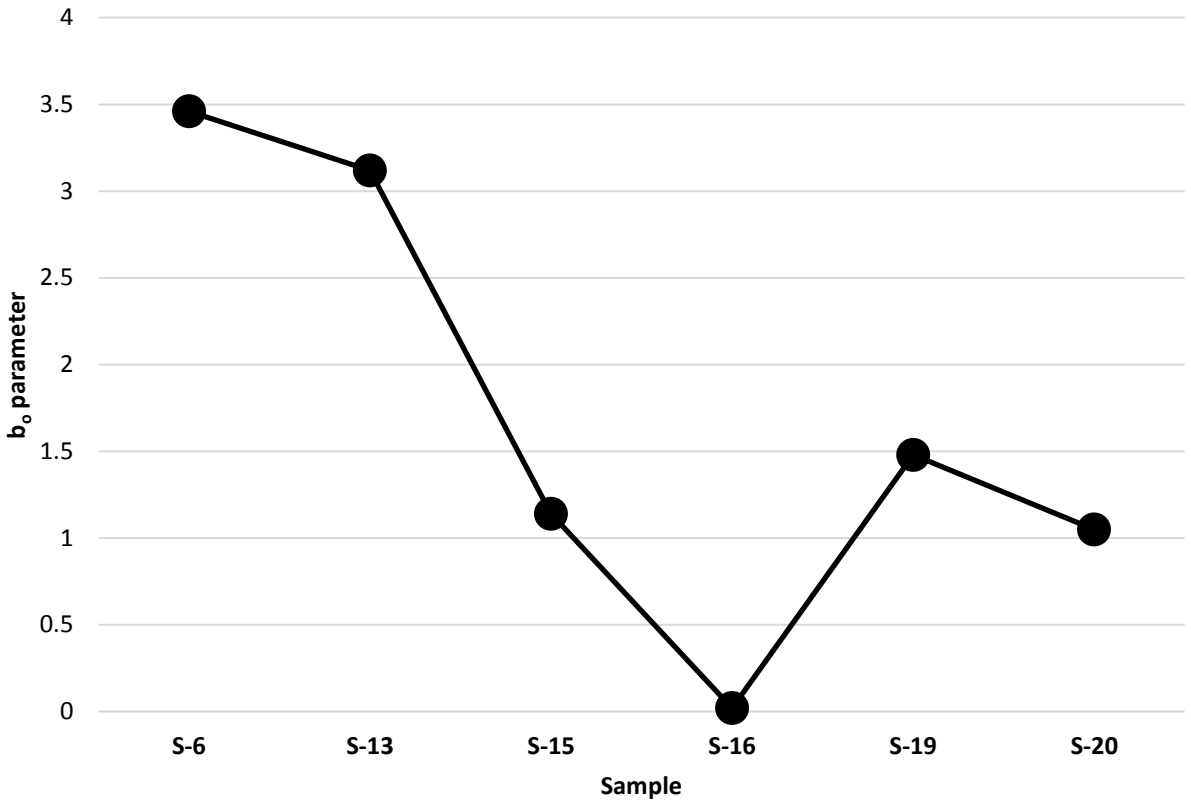

Figure 3-4: Estimated b parameter for oil phase (data given in **Table 3-2**)

3.7 UTKR3P PARAMETER SENSITIVITY ANALYSIS ON

In this section, we perform a sensitivity analysis of relative permeability parameters. For the base case scenario, we selected a set of two-phase relative permeability curves as shown in **Figure 3-5** and extracted the relative permeability parameters from it by curve fitting. The parameters for Phase-2 in three-phase flow of (Phase-1 (PH1), Phase-2 (PH2), and Phase-3 (PH3)) are listed in **Table 3-3**. Note that residual saturations, b parameter, and critical saturations are characteristic quantities for all phases. We also investigate the trapping-number dependency where two sets of parameters are listed: capillary dominated flow (low trapping number condition) and viscous/gravitational dominated flow (at high trapping number state). **Figure 3-6** represents the variation of θ parameter with trapping number (capillary desaturation effect).

Figure 3-7 shows the calculated isoperms of PH2 in a ternary saturation diagram. We increased the trapping number or its parameter (T_i) in **Figure 3-8A-D** and demonstrated that as the capillary forces decrease, the curvature of PH2 isoperms decreases. It states that by increases the trapping number, the dependency of phase relative permeability to other phases decreases and, in turn, relative permeability values increase. **Figure 3-9** depicts the variation of two-phase relative permeabilities with trapping number when the third phase is at critical saturation.

Figure 3-8E-J demonstrate the effect of two-phase relative permeability parameters on isoperms. They also compare the significance of non-unique relative permeability parameters on isoperms. For example, **Figure 3-8E** shows that by increasing both k_{r21}^{0L} and k_{r23}^{0L}, the oil isoperms are obtained at lower saturation values of PH2 than those in the base case. In addition, unequal values of two-phase endpoint relative permeabilities result in a distorted shape for the higher-value isoperms.

Figure 3-8G-J demonstrate the effect of relative permeability curvatures on isoperms. **Figure 3-8G** shows that selecting a higher value for the 1st curvatures in two-phase flow, results in a lower relative permeability compared to base case for a specified saturation. In contrary, increasing the 2nd curvature returns a higher relative permeability and shift the isoperms toward the PH2 base (see **Figure 3-8**I). Unequal two-phase curvatures result in asymmetric isoperms with respect to height of PH2.

Figure 3-8K-N reveal the vital role of residual saturations on PH2 isoperms. Not only does the variation of PH2 residuals (S_{2r1}^{L} and S_{2r3}^{L}) shift the isoperms and distort the shape of isoperm particularly at lower saturation values, but also the variation of residual saturations of other phases severely affect PH2 relative permeabilities. In addition, **Figure 3-8O-R** highlight the crucial role of *b* parameter in relative permeability behavior particularly at low saturations where the curvature of isoperms varies.

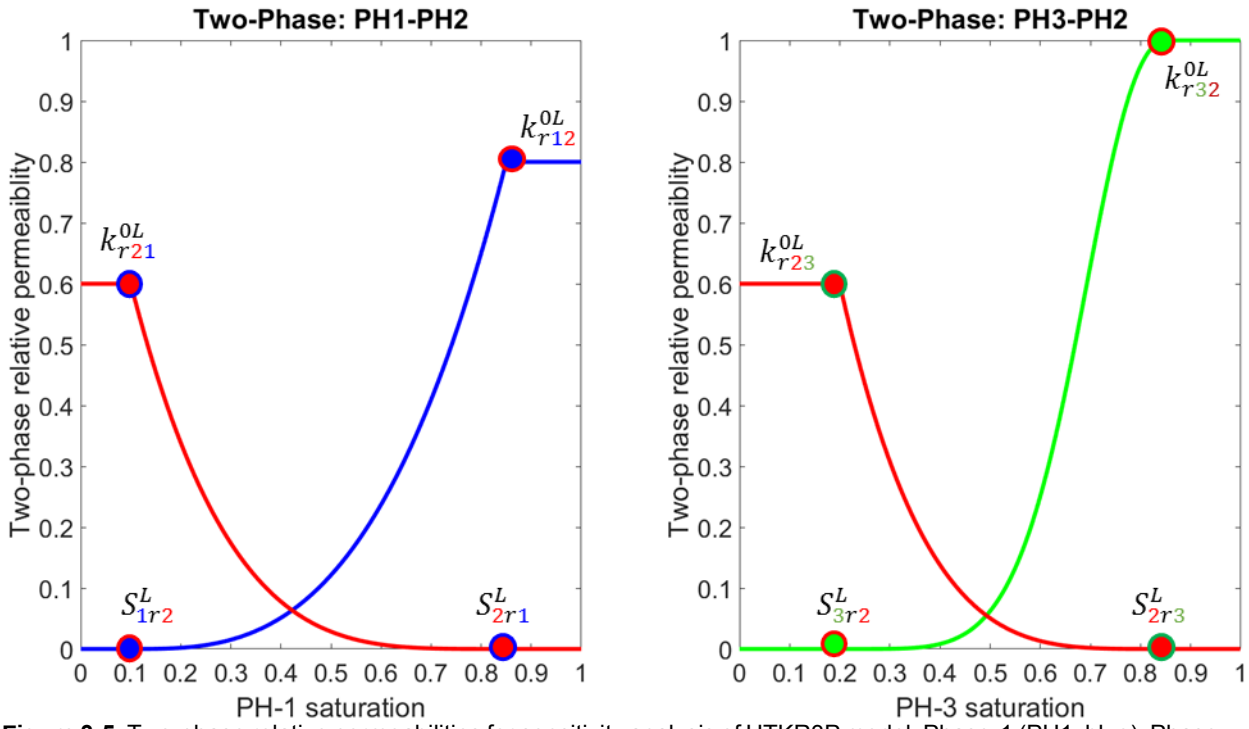

Figure 3-5: Two-phase relative permeabilities for sensitivity analysis of UTKR3P model: Phase-1 (PH1, blue); Phase-2 (PH2, red); Phase-3 (PH3, green).

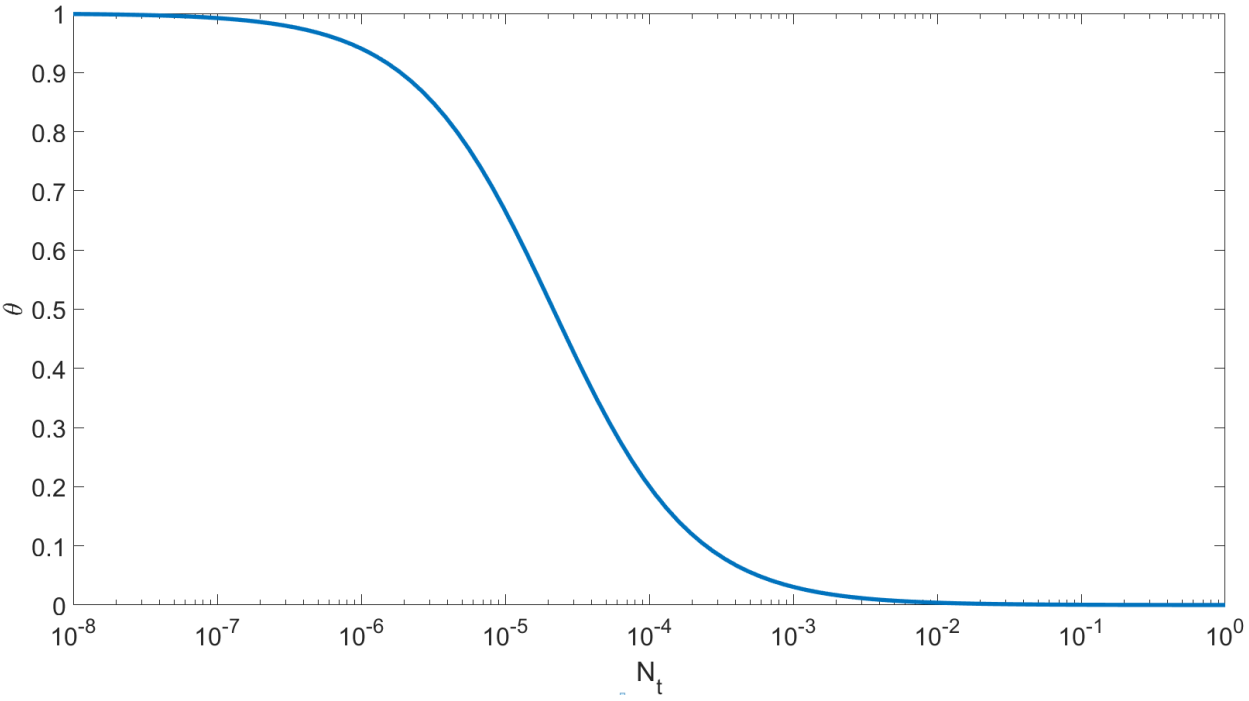

Figure 3-6: Variation of θ parameter with trapping number (see **Eq. 3-5** to **Eq. 3-7**)

Table 3-3: UTKR3P parameters for base case scenario in sensitivity analysis

Two-phase data at capillary-dominated condition (Low trapping number)	**Value**
Residual saturation of PH1 ($\boldsymbol{S^{L}_{1r2} = S^{L}_{1r3}}$)	0.10
Residual saturation of PH2 ($\boldsymbol{S^{L}_{2r1} = S^{L}_{2r3}}$)	0.15
Residual saturation of PH3 ($\boldsymbol{S^{L}_{3r1} = S^{L}_{3r2}}$)	0.20
End-point relative permeability for PH2 ($\boldsymbol{k^{0L}_{r21} = k^{0L}_{r23}}$)	1.0
1st curvature of relative permeability for PH2 ($\boldsymbol{C^{L}_{121} = C^{L}_{123}}$)	4.0
2nd curvature of relative permeability for PH2 ($\boldsymbol{C^{L}_{221} = C^{L}_{223}}$)	0.0
Two-phase data at viscous/gravitational dominated condition (High trapping number)	**Value**
Residual saturation of all phases $\left(\boldsymbol{S^{H}_{jri}}, j \neq i\right)$	0.0
End-point relative permeability for PH2 ($\boldsymbol{k^{0H}_{r21} = k^{0H}_{r23}}$)	0.8
1st curvature of relative permeability for PH2 ($\boldsymbol{C^{H}_{121} = C^{H}_{123}}$)	1.0
2nd curvature of relative permeability for PH2 ($\boldsymbol{C^{H}_{221} = C^{H}_{223}}$)	0.0
Trapping parameters *	**Value**
Trapping number ($\boldsymbol{N_{ti}}$)	10^{-8}
Trapping number parameter ($\boldsymbol{T_i}$)	1585
Trapping number parameter ($\boldsymbol{\tau_i}$)	0.9
General phase parameters *	**Value**
b_i parameter in **Eq. 3-4**	0.0
Critical saturation ($\boldsymbol{S_{ci}}$)	0.0

***** i denotes all phases (PH1, PH2, and PH3)

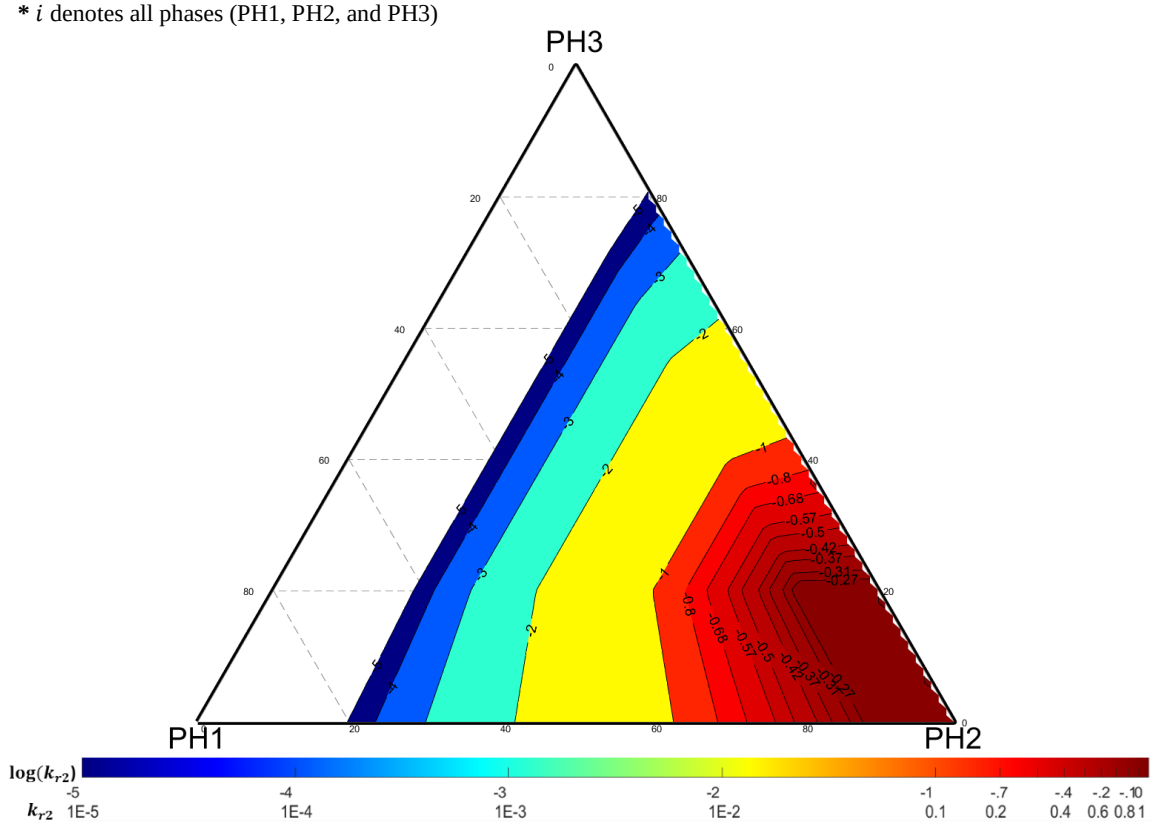

Figure 3-7: Phase-2 isoperms calculated using the UTKR3P model (Base case scenario, **Table 3-3**)

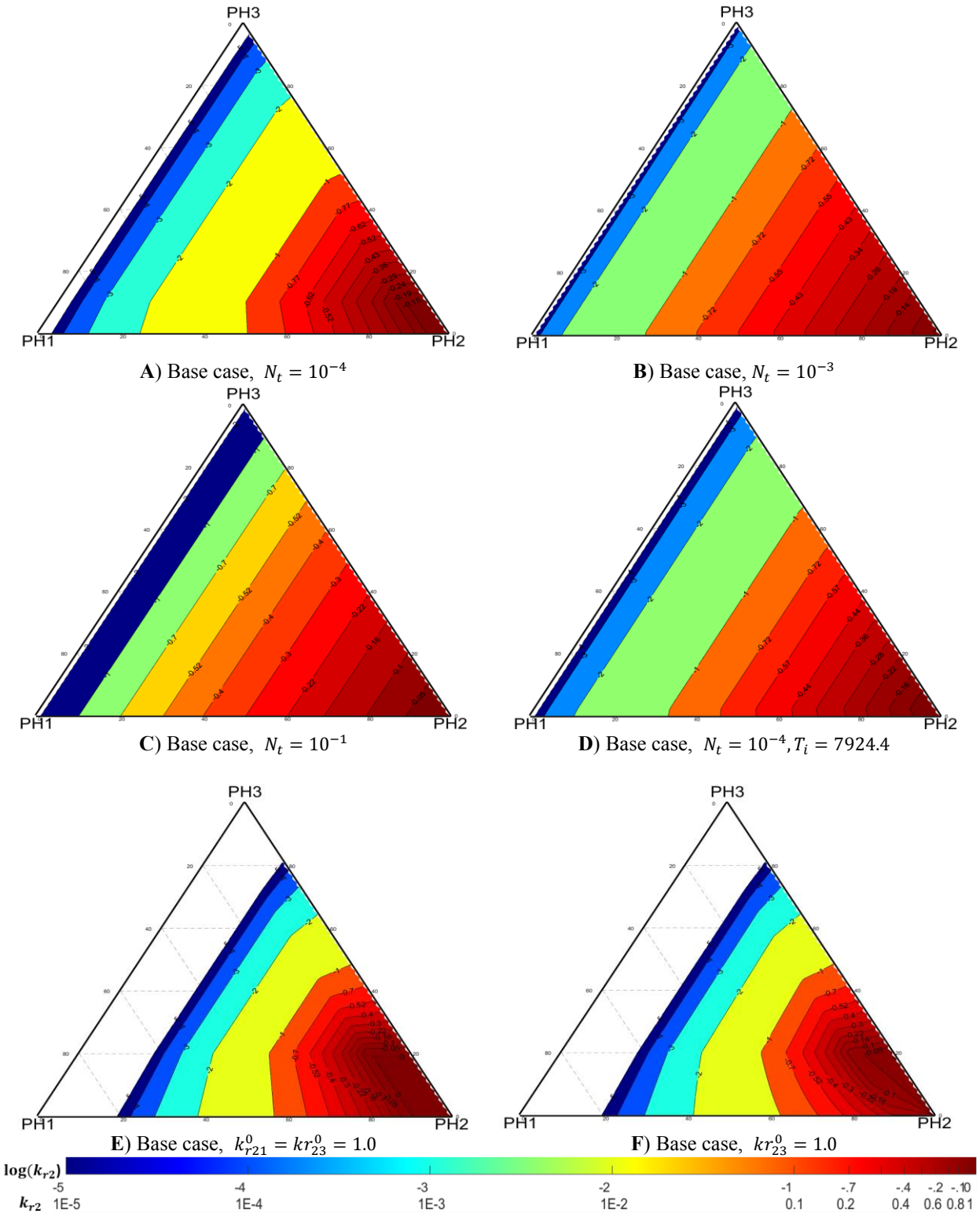

A) Base case, $N_t = 10^{-4}$

B) Base case, $N_t = 10^{-3}$

C) Base case, $N_t = 10^{-1}$

D) Base case, $N_t = 10^{-4}, T_i = 7924.4$

E) Base case, $k^0_{r21} = kr^0_{23} = 1.0$

F) Base case, $kr^0_{23} = 1.0$

Figure 3-8: Sensitivity analysis of phase-2 isoperms with relative permeability parameters

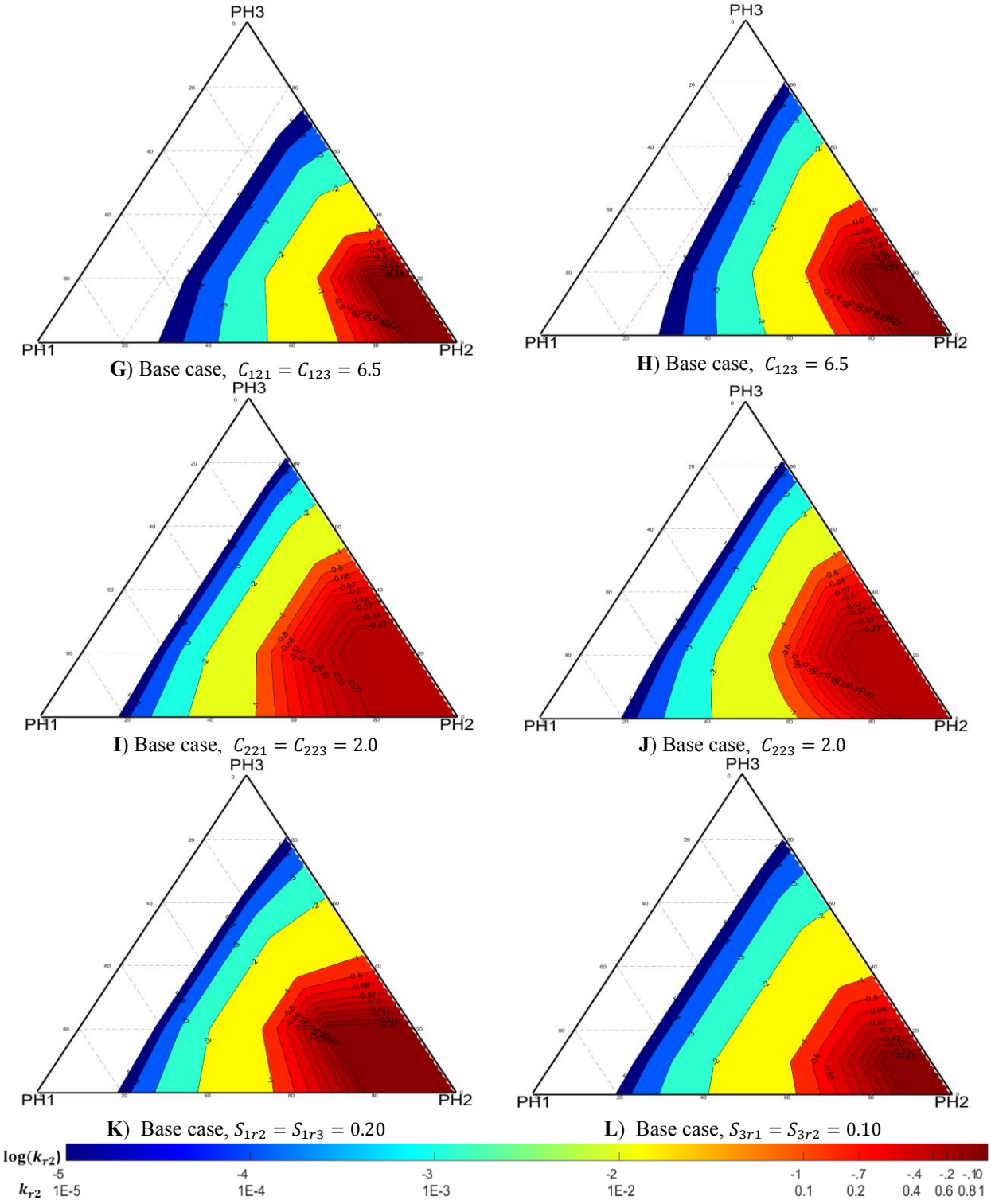

G) Base case, $C_{121} = C_{123} = 6.5$

H) Base case, $C_{123} = 6.5$

I) Base case, $C_{221} = C_{223} = 2.0$

J) Base case, $C_{223} = 2.0$

K) Base case, $S_{1r2} = S_{1r3} = 0.20$

L) Base case, $S_{3r1} = S_{3r2} = 0.10$

Figure 3-8 (cont'd): Sensitivity analysis of phase-2 isoperms with relative permeability parameters

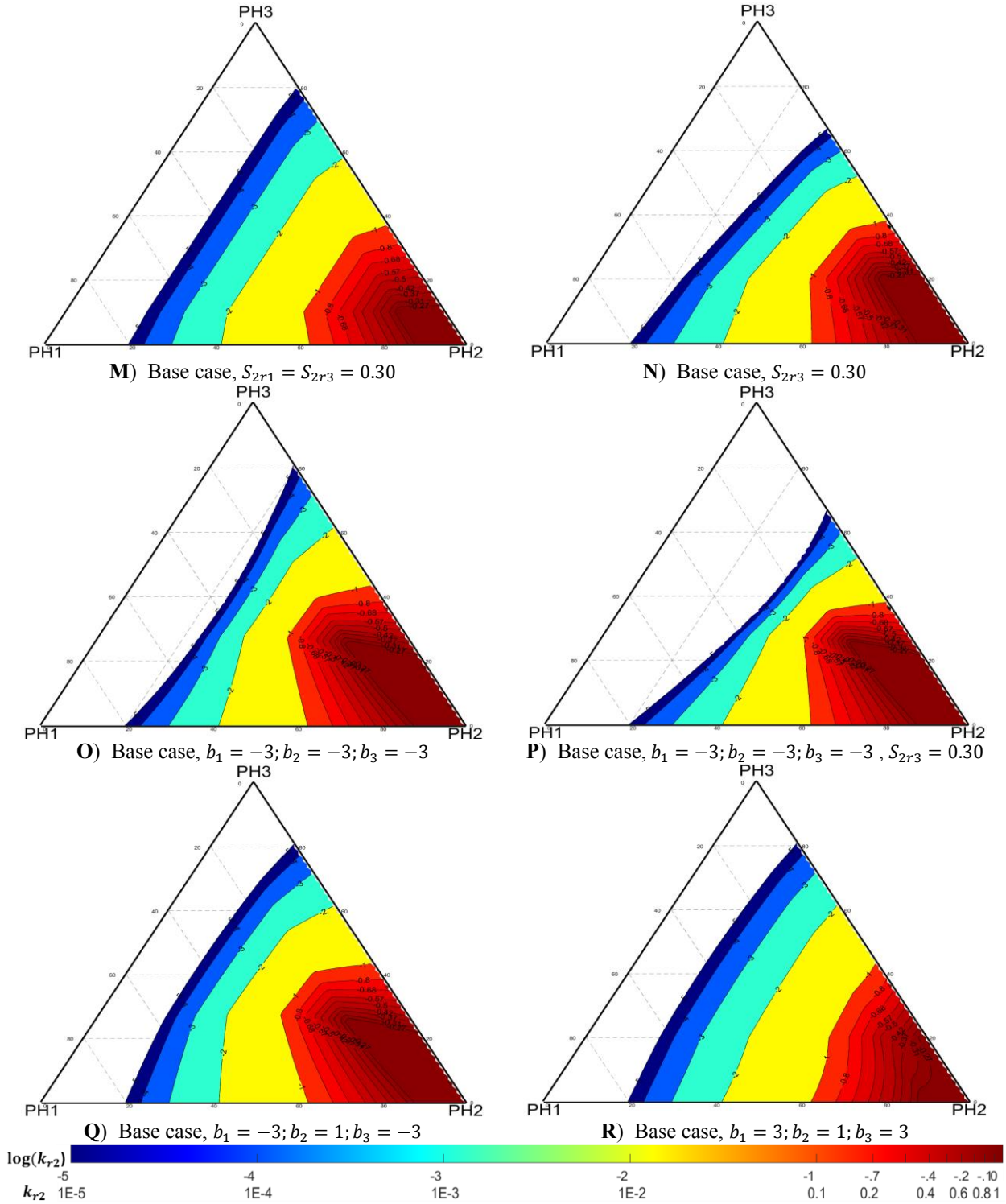

M) Base case, $S_{2r1} = S_{2r3} = 0.30$

N) Base case, $S_{2r3} = 0.30$

O) Base case, $b_1 = -3; b_2 = -3; b_3 = -3$

P) Base case, $b_1 = -3; b_2 = -3; b_3 = -3$, $S_{2r3} = 0.30$

Q) Base case, $b_1 = -3; b_2 = 1; b_3 = -3$

R) Base case, $b_1 = 3; b_2 = 1; b_3 = 3$

Figure 3-8 (cont'd): Sensitivity analysis of phase-2 isoperms with relative permeability parameters

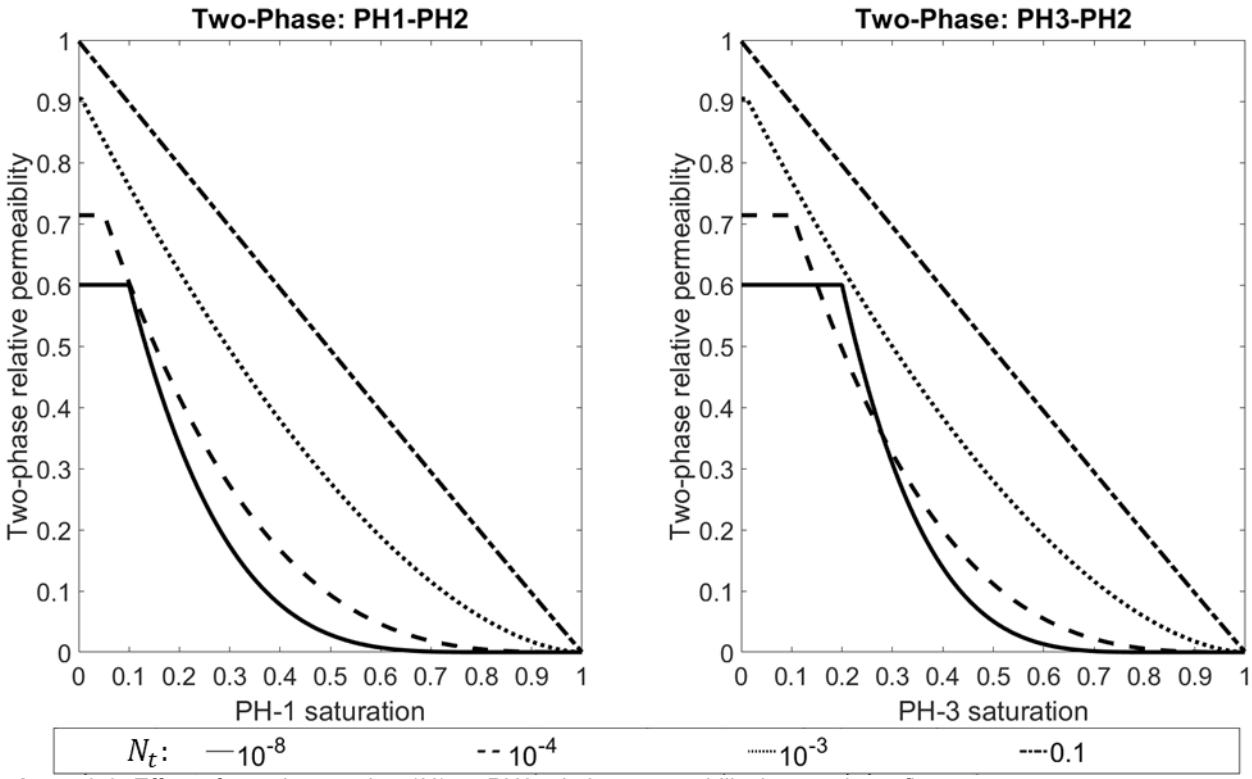

Figure 3-9: Effect of trapping number (N_t) on PH2 relative permeability in two-phase flow

3.8 VALIDATION OF UTKR3P MODEL

We validated the proposed model using the relative permeability data of Donaldson (**1966**), Oak (**1990**, **1991**, **1992**), Maini *et al.* (**1990**) and Baker (**1993**). In general, the UTKR3P model captures the relative permeability trends for water- and oil- wet rocks even in saturation range where phase relative permeability is a function of one saturation. We present the results of the calculated and measured relative permeability data of intermediate-wet samples on Berea sandstone core treated with a silane wetting agent (**Oak, 1991**). **Figure 3-10** exhibits six measured two-phase relative permeabilities on the sides of ternary diagram. Inside the ternary diagram, we show the saturation path of a gas flood (DDI process, see **Saturation history** in Appendix A) together with the measured three-phase gas relative permeabilities. The ternary diagram shows only the measured three-phase gas isoperms in the decreasing water saturation, decreasing oil saturation and increasing gas saturation (DDI) direction. The two-phase data provided six sets of endpoints,

curvature, and residual saturations as input parameters to the UTKR3P model.

We developed a MATLAB code to history match three set of three-phase relative permeabilities (i.e., water (Phase-1), oil (Phase-2), gas (Phase-3)). The code is based on a multi-objective optimization technique (minimizing three SEE_j, j=1,2,3) and applies the derivatives of the UTKR3P model with respect to saturations (see **Appendix E**).

Figure 3-11 shows the trend of measured and calculated relative permeability for different phases. There is a good agreement between the measured and calculated relative permeability values considering only one matching parameter per phase (b_j) is used and a very narrow range of saturations were experienced in the experiment. The history matched b_j parameters and the SEEs are given for each phase in **Figure 3-11**.

The three-phase data of Oak (**1991**) suggested that water relative permeability depends only on water saturation (i.e., two- and three-phase water relative permeability values were identical). The gas relative permeabilities were a function of both gas saturation and saturation history and were the same in two- and three-phase flow. However, oil relative permeability was varied not only with oil but with saturations of water and gas and with the saturation history. This observation suggests that there will be more experimental errors associated with the oil phase than the other two phases due to more complex dependency of oil relative permeability on three saturations and saturation trajectories. There are other errors associated with data for low saturations (i.e., errors in saturation measurements) since the saturation was measured by an x-ray absorption method and reported uniformly as an average over the core length, error due to saturation history, etc. While this test provides promising results, further examination of different aspects of the proposed model at various wettability conditions with different fluid(s) components is indispensable.

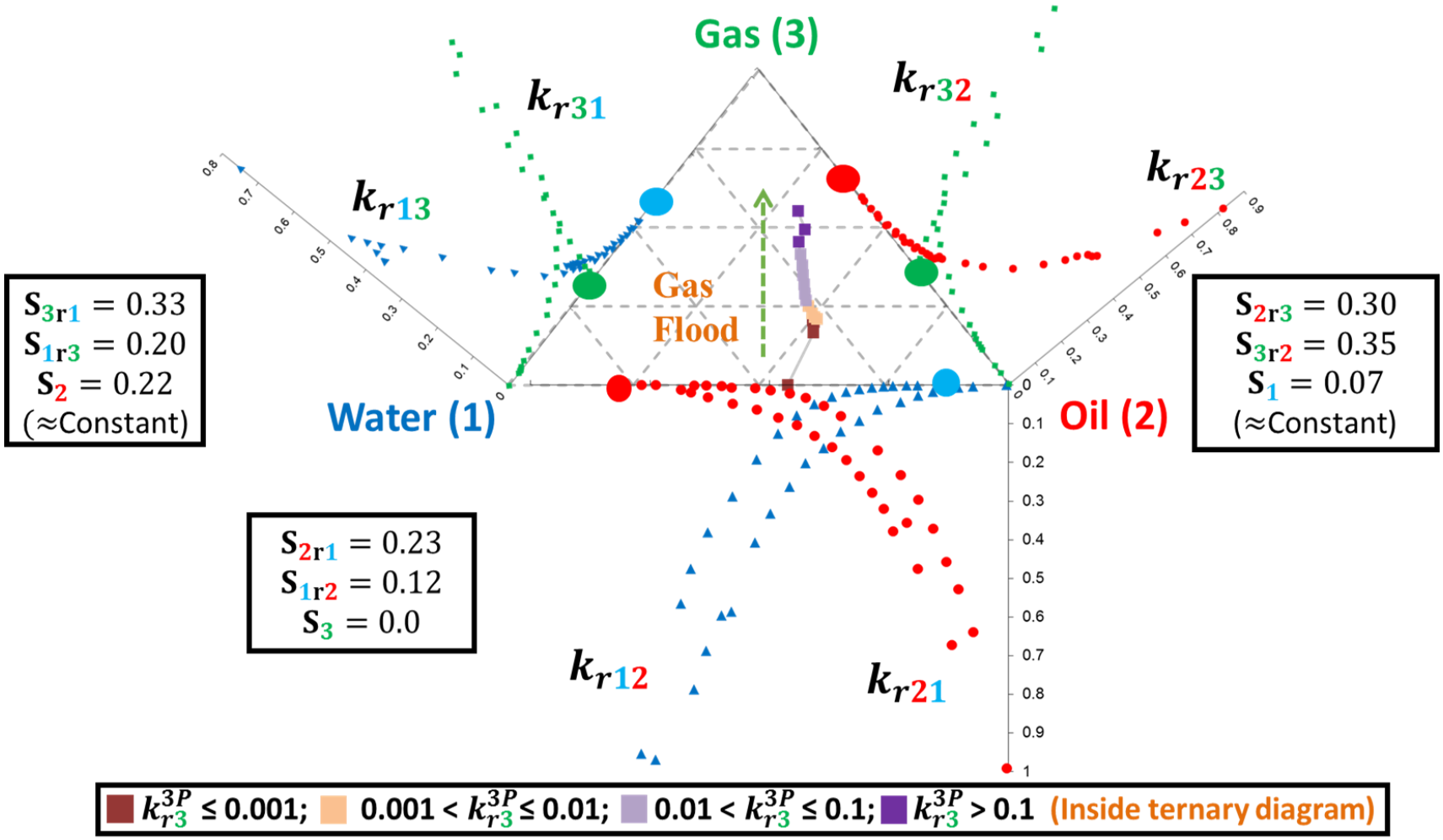

Figure 3-10: Saturation trajectory of a gas flood (DDI process) in an intermediate-wet sandstone rock (sample 15, Oak, **1991**) (inside the ternary diagram). The curve also represents measured three-phase gas relative permeabilities (k_{r3}^{3P}) categorized in four colors. Three sets of measured two-phase relative permeability data (six curves of two-phase relative permeabilities) are shown on three sides of the ternary diagram. Coloring index: Phase-1 (water, blue triangle), phase-2 (oil, red circle), and phase-3 (gas, green diamond). Graph also shows two-phase residual saturations measured at a constant saturation of the third phase.

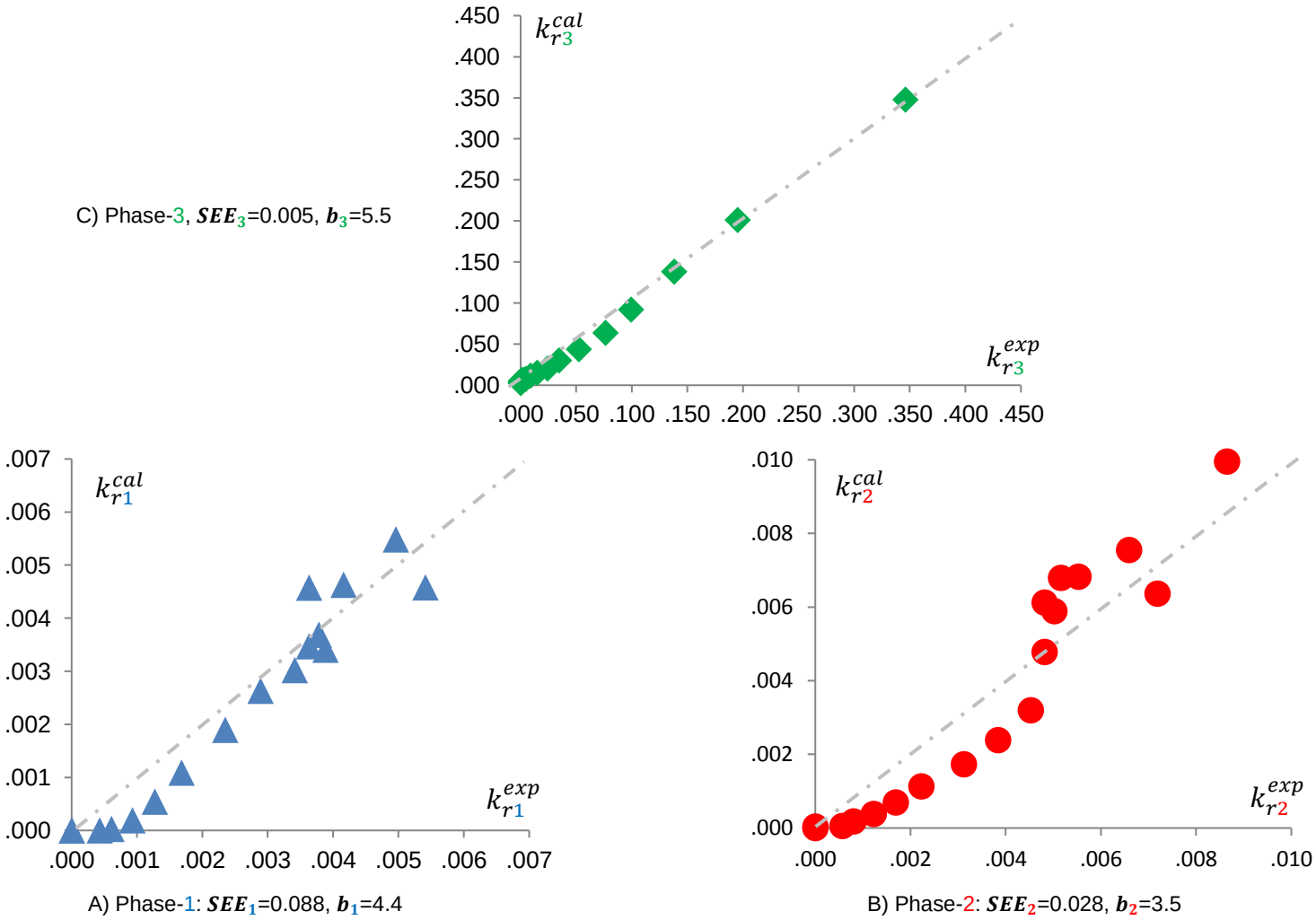

Figure 3-11: Correlation between calculated 3-phase relative permeability (k_{rj}^{cal}) and measured 3-phase data (k_{rj}^{exp}) j=1,2, 3 (see **Figure 3-10**)

3.9 BENCHMARK AGAINST OTHER RELATIVE PERMEABILITY MODELS

We benchmark the oil relative permeability calculated using UTKR3P model against the widely accepted three-phase relative permeability models for an intermediate-wet rock sample (**Oak, 1991**). The measured isoperms are plotted in **Figure 3-12**: Calculated oil isoperms by UTKR3P model (solid lines) and measured values (Intermediate-wet samples, Oak data The models include modified Stone I (**Stone, 1970**) coupled with Fayers' model (**1984**), modified Stone II (**Stone, 1973**), Baker I (or segregated-flow model) (**1988**), and Baker II (or linear-isoperm model) (**1988**). Note that for the Stone I and Stone II models, we use the modified formulations as proposed by Aziz and Settari (**1979**). We applied the Fayer and Matthews correlation (**1984**) (see **Table 2-7**) to evaluate the minimal saturation (S_{om}), an adjustable parameter in Stone I method.

Comparing oil isoperms calculated from these three-phase relative permeability models (**Figure 3-12** to **Figure 3-17**) reveals the flexibility of the UTKR3P model in obtaining an acceptable match against laboratory data (SEE_o=0.03). Note that the commonly accepted relative permeability models fail to match the curvature of measured isoperms.

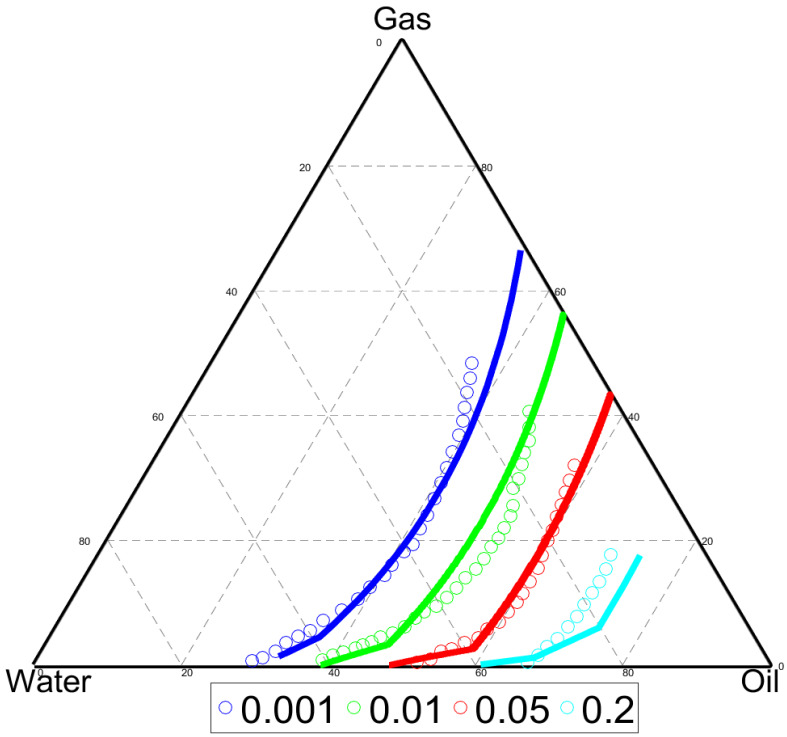

Figure 3-12: Calculated oil isoperms by UTKR3P model (solid lines) and measured values (Intermediate-wet samples, Oak data (**1991**).

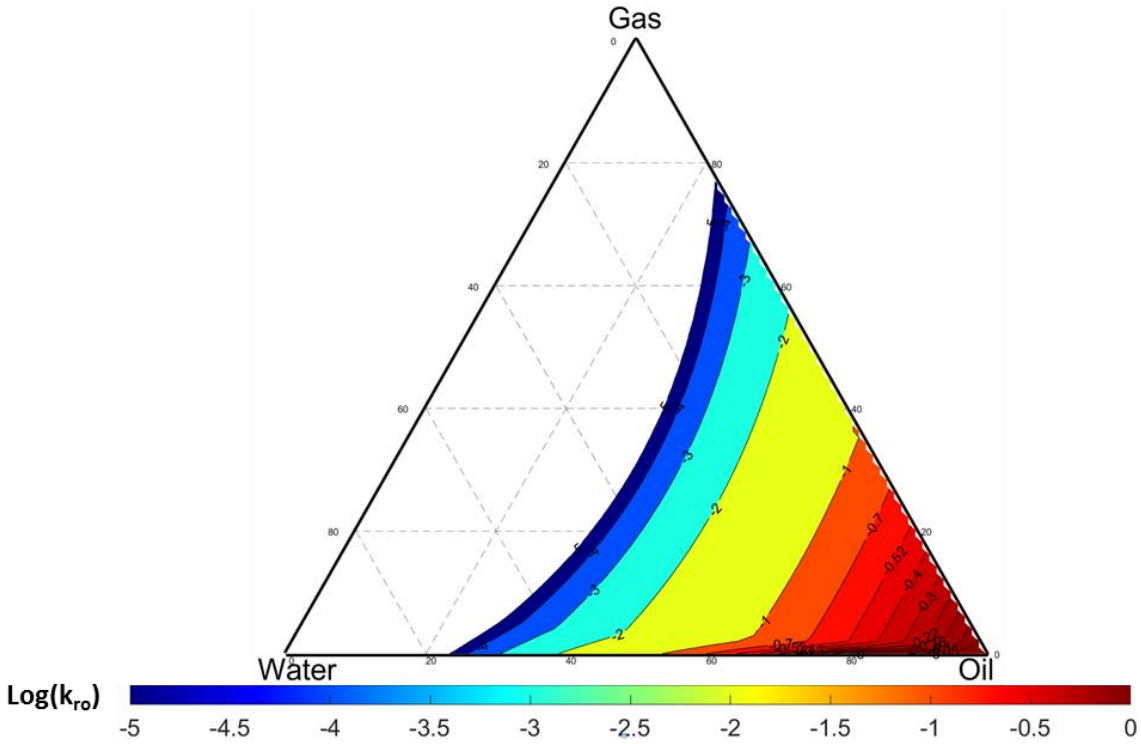

Figure 3-13: Calculated oil isoperm contours (in log-scale) by UTKR3P model (see **Figure 3-12**)

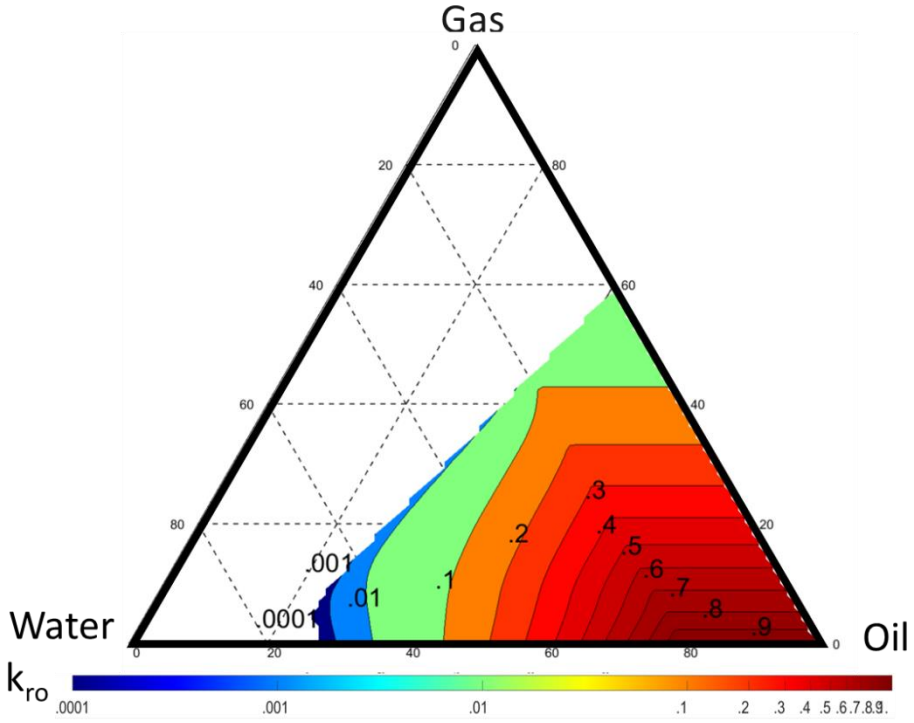

Figure 3-14: Oil isoperm contours calculated using modified Stone I model (**Aziz & Settari, 1979**) coupled with Fayer and Matthews correlation (**1984**)

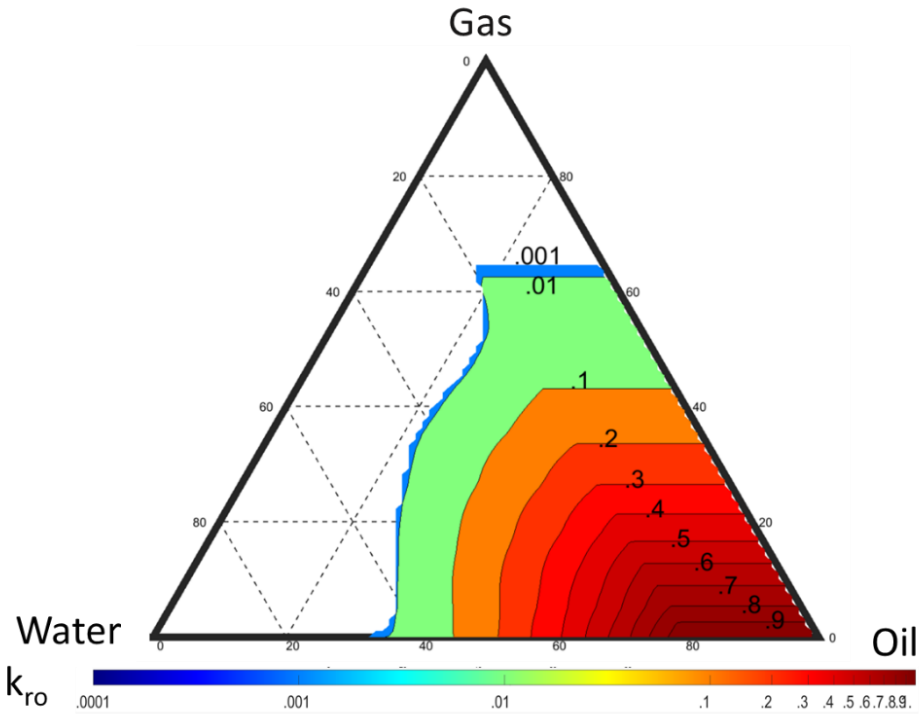

Figure 3-15: Oil isoperm contours calculated using modifed Stone II model (**Aziz & Settari, 1979**)

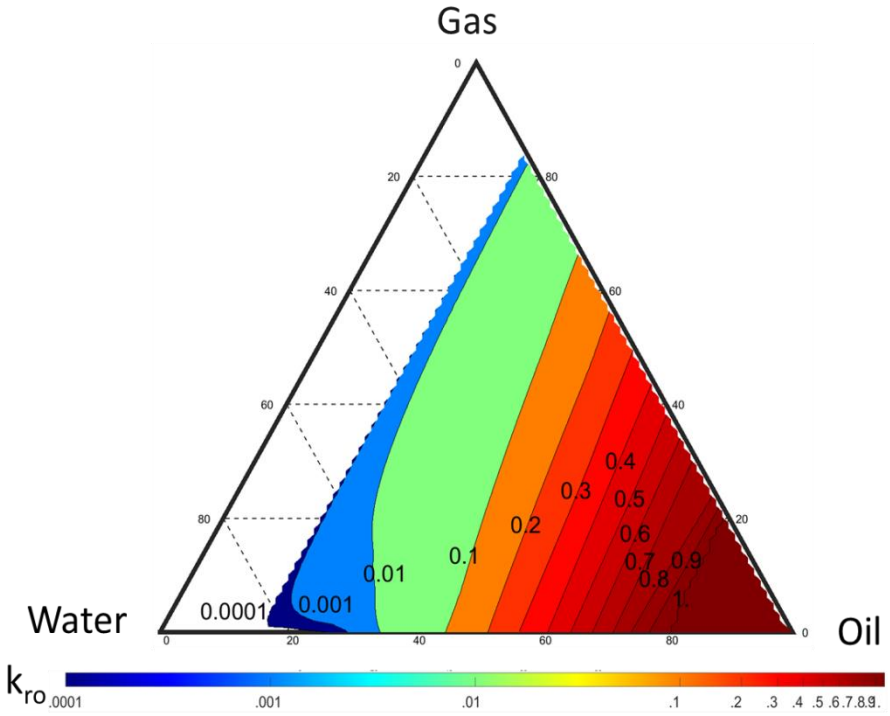

Figure 3-16: Oil isoperm contours calculated using Baker I model (**1988**) (segregated-flow model)

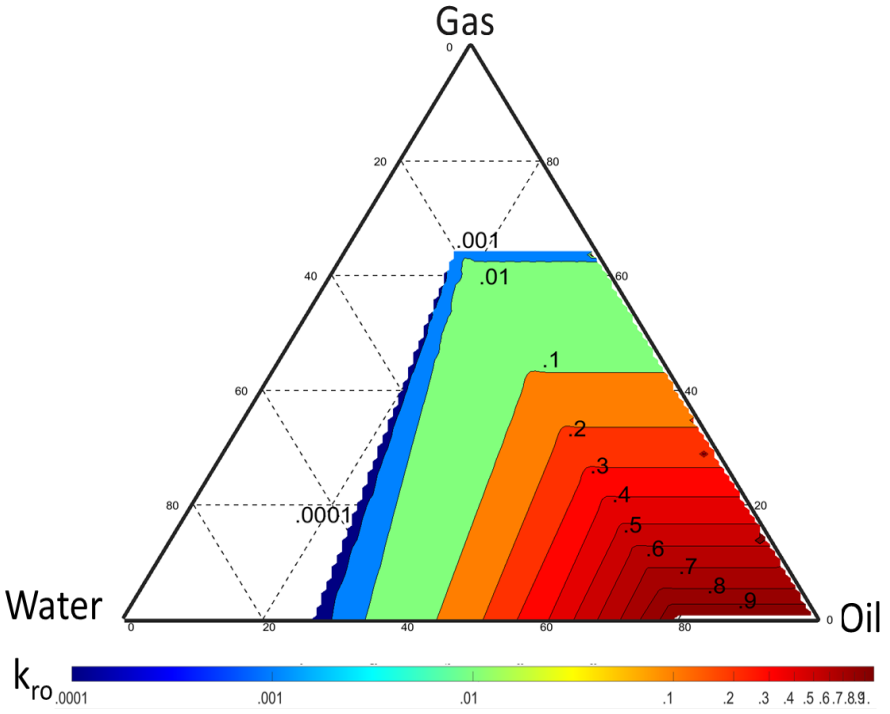

Figure 3-17: Oil isoperm contours calculated using Baker II model (**1988**) (linear-isoperm model)

3.10 KEY FEATURES OF THREE-PHASE RESIDUAL SATURATION MODEL

1) The three-phase residual saturation model approaches to appropriate two-phase residual saturation limits.
2) Its mathematical function confirms that residual saturation encapsulates in an acceptable saturation range($S_{jr}^{3P} \in [S_{jc}, S_j]$).
3) The residual saturations evaluated from this formalism are saturation history dependent and different than those of two-phase flow. The experimental results support the non-unique behavior of residual saturation in macroscopic scale and reported by several investigators (see **Capillary trapping** in Chapter 2).
4) A distinct feature residual saturation model is its capability to change the curvature of isoperms while keeping all other relative permeability model parameters constant.

3.11 KEY FEATURES OF UTKR3P MULTIPHASE RELATIVE PERMEABILITY MODEL

1) This mathematically simple function is general and applicable to different phases without phase labeling from flash calculation.
2) When fluid composition yields the variation of number of phases (two- to three-phase or vice versa) the relative permeability values vary accordingly and seamlessly without any discontinuity in the relative permeability function or its derivative.
3) It applies to different wettability conditions. The *b* parameter varies when wettability state changes. Note that the other relative permeability parameters such as two-phase end-point relative permeabilities, curvatures, and residual saturations may also vary depending on rock wettability.
4) The developed model replicates the reported shapes of two- and three- phase relative permeability curves in extreme saturations reported in the literature.

5) Linear saturation-weighted interpolation scheme in parameter level ensures that the end-point relative permeability and the exponents lie between the two-phase values. This assumption is fair based on the reviewed published experimental results.
6) Linear saturation-weighted interpolation scheme in relative-permeability-parameter level confirms that functional format of the relative permeability model is honored in the entire saturation space. Here, the unacceptable relative permeability values are avoided which would otherwise be estimated by applying other methods, e.g., saturation-weighted interpolation method in the relative permeability level as performed in other three-phase models, e.g., Baker (**1988**) and Blunt (**2000**) models.

3.12 SUMMARY AND CONCLUSIONS

Three-phase relative permeability is an essential element in modeling EOR processes and must be accurately calculated in a predictive model. In the following, we summarize the impact of four critical parameters on relative permeabilities and the current state of modeling their effects using the three-phase relative permeability correlations.

(i) ***Wettability state***: hydrocarbon reservoirs possess a broad range of wettability states. Both rock wettability and fluid speeding have remarkable impacts on the performance of several EOR applications. However, many empirical relative permeability models are based on experimental results for strong wettability conditions. Hence, using these relative permeability models for the intermediate—and oil/wet states become questionable.

Three-phase relative permeability calculation in non-water-wet media (i.e., intermediate-wet/oil-wet states) is problematic. In strong water-wet condition, relative permeability of water and gas primarily depend on their saturation. Hence, two-phase relative permeability can be used in three-phase flow modeling. Relative permeability of oil, however, depends on two saturations. Also, for the non-water-wet media, identification of the degree of wettability is not a trivial task.

Also, a general relative permeability model (i.e., applicable to various phases) is an indispensable element of characterizing the composition demanding processes. This feature assists in modeling a composition-dependent relative permeability without labeling the phases. Moreover, it reduces the coding/debugging efforts when the model is implemented into a reservoir simulator.

The developed three-phase relative permeability models are based on measured data in strong wettability conditions for a particular phase. The widely used relative permeability models, therefore, become questionable when applied to the non-water-wet state or to various phases.

(ii) ***Extreme saturations***: EOR and gas storage projects target extreme saturation region (i.e., the lowest level of hydrocarbon stranded in the reservoir and highest range of gas inventory). When extreme saturations are approached, the effective mechanisms of fluid configuration based

on the rock wettability may result in a different fluid displacement behavior from those in normal saturation range. Laboratory measurement reported an inverse S-shape relative permeability curve for non-wetting fluids at high saturation in non-water-wet media. Only two of the reviewed relative permeability models can capture this phenomenon.

At low saturation region, there is a change in the slope of relative permeability curve. For modeling low saturation region, the conventional assumption is that intermediate-wet fluid spreads over the wetting fluid and that relative permeability and saturation have a quadratic relationship. We showed that this assumption is not always valid in that even in a simple pore structure (e.g., pore corner angle) and equilibrium spreading coefficient significantly impact the formation of a stable film layer of intermediate-wet fluid between wetting and non-wetting fluids.

(**iii**) ***Saturation history***: relative permeability is saturation path dependent and must be included as a dynamic property in reservoir simulation. The characteristic properties of a unique saturation combination are different when the specified saturation is approached from various saturation trajectories (or path). In that many EOR applications and the underground CO_2 sequestration involve in variation both in saturation direction and path, a dynamic relative permeability is required in characterizing fluid flow. Saturation direction varies when a cyclic injection scheme is applied or during the post-injection period in CO_2 injection sites. Saturation path changes when same process is repeated during a multicyclic project (e.g., primary, secondary, and tertiary gas injection). Here, relative permeabilities for the same specified saturation become variable at different saturation routes. Undeservedly, the available relative permeability models ignore the impact of saturation path in their formulations.

(**iv**) ***Non-unique relative permeability***: all too often, there is an asymmetric behavior of relative permeability both between two- and three-phase flow and between two different fluid pairs. The former describes the significant difference between two- and three-phase relative permeabilities. The latter addresses non-unique values of relative permeability parameters such as

a non-unique endpoint relative permeability of oil when flows with water or gas. Currently, relative permeability models do not adequately capture the discussed latter variation in their formulations.

Due to the discussed limitations of the current relative permeability models, we developed a general three-phase relative permeability model (UTKR3P) applicable to water/oil/gas phases. Relative permeability parameters are calculated based on a linear saturation-weighted interpolation between two-phase parameters. Two-phase parameters are calculated when saturation of one-phase approaches the critical saturation. The residual saturation term adds the saturation-path dependency in the formulation of the developed model. The free model parameter b in the three-phase residual saturation formulation varies with rock wettability and fluid composition. Moreover, a trapping-number-dependent relative permeability parameters provides the inclusion of capillary desaturation effect in UTKR3P model.

Based on the fluid and experimental results, there are minimum three and maximum five parameters per phase in the UTKR3P model when a capillary-dominated flow is modeled (low trapping number). These parameters for each phase j include ($k_{rj}^0, C_{1j},$ and S_{jr}). k_{rj}^0 and C_{1j} parameters can be calculated using **Eq. 3-3**. The residual saturation term (S_{jr}) is calculated using the free model parameter b in **Eq. 3-4** and two-phase residual saturation. Each three-phase parameter requires a pair of measured two-phase parameters (e.g., $k_{rj}^0 = f(k_{rjl}^0, k_{rjm}^0)$). Six required input parameters are extracted from the 2D tables reported in the two-phase measurements. If there is a minimum phase saturation that cannot be removed in the measurements, the critical saturation (S_{jc}) is added to the model as a measured and fixed fluid property in two and three-phase flow. If the second curvature (C_{2j}) is anticipated, e.g., in modeling of non-wetting fluids in the intermediate-wet states, the number of parameters is increased to five. If the optional high trapping number region in saturation space is effective, then three other parameters per phase are added to the model including $N_{Tj}, T_j,$ and τ_j. Note that each process requires specific set of the discussed input parameters.

The UTKR3P model generates consistent and continuous set of relative permeability curves. Note that there are kinks in the dynamic relative permeability curves due to natural interactions among fluids. For example, when saturation of one phase approaches to residual saturation, it is reflected on the relative permeability curve of the others phases as a kink. These natural kinks are captured by the UTKR3P model.

We showed the validation of UTKR3P model against a set of relative permeability data for water, oil, and gas phase in two and three-phase flow in an intermediate-wet sample. Furthermore, we investigated the impact of rock wettability and the interacting forces on oil isoperms by changing the b parameter and trapping number, respectively. The capability of UTKR3P model to match experimental results of an intermediate-wet sample was demonstrated for which four other three-phase relative permeability models did not capture the curvature of isoperms.

Chapter 4: **Three-Phase Hysteresis Modeling (UTHYST Model)**

In this chapter, we introduce and validate a three-phase hysteresis model called UTHYST. First, we review the impacting parameters on hysteresis, particularly on capillary trapping. We then discuss the features of a reliable three-phase hysteresis model and the underlying assumptions of the UTHYST model.

4.1 IMPACTING PARAMETERS ON THREE-PHASE HYSTERESIS MODEL

We noted in **Hysteresis** section of Chapter 2 that for multiphase flow in porous media, hysteresis depends on contact angle hysteresis and capillary trapping. In addition, the contact-angle hysteresis is coupled with the wettability alteration in the saturation-history-dependent processes. When the wettability alteration occurs (see **Rock wettability** in Appendix A), it induces a change in phase trapping and contact angles. We discussed that pore wettability depends *only* on contact angle for a flat surface. For the rocks with specified roughness, however, one may expect that both contact angle and pore structure control the pore wettability (**Fenwick & Blunt, 1988**; **Øren & Pinczewski, 1995**). If a rock surface roughness induces hysteresis in the contact angle, it is transformed to the wettability alteration and vice versa.

One key and standard feature for the hysteresis models to distinguish the increasing and decreasing saturation processes is the free phase saturation concept (see **Saturation** in Appendix A). Free saturation demonstrates the movable fluid currently in place depending on the current phase-trapping condition. Therefore, we conclude that capillary trapping (see **Capillary trapping** in Chapter 2) is the crux of hysteresis in relative permeability modeling. In the following, we review three-phase non-wetting phase trapping and the key impacting parameters on it based on the observed lab and field results.

Figure 4-1 is a compilation of the experimentally measured behavior of non-wetting phase initial-trapped saturation for various rocks and wettability states. They include sandstone rocks

(**Geffen et al., 1952**; **Crowell et al., 1966**; **McKay, 1974**; **Oak, 1990**, **1991**, **1992**; **Ma & Youngren, 1994**; **Irwin & Batycky, 1997**; **Jerauld, 1997b**; **Kralik et al., 2000**; **Akbarabadi & Piri, 2013**), carbonate rocks (**Irwin & Batycky, 1997**; **Al-Menhali & Krevor, 2016**), and sandpack samples (**Al-Mansoori et al., 2009**; **Amaechi et al., 2014**). We also demonstrated the constraining and predictive Land curves from the Land formalism (see **Eq. 2-2**). The depicted Land coefficients of 0, 1, 2, and 4 are equivalent to residual saturation of 100%, 50%, 33%, and 20%, respectively. Note that the curves are plotted withdrawing the effective saturation definition, viz., $S^* = S$, due to either incomplete access to the required data or because of the variation of the connate water saturation resulting in inconsistent data. The 1:1 line represents no fluid production condition under which all the initial gas saturation is entrapped. These curves are plotted to assist in visualization purpose without intending to match a specific set of the experimental results.

Figure 4-2 summarizes the gas trapping for the samples above in a box plot. The vertical boxes give the likely range of variation (interquartile range (*IQR*): range over which 75% of the measured non-wetting phase trapping fall, i.e., between first and third quartiles). The whiskers (extended vertical lines) on two sides of the boxes give the inner fence ($1.5\times IQR$). The suspected outliers ($1.5\times IQR$ or more below the first quartile and $1.5\times IQR$ or more above the third quartile) are in colored circles. A review of the experimental results in **Figure 4-1** and **Figure 4-2** reveals the followings:

1) The non-wetting trapped saturation monotonically increases at lower initial saturation region. The level of trapping approaches to the initial saturation.
2) At higher initial saturations, some of the experimental results show a zero-slope trapping line consistent either with the piecewise linear model of Aissaoui (**1983**) or with the hyperbolic form of Jerauld's model (**Jerauld, 1997b**). The former predicts a breaking point beyond that no trapping occurs; the latter predicts a modified form of the Land equation

where a zero-slope trapping is approached at the highest initial saturation region.

3) As the maximum saturation increases, the uncertainty of predicting trapping behavior increases. It implies that some other factors are also effective for the non-wetting trapping at high initial saturation. These include, but are not limited to, microscopic pore structure such as pore geometry, size distribution and topology, together with the fluid configuration in porous media.

There have been attempts to relate these microscopic pore-scale properties to the macroscopic Darcy-scale of fluid flow via the porosity parameter. Several researchers reported a lower level of maximum trapping as the rock porosity increases, and that attempted to correlate maximum trapping to the macroscale properties like porosity and microporosity (**Yuan, 1981**; **Jerauld, 1997a**; **Holtz, 2002**; **Suzanne et al., 2003**). Holtz (**2002**) proposed a linear inverse relation between maximum-trapping and porosity. Jerauld (**1997a**) and Suzanne et al. (**2003**) noted that microporosity does not contribute in non-wetting trapping. These conclusions assist in field-scale modeling. Nevertheless, they are not general statements in that the selected macroscale properties cannot adequately represent the required pore-level characteristics of trapping, at least, when they are unassisted. That explains the scattered trend of maximum-trapping-porosity in more heterogeneous carbonate rocks.

In addition, pore aspect ratio (pore-body to pore-throat size) (see **Pore structure** in Appendix A) has implications on fluid trapping (**Jerauld, 1997a**; **Wardlaw & Cassan, 1978**). In the study of gas trapping in the intermedia-wet samples of Prudhoe Bay reservoirs, Jerauld (**1997a**) explained the observed correlation between non-wetting phase trapping and porosity through the level of aspect ratio. He contributed the higher phase trapping to a higher aspect ratio and choke-off mechanism. It describes the scattered trapping data in more heterogeneous rocks. The sedimentation process leads to the variation of the pore

geometry parameters and, in turn, the change of the aspect ratio.

4) As the rock heterogeneity increases, the level of trapping increases. In most cases, the level of trapping decreases as moving from vuggy carbonates to homogeneous consolidated sandstones to sand packs.

5) Although non-wetting fluid is trapped at all wetting states, the intermediate-wet condition gives lower trapping values than strong wettability conditions. We compared the observed trapping behavior of supercritical CO_2 ($scCO_2$), gaseous CO_2 (gCO_2), and nitrogen in the water-wet sandstone (data: Akbarabadi and Piri (**2013**)) and mixed-wet carbonate (data: Al-Menhali and Krevor (**2016**)) rocks. It shows that as the degree of non-wetness between displacing and displaced phases increases, a higher trapping is expected.

6) Fluid morphology impacts the level of non-wetting trapping. If the length of the non-wetting phase globules is several pore diameters, capillary heterogeneity in a representative elementary volume controls the trapping level; otherwise, for the non-wetting fluids consisting of disconnected bubbles, primarily, the local capillary pressure controls bubble trapping resulting in high phase trapping than that of globules. It is consistent with the results of non-wetting trapping experiments of Zuo and Benson (**2014**). They examined a process-dependent CO_2 trapping in Berea sandstone samples. The water imbibition to the core containing dissolved CO_2 resulted in a higher CO_2 trapping level than that of CO_2 as introduced by drainage.

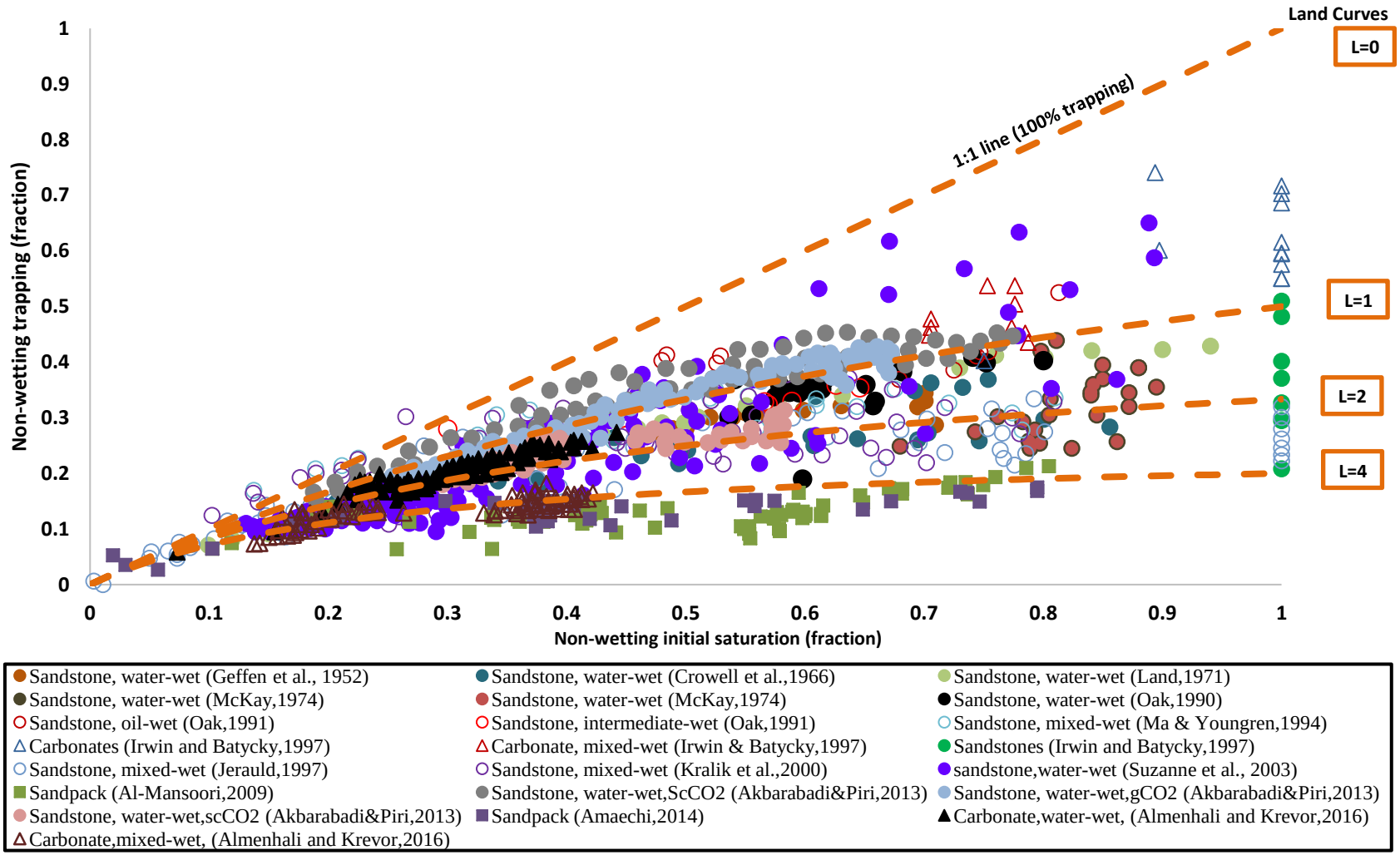

Figure 4-1: Crossplot of gas Initial-trapping experimental results for sandstone (circles), carbonates (triangles), and sandpacks (squares) with a broad wettability preference (filled symbols represent water-wet samples). Dash curves show Land curves (see **Eq. 2-2**, a=0, d=1) with four Land coefficients (L=0,1,2 and 4).

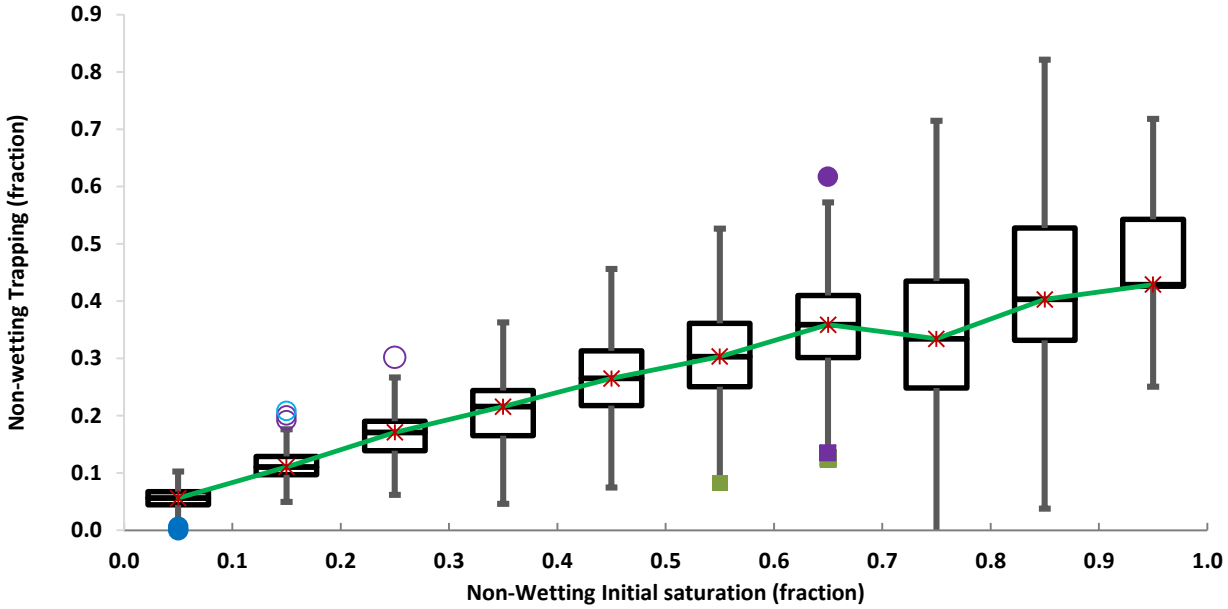

Figure 4-2: Box plot of non-wetting phase trapped saturation for the sandstone, carbonate, and sandpack. The vertical boxes give the likely range of variation (IQR). The whiskers on the bottom and top side of each column are the inner fences (1.5×IQR). The suspected outliers are given in colored shapes (circles and rectangle) consistent with color and shape presented in **Figure 4-1**. The stars show the median of each column connected to the solid green line.

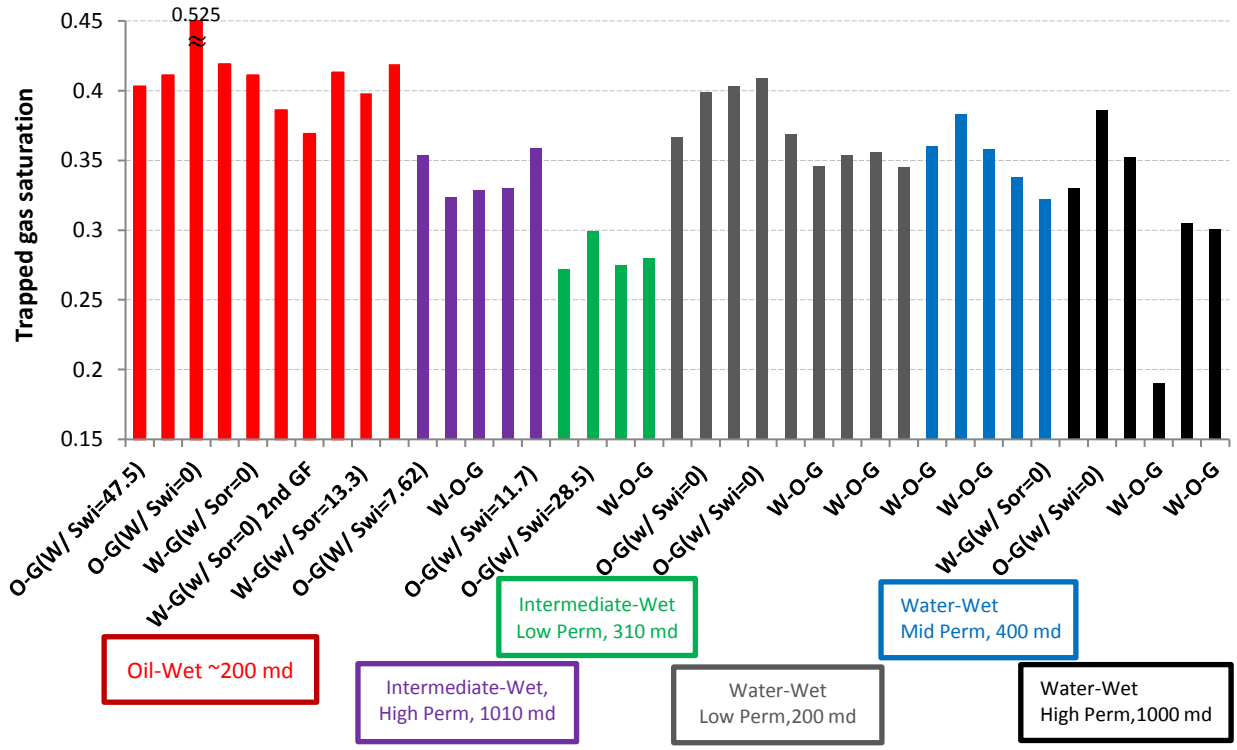

Figure 4-3: Measured trapped gas saturation for Berea sandstone cores with different wettability (Data: Oak, **1990**; **1991**; **1992**).

In conclusion, reviewing the initial non-wetting phase saturation results reveals that there is a broad range of initial-trapped saturation. We relate this significant variation to pore structure, rock wettability, fluid spreading and configuration, and pore filling sequence in three-phase flow.

4.2 LIMITATIONS OF CURRENT HYSTERESIS MODELS

The present three-phase hysteresis models add extensive numerical cost to compositional reservoir simulation due to their formulation. Hysteresis is a history-dependent natural phenomenon and requires that the associated model properties to be stored at each time level. This feature of hysteresis makes it a memory-intensive computation. In relative permeability application, for example, the prior saturation of grid blocks is stored together with other required parameters of the hysteresis model. With the current models also an adjustment is necessary to switch between the first and consequent cycles. Consequently, mathematically sophisticated hysteresis models lead to both memory demanding and computationally expensive numerical simulations.

In addition, the three-phase hysteresis models are not general. Each model is specifically developed for measured data for a particular fluid type, rock type, and saturation trajectory. A generalized formulation including these parameters is expected.

4.3 PREMISES OF UTHYST MODEL

Based on the studied laboratory/field experimental results, the following are the premises of developing a three-phase hysteresis model:

1. In the absence of interphase mass exchange, the non-wetting phase trapping increases monotonically in the decreasing phase saturation processes. This presumption is supported with the experimental results and states that once a phase trapping occurs, it is not remobilized when capillary forces dominate viscous and gravitational forces.
2. There is no trapping when phase saturation increases continuously.
3. The dendritic saturation (see **Dendritic/non-conductive** saturation in Appendix A) does not interfere the capillary trapping and is excluded from the modeling.
4. Compositional exchanges between the trapped phase and the displacing fluids may reduce the phase trapping. These processes include but are not limited to, miscible displacement, near-critical fluid flow, and chemical-EOR processes. When a process experiences significant mass transfer between two phases, the capillary force will diminish. It leads to the lowering of phase trapping. Here, the monotonicity of the phase trapping curve is not valid.
5. Land's trapping coefficient in **Eq. 2-2** represents the initial-trapped correlation. Land coefficient is not unique for two- and three-phase flow (**Skauge & Larsen, 1994**; **Egermann et al., 2000**; **Spiteri & Juanes, 2006**; **Shahverdi et al., 2011**). In addition, the Land coefficient is not constant within the multicycle processes (i.e., hysteresis cycles). Here, a particular value of Land coefficient is assigned to each cycle depending on the maximum possible phase trapping for that cycle. Land coefficient depends on parameters affecting initial-trapped behavior such as pore geometry and network topology, fluid configuration, and fluid spreading. Among others, several impacting parameters are

relevant including IFTs, contact angles, rock permeability, pore size distribution, and rock wettability. For example, investigating Oak's three-phase gas relative permeability data (**Oak, 1990**; **1991**) revealed that for the same fluids, Land coefficient increased as the rock permeability increased lowering the level of non-wetting phase trapping. For these three-phase relative permeability measurements, the Land coefficient increased as the fluid-pair IFTs decreased. Spiteri and Juanes **(2006)** studied Oak's experiments and concluded that the Land coefficient is far from being constant. Element et al. (**2003**) conducted multicycle gas injection in both water- and intermediate-wet samples and concluded that to match their experimental results a dynamic Land coefficient was required for hysteresis cycles.

6. The presence of a conjugate phase impacts the level of phase trapping in multicycle processes. Conjugate-phase is defined as a mobile phase impacting the relative permeability of phase *j* as reported in the literature (**Jerauld, 1997b**; **Larsen & Skauge, 1998**; **Kralik et al., 2000**). Larsen and Skauge (**1998**) proposed a cycle-dependent relative permeability model taking into account the impact of water saturation at the start of the current cycle on gas relative permeability. The designation of the conjugate phase is currently arbitrary due to the lack of experimental results. In the sense of phase trapping, we consider water, oil, and gas as the conjugate phase for the gas, water, and oil trapping.
7. A cycle-dependent relative permeability exists in three-phase flow within multicycle processes. The relative permeability decreases at a specified saturation as cycle number increases.

4.4 UTHYST MODEL

We develop a general three-phase hysteresis model honoring the pore- and core-scale observations. The model calculates dynamic capillary trapping in a multicycle process. The trapped saturation within each cycle *n* is initially calculated by,

$$\left(S_{jt}\right)_n = min\left\{S_j, S_{jt}^I + \left(\Delta S_{jt}\right)_n \left(\frac{1 - S_m^I}{1 - S_{cm}}\right)^{\alpha_j}\right\}. \qquad \textbf{Eq. 4-1}$$

where, S_{jt}^I is the cumulative trapped saturation at the start of cycle *n*, $\left(\Delta S_{jt}\right)_n$ denotes the capillary trapping during cycle *n*, and the set of parentheses on the right hand side of **Eq. 4-1** introduces the effect of saturation of conjugate phase (m) at the start of cycle *n* (S_m^I) relative to the conjugate phase critical saturation (S_{cm}). Note that α_j is the free parameter of the UTHYST model and addresses the degree of reduction of relative permeability due to the conjugate phase. Phase trapping during the current cycle is estimated based on the Land formalism:

$$\left(\Delta S_{jt}\right)_n = \frac{S_j^{max} - S_j}{1 + (L_j)_n \left(S_j^{max} - S_j\right)}. \qquad \textbf{Eq. 4-2}$$

Here, to evaluate the effective phase trapping, we define a modified Land coefficient. It enables us to honor pore filling sequence in porous media.

$$(L_j)_n = \frac{1}{S_{jr}^M - S_{jt}^I} - \frac{1}{\left(S_j^M\right)_n - S_j^I}, \qquad \textbf{Eq. 4-3}$$

where superscript *M* denotes the maximum saturation obtained within the current cycle. Note that the dynamic evaluation of residual saturation results in a saturation-path dependent Land coefficient. Otherwise, one can apply a fixed Land coefficient and still obtains a cycle-dependent

hysteresis model.

This model results in no phase trapping in saturation increasing half-cycles in agreement with the physical process reported in laboratory and field results. The trapped saturation at capillary dominated flow shows a monotonically increasing behavior in decreasing phase saturation processes. We provide the analytical derivative of the UTHYST model in **Appendix F**.

The UTHYST model can be applied to a general purpose relative permeability model using the free saturation concept ($S_{jf} = S_j - S_{jt}$). For both increasing and decreasing saturation processes, relative permeability of phase j can be described as,

$$k_{rj} = k_{rj}(S_{jf}). \qquad \textbf{Eq. 4-4}$$

Here, relative permeability of each phase is calculated using the formulation of the adopted relative permeability model. The free saturation is used rather than total saturation.

4.5 COMPOSITIONAL EFFECT ON HYSTERESIS AND PHASE TRAPPING

The compositional effects due to mass transfer are included using the capillary-desaturation curves similar to the trapping number-dependent residual saturation (see **Trapping number effect** in Chapter 3):

$$\left(S_{jt}\right)_n^{corr} = S_{jt}^{min} + \theta_{j,n}\left(\left(S_{jt}\right)_n - S_{jt}^{min}\right), \quad \text{i} = \text{phase m or l.} \qquad \textbf{Eq. 4-5}$$

Here, S_{jt}^{min} is the trapping saturation experimentally measured including the compositional effects, $\left(S_{jt}\right)_n$ in the parentheses is the trapped saturation calculated from **Eq. 4-1**, and θ_j is the trapping coefficient calculated from **Eq. 3-7**. As the effective viscous/gravitation forces dominate capillary forces, the trapped phase saturation reduces in par with the experimental results (see

Trapped phase mobilization in Chapter 2).

4.6 KEY FEATURES OF PROPOSED UTHYST MODEL

1) The UTHYST model offers a simple and general approach to calculating phase trapping in multicycle processes for different rock wettabilities.
2) It is valid for processes where saturation decreases and increases and adopts free saturation concept, i.e., the difference between total saturation and trapped saturation.
3) This model applies to any relative permeability model and results in a cycle-dependent relative permeability.
4) The saturation path effect on phase trapping is incorporated in a dynamic Land coefficient. In the absence of significant variation in saturation path, a constant Land coefficient can be applied while generating a set of cycle-dependent relative permeability curves.

4.7 COMMENTS ON CYCLE-DEPENDENT RELATIVE PERMEABILITY MODEL

The UTHYST model evaluates phase trapping in porous media within a multicycle process and results in a cycle-dependent relative permeability as reported in the literature (see **Hysteresis modeling in relative permeability** in Chapter 2). Cycle indicates a successive increasing and decreasing phase saturation, respectively and is local phase-history dependent. In particular, cycles are independent of the overall process applied in the prospect. In other words, it entails the phase index according to the decreasing phase history which is not necessarily following the fluid injection scenario. For example, for the secondary gas injection in a WAG process (XXI), the cycle number for gas phase in each grid block is calculated with respect to the gas saturation stored for that grid-block. If the gas saturation increases compared to previous time level, a new gas cycle starts; the gas cycle number for that grid block is constant all through increasing and decreasing

gas saturation within that grid block; consecutive gas cycle will start by gas saturation increasing after a half-cycle saturation decreases within the specified grid-block.

Strictly speaking, phase saturation from the simulation results oscillates due to numerical instabilities and results in the redundant and non-physical switching of saturation direction. This may be responsible for slow or non-convergence of numerical simulation and must be avoided. We define a saturation tolerance parameter (ε_h) to control switching of phase saturation direction and name it *SATTOLHYST*. Any saturation variation in grid-block *k* in the current time level (*t*) below the user defined tolerance is ignored and the phase saturation direction index (*PID: increasing or decreasing*) from the last time level (*t-1*) will be taken,

$$\forall \left(S_{k,j}^{t} + \varepsilon_h < S_{k,j}^{t-1} \middle| S_{k,j}^{t} - \varepsilon_h > S_{k,j}^{t-1}\right), PID_{k,j}^{t} = PID_{k,j}^{t-1}. \qquad \textbf{Eq. 4-6}$$

4.8 VALIDATION OF UTHYST MODEL

In this section, we first evaluate the performance of the UTHYST model for the gas trapping. Here, we use the saturation path resulted in a synthetic model of a three-cycle WAG injection scheme as shown in **Figure 4-4**. The starting (A) and ending (M) points of this coupled DDI and IDI processes are highlighted in **Figure 4-4**. Relative permeability parameters are listed in **Table 4-1**.

Table 4-1: Relative permeability data used in WAG simulation case study for verification of UTHYST model

Two-phase relative permeability data	Value
Residual water saturation $(\boldsymbol{S}_{\mathrm{wr}o} = \boldsymbol{S}_{\mathrm{wr}g})$	0.10
Residual oil saturation $(\boldsymbol{S}_{orw} = \boldsymbol{S}_{\mathrm{o}rg})$	0.10
Residual gas saturation $(\boldsymbol{S}_{grw} = \boldsymbol{S}_{gro})$	0.33
End-point gas relative permeability ($\boldsymbol{k}^{\boldsymbol{0}}_{\boldsymbol{rgw}} = \boldsymbol{k}^{\boldsymbol{0}}_{\boldsymbol{rgo}}$)	1.0
1st curvature of gas relative permeability curve $(\boldsymbol{C}_{\boldsymbol{1}gw} = \boldsymbol{C}_{\boldsymbol{1}go})$	3.0
2nd curvature of gas relative permeability curve $(\boldsymbol{C}_{\boldsymbol{2}gw} = \boldsymbol{C}_{\boldsymbol{2}go})$	0.0
General phase parameters	**Value**
b parameter in **Eq. 3-4** ($\boldsymbol{b}_w$ / $\boldsymbol{b}_o$ / $\boldsymbol{b}_g$)	0.0/0.0/1.0
Critical saturation $(\boldsymbol{S}_{cw}$ / $\boldsymbol{S}_{co}$ / $\boldsymbol{S}_{cg})$	0.1/0.0/0.0

We note that both water and gas saturation do not monotonically vary in a fixed saturation direction. For example, gas saturation at t=4 (dimensionless unit) decreases in a DDI saturation direction. Hence, we selected an appropriate saturation tolerance parameter that avoid a redundant switching between decreasing and increasing saturation directions ($\varepsilon_h = 0.02$). **Figure 4-5** demonstrates the saturation direction identification values for gas phase. Three increasing gas saturation (XXI, $PID_g = 1$) and three decreasing gas saturation directions (XXD, $PID_g = 0$) were identified. In addition, **Figure 4-5** shows the calculated trapped gas saturation versus time at a fixed conjugate phase reduction factor ($\alpha_g = 0.5$). During a XXI saturation direction, no gas is trapped (flat lines). As a XXD saturation direction starts, an increased trapped gas saturation is calculated. Moreover, there is a point where gas saturation and trapped saturation are identical to avoid non-physical results (point M). **Figure 4-6** depicts the variation of trapped gas saturation for

four selected values of α. It shows the increased gas trapped saturation by decreasing the conjugate phase reduction factor. **Figure 4-7** represents the calculated gas relative permeability for the selected reduction factors. It highlights the cycle-dependent relative permeabilities calculated by the UTHYST model. At a point with an identical gas saturation, e.g., $S_g = 0.6$, as trapped gas saturation increases for each cycle and/or by reduction factor, gas relative permeability decreases both for the XXI and XXD saturation directions compared to that of primary XXI.

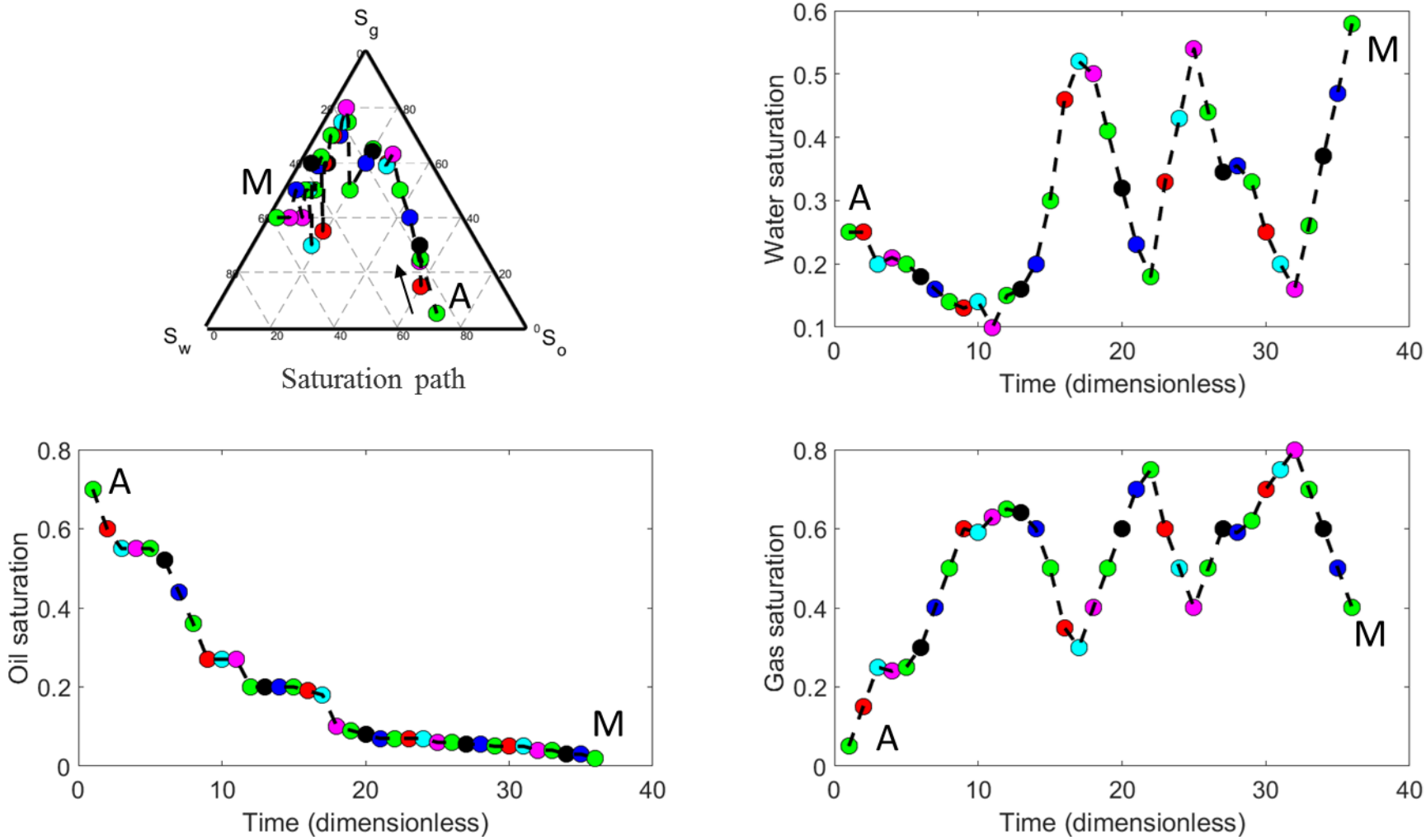

Figure 4-4: Saturation path (A→M) for a three-cycle WAG process in validating the UTHYST model (color format is identical in all graphs)

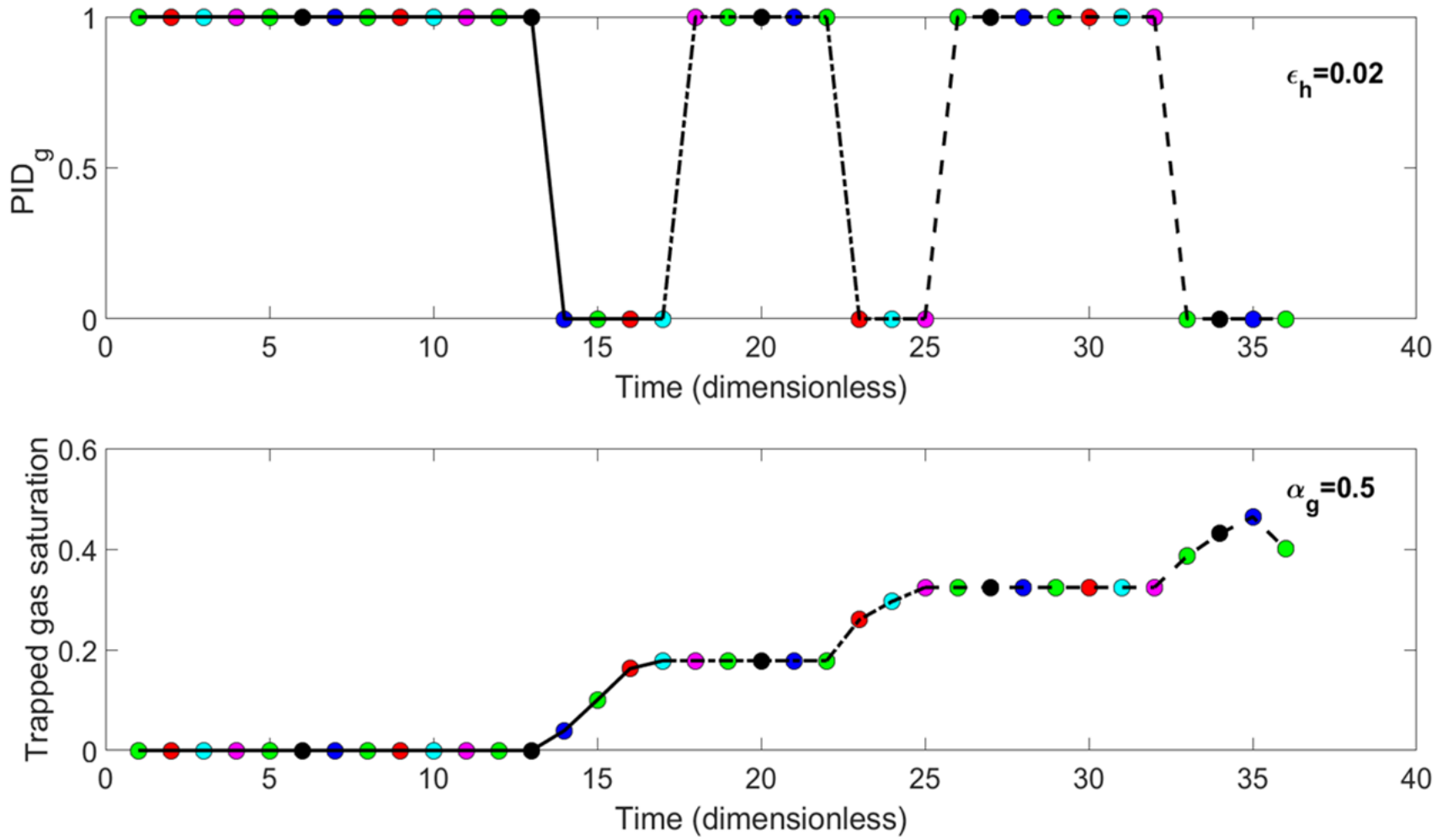

Figure 4-5: Saturation direction identification and calculated trapped gas saturation variation in three-cycle WAG process. 1st cycle; solid line; 2nd cycle; dash-dotted line; 3rd cycle: dash line (saturion history: **Figure 4-4**).

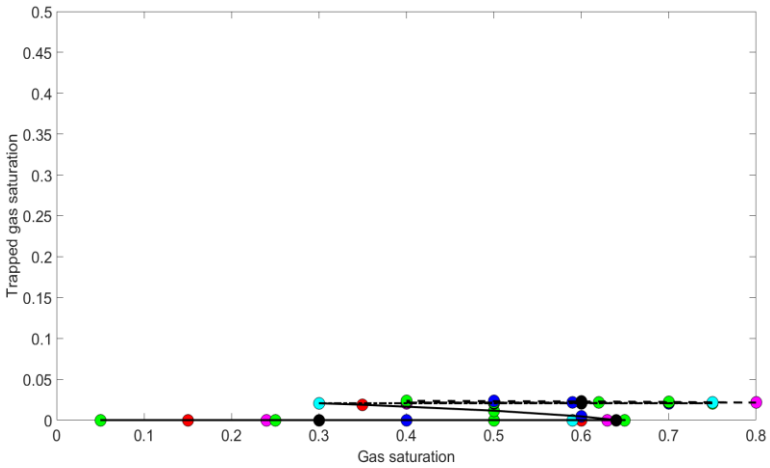

A) $\alpha_g = 8.0$

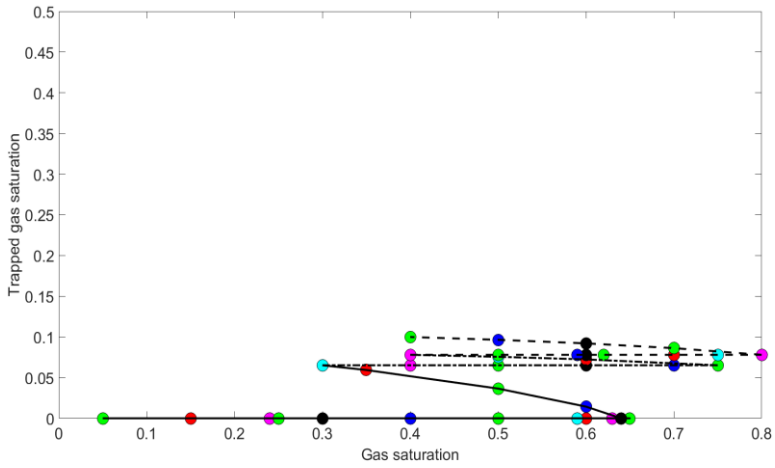

B) $\alpha_g = 4.0$

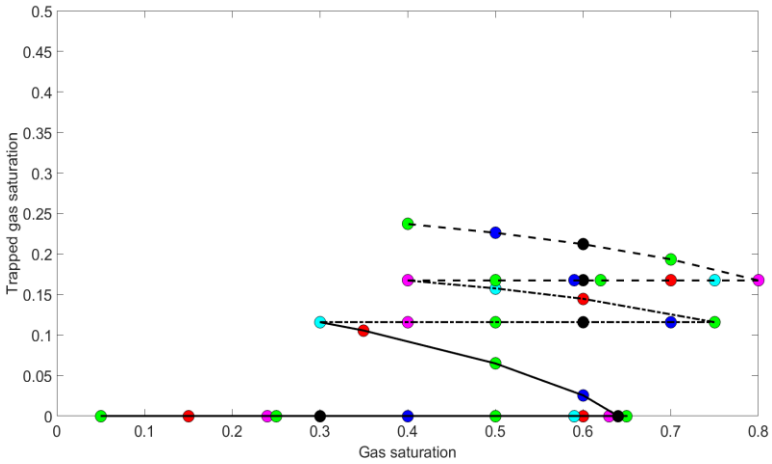

C) $\alpha_g = 2.0$

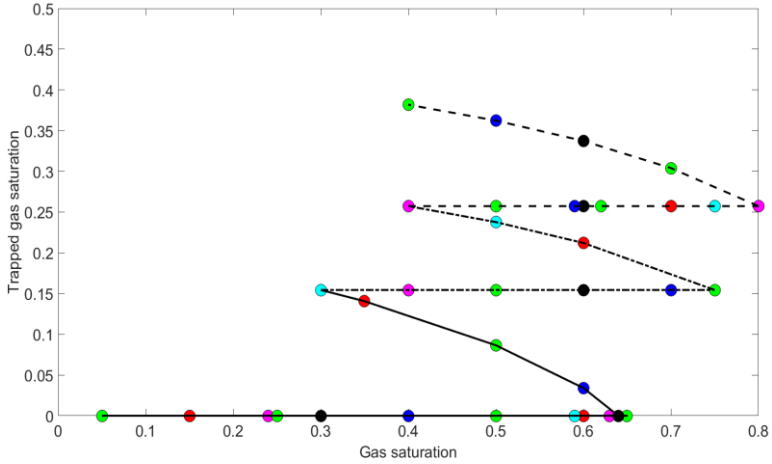

D) $\alpha_g = 1.0$

Figure 4-6: Sensitivity analysis of gas trapping with reduction factor (α_g) in UTHYST model. 1st cycle: solid line; 2nd cycle: dash-dotted line; 3rd cycle: dash line (saturion history: **Figure 4-4**).

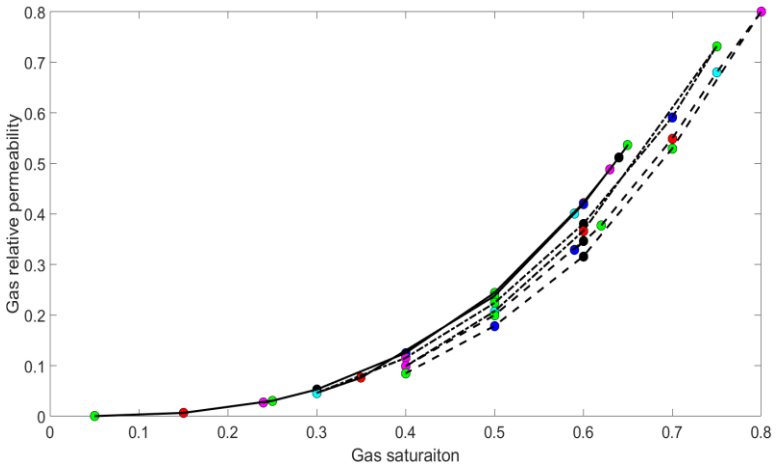

A) $\alpha_g = 8.0$

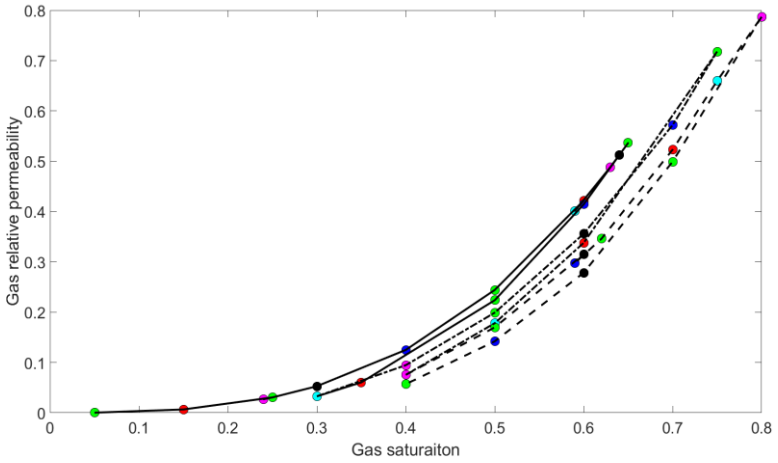

B) $\alpha_g = 4.0$

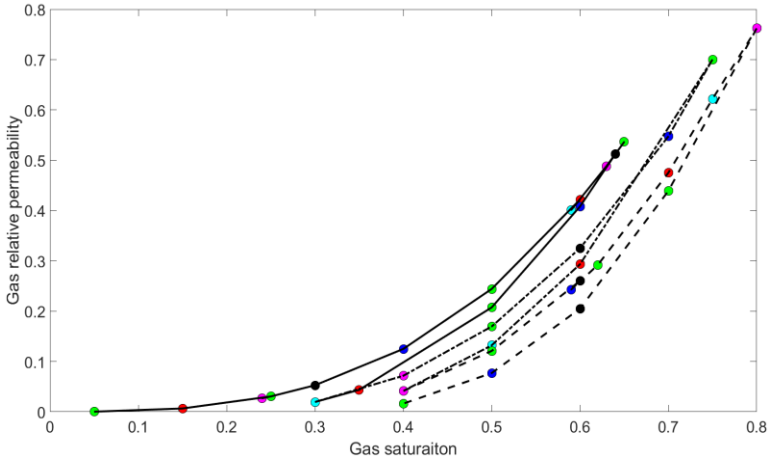

C) $\alpha_g = 2.0$

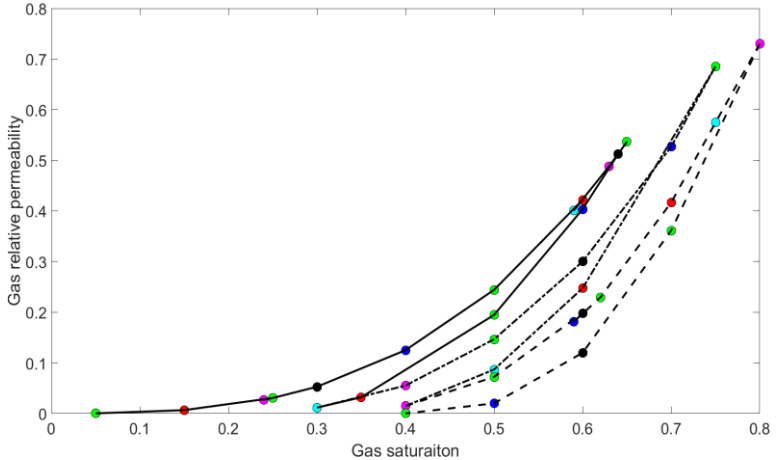

D) $\alpha_g = 1.0$

Figure 4-7: Sensitivity analysis of gas relative permeability with reduction factor (α_g) in UTHYST model. 1st cycle: solid line; 2nd cycle: dash-dotted line; 3rd cycle: dash line (saturion history: **Figure 4-4**).

4.9 BENCHMARK AGAINST OTHER HYSTERESIS MODELS

We benchmark the gas relative permeability calculated using the UTHYST model against two widely accepted hysteresis models for the case study reviewed earlier (see **Validation of UTHYST model**). The benchmarking models include two-phase Carlson model (**Carlson, 1981**) and three-phase Larsen and Skauge model (**Larsen & Skauge, 1998**). Carlson model reproduces a reversible set of hysteretic relative permeability curves. Indeed, there is only one curve for the increasing saturation direction (XXI) and one curve represents the decreasing gas saturation process (XXD) irrespective of the cycle number (see **Figure 4-8**). However, as **Figure 4-9** demonstrates, the Larsen and Skauge model results in a cycle-dependent relative permeability curves with different set of curves for each injection cycles. In the Larsen and Skauge hysteresis model, we evaluated the hysteresis effect by selecting three reduction factors (α_{LS}) to investigate the impact of water phase saturation on gas relative permeability. Note that for both hysteresis models, the Land coefficient calculated from the gas residual saturation was constant (L=2.0).

Comparing **Figure 4-7**, **Figure 4-8** and **Figure 4-9** reveals that the relative permeability curves of first WAG cycle are identical for two- and three-phase hysteresis model. For the three-phase hysteresis models, the higher α_{LS} value in the Larsen and Skauge model or a lower α value in the UTHYST model result in a more prnounced effect of water saturation on the reduction of gas relative permeability within the second and third cycles.

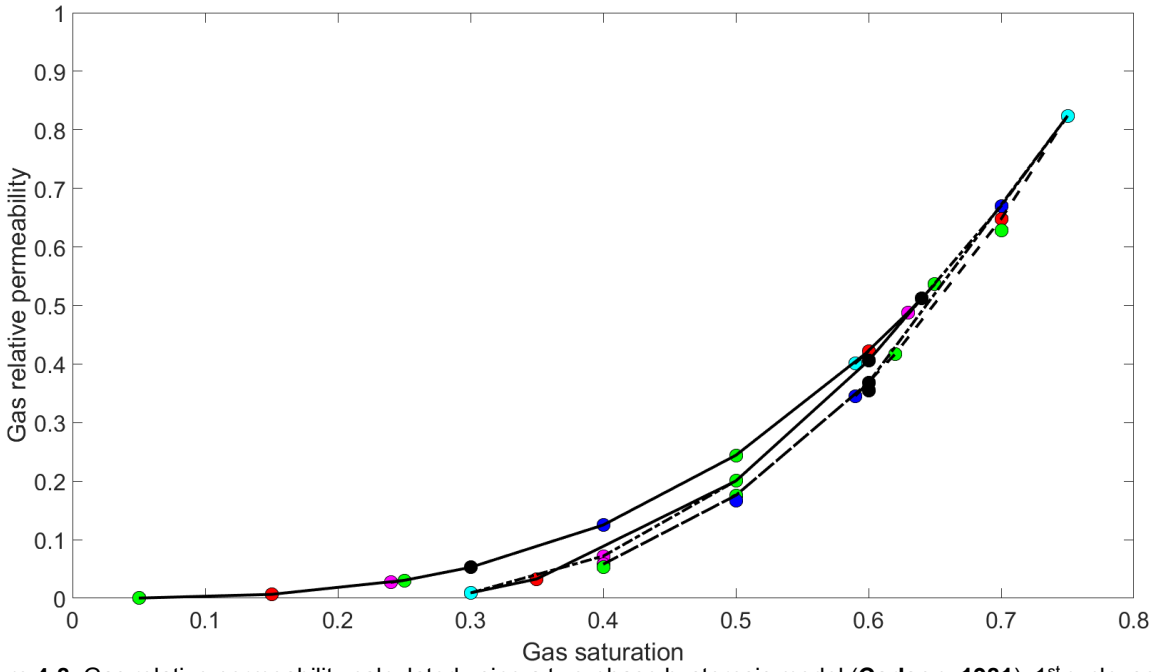

Figure 4-8: Gas relative permeability calculated using a two-phase hysteresis model (**Carlson, 1981**). 1st cycle: solid line; 2nd cycle: dash-dotted line; 3rd cycle: dash line

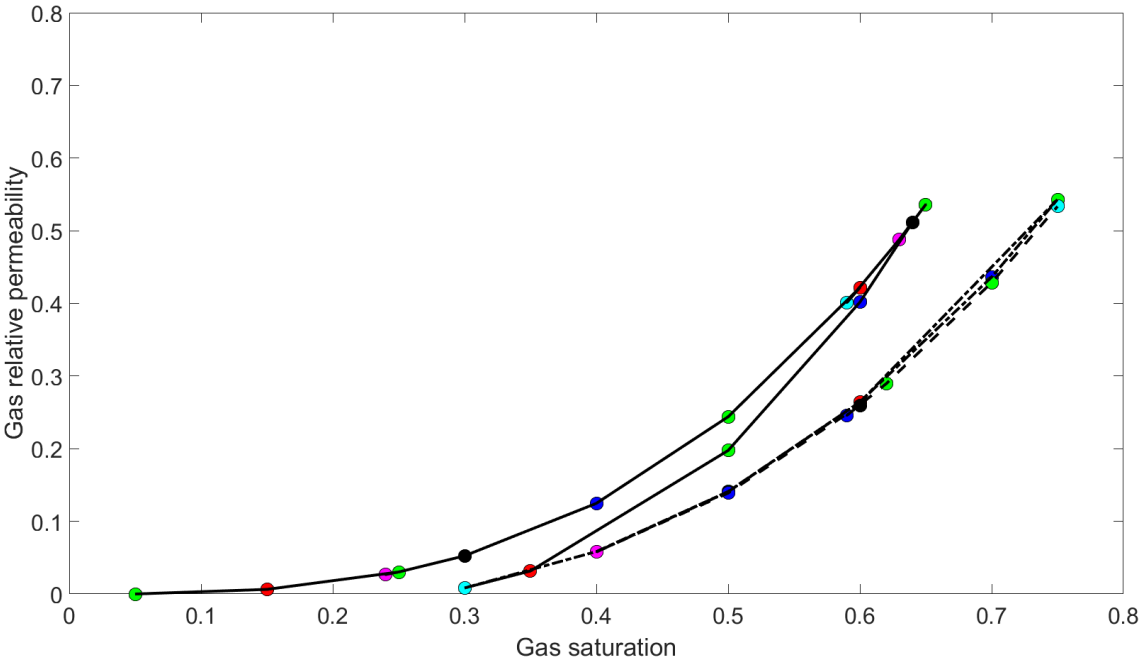

Figure 4-9A: Gas relative permeability calculated using the Larsen and Skauge model (**1998**) with $\alpha_{LS} = 0.5$. 1st cycle: solid line; 2nd cycle: dash-dotted line; 3rd cycle: dash line

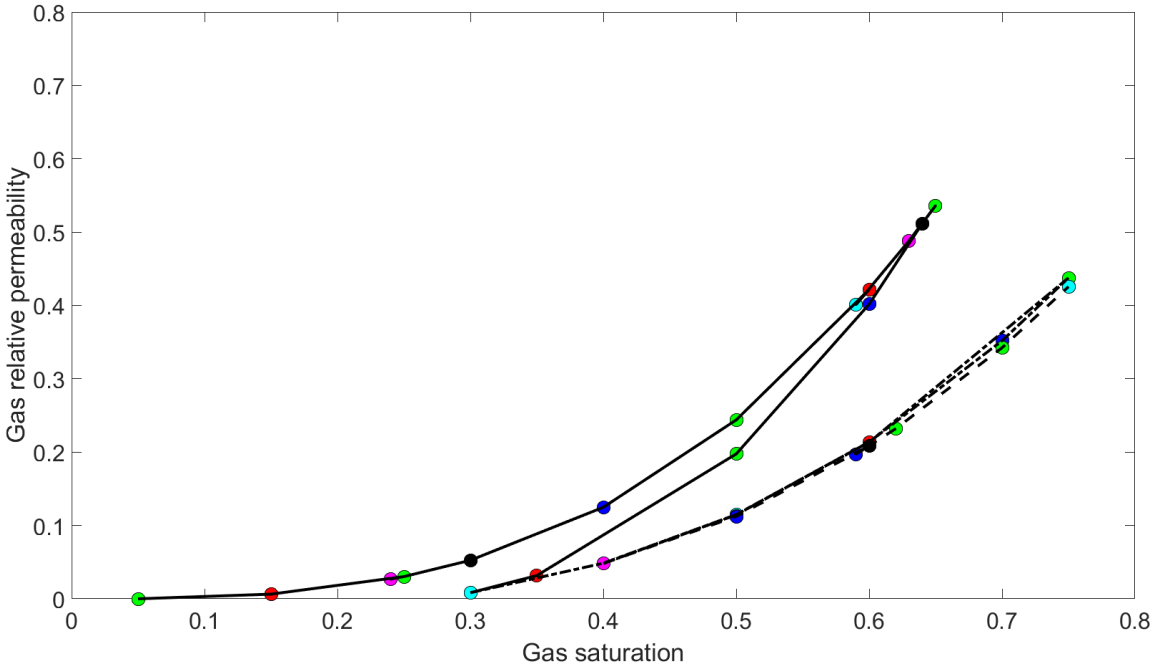

Figure 4-9B: Gas relative permeability calculated using the Larsen and Skauge model (**1998**) with $\alpha_{LS} = 0.8$. 1st cycle: solid line; 2nd cycle: dash-dotted line; 3rd cycle: dash line

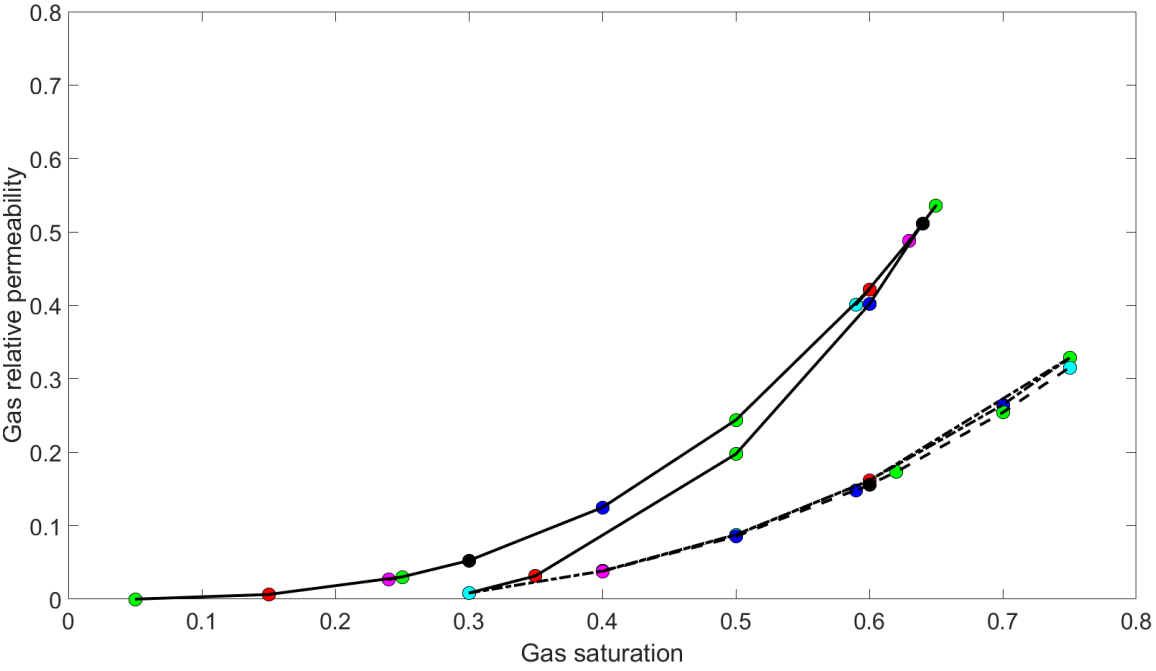

Figure 4-9C: Gas relative permeability calculated using the Larsen and Skauge model (**1998**) with $\alpha_{LS} = 1.2$. 1st cycle: solid line; 2nd cycle: dash-dotted line; 3rd cycle: dash line

4.10 SUMMARY AND CONCLUSION

Hysteresis phenomena govern the physics of multiphase flow in multicycle processes. Capillary trapping and hysteresis play a substantial role on the techno-economic performance of multicycle processes and natural gas storage projects. Accurate modeling of hysteresis requires fundamental understanding of the impacting parameters on the complex multiphase flow in porous media.

Capillary trapping is key to characterizing hysteresis in a multicycle process. In the absence of interphase compositional variations, trapped saturation in a consolidated rock increases monotonically in a decreasing saturation direction and remains constant in the increasing saturation direction. Land equation describes that the difference of reciprocal of initial and trapped saturation is constant. The constant Land coefficient is valid objective to the fixed experimental saturation history and is not unique in multicycle processes. As the number of phases, saturation direction, or saturation trajectory vary, the Land coefficient varies. Trapped saturation also depends on the saturation of a conjugate phase.

For three-phase applications, the observed cycle-dependent relative permeability contradicted the underlying assumption of two-phase hysteresis models. The cycle dependency of relative permeability introduced the three-phase hysteresis modeling concept.

The developed three-phase hysteresis model in this chapter provides a simple approach to calculate capillary trapping. Furthermore, the calculated trapped saturation provides insights to the degree of gas inventory in natural gas storage and CO_2 sequestration processes. Incorporating the trapped saturation to a relative permeability model represent the hysteresis effect and results in the cycle-dependent relative permeability curves.

Capillary trapping is a saturation-history-dependent quantity. It requires both saturation direction and path to be incorporated in the relative permeability model. While some processes are involved in a significant variation of saturation trajectory (path), the saturation direction may not

vary or vice versa. The impact of coupled saturation path and direction for multicycle processes can be modeled using the UTHYST model. The saturation path effect in the absence of a variation in the saturation direction, however, is incorporated using the UTKR3P model. It delineates the significance of developing an integrated toolbox including a relative permeability and a hysteresis model.

Chapter 5: **Compositional Relative Permeability Modeling (UTPGE framework)**

This chapter introduces a general framework for incorporating compositional effects as applied to relative permeability model. The proposed approach is general— applicable to any hydrocarbon and non-hydrocarbon phases— and generates spatial-temporal distributions of relative permeability over the entire composition and saturation spaces. In particular, it is a pragmatic approach for modeling processes involved in an intensive interphase mass transfer (see **Fluid composition** in Chapter 2). The proposed framework is an extension of the model proposed by Yuan and Pope (**2012**) for the hydrocarbon phase relative permeability.

The general framework unifies thermodynamics, petrophysics, and geochemistry to enhancing relative permeability model (UTPGE framework). Some features of the UTPGE framework include (**i**) adding explicitly the pressure, temperature, and compositional effects, (**ii**) incorporating geochemical effects on aqueous relative permeability, (**iii**) scanning of water-hydrocarbon fluid system when single-phase hydrocarbon is bounded between the immiscible oil and gas phases, and (**iv**) generating an EOS-dependent hydrocarbon relative permeability without the arbitrary phase-splitting as oil or gas.

In the following, we first introduce the UTPGE framework and review the keystone of the modeling approach, viz., molar GFE calculation, for two composition-demanding processes. The case studies then provide discussion on applying the UTPGE framework for more accurate modeling of compositional relative permeability and insight into the impacting parameters for methods such as modified-salinity waterflood and near critical fluids. Specifically, we provide two detailed examples, one for the aqueous phase and a second for the hydrocarbon.

5.1 GENERAL UTPGE FRAMEWORK

The phase molar Gibbs free energy (GFE) is evaluated based on components mole fraction and partial molar GFE at specified pressure (P), temperature (T), and composition (θ) and by neglecting the capillary pressure term as,

$$\underline{G_j}(T,P,\theta) = \sum_{i=1}^{N_j} \theta_{ij}\bar{G}_{ij}, \qquad \textbf{Eq. 5-1}$$

where θ_{ij} denotes the mole fraction of component i in phase j and $\bar{G}_{ij}$ is partial molar GFE of component i in phase j at P and T. The partial molar GFE of component i in phase j (chemical potential) for the real mixtures is defined based on the following general formulae relating two GFE values at identical P and T as (**Prausnitz et al., 1999**),

$$\bar{G}_{ij}(T,P,\theta) = \underline{G_{ij}^{\square}}(T,P,\theta_i^{\square}) + RTln\left(\frac{f_{ij}(T,P,\theta_{ij})}{f_{ij}^{\square}(T,P^{\square},\theta_{ij}^{\square})}\right), \qquad \textbf{Eq. 5-2}$$

where for component i in phase j, f_{ij} is the fugacity at P, T, and θ. $f_{ij}^{\square}$ denotes the ideal fugacity in a reference pressure and composition and T based upon the phase state, and $\underline{G_{ij}^{\square}}$ expresses the chemical potential at an ideal state. As will be noted, both $\underline{G_{ij}^{\square}}$ and $f_{ij}^{\square}$ are defined using a convenient standard state of phase, e.g., aqueous, hydrocarbon, or solid phase including T, reference pressure ($P^{\square}$), and reference composition ($\theta_{ij}^{\square}$). Thus, these phase-dependent quantities result in a non-unique value for the general ideal state of the GFE quantity.

Defining the fugacity (or activity) of component i in phase j as,

$$a_{ij} = \frac{f_{ij}(T,P,\theta_{ij})}{f_{ij}^{\square}(T,P^{\square},\theta_{ij}^{\square})}, \qquad \textbf{Eq. 5-3}$$

and combining **Eq. 5-1** and **Eq. 5-2**, results in the following general expression for the phase molar *GFE*,

$$\underline{G_j}(T,P,\theta) = \sum_{i=1}^{N_j} \theta_{ij}\left[\underline{G_{ij}^{\square}}(T,P,\theta_i^{\square}) + RTln(a_{ij})\right]. \quad \textbf{Eq. 5-4}$$

Because $\underline{G_j^{\square}} = \sum_{i=1}^{N_j} \theta_{ij}\left(\underline{G_{ij}^{\square}}(T,P,\theta_i^{\square})\right)$, we finalizes the molar GFE evaluation for any specific phase and specific P, T, and θ as,

$$\underline{G_j}(T,P,\theta) = \underline{G_j^{\square}}(T,P) + RT\sum_{i=1}^{N_j} \theta_{ij}ln(a_{ij}). \quad \textbf{Eq. 5-5}$$

Figure 5-1 reviews the algorithm for composition-dependent relative permeability g for any phase. As **Figure 5-1** states, one can select the interphase composition rather than the bulk-phase approach. It provides a detailed and more accurate modeling approach of multiphase compositional relative permeability than the approach based on the bulk-phase-dependent parameters. This general method relates two-phase relative permeability properties to the bulk phase property and an interface property of the specified phase in equilibrium with its counterpart phase(s). The phase molar Gibbs free energy (GFE) represents the bulk property. A thermodynamic property should represent the interphase property. Although the GFE of interphase seems trivial, it is computationally expensive. As described below, we employ interfacial tension in numerical simulation and avoid evaluating the interphase composition and the exact location of interphases.

For the closed system of interest, the fluid-pair IFT (σ) represents the increase in the Gibbs free energy per increase in surface area at constant P, T, and number of moles of each interphase component. Based on the Gibbs theorem (**Gibbs, 1875-1878**; **Kirkwood & Oppenheim, 1961**), total Gibbs free energy of a closed system (G^t) including two immiscible phases α and β divided by an infinitely thin interphase γ with interfacial area (A) can be expressed as,

$$G^t = G^\alpha + G^\beta + G^\gamma + \sigma A. \quad \textbf{Eq. 5-6}$$

For the constant overall composition (N), P, and T, one can relate IFT to the variation of interphase Gibbs free energy (G^γ),

$$\sigma \propto \left(\frac{\partial G^\gamma}{\partial A}\right)_{T,P,N}. \quad \textbf{Eq. 5-7}$$

Eq. 5-7 states that IFT may be a suitable representation of G^γ. This approach can be readily implemented in a compositional reservoir simulator in that IFT values are generally evaluated in reservoir simulators.

Guggenheim (**1940**) pointed out that the thermodynamics properties must be assigned to the interphase with a finite volume. Adding a thin molecular layer does not significantly impact the accuracy of the total Gibbs free energy calculation. It is of particular importance because the crucial dividing interphase location is an uncertain parameter. We then follow the Gibbs theorem without losing generality.

Now, we have twos set of parameters: the bulk thermodynamic property as represented by GFE and an interface property as represented by IFT. A texture mapping technique evaluates the function of two variables (GFE, IFT) on a rectilinear 2D grid in unsampled locations of compositional space. Providing a dataset of known compositions (Q), we create an interpolation function among the GFE and IFT. We then lift the vertices of the generated Delaunay triangulation (**Lee & Schachter, 1980**) for the Q-set and evaluate the interpolant at any query point X.

Among various multivariate interpolation approaches, we adopt a bilinear GFE-IFT weighted interpolation scheme. If the size of the Q data set increases (i.e., the compositional analysis of produced oil and gas in SCAL analysis), the interpolation scheme can be extended to the more accurate methods such as bicubic interpolation. Here, our focus is to introduce the

framework; the bilinear interpolation scheme thereby was found to be sufficient.

The coupled GFE-IFT approach appeals to a variety of subsurface processes/conditions. (**i**) When there are more than one non-aqueous phase and those phases interact with aqueous disproportionally. For example, the mass-transfer between aqueous and non-hydrocarbon gases are entirely different than that with the hydrocarbon liquids. The dissolution of supercritical CO_2 and acid gases in aqueous phase alters the phase behavior and thermodynamic properties of the aqueous phase substantially when compared to liquid hydrocarbon. (**ii**) When two-phase relative permeability parameters are dissimilar. The end-point relative permeability, residual saturation, relative permeability curvature constants are not necessarily unique in water-oil-gas, water-gas, water-oil, water-non-hydrocarbon liquids particularly for non-water-wet media. This necessitates distinguishing between the two-phase parameters and their level of alteration. The reasoning highlights the importance of applying a parameterized relative permeability model, e.g. the UTKR3P model.

5.1.1 General approach in compositional relative permeability measurement and simulation

For the particular process and fluid system, we run a simulation study to identify the extreme values of phase molar GFE over saturation and composition spaces. The evaluated composition, pressure, and temperature are then the initial condition at which the two-phase laboratory relative permeability measurements are conducted. For example, for a near-miscible gasflood, we initially identify the GFE of mixture and hydrocarbon phases. This yields the selection of the lowest and highest GFE values such as the most liquid-like and gas-like hydrocarbons, respectively.

The laboratory measurements are then conducted based on these fluid compositions. This procedure confirms that during the simulation study of compositional relative permeability, no unsecured extrapolation will be required. The measured relative permeability together with the

phase bulk composition and IFT values are input parameters to the UTPGE framework. We then map relative permeability parameters (endpoints, residual saturations, and curvatures) on the integrated GFE-IFT space. The parameters of any query points during the simulation study are selected from the evaluated maps.

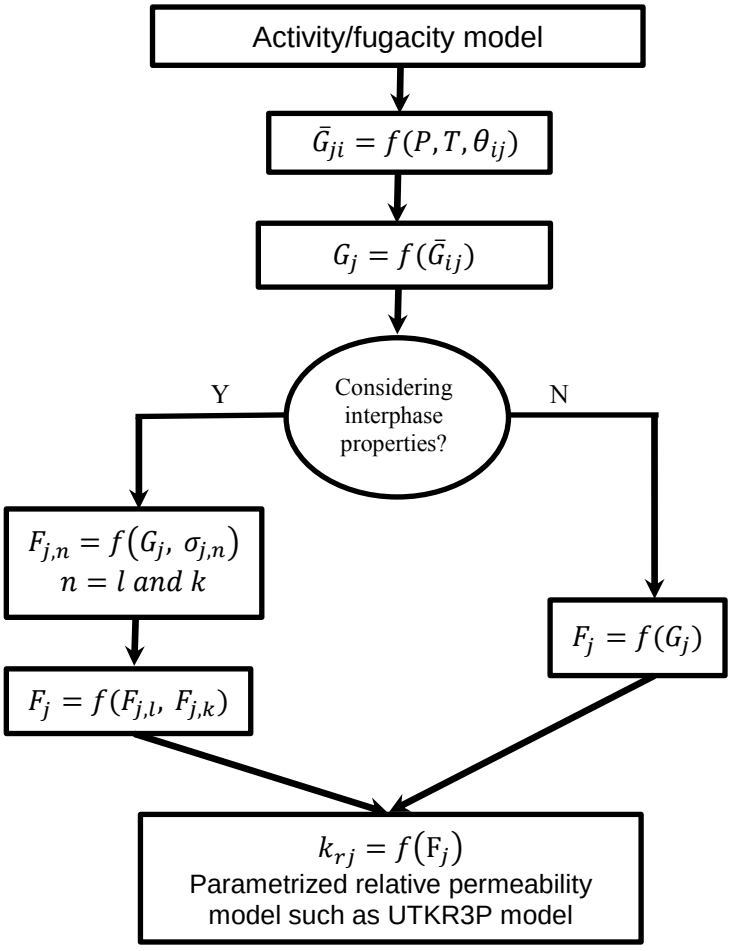

Figure 5-1: General UTPGE framework for modeling composition-dependent relative permeability

5.2 COMPOSITION-DEPENDENT AQUEOUS RELATIVE PERMEABILITY

As noted in **Chapter 2**, aqueous phase dynamically exchanges components with the surrounding phases in porous media within several petroleum, hydrology, and environmental applications. Discussions of **Fluid composition** in Chapter 2 delineates the crucial role of mass exchange on aqueous relative permeability. As explained in the following, the UTPGE framework provides a straightforward approach to model the compositional aqueous relative permeability.

5.2.1 Review of aqueous Gibbs free energy framework

Figure 5-2 displays the overall context of the proposed aqueous relative permeability calculation procedure based on the general UTPGE framework (**Figure 5-1**). One requires aqueous speciation results to evaluate the activity coefficient and GFE of aqueous components (i.e., water and other species in the comprehensive model as noted later). Next, if the bulk properties are the only critical parameter for the compositional-dependent relative permeability, the parameters for the aqueous phase are directly evaluated based on a *linear* GFE-averaged interpolation scheme between the reference and current state.

By adopting both bulk and interface properties to assess composition-dependent parameters, we require IFT between aqueous and other phases. For the water-hydrocarbon IFT, we apply the correlation of Firoozabadi and Ramey (**1988**) as modified by Sutton (**2009**). Next, we review the GFE calculation for the aqueous phase.

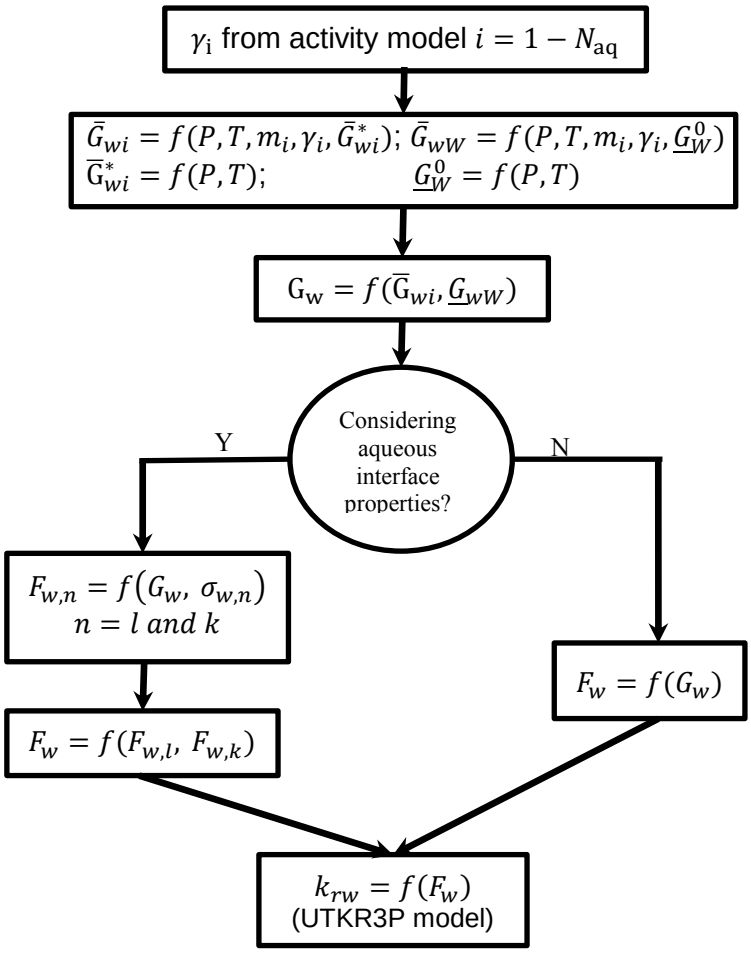

Figure 5-2: UTPGE framework for modeling composition-dependent aqueous relative permeability

5.2.2 **Gibbs free energy of Aqueous phase**

Aqueous GFE is calculated from aqueous speciation results (i.e., species activity and concentration). Neglecting the capillary pressure, for an aqueous system constituting of N_{aq} aqueous components at a specific temperature (T), pressure (P), and composition, one may extracts the GFE of non-ideal aqueous phase (G_w) from **Eq. 5-1** as a sum of the contributions from water and other components:

$$G_w(T, P, w_i) = c_W \bar{G}_{wW} + \sum_{j=1}^{N_{aq}-1} c_j \bar{G}_{wj}, \qquad \textbf{Eq. 5-8}$$

where c_W and c_j denote a convenient form of concentration of water (W) and any other component in the aqueous system (w), respectively. Here, N_{aq} is the number of aqueous components, $\bar{G}_W$ and $\bar{G}_j$ denote the partial molar GFE of water and other components in the aqueous system, respectively. Note that for a reactive aqueous system, although the concentration of reactive components varies according to stoichiometric coefficient and reaction extent of the components, **Eq. 5-8** holds for GFE calculation of total system. The partial molar GFEs for water ($\bar{G}_{wW}$) and electrolyte components ($\bar{G}_{wj}$) are expressed by,

$$\bar{G}_{wW}(T,P,w_W) = \underline{G}^0_W(T,P) + RTln(w_W\gamma_W), \qquad \textbf{Eq. 5-9}$$

$$\bar{G}_{wj}(T,P,w_j) = \bar{G}^*_j(T,P) + RTln(w_j\gamma_j), \qquad \textbf{Eq. 5-10}$$

where $\underline{G}^0_W$ represent the standard state GFE for pure solvent (water), $\bar{G}^*_j$ denotes the apparent standard-state (or apparent reference) partial GFE for any solute, and γ_j denote the component activity coefficient due to non-ideality of the solution. Note that the standard state GFE is pressure and temperature dependent but is independent of composition. For solute components, the standard state GFE is the GFE of those components in a hypothetical ideal solution of a solvent at a given temperature and pressure. The ideal solution is defined based on a non-zero concentration of solute where the solute activity coefficient approaches one. The water standard state GFE, however, is pure-water reference state (**Prausnitz et al., 1999**). For the aqueous system, w_i is represented in molality scale to alleviate the required density data. The pressure- and temperature-dependent apparent standard-state GFEs are calculated based on the HKF EOS (**Helgeson, 1969**; **Helgeson & Kirkham, 1974**; **Helgeson et al., 1981**; **Oelkers et al., 1995**) as described in **Appendix G**. For the electrolytes not provided in the HKF tables, we use the apparent standard-state GFEs (evaluated at 25 ℃ and 1 atm) in NIST tables corrected for the specified pressure and temperature based on an approximation method (**Sandler, 2006**). We discuss this method in **Appendix H**. Venkatraman (**2014**) successfully applied this approximation method for modeling the acid-gas

solubility in the aqueous phase.

Figure 5-3 and **Figure 5-4** depict the variation of isothermal apparent standard GFE ($\bar{G}_j^*$) with pressure for a broad range of pressure and temperature in field applications ($T = 50 - 300$ ℃; $P = 10 - 150$ MPa) based on the HKF-EOS for selected cations and anions in an aqueous solution, respectively. They reveal that although the studied cations have a monotonic behavior with respect to standard GFE within the shown pressure and temperature range, a natural non-monotonicity exists in thermodynamic behavior of some anions, e.g., Cl^- and HS^-. This must be taken into account when the GFE-dependent relative permeability model is applied. **Figure 5-5** compares the behavior of reference GFE ($\bar{G}^*/RT$) of NaCl salt when outlined in molar (*kJ/mole*) and dimensionless representations. It implies that the non-monotonicity can be concealed if one plots the dimensionless GFE in lieu of the molar format. It leads to erroneous results if one naïvely concludes that the electrolyte apparent standard GFE naturally obeys a monotonic behavior.

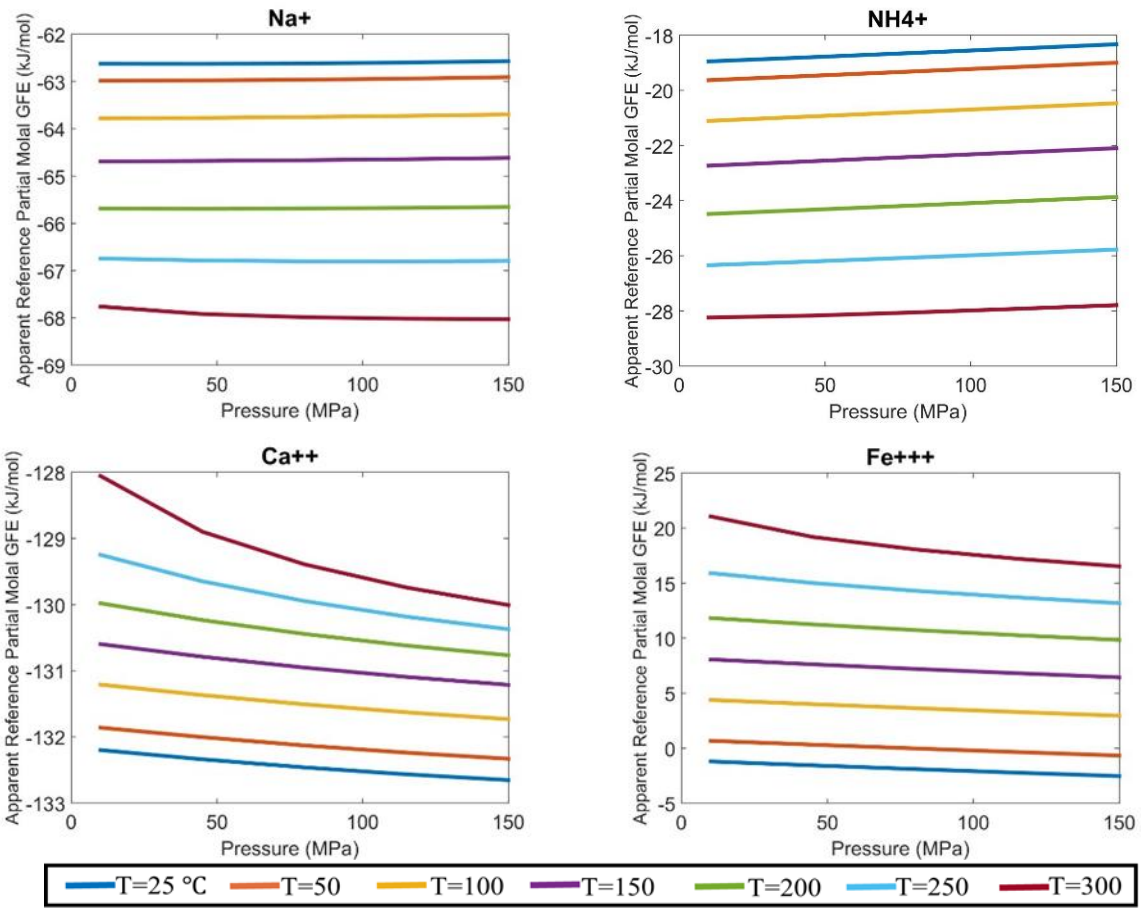

Figure 5-3: Variation of isothermal apparent standard GFE of selected cations with pressure

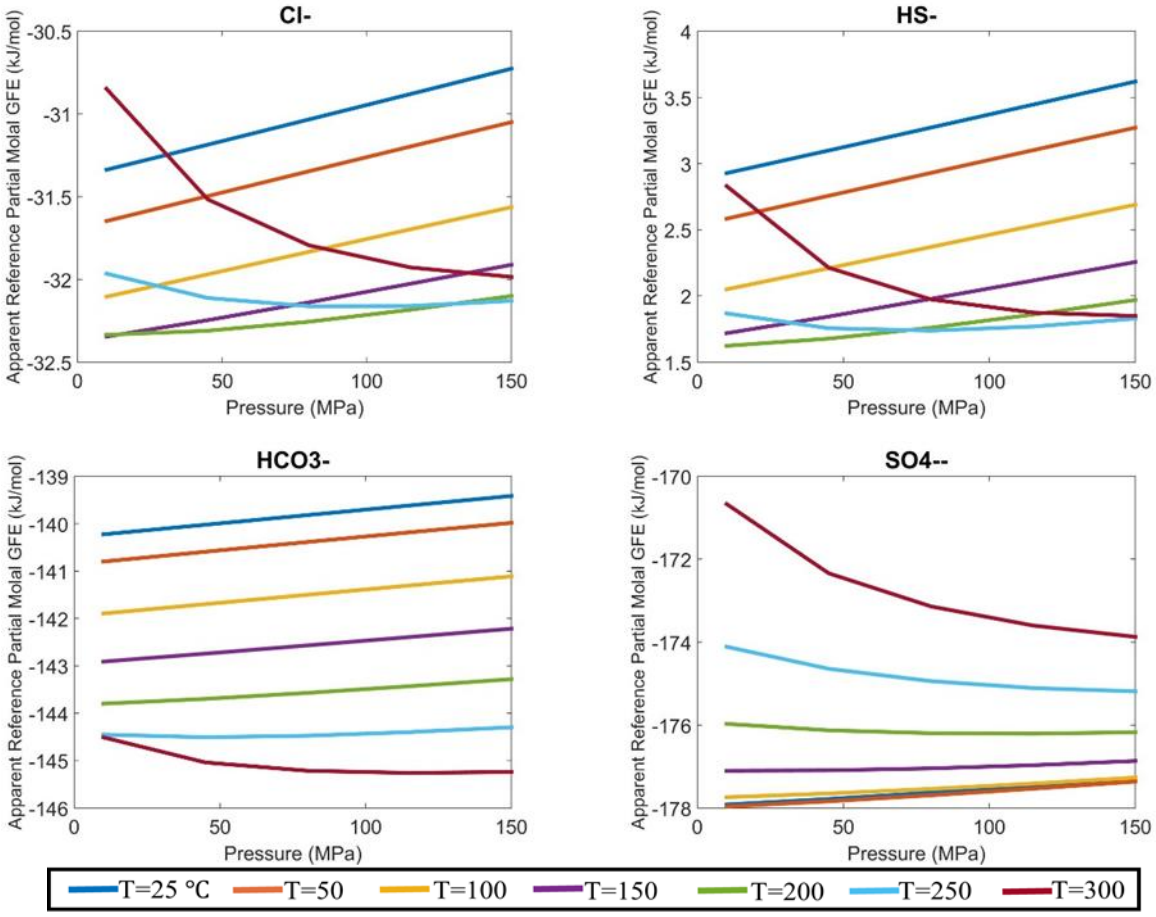

Figure 5-4: Variation of isothermal apparent standard GFE of selected anions with pressure

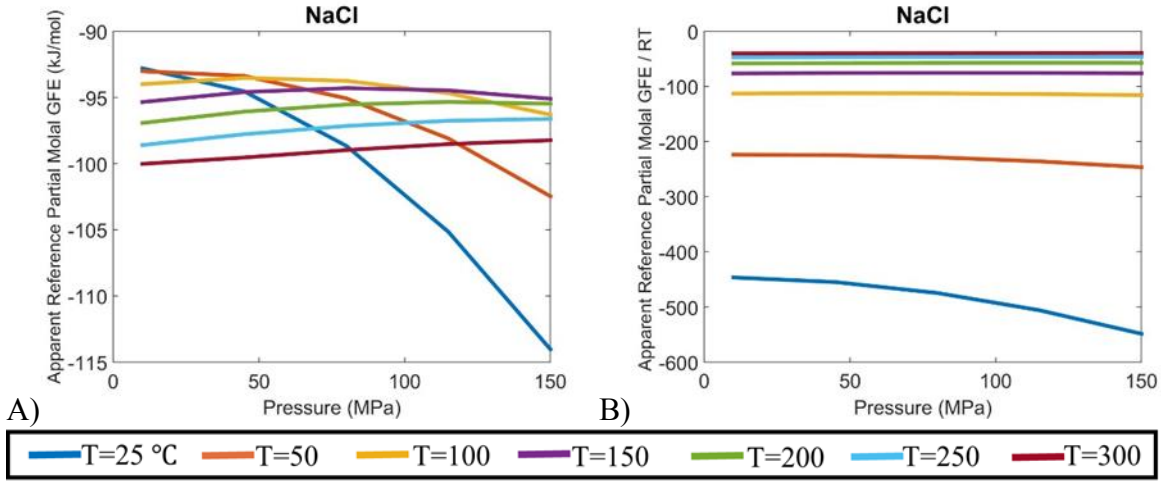

Figure 5-5: Variation of Isothermal apparent standard GFE of NaCl with pressure: A) molar GFE (kJ/mole) and B) dimensionless GFE (G/RT)

5.2.2.1 Aqueous activity modeling

As discussed in **Appendix C**, numerous electrolyte activity models have been developed to cover several interaction levels in aqueous electrolyte solutions: charge-charge, charge-dipole, and dipole-dipole interactions. The starting point of these models, in general, is to divide a general electrolyte activity model into non-electrolyte and electrolyte sections. They then relate the activity model to an excess thermodynamic property, e.g., molar Gibbs free energy or molar Helmholtz free energy. Next, they attempt to capture the complex short- and long-range interplays among solute ions, solute molecules, and solvent molecules.

The non-electrolyte section of excess property incorporates short-range repulsive and dispersive interactions. An EOS, local composition model, or empirical model may represent these short- to intermediate-range interactions. The electrolyte contribution is to cover long-range charge-charge and charge-multipole interactions in the excess thermodynamic property.

A theoretical model based on the Poisson-Boltzmann or integral theory as represented by the Debye-Hückel or MSA and their variants, respectively, may characterize the long-range interactions. Many investigators believe that the modern MSA approach is superior to the conventional Debye-Hückel type approach due to increased level of ion-ion and ion-solvent interactions. From a practical and field-scale application perspective, however, there is no compelling reasoning to prefer the more complicated MSA approach in lieu of the Debye-Hückel type approach. Indeed, several researchers (**Zuckerman et al., 1997**; **Paricaud et al., 2002**; **Lin et al., 2007**) have demonstrated that there is a good agreement among numerical results from a range of variants of the both Debye-Hückel and MSA models against experimental electrolyte data.

5.2.3 Reduced form of aqueous Gibbs free energy framework

Ionic strength may conditionally represent the GFE of the aqueous system. This has been shown

based on the detailed study of various samples at a broad range of temperature and composition. **Table 5-1** lists water speciation results for five samples. We then evaluated the required activity and osmotic coefficients for the UTPGE framework in two ways: (**i**) by analyzing the aqueous system in the PHREEQC package (**pH**-**RE**dox-**EQ**uilibirum in **C** programming language) —an open-source state-of-the-art geochemical package of the USGC (**Parkhurst & Appelo, 2013**) and adopting Pitzer model (**Pitzer, 1973a**) (see **Pitzer formulation** in Appendix C) and B-dot model (Helgeson and coworkers, **1969**; **1974**; **1981**) (see **Table C-2** in Appendix C), and (**ii**) by implementing the Pitzer formulation into an in-house developed code. We considered seventeen geochemical reactions and carbon dissolution, opted the possible cation-exchange with clays, if required, but excluded the redox state from our simulation studies. In that the ionic activity behavior in the specified range of composition and temperature/pressure is approximately identical in two models, we only report the results of Pitzer's model. In addition, we excluded the solid surface energy in modeling GFE using the UTPGE framework.

Figure 5-6 depicts the non-ideal behavior of ionic species of these samples along with water activity at the designated temperature and the associated pure-water saturation pressure (P^{sat}): activity coefficient of electrolytes behaves non-monotonically as overall concentration of the solution increases.

We then evaluated the appropriate isothermal apparent standard GFE of each species at the query pressure and temperature using the HKF-EOS model (see **Appendix G**). Integrating the activity of water component and all other aqueous species completes the calculation procedure for the aqueous GFE (see **Figure 5-2**).

Figure 5-7 represents dimensionless GFE (G/RT) variation with temperature for each sample with unique ionic strength. **Figure 5-7** also reports that as ionic strength increases, isothermal GFE decreases. **Figure 5-8** indicates that excluding pressure effects, molar GFE and

ionic strength are correlated for the studies samples. They approach pure-water GFE at the designated pressure and temperature at the high diluted state. **Figure 5-8** implies that the molar GFE of the aqueous system is highly correlated with variation of water activity with ionic strength for the studied samples. This occurs due to the dominant effect of activity and partial molar GFE of water component in the overall behavior of studied aqueous systems. **Figure 5-8** shows that by neglecting the pressure effect on electrolyte behavior for samples in **Table 5-1**, irrespective of the internal aqueous composition, the ionic strength ($molal$ unit) expresses the molal GFE (G) ($kJ/mole$ unit) as,

$$G = -7.1 \times I - 251.1. \qquad \textbf{Eq. 5-11}$$

This correlation lends credence to the idea that ionic strength may represent, in particular, circumstances, the behavior of GFE. Consequently, a straightforward relation of the compositional effects with the ionic strength of the solution can be taken into account as a reduced form of the general proposed framework. In addition, one may facilitate further simplifications of the UTPGE framework if complete water analysis is not acceptable— the ionic composition of the aqueous phase is unknown or unreliable. One could estimate ionic strength using electrical conductivity and/or total dissolved solids (TDS). Griffin and Jurinak (**1973**) suggested the following relation: $I = 1.6 \times 10^{-5} \times SC \quad (if\ I < 0.5)$, where SC is specific conductance in $\mu S/cm$. Langelier (**1936**) proposed applying TDS (i.e., $I = 2.5 \times 10^{-5} \times TDS$, where the unit of TDS is mg/L).

Table 5-1: Chemical analysis (ppm), ionic strength, and GFE of aqueous phase for five samples

Ions	Fresh Water	Formation Water-1	Formation Water-2	Geothermal-1	Geothermal-2
	(Kazempour et al., 2013)		(Sorop et al., 2015)	(McCoy et al., 1981)	
Na^+	40	2430	96297	32190	48281
K^+	5	66	1403	454	988
Ca^{2+}	12	300	3633	7870	18305
Mg^{2+}	3	47	1990	910	2320
Ba^{2+}	0	20	35	0	0
Sr^{2+}	1	26	125	1	1
Cl^-	18	4343	162125	50300	91387
Fe^{3+}	0	0	0	33	56
SO_4^{2-}	0	7	0	444	7
HCO_3^-	110	512	0	606	208
TDS (ppm)	**215**	**8410**	**265608**	**103925**	**190904**
Temperature (℃)	45	45	45	132	177
Ionic strength (M)	**0.003**	**0.138**	**6.161**	**1.754**	**3.289**
G/RT (T, P^{sat})	**-94.9**	**-95.3**	**-111.0**	**-75.0**	**-69.6**

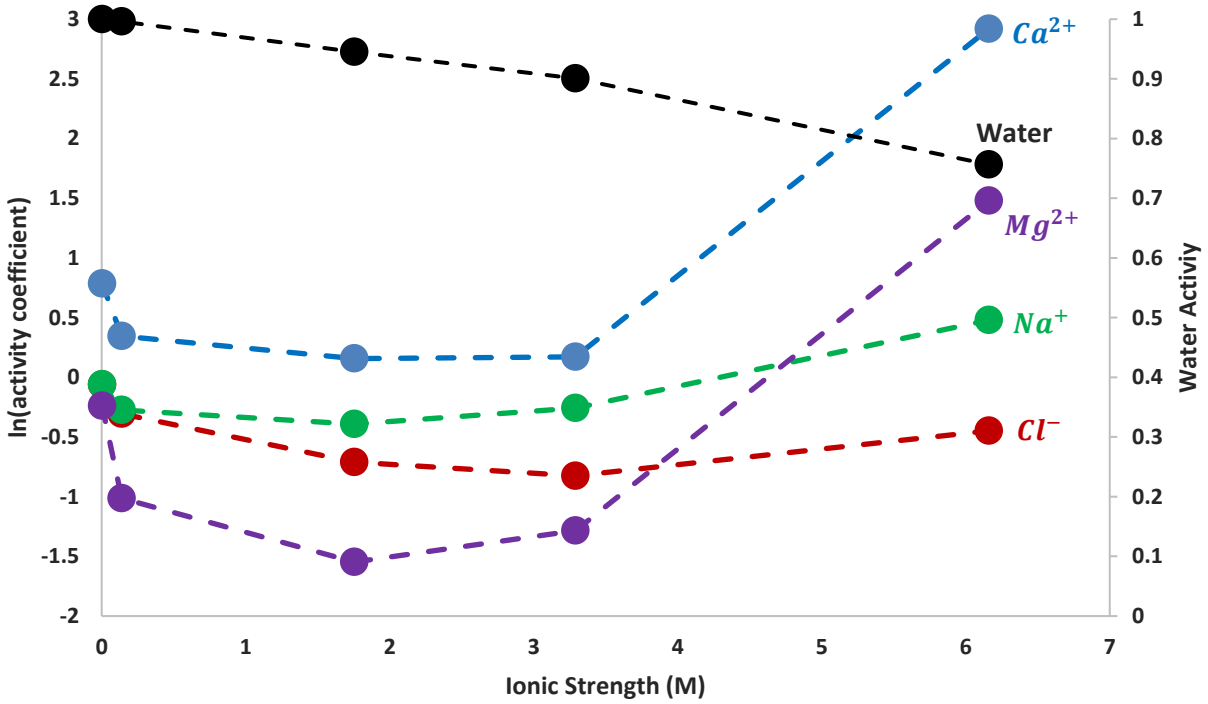

Figure 5-6: Variation of activity coefficient of four species (left axis) and water activity (right axis) with ionic strength (see **Table 5-1**)

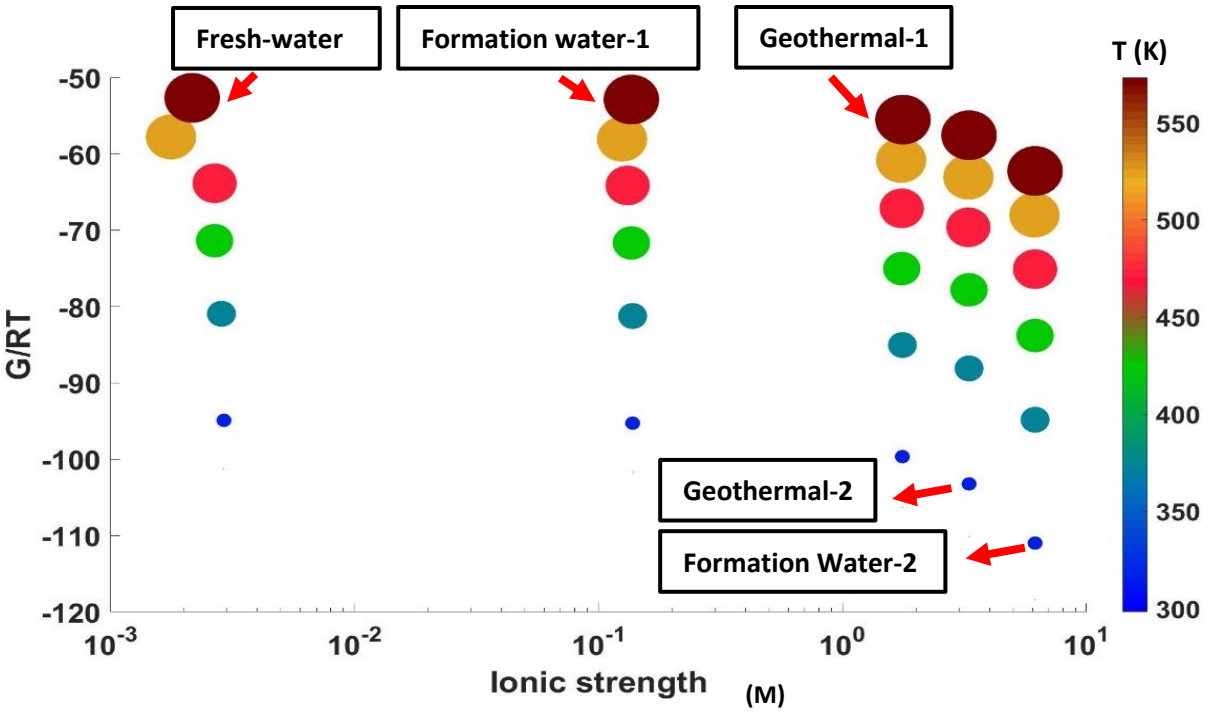

Figure 5-7: Variation of aqueous dimensionless GFE with temperature and ionic strength (according to size and color of bubbles) of studied samples (see **Table 5-1**)

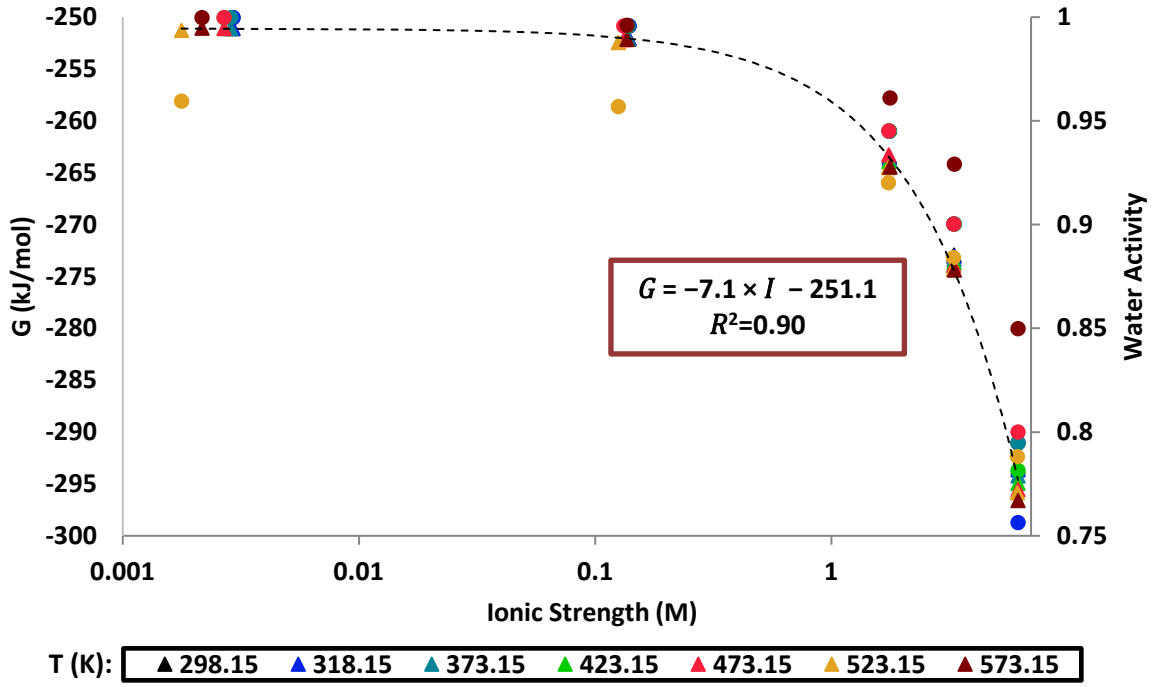

Figure 5-8: Variation of aqueous molal Gibbs free energy (G) (left axis, triangles) and water component activity (right axis, circles) with ionic strength and temperature for studied samples (see **Table 5-1**)

5.2.4 Application of UTPGE framework to model low-salinity waterflood (Case AQ1)

We apply the UTPGE model to a low-salinity waterflood to demonstrate the straightforward application of this general framework (Case AQ1). The reference high salinity state (HS) is the Formation Water-2 (**Sorop et al., 2015**) in **Table 5-1**. The reference low-salinity state (LS) is the diluted formation water by 167 times (TDS≅1600 ppm). First, we evaluate the reference relative permeability values at low- and high-salinity conditions. We then apply the UTPGE framework to calculate relative permeability curves at any query states.

Figure 5-9 represents the measured and calculated relative permeability data using the UTKR3P relative permeability model for water and oil relative permeability did not exceed 0.04). Note that oil relative permeability shows an S-shape behavior which can readily be modeled applying the UTKR3P model. Next, we update the relative permeability parameters for any selected pressure, temperature, and composition in a range of LS and HS conditions. For an arbitrary middle composition (MS) (I=3.5 M), the GFE is evaluated either by calculating the detailed aqueous speciation or by estimating using **Eq. 5-11**. Here, our purpose is conceptual rather than to match specific data. As a result, we applied the latter method to evaluate the dimensionless GFE (G/RT= -104.3). The water and oil relative permeability parameter ($k_{rj}^0, C_{1j}, C_{2j}, and\ S_{rj}$) are interpolated based on the reference GFEs for LS and HS (G^{LS}/RT= -102.3 and G^{HS}/RT=-111.4). **Figure 5-10** presents the calculated relative permeabilities curves.

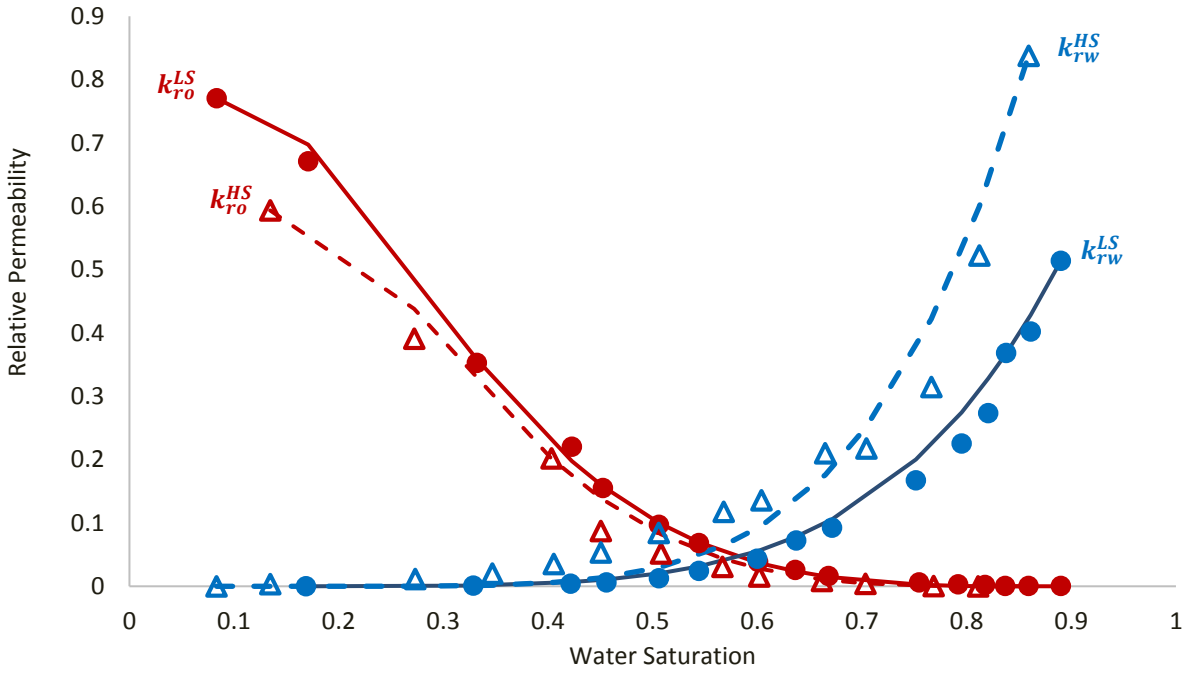

Figure 5-9: Water (blue) and oil (red) relative permeability at LS and HS conditions in Case AQ1 (sample Formation Water 2, **Table 5-1**). Measured LS data (filled circle) and measured HS data (empty triangle); calculated LS curves (dashed lines) and calculated HS curves (solid lines)

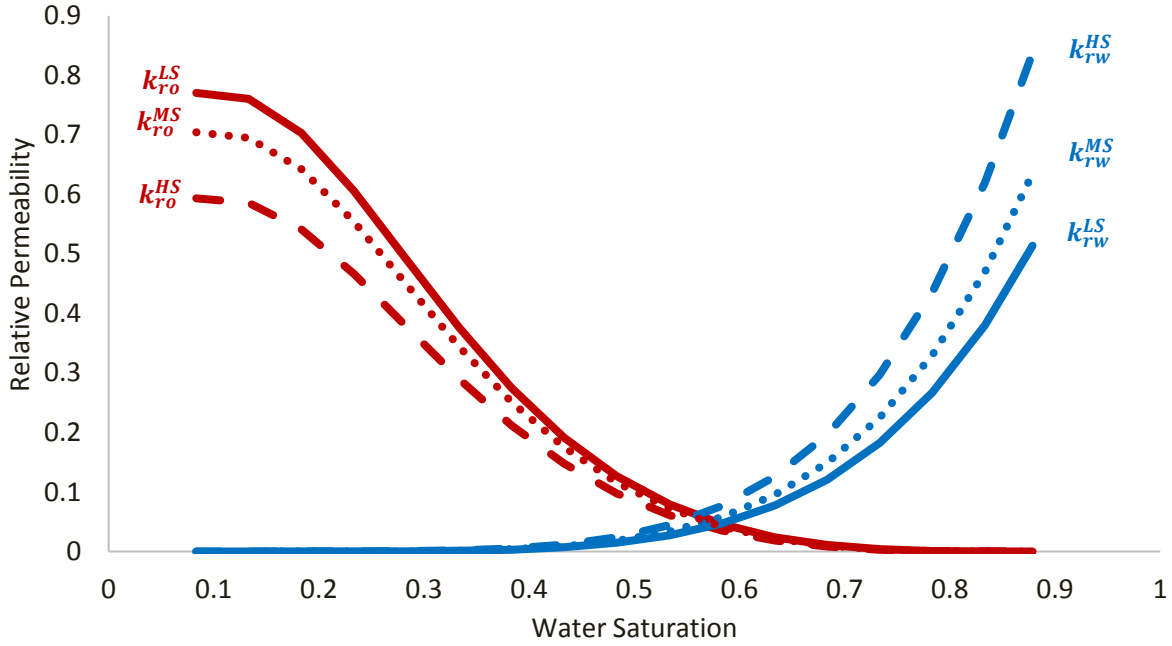

Figure 5-10: Water and oil relative permeability at LS, MS, and HS conditions in Case AQ1 (sample Formation Water 2, **Table 5-1**). Water (blue) and oil (red); calculated HS curves (dashed lines); calculated LS curves (solid lines); calculated compositional MS curves (dotted lines)

Comparison of general and simplified UTPGE frameworks

The general UTPGE framework takes into account the contribution of each electrolyte explicitly. Reduced form of the framework, however, formulates GFE as a function of total aqueous concentration. This may lead to erroneous results if the relative permeability is sensitive to particular set of ionic concentrations. For example, **Figure 5-11** depicts GFE variation with concentration of one particular salt, e.g. NaCl, for a constant ionic strength solution. Two cases are demonstrated in which the overall concentration is renormalized on either one or four salt(s) to keep the ionic strength constant (I= 6.148 M). It reveals that the water activity varied between 0.758 to 0.854 and that aqueous GFE may change up to 10% compared to that of the starting sample. As a result, if internal composition of the aqueous is a substantial decision-making parameter, the general framework is recommended. This is of particular concern for cases with significant ion-exchange capacity where the possible exchange of cations may keep the overall concentration constant while the concentration of the individual and important species of aqueous varies.

We conclude that for the range of temperature of the studies samples and by neglecting the pressure effect, the GFE of an aqueous system may be represented by the ionic strength of that system. Hence, either of the approaches (GFE or I) are suitable for modeling the low salinity waterflood. It is in accordance with the principle that Korrani et al. (**2014**) applied for the modeling of low salinity waterflood (see **Table 2-1**). They used an ionic-strength-weighted interpolation scheme to estimate relative permeability of a modified salinity waterflood. If the aqueous composition varies while having an equal ionic strength, application of the ionic strength as the weighting parameter may lead to the erroneous results.

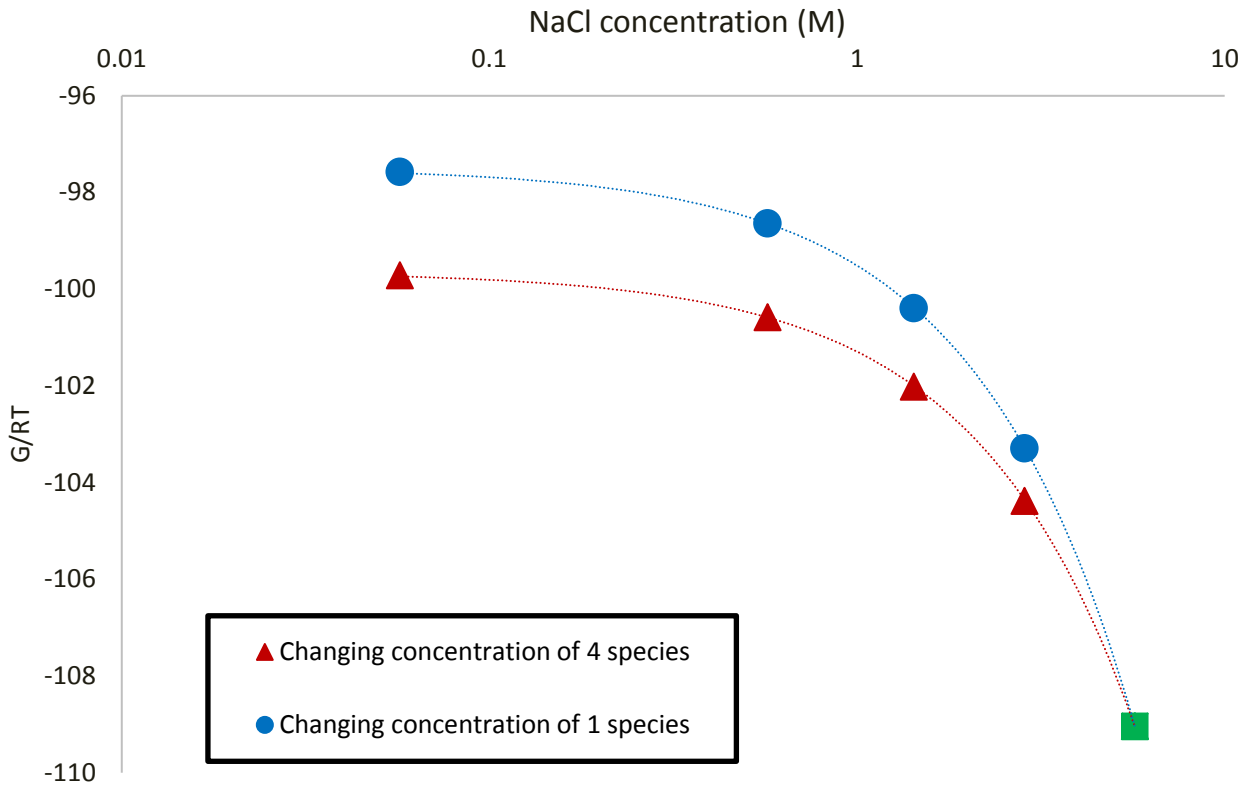

Figure 5-11: Variation in aqueous molar GFE with concentration of one salt (NaCl) while keeping ionic strength constant (I=6.16 M) by renormalizing the overall mixture concentration either by varying concentration of one or four species. Variation of concentration of Ca^{2+} (blue circles); variation of concentration of K^{+}, Mg^{2+}, Ba^{2+}, and Ca^{2+} (red triangles); concentration of original sample (green rectangle) (data: Formation water-2, **Table 5-1**)

5.3 COMPOSITION-DEPENDENT HYDROCARBON RELATIVE PERMEABILITY

In this section, we demonstrate the application of the developed UTPGE framework in modeling hydrocarbon relative permeability for near-critical fluids, and near-miscible displacements. First, we tailor the general UT-PGE framework to the hydrocarbon phase. We then illustrate the unique features of this framework in modeling processes involved in an intensive interphase mass transfer.

As Yuan and Pope (**2012**) stated, the GFE-dependent relative permeability approach does not require the conventional phase characterization and labeling. It eliminates the dependency of a successful relative permeability modeling to correct phase identification which is particularly useful if phase-flipping issue is probable. The conventional relative permeability calculation approach requires the designated phase saturation and phase relative permeability parameters. The labeled phase is based on a phase characterization quantity like phase mass density. Mass densities, however, may induce compositionally inconsistent results to numerical modeling in certain conditions. There are instances in which mass density of phases physically cross. For example, when a CO_2-rich liquid phase and a hydrocarbon-rich liquid coexists in a fluid system at low temperature (**Khan, 1992**). Besides, the unphysical phase flipping issue due to the near-miscible condition in numerical reservoir simulation is another source of the incorrect phase characterization based on mass densities (**Jerauld, 1997b**; **Yuan & Pope, 2012**; **Beygi et al., 2015**).

The UTPGE framework improves the Yuan and Pope method (**2012**) in two manners: (**i**) it explicitly adds the reference molar Gibbs free energy quantity into the functional formulation of the compositional relative permeability model. (**ii**) It improves and expands the relative permeability calculation by introducing the interface composition to the model. The former is crucial to extend the accuracy of the model on the temperature and pressure of the fluid system. The latter is beneficial when the relative permeability parameters of fluid pairs differ. For example,

the end point relative permeability of oil-water is different than that of the oil-gas flow. Moreover, the IFT-dependent term incorporates, at least, two set of relative permeability parameters with different IFT values. The fluid system then may span the composition space at low and high IFT values with the designated relative permeability parameters.

5.3.1 Review of hydrocarbon Gibbs free energy framework

Figure 5-12 displays the algorithm of the proposed compositional hydrocarbon relative permeability modeling. The input parameters to the UTPGE framework include overall hydrocarbon composition (z), pressure, temperature, and PVT properties of each component. First, we perform the phase equilibrium calculation including a stability analysis followed by a flash calculation. Here, our purpose is conceptual rather than to match general data. We therefore perform a two-phase flash calculation and avoid the states at which three-phase hydrocarbon may exists.

For the stability analysis of overall composition *z*, we follow the strategy of Trangenstein (**1987**) to minimize the change-in-GFE (ΔG) function with respect to a trail phase mole fraction,

$$\Delta G = \sum_{i=1}^{N_h} y_i[\bar{G}_i(y) - \bar{G}_i(z)], \qquad \textbf{Eq. 5-12}$$

and,

$$\min f(y) = \sum_{i=1}^{N_h} \frac{\partial(\Delta G)}{\partial y_i}, \ \text{subject to: } x_{N_h} = 1 - \sum_{i=1}^{N_h - 1} y_i \geq 0 \qquad \textbf{Eq. 5-13}$$

where y_i denotes the mole fraction of *i* in the trail phase (*y*). Perschke (**1988**) discusses the required procedure for the stability analysis of hydrocarbon mixtures in detail. We use the DIRECT algorithm (**Jones et al., 1993**) for evaluating the global minimum of the multi-variate ΔG function. Saber (**2011**) applied the DIRECT algorithm to the ill-defined hydrocarbon mixtures at the near-critical condition and concluded that this deterministic approach outperforms the fast simulated

annealing, interval Newton, and tunneling methods. The simple **DI**viding **RECT**angles (DIRECT) method applies the Lipschitzian approach without specifying the Lipschitz constant and transforms the objective function into a hyper-cube – a unit imaginary domain. It is a fast approach for global optimization as required in stability analysis.

Providing the composition of each phase *h* together with total molar ratio of each phase L_j, we evaluate the phase molar density of each phase j $\left[\xi_j = 1/V_j = P/\left(Z_j RT\right)\right]$ as required for the following quantities: (**i**) phase mass density, (**ii**) phase saturation, and (**iii**) hydrocarbon-pair IFT calculation. Finally, we evaluate the phase molar GFE using **Eq. 5-16** to **Eq. 5-19**. It also requires the ideal gas properties as described in **Appendix I**. This step completes the required thermodynamics parameters of compositional-dependent relative permeability modeling.

Next, if the bulk properties are the only critical parameters for the relative permeability modeling, the parameters for the hydrocarbon phase are directly evaluated based on a *linear GFE-average* interpolation scheme between the reference and the current state. By adopting both bulk and interface properties to assess composition-dependent parameters, we also require IFT between aqueous and the other phases. For the optional bilinear approach, we estimate the IFT pairs according to each fluid pair. For the IFT between the liquid- and vapor-like hydrocarbon fluid pairs, we use the Macleod-Sudgen correlation (**Reid et al., 1987**).

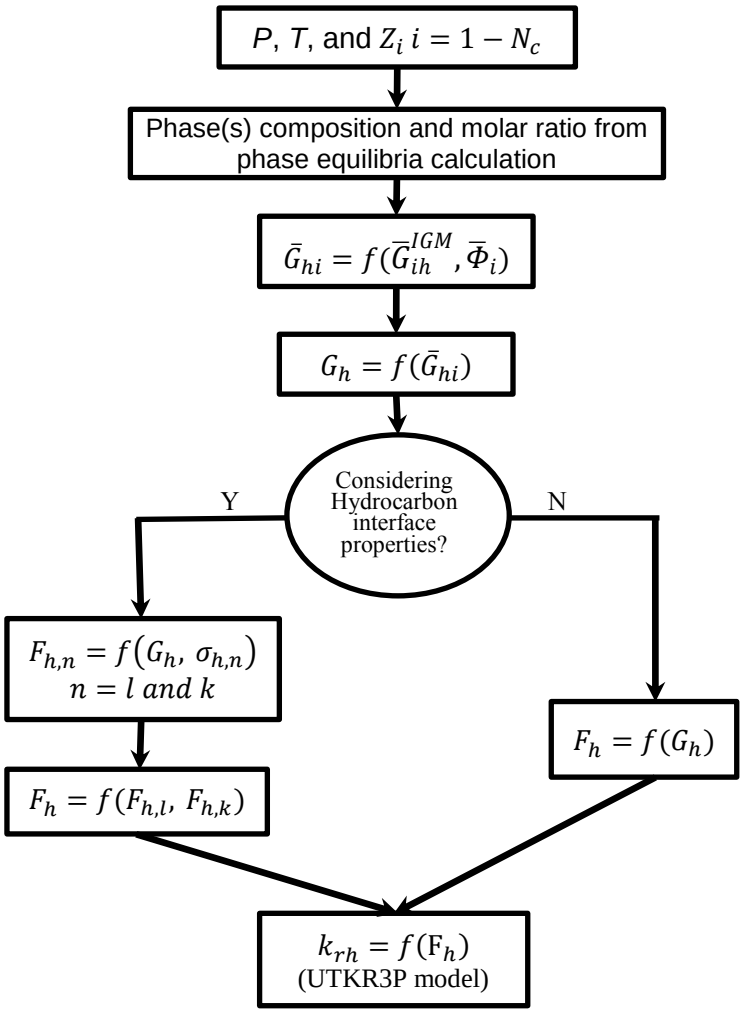

Figure 5-12: UTPGE framework to calculate composition-dependent hydrocarbon relative permeability

In the following section, we review the GFE calculation for the hydrocarbon phases. We then show case studies with the above procedure in evaluating the compositional relative permeability of hydrocarbon phase(s).

5.3.2 **Hydrocarbon Gibbs free energy**

Equation-of-states with simple mixing rule, e.g. one-fluid van der Waals mixing rule, can be used to evaluate the fugacity of hydrocarbon mixtures. The partial molar GFE of component *i* in real hydrocarbon mixture (phase *h*) is expressed by,

$$\bar{G}_{ih} = \bar{G}_{ih}^{IGM} + RTln\bar{\Phi}_i, \qquad \textbf{Eq. 5-14}$$

where $\bar{\Phi}_i$ is the fugacity coefficient of component *i* calculated from the EOS and $\bar{G}_{ih}^{IGM}$ is the molar GFE in hypothetical ideal gas mixture state. This property is evaluated based on the following equation,

$$\bar{G}_{ih}^{IGM}(T, P, x_i) = \underline{G}_i^{\square}(T, P) + RTlnx_i, \qquad \textbf{Eq. 5-15}$$

where x_i is the mole fraction of component *i* in hydrocarbon mixture and $\underline{G}_i^{\square}$ is the pure component GFE as an ideal gas. The first term on RHS of **Eq. 5-15** is the GFE of a hypothetical ideal gas at specified pressure and temperature. Combining **Eq. 5-1**, **Eq. 5-14**, and **Eq. 5-15** finalizes the molar GFE calculation for a hydrocarbon mixture:

$$\begin{aligned} \underline{G}_h = \sum_{i=1}^{N_h} x_i \bar{G}_{ih} &= \sum_{i=1}^{N_h} x_i \, \underline{G}_i^{\square}(T, P) + RT \sum_{i=1}^{N_h} x_i \, lnx_i + RT \sum_{i=1}^{N_h} x_i \, ln\bar{\Phi}_i \\ &= \sum_{i=1}^{N_h} x_i \, \underline{G}_i^{\square}(T, P) + RT \sum_{i=1}^{N_h} x_i \, ln(x_i\bar{\Phi}_i), \end{aligned} \qquad \textbf{Eq. 5-16}$$

where $\underline{G}_i^{\square}$ is pressure- and temperature-dependent reference GFE of pure component *i* and $\bar{\Phi}_i$ denotes the fugacity coefficient of component *i*. Note that **Eq. 5-16** for the hydrocarbon phase is in consistent with the definition as generally defined by **Eq. 5-5**.

The $\underline{G}_i^{\square}$ quantity is based on the ideal-gas state and is expressed by the component GFE definition for an ideal gas mixture,

$$\underline{G}_i^{\square}(T, P) = \underline{H}_i^{\square}(T) - T\underline{S}_i^{\square}(T, P), \qquad \textbf{Eq. 5-17}$$

where $\underline{H_i^{\square}}\,(T,P)$ is the pure component enthalpy of an ideal gas state and is a monotonic functions of temperature and $\underline{S_i^{\square}}\,(T,P)$ is the pure component ideal-gas entropy depending on pressure and temperature:

$$\underline{H_i^{\square}}\,(T) = \underline{H_i^{\square}}\,(T^0, P^0 = 1\ atm) + \int_{T^0,P=0}^{T,P=0} c_{Pi}^{*} dT,$$
$$\underline{S_i^{\square}}\,(T,P) = \underline{S_i^{\square}}\,(T^0, P^0 = 1\ atm) + \int_{T^0,P=0}^{T,P=0} \frac{c_{Pi}^{*}}{T} dT - Rln\frac{P}{P^0}, \qquad \textbf{Eq. 5-18}$$

where c_P^* is the ideal gas molar heat capacity at constant pressure as a function of temperature. Although many analytical equations are available for industrial applications, the most notable ones are the polynomials with varying number of terms. Alternatively, for the molar ideal-gas entropy, one may apply the available formulations, e.g., API technical book procedure (**Daubert & Danner, 1997**). **Appendix I** further discusses the ideal gas molar heat capacity and molar entropy modeling.

The fugacity coefficients in **Eq. 5-16** is calculated based on the following equation for the Peng-Robinson EOS (**Sandler, 2006**),

$$ln\bar{\Phi}_{ih}(T,P,h_i) = \frac{b_i}{b_{mix}}\left(Z_{mix}^h - 1\right) - ln\left(Z_{mix}^h - \frac{b_{mix}P}{RT}\right) - \frac{a_{mix}}{2\sqrt{2}b_{mix}RT}\left[\frac{2\sum_n h_n a_{in}}{a_{mix}} - \frac{b_i}{b_{mix}}\right] ln\left[\frac{Z_{mix}^h + \left(1+\sqrt{2}\right)\frac{b_{mix}P}{RT}}{Z_{mix}^h + \left(1-\sqrt{2}\right)\frac{b_{mix}P}{RT}}\right], \qquad \textbf{Eq. 5-19}$$

where *h* denotes the vapor or liquid state, h_m is the mole fraction of component m in the specified state, Z_{mix}^h is the desired state root for the compressibility factor, a_{mix} and b_{mix} are calculated based on the applied mixing rule for the desired state, e.g., one-fluid van der Waals mixing rule for the hydrocarbon mixture, a_{in} from the mixture rule $\left(a_{in} = \sqrt{a_{ii}a_{nn}}(1-k_{in})\right)$ where k_{in} are binary interaction parameters found by fitting the EOS to mixture data. Next, we summarize the required procedure to evaluate the compositional-dependent hydrocarbon phase relative

permeability.

5.3.3 Application of UTPGE framework to hydrocarbon phase modeling

In this section, we demonstrate four case studies using a MATLAB code. The developed code applies the UTPGE framework to the entire saturation and composition spaces in a single time step (i.e., fixed pressure, temperature, and overall composition). It performs the stability analysis and flash calculation and calculates the hydrocarbon molar GFE.

The aqueous modeling section of the UTPGE framework (see **Compositional aqueous relative permeability**) assists in the modeling of dissolution of hydrocarbon and non-hydrocarbon components in aqueous phase. We intend to exhibit features of the developed framework on a conceptual basis rather than to match specific data. Hence, we model the aqueous phase as pure water component with no interphase mass transfer with other phases. In addition, we simplify the modeling procedure by ignoring the water component vaporization and exclude water component from phase equilibria calculation.

5.3.3.1 Case H1

We perform simulation studies to better understand the behavior of molar GFE in single- and two-phase hydrocarbon flow (two phase water-hydrocarbon and three-phase water/HC Phase-1/HC Phase-2). First, we conduct a solvent injection test (Case H1-A). The initial oil composition is equimolar mixture of normal heptane (nC_7) and normal decane (nC_{10}). The injectant solvent (50% methane (C_1) and 50% normal butane (nC_4)) enriches the initial fluid within an isothermal process (T=145 °F). **Figure 5-13** shows the composition path (A-M) of the solvent injection process in a pseudo ternary diagram where each apex represents 100% mole fraction of C_1, C_4, and combined C_7 and C_{10} components. In the pressure-composition phase envelope, we construct three constant vapor mole fractions of 0% (liquid-vapor boundary), 20% and 50% (V=0.0, 0.2, and 0.5). We then evaluate the composition and pressure combinations resulting in the specified vapor mole fraction

values. **Figure 5-14** depicts the variation of pressure as the solvent mole fraction increases along the composition path A-M. **Figure 5-15** demonstrates the variation of HC phase-2 (gaseous phase) saturation. It also confirms that vapor mole fraction approximately remains constant at the selected values through the injection process. **Figure 5-16** shows the calculated equilibrium ratio (K-value) of each component and that the K-values approach to a unique value (k_i=1.0, i=component 1-4) at high pressures.

Figure 5-17 illustrates the variation of molar GFE of the single hydrocarbon phase (gas) with pressure. The non-monotonic behavior close to the maximum pressure (or solvent mole fraction) implies that at a fixed temperature, pressure, and saturation, the molar GFE is not unique. **Table 5-2** lists the calculated physical quantities of two selected compositions at an approximately constant pressure (points D and M in **Figure 5-17**). It reveals that although pressure and temperature remain constant, the variation of internal composition of the single phase flow (two-phase water-hydrocarbon phase) forces the variation in the mass density and GFE. If the GFE is the single interpolating parameter in evaluating the compositional relative permeability, at a fixed saturation we observe two different relative permeability values. We further investigate this feature of the GFE-averaged interpolation scheme in **Case H2** and **Case H3**.

Figure 5-18, and **Figure 5-19** depict the GFE variation of each hydrocarbon phase in equilibrium at a three-phase flow (two hydrocarbon phases and water) together with the mixture GFE. They also show the continuous behavior of GFE as the number of phases changes. They describe that as one of the hydrocarbon phases disappears the total GFE of the hydrocarbon system follows the GFE of the other phase. The continuity in the GFE behavior when pressure, composition, or temperature varies plays the crucial role in a consistent compositional modeling when the relative permeability parameters are GFE-dependent.

Next, we conduct a constant composition expansion (CCE) test on the $CO_2/C_1/FC_6$ fluid

system (Case H1-B). We adopt four constant overall composition as listed in **Table 5-3** and perform the isothermal experiment at T=260 °F for a pressure range of 500-2500 psia.

Figure 5-20 shows the liquid dropout as predicted by the simulated CCE experiments. It explains that the liquid dropout increases from the composition B1 to B4. Composition B4 reaches 100% liquid volume approximately at P=1700 psia. The broad range of liquid dropout facilitate an extensive evaluation of GFE for the fluid system at the designated temperature.

Figure 5-21 to **Figure 5-24** provide the variation of single phase and two-phase equilibrium hydrocarbons and those of overall mixture with pressure for the studied samples (b1 to B4, respectively). It states that GFE of hydrocarbon phases approaches together near the saturation point of each sample. These figures also express the rewarding feature of molar GFE of each fluid system: as one of the phases disappears, the GFE remains continuous. For instance, **Figure 5-21** states that as HC Phase-1 (liquid) disappears (Case H1-B1: P< 550 psia and P> 1900 psia), the GFE of single-phase HC follows the GFE of HC Phase-2 (vapor). In opposition, **Figure 5-24** describes that when the HC Phase-2 (vapor) disappears (Case H1-B4: P> 1700 psia), the GFE of single-phase HC follows the GFE of HC Phase-1 (liquid). Note that **Figure 5-21** to **Figure 5-24** demonstrate that although hydrocarbon phase-1 shows a monotonically decreasing GFE as pressure reduces, the hydrocarbon phase-2 shows a non-monotonic behavior.

Table 5-2: Physical properties of two points (D and M) in single-phase flow (Case H1-A)

Point	Temperature (°F)	Pressure (psia)	Composition $C_1/nC_4/nC_7/nC_{10}$	Hydrocarbon Saturation	Mass density (lbm/ft^3)	GFE
D	145	1605	0.406/0.406/0.094/0.094	1.0	31.6	-32.5
M	145	1599	0.498/0.498/0.002/0.002	1.0	23.2	-22.5

Table 5-3: Mixture composition of Case H1-B samples in CCE experiment (T=260 °F)

Sample	Composition $CO_2/C_1/FC_6$
B1	0.40/0.40/0.20
B2	0.25/0.50/0.25
B3	0.34/0.37/0.29
B4	0.50/0.10/0.40

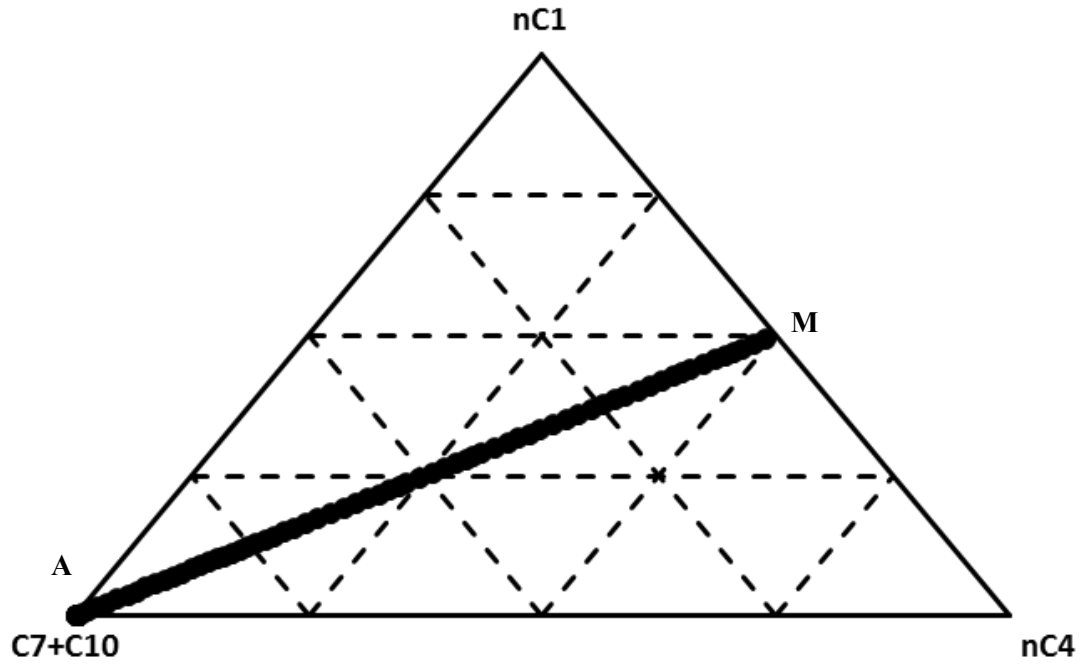

Figure 5-13: Composition path for the solvent injection experiments (Case H1-A)

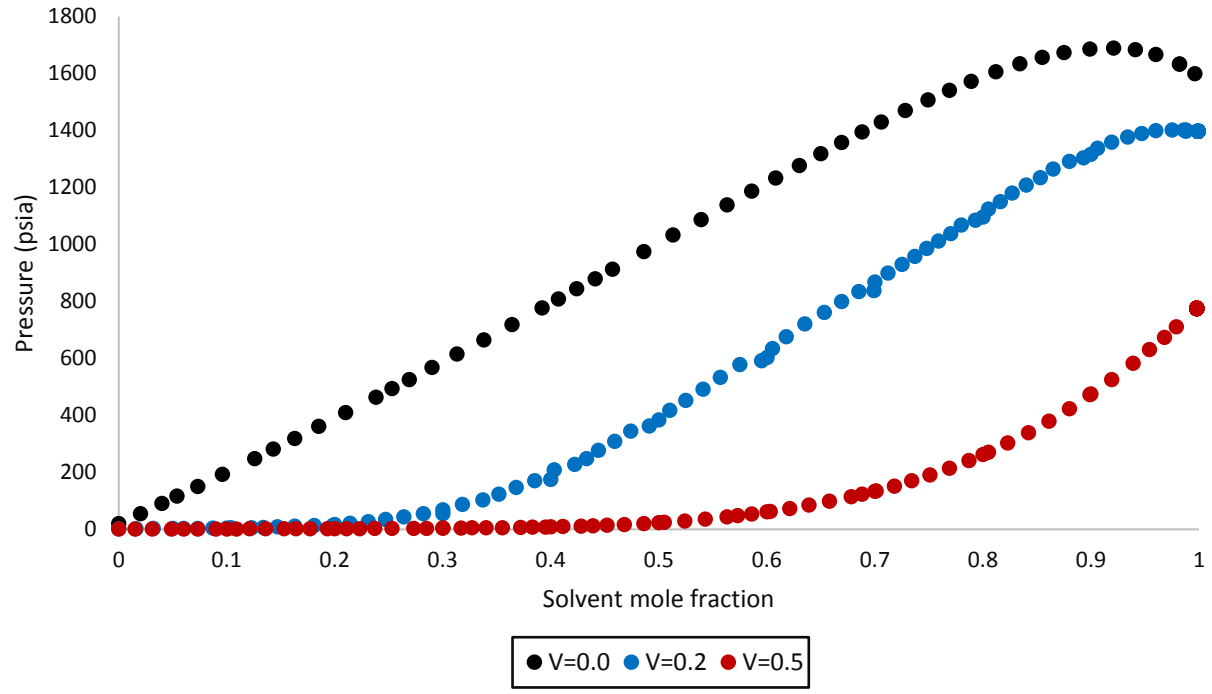

Figure 5-14: Variation of solvent mole fraction in three solvent injection processes (Case H1-A)

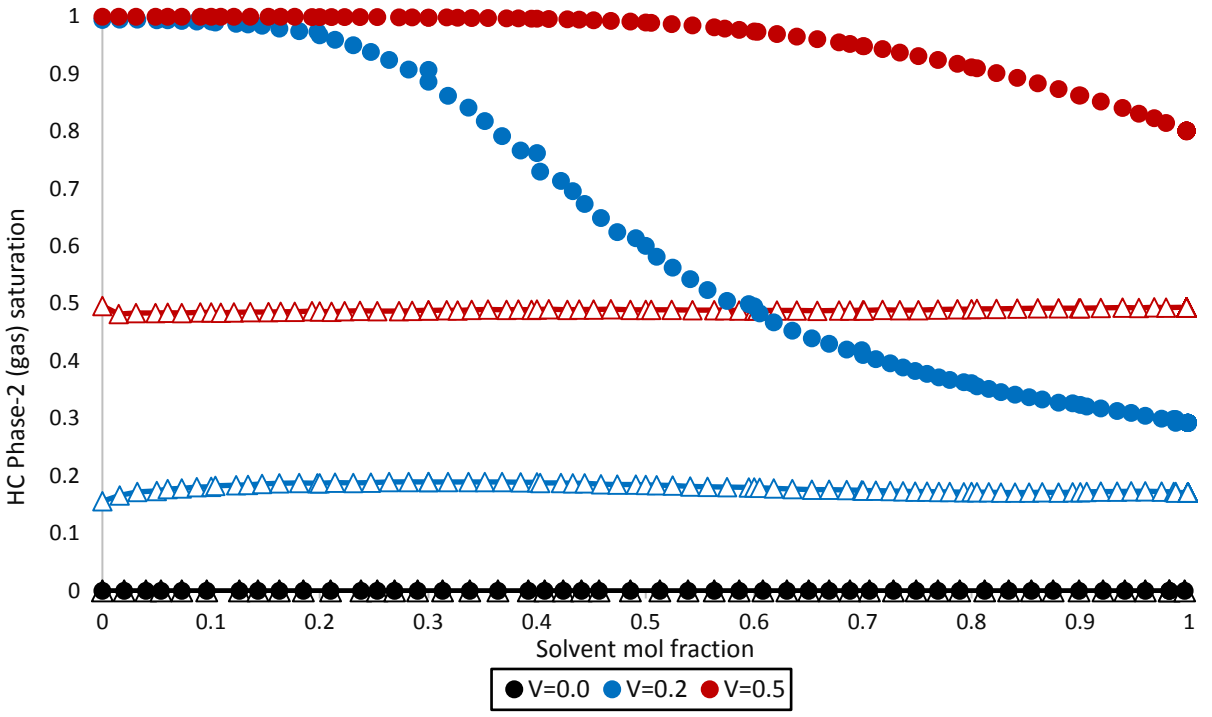

Figure 5-15: HC Phase-2 (gas) saturation (circles) and vapor content (triangles) in three solvent injection experiments (Case H1-A)

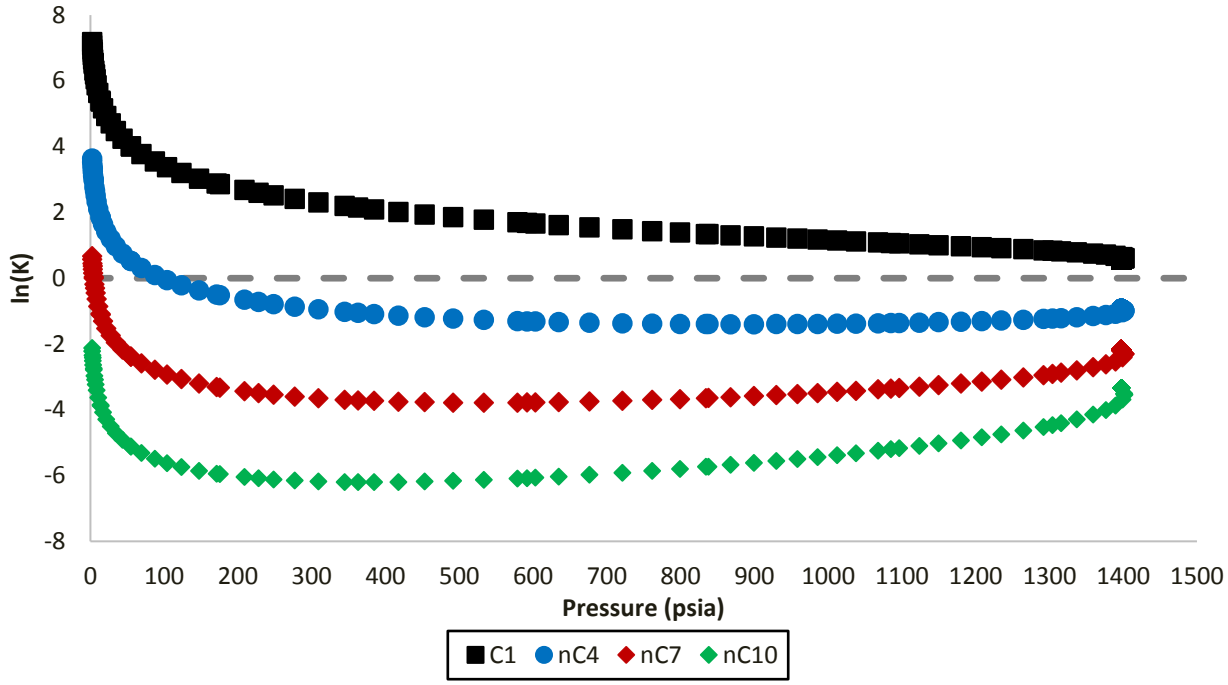

Figure 5-16: Equilibrium ratio of hydrocarbon mixture in gas injection processes (Case H1-A)

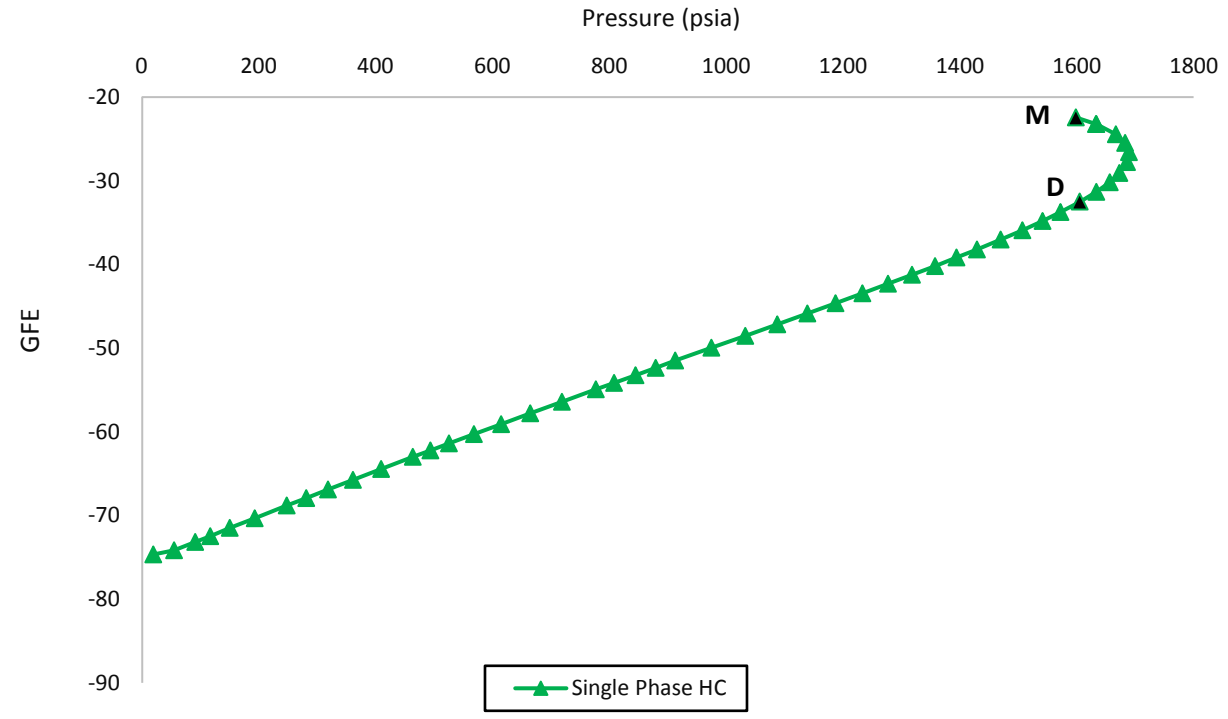

Figure 5-17: Single-phase hydrocarbon (oil) GFE during solvent injection (Case H1-A,V=0.0)

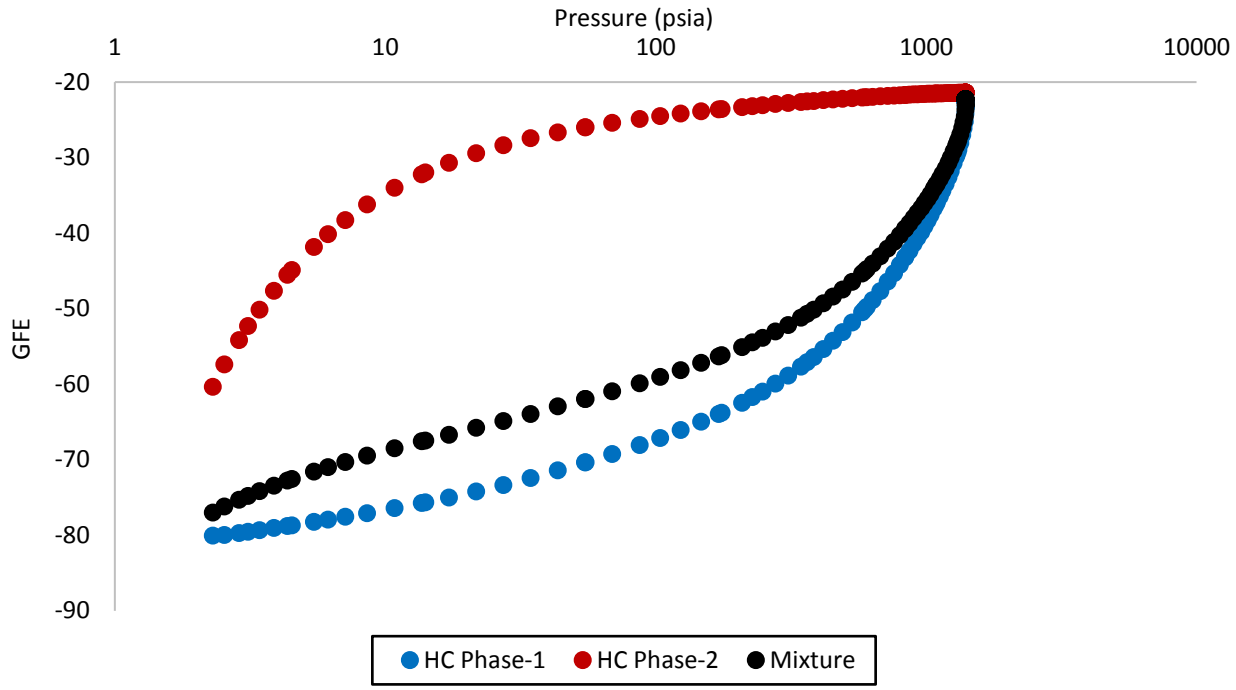

Figure 5-18: Hydrocarbon and mixture GFE during solvent injection (Case H1-A,V=0.2)

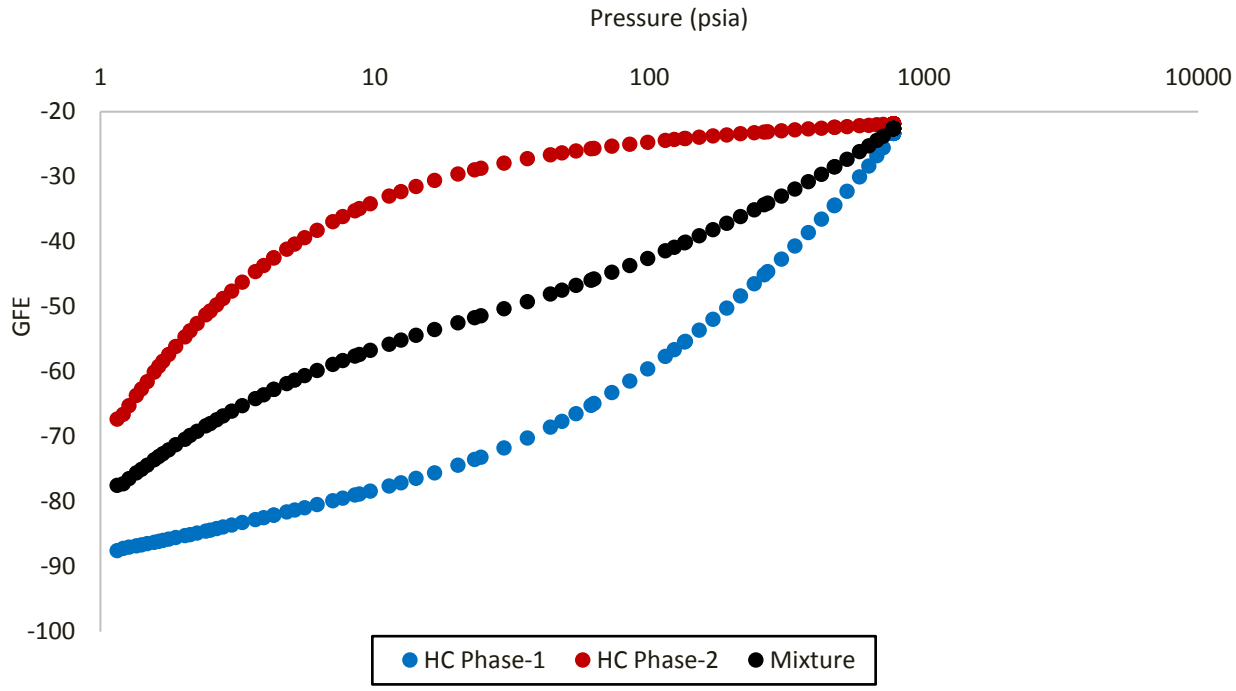

Figure 5-19: Hydrocarbon and mixture GFE during solvent injection (Case H1-A,V=0.5)

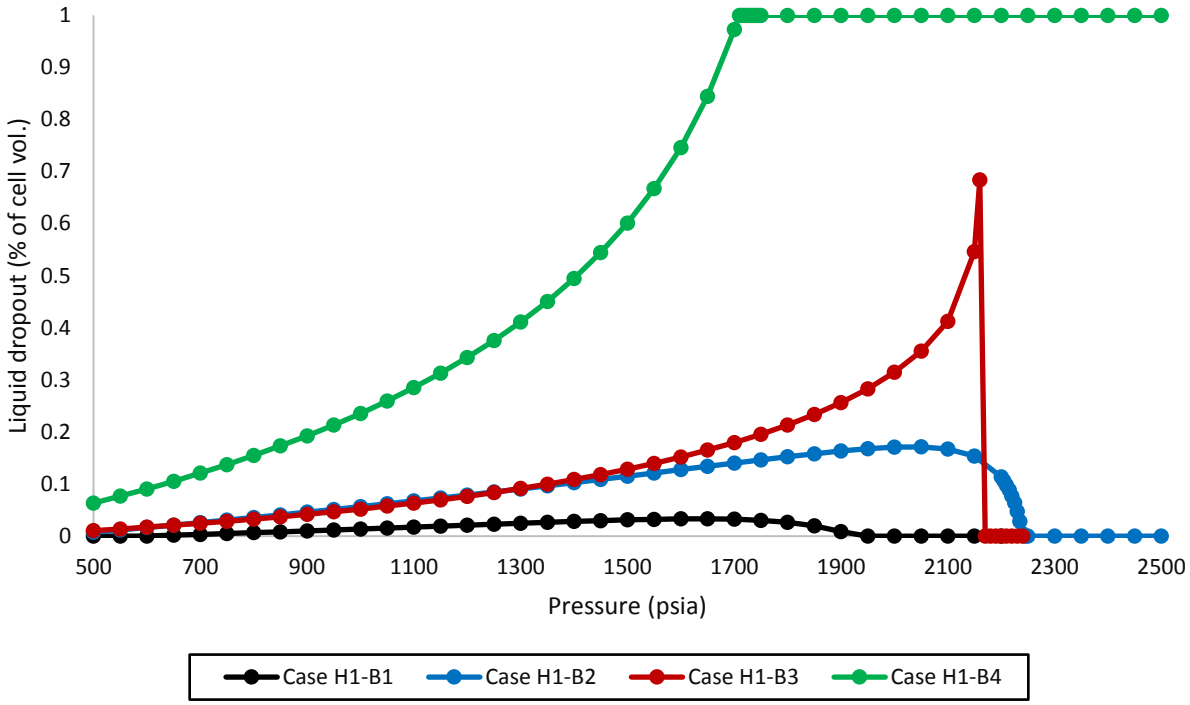

Figure 5-20: Liquid dropout in CCE experiment (Case H1-B)

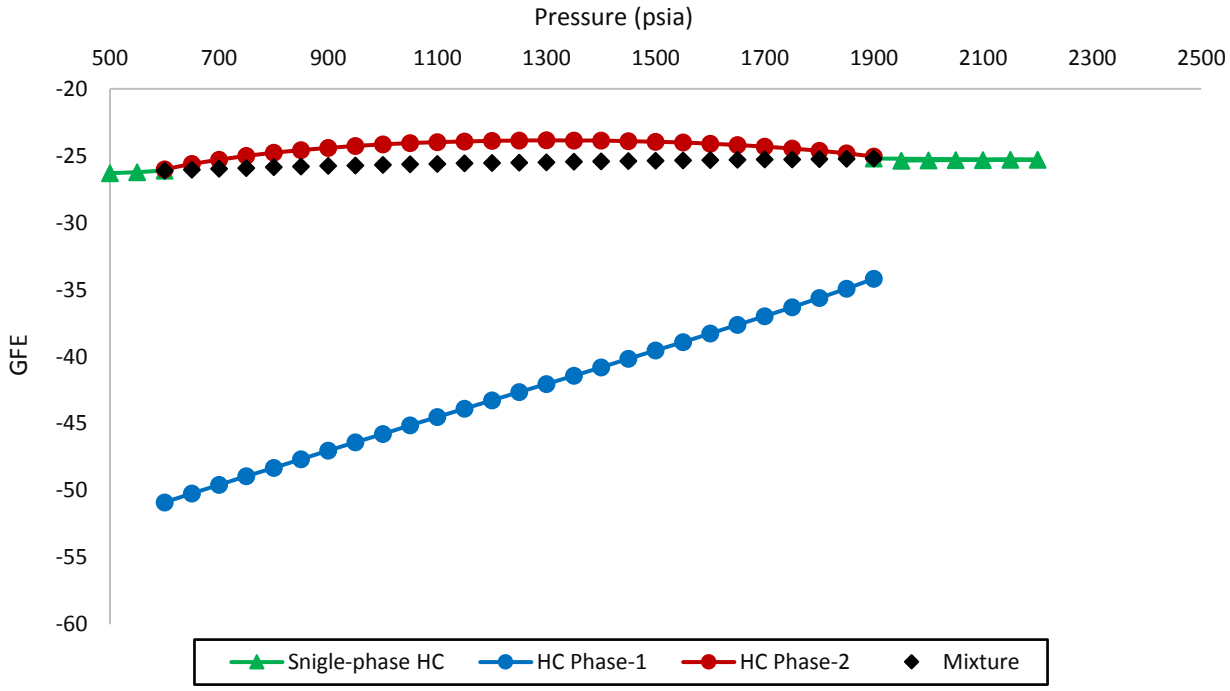

Figure 5-21: GFE variation in CCE experiment (Case H1-B1)

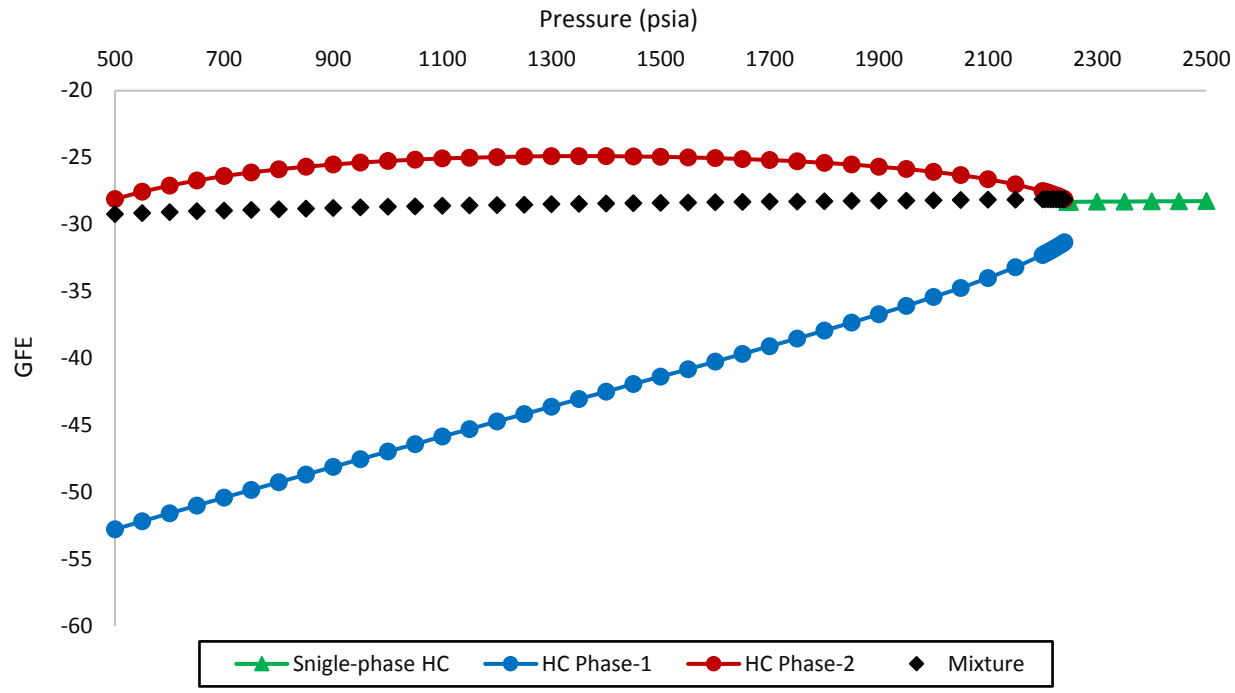

Figure 5-22: GFE variation in CCE experiment (Case H1-B2)

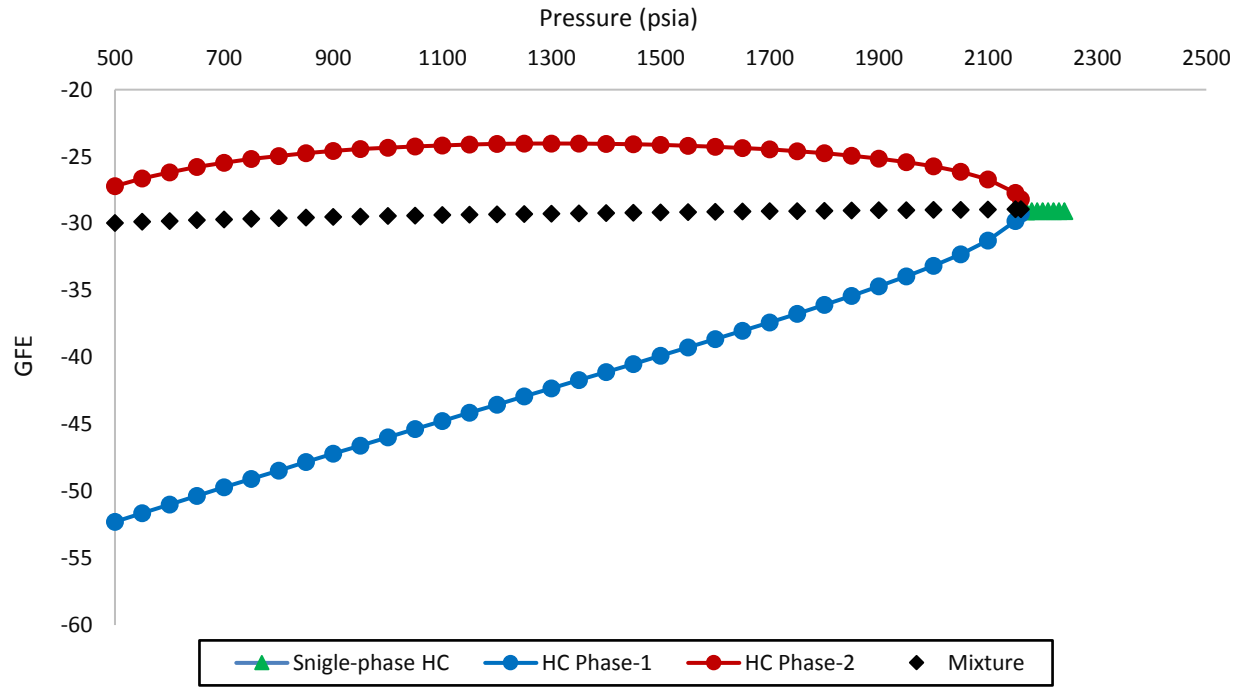

Figure 5-23: GFE variation in CCE experiment (Case H1-B3)

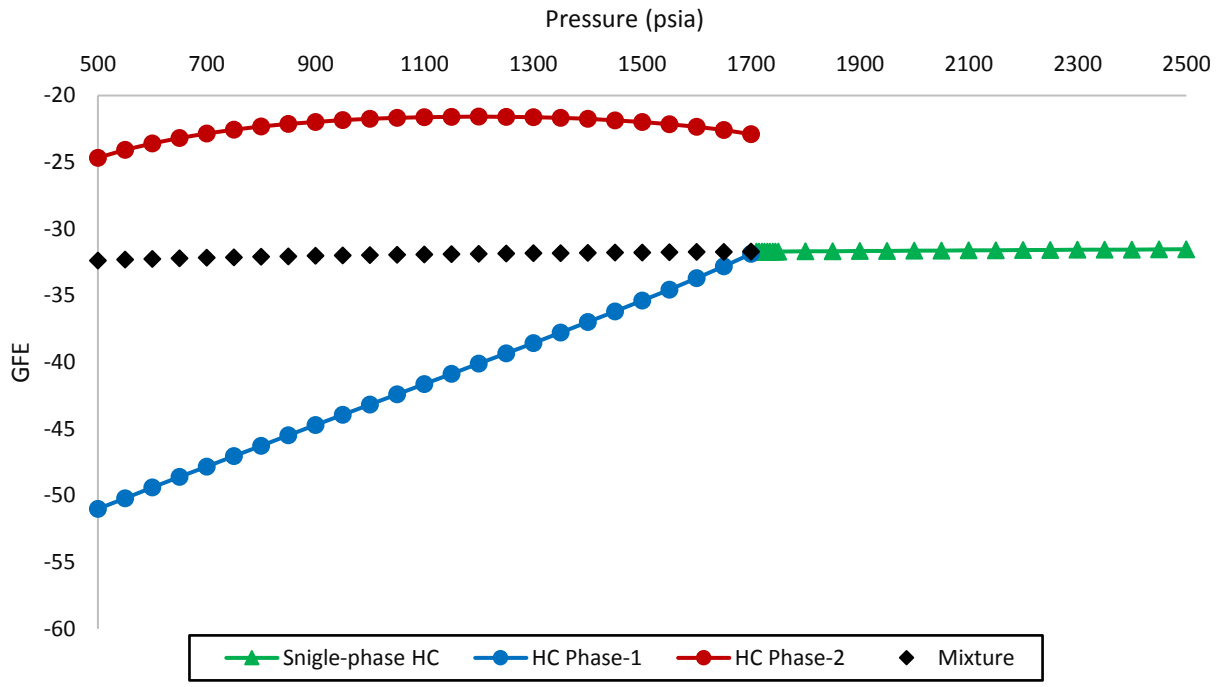

Figure 5-24: GFE variation in CCE experiment (Case H1-B4)

5.3.3.2 Case H2

We apply the UTPGE framework to the four-component system of $H_2O/CO_2/C_1/FC_6$ and demonstrate the composition-dependent relative permeability as predicted by this approach. The water saturation (phase-1) in this example is constant (S_1=0.1), and we focus on the simulation of the hydrocarbon phase(s). **Table 5-4** lists the required parameters of each component in phase equilibria calculations.

The simulations span entire composition space at a fixed temperature (T=260 °F) and two pressures (P=1750 psia and 2000 psia). The lower pressure is slightly above the minimum miscibility pressure (MMP) of solvent injection (component Z_1: CO_2) into the equimolar feed composition of Z_2 and Z_3: based on the cell-to-cell simulation and the key tie-line semi-analytical approaches, MMP is 1725 and 1735 psia, respectively. The higher pressure is below the critical

point of CO_2 injection into an equimolar feed of methane and hexane (critical pressure=2080 psia at CO_2 mole fraction of 0.44). The selected pressures demonstrate the variation of phase behavior and its impact on the relative permeability modeling.

Figure 5-25 (and **Figure 5-26**) shows the ternary composition diagram where two-phase region is bounded with vapor and liquid saturation curves. It also highlights the tie-lines with decreasing length as the critical point (X) is approached. **Figure 5-27** (and **Figure 5-28**) depicts the compositional variation of single-phase hydrocarbon at P=1750 (and 2000 psia). In that the UTPGE framework does not require to label a phases as oil/gas/etc., we just name the hydrocarbon phases in a numerical order (i.e., hydrocarbon (HC) phase-1, HC phase-2, etc.). As **Figure 5-29** indicates, the variation of single-phase mass density is continuous and noticeable in the compositional space. Besides, **Figure 5-29** implies that although the phase-labeling approach (i.e., using a reference mass density ($\rho^{ref} = 25\ lb/ft^3$)) works flawlessly for the single-phase region away from critical zone, as the near-critical region approaches the density of single-phase hydrocarbon (oil or gas) approaches to the reference density value. Hence, as **Figure 5-30** illustrates, the proper phase identification is problematic in region where the composition of two hydrocarbon phases are close to each other. In a computational domain, it translates to the possibility that while the phase is labeled as oil at one time-level, it would be labeled as gas in the next time-level or vice versa. It highlights the possibility of encountering the phase-flipping issue during the simulation of the near-critical displacement leading to the discontinuity in the relative permeability curves.

Figure 5-31 (and **Figure 5-32**) indicates the variation of GFE of the hydrocarbon phases with equilibrium ratio of CO_2 component ($K_i^{eq} = y_i/x_i$ where x and y are the mole fraction of the component i in HC phase-1 and -2, respectively) at the specified pressure. It also shows the GFE of overall composition. Although the GFE of HC phase-1 shows a monotonic behavior with respect

to the K-values of Z_1 component, the second hydrocarbon shows a non-monotonic behavior. It may result in the erroneous results if the relative permeability of each phase is correlated *only* with the GFE. Particularly, two different compositions of the like hydrocarbon phase (as represented by K-values here) show identical GFE and, in turn, identical relative permeability whereas one speculates dissimilar relative permeabilities for these two hydrocarbons. Nonetheless, for this particular example, the level of non-monotonicity is negligible and we keep the molar GFE as the unique functional parameter for the compositional relative permeability estimation. As noted, the complete UTPGE framework couples GFE and IFT as will be reviewed in **Case H4**.

Figure 5-33 (and **Figure 5-34**) represents total iso-GFE, (i.e., contours of constant GFE, in a ternary composition diagram at the desired pressures). It illustrates the directional contours towards the heaviest component (C_6). The most gas-like component has the highest GFE value. Furthermore, the direction and absolute values of the total GFE of the system is unique and independent of the operating pressure.

In the following, we plot **Figure 5-35** to **Figure 5-40** and **Figure 5-45** to **Figure 5-48** based on the composition of each equilibrium phase. **Figure 5-43** and **Figure 5-44** represent the compositional variation of hydrocarbon phases with respect to the mixture composition.

Figure 5-35 (and **Figure 5-36**) describes the monotonic behavior of the GFE of a single-phase hydrocarbon in two-phase water-hydrocarbon flow: it increases from most liquid-like fluid to its maximum value at the most gas-like fluid. At the near-critical zone, the GFE varies slowly without encountering any discontinuity.

Figure 5-37 (and **Figure 5-39**) shows the relative permeability calculated based on the phase-labeling approach in which we designate the phases as either oil or gas. Note that saturation is constant in this region (S_o or S_g=0.9). This figure demonstrates a constant value based on the endpoint relative permeability of oil or gas phases. We do not attempt to show the phase flipping

issue. If a slight change occurs in the overall composition and even if the numerical errors are neglected, the possibility of an incorrect phase labeling at the next time level is plausible.

Figure 5-38 (and **Figure 5-40**) illustrates the composition-dependent relative permeability of single-phase hydrocarbon. Not only is there a transition zone from oil- to gas-like behavior, but also the single hydrocarbon in region of lower (or higher) mass density values does not return a unique relative permeability. It means that as the internal composition of any hydrocarbon phase varies, its relative permeability changes even if the hydrocarbon saturation is invariant.

Figure 5-41 (and **Figure 5-42**) describes the saturation variation of HC phase-1 and phase-2 for three-phase flow in the compositional space of each HC phase. It demonstrates that saturation of hydrocarbons become equivocal near the critical region, viz., where it is considered as the bottleneck of the conventional phase-labeling approach. The scatter plot of **Figure 5-43** (and **Figure 5-44**) shows the compositional variation of HC phase-1 with overall mixture composition. The saturations of two HC phases are complementary both in the compositional space of the HC phases and the overall mixture ($S_{HC1} + S_{HC2} = 1 - S_w$).

Figure 5-45 (and **Figure 5-47**) shows the calculated relative permeability based on the conventional phase-labeling approach. **Figure 5-46** (and **Figure 5-48**) shows the compositional relative permeability based on the GFE-averaged interpolation scheme. Comparison of the calculated relative permeabilities in composition space based on the phase-labeling and composition-dependent approaches reveals that the relative permeability values are approximately identical in the non-critical region. As the critical point is approached, however, the deviation of the calculated relative permeability values from the two methods increase.

Figure 5-49 to **Figure 5-52** represent the calculated relative permeability for HC phase-1 and phase-2 in the integrated saturation-composition spaces based on the UTPGE framework. **Figure 5-49** (and **Figure 5-51**) also demonstrates the variation of single hydrocarbon relative

permeability in two-phase water-HC phase-1 flow. It replicates the results of **Figure 5-38** (and **Figure 5-40**) and highlights the non-unique single-phase relative permeability when the composition varies but saturation is constant.

Figure 5-53 (and **Figure 5-54**) shows the variation of calculated relative permeability with saturation for both hydrocarbon phases using both methods. It implies that both methods replicate the expected curves of relative permeability. The relative permeability values are in good agreement in lower saturation region. The scatter plot in **Figure 5-55** (and **Figure 5-56**), however, demonstrates that the correlation between the modeled relative permeability of each hydrocarbon is weak as relative permeability increases. It is an expected behavior of the composition-dependent relative permeability: based on the operating condition (i.e., composition, pressure, and temperature), the molar GFE of each phase deviates from the extreme side (i.e., GFE of the most oil- and gas-like fluids). That compels the relative permeability parameters to be estimated differently than the immiscible values used in the phase-labeling approach. As a result, the composition-dependent relative permeability of HC phase-1 overestimates those of the phase labeling approach (viz., calculated suing the immiscible parameters). The composition-dependent relative permeability of HC phase-1, however, has smaller values than those of phase-labeling approach. It is rational when is perceived based on the imposed operational condition and the level of miscibility of the interacting fluids.

Table 5-4: PVT properties of components (Case H2)

Component no.	Component name	Critical pressure (*psi*)	Critical temperature (*R*)	Critical molar volume ($ft^3/lbmol$)	Molecular weight	Acentric factor	Parachor
Z_1	CO_2	1069.87	547.6	1.5057	44.010	0.225	78.0
Z_2	C_1	667.20	343.1	1.5858	16.043	0.008	77.0
Z_3	FC_6	477.03	913.5	5.5103	86.000	0.275	250.1

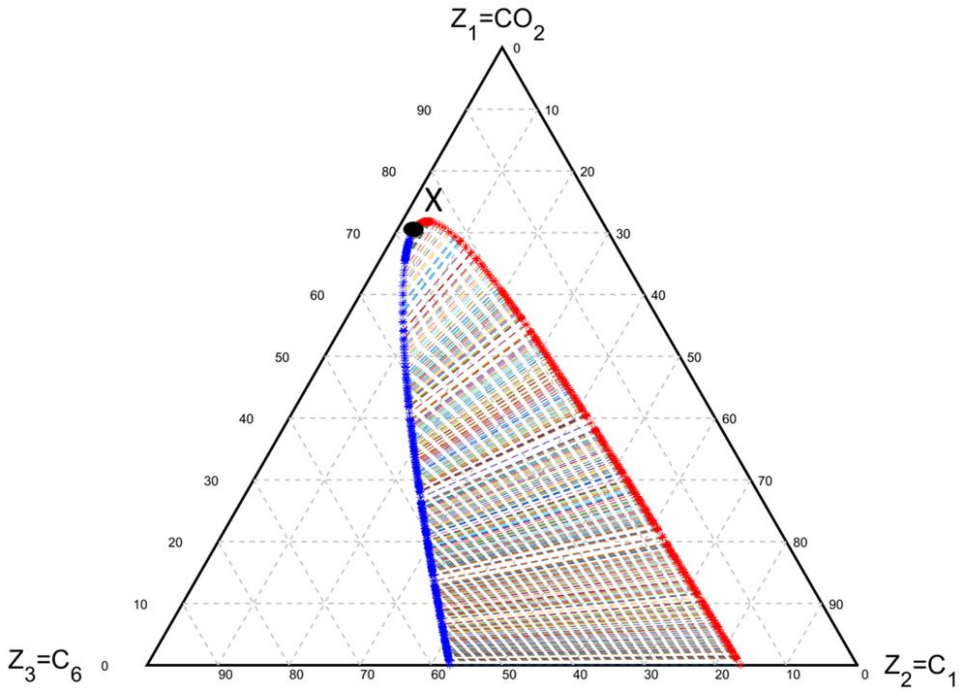

Figure 5-25: Two-phase envelope (red: vapor, blue: liquid) and tie-lines in ternary composition plot (Case H2, T=260 °F, P=1750 psia)

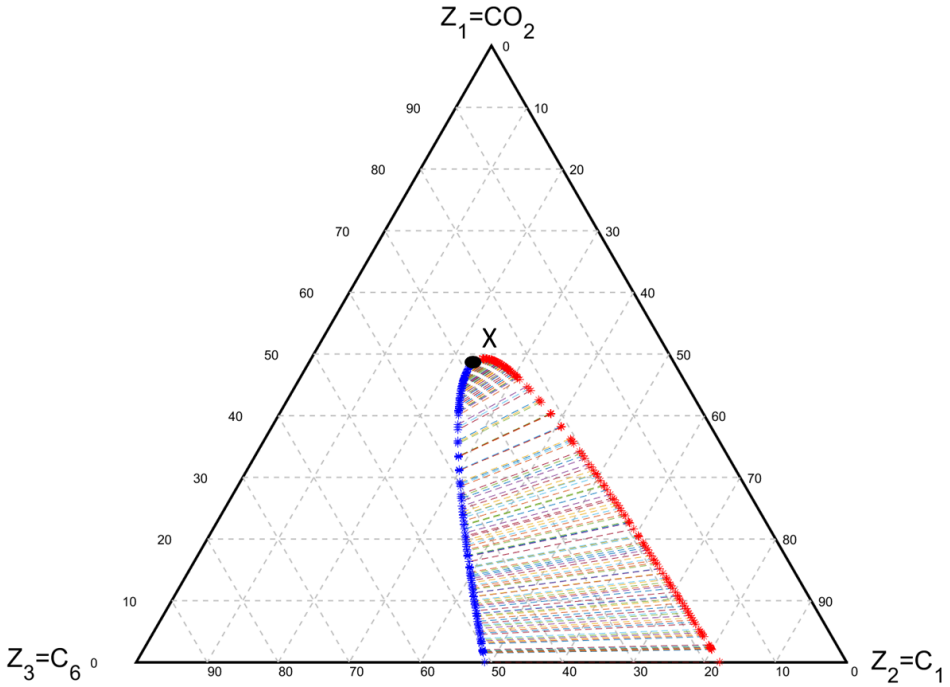

Figure 5-26: Two-phase envelope (red: vapor, blue: liquid) and tie-line indices (right) in ternary composition plot (Case H2, T=260 °F, P=2000 psia)

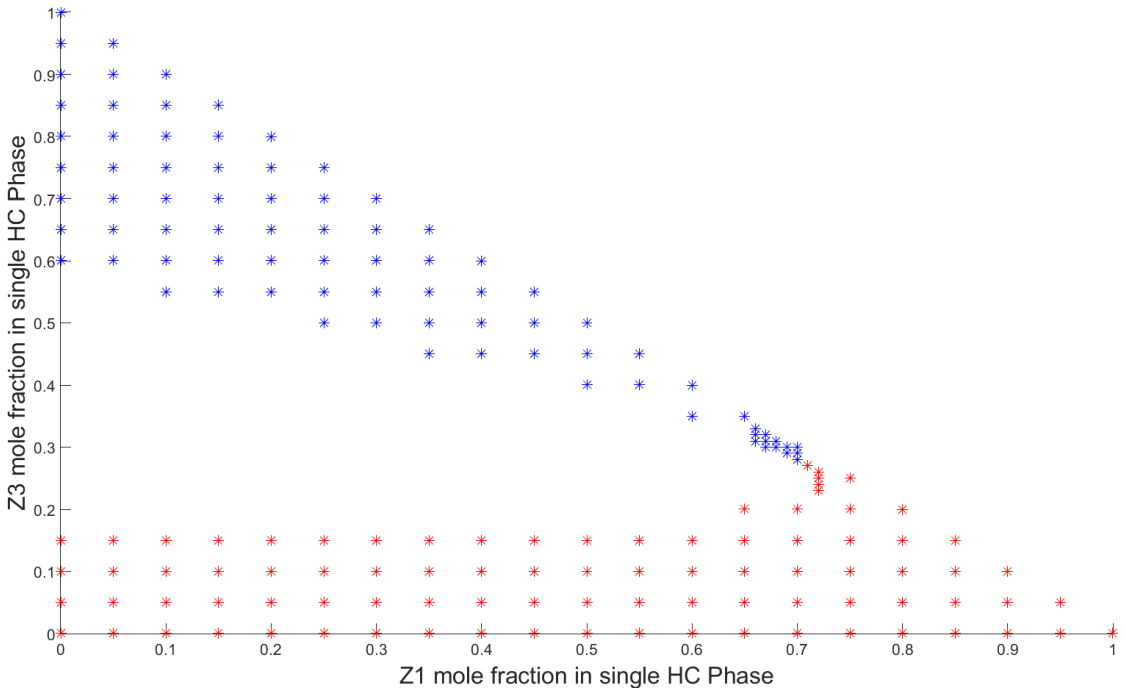

Figure 5-27: Compositional variation (mole fraction of components 1 and 3) in single hydrocarbon phase region: HC phase-1 (blue) or HC phase-2 (red) (Case H2, P=1750 psia)

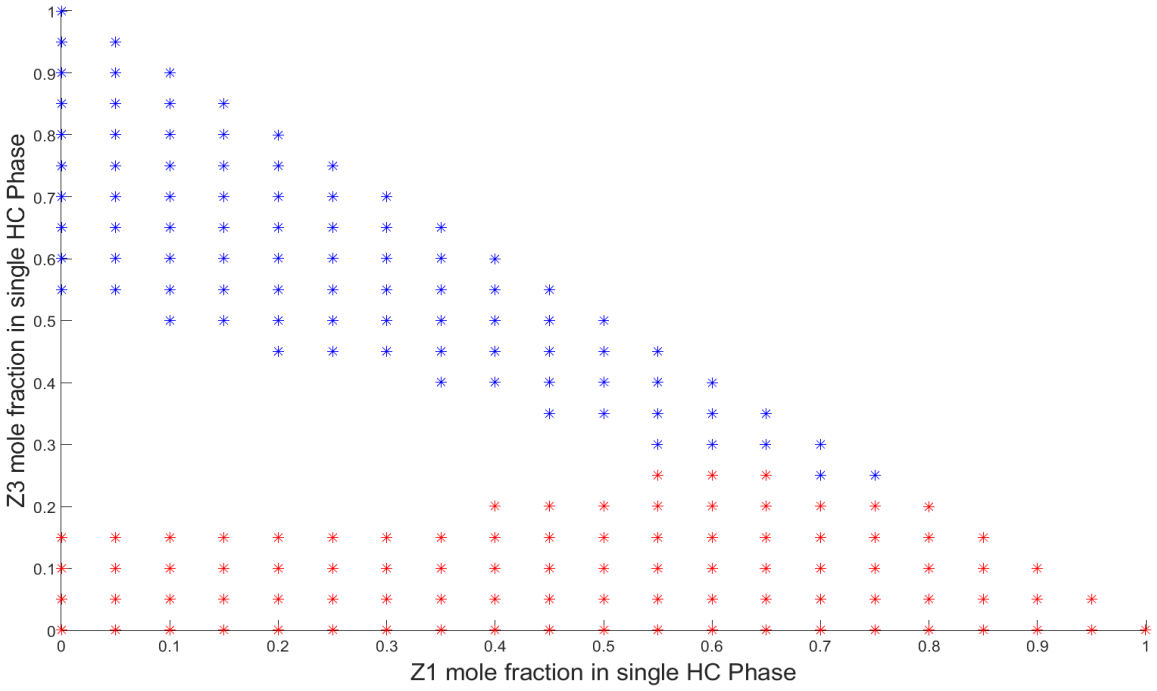

Figure 5-28: Compositional variation (mole fraction of components 1 and 3) in single hydrocarbon phase region: HC phase-1 (blue) or HC phase-2 (red) (Case H2, P=2000 psia)

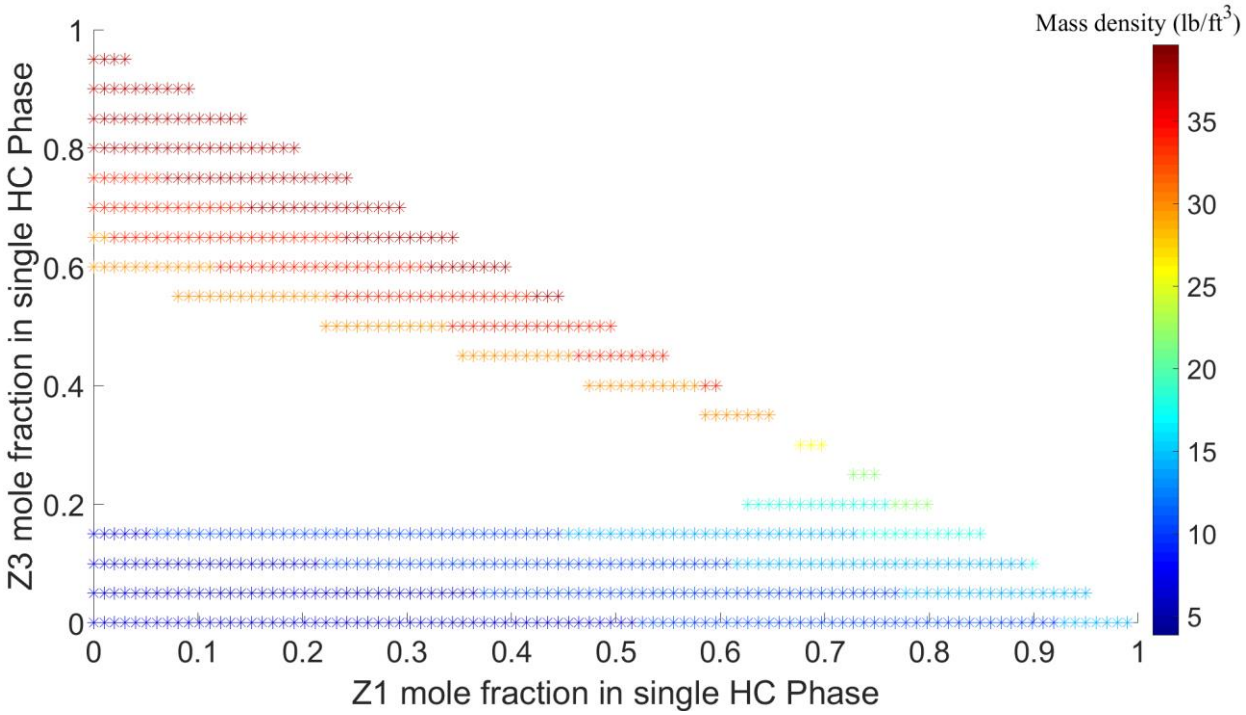

Figure 5-29: Compositional variation of single-phase hydrocarbon mass density (Case H2, P=1750 psia)

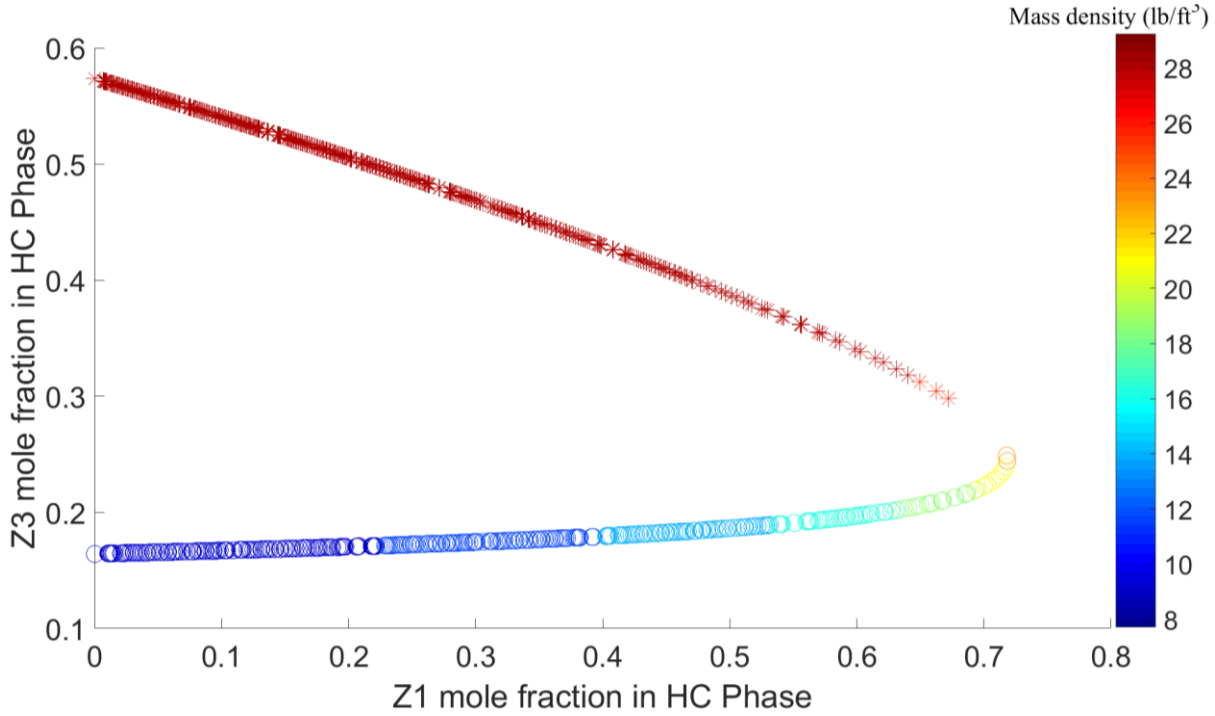

Figure 5-30: Compositional variation of hydrocarbon mass-density in three phase flow: HC phase-1 (stars) and HC phase-2 (circles) (Case H2, P=1750 psia)

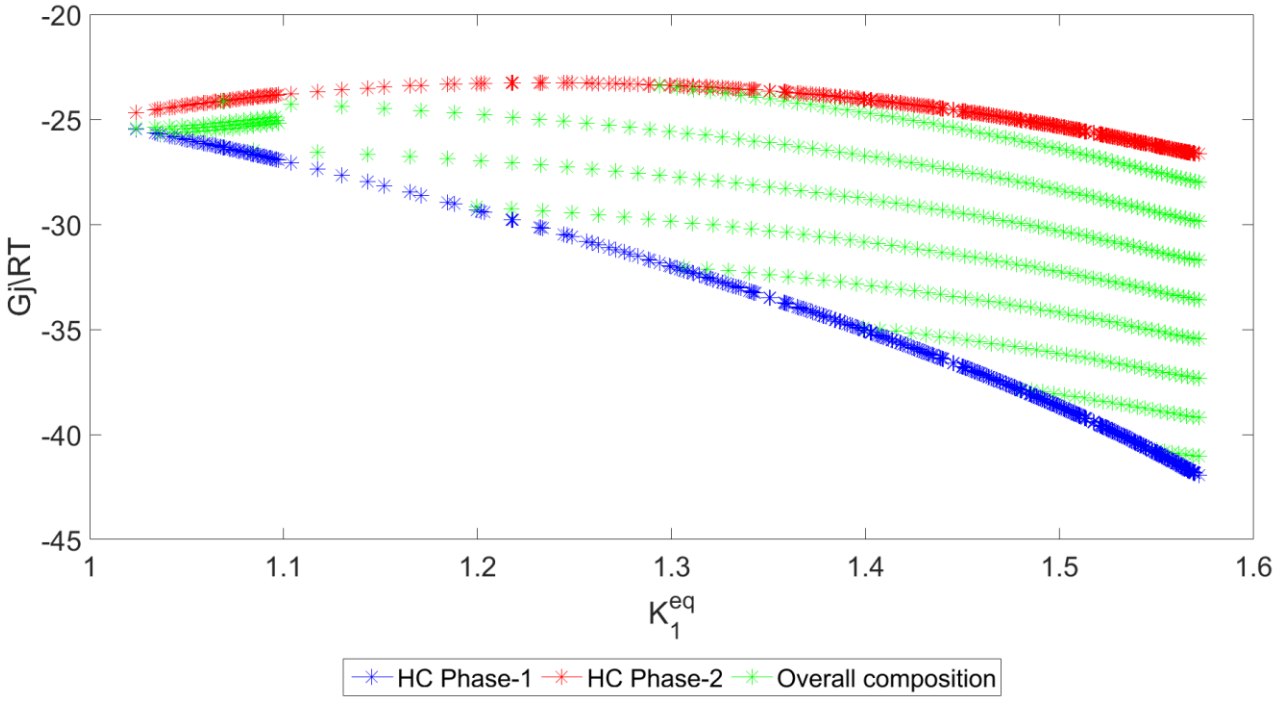

Figure 5-31: Variation of phase GFE (G/RT) with equilibrium ratio of CO_2 component (Case H2, P=1750 psia)

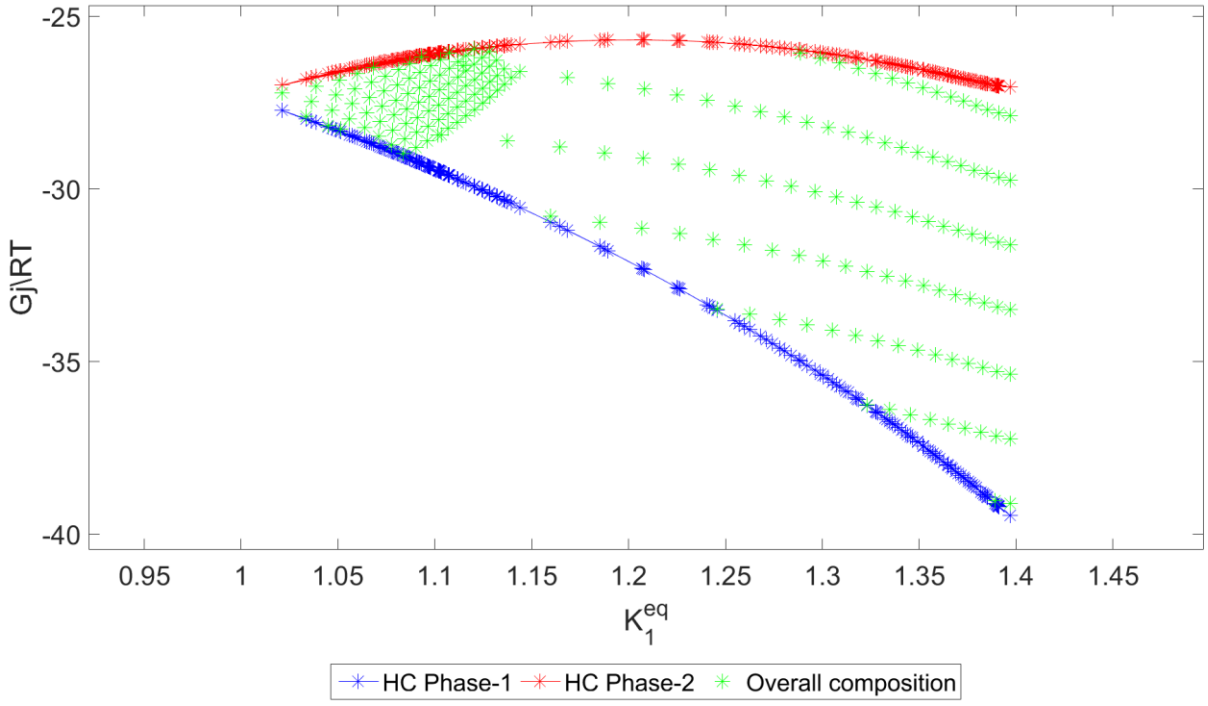

Figure 5-32: Variation of phase GFE (G/RT) with equilibrium ratio of CO_2 component (Case H2, P=2000 psia)

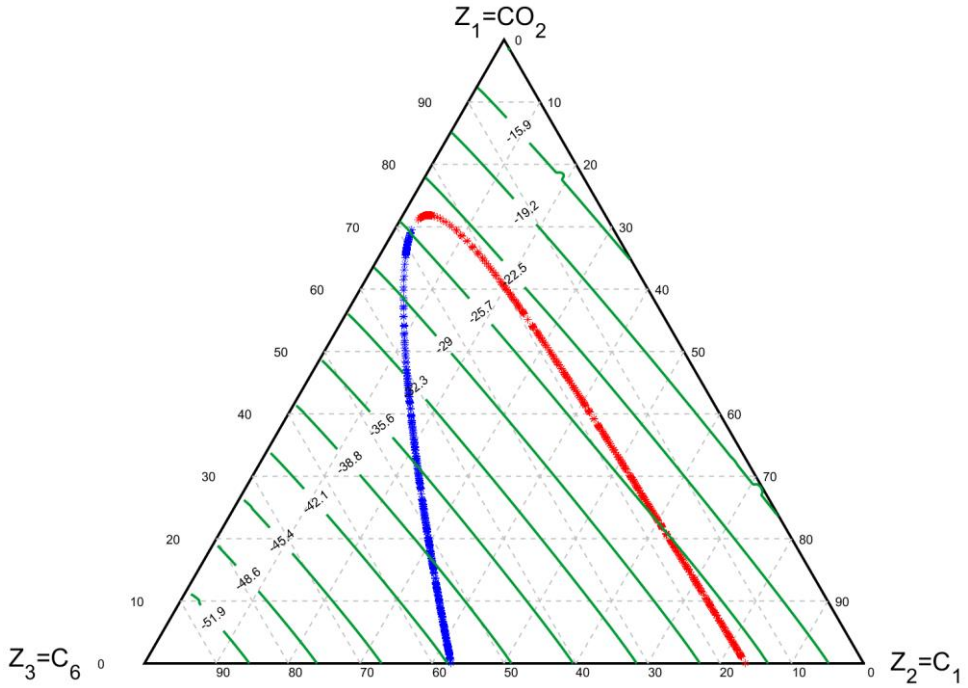

Figure 5-33: Iso-GFE (green) and two-phase envelope (vapor: red, liquid: blue) in composition ternary plot (Case H2, P=1750 psia)

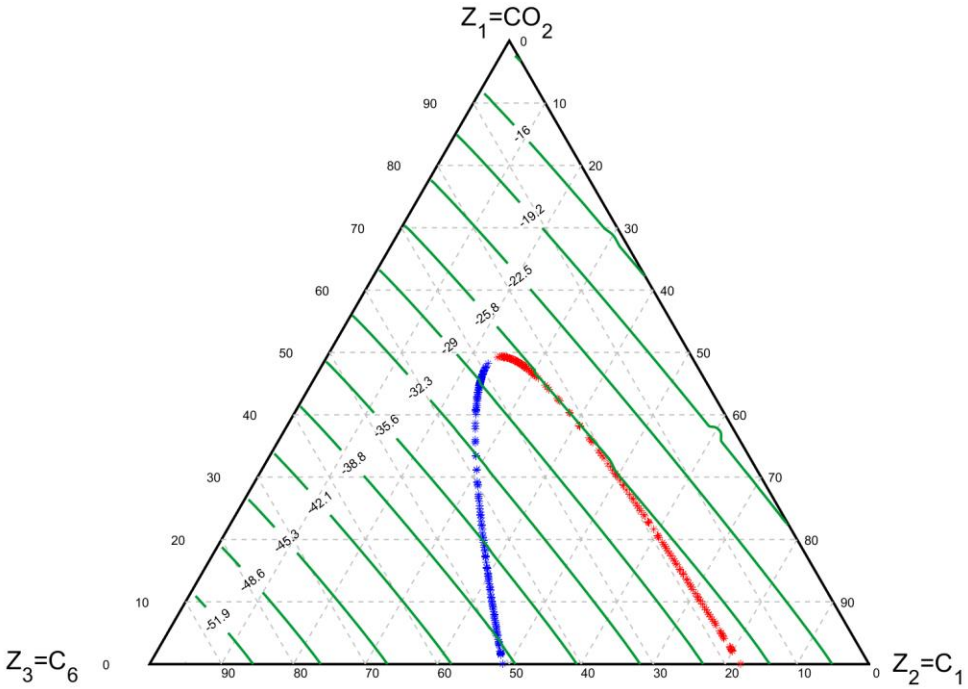

Figure 5-34: Iso-GFE (green) and two-phase envelope (vapor: red, liquid: blue) in composition ternary plot (Case H2, P=2000 psia)

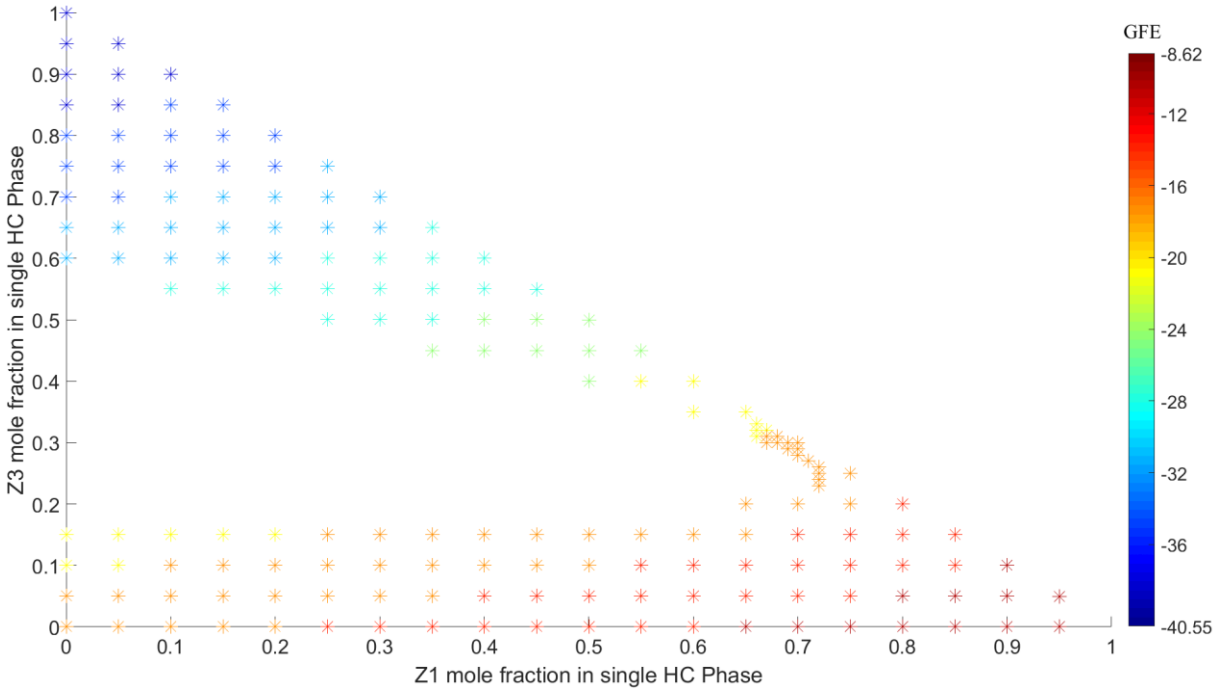

Figure 5-35: Variation of GFE (G/RT) of single-phase hydrocarbon with its composition (Z_1 and Z_3 components) (two-phase water-hydrocarbon flow) (Case H2, P=1750 psia)

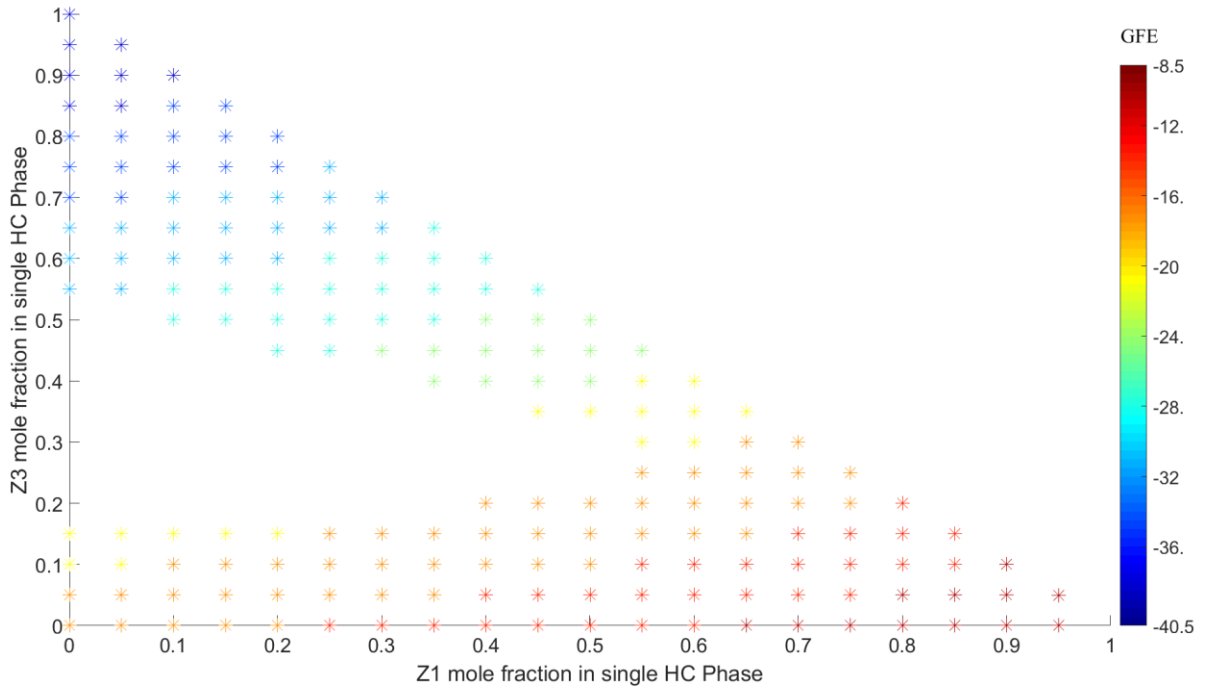

Figure 5-36: Variation of GFE (G/RT) of single-phase hydrocarbon with its composition (Z_1 and Z_3 components) (two-phase water-hydrocarbon flow) (Case H2, P=2000 psia)

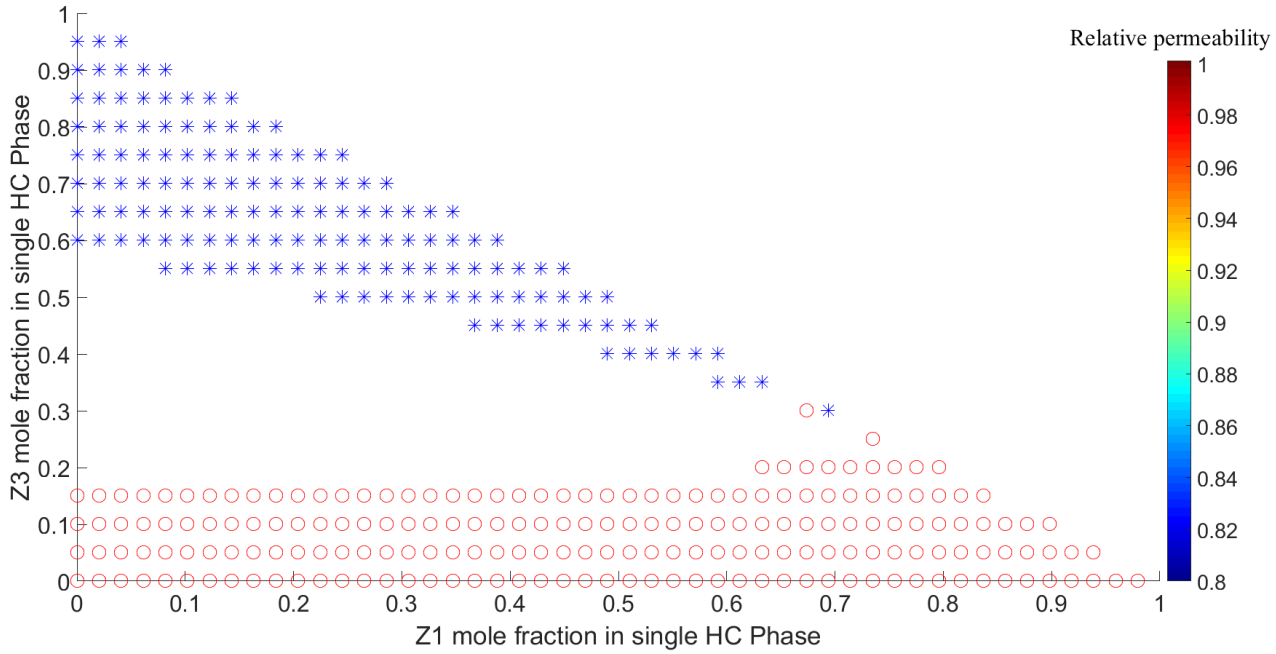

Figure 5-37: Calculated relative permeability of single-phase hydrocarbon (2-phase water-oil/gas flow) based on phase-labeling approach: oil (star), gas (circle) (Case H2, P=1750 psia)

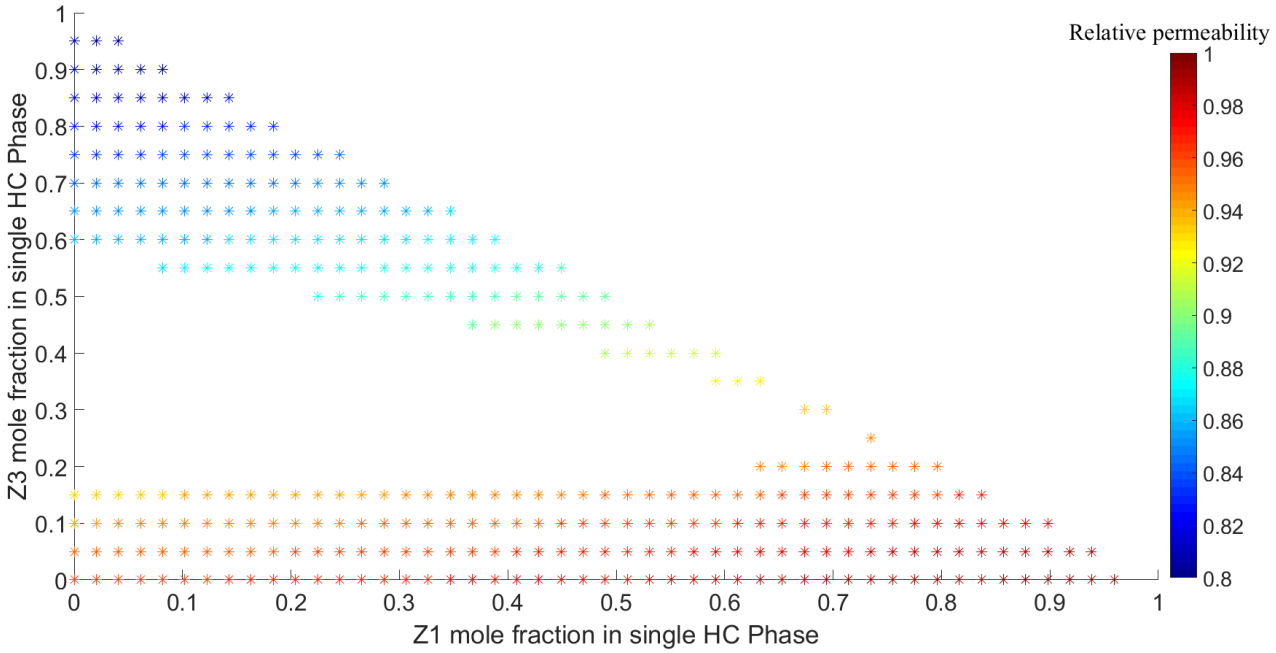

Figure 5-38: Composition-dependent relative permeability (GFE-based) of single-phase hydrocarbon (two-phase water-HC phase-1 flow) (Case H2, P=1750 psia)

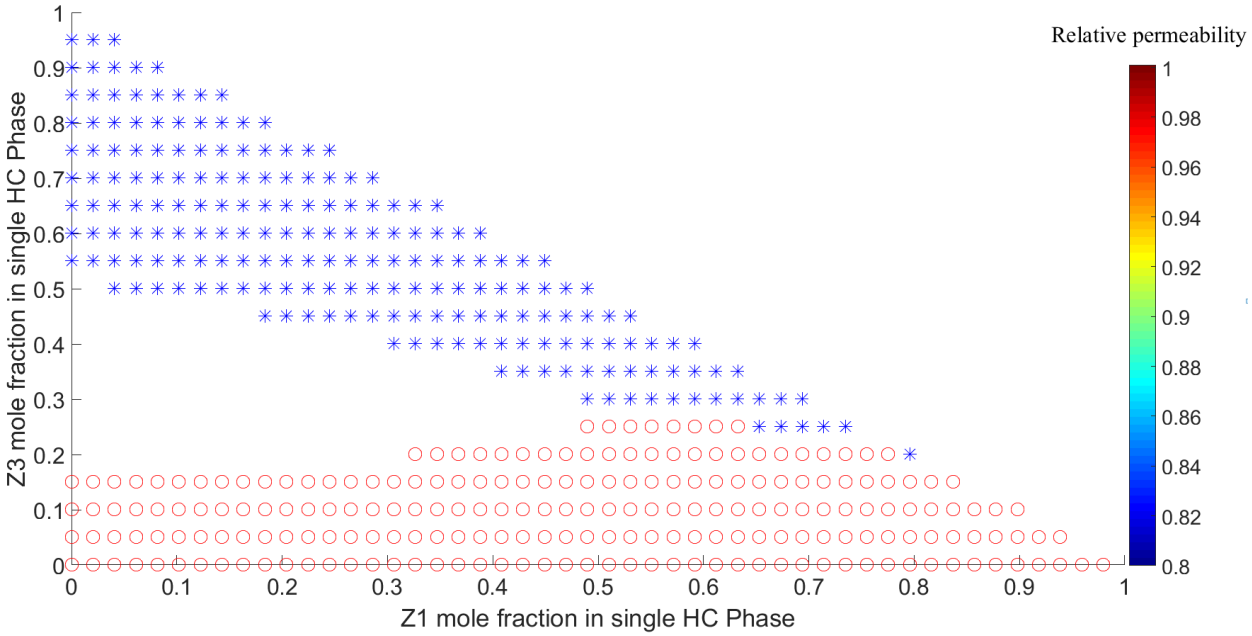

Figure 5-39: Calculated relative permeability of single-phase hydrocarbon (2-phase water-oil/gas flow) based on phase-labeling approach: oil (star), gas (circle) (Case H2, P=2000 psia)

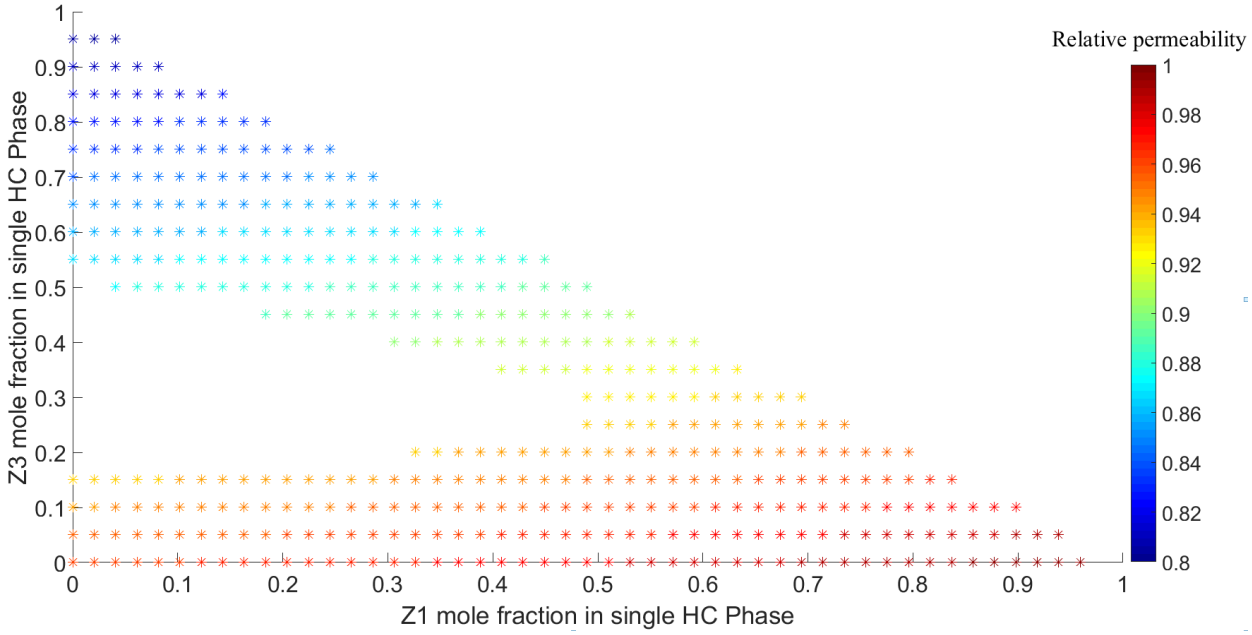

Figure 5-40: Calculated composition-dependent (GFE-averaged) relative permeability of single-phase hydrocarbon (two-phase water-HC phase-1 flow) (Case H2, P=2000 psia)

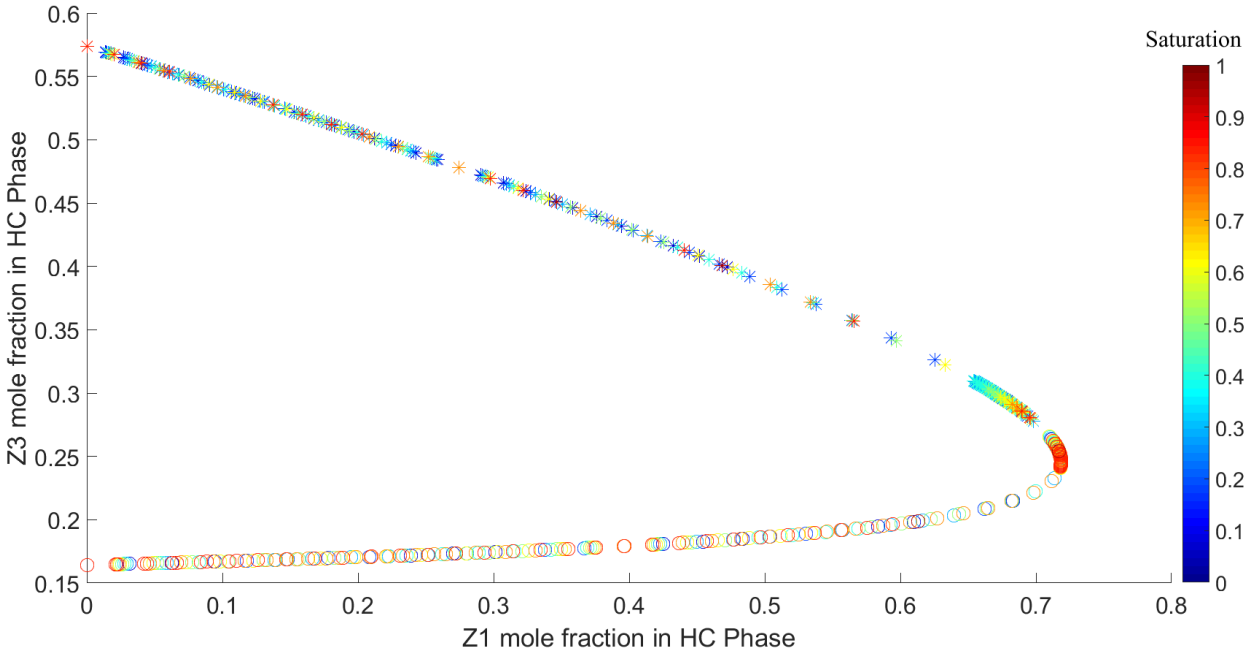

Figure 5-41: Compositional variation of hydrocarbon saturation in three-phase flow: HC phase-1 (stars) and HC phase-2 (circles) (Case H2, P=1750 psia)

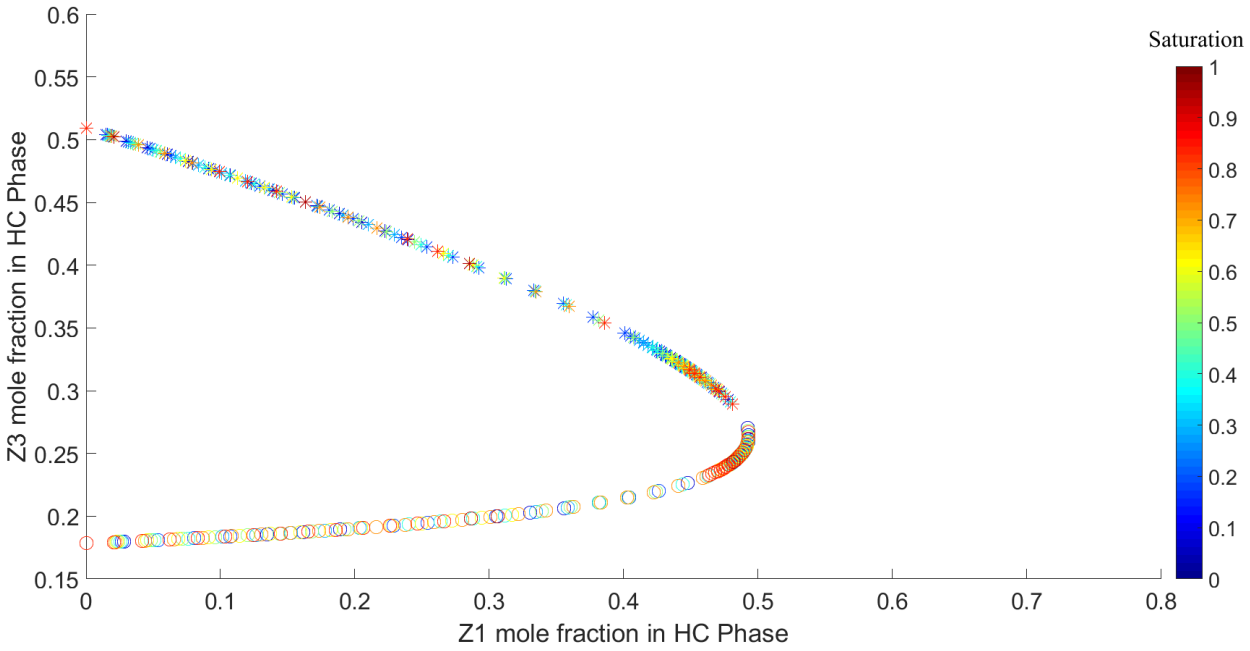

Figure 5-42: Compositional variation of hydrocarbon saturation in three-phase flow: HC phase-1 (stars) and HC phase-2 (circles) (Case H2, P=2000 psia)

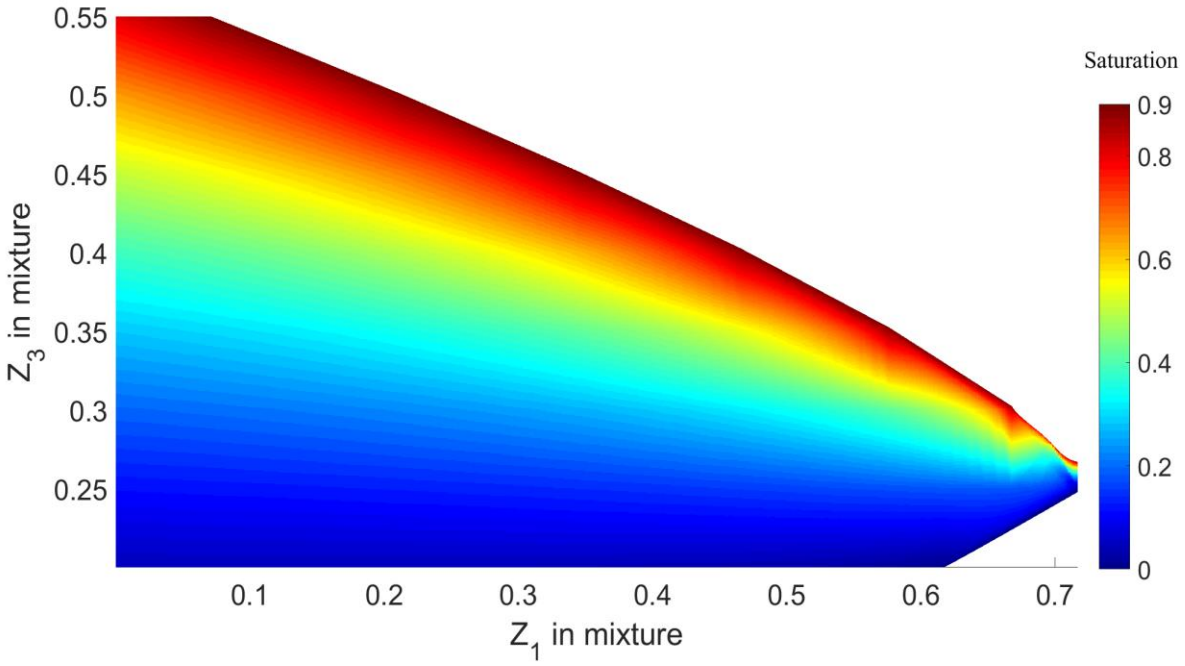

Figure 5-43: Scatter plot of compositional variation of HC phase-1 saturation with mixture composition (Case H2, P=1750 psia)

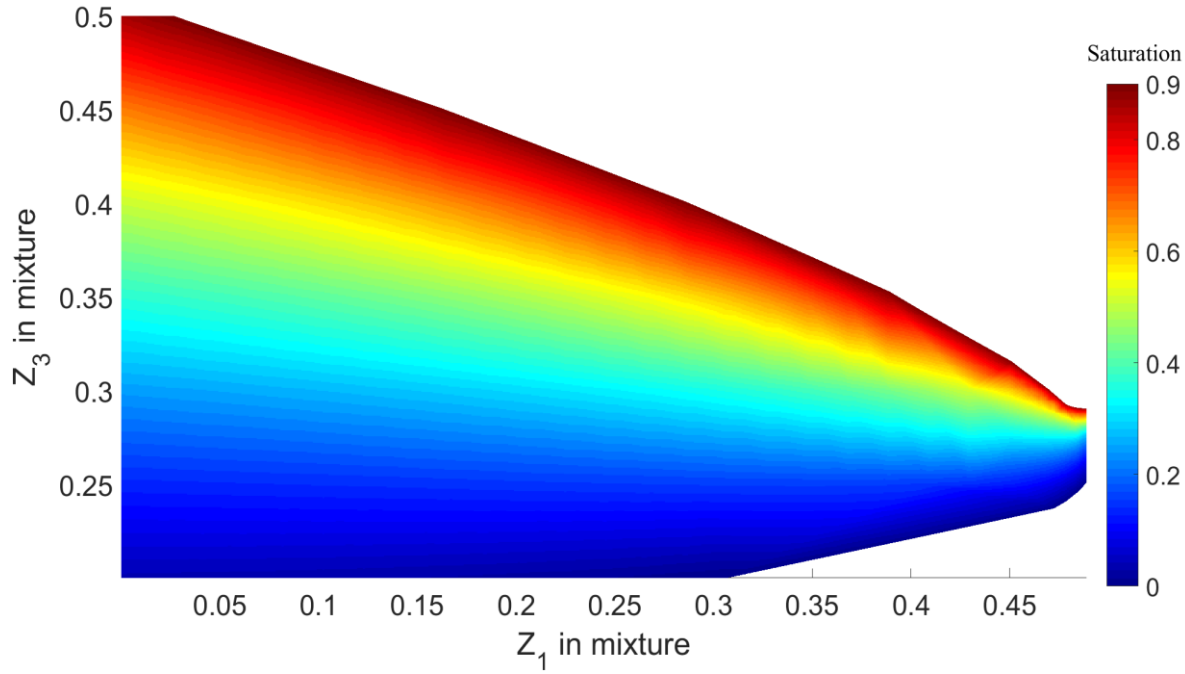

Figure 5-44: Scatter plot of compositional variation of HC phase-1 saturation with mixture composition (Case H2, P=2000 psia)

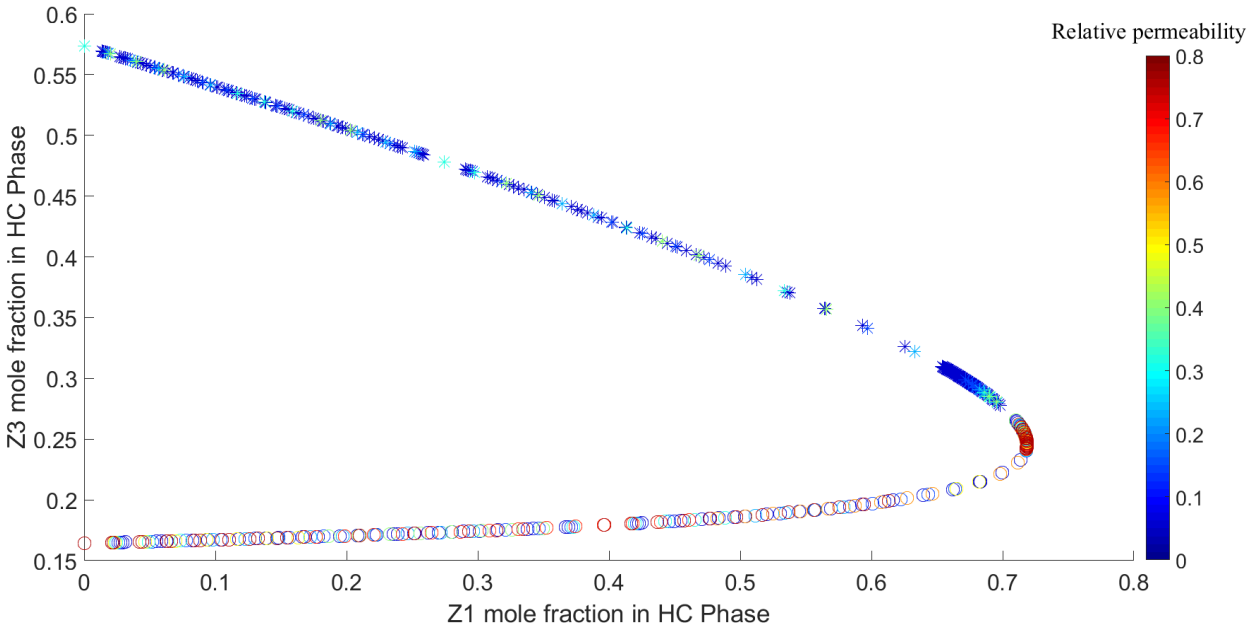

Figure 5-45: Calculated conventional (based on phase-labeling approach) relative permeability of hydrocarbons in three-phase: oil (star), gas (circle) (Case H2, P=1750 psia)

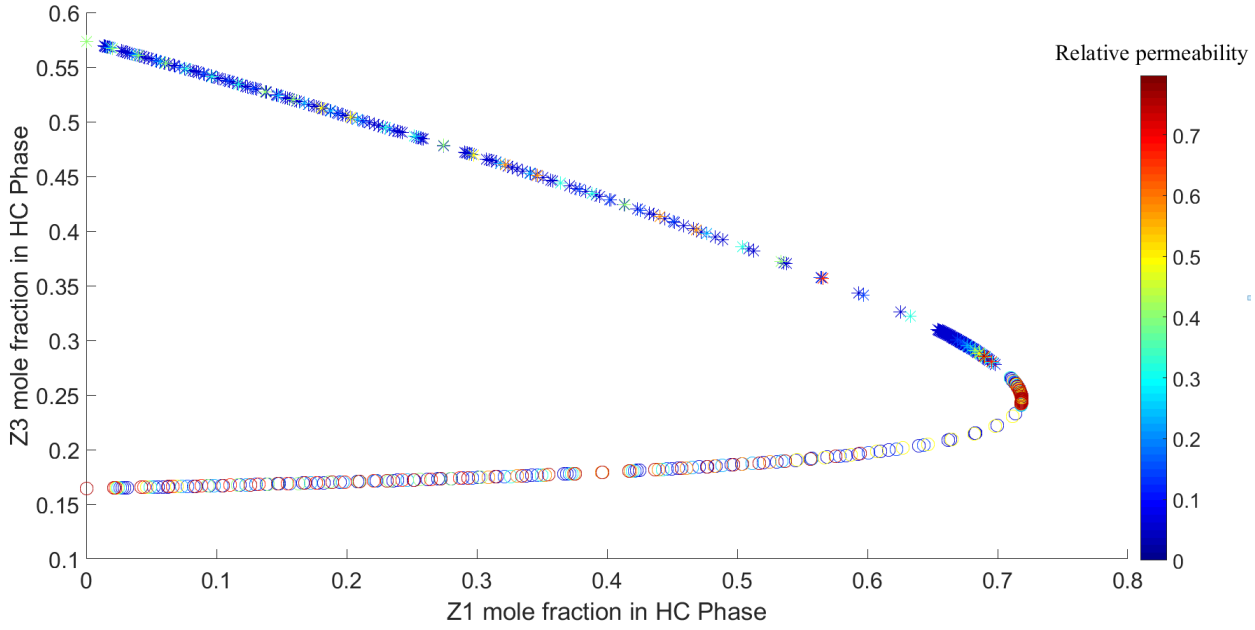

Figure 5-46: Calculated composition-dependent (GFE-averaged) relative permeability of hydrocarbons in three-phase: HC phase-1 (star), HC phase-2 (circle) (Case H2, P=1750 psia)

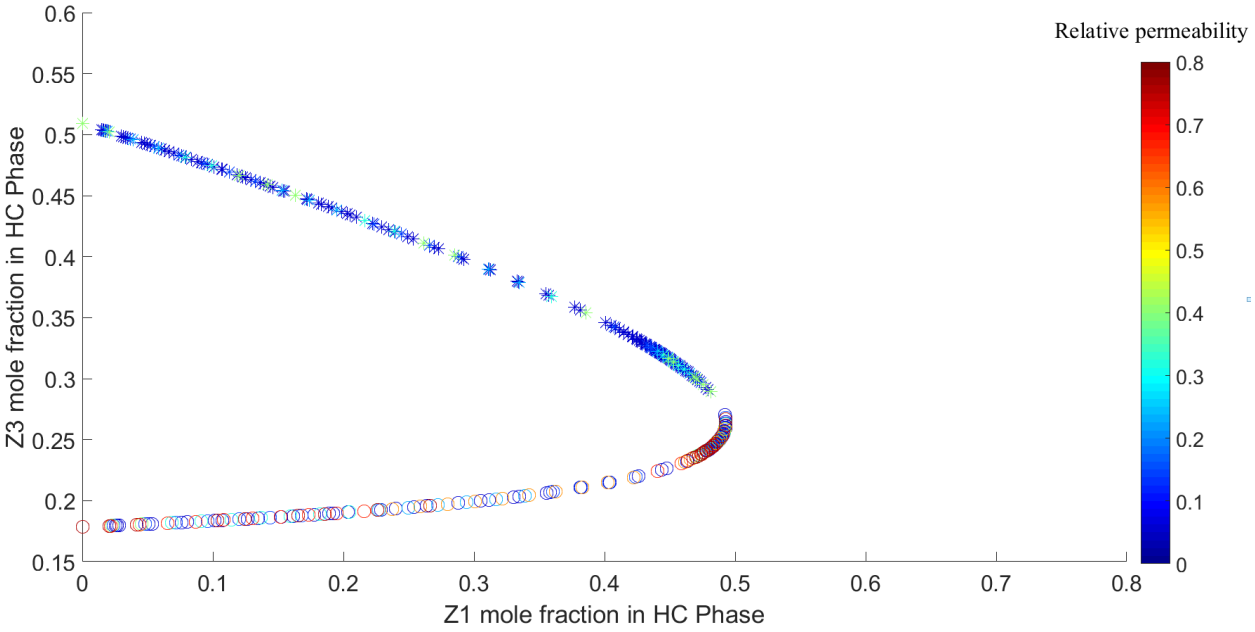

Figure 5-47: Calculated conventional (based on phase-labeling approach) relative permeability of hydrocarbons in three-phase: oil (star), gas (circle) (Case H2, P=2000 psia)

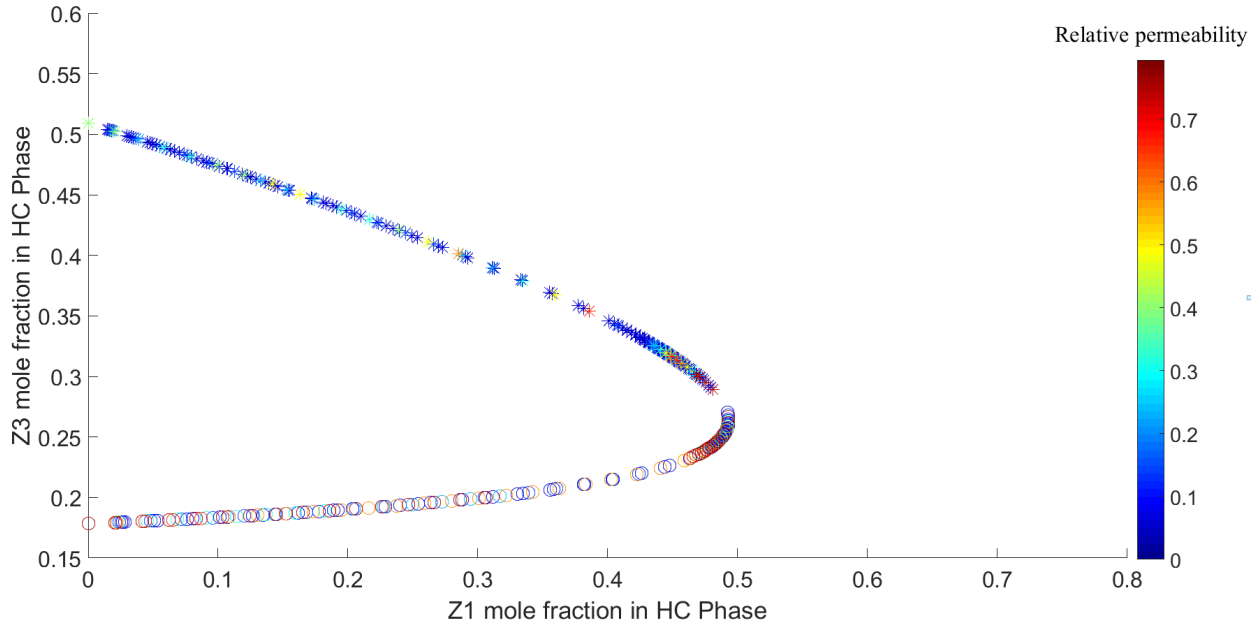

Figure 5-48: Calculated composition-dependent (GFE-averaged) relative permeability of hydrocarbons in three-phase: HC phase-1 (star), HC phase-2 (circle) (Case H2, P=2000 psia)

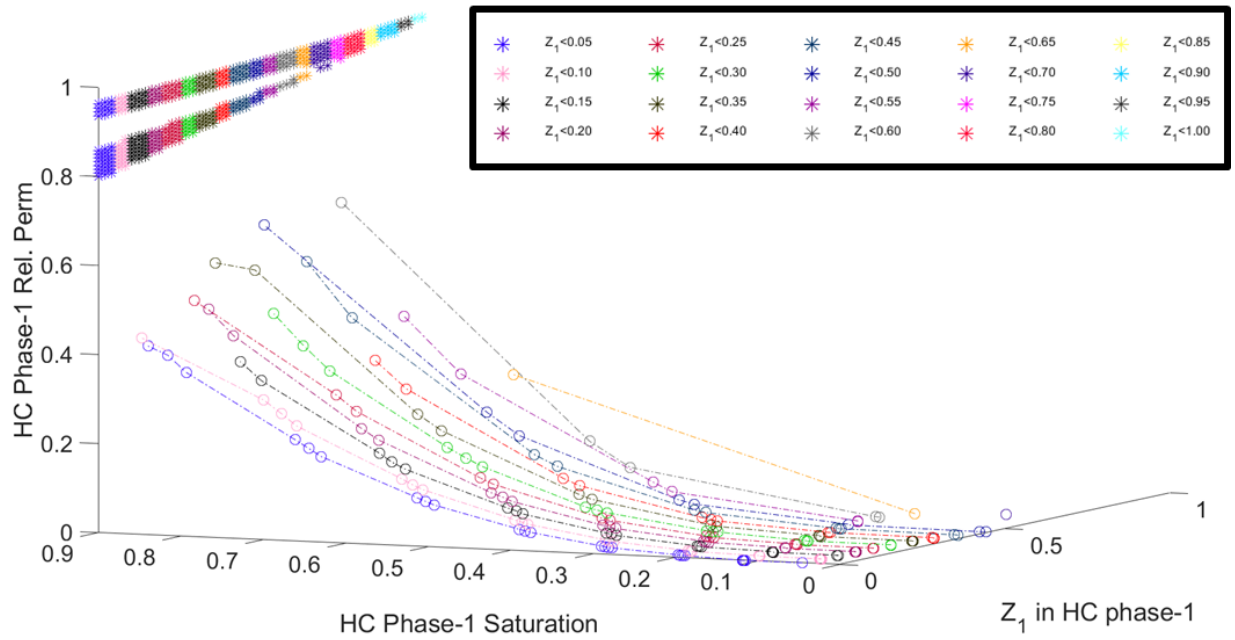

Figure 5-49: Variation of HC phase-1 relative permeability with saturation and composition (Z_1 in HC phase-1) in two phase (stars) and three-phase (dotted lines) flow (Case H2, P=1750 psia)

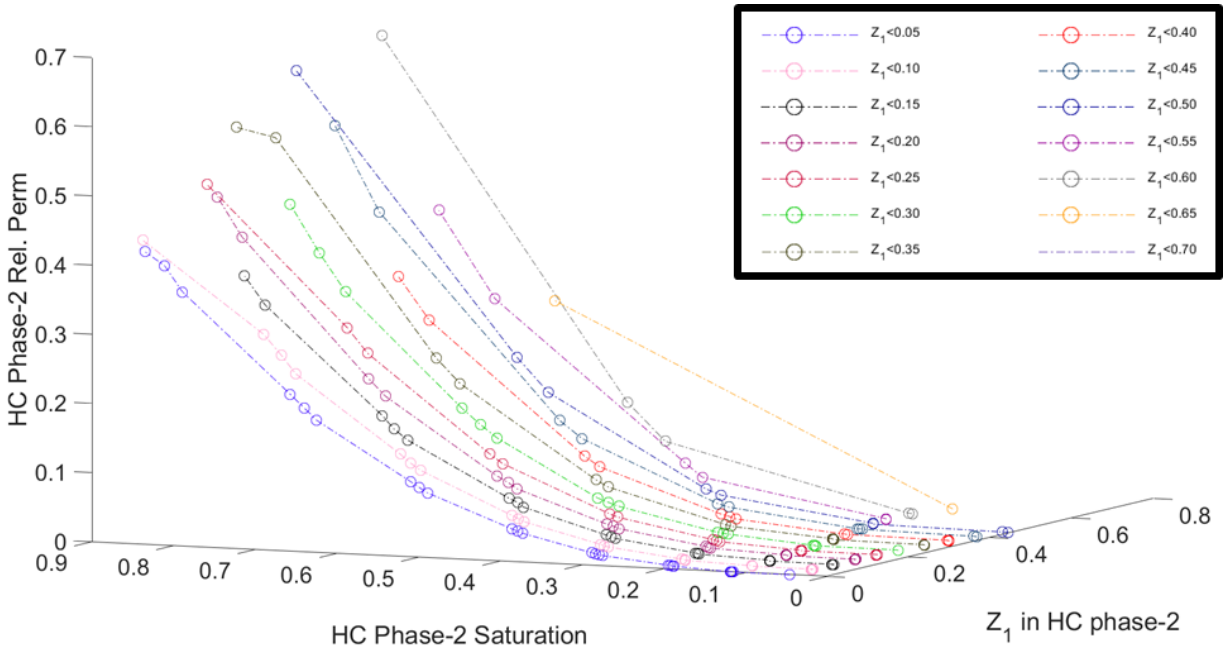

Figure 5-50: Variation of HC phase-2 relative permeability with saturation and composition (Z_1 in HC phase-2) in three-phase flow (Case H2, P=1750 psia)

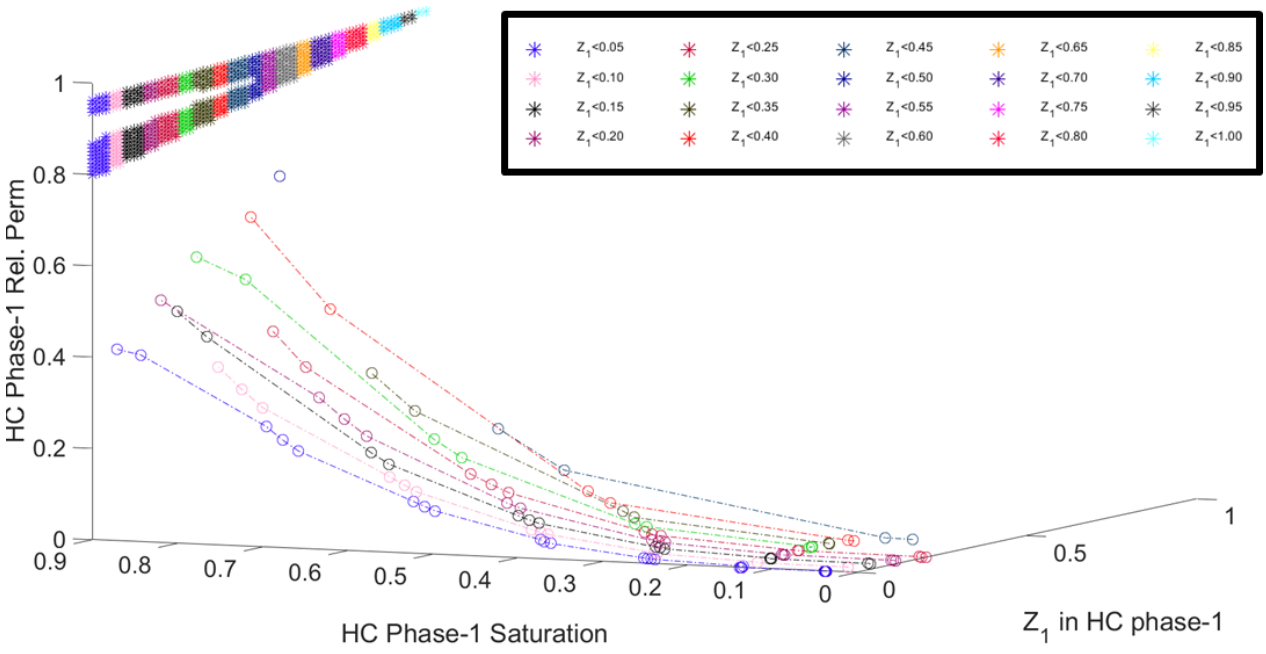

Figure 5-51: Variation of HC phase-1 relative permeability with saturation and composition (Z_1 in HC phase-1) in two phase (stars) and three-phase (dotted lines) flow (Case H2, P=2000 psia)

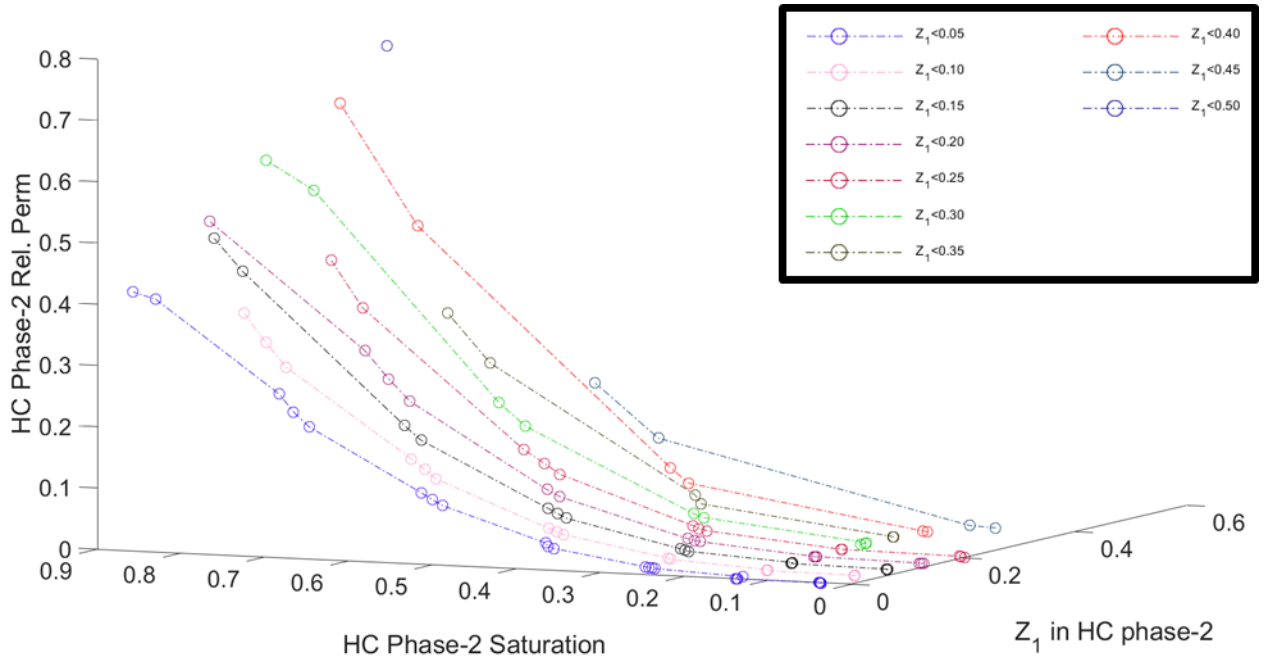

Figure 5-52: Variation of HC phase-2 relative permeability with saturation and composition (Z_1 component in HC phase-2) in three-phase flow (Case H2, P=2000 psia)

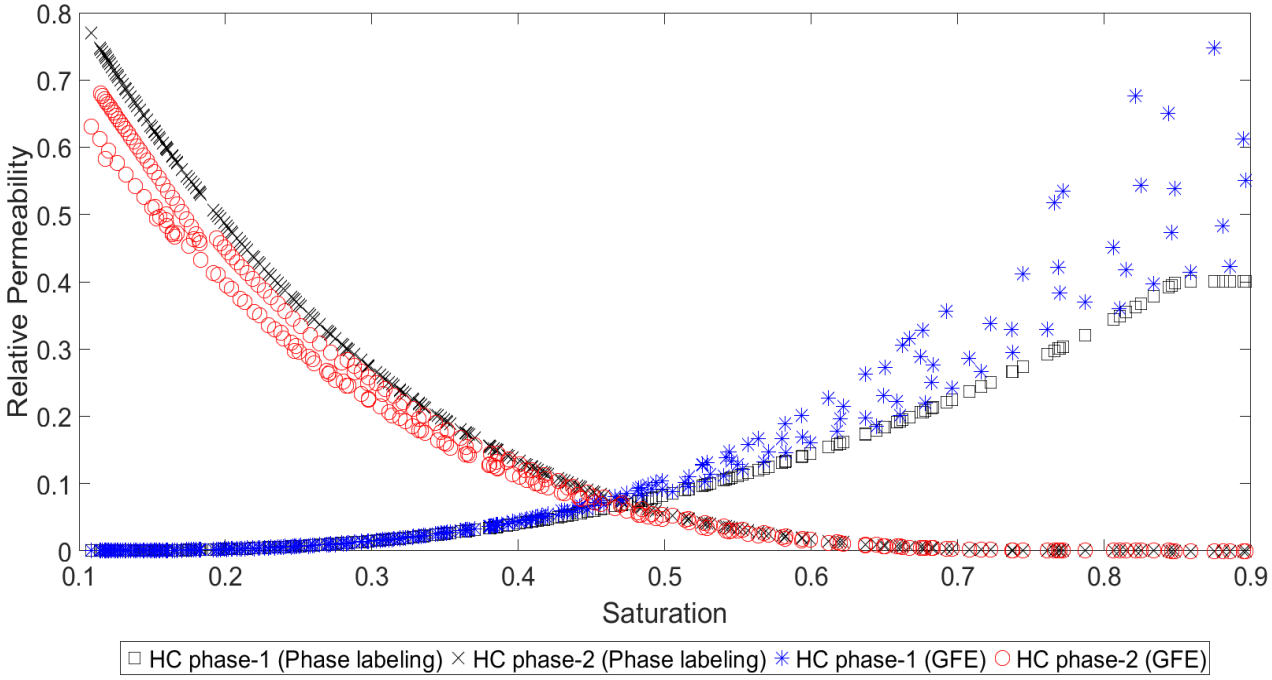

Figure 5-53: Calculated HC phase-1 and HC phase-2 relative permeability in three-phase flow using composition-dependent and phase-labeling approaches (Case H2, P=1750 psia)

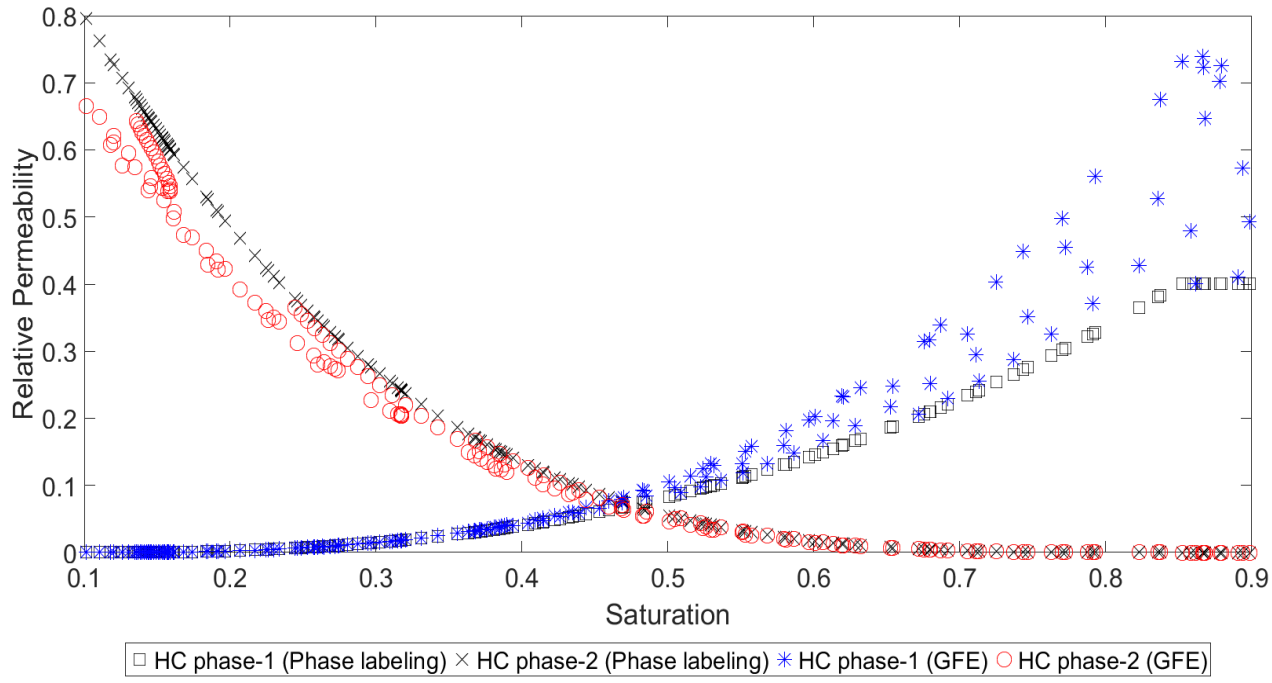

Figure 5-54: Calculated HC phase-1 and HC phase-2 relative permeability in three-phase flow using composition-dependent and phase-labeling approaches (Case H2, P=2000 psia)

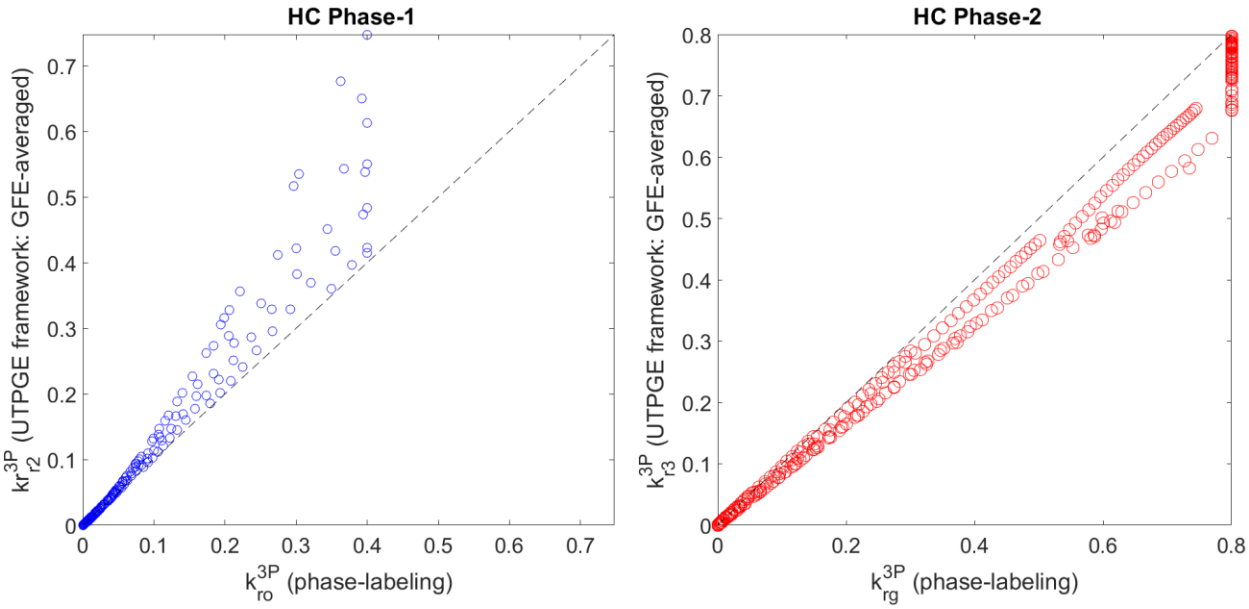

Figure 5-55: Correlation between modeled relative permeability of HC phases based on UTPGE framework (GFE-averaged) and phase-labeling approach: A) HC phase-1 (k_{r2}^{3P}) and oil phase; B) HC phase-2 (k_{r3}^{3P}) and gas phase (Case H2, P=1750 psia)

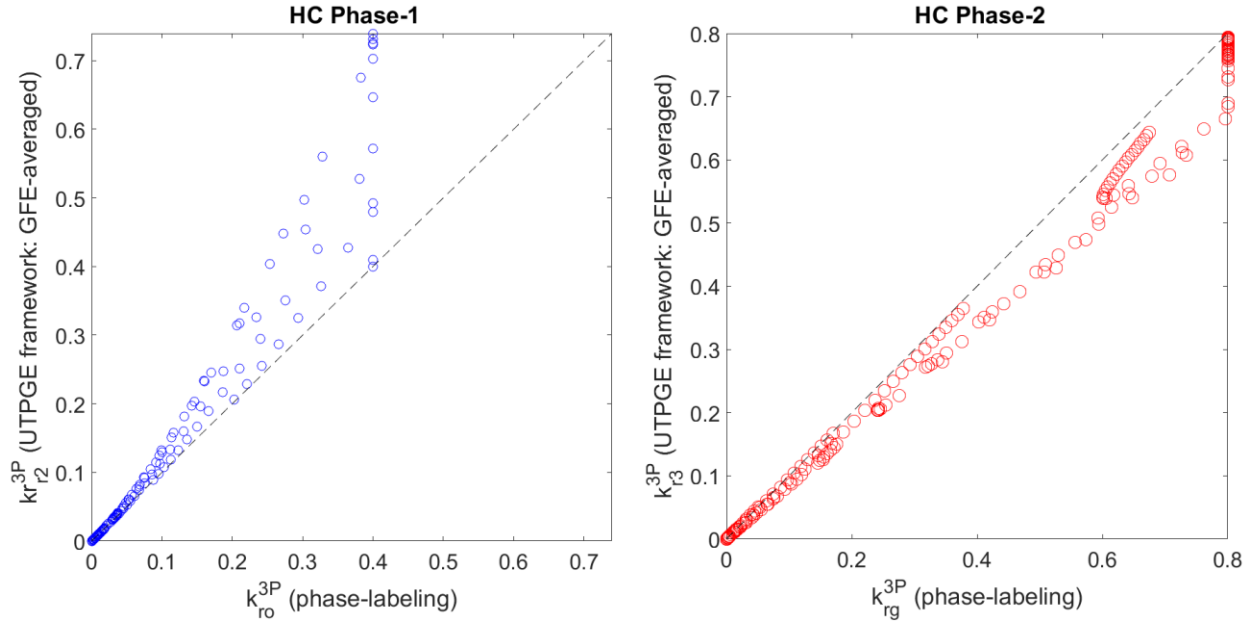

Figure 5-56: Correlation between modeled relative permeability of HC phases based on UTPGE framework (GFE-averaged) and phase-labeling approach: A) HC phase-1 (k_{r2}^{3P}) and oil phase; B) HC phase-2 (k_{r3}^{3P}) and gas phase (Case H2, P=2000 psia)

5.3.3.3 Case H3

In this example, we investigate pressure and composition effects on oil and gas relative permeability within a solvent injection into a butane-decane mixture. The solvents include CO_2, N_2, methane, or ethane. The basis of oil and gas relative permeability is the laboratory measured values of 0.4 and 1.0 when the experiments conducted with pure decane and CO_2 component, respectively, at reservoir pressure of 4500 psi. The reservoir and laboratory temperature are constant (T=160 °F).

Figure 5-57 shows two-phase envelope of $CO_2/nC_4/nC_{10}$ system at a nominal pressures of 1500 psia. **Figure 5-58** depict variation of the GFE and end-point relative permeability of the injected solvents together with those of pure decane. They highlight the variation of gas end-pint relative permeability for the pure solvents. Gas end-point relative permeability becomes approximately 7% lower when switching from the CO_2 to methane solvent.

In addition, **Figure 5-58** implies that for the designated in-place mixture (pure decane, oil) and solvent (gas), the variation of end-point relative permeability of both oil and gas phases slightly vary with pressure: the relative variation of oil and gas relative permeability with respect to the measured laboratory values are $\pm$5% and $\pm$1%, respectively. This result is in accordance with the general speculation that if pressure does not induce intensive mass-transfer and non-equilibrium conditions to a designated fluid system, it hardly impact relative permeability.

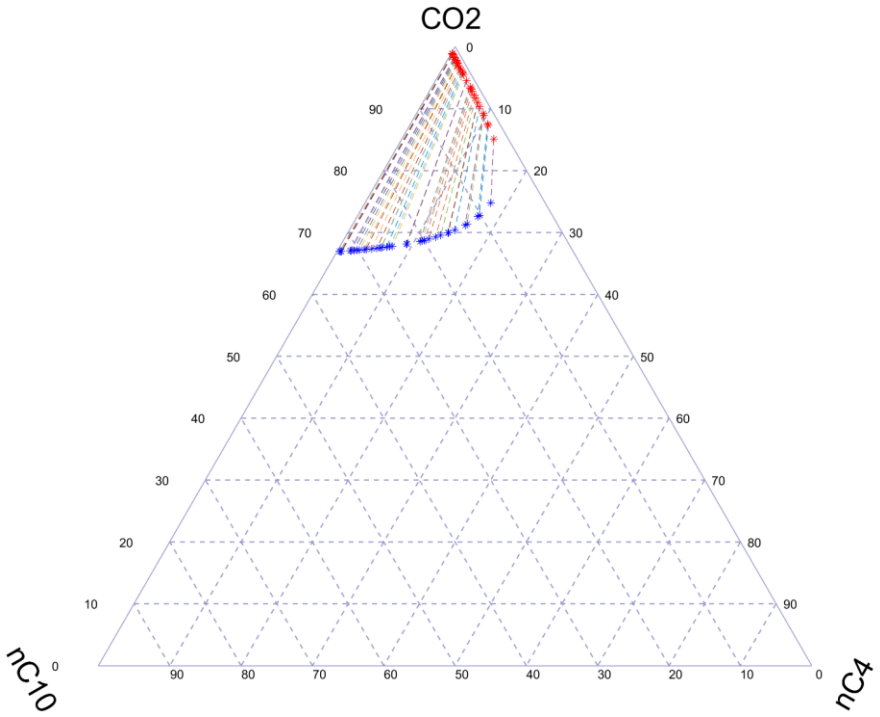

Figure 5-57: Two-phase envelope (vapor: red, liquid: blue) in composition ternary plot (Case H3: $CO_2/nC_4/nC_{10}$ system, P=1500 psia)

Table 5-5: GFE of components and phase end-point relative permeability (Case H3)

Components	Pressure (psi)	1500	2500	3500	4500	7000	10000
CO_2	GFE	-12.48	-12.28	-12.14	-12.01	-11.71	-11.38
	k_r^0-PH_2	0.996	0.998	0.999	**1.000**	1.002	1.005
N_2	GFE	-15.97	-15.96	-15.99	-16.04	-16.23	-16.54
	k_r^0-PH_2	0.969	0.969	0.969	0.968	0.967	0.964
C_1	GFE	-20.73	-20.37	-20.15	-19.96	-19.55	-19.11
	k_r^0-PH_2	0.931	0.934	0.936	0.937	0.941	0.944
C_2	GFE	-20.12	-19.91	-19.72	-19.54	-19.13	-18.68
	k_r^0-PH_2	0.936	0.938	0.939	0.941	0.944	0.947
nC_{10}	GFE	-89.70	-89.20	-88.71	-88.22	-87.01	-85.57
	k_r^0-PH_1	0.388	0.392	0.396	**0.400**	0.410	0.421

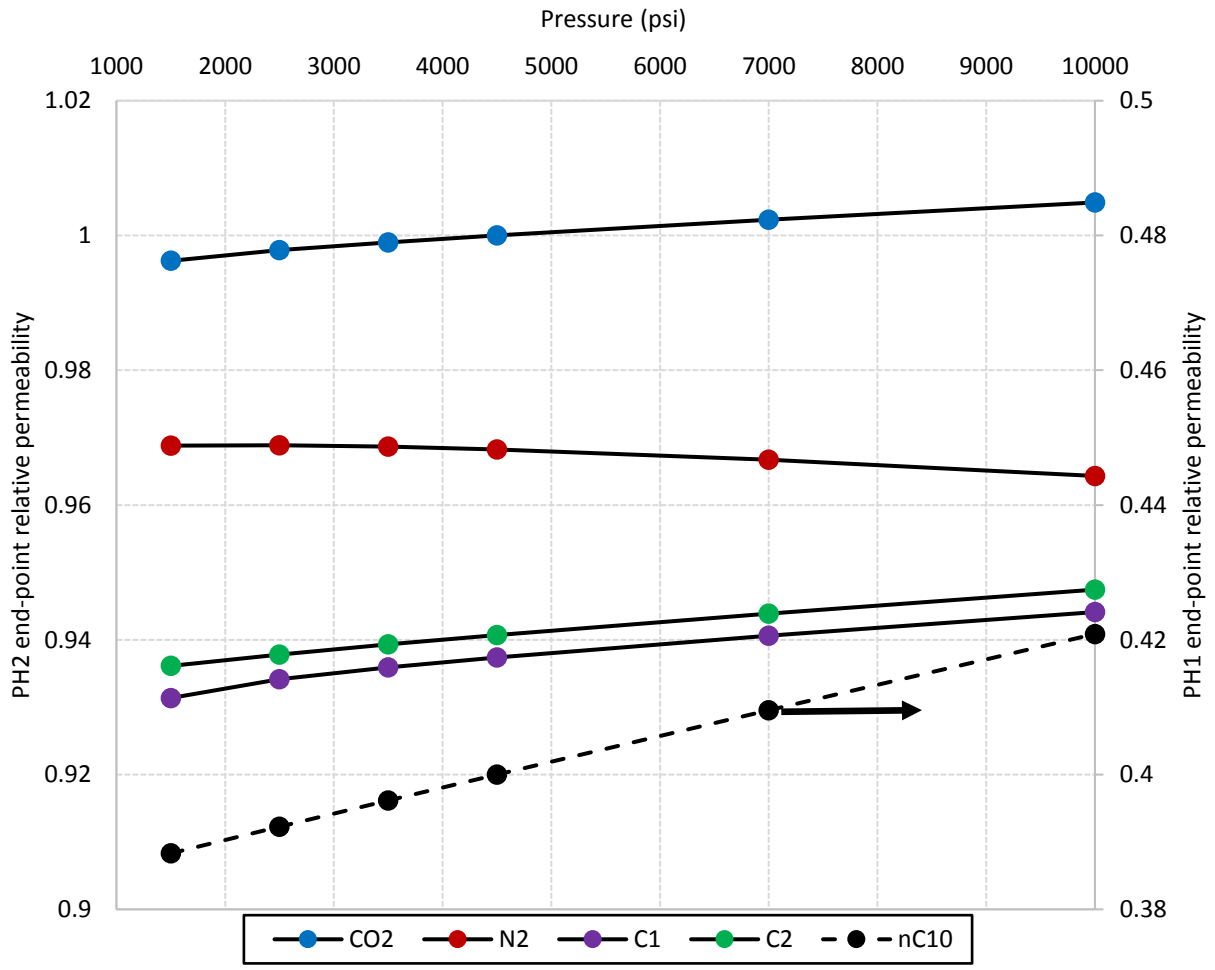

Figure 5-58: Variation of end-point relative permeability of PH-2 (gas, left axis) and PH-1 (oil right axis) with pressure (Case H3)

5.3.3.4 Case H4

In this case study we aim to incorporate both the GFE and IFT in modeling the compositional relative permeability. We use the fluid system of **Case H2**. The GFE-IFT dependent modeling approach spans the entire composition and saturation spaces. The complete compositional relative permeability modeling based on the coupled GFE and IFT may include data points from the immiscible, near-miscible, and miscible processes. The model then applies a bilinear GFE-IFT-average interpolation scheme between the current and reference relative permeability parameters (i.e., end-point relative permeability, functional curvature, and residual saturations).

Table 5-6 describes the properties of the input data points in two- and three-phase flow. Points A and B describes the most oil- and gas-like fluids in two-phase flow. The end-point of data points A and B are not identical to represent different fluid behavior in water-hydrocarbon flow. Points C-1 and C-2 replicate the end-point oil relative permeability data point with measured oil and gas composition and IFT. Points D-1 and D-2 represent the end-point gas relative permeability data point with the pertinent composition and IFT. Note that oil (and gas) relative permeability parameters for data points C and D are identical. It is because these two points represents two immiscible data points in a conventional relative permeability dataset in which all oil (or gas) points in a relative permeability curve have identical set of relative permeability parameters.

Figure 5-59 shows the input compositional (GFE and IFT) data surface of points A-D lifted for their associated and normalized relative permeability parameters ($F: k_r^0, S_r,$ and C_1). **Figure 5-60** illustrates the variation of calculated end-point relative permeability of hydrocarbon in two- and three-phase flow on the compositional GFE-IFT surface. It highlights the capability of the complete UTPGE framework in estimating the consistent and continuous relative permeability parameters.

Figure 5-61 compares the conventional HC phase-1 relative permeability with the compositional approaches as presented by the UTPGE framework. The compositional model depends either on the GFE or on the integrated GFE and IFT quantities. **Figure 5-61** describes that while the former method estimates the expected relative permeability values qualitatively, the latter method reproduces more representative immiscible, near-miscible, and miscible relative permeability curves.

Table 5-6: Data points for two- and three-phase flow (Case H4)

Input data	GFE	IFT	End-point relative permeability	Relative permeability curvature	Residual saturation	Comment
A	-55.19	0.0	0.8	1.0	0.0	Most oil-like fluid
B	-12.59	0.0	1.0	1.0	0.0	Most gas-like fluid
C-1	-41.44	0.787	0.4	2.5	0.20	Immiscible oil end-point
C-2	-26.49	0.787	0.8	4.5	0.15	Immiscible residual gas
D-1	-35.48	0.274	0.4	2.5	0.20	Immiscible residual oil
D-2	-24.18	0.274	0.8	4.5	0.15	Immiscible gas end-point

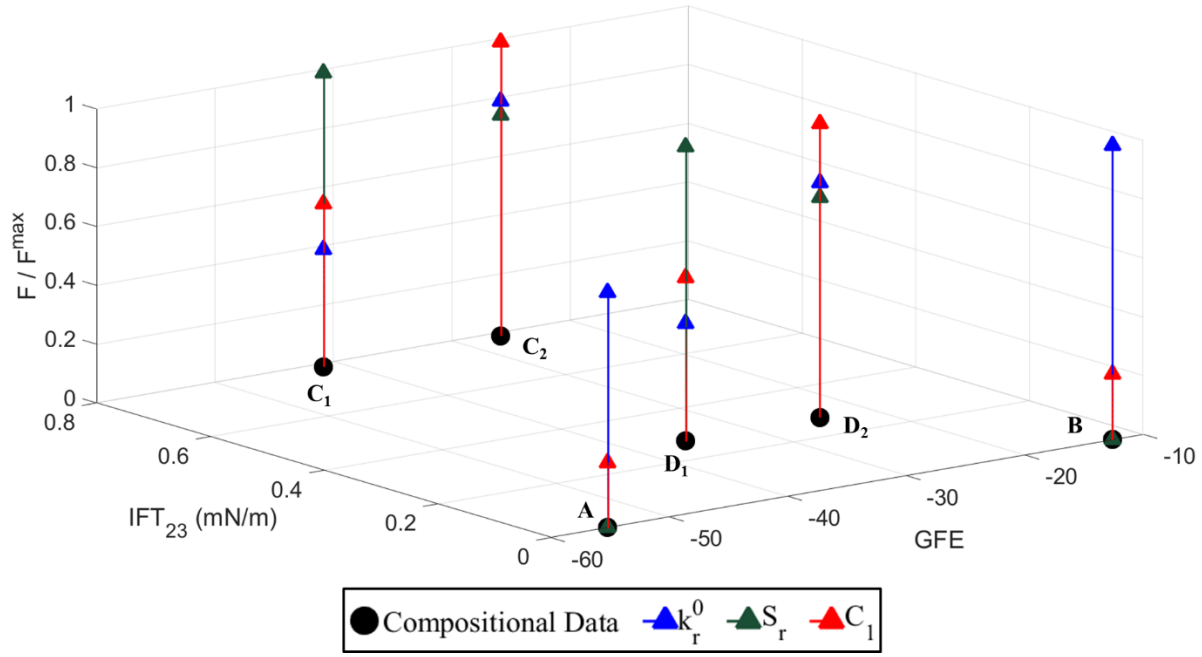

Figure 5-59: Normalized input relative permeability parameters (endpoint, residual, and curvature) in GFE and IFT_{23} (between HC phase-1 and HC phase-2) space (Case H4)

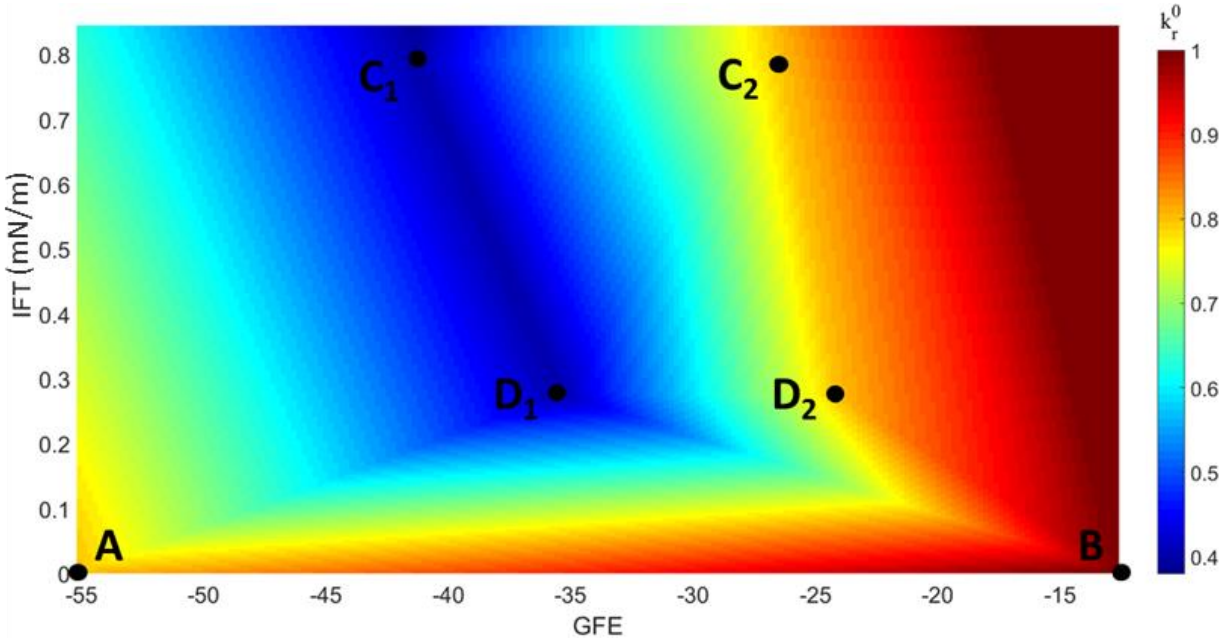

Figure 5-60: Modeled end-point relative permeability variation with GFE and IFT together with given data points: A-D (Case H4).

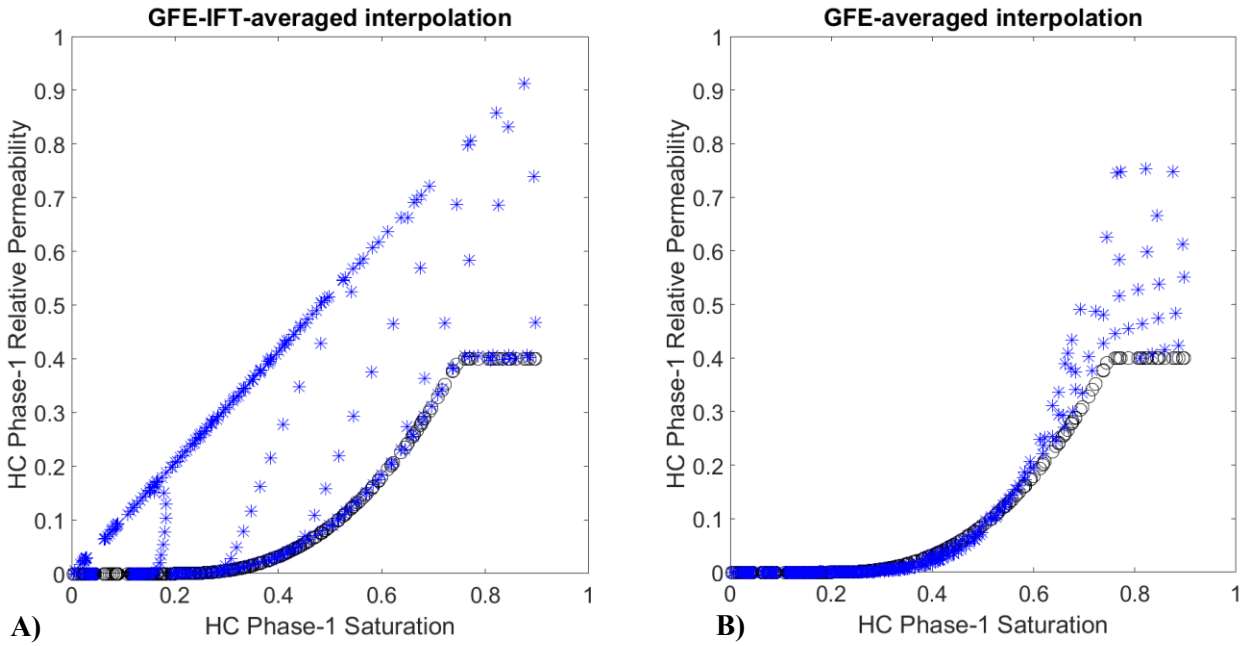

Figure 5-61: Comparison of modeled conventional (phase-labeling approach: black circles) and compositional relative permeability of HC phase-1 (blue star) for Case H4: **A**) GFE-IFT dependent model (bilinear approach); **B**) GFE-dependent model (linear approach).

5.4 SUMMARY

The established results of the case studies in this chapter demonstrated that the UTPGE framework is a viable tool to model the compositional relative permeability more accurately when compositional variation is significant. The proposed captures the impact of both bulk and interphase composition effects on relative permeability for various phases. We noted that the reference-state GFE of components is pressure and temperature dependent and must be included in the calculation of phase GFE. We showed examples of aqueous and hydrocarbon phases. In the following, we describe some of the implications of the studied case studies.

Case AQ1 stated one of the rewarding features of the UTPGE framework: geochemical-dependent aqueous phase relative permeability. The complex aqueous fluid involved in both internal mass-transfer and interphase equilibrium chemical reactions with solid phase(s) and yielded several species. Moreover, the results demonstrated that the chemical reactions play an interim role in evaluating the molar GFE of aqueous system. Although geochemical reactions impact the overall behavior of fluid mobility, considering them in any geochemical package paves the ways in reservoir simulation. In particular, one requires to import the speciation results from a geochemical package to calculate the molar GFE of each existing species. We imported the speciation results from the PHREEQC package (**Parkhurst & Appelo, 2013**). We also showed that, in certain circumstances, the molar GFE and ionic strength of the aqueous phase are interrelated and that one may substitute the more computationally expensive molar GFE calculation with the ionic strength.

The results of **Case H1** revealed that the GFE of hydrocarbon fluids is a continuous function even in conditions in which phases appear/disappear. This concrete thermodynamically-consistent behavior of the molar GFE of the studied fluid systems is the cornerstone of compositional relative permeability using the GFE of each phase. We noticed that the GFE may

show non-monotonic behavior for a specified pressure, temperature, and composition. That sheds light to the requirement of providing a complementary quantity to incorporating the interphase composition effect in the proposed approach to complete compositional relative permeability modeling.

The established results of **Case H2** demonstrated the calculation procedure of relative permeability in an integrated composition-saturation space. They revealed that the UTPGE framework provides continuous and consistent results in modeling the relative permeability of both three-phase flow and two-phase water-hydrocarbon flow. More importantly, they confirmed the shortcoming of phase-labeling approach in modeling near-critical fluid systems. They also illustrated the impact of phase composition on the different relative permeability values of a single-phase hydrocarbon (two-phase water hydrocarbon flow).

Case H3 highlighted the possibility of reevaluation of a given measured relative permeability data when the overall composition of existing phases varies. Strictly speaking, one can transform the laboratory relative permeability curves to a specified pressure, temperature, and composition. It is beneficial when the laboratory conditions cannot represent the high reservoir pressure/temperature or the dynamic variation in the composition of the in-situ fluid. The corrected relative permeability parameters or tables by the proposed framework then are the input parameters to the numerical reservoir simulators.

Not only do both phase composition and saturation impact relative permeability in a particular range of fluid composition, the composition and saturation of other phases in three-phase flow may change the relative permeability of a designated phase. We added this functionality through the composition of the interphase or equivalently the IFT values.

Case H4 showed that implementing the full UTPGE framework (i.e., GFE-IFT weighted interpolation scheme) provides a pragmatic approach in modeling relative permeability in

composition-saturation space where both internal and interphase effects are added. We applied the UTPGE framework to a near critical fluids including the problematic liquid dropout close to the wellbore (**Case H4)**. It is beneficial when the number of existing fluids varies dynamically when the reservoir pressure changes. Nevertheless, we did not consider the impact of viscous forces on relative permeability. One can substitute the IFT term with trapping number to include gravitational, viscous, and capillary forces. Alternatively, we first evaluate the impact of trapping number on relative permeability parameters (see **Trapping number effect** in Chapter 3). We then import the corrected quantities into the compositional UTPGE framework.

Note that here we assume that the fluid system does not alter rock wettability. Nevertheless, the UTPGE framework is general and is capable of modeling this effect: it demands an integrated model incorporating the aqueous, hydrocarbon, and non-hydrocarbon phases. One requires to include the geochemical reactions in the functional form of the UTPGE framework. The Gibbs free energy model includes the chemical reactions: the equilibrium (or non-equilibrium) reactions have interim impact on the phase molar GFE. The rock wettability effect, variation of the GFE with the equilibrium and non-equilibrium reactions, and relative permeability can be integrated.

Chapter 6: **Application of UTKR3P and UTHYST Models**

The objective of this chapter is to validate and apply the UTKR3P and UTHYST models as implemented into IPARS and UT-DOECO2 compositional reservoir simulators. The enhanced reservoir simulator and the relevant discussions are included in **Appendix J** and **Appendix K**, respectively. We deploy the implemented models to examine four case studies as summarized in **Table 6-1**.

Table 6-1: Summary of applied simulator and objectives of each case study

Case Study	Simulator	Objective
S1	IPARS	Sensitivity analysis on parameters of UTKR3P model to examine impact of two-phase relative permeability parameters on oil recovery
S2	IPARS	Investigating hysteresis and capillary trapping effects on the performance of an immiscible WAG injection scheme
S3	UT-DOECO2	Examining hysteresis effect (i.e., UTHYST model) on the performance of a tapered WAG injection scheme applied to an intermediate-wet rock.
S4	UT-DOECO2	Modeling low-tension gas flood

6.1 UTKR3P MODEL VERIFICATION (CASE S1)

In this section, we verify the robustness of the implemented UTKR3P model in IPARS compositional reservoir simulator. The impact of variation of the parameters of UTKR3P model on oil recovery in a WAG process for a synthetic and homogenous 3D reservoir is investigated. One pseudo component (C_7-C_{15}) was used to represent a fairly heavy oil with Peng-Robinson equation of state (**Peng & Robinson, 1976**). **Table 6-2** and **Table 6-3** illustrate a summary of fluid and reservoir properties. Note that **Table 6-2** gives the data for all case studies in this chapter. **Table 6-4** lists the reference relative permeability data (Base case). The two-phase capillary pressure of water-oil (P_{cow}) and gas-oil (P_{cgo}) are modeled using the van Genuchten model (**1980**) ($P_{cij} = \alpha_{ji}^{-1}.\left(\bar{S}_j^{n_{ji}/(1-n_{ji})} - 1\right)^{n_{ji}^{-1}}$, where $\bar{S}_j$ is normalized saturation of wetting fluid, α_{ji} and n_{ji} are fitting parameters). We do not include hysteresis effect in modeling of this case study. One-quarter

of a five-spot well pattern is modeled. Two wells (i.e., an injector and a producer) are located at the opposite corners of the reservoir model. The injection and production wells are pressure constrained (injection bottom-hole pressure (BHP)=5500 psia; production BHP=4500 psia) and penetrate all layers in z-direction (wellbore radius (r_w) =0.5 ft; skin factor=0.0). A WAG injection scheme with a WAG ratio of 1:1 is applied with six cycles of N_2 and water injection where each half-cycle lasts 30 days (i.e., total injection period is 360 days).

We performed a deterministic sensitivity analysis to investigate the impact of two-phase relative permeability parameters on oil recovery. Each parameter was varied in a $+/-$ 50% range. The oil recovery factor for the base case scenario is 40.47% at the end of injection period. **Table 6-5** lists the effect of 15 two-phase flow parameters on oil recovery (i.e., k_{rij}^0 and C_{1ij} and C_{2ij} where *i,j*=1,2,3, i≠j). Here, by introducing the second curvature, the relative difference between oil recovery factor in Base case and updated values is up to 40%. The tornado diagram in **Figure 6-1** compares the relative impact of k_{rij}^0 and C_{1ij} quantities on oil recovery. The comparative charts illustrate that for this case study, two-phase parameters of different fluid pairs have non-unique impact on oil recovery. For example, the end-point oil relative permeability to water (k_{r21}^0) has the significant impact on oil recovery (The relative difference between oil recovery in Base case and $k_{r21}^0 = 0.3$ is 33.1%). The variation of end-point oil relative permeability to gas (k_{r23}^0), however, has a negligible effect on oil recovery (The relative difference between oil recovery in Base case and $k_{r23}^0 = 0.3$ is 2.9%). The result of this bar chart, however, are case specific. For instance, if the oil displacement by gas is the controlling mechanism, the impact of gas-related relative permeability parameters dominates those of water. The complicated three-phase flow in non-water-wet medium makes it difficult to quantify the most uncertain parameters in reservoir simulation. A parametrized-level model like UTKR3P model can assist to quantify the relevant uncertainties more accurately than relative permeability tables and parametric models with

constant relative permeability parameters like equal oil-water and oil-gas end-point relative permeability, curvature, or residual saturation.

Table 6-2: Fluid component properties (Case S1-Case S4)

	Critical temperature ($°R$)	Critical pressure (psi)	Critical compressibility	Acentric factor	Molecular weight	Parachor	Volume shift parameter
CO_2 (injectant)	1069.9	547.6	1.506	0.225	44.01	49.0	0.000
N_2 (injectant)	226.6	492.3	0.2742	0.040	28.01	84.0	0.000
C_1	343.1	667.2	0.2873	0.008	16.04	71.0	0.000
C_2-C_3	612.0	658.6	0.2852	0.127	36.27	132.5	-0.092
C_4-C_6	835.1	487.5	0.2716	0.240	70.42	231.4	-0.042
C_7-C_{15}	1086.4	329.4	0.2621	0.609	137.84	404.3	0.067
C_{16}^+	1444.9	258.8	0.2837	1.042	317.90	831.9	0.225

Binary interaction coefficient for Peng-Robinson EOS					
	C_1	**C_2-C_3**	**C_4-C_6**	**C_7-C_{15}**	**C_{16}^+**
CO_2	0.055	0.055	0.055	0.095	0.095
N_2	0.155	0.155	0.155	0.155	0.155

Table 6-3: Reservoir and fluid properties (Case S1)

Variable	Values	Variable	Values
Reservoir dimensions (*ft*)	850×850×40	Rock compressibility (*1/psi*)	5×10^{-6}
Grid-block size (*ft*×*ft*×*ft*)	170×170×10	Reservoir initial pressure (*psia*)	5000
Porosity	0.25	Reservoir temperature (°*F*)	220
Permeability in X- and Y-directions (md)	1010	Water formation volume factor (*rb/STB*)	1.0
Permeability in Z-direction (md)	202	Water stock tack density (*lbm/scf*)	62.24
Initial saturations: Phase-1/Phase-2/Phase-3	0.2/0.8/0.0	Original oil in-place (*KSTB*)	1000.65
Water compressibility factor (*1/psi*)	3.3×10^{-6}	$\alpha_{wo}/\alpha_{og}/n_{wo}/n_{og}$ in P_c model	3/2.5/3/2.5

Table 6-4: Reference relative permeability data (Case S1)

$S_{1r2} = S_{1r3}$	0.10	$S_{2r1} = S_{2r3}$	0.2	$S_{3r1} = S_{3r2}$	0.25
$k^0_{r12} = k^0_{r13}$	0.4	$k^0_{r21} = k^0_{r23}$	0.6	$k^0_{r31} = k^0_{r32}$	0.9
$C_{112} = C_{112}$	3.0	$C_{121} = C_{123}$	4.0	$C_{131} = C_{132}$	5.0
C_{2ji}, j,i=1,2,3	0.0	b_j, j=1,2,3	0.0	S_{cj}, j=1,2,3	0.0

* 1, 2, and 3 represent water, oil, and gas phases, respectively

Table 6-5: Sensitivity analysis of 2-phase relative permeability parameters on recovery factor (Case S1)

Parameter	Relative variation of Base case						
	-50%	-30%	-10%	0%	10%	30%	50%
	Oil recovery factor (%)						
k_{r13}^{0}	40.43	40.43	40.45	**40.47**	40.48	40.52	40.56
k_{r31}^{0}	40.52	40.49	40.48	**40.47**	40.45	N.A.	N.A.
k_{r32}^{0}	40.59	40.53	40.47	**40.47**	40.45	N.A.	N.A.
C_{113}	40.89	40.67	40.50	**40.47**	40.47	40.51	40.55
C_{131}	39.96	40.21	40.41	**40.47**	40.49	40.62	40.73
C_{132}	40.02	40.24	40.41	**40.47**	40.47	40.51	40.44
C_{123}	41.83	41.20	40.69	**40.47**	40.27	39.86	39.56
k_{r23}^{0}	39.28	39.77	40.24	**40.47**	40.67	41.07	41.43
k_{r12}^{0}	38.81	39.33	40.03	**40.47**	40.90	41.79	42.70
C_{112}	52.65	47.36	42.29	**40.47**	39.21	38.08	37.64
C_{121}	53.95	47.33	42.48	**40.47**	38.64	35.56	33.02
k_{r21}^{0}	27.09	33.15	38.10	**40.47**	42.70	46.69	50.51
	Value						
	0.0	**0.1**	**0.5**	**0.8**	**1.1**	**1.3**	**1.5**
C_{221}	**40.47**	42.66	48.87	52.20	54.49	55.73	56.81
C_{223}	**40.47**	40.67	41.42	41.90	42.32	42.58	42.82
$C_{231} = C_{232}$	**40.47**	40.44	40.36	40.36	40.39	40.40	40.41

* N.A.: Not applicable

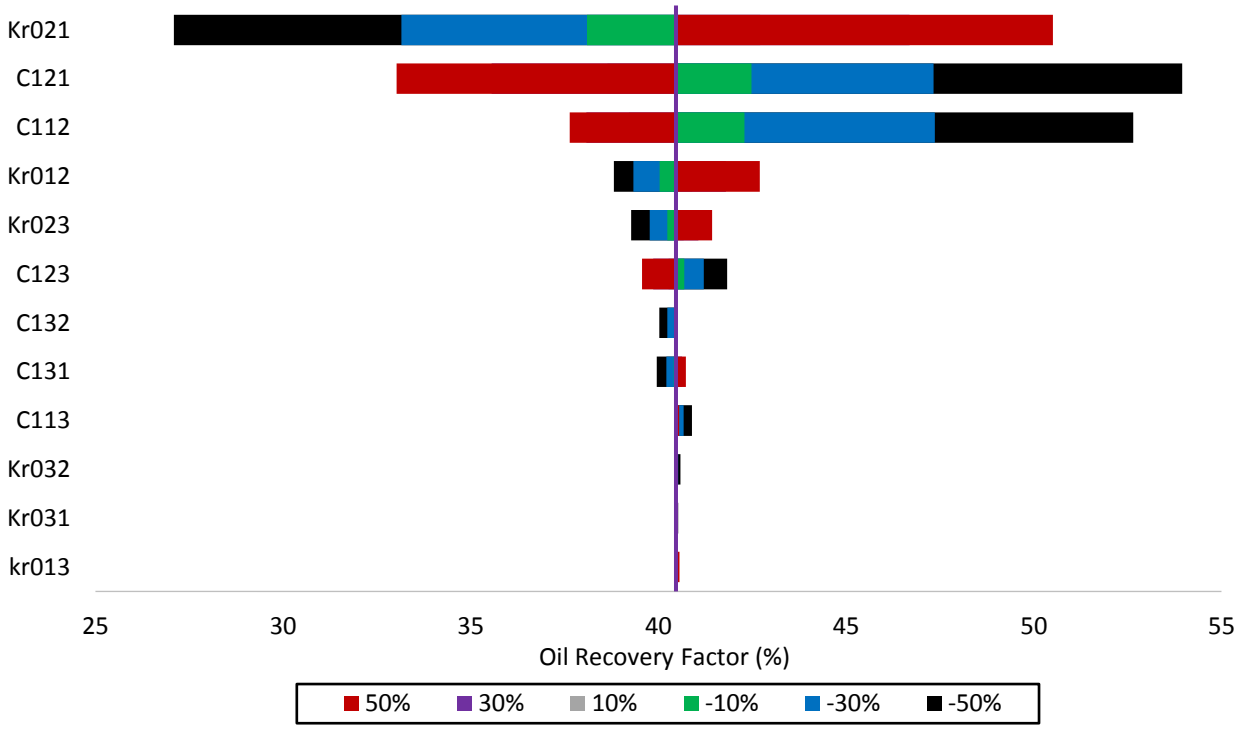

Figure 6-1: Sensitivity analysis to study the impact of relative permeability parameters on oil recovery (Case S1)

6.2 N_2-WAG (CASE S2)

We aim to study the effect of hysteresis and capillary trapping on the performance of the immiscible WAG injection scheme using the IPARS simulator. For WAG injection strategy, the reservoir heterogeneity (i.e., as represent by the Dykstra-Parsons coefficient and dimensionless correlation length in X-, Y-, and Z-directions) (**Ghomian, 2008**). Hence, we model a stochastically generated permeability field with an average permeability of 200 md. **Table 6-2** and **Table 6-6** list the fluid, initial composition, and reservoir properties. The fluid displacement is capillary dominated ($N_t = 10^{-8}$). Six components represent oil with the Peng-Robinson equation of state (**Peng & Robinson, 1976**). **Table 6-7** provides relative permeability data and hysteresis parameters. In this study, capillary pressure is not modeled (i.e., $P_{c21} = P_{c32} = 0$). The simulation model presents a five-spot pattern including one injection well and four production wells. **Figure 6-2** shows the location of wells and permeability distribution in x- and y-directions (k_x and k_y). The injection and production wells are pressure constrained (injection BHP=4000 psia; production BHP=1000 psia) and penetrate all layers in z-direction. A six-cycle WAG injection scheme with a WAG ratio of 1:1 is applied with six cycles of N_2 and water injection where each half-cycle lasts 30 days (i.e., total injection period is 360 days). We ran two simulation cases without hysteresis (Case S2A) and with hysteresis (Case S2B) option. The UTKR3P model for relative permeability calculation and UTHYST model for hysteresis option are applied.

We focus on a particular grid-block M located in the second bottom layer of the injection well (see **Figure 6-2**) for the relative permeability and hysteresis. **Figure 6-3** depicts variation of trapped gas saturation with total gas saturation for gridlock M in Case S2B. It shows that as the total gas saturation in each cycle decreases (e.g., during water injection half-cycle), trapped gas accumulates. In the increasing gas saturation, however, the trapped gas saturation remains constant. **Figure 6-4** demonstrate the variation of total gas saturation in both cases for grid block

M. It highlights the impact of gas trapping in a higher total gas saturation value within different cycles for Case S2B. Nonetheless, both cases resulted in equal total gas saturation during the first gas flood (i.e., 0-30 days). **Figure 6-5** reports the calculated gas relative permeabilities for both cases. In general, gas mobility is higher in Case S2A than Case S2B. The difference between gas relative permeability in Cases S2A and S2B is one order of magnitude at the end of the sixth WAG cycle. This has implications on hydrocarbon recovery and operational considerations. For example, the design of a produced-gas processing capacity may suffer from inaccurate modeling of gas trapping.

Figure 6-6 and **Figure 6-7** compare the gas saturation distribution for Cases 1A and 1B at the end of the third waterflood (t=180 day) and end of the sixth waterflood (t=360 days), respectively. Here, the cross sections of injection and production wells are highlighted while the rest of the reservoir is shown with opacity of 30%. These figures address the significant gas saturation stranded in the reservoir when hysteresis option is included. The vertical aspect ratio (VAR) for the 3D visualization purpose of the reservoir is 10.

Figure 6-8 and **Figure 6-9** illustrate spatial gas saturation distribution, quartiles of average reservoir pressure, oil saturation, and gas saturation, together with gas saturation histogram for both cases at the end of the third waterflood (t=180 day) and end of the sixth waterflood (t=360 days). They demonstrate that after 6 cycles of WAG injection, gas saturation left in the reservoir is significant when hysteresis option is included. In addition, for this case, oil recovery is higher for Case S2A than Case S2B (i.e., higher remaining oil saturation in hysteresis case). It is due to the reduced gas mobility in Case S2B. Indeed, the difference in average reservoir pressure between Case S2A and S2B is approximately 1000 psi (see pressure quartiles in **Figure 6-8** and **Figure 6-9**).

Figure 6-10 shows that by excluding the hysteresis effect the rate of water and gas injection

increase as the cycle number increases. **Figure 6-11**, however, reveals that well injectivity decreases when hysteresis effect is included. The abnormal well injectivity issue in hysteresis case is due to the elevated gas trapped saturation around the wellbore (viz., also reflected in an increased reservoir pressure).

Table 6-8 lists the cumulative injection and production fluids for both cases. It shows that although the cumulative oil production was reduced in Case S2B, the oil production per equivalent fluid injection was greatly improved when hysteresis was included (i.e., 1.14% and 8.99% for Case S2A and Case S2B, respectively). This analysis highlights the critical role of hysteresis effect in a multicycle process.

Table 6-6: Reservoir properties and initial fluid composition (Case S2)

Variable	Values	Variable	Values
Reservoir dimensions (*ft*)	850×850×40	Initial water/oil/gas saturation	0.45/0.55/0.0
Grid-block size (*ft*×*ft*×*ft*)	50×50×10	Rock compressibility (*1/psi*)	5×10^{-6}
Porosity	0.25	Initial reservoir pressure (*psia*)	3000
Dykstra-Parsons coefficient (for permeability in x- and y-directions)	0.8	Reservoir temperature (°*F*)	220
Correlation length in x-, y-, and z-directions (*ft*)	850/850/10	Water formation volume factor (*rb/STB*)	1.0
Ratio of permeability in x-direction to z-direction	5.0	Water stock tack density (*lbm/scf*)	62.24
Water compressibility factor (*1/psi*)	3.3×10^{-6}	Original oil in-place (*MSTB*)	2751.8

Initial oil composition					
N_2	**C_1**	**C_2-C_3**	**C_4-C_6**	**C_7-C_{15}**	**C_{16}^+**
0.0	0.15	0.10	0.10	0.15	0.50

Table 6-7: Relative permeability data and hysteresis parameters (Case S2)

$\boldsymbol{S_{1r2}}$	0.20	$\boldsymbol{S_{1r3}}$	0.30	$\boldsymbol{S_{2r1}}$	0.35
$\boldsymbol{S_{2r3}}$	0.10	$\boldsymbol{S_{3r1}}$	0.10	$\boldsymbol{S_{3r2}}$	0.05
$\boldsymbol{k^0_{r12}}$	0.2	$\boldsymbol{k^0_{r13}}$	0.3	$\boldsymbol{k^0_{r21}}$	0.7
$\boldsymbol{k^0_{r23}}$	0.9	$\boldsymbol{k^0_{r31}}$	0.9	$\boldsymbol{k^0_{r32}}$	1.0
$\boldsymbol{C_{112}}$	3.5	C_{113}	3.0	C_{121}	4.5
$\boldsymbol{C_{123}}$	4.0	$\boldsymbol{C_{131}}$	5.0	$\boldsymbol{C_{132}}$	4.5
$\boldsymbol{C_{2ji}}$, **j,i=1,2,3**	0.0	$\boldsymbol{b_j}$, **j=1,2,3**	0.0	$\boldsymbol{S_{cj}}$, **j=1,2,3**	0.0
$\boldsymbol{\alpha_3}$	1.0	$\boldsymbol{L_3}$	4.0	$\boldsymbol{\varepsilon_h}$	0.001

***** 1, 2, and 3 represent water, oil, and gas phases, respectively

Table 6-8: Cumulative injected and produced fluids at 360 days (Case S2)

	WCUMI (KSTB)	GCUMI (MMscf)	WCUMP (KSTB)	OCUMP (STB)	GCUMP (MMscf)
Case 2A	2940.5	26392.0	2821.1	85676	26511.7
Case 2B	140.7	662.0	443.3	50463	384.8

* XCUMI: cumulative injection; XCUMP: cumulative production; W: Water; O: Oil; G: Gas

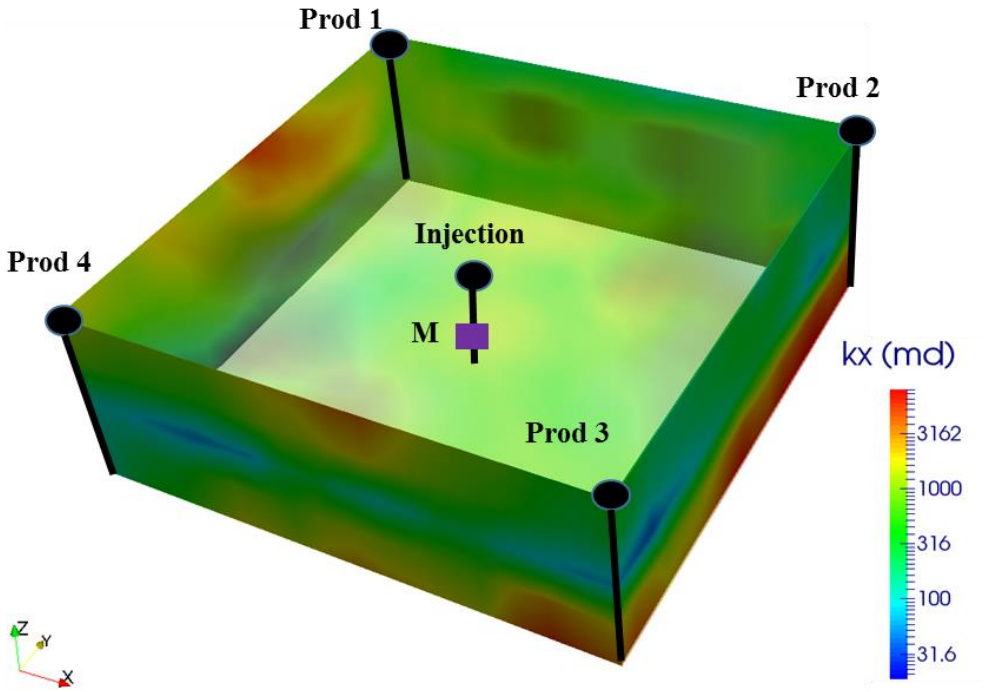

Figure 6-2: Permeability distribution (in x-direction: k_x) and location of wells (Case S2). Grid-block M highlighted in purple is tracked for its saturaiton and relative permeaiblity profiles

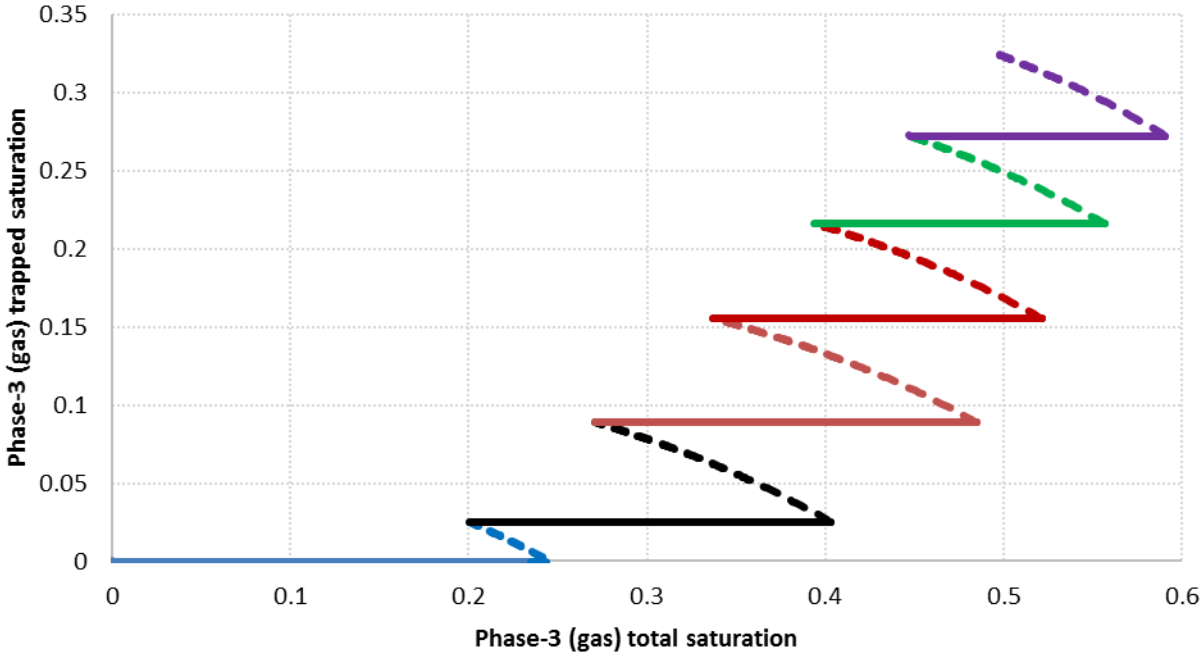

Figure 6-3: Phase-3 (gas) trapped saturation profile for grid block M (see **Figure 6-2**) for Case S2B. 1st cycle: blue; 2nd cycle: black; 3rd cycle: orange; 4th cycle: red; 5th cycle: green; 6th cycle: purple. Gas injection half-cycle (solid line) and water injection half-cycle (square dot)

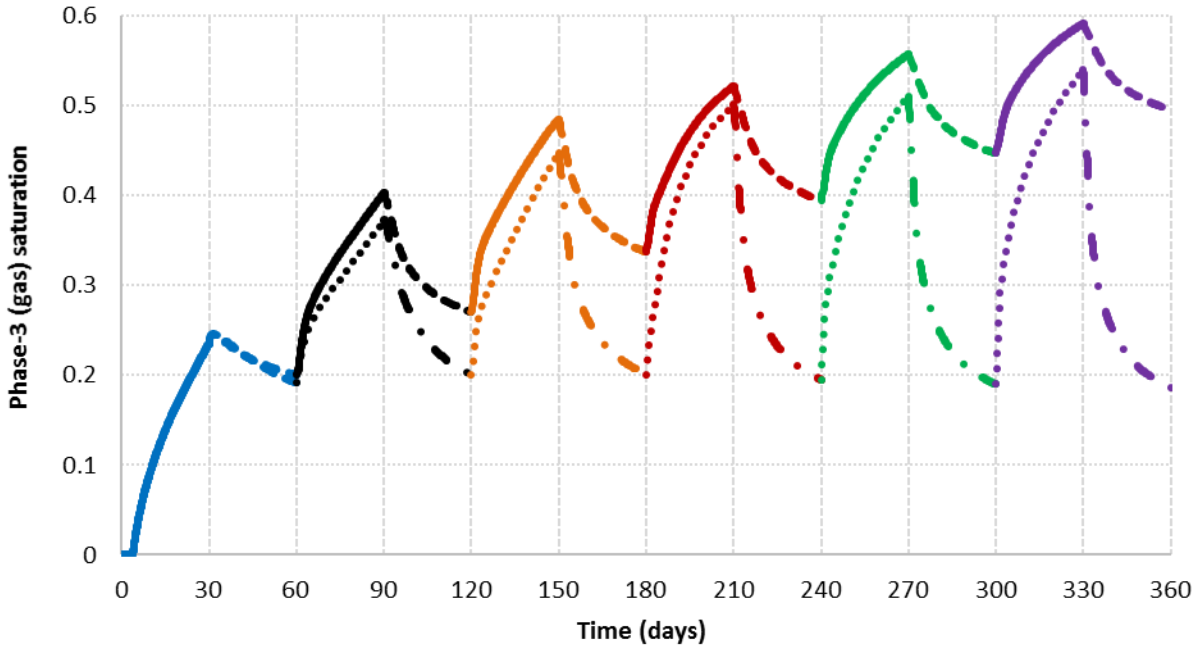

Figure 6-4: Phase-3 (gas) saturation profile for grid block M (see **Figure 6-2**) for Cases S2A and S2B. 1st cycle: blue; 2nd cycle: black; 3rd cycle: orange; 4th cycle: red; 5th cycle: green; 6th cycle: purple. Gas injection half-cycle: without hysteresis (round dot) and with hysteresis (solid line); water injection half-cycle without hysteresis (dash dot) and with hysteresis (square dot)

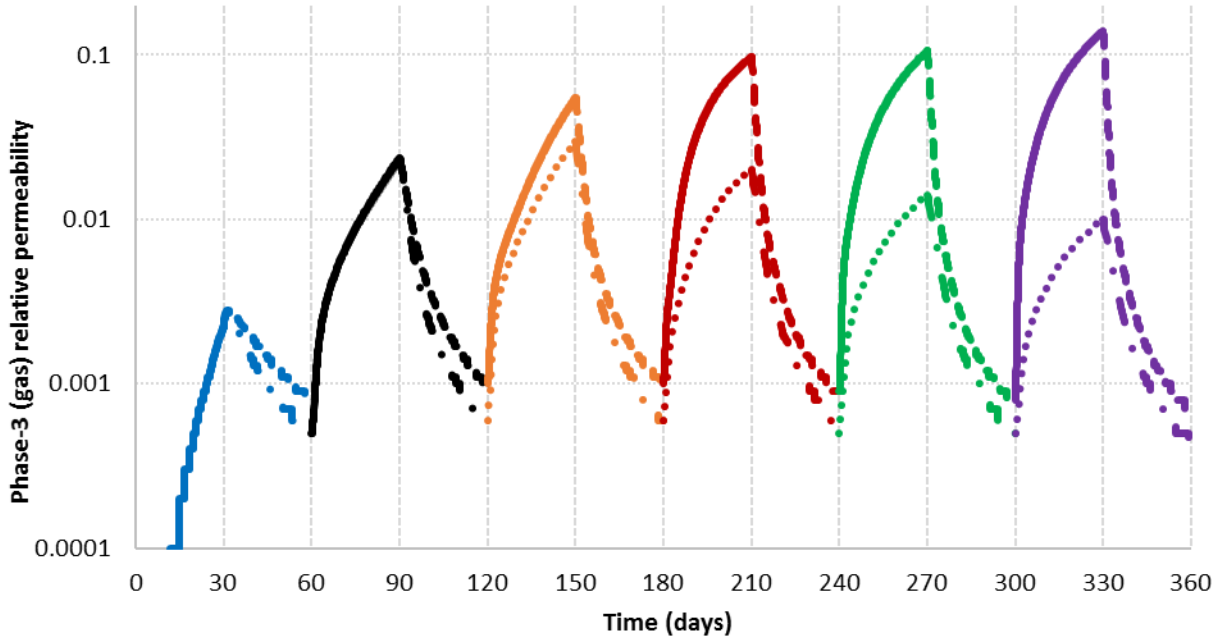

Figure 6-5: Phase-3 (gas) relative permeability profile for grid block M (see **Figure 6-2**) for Cases S2A and S2B. 1st cycle: blue; 2nd cycle: black; 3rd cycle: orange; 4th cycle: red; 5th cycle: green; 6th cycle: purple. Gas injection half-cycle: without hysteresis (round dot) and with hysteresis (solid line); water injection half-cycle without hysteresis (dash dot) and with hysteresis (square dot)

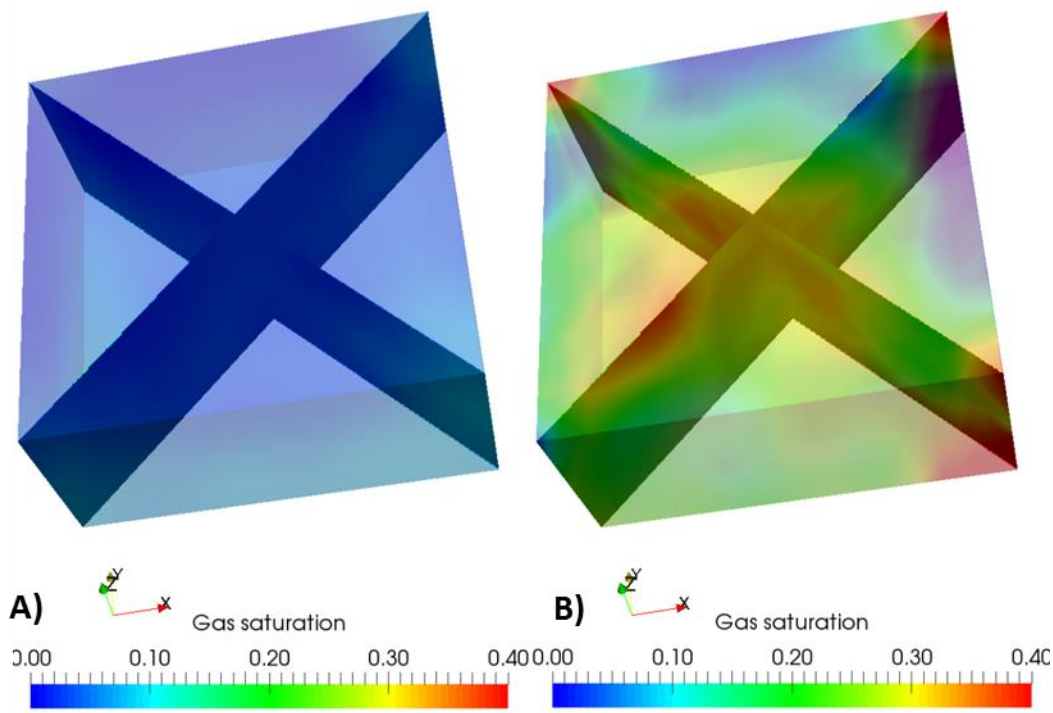

Figure 6-6: Spatial gas saturation distribution at the cross sections of injection and production wells at the end of 3rd cycle (180 days) for **A**) Case S2A and **B**) Case S2B. Vertical aspect ratio (VAR)=10.

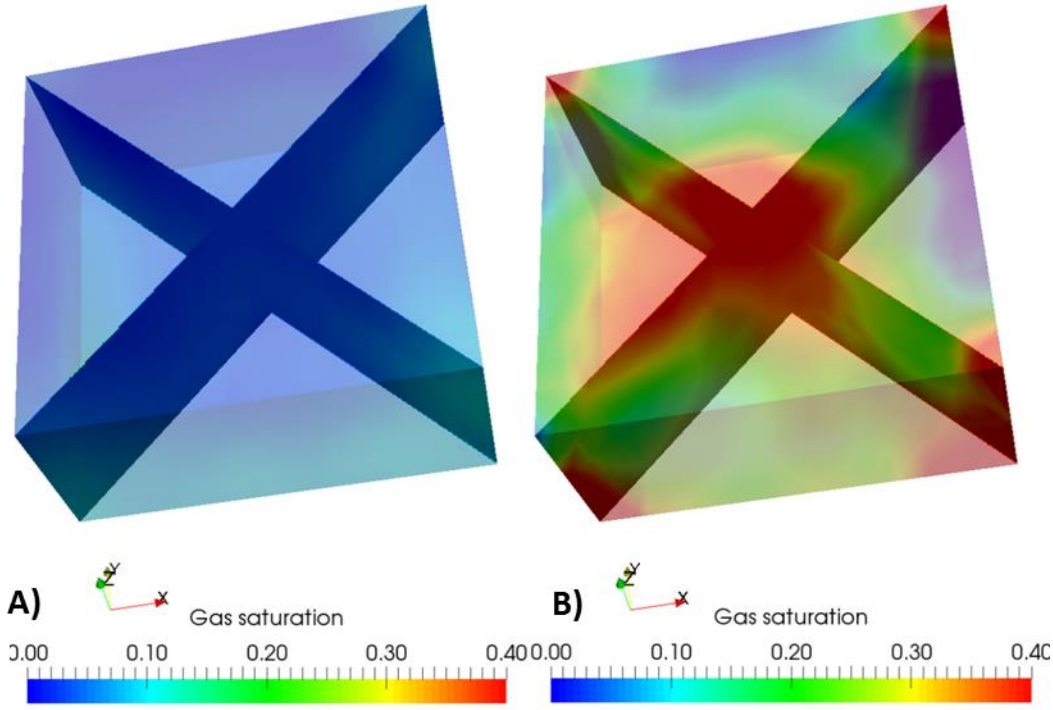

Figure 6-7: Spatial gs saturation distribution at the cross sections of injection and production wells at the end of 6th cycle (360 days) for **A**) Case S2A and **B**) Case S2B. VAR=10.

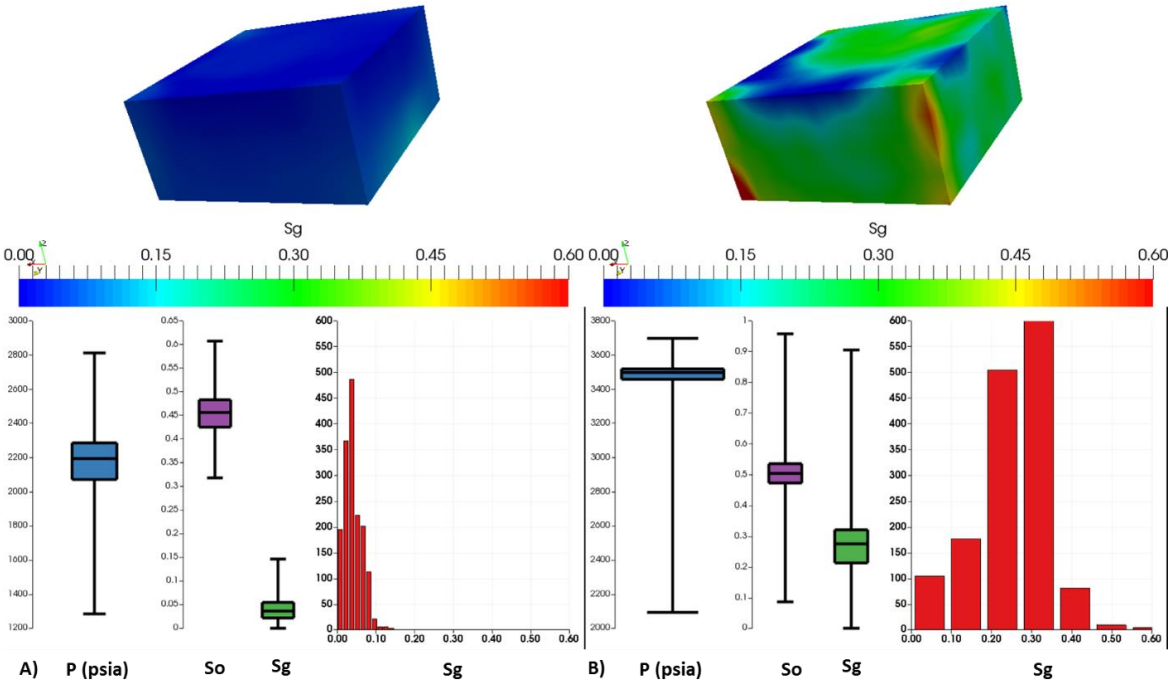

Figure 6-8: Spatial gas saturation (S_g) at the end of 3rd cycle (180 days) (top figures), average pressure (P), oil saturation (S_o) and S_g quartiles, and S_g histogram (bottom figures) for **A**) Case S2A and **B**) Case S2B. VAR=10.

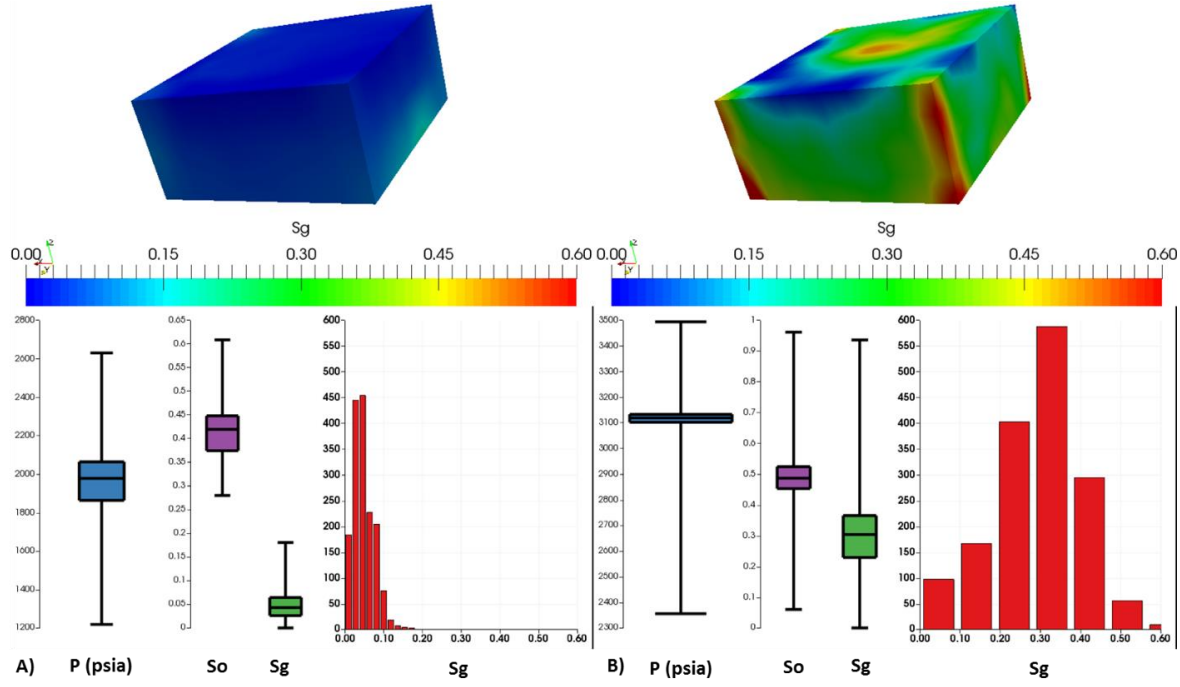

Figure 6-9: Spatial gas saturation (S_g) at the end of 6th cycle (360 days) (top figures), average pressure (P), oil saturation (S_o) and S_g quartiles, and S_g histogram (bottom figures) for **A**) Case S2A and **B**) Case S2B. VAR=10.

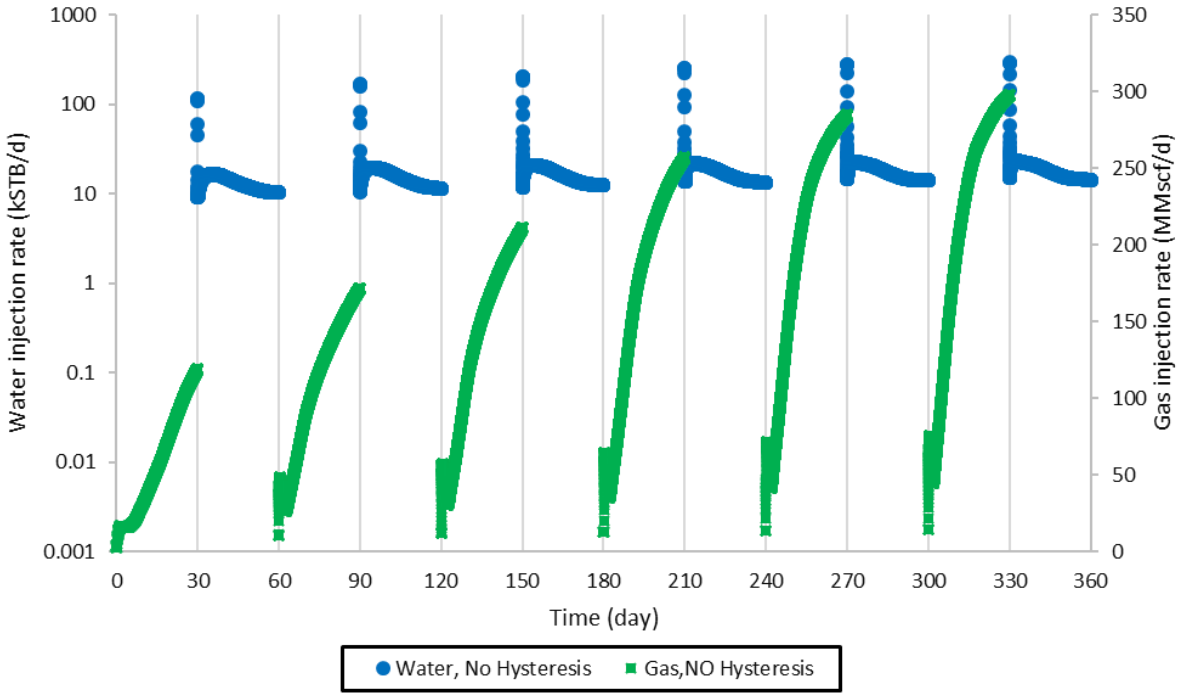

Figure 6-10: Water and gas injection rate in Case S2A

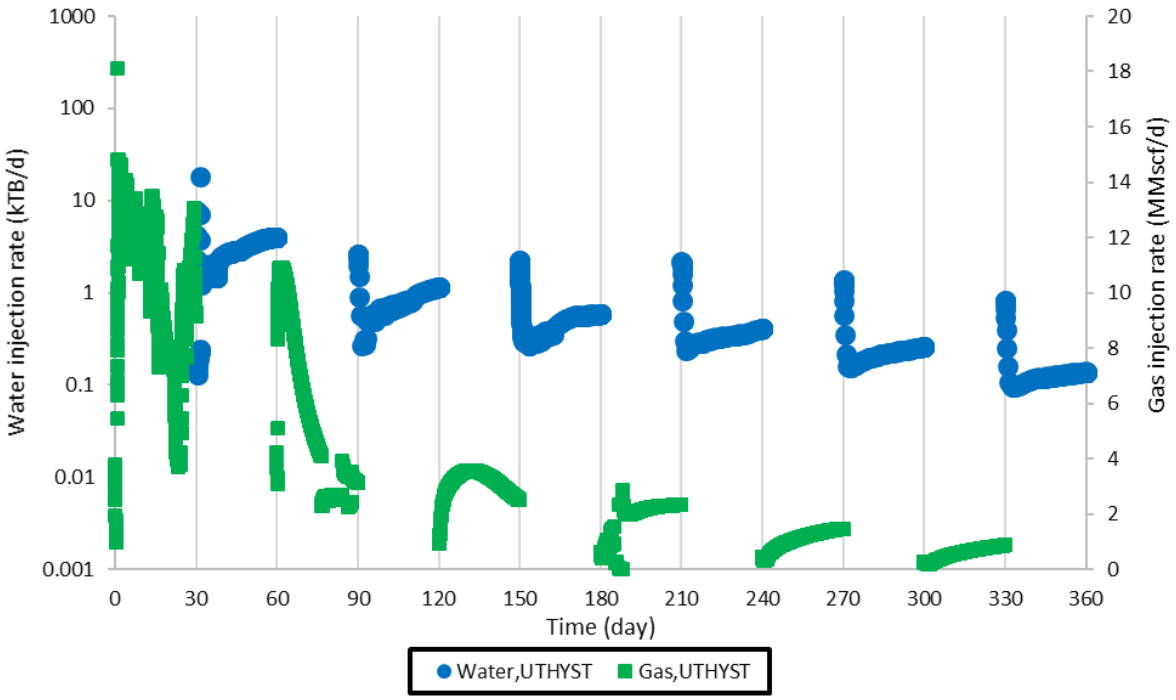

Figure 6-11: Water and gas injection rate in Case S2B

6.3 CCUS (CASE S3)

In this case, we probe the impact of hysteresis on the performance of a carbon capture, utilization and storage (CCUS) (i.e., a coupled CO_2-EOR and sequestration process) case study. We aim to examine the integrated UTKR3P and UTHYST models as implemented into the UT-DOECO2 simulator. A capillary dominated fluid displacement ($N_t = 10^{-8}$) in an isothermal process is modeled. Although CO_2 dissolution into aqueous phase play a key role on the performance of CO_2-EOR and sequestration application, in this study, we did not include CO_2 solubility in aqueous phase. Furthermore, neither the impact of geochemical reactions nor the geomechanical effects were modeled. **Table 6-9** lists the reservoir properties and original fluid composition. **Table 6-10** provides a set of relative permeability data for an intermediate-wet rock together with hysteresis parameters. One quarter of a five-spot well pattern is simulated including an injector and a producer wells located at the opposite sites of the reservoir. **Figure 6-12** illustrates permeability (k_x and k_y) distribution and location of the wells. Both injection and production wells are constant total molar injection constrained and penetrate all layers in z-direction (r_w=0.5 ft; skin factor=0.0). A tapered WAG injection scheme is applied with variable WAG ratio to enhance the overall performance of process. In the tapered fashion, the water half-cycle volume increases by cycle number (i.e., wetting the WAG) (**Jarrell et al., 2002**). **Table 6-11** describes the implemented WAG strategy. Cumulative fluid injection volume during 480 days is 1.3 PV. We ran three simulation cases: one without hysteresis (Case S3A) and two cases including hysteresis by applying the UTHYST models. The latter has two saturation tolerance value (see **Eq. 4-6**): $\varepsilon_h = 0.001$ (Case S3B) and $\varepsilon_h = 0.003$ (Case S3C). The UTKR3P model for relative permeability calculation is applied together with UTHYST model.

Figure 6-13 demonstrates the variation of gas saturation for Cases S3A and B. Here, we inferred that the capillary trapping (i.e., increased gas retention in the reservoir) due to including

the hysteresis effect increase during the chase water injection. **Figure 6-14** compares the spatial saturation distribution for the defined cases at the end of the first waterflood (i.e., total injected fluid is 0.33 PV) and during the chase water injection (i.e., total injected fluid is 1.25 PV). We note that gas has a propensity to be located in the higher permeability regions and that the capillary trapping (Case S3B) is higher in higher permeability area of this heterogeneous reservoir. Moreover, **Figure 6-14** shows qualitatively that waterflood particularly the chase water injection yields a higher spatial gas saturation distribution (**Figure 6-14A** with **C and Figure 6-14B** with **D**). In addition, the degree of gas retention in reservoir significantly increases as the hysteresis option is included (compare **Figure 6-14A** with **B** and **Figure 6-14C** with **D**). **Figure 6-16** compares oil recovery for three cases where the total injected gas and water is identical for three cases (see **Figure 6-15**). Including the hysteresis effect (Case S3B and S3C) resulted in a higher oil recovery than no hysteresis case (Case S3A). We conclude that for this case study the control of gas mobility has a noticeable impact on oil recovery. As the three-phase hysteresis option is included, the degree of capillary trapping is considered by which gas relative permeability decreases.

Figure 6-17 compares the degree of gas retention in the reservoir for three cases. It emphasizes that as hysteresis effect is included to the modeling (S3B and S3C), the amount of gas retention increased by 393% compared to no hysteresis case (S3A) at the end of chase water injection period. In addition, by increasing the saturation tolerance parameter, the degree of gas hysteresis decreases and is represented by a lower gas retention for Case S3C than Case S3B. We then evaluate the CO_2 inventory over the injection period (i.e., 480 days). Here, the dimensionless inventory parameter is defined as the ratio between the amount of gas retention to cumulative injected gas at a specified time (i.e., ton/ton). **Figure 6-18** reveals that including hysteresis effect increases gas inventory capacity in reservoir compared to non-hysteresis case. Next, we evaluated

the CO_2 utilization factor as defined by the volume ratio of oil production per injected CO_2 (STB/ton). **Figure 6-19** highlights the increased amount of calculated CO_2 utilization factor when hysteresis is effective. Again, the amount of calculated values for carbon utilization factor decreases as the saturation tolerance parameter increases in par with earlier results (see **Figure 6-17**). Note that the increased trapped gas saturation for a rate-controlled well yields pressurizing the reservoir. The average reservoir pressure for the hysteresis cases is significantly higher than the no-hysteresis case (e.g., 7160 psi and 5840 psi in Cases S3B and S3C, respectively, compared to 1340 psi in Case S3A at the end of injection period as shown in **Figure 6-20**). The results of the critical role of hysteresis and capillary trapping in this case study are in agreement with the simulation studies conducted for CO_2 inventory in saline aquifers and the stranded oil reservoirs (**Ghomian, 2008**; **Kumar et al., 2004**).

Table 6-9: Reservoir properties (Case S3)

Variable	Values	Variable	Values
Reservoir dimensions (*ft*)	700×700×30	Water compressibility factor (*1/psi*)	3.3×10^{-6}
Grid-block size (*ft*×*ft*×*ft*)	20×20×10	Initial water/oil/gas saturation	0.45/0.55/0.0
Average horizontal permeability (md)	1100	Rock compressibility (*1/psi*)	5×10^{-6}
Reference depth (ft)	7500	Initial reservoir pressure (*psia*)	1500
Porosity	0.25	Reservoir temperature (°*F*)	220
Dykstra-Parsons coefficient (for permeability in x- and y-directions)	0.75	Initial water molar density (*lb-mol/scf*)	3.480
Correlation length in x-, y-, and z-directions (*ft*)	700/700/10	Initial oil molar density (*lb-mol/scf*)	0.263
Ratio of permeability in x-direction to z-direction	10.0	Initial oil viscosity (cP)	21.62

Initial oil composition					
CO_2	**C_1**	**C_2-C_3**	**C_4-C_6**	**C_7-C_{15}**	**C_{16}^+**
0.0	0.05	0.10	0.10	0.15	0.60

Table 6-10: Relative permeability data and hysteresis parameters (Case S3)

$S_{1r2} = S_{1r3}$	0.10	$S_{2r1} = S_{2r3}$	0.1	$S_{3r1} = S_{3r2}$	0.25
$k^0_{r12} = k^0_{r13}$	0.4	$k^0_{r21} = k^0_{r23}$	0.6	$k^0_{r31} = k^0_{r32}$	1.0
$C_{112} = C_{112}$	3.0	$C_{121} = C_{123}$	4.0	$C_{131} = C_{132}$	5.0
C_{2ji}, j,i=1,2,3	0.0	b_j, j=1,2,3	0.0	S_{cj}, j=1,2,3	0.0
α_3	1.0	L_3	3.0	ε_h	0.001

* 1, 2, and 3 represent water, oil, and gas phases, respectively

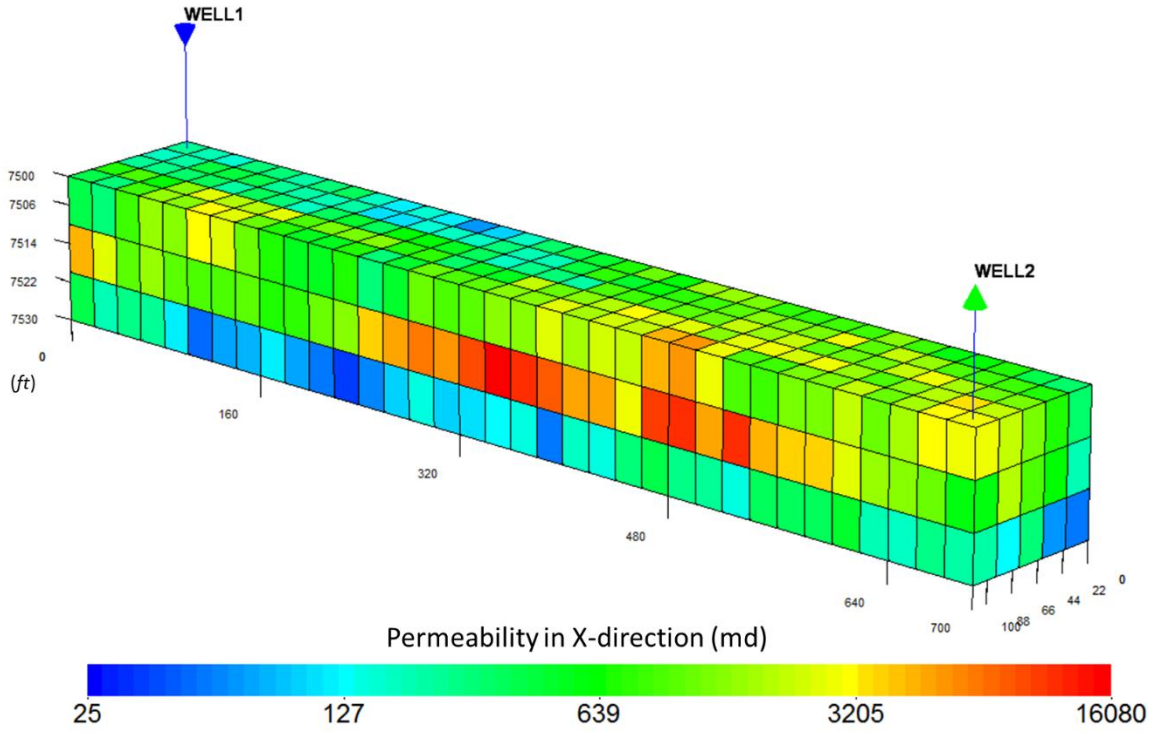

Figure 6-12: Permeability distribution and location of wells (injection well: WELL1, and production well: WELL2) (Case S3)

Table 6-11: Tapered WAG injection scheme (Case S3)

	Continuous CO_2 Injection	Cycle 1	Cycle 2	Cycle 3	Cycle 4	Chase water
Total slug size (PV)	0.3	0.3	0.2	0.1	0.1	0.3
WAG ratio	0.0	0.1	0.5	1.0	1.5	Inf.
CO_2 slug size (PV)	0.30	0.27	0.13	0.05	0.04	0.00
Water slug size (PV)	0.00	0.03	0.07	0.05	0.06	0.30
CO_2 slug duration (days)	60.0	30.0	30.0	30.0	30.0	0.0
Water slug duration (days)	0.0	30.0	30.0	30.0	30.0	90.0

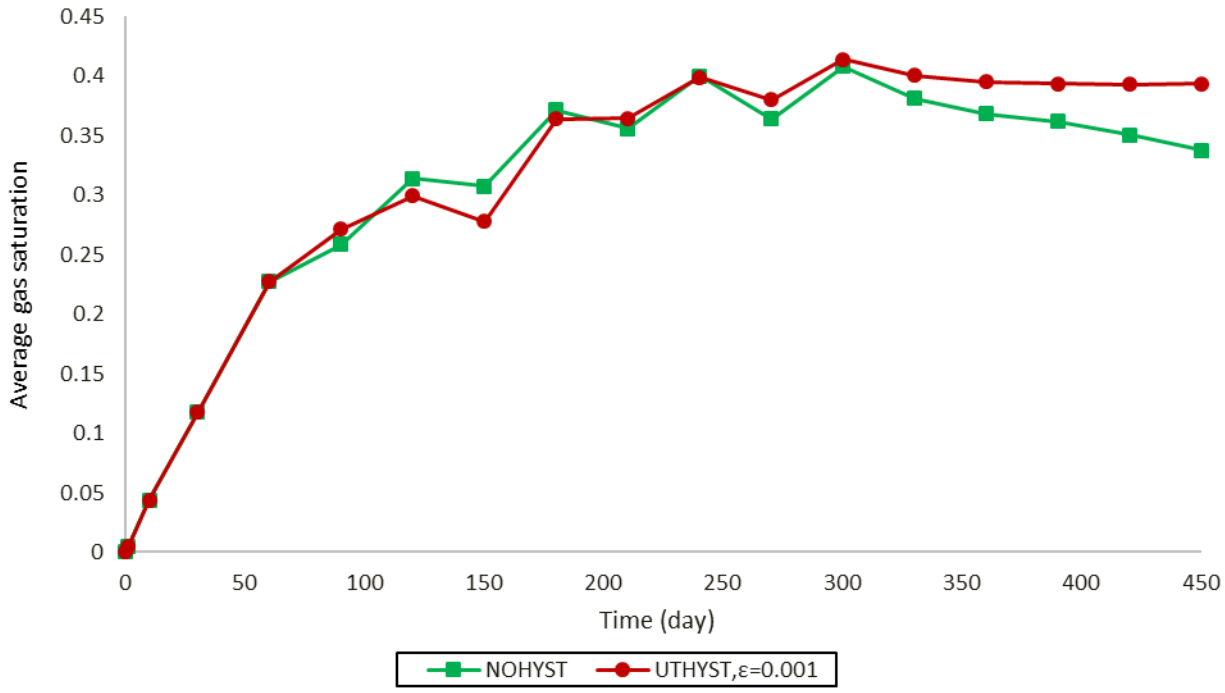

Figure 6-13: Variation of average gas saturation in Case S3A and S3B

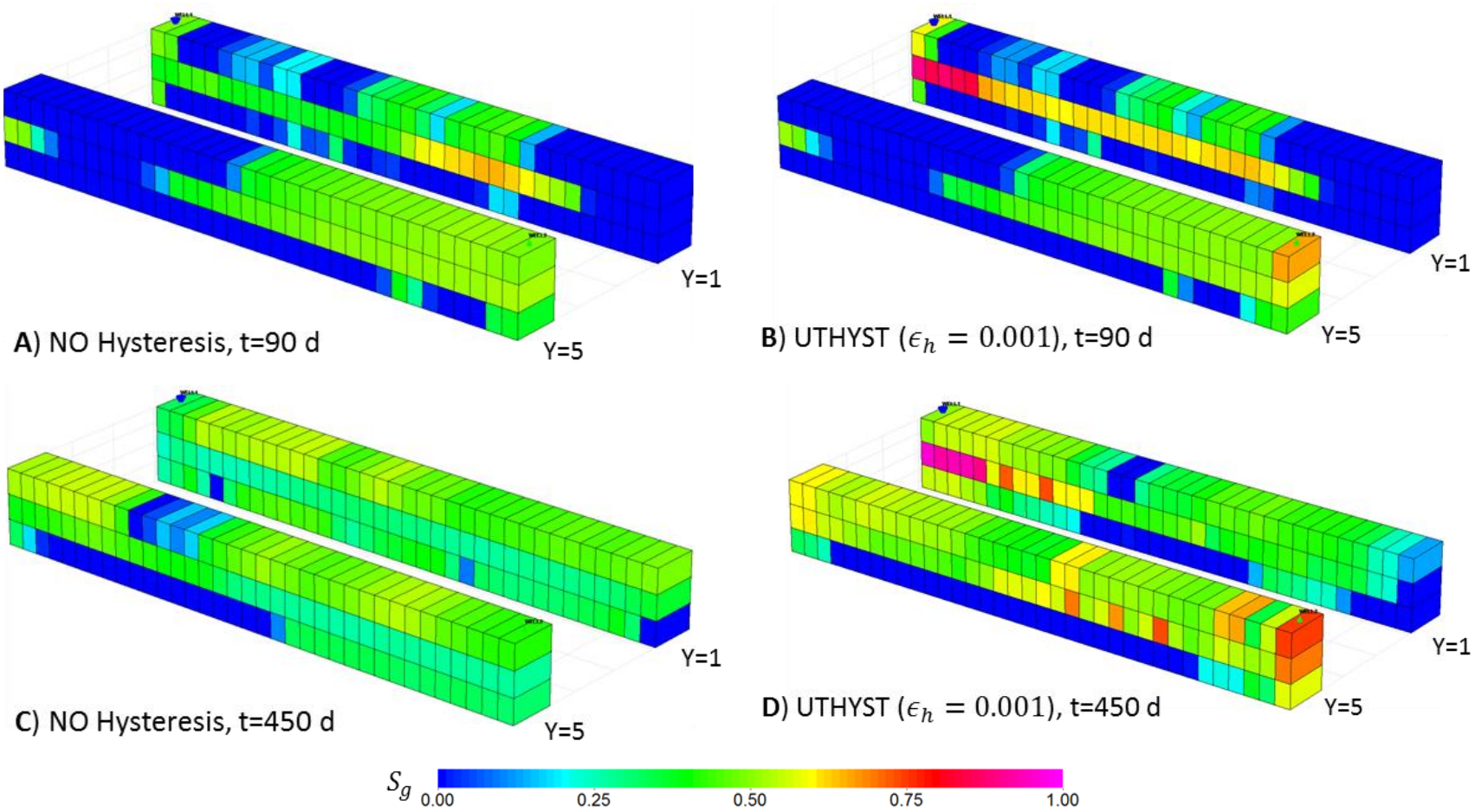

Figure 6-14: Spatial gas saturation distribution for grid blocks located at Y=1 and Y=5 for **A**) Case S3A, t=90 days, **B**) Case S3B, t=90 days, **C**) Case S3A, t=450 days, **D**) Case S3B, t=450 days. Aspect ratio in Y- and Z- directions are 3.

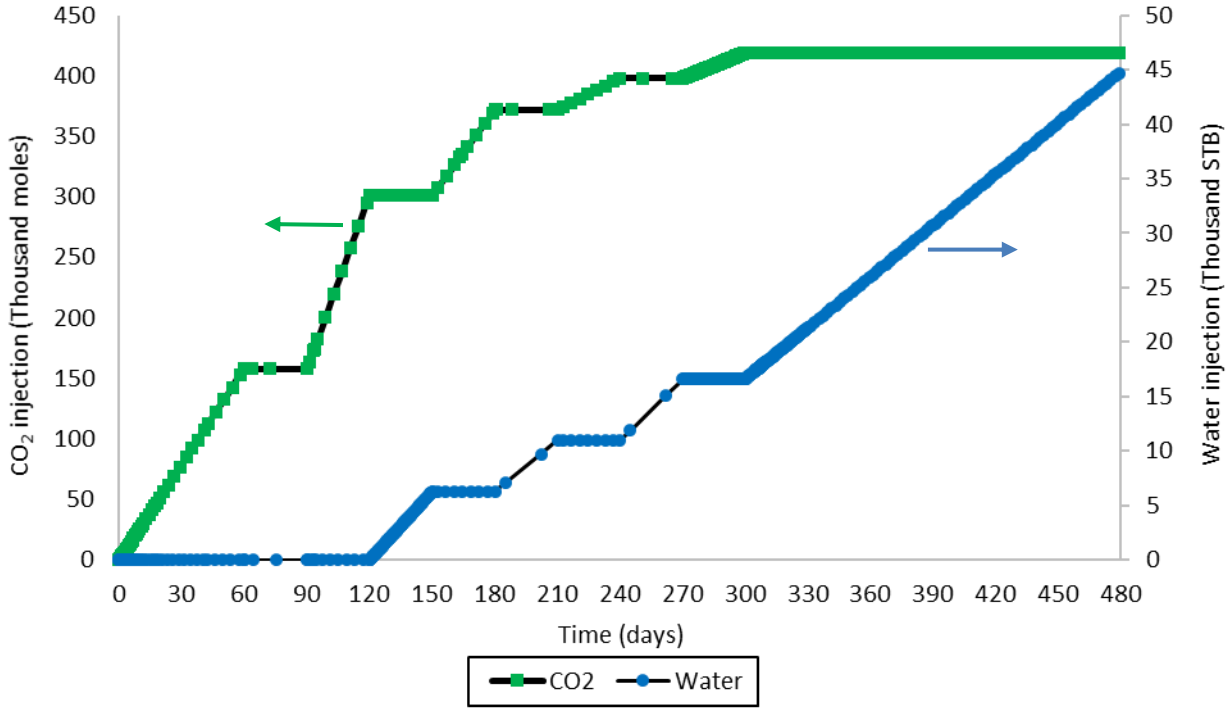

Figure 6-15: Cumulative CO_2 and water injection in Cases S3 (Case S3A, S3B, and S3C)

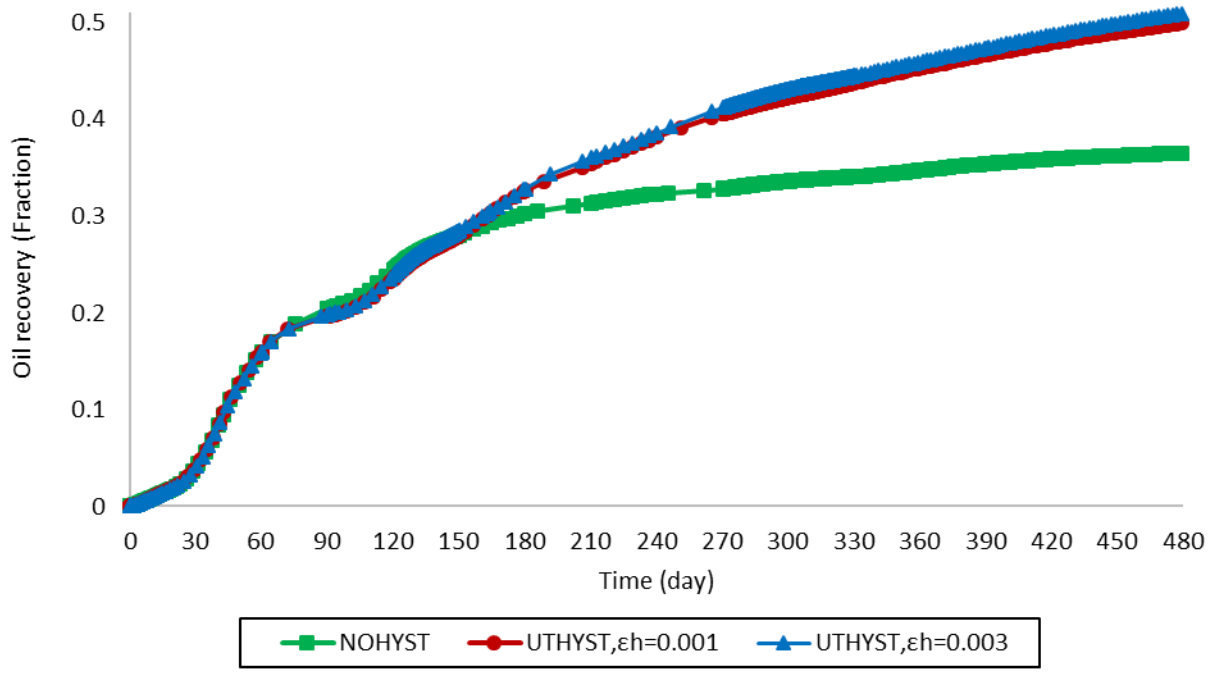

Figure 6-16: Oil recovry facor (Case S3)

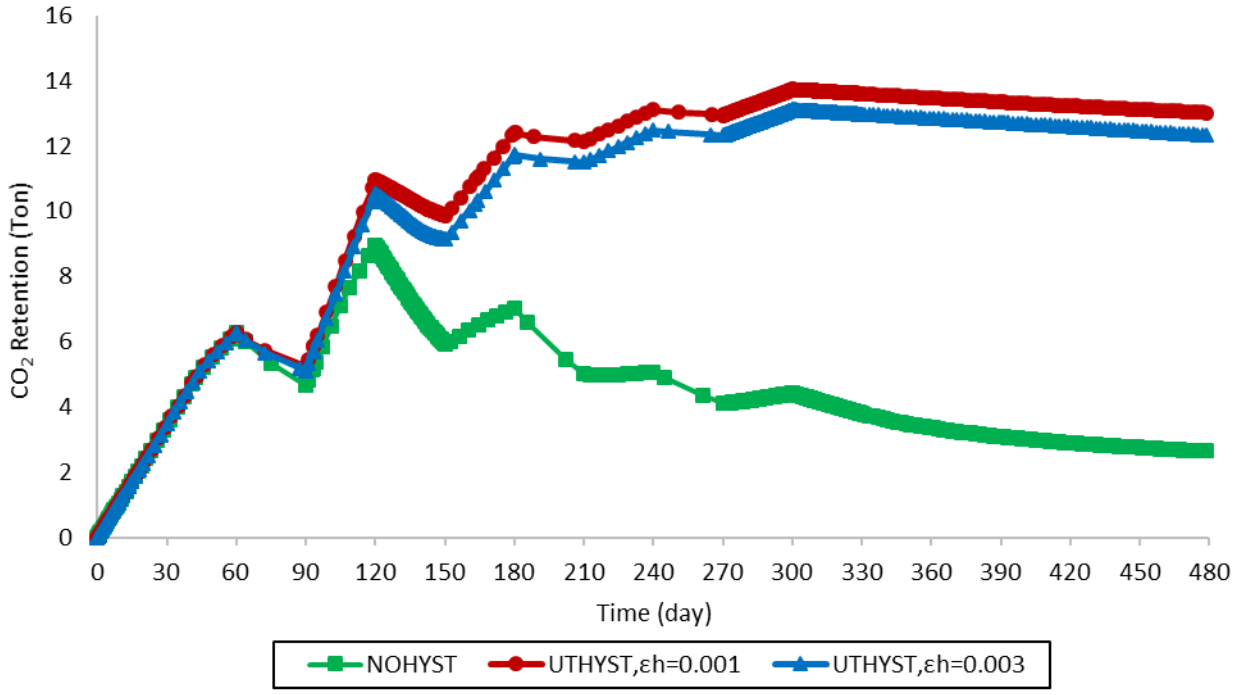

Figure 6-17: CO_2 retention in Case S3

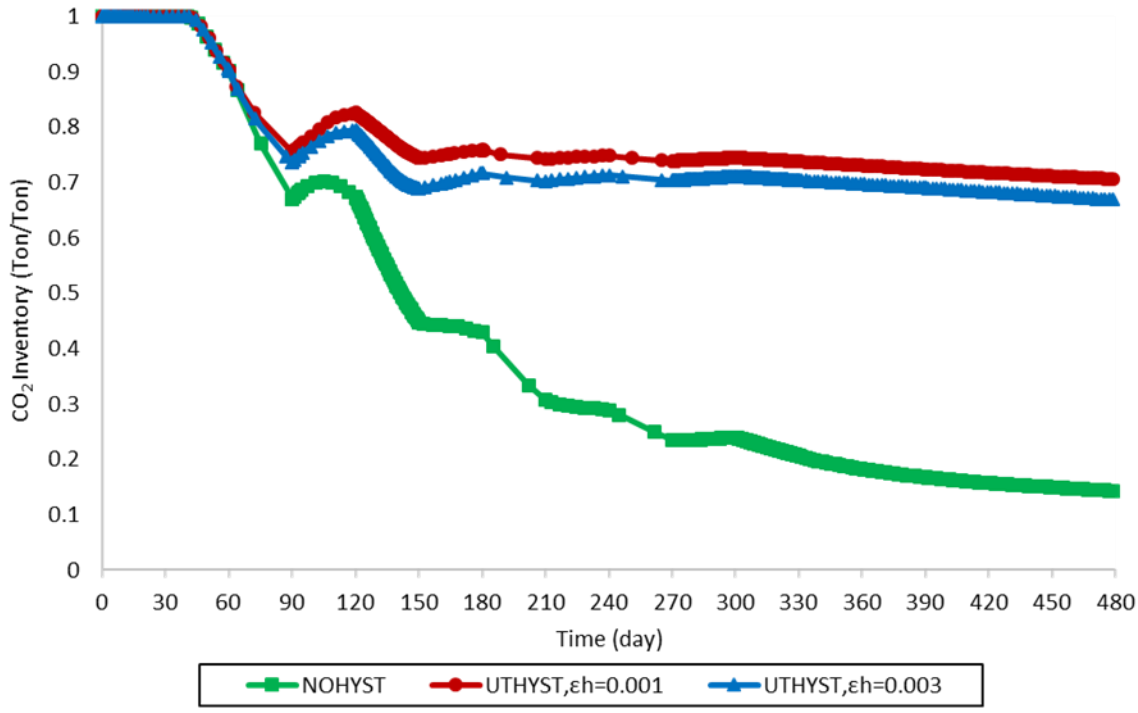

Figure 6-18: CO_2 inventory in Case S3

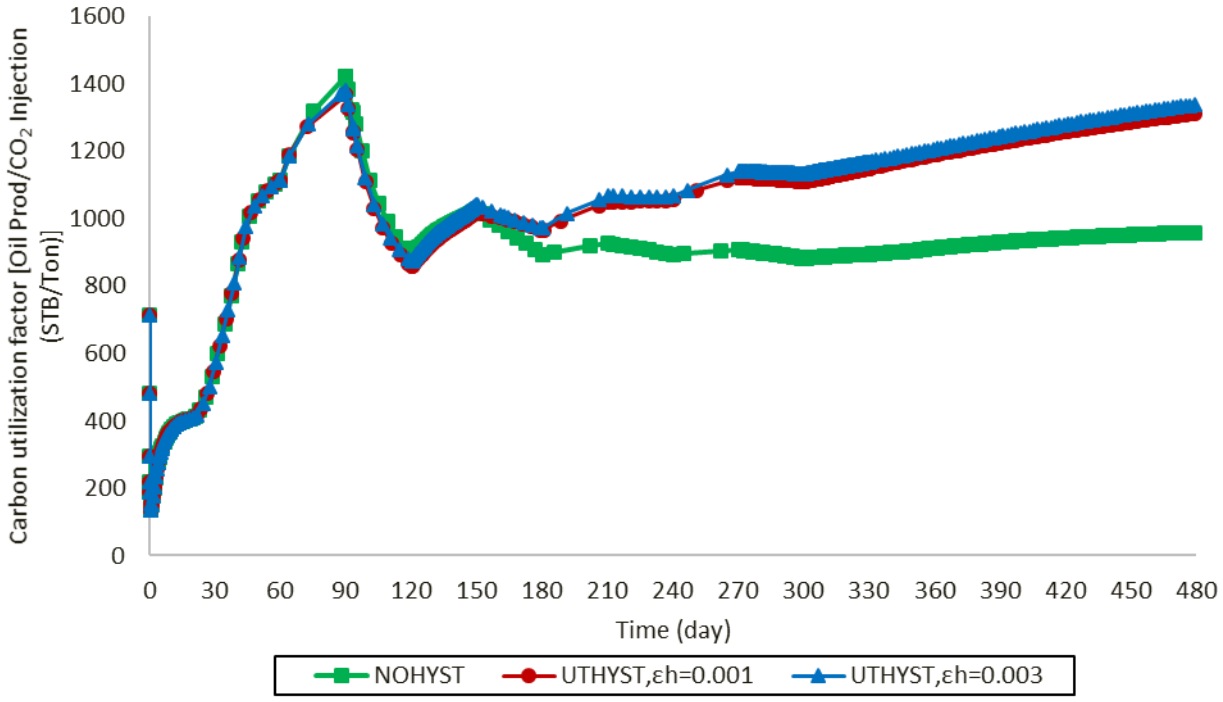

Figure 6-19: CO_2 utilization in Case S3

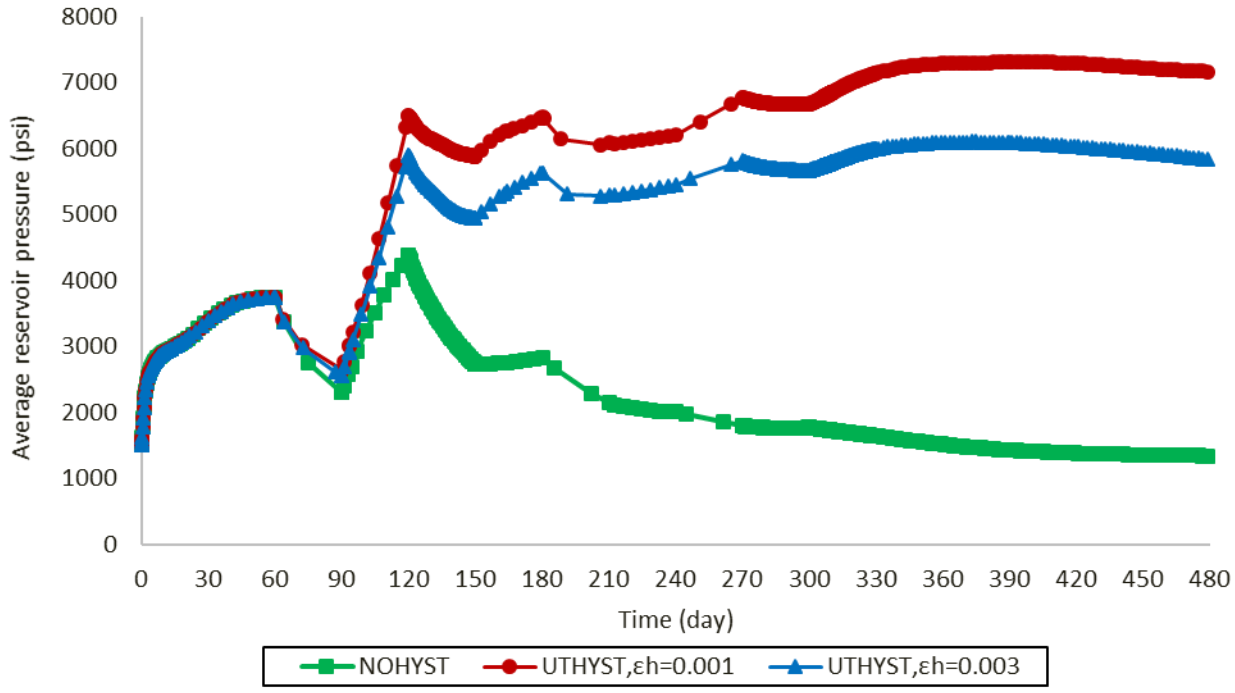

Figure 6-20: Average reservoir pressure in Case S3

6.4 LOW-TENSION GAS FLOOD MODELING (CASE S4)

In this section, we investigate the effect of hysteresis on capillary trapping and performance of the low-tension gas flood as conducted in a synthetic, low permeability, mature water flooded oil reservoir. Here, low saturations are key characteristic of fluid displacement. Two mechanisms for producing the large resource of stranded oil (i.e., no initial mobile oil saturation) are lowering capillary trapping to mobilize oil and increasing sweep efficiency. To model the low-tension gas flood process, we enhanced the UT-DOECO2 simulator based on the framework discussed in **Appendix L**. We conceptually validate the framework using a synthetic reservoir with experimental results for model parameters, e.g. PVT, surfactant parameters, oil composition effect on surfactant phase behavior, foam model parameters, multiphase relative permeability at low and high trapping numbers, and hysteresis. Note that we exclude three-phase liquids (oil/water/microemulsion) in our modeling. Neglecting the separate microemulsion phase impacts foam generation and flow. In addition, it induces the possibility of water fingering through the oil that will not be modeled in this study.

The reservoir is $300\times10\times100$ ft discretized in 300 grid cells ($30\times 1\times 10$) and is homogenous with one high-permeability streak in the fourth top layer replicating the low-perm, intermediate-wet sample of Oak (**1991**). One-quarter of a five-spot well pattern is modeled: two wells, an injector and a producer, which are located at the opposite corners of the reservoir model (see **Figure 6-21**). The injection well is rate controlled with switching option to bottom-hole pressure control of 3000 psi. The production well is pressure constrained with producing a bottom-hole pressure of 1500 psia. Four-component oil composition is modeled with Peng-Robinson Equation-of-State. **Table 6-12** and **Table 6-13** describe a summary of the reservoir and fluid properties. **Table 6-14** addresses the UT-foam model parameters, surfactant properties, and oil composition effect based on two sets of experimental results versus EACN.

Simulation cases start with a low-tension surfactant slug of 1% (volume fraction) to reduce water-oil interfacial tension and mobilize the residual oil followed by four different injection schemes with or without hysteresis option as summarized in **Table 6-15**. Note that for the foam cases, we apply two surfactants (i.e., one to reduce oil-water IFT (low-tension surfactant or LT) and one to stabilize foam (SF). Fluid injection schemes include chase water (Case S4A), water-alternate-gas (WAG) (Case S4B), foam surfactant-alternate-gas injection (SAG) (Case S4C), and in-situ foam generation with aqueous surfactant-gas co-injection (CoInj) (Case S4D). The injection salinity is 0.13 meq/mL. The WAG ratio is 1:1 and half-cycle size is 60 day starting with water injection followed by N_2 injection. For Cases S4B-D, the cumulative water and gas injection are close to 36,500 STB and 14.5 MMSCF, respectively (i.e., 5 PV injection after 990 days).

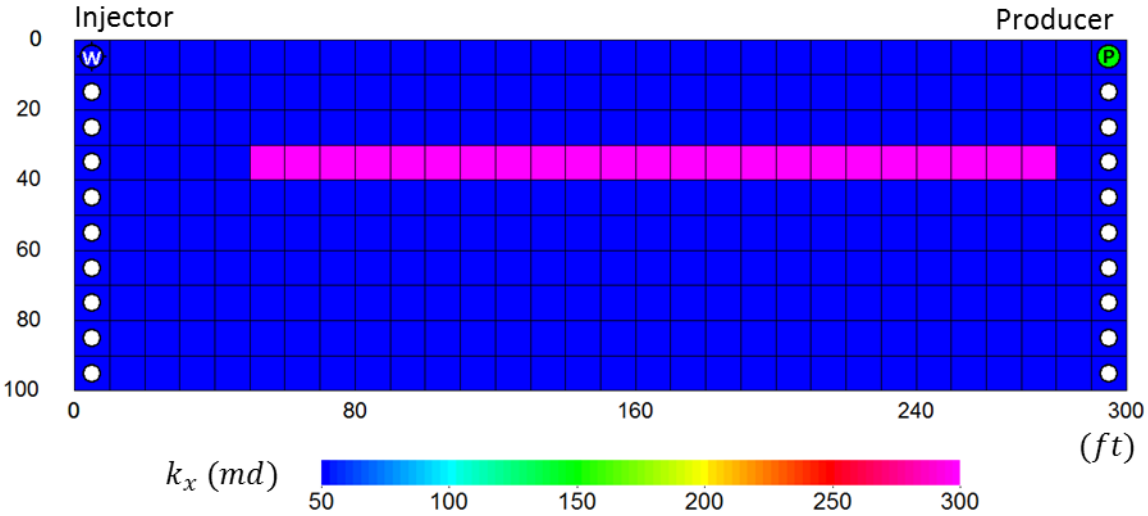

Figure 6-21: Spatial permeability distribution and well location (Case S4)

Figure 6-22 compares oil recovery for the simulation cases. In highlights that the foam mobility control methods (Cases S4C and S4D) yield higher oil recovery. When the UTHYST three-phase hysteresis option is on, the incremental oil recovery by SAG (Case S4C) and CoInj (Case S4D) schemes over WAG (Case S4B) strategy are 7.2% and 9.8%, respectively. The

generated foam mitigates the gas override to the high permeable zone/top layers. It results both in an improved vertical gas conformance at the injector well and in areal sweep efficiency. Although co-injection plan is sufficient to increase oil recovery due to the continuous in-situ foam generation, it elevates the injection flowing BHP and brings injectivity and consequently operational issues. While flowing BHP fluctuates due to the alternate fluid injection strategy in WAG and SAG cases (Cases S4B and S4C), it continuously boosts for the co-injection scheme due to the constant in-situ foam generation close to the wellbore.

Figure 6-22 reveals that the impact of hysteresis option is not unique and is process dependent. **Figure 6-23** compares the injection well flowing BHP for water injection and three multicycle processes when the hysteresis option is applied using the UTHYST model ($\alpha_3 = 6.0$). **Figure 6-24** compares spatial oil distribution for three cases at the end of injection period where the high permeable area is highlighted in a red box. It reveals the foaming strategies (S4C and S4D) have the potential to boost the areal sweep efficiency and mobilize oil through the low-tension process compared to WAG injection scheme.

As **Figure 6-25** and **Figure 6-26** imply, a key parameter that yield a higher oil recovery in SAG and CoInj schemes compared to WAG is the increased gas entrapment (compare Cases S4B-3 and S4C-3). These figures emphasize the potential of UTHYST model to effectively model the monotonic increase in gas entrapment. The increased trapped gas saturation is reflected by an increased total gas saturation in reservoir. As the UTHYST parameter (α_3) increases (from 6 to 9), the gas trapping within each cycle decreases and approaches to the predicted values of the Carlson model. **Figure 6-26** and **Figure 6-27** illustrate phase-3 (gas) relative permeability and phase trapping for grid block M within Case S4B-3. They reveal the cycle dependency of gas relative permeability due to capillary trapping effect. Note that here the saturation path dependency incorporated in the UTKR3P model is not modeled, viz., *b* parameter value is set to zero. As a

result, the cycle dependency is only because of the saturation direction effect as added through the UTHYST model. Gas relative permeability substantially decreases as the cycle number increases. Indeed, there is a 40% difference between the calculated relative permeability values at a constant gas saturation (S_3=0.47) from the first to the last cycle.

Table 6-12: Fluid and reservoir properties (Case S4)

Initial pore volume= 53.42 MSTB and porosity=0.2
Horizontal permeability=50 md and k_v/k_h=1.0 (except for high permeable streak)
T=90°F and $P^{initial}$=1500 psia
$S_w^{initial}$ =0.65, $S_o^{initial}$ =0.35, Initial salinity (meq/mL)=0.10
Initial oil composition: N_2=0.0%; C_{10} =30.0%; C_{15}=40.0%; C_{20}=30.0% EACN of oil composition: N_2=0; C_{10} =10; C_{15}=15; C_{20}=20
Formation compressibility =3×10^{-6} 1/psi

* 1, 2, and 3 represent water/microemulsion, oil, and gas phases, respectively

Table 6-13: Relative permeability model parameters (Case S4)

$\boldsymbol{S_{1r2}^L = S_{1r3}^L}$	0.20	$\boldsymbol{S_{3r1}^L = S_{3r2}^L}$	0.35
$\boldsymbol{S_{2r1}^L}$	0.35	$\boldsymbol{S_{2r3}^L}$	0.25
$\boldsymbol{k_{r12}^{0L} = k_{r13}^{0L}}$	0.12	$\boldsymbol{k_{r31}^{0L} = k_{r32}^{0L}}$	0.90
$\boldsymbol{k_{r21}^{0L}}$	0.70	$\boldsymbol{k_{r23}^{0L}}$	0.70
$\boldsymbol{C_{112}^L = C_{112}^L}$	2.00	$\boldsymbol{C_{131}^L = C_{132}^L}$	2.50
$\boldsymbol{C_{121}^L}$	2.16	$\boldsymbol{C_{123}^L}$	2.70
$\boldsymbol{C_{1ji}^H}$, j,i=1,2,3	1.0	$\boldsymbol{C_{2ji}^L = C_{2ji}^H}$, j,i=1,2,3	0.0
$\boldsymbol{S_{jri}^H}$, j,i=1,2,3	0.0	$\boldsymbol{k_{rji}^H}$, j,i=1,2,3	1.0
$\boldsymbol{b_j}$, j=1,2,3	0.0	Gas hysteresis parameter $(\boldsymbol{\alpha_3})$	6.0

* 1, 2, and 3 represent water/microemulsion, oil, and gas phases, respectively

Table 6-14: Surfactant, microemulsion, and foam model parameters (Case S4)

UT-Foam model parameters				
$R_{ref} = 200; S_w^* = 0.3; S_o^* = 0.25; C_s^* = 0.001;\ \varepsilon = 0.01;\ \sigma = 1; u_{g,ref} = 1\ (ft/day)$				
Surfactant parameters				
Surfactant compressibility (at P=14.65 psia) = 0.; CMC=0.001; IFT model parameter (**Huh, 1979**) =0.3				
Compositional aqueous phase viscosity parameter: $\alpha_{v1} = 1.5;\ \alpha_{v2} = 1.3;\ \alpha_{v3} = 3.0;\ \alpha_{v4} = \alpha_{v5} = 1.$				
Oil composition effect on microemulsion phase behavior (Two sets of parameters vs. EACN)				
1st solubility experiment parameters:	2nd solubility experiment parameters:			
# of hydrocarbon components in experiment: 1	# of hydrocarbon components in experiment: 1			
$EACN_1$=10	$EACN_1$=20			
$C_{SEOP,1} = 0.26;\ \sigma_0 = 25;\ \sigma_1 = 40;$ $(C_{SEU} - C_{SEL})_1 = 0.2$	$C_{SEOP,1} = 0.30;\ \sigma_0 = 8;\ \sigma_1 = 18;$ $(C_{SEU} - C_{SEL})_1 = 0.3$			
Hydrocarbon dissolution vs. surfactant concentration				
$C_s(\frac{\mathbf{lb_m\ surfactant}}{\mathbf{lb_m water - hydrocarbon\ solution}})$	**Component partition coefficient**			
	N_2	**C_{10}**	**C_{15}**	**C_{20}**
0.10	0.0	0.0008	0.0008	0.0008
0.20	0.0	0.0020	0.0020	0.0080
0.70	0.0	0.0080	0.0115	0.0115
0.99	0.0	0.0115	0.0115	0.0115

Table 6-15: Summary of simulation cases and oil recovery factor after 5 PV injection (Case S4)

Case	**Injection scheme**		**Gas hysteresis option**	**Oil RF (%)**
	Surfactant slug	**Drive**		
S4A	1% SI	Water	Not applicable	13.62
S4B-1	1% SI	WAG	No	25.85
S4B-2			Carlson Model	27.28
S4B-3			UTHYST Model	28.93
S4C-1	1% SI	0.1% SAG	No	30.29
S4C-2			Carlson Model	30.63
S4C-3			UTHYST Model	36.12
S4D-1	1% SI	0.1% CoInj	No	38.36
S4D-2			Carlson Model	38.55
S4D-3			UTHYST Model	38.69

* SI: Low-tension surfactant, SF: Foaming surfactant; WAG: water alternate gas; SAG: surfactant alternate gas; CoInj: SF-gas co-injection

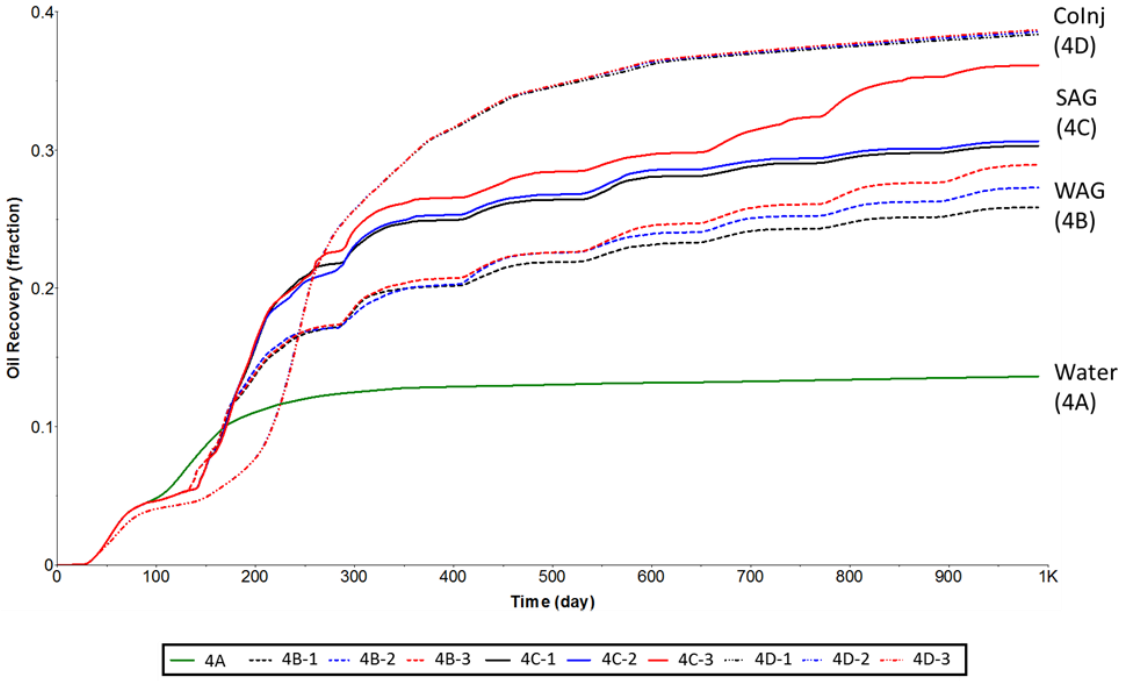

Figure 6-22: Oil recovery for different processes listed in **Table 6-15** (Case S4)

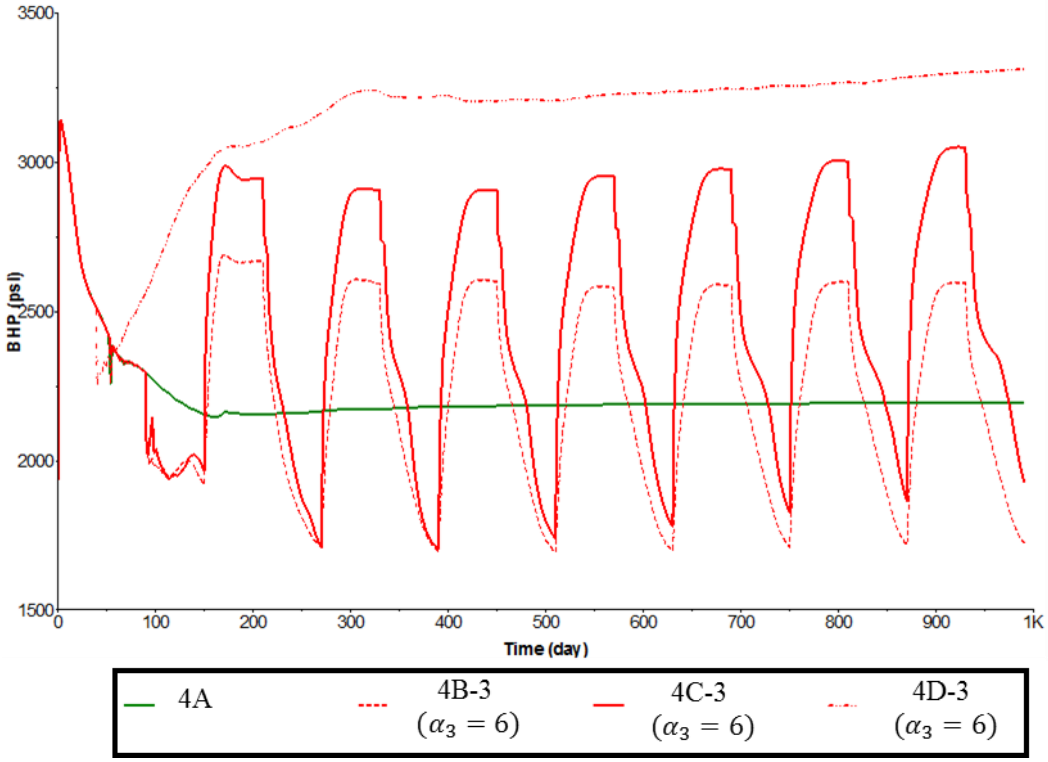

Figure 6-23: Comparison of injection well BHP between multicycle processes and waterflood (Case S4)

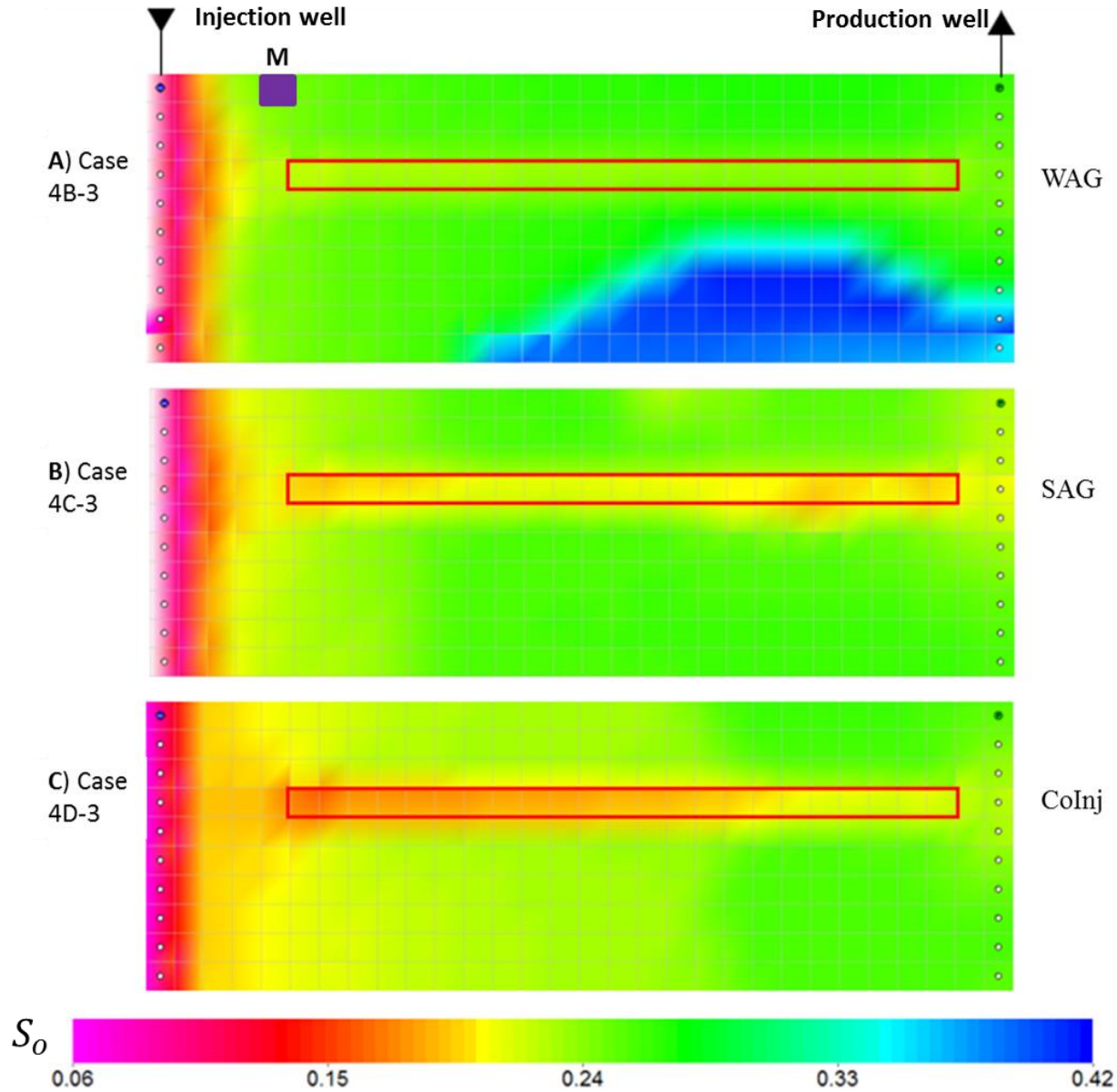

Figure 6-24: Phase-2 (oil) saturation distribution for three cases after 5 PV injection (high permeable streak highlighted in red box). Saturation and relative permeaiblity profiles of grid-block M (5,1,1) highlighted in purple are tracked (Case S4).

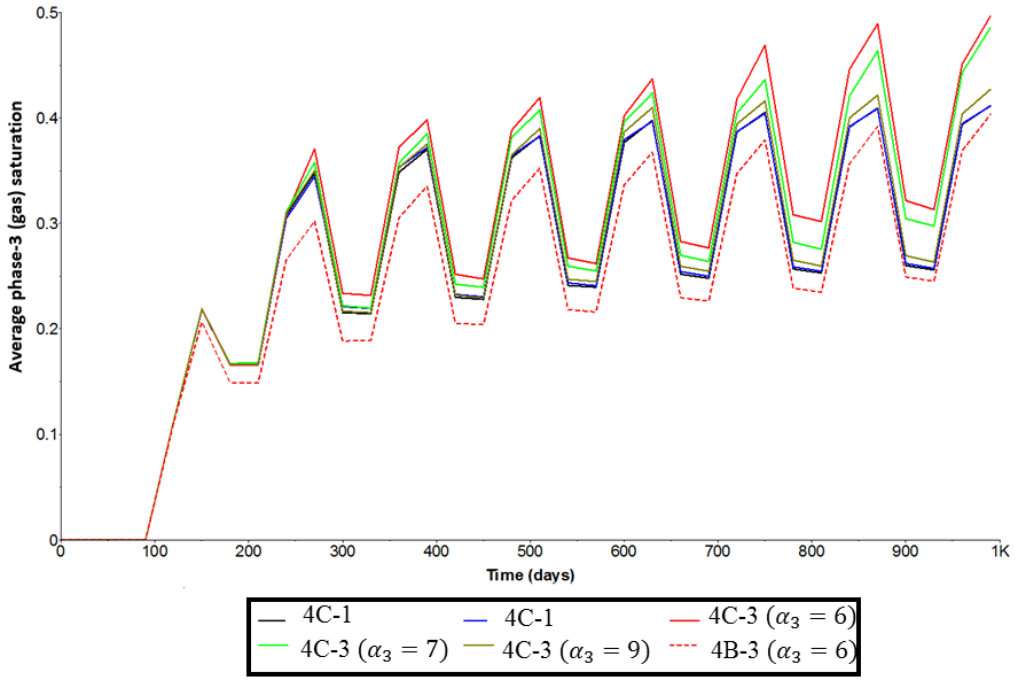

Figure 6-25: Average phase-3 (gas) saturation within WAG and SAG processes including UTHYST model (Case S4B and S4C)

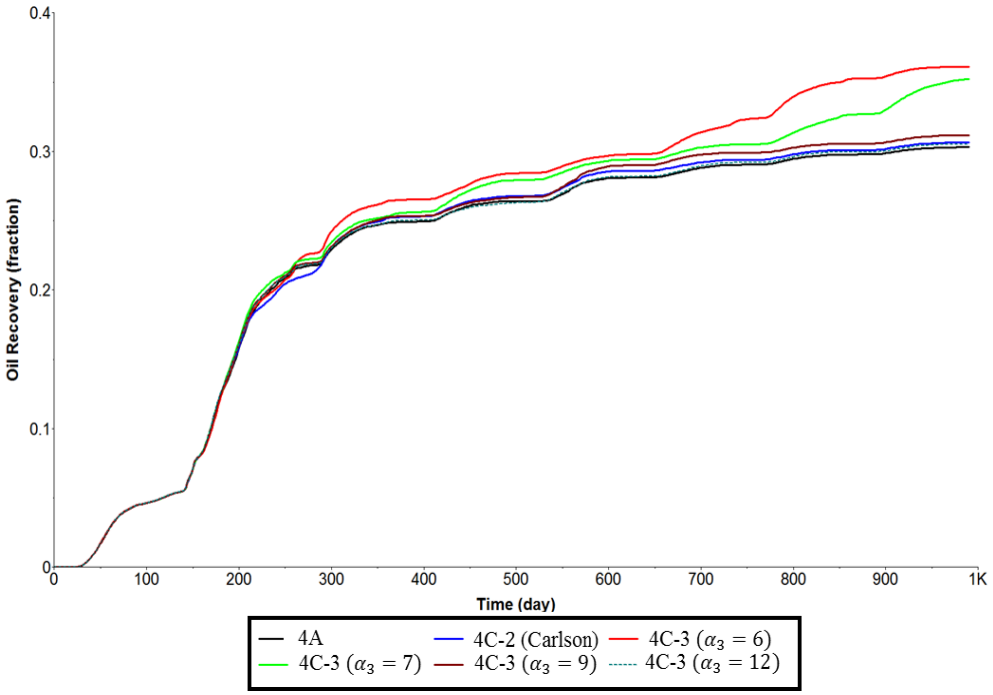

Figure 6-26: Impact of 2-phase (Carlson model) and 3-phase (UTHYST) hysteresis model on oil recovery (Case S4C)

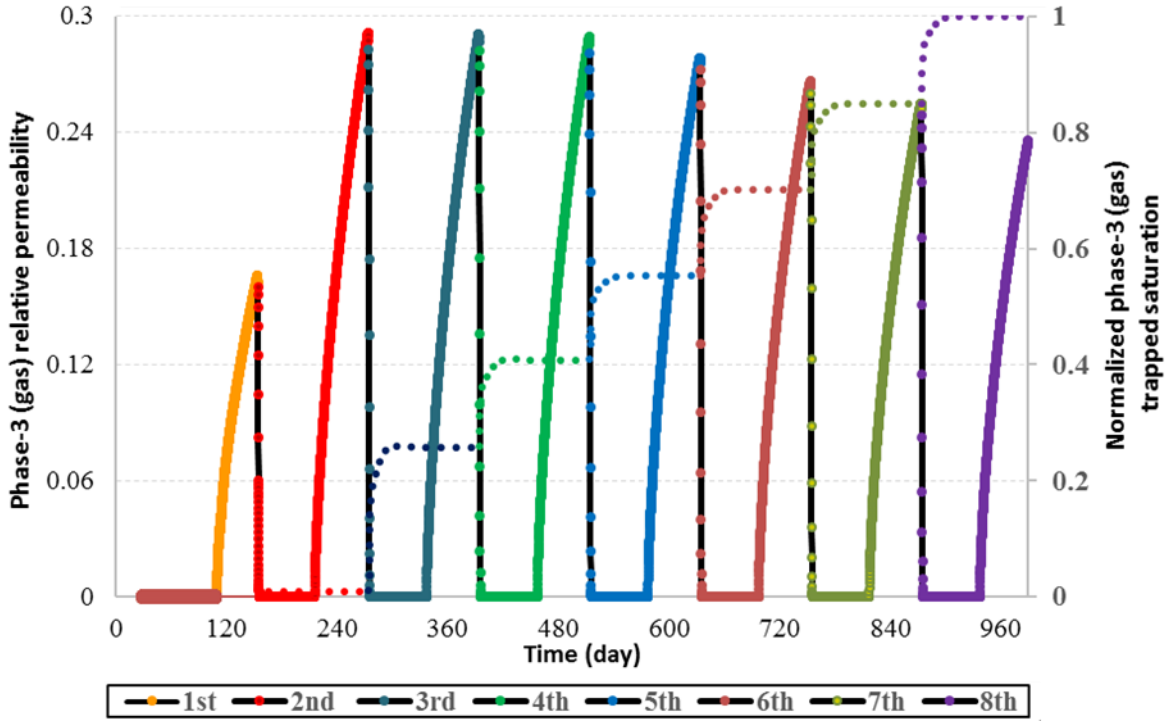

Figure 6-27: Phase-3 (gas) relative permeability (solid line) and normalized trapped saturation (dash line) in Case S4B-3 for grid-block M

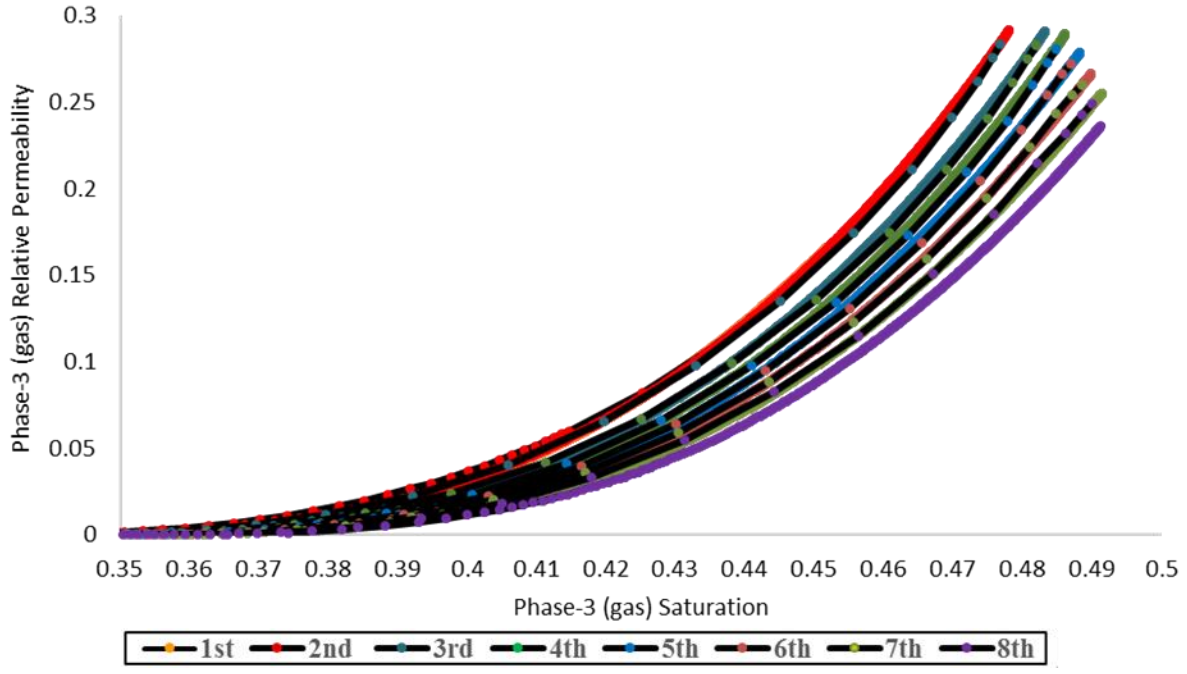

Figure 6-28: Phase-3 (gas) relative permeability in Case S4B-3 for grid-block M

6.5 SUMMARY AND CONCLUSION

In **Case S1**, we used IPARS simulator and highlighted the importance of including a parametrized-level relative permeability model on the decision making of an EOR process. We also addressed the requirement of incorporating a particular set of relative permeability parameters in two-phase flow. We ran a multicycle N_2-WAG injection scheme and applied the UTKR3P model. The example included a sensitivity analysis to study the impact of relative permeability parameters on oil recovery. We showed that incorporating the parameterized relative permeability model provides a ranking tool that can assist in uncertainty quantification and history matching. we also demonstrated that two-phase relative permeability for two different fluid pairs do not have a unique contribution. For example, oil endpoint relative permeability in two-phase oil-water and oil-gas must be included separately in reservoir simulation.

In **Case S2**, we used IPARS simulator and emphasized on the crucial role of hysteresis and capillary trapping in the design of gas storage/EOR processes. We performed a multicycle immiscible WAG injection scheme in the compositional mode and demonstrated that the degree of gas stranded in the reservoir significantly varies with and without including the hysteresis effect. We also showed the severe reduction of well injectivity (i.e., both for water and gas) when the hysteresis effect was included.

In **Case S3**, we used UT-DOECOE simulator and addressed the impact of capillary trapping and hysteresis on a CCUS process (i.e., coupled CO_2-EOR and sequestration). The results of the tapered WAG injection scheme confirmed that hysteresis has a pronounced effect on CO_2 inventory, CO_2 utilization factor, reservoir pressurizing, and oil recovery. It also implies that including the hysteresis effect in reservoir modeling of natural gas storage processes significantly affects the techno-economic performance of the operation.

In **Case S4**, we applied the developed framework in **Appendix L** for modeling low-tension

gas flooding as implemented into UT-DOECO2 simulator. Here, two different surfactants are modeled to (i) mobilize oil by ultra-low interfacial tension and (ii) control gas mobility by generating in-situ foam. We illustrated the incorporation of UTHYST model to generate cycle-dependent relative permeability in multicycle processes such as WAG and SAG. The simulation results showed that gas relative permeability of a designated grid-block could be reduced by as much as 40% from first to the last cycle.

Chapter 7: **Conclusions and Recommendations for Future Research**

7.1 SUMMARY

In this dissertation, we covered three subjects: three-phase relative permeability, three-phase hysteresis, and compositional relative permeability modeling. According to the objectives stated in **Chapter 1**, the main contributions of this study are listed as follows on the order of the presented chapters.

1) Currently, the existing three-phase relative permeability models do not adequately capture the fundamentals of fluid flow behavior (**i**) in intermediate-wet/oil-wet media, (**ii**) in extreme saturation regions, and (**iii**) in saturation-history dependent processes. In addition, the widely used relative permeability correlations (**iv**) are applied to a particular phase(s) and (**v**) do not include the compositional effects explicitly.
2) We investigated the impact of rock geometry and topology, spreading coefficient, and rock wettability on the existence of a stable fluid layer in three-phase flow.
3) We developed and validated a three-phase relative permeability model (i.e., UTKR3P) including the recommended features that do not hold in any other relative permeability models.
4) We investigated the validity of the UTKR3P model both mathematically and physically. The functional form of the formulation and the derivative (i.e., both analytically and numerically) of UTKR3P model are valid over the entire saturation space. From a mathematical perspective, we examined the variation of relative permeability for several saturation paths spanned over a broad range of saturation space. In the absence of discontinuities due to physical phenomena, we did not observe any inconsistent relative permeability curves.
5) We evaluated the impact of wettability on the curvature of isoperms in saturation space. We demonstrated the significant impact of residual saturation estimation on the behavior of isoperms particularly at low saturation region for all three phases.

6) We developed and validated a three-phase hysteresis model (i.e., UTHYST) applicable to multicycle processes. The main contribution of UTHYST model is to calculate capillary trapping both in increasing and decreasing saturation directions. We assessed the capability of the UTHYST model to generate cycle-dependent relative permeability curves.
7) We included the impact of compositional variation of trapped saturation to the UTHYST model. This option captures the non-monotonic behavior of capillary trapping. The non-monotonicity can be due to the significant compositional exchange (e.g., solubilization or vaporization) between the trapped and displacing fluids.
8) We developed a simple saturation-direction-identification procedure including a saturation tolerance parameter. Including the tolerance parameter reduces the number of saturation direction switching when simulation results yield to an oscillation of the saturation values due to the numerical instabilities. The redundant number of alternative saturation directions is computationally expensive and not physically required. This leads to have slow- or non-convergence simulation and must be avoided. As the tolerance parameter increases, the number of switches between saturation directions decreases.
9) The developed UTKR3P and UTHYST models were implemented into two in-house compositional reservoir simulators: IPARS and UT-DOECO2. We verified the implemented models in both simulators.
10) We examined the impact of two-phase parameters on the performance of the UTKR3P model in the modeling of an immiscible WAG process.
11) We demonstrated the significant effect of hysteresis in gas inventory and retention for a CCUS process. This task was accomplished by applying the integrated UTKR3P and UTHYST models.
12) We applied a framework for modeling the low-tension gas flood as a hybrid gas-chemical EOR

method in which two surfactants are modeled to (**i**) mobilize oil by ultra-low interfacial tension and (**ii**) control gas mobility by generating in-situ foam.

13) We developed a general framework for modeling the compositional relative permeability. The developed framework unifies thermodynamics, petrophysics, and geochemistry to enhancing the modeling of relative permeability. The general framework was applied to the aqueous phase and hydrocarbon phases.
14) We examined the UTPGE framework for several fluid systems and obtained the consistent and continuous relative permeability curves within the entire composition space.

7.2 CONCLUSIONS

We conclude the followings based on the compelling facts presented in Chapter 2 and this research in Chapters 3-6.

7.2.1 Three-phase relative permeability

1) Careful study of available relative permeability models gave a wrong isoperm curvature compared to the measured three-phase relative permeability in intermediate-wet state (**Oak, 1991**). The curvature was correctly represented with the UTKR3P model.
2) The UTKR3P model is a versatile, simple, and flexible in the selection of wettability states. The proposed model was validated against the intermediate- and oil-wet laboratory data in addition to water-wet condition. The free parameter *b* in residual saturation formulation varies as the rock wettability alters.
3) We demonstrated that the UTKR3P model captures the saturation-path dependency using the dependency of residual saturation to the probed saturation trajectory.
4) Our detailed investigation of fluid spreading at low saturation region revealed that the fluid spreading is non-monotonic even in a pore scale. In addition, the spreading is both pore-geometry and wettability dependent.

5) We showed that the UTKR3P model captures the inverse S-shape relative permeability curve of the non-wetting fluids in an intermediate-wet state.
6) There is always only one fitting parameter per phase ($b_j, j = 1, 2, 3$). The other required parameters of the UTKR3P model are process dependent. If a capillary-dominated flow is modeled, maximum nine parameters per phase are required (i.e., four pairs of two-phase quantities (i.e., $k^0_{rji}, C_{1ji}, C_{2ji}, S_{jri}\ \ j \neq i$) extracted from two-phase measured relative permeability data and one critical saturation (S_{jc})). The minimum number of the required parameters is three per phase (i.e., k^0_{rj}, C_{1j}, S_{jr}). If the optional high trapping number region in saturation space is modeled, maximum three other parameters per phase are required (i.e., N_{Tj}, T_j, τ_j).

7.2.2 **Three-phase hysteresis**

7) We illustrated that incorporating the hysteresis effect in modeling multicycle processes captures the reduction of well injectivity. In addition, it was demonstrated that the Land coefficient in initial-trapped saturation relationship varies in multicycle processes. In addition, the Land coefficient varies as the rock wettability changes.
8) The proposed methodology to identify the saturation direction of each phase within the multicycle processes is simple and fast. The selection of the tolerance parameter imposes a trade-off between accuracy of reproducing the physical behavior of fluid displacement and the computational cost of identifying the saturation direction.
9) Our three-phase hysteresis model contributes in generating a set of cycle-dependent relative permeability curves for multicycle processes. The dynamic relative permeability curves from the UTHYST model ensures three characteristics of capillary trapping in multicycle processes including (**i**) the monotonic behavior, (**ii**) the effect of the conjugate phase, and (**iii**) the dynamic Land coefficient.

10) The UTHYST model has three input parameters per phase with hysteresis effect ($L_j, S_{cj},$ and α_j) where only one parameter is a matching parameter (α_j).

7.2.3 Compositional relative permeability

Accurate modeling of the composition demanding processes requires a consistent and continuous relative permeability curves over the entire saturation and composition spaces. Fluids may involve in an extensive compositional exchange with their surroundings in EOR processes. For example, the interactions of aqueous phase with solid rock, liquid and gaseous hydrocarbon and non-hydrocarbon phases affects the overall performance of a diverse range of processes such as low-salinity water flood and CO_2 sequestration in saline aquifers. In addition, the complex fluids have remarkable compositional variation and yield uncertainty in modeling fluid displacement.

Relative permeability is composition dependent. In the absence of capillary desaturation effect and regarding incorporating a general inclusion of compositional effects on relative permeability few attempts have been made. When an aqueous system dynamically exchanges components with solid/liquid/gas phase within geochemical reactions, gas solubility, and water evaporation, the relative permeability varies even though the effective IFT required in the capillary desaturation curve may not be held.

11) Both bulk and interphase compositions impact relative permeability. While the bulk-phase composition changes the relative permeability of a specified phase, the interacting fluids with that phase also affect its relative permeability (viz., different relative permeability parameters for a specified fluid when is displaced with two separate phases). It implies that the interphase composition must be included in composition-dependent relative permeability modeling.
12) Coupling relative permeability and fluid phase behavior is an effective technique to incorporate the compositional effects together with the effects of pressure and temperature into fluid displacement characterization. Molar Gibbs free energy (GFE) is an appropriate quantity to

represent phase behavior of the fluid system and is in par with the imposed criteria to the reservoir simulation grid-blocks (i.e., holding a constant pressure and temperature).

13) We showed that the GFE of all fluid systems we studied is unconditionally continuous particularly when phases appear/disappear. More specifically, the GFE is continuous when a fluid composition passes through a path starting from a two-phase, to a three-phase, and finally to another set of two-phase flow.
14) We highlighted that the GFE of phases may have a non-monotonic behavior for a specific pressure, temperature, and composition conditions. A complementary quantity to completing the composition-dependent relative permeability modeling is required. We concluded that the interface composition as represented by IFT is an appropriate parameter in modeling three-phase relative permeability in compositional model.
15) We believe that pressure and temperature can impact relative permeability depending on the fluid composition and rock property. We noticed that temperature may significantly change the GFE of the aqueous phase.
16) The apparent standard partial molal GFE of electrolyte solution is pressure and temperature dependent. We demonstrated that neglecting this quantity particularly for anions such as sulfate ion in the aqueous phase yields to an inaccurate GFE value. We also demonstrated that the reference-state GFE of components are pressure- and temperature- dependent quantities and should not be neglected in the GFE calculation.
17) The published approaches for modeling low-salinity water flood are incomplete. They do not include the impact of each electrolyte in the aqueous solution and exclude the effect of temperature. Our framework is general and includes the effect of each electrolyte explicitly, temperature, and pressure in modeling aqueous relative permeability.
18) In certain circumstances, the molar GFE and ionic strength of the aqueous phase are

interrelated (i.e., linear relationship) and that one may substitute the more computationally expensive molar GFE calculation with ionic strength.

19) We illustrated that the integrated GFE-IFT modeling approach yields a more accurate relative permeability than GFE approach when two-phase relative permeability parameters are dissimilar or when a non-monotonicity is observed in the GFE of phase(s).

20) We confirmed that the UTPGE framework can be applied to calculate compositional relative permeability within several EOR processes including near-critical fluids in two- and two-phase flow. We also showed that the proposed framework can be applied to provide representative SCAL data when the laboratory and field conditions (pressure, temperature, or composition) differ.

7.3 RECOMMENDATIONS FOR FUTURE WORK

In the following, we review some unresolved issues that could be a continuation of this work and confirm a more accurate representation of the three-phase flow in porous media. The recommendations are categorized to three-phase relative permeability, three-phase hysteresis, and composition-dependent relative permeability modeling.

7.3.1 Three-phase relative permeability modeling

1) Relative permeability is a second-order tensor and scale-dependent. In multiphase flow, fluid configuration, as represented by fluid saturation in core-scale, may impact the in-situ anisotropy in porous media. This statement highlights the importance of incorporating a variable relative permeability in different coordinates in three-dimensional anisotropic models. This methodology alleviates the application of mathematical models to upscale relative permeability when transferring on the boundaries of scales of interest, from pore- to core- to field-scale.

2) The investigations of a geomechanical-dependent and dynamic relative permeability in the

essence of laboratory measurements and modeling is required. The impact of rock mechanics effects on relative permeability may become crucial in particular applications in which pore structure varies.

3) Currently, the capillary desaturation effect has not thoroughly been examined in three-phase flow. Hence, we excluded the impact of displacing phase on trapping-number dependent quantities. In particular, the same capillary desaturation curve is assigned when either water or gas displaces oil. A pragmatic approach to correctly select the in-situ displacing phase must be developed. Also, two measured desaturation curves are required to complete modeling of capillary desaturation effect in the three-phase flow.
4) The compositional effect on *b* parameter in the three-phase residual saturation may be crucial when there is significant mass transfer and must be further investigated.
5) An integrated capillary pressure and relative permeability model is crucial in modeling three-phase flow. We recommend to use a reliable three-phase capillary pressure model applicable in both saturation and composition spaces.

7.3.2 **Three-phase hysteresis modeling**

6) A detailed modeling and experimental validations are required to include the impact of mobilization of trapped fluids when there is a meaningful composition exchange between displacing and trapped fluids.
7) Conjugate phase definition is arbitrary and constant in current version of the UTHYST model. Further laboratory examinations are recommended to accommodate a practical method for the selection of conjugate phase within various wettability conditions.
8) A methodology must be developed for the calculation of maximum trapped saturation (S_{jt}^{M}) based on rock properties such as pore morphology, size/throat distribution, and wettability. Assigning the S_{jt}^{M} is currently arbitrary among hysteresis models. This quantity, however, is

an input parameter in reservoir simulation studies. Although there have been attempts to relate the microscopic phase trapping to the macroscopic Darcy-scale porosity, the scattered in S_{jt}^{M} is not acceptable. Furthermore, microporosity does not contribute to fluid trapping.

9) Investigate the trapping behavior within a multicycle process in unconsolidated rocks.

7.3.3 Composition-dependent relative permeability modeling

10) While this study advocates the impact of geochemical reactions on relative permeability through a composition-dependent relative permeability model, measurements are required to further investigate the geochemical-dependent relative permeability.
11) Include capillary pressure term in the functional form of the integrated GFE and IFT formulation to enhancing relative permeability modeling. It then necessitates capillary pressure to explicitly be added to phase behavior modeling in compositional simulation.
12) Develop a more mechanistic interpolation scheme based on additional laboratory data to enhance the modeling of relative permeability using the integrated GFE-IFT.
13) Study the complex fluids (e.g., fluids involved in significant wax/asphaltene precipitation, compositional grading reservoirs, and surfactant flood) using the UTPGE framework.
14) Develop an electrolyte EOS (eEOS) that spans the entire composition space and covers typical range of pressure and temperature in subsurface applications to accurately characterizing electrolyte solutions.

Appendix A: Terminology

In this appendix, we present the terminology of typical parameters in petroleum literature as have been used in this dissertation. Some of these parameters are equivocal, and the author adopts a convention to define the parameters and apply them in a consistent matter. The definitions are sorted in an alphabetical order.

CAPILLARY AND TRAPPING NUMBER

The capillary number expresses the ratio of viscous to capillary forces. It addresses the active forces counteracting on trapping-remobilization of a trapped phase in porous media. Many variations of the capillary number definition have been published focusing on impacting parameters on both viscous and capillary forces including, but not limited to, rock permeability, porosity, contact angle, viscosity, fluid velocity, IFT, phase potential, and phase relative permeability (**Brownell & Katz, 1947**; **Delshad et al., 1987**; **Green & Willhite, 1998**; **Jerauld, 1997b**; **Moore & Slobod, 1955**; **Pennell et al., 1996**).

As the capillary number increases either through lowering the effective capillary forces or increasing the viscous forces on the displaced phase, there is a critical value beyond which the trapped saturation decreases precipitously— capillary-desaturation effect. This important effect may be recognized as a process in which effective forces on the trapped phase play the primary role and mass-transfer has a secondary effect. Although interphase mass transfer changes the IFT between displacing-displaced fluid, it has a distinguished contribution on particular fluid displacements as discussed in **Capillary trapping** in Chapter 2.

The dimensionless Bond number represent the magnitude of the gravitational to capillary forces (**Perry & Chilton, 1973**). The trapping number integrates gravitational forces with viscous and capillary forces and can be applied as a tool to measure the extent of trapped phase

remobilization excluding interphase mass transfer and spreading effect (see **Fluid spreading**). The trapping number couples the Bond number with the capillary number. For a general case where the active gravitational and viscous forces on the displaced phase are not collinear, the trapping number for phase *j* displaced by displacing phase *i* is calculated by (**Jin, 1995**; **Pope et al., 2000**),

$$N_{Tj} = \frac{\left|\vec{\vec{k}}.\left[\vec{\nabla}\Phi_i + g(\rho_i - \rho_j)\vec{\nabla}D\right]\right|}{\sigma_{ji}}, \quad \text{i} = \text{phase m or l.} \qquad \textbf{Eq. A- 1}$$

where the term inside the bracket of the nominator expresses the coupled viscous and gravitational forces, and all the parameters are defined in **Glossary**.

Accurate representation of fluid flow in a heterogeneous and anisotropic porous medium requires the full tensor permeability. Rather than conventional approach of selecting the principal directions of permeability tensor on the axes of modeling coordinate system, we then require additional elements to treat the permeability tensor. Moreover, the x-y-z coordinate of the porous medium can be obtained by a two-level rotation of the planes of the coordinate system.

CONTACT-ANGLE HYSTERESIS

The contact-angle hysteresis is a natural phenomenon and plays a key role in many industrial processes particularly in chemical and metallurgical applications (**De Gennes et al., 2004**). It refers to the difference between the contact angles in advancing and receding processes at a particular velocity (**Eral et al., 2013**). In petroleum industry, it is equivalent to the hysteresis existing between the increasing non-wetting fluid saturation and the increasing wetting fluid saturation processes (**Morrow, 1975**). The static contact-angle hysteresis addresses the difference between the maximum (advancing) and the minimum (receding) contact angles at zero velocity. It may approach to as high as 100° (**Morrow, 1975**) and induces a local minimum on the Gibbs free energy (**Marmur & Bittoun, 2009**). Depending on the capillary number, viz., fluid velocity, the deference between the advancing and receding contact angles increases (**Eral et al., 2013**). The

contact angle hysteresis is controlled by several pore-scale parameters including local wettability heterogeneity, pore topology (surface roughness), and the aqueous and oil compositions and contaminations (to alter rock wettability) (**Adamson, 1960**; **Morrow, 1975**; **Paterson et al., 1998**; **Yang et al., 1999**).

EOR AND IOR

The EOR techniques constitute of thermal, chemical, solvent, and microbial injection methods. EOR mainly contributes to any injection method by which the hydrocarbon recovery or the field economic improves.

Improved oil recovery (IOR) is a general term and refers to any activity to effectively increase the in-place hydrocarbon recovery or production rate. The IOR must explicitly meet the predefined economic criteria of a particular field. Not only does the IOR encompasses the EOR but also covers any reservoir management technique contributing to the continued/elevated production rate and hydrocarbon recovery. The reservoir management techniques constitute the water management, injection and production management, in-fill drilling, well-stimulation, smart wells, and conformance control among others.

The starting point of EOR/IOR conventionally was speculated at the end of the primary and secondary production schemes. The secondary production addresses the activities to maintain the reservoir pressure over the range of a desired production. From a more recent perspective, however, the EOR/IOR methods may start along with the primary production from a green field.

FLUID CONFIGURATION IN MULTIPHASE FLOW: LAYERING VS. TRAPPING

Fluid configuration and spreading in multiphase displacement is strongly related to rock wettability, pore structure, and equilibrium spreading coefficient (**Øren & Pinczewski, 1995**; **van Dijke & Sorbie, 2002**). The fluid distribution in porous media is achieved by a balance between interfacial tensions, contact angles, local capillary pressure, and pore structure. It also has

implications on the fluid spreading and film flow in porous media.

Phase trapping and film flow (see **Layer drainage**) are common phenomena in low saturation region and have implications on fluid recovery. Investigators have identified the layer drainage (or film flow) for the intermediate phase such as oil in a water-wet rock. The layer-drainage depends on pore structure, contact angles, and rock wettability. If the film flow does not occur, however, the flowing phase becomes disconnected and eventually trapped. It is therefore crucial to identify the possibility of layer drainage in porous media. Presumption of a layer drainage is common in relative permeability modeling. As we will show, however, existence of layer drainage depends upon the rock wettability and pore geometry. In the following, we conduct an analytical study to investigate the possibility of layer-drainage existence as the rock wettability changes.

The necessary condition for film flow (i.e., the existence of a fluid layer (in this case PH-2) sandwiched between two other fluids in pores where PH-1 is the wetting fluid) is based on the geometrical relationship between the pore corner angle (2β) and the fluid contact angles (**Figure A-5**). Assuming that there is only one curvature exists in the plane of the wedge and the contact of PH1-PH2 interface with the solid does not coincide with the PH3-PH2 contact, one may derive the required condition for the existence of a continuous layer of PH-2 as (**DiCarlo et al., 2000**; **Fenwick & Blunt, 1988**; **Øren & Pinczewski, 1995**),

$$\theta_{21} + \beta < \frac{\pi}{2} \text{ and } \theta_{23} + \beta < \frac{\pi}{2}. \qquad \textbf{Eq. A-2}$$

Eq. A-2 implies the significance of contact angles on fluid spreading, fluid displacement, and pore filling. Dynamic contact angle measurement is a tedious task is laboratory. Consequently, researchers identified correlations to evaluate contact angles that fulfill the required relationship between interfacial tension and contact angles, e.g., Bartell-Osterhof equation (**Bartell &**

Osterhof, 1927; **Øren & Pinczewski, 1994**; **Zhou & Blunt, 1997**). Contact angles between non-wetting fluid (PH-3) and either of other fluids (PH-1 and PH-2) can be determined based on the coupling of equilibrium spreading coefficient and contact angles between more wetting fluids (**van Dijke & Sorbie, 2002**).

$$cos\theta_{32} = \frac{1}{2\sigma_{32}}\{C_{s2}^{eq} cos\theta_{21} + C_{s2}^{eq} + 2\sigma_{32}\},$$
$$cos\theta_{31} = \frac{1}{2\sigma_{31}}\{(C_{s2}^{eq} + 2\sigma_{21})cos\theta_{21} + C_{s2}^{eq} + 2\sigma_{32}\}, \quad \textbf{Eq. A-3}$$

where C_{s2}^{eq} is the equilibrium spreading coefficient, viz., $C_{s2}^{eq} = \min(0, C_{s2})$ (**Rowlinson & Widom, 1989**).

Next, we investigate the impact of pore geometry on the fluid configuration and fluid spreading capacity in a simple analytical analysis. We evaluate the maximum allowed pore angle ($\max(2\beta)$) within which a stable fluid layer exists. We vary IFTs between two fluid pairs ($\sigma_{12}\ and\ \sigma_{23}\ \in [0,60]\ mN/m$), fix the third fluid-pair IFT ($\sigma_{13} = 72\ mN/m$), and use a value of 10° as the constraint for pore half-angle (possible range of half contact-angle: $10° < \beta < 80°$).

Figure A-1 shows the variation of maximum half-angle of the pore corner with IFTs and the equilibrium spreading coefficient (C_{s2}^{eq}). It implies that as the IFT of one fluid pair increases, only a narrower range of pore angles provide fluid-layer spreading. Also, the spreading in wider angle pores are only accessible through a high spreading coefficient, viz., when equilibrium spreading coefficient approaches zero.

Figure A-2 to **Figure A-4** assess the fluid-layer-spreading in pores with variable geometry and fluid contact angles. They compare the variation of maximum half-angle of the pore corner with one fluid-pair IFT (σ_{12}) and the contact angle (θ_{12}) while keeping two other IFTs (σ_{13} and σ_{23}) constant. The other required contact angles are evaluated based on **Eq. A-2**. These figures imply that the spreading of a fluid-layer has non-monotonic behavior even on the pore scale. Besides, the fluid spreading is just expected on the wider pore angles at the strongly water-wet

state. This observation is consistent with the experimental results (**Abdallah et al., 2007**; **DiCarlo et al., 2000**; **Iglauer et al., 2013**). They confirm that for the fixed IFTs, the fluid layer form only on the sharp pore corners as θ_{12} increases. Besides, as σ_{23} decreases, only a small window of equilibrium spreading coefficients exist in which fluid-layer may form at a wide range of pore geometries. Otherwise, the film layer collapses and that PH-2 becomes disconnected.

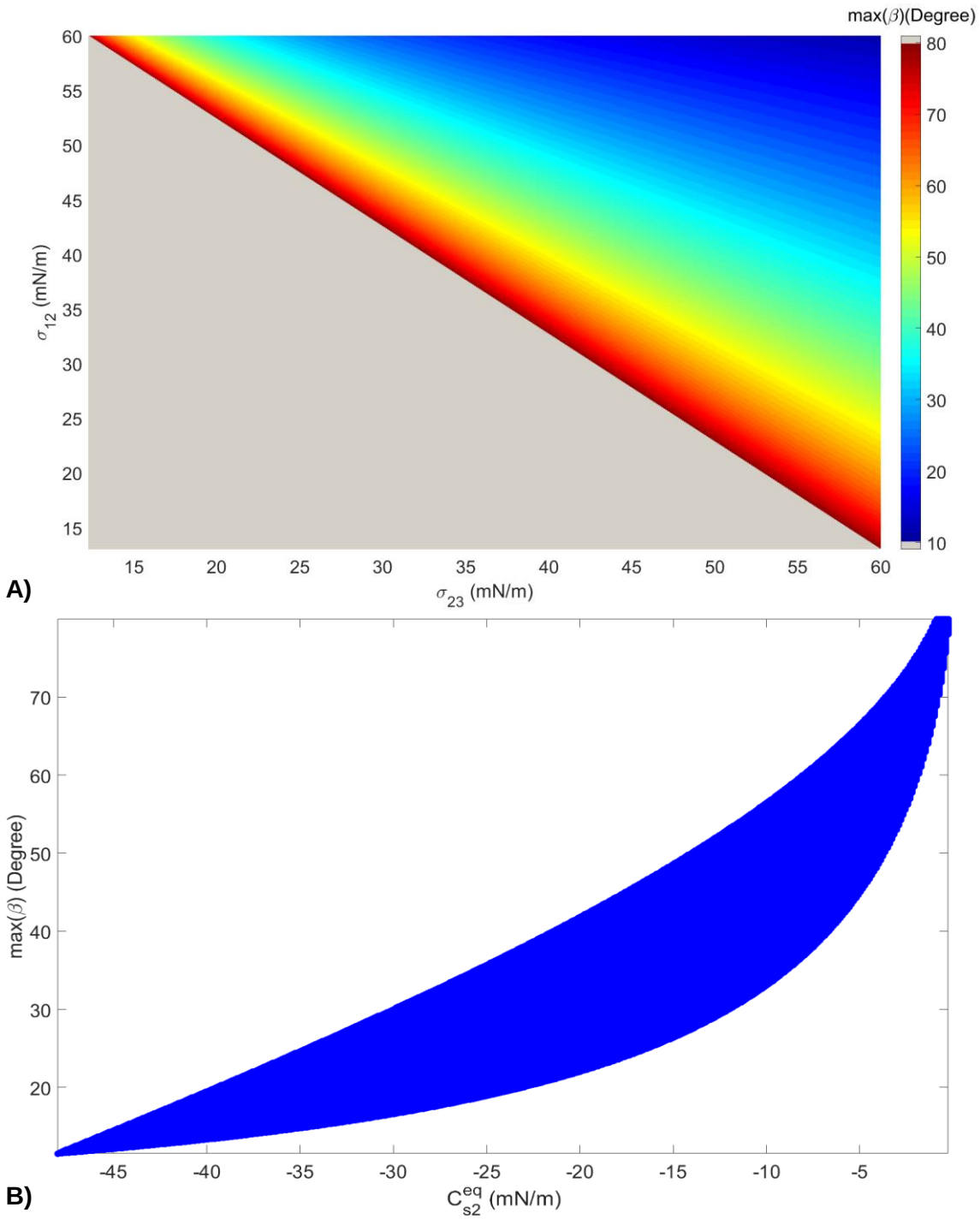

Figure A-1: Variation of the maximum allowed half-angle of the pore corner ($10° \leq \max(\beta) \leq 80°$) in which a stable oil (fluid 2) layer forms in multiphase displacement in a water-wet (PH-1) porous media (Note: fixed $\sigma_{13} = 72\ mN/m$). **A**) variation of pore corner half-angle with two IFTS (σ_{12} and $\sigma_{23} \in [0,60]\ mN/m$) in the upper triangle where the color map shows $\max(\beta)$. **B**) variation of pore corner half-angle with equilibrium spreading coefficient (due to variation of two IFTs) in a water-wet porous medium where blue region shows $\max(\beta)$.

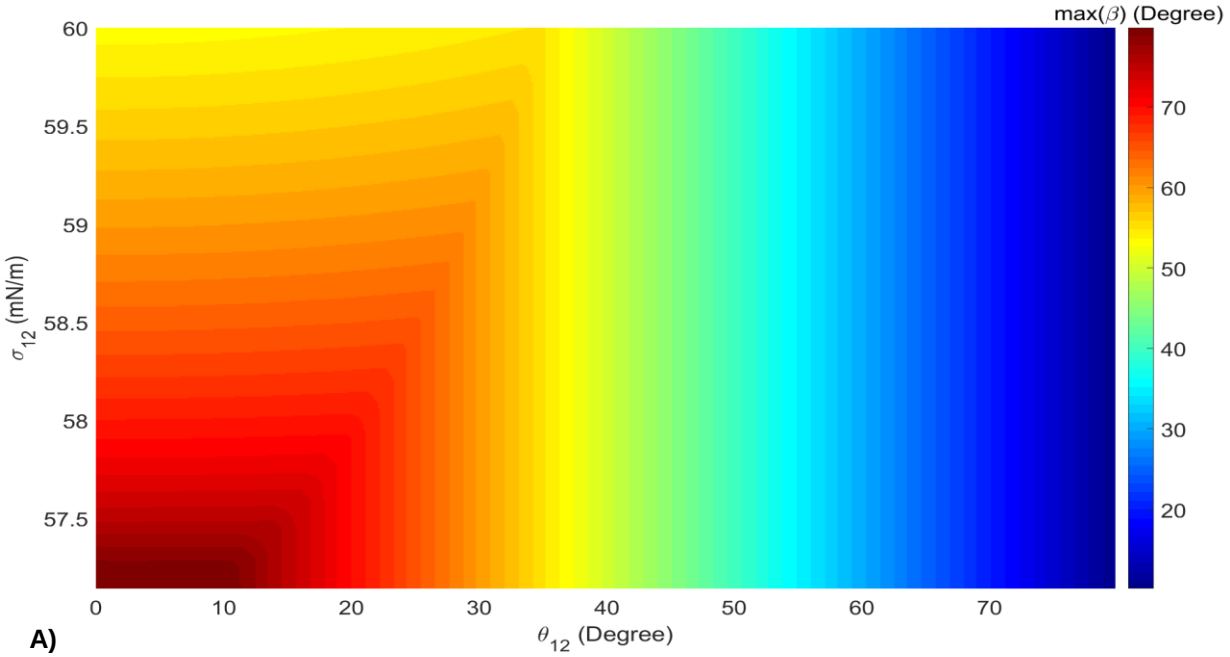

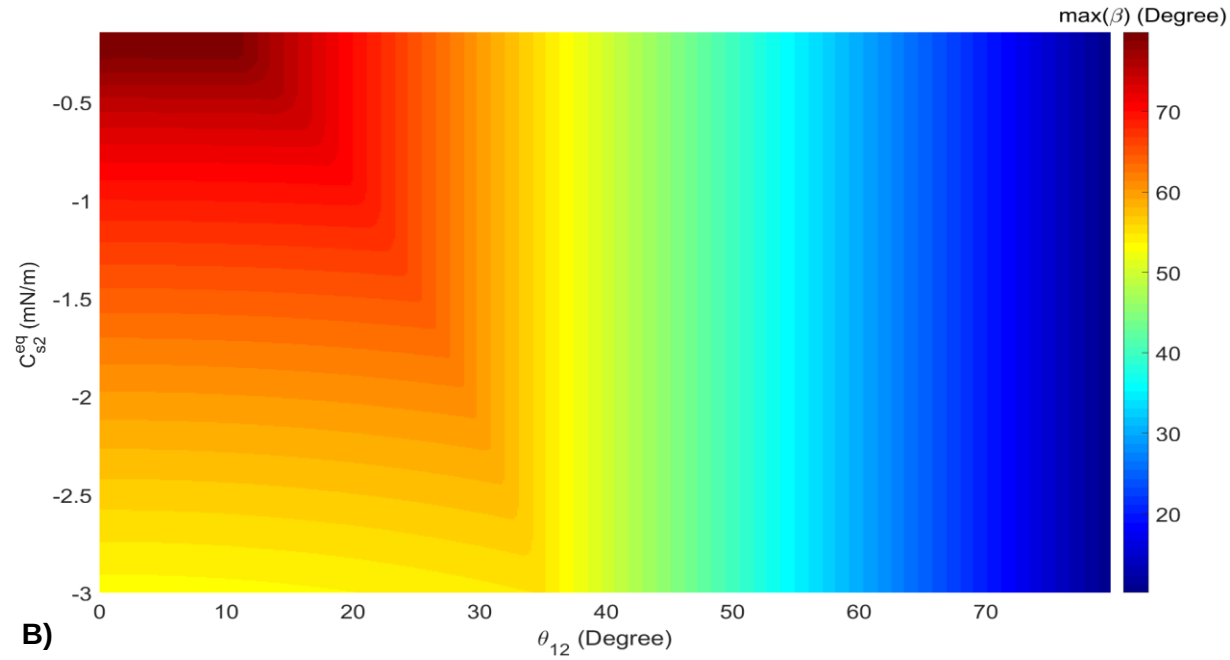

Figure A-2: Variation of maximum half-angle of the pore corner ($10° < \max(\beta) < 80°$) leading to the formation of a stable oil (PH-2) layer in multiphase displacement with varying wettability (oil-water contact angle) ($0° \leq \theta_{12} \leq 90°$). (Note: fixed $\sigma_{13} = 72\ \mathrm{mN/m}$ and $\sigma_{23} = \mathbf{15}\ \mathrm{mN/m}$): **A**) variation of pore corner half-angle with contact angle and one IFT where the color map shows $\max(\beta)$; **B**) variation of pore corner half-angle with contact angle and equilibrium spreading coefficient (color map shows maximum value of pore corner half-angle).

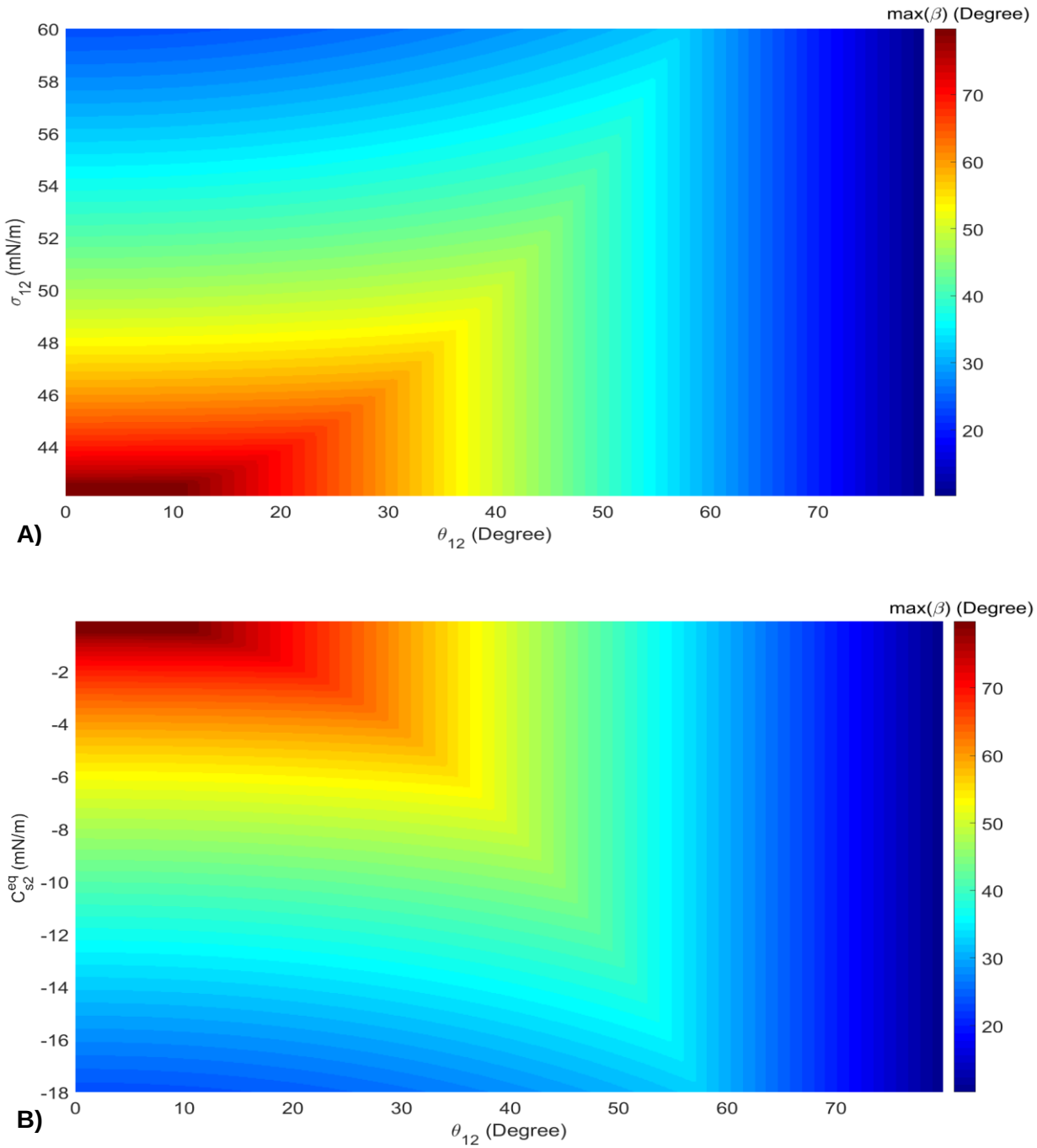

Figure A-3: Variation of maximum half-angle of the pore corner ($10° < \max(\beta) < 80°$) leading to the formation of a stable oil (PH-2) layer in multiphase displacement with varying wettability (oil-water contact angle) ($0° \leq \theta_{12} \leq 90°$). (Note: fixed $\sigma_{13} = 72$ mN/m and $\sigma_{23} = \mathbf{30}$ mN/m): **A**) variation of pore corner half-angle with contact angle and one IFT where the color map shows $\max(\beta)$; **B**) variation of pore corner half-angle with contact angle and equilibrium spreading coefficient (color map shows maximum value of pore corner half-angle).

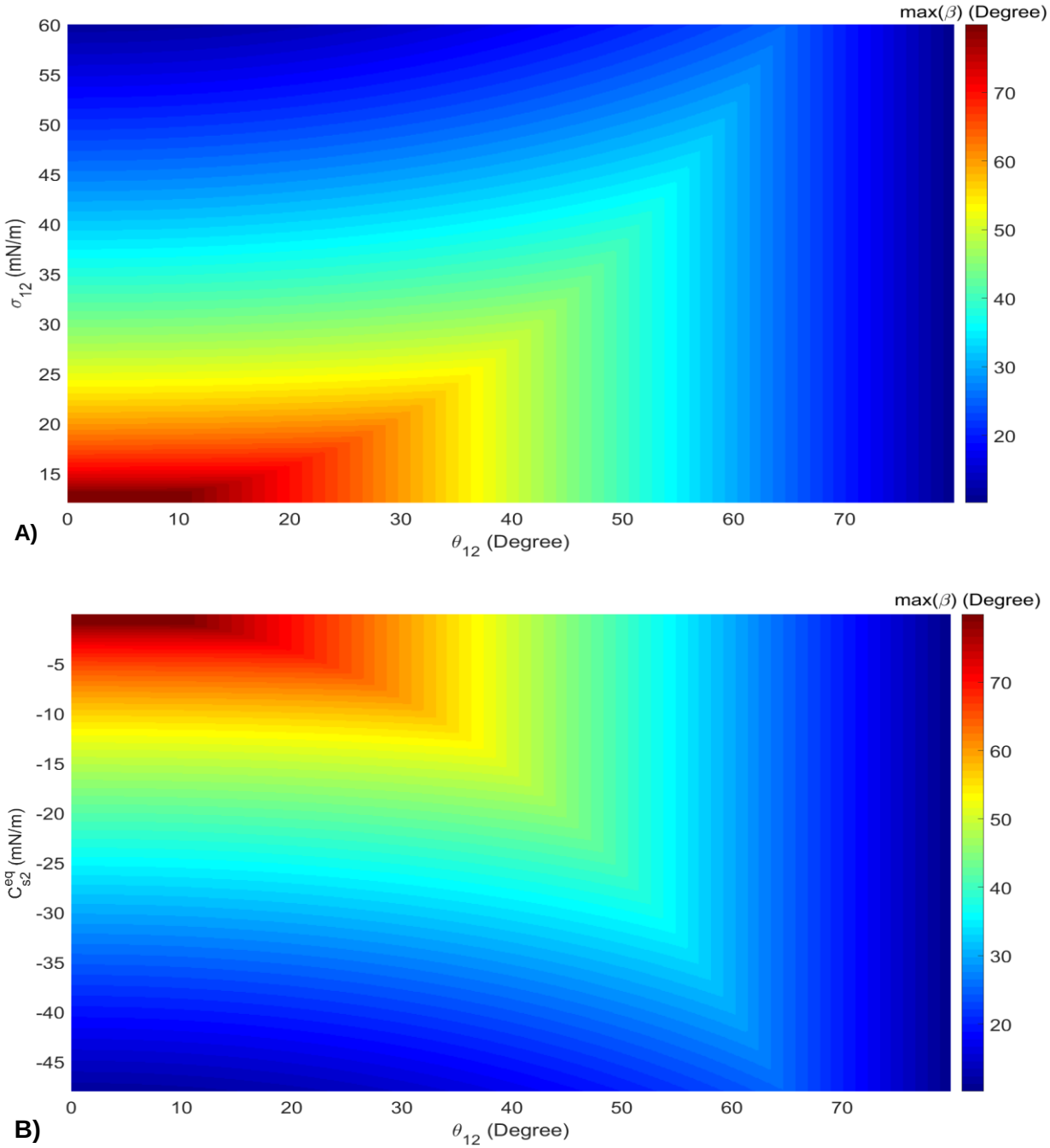

Figure A-4: Variation of maximum half-angle of the pore corner ($10° < \max(\beta) < 80°$) leading to the formation of a stable oil (PH-2) layer in multiphase displacement with varying wettability (oil-water contact angle) ($0° \leq \theta_{12} \leq 90°$). (Note: fixed $\sigma_{13} = 72\ \mathrm{mN/m}$ and $\sigma_{23} =$ **60** $\mathrm{mN/m}$): **A**) variation of pore corner half-angle with contact angle and one IFT where the color map shows $\max(\beta)$; **B**) variation of pore corner half-angle with contact angle and equilibrium spreading coefficient (color map shows maximum value of pore corner half-angle)

FLUID SPREADING

In petroleum engineering and hydrology, it is generally believed that the mere role of wettability state on two-phase flow is replaced by interaction between the wettability (fluid/solid) and spreading coefficient (fluid/fluid) or directly contact angle and IFT for three-phase flow (**Abdallah et al., 2007**; **Øren & Pinczewski, 1994**; **van Dijke & Sorbie, 2002**). Three-phase displacement processes and pore-scale mechanisms in physically etched micromodels revealed that fluid configurations can be categorized based on the phase spreading coefficient (C_s) defined as a balance of interfacial tensions (**Abdallah et al., 2007**; **Adamson, 1960**; **Øren & Pinczewski, 1995**):

$$C_{s2} = \sigma_{13} - (\sigma_{12} + \sigma_{23}), \qquad \textbf{Eq. A-4}$$

where σ_{ij} denotes IFT between phases i and j. Phase spreading may further be characterized as initial (C_{s2}^{I}) and equilibrium coefficients (C_{s2}^{eq}). The initial spreading coefficient is based on fluid-pair IFTs measured without interference from the third phase. The equilibrium (or effective) spreading coefficient, however, represents the system has reached thermodynamic equilibrium (i.e., interactions of IFT pairs at the presence of the third fluid are considered (**Zhou & Blunt, 1997**)).

Three situations are discernable: (**i**) if $C_{s2}^{I} < 0$, a three-phase contact line exists, viz., non-spreading system. Otherwise, (**ii**) if $C_{s2}^{eq} \approx 0$, a macroscopically thick and stable and hydraulically conductive film of phase 2 forms between the wetting- and non-wetting-phases (phase 1 and phase 3, respectively); or, (**iii**) if $C_{s2}^{eq} < 0$, only a molecular film is formed (**Sahni et al., 1998**; **Zhou & Blunt, 1997**).

In a non-spreading oil case, oil is wetting relative to gas and water or gas could be the wetting phase in non-water wet media depending on gas-water contact angle. This demonstrates that contact angle plays a crucial role in fluid configurations in porous media. Irrespective of rock

wettability condition, oil is always the wetting phase to gas and cannot be named as a non-wetting phase in three-phase conditions. In oil-wet pores, oil is wetting relative to other phases and gas and water are not in direct contact (**Øren & Pinczewski, 1995**; **van Dijke et al., 2001**). However, gas is not necessarily the non-wetting phase. The gas-water contact angle, identified by the difference between oil-water and gas-oil IFTs, determines the intermediate-wetting phase in oil-wet rocks (**van Dijke et al., 2001**). If oil-water IFT is larger than that of gas-oil, then gas and water phases behave as intermediate- and non-wetting phases, respectively (i.e., *water repellent*) with an apparent gas-wetting characteristic. In a water repellent system, both oil and gas preferentially are the wetting fluids than water (**Oak, 1992**; **Schneider & Owens, 1970**; **Tang & Firoozabadi, 2000**).

LAYER DRAINAGE

Layer drainage (or film flow) states that oil resides between gas in the center of a pore and water attached to the rock surface. The oil saturation is proportional to the occupied oil layer area. Relative permeability is proportional to the square of the area filled with oil (hydrodynamic conductance and Poiseuille type flow in the pipe-like domain (**Dullien, 1992**). As a result, $k_{ro} \propto S_o^2$ (**Blunt, 2000**; **DiCarlo et al., 2000**). This sandwiched oil keeps its continuity and very-low mobile oil saturation is achieved though the production rate is quite low. Gas plays a critical role in this behavior: the lower the amount of injected free gas, the higher residual oil saturation. Note that water in non-water-wet samples, however, does not show the quadratic form and becomes trapped. It is due to the fact that water possesses a negative equilibrium spreading coefficient in non-water media.

IONIC STRENGTH

In order to calculate a solution activity with the dissolved ions, the ionic strength is an important parameter presenting the electrical interaction. Lewis and Randall (**1921**) introduced this concept

to measure the concentration of all ions in the solution where the dissolved compound dissociate into ions. In general, the ionic strength of solution is defined as,

$$I = 0.5 \sum_{i=ions} z_i^2 m_i, \qquad \textbf{Eq. A- 5}$$

where z_i is valence of ion and m_i is ion molality and the summation is over all ions in solution. For example, for a mixture of anionic surfactant and salts, e.g., sodium dodecyl benzenesulfonate (1)-sodium chloride (2)-calcium chloride (3) in a microemulsion phase, the total ionic strength is calculated by:

$$I = 0.5 \sum_{i=1}^{3} z_i^2 m_i = 0.5 \times \{m_{RSO3-} + m_{Na^+} + m_{Na^+} + m_{cl^-} + 4m_{Ca^{2+}} + 2m_{cl^-}\}$$
$$= m_{RNaO3S} + m_{NaCl} + 3m_{CaCl_2}.$$

If complete water analysis is not acceptable- ionic composition of the aqueous phase is unknown or unreliable- one could estimate ionic strength by means of electrical conductivity and/or total dissolved solids (TDS). Griffin and Jurinak (**1973**) suggested the following relation: $I = 1.6 \times 10^{-5} \times SC \quad (if\ I < 0.5)$, where SC is specific conductance in $\mu S/cm$. Langelier (**1936**) proposed using TDS (mg/L), $I = 2.5 \times 10^{-5} \times TDS$.

GAS UTILIZATION FACTOR

In the gas injection context, the optimal utilization of the injecting fluid is a critical parameter in the technical-economic assessment of the implemented process. For example, in the CCUS process, one desire to efficiently store the CO_2 in natural subsurface resources and increase hydrocarbon recovery. The natural resources to sequester the significant amount of CO_2 include hydrocarbon reservoirs and deep saline aquifers. The efficient utilization of the CO_2 entails both the highest incremental oil recovery and the maximum CO_2 inventory.

MOBILITY/CONFORMANCE CONTROL

Mobility ratio addresses the mobility of displacing fluid (D) divided by that of the displaced fluid (d) as:

$$M_{Dd} = \frac{k_{r,D}/\mu_D}{k_{r,d}/\mu_d}. \qquad \textbf{Eq. A- 6}$$

A large value of mobility ratio ($M_{Dd} > 1$) is unfavorable for fluid displacement resulting in viscous fingering of the displacing (injectant) fluid. It is to the extent that a major challenge of evolving gas-based EOR methods is poor macroscopic sweep efficiency and microscopic displacement efficiency due to adverse mobility ratio.

Mobility control techniques assist in reducing the mobility ratio and, in turn, suppressing the problems associated with the fingering and channeling effect. To diminish the unstable displacement via the mobility control agent, one may intend to either reduce the relative permeability or increase the viscosity, viz., thickening, of the displacing fluid. Polymers and foam are the widely accepted agents to control the liquid injectants. Foams are also applicable to reduce the mobility of the gas/steam injectants.

Conformance control techniques intend to direct the injected fluid preferentially into the designated area of the reservoir to reduce bypassing the resident hydrocarbons, particularly in heterogeneous reservoirs. The conformance control agents like polymer, the cross-linker gels, and foam block or reduce flow of injectant fluid through high permeability streaks and/or natural fractures, divert the injectant fluid to low permeability zone and improve sweep efficiency. The conformance control treatment is applicable both at the near wellbore and deeper in the reservoir.

PORE STRUCTURE

Pore structure as a general terminology includes several pore-related parameters like pore size, geometry, topology, tortuosity, and cementation among others. Pore structure significantly impacts

the fluid flow and dynamics in porous media (**Dullien, 1992**). In the following, we briefly review pore size and topology as being applied in this dissertation.

Pore size

The pore-size distribution is a statistical tool to qualitatively relate petrophysical properties as an indispensable element of petrophysical characterization of reservoir rocks (**Arche, 1950**). Unfortunately, there is no theoretical definition for the pore size due to the measurement-method-dependent pore size determination (**Dullien, 1992**). Pore-size distribution is the probability density function (PDF) of a characteristic pore size and returns the pore volume distribution. Based on the PDF and the measurement methods, several definitions are discernable as compiled by Basan (**1997**). A widely accepted pore-size distribution definition addresses the incremental pore volume versus logarithmic pore-throat radius derived from a mercury injection capillary pressure (MICP) curves (**Peters, 2012**).

Pore sizes may span a vast spectrum from submicron, viz., micro- and ultra-pores, to very large void spaces, viz., vugs or caverns (**Dullien, 1992**). Pore throat is the narrow pore space connecting two larger pore volumes.

Pore geometry

Pore geometry is a complex function of (**i**) pore and throat size, (**ii**) pore configuration such as tortuosity and surface area, (**iii**) pore particulate system such as sorting, packing, and shape, and (**iv**) the porous system like intergranular, vuggy, and fractured media (**Dernaika et al., 2013**; **Dullien, 1992**; **Wardlaw, 1982**).

Pore topology

Pore topology reflects the spatial interconnectedness of a porous medium. The network topological parameters include the number of isolated clusters, the number of alternate paths in which fluid

can flow within a pore network, and coordination number defined as the mean number of pore throats emanating from a pore body (i.e., reflecting spatial connectivity of pore space).

Coordination number as the primary measure of a network topology for regular packing of spheres, Berea Sandstone samples, and glass bead packs varies between 1-2 for the non-distinct pores to large values for three-dimensional icosahedral lattices (=12) and random Voronoi networks filled with polyhedra (≅16). A realistic for coordination number range is 3-8 (**Chatzis et al., 1983**; **Dong et al., 2007**; **Jerauld & Salter, 1990**; **Yuan, 1981**; **Zhao & MacDonald, 1993**).

RELATIVE PERMEABILITY

Relative permeability expresses the reduction factor in a fluid mobility when other fluids exist in a porous medium. It acts as a bridge among several inter-related fields of study, e.g., reservoir engineering, petrophysics, petrology, and thermodynamics and has pronounced implications in EOR applications (**Lake et al., 2014**) and fluid displacement and recovery.

Darcy's law presents the flux of a single-phase in porous media replicating a homogenized Navier-Stokes equation (**Bear & Bachmat, 1990**). A phenomenological extension then made the application of this constitutive law possible in multiphase flow modeling through the relative permeability term (**Wyckoff & Botset, 1936**). For the solution of mass balance of phase *j* in an anisotropic and multi-dimensional porous medium (Ω), Darcy's constitutive law expresses the relation between fluid velocity in the direction of flow ($u_{i,j}$) and fluid potential (Φ_j): $u_{i,j} = \lambda_j \, \partial\Phi_j/\partial x \;\; x \in \Omega$, where λ_j is fluid mobility defined as effective (phase) permeability to fluid viscosity ($\lambda_j = k_j/\mu_j$). Relative permeability, in turn, expresses effective permeability as a fraction of a base permeability, viz., $k_{rj} = k_j/K$, where *K* is the second-rank permeability tensor (**Bear, 1972**).

As Standing (**1975**) noted, the base permeability (k_j) is an arbitrary reference parameter but commonly applied ones are (**i**) absolute permeability, (**ii**) dry air permeability, and (**iii**)

effective permeability of one of the hydrocarbon phases at connate water saturation.

ROZ/TZ

Residual oil zone (ROZ) and transition zone (TZ) are stranded regions in hydrocarbon reservoirs. ROZ/TZ primarily includes oil at saturation below water-flooded residual oil saturation. They account for a substantial amount of reserve in the hydrocarbon reservoirs of the United States. Harouaka et al. (**2014**) estimated that ROZ/TZ in 5 Permian Basins contain 30.7 Bbbl oil-in-place in which oil located below the oil-water-contact is exploited particularly thorough CO2-EOR. It is noteworthy that in spite of the emerging CO2-EOR techniques and their potential to recover a substantial amount of oil from the ROZ/TZ regions, still more compelling research is required to increase the effectiveness of CO_2-EOR applications in production from stranded oil zones and their associated low-saturation region.

ROCK WETTABILITY

Wettability is defined as the relative tendency of one fluid to coat the solid surface spontaneously in the presence of the other fluid(s) (**Craig, 1971**). This crucial parameter in petroleum engineering application depends on contact angle between fluids and pore geometry. The wettability preference of a flat surface is obtained based on the contact angle between a designated fluid pair. In more complicated pore structures in rocks, however, the wettability state is also dependent on the pore geometry. As a result, the wettability preference of the petroleum reservoir rock (initially strongly water-wet state) may be altered substantially within the displacement process even if the contact angles remain constant. Rock wettability alters in various ways making the pore occupancy very complicated for the multiphase systems (**Kovscek et al., 1993**; **Morrow, 1990**; **Treiber & Owens, 1972**).

The initial wettability state is strongly water-wet. For decades, the petroleum industry believed that rock-wettability is in the water-wet state in that even with oil migration into the rock,

the siliceous surfaces keep the water affinity. Besides, in reservoir simulation area, a variety of reservoir-fluid adjusting parameters along with the complicated task to measure the wettability through the reservoir conceal the rock wettability role as a primary impacting parameter.

In general, wettability in the porous medium may be classified as either homogeneous or heterogeneous. The homogeneous case can be categorized by measuring contact angle (CA) as water-wet, intermediate-wet (or neutral-wet), and oil-wet. The contact angle is the measure of wettability of solid through the denser phase. The range of the contact angle for selecting the wettability state, however, is not unique. Tieber et al. (**1972**) examined the wettability of 55 reservoirs using the contact angle measurement and found that sandstone reservoirs were 43% water-wet, 7% intermediate-wet, and 50% oil-wet. The examined carbonate reservoirs were 8% water-wet, 8% intermediate-wet, and 84% oil-wet. Based on their examination, the reservoirs are classified as water-wet (CA=0°-75°), intermediate-wet (CA=75°-105°), and oil-wet (CA=105°-180°) states. Morrow (**1976**) examined the contact angle of cores with porosity ranging from 16% to 47.5%. He measured the contact angle both on a smooth surface (intrinsic angle) and on a rough surface for both drainage (RCA) and imbibition tests (**MacAllister et al., 1993**). The investigator redefined the wettability labeling based on the contact angle hysteresis as water-wet (ACA=0°-62°), intermediate-wet (A(R)CA=62°-133°), and oil-wet (RCA=133°-180°) states. Morrow (**1976**) concluded that this reclassification will increase the number of intermediate-wet states presented by Tieber et al. (**1972**) for both sandstone (from 7% to 33%) and carbonate (from 8% to 64%) core samples. Chilingar and Yen (**1983**) selected the $90° \pm 10°$ range for the intermediate-wet state and observed that 80% of the carbonate surfaces in their studies were oil-wet, and 12% were intermediate-wet.

In the absence of gas, two intermediate-wet states for heterogeneous wettability are generally recognized: fractional-wet (**Brown & Fatt, 1956**) and mixed-wet (**Salathiel, 1973**).

Fractional-wettability state implies spotted and heterogeneous wetting (*dalmatian wetting*) where scattered areas of the rock are strongly oil-wet whereas the rest of the rock surface is strongly water-wet or vice versa. This heterogeneity happens due to the irregularities in the rock geochemistry spanning the porous medium where the rock surface is composed of minerals with different surface chemical properties having different wettability alteration tendency.

The mixed-wettability state refers to the coexistence of water-wet and oil-wet pores on the porous medium categorized based on the pore size distribution (i.e., either smaller pores (MWS) or larger pores (MWL) are in the oil-wet state). It is theoretically believed that rock has a tendency to reveal an MWL wettability state (**Salathiel, 1973**): if oil with surface active components is accumulated in a reservoir during the primary drainage, it displaces the water from the larger pores. The wettability of this surface area is gradually altered to oil-wet. Skauge and Ottesen (**2002**), however, found both MWS and MWL wettability conditions in their experimental analysis of 13 North Sea sandstone reservoirs.

Pore wettability depends *only* on contact angle for a flat surface. For rocks with specified non-flat surfaces, however, pore wettability depends on both contact angles and pore structure (**Fenwick & Blunt, 1988**; **Øren & Pinczewski, 1995**): a coupled corner-angle of a pore and contact angle may characterize a pore either as water-wet or oil-wet depending on the fluid curvature. More precisely, for a half angle of the pore corner (β) as schematically shown in **Figure A-5**, we define the following relation:

$$\begin{cases} \theta_{12} < \frac{\pi}{2} - \beta: & \text{water } (\mathrm{PH}-1) - \text{wet pore}, \\ \frac{\pi}{2} - \beta < \theta_{12} < \beta - \frac{\pi}{2}: & \text{intermediate} - \text{wet pore}, \\ \theta_{12} > \frac{\pi}{2} - (\pi - \beta) = \beta - \frac{\pi}{2}: & \text{oil } (\mathrm{PH}-2) - \text{wet pore}. \end{cases} \qquad \textbf{Eq. A- 7}$$

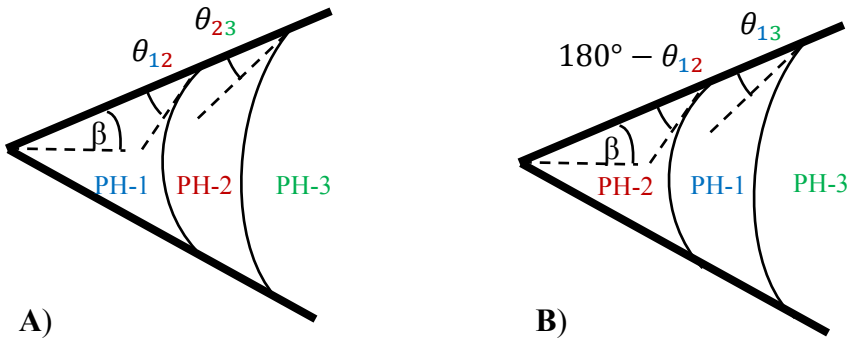

Figure A-5: A schematic representation of the fluid configuration in a corner pore with half-angle β within a **A**) water-wet (PH-1) rock **B**) oil-wet (PH-2) rock (Courtesy to **DiCarlo et al., 2000**).

In the core- and field-scale applications, however, one cannot predict in priori the overall rock wettability due to the complicated pore structure and the level of added heterogeneity.

SATURATION

In the literature, there are plethora of saturation-related quantities defined for the desired subsurface processes and applications. The widely used phase saturation definitions include critical, connate, irreducible, dendritic, trapped, free or flowing, effective, residual, and remaining saturation among others. The saturation history definitions include drainage and imbibition coming after ordinal numbers-- primary, secondary, tertiary, and so on. These quantities are not necessarily unique, independent and required. They even might not address a clear set of process/fluid characteristics. Different investigators may adopt ad-hoc formalism constituting of some of these parameters. From the application point of view, however, one should select and apply a minimum number of process-dependent and well-known set of parameters.

We apply primarily three parameters: (**i**) trapped (or residual saturation), (**ii**) critical, and (**iii**) free (or flowing) saturation for the modeling purposes in **Chapter 3** and **Chapter 4**. Yet, for the clarification purpose, we briefly review the selected saturation parameters as will be referred to in this dissertation.

Effective saturation

The effective saturation is an interim parameter to relax redundant parameter estimation in analytical and numerical calculations. It is plausible to adopt an ad-hoc definition for the quite applicable effective saturation. Two of the most applied definitions for the effective saturations have a subtracting and dividing origin. For instance, one may define effective saturation as the difference between the total saturation and minimum attainable saturation to avoid introducing stagnant and redundant critical saturation to a desired formulation ($S_j^* = S_j - S_{jc}$). Also, one may divide the phase saturation by maximum attainable saturation in porous media ($S_j^* = S_j/(1 - S_{ic})$) where *i* could by connate water saturation or phase *j* critical saturation.

Connate and critical saturation

These quantities refer to the lowest saturation attainable in the core samples. The connate saturation addresses the initial water saturation in the reservoir.

Critical saturation can be defined as the minium saturation attainable during the project lifetime. More specificly, the critical saturation is the saturation of fluids below which they do not flow in prous media irrespective of the capillary/trapping number. This definition resembles the irreducible or residual saturaiton.

These petrophysical quantities facilitate modeling effective saturation. Also, they assist in the modeling of dendritic phase saturation. Experimental results show that core sample cannot drain below a minimum phase saturation. This stagnant fluid can be due to phase trapping in microporosity among others.

Dendritic/non-conductive saturation

A non-wetting fluid in porous media may occupy a fraction of pore volume without contributing in electrical or hydraulic conductivity. This portion of fluid is contained in pores from which they cannot escape. They appear as tree-like branches in porous media and that the associated fluid

saturation is called *dendritic* saturation. The entry capillary pressure of control the dendritic pores in porous media and that the pore-to-throat size is an important parameter in the level of dendritic saturation as observed in porous media. Dullien et al. (**1977**) measured the dendritic saturation in a capillary-saturation experiment on Berea sandstone samples. Other investigators identified dendritic saturations based on the network-level analysis (**Chatzis, 1980**; **Chatzis & Dullien, 1985**; **Mohanty & Salter, 1982**).

Free or flowing saturation

This is the fraction of phase saturation contributing in fluid mobility within porous media. It is defined as the difference between total saturation and trapped saturation.

Irreducible saturation

Irreducible water saturation is a well-established petrophysical paramters and addresses the water volume that cannot be produced in the conventional primary production mechansims (i.e., low trapping number values). For example, consider a decreasing water saturation process operated in a water-wet rock till the water production stopped completely. The irreducible saturaiton refers to the remaining immobile water saturation in the sample.

Further, investigators categorized the irreducible water in a shaly and water-wet medium with high-clay content into two general bounding levels: (i) clay-bound water including the hydration water attached to clay surface area, the trapped water in the dead-ends, and by-passed water and (ii) the capillary-bounded water (**Peveraro & Thomas, 2010**).

Residual saturation

see Trapped saturation.

Trapped saturation

Trapped, residual, and remaining saturation are ambigueous terms defined in the petroleum

literature. The remaining saturation refers to the total volume of fluid left in the reservoir: it does not necessarily point to the trapped fluid in a pore scale. The operational and economic considerations like water-cut and gas-oil-ratio are among the sources of remaining saturaitons. For instance, if one designates a particular water-cut for a sepficied field, the oil production will be ceased by achieving the set vlaue irrespective of that mobile fluid that still exists in the reservoir. Although for practical prurposes the remaining saturaiton suffices, from the pore-scale perspective, the incomplete defintion remaining saturaiton does not describe the pore-scale fluid displacement.

Trapped, residual, and irreducible saturation terms address the immobile phase left in porous media following a particular applied process. As noted earlier, irrudicble saturation points to the immobile wetting fluid. Between the trapped and residual saturaiton, however, there is not consensus in the literature. Some investigators have prefered the trapped saturation for the discussion of immobile oil saturation while others use the residual oil saturation. While one may select the trapped gas saturaiton to address the immobile gas for a designated process, others may prefer the residual gas saturation. In this dissertation we use trapped and rediual terminology interchangeably except otherwise noted.

Trapped (or residual) saturaiton is a process dependent quantity. In the following, we discuss three examples of common trapping definitions in the petroleum and hydrology industries. Residual oil saturation to water addresses the immobile oil stranded in the reservoir and cannot be produced with the as-is waterflood even if the water injection would have continued for several pore volumes. This trapping mainly occurs due to the interaction of the applied forces on the displacing fluid. For the typical primary hydrocarbon recovery applciation where gravity does not assit, the capillary force dominate the viscous and gravitational forces. This lead to the capillary trapping due to local pore-scale heterogeneity or change in saturation history.

For the gas-based EOR application, the trapped terminology is more complicated. Not only

does the capillary trapping play a crucial role, but also the physics of the interacting fluids interfer. Lake et al. (**Lake et al., 2014**) discuss two impacting paramters on phase trapping in solvent-EOR applications: water blocking and phase behavior effecs. The trapped oil saturaiton by either of these principles, however, is producble providing enough contacting time and the displacing fluids.

CO_2 sequestration in underground resources involves several trapping mechanisms. They include (**i**) the primary structural trapping in the impermeable cap rock(s), (**ii**) the effective dissolution trapping with extensive amount of dissolved CO_2 stored in aqueous phase, (**iii**) the slow mineral trapping (CO_2 mineralization), and (**iv**) the fast and essential capillary (or residual) trapping in a capillary dominated displacement (**Bachu et al., 1994**; **Delshad et al., 2010**; **Iglauer, 2011**; **Pruess & García, 2002**; **Pruess et al., 2003**). The capillary trapping may also be categorized to local capillarity in more heterogeneous reservoirs and the conventional residual trapping (**Saadatpoor, 2012**).

For multiphase flow, the displacing fluid in proiri is not distinctive. Either water or gas may displace oil in a process involved in multiphase flow, e.g., gas mobility control techniques. In this situation, we opt the three-phase trapped (or residual) saturation for phase ($S_{jr}^{3P} = S_{jt}^{3P}: S_{or}^{3P}, S_{gr}^{3P}$) to distinguish that from that of two-phase flow ($S_{jr}^{2P} = S_{jt}^{2P}: S_{orw},\ S_{org},\ S_{gtw}$).

SATURATION HISTORY

In multiphase flow, saturation history varies frequently: either saturation direction or saturation path may change while the overall saturation is fixed. In general, saturation direction refers to hysteresis phenomenon. The saturation path adds one level of detail for hysteresis effect: it may address the impact of overall initial saturation on fluid displacement in porous media. For example, the phase trapping is a saturation-path-dependent phenomenon. Next, we first define the saturation direction followed by saturation path.

Saturation direction

drainage and imbibition are widely accepted notions referring to the saturation direction. Conventionally, these terms infer the wettability condition of a specified porous medium: drainage refers to the process in which non-wetting-phase saturation increases; and, imbibition states a process in which wetting-phase saturation increases. These terms are valid for two-phase flow and under a strong wettability condition. As the degree of freedom increases in three-phase flow, the drainage and imbibition turn to ambiguous terms: they are not valid statements for mixed- or neutral-wettability states. As a result, we avoid the ambiguous nomenclature and, in turn, adopt terminology of saturation direction as proposed by Saraf et al. (**1982**) in a general wettability condition.

The nomenclature by Saraf et al.'s (**1982**) denotes the overall saturation direction using the direction of saturation change for each phase. For a fluid flow of maximum of three phases in a porous medium, different processes are discernable as denoted in a three letter format of XYZ where X, Y, and Z stand for water, oil and gas saturation direction, respectively. Each letter may indicate increasing (I), decreasing (D), or constant (C) saturation depending on the phase saturation direction. Fifteen physically possible cases can be considered: 5 cases follow an oilflood (XIX), and the rest are either waterflood or gasflood (IXX or XXI) of which 12 cases are distinct processes. Six saturation direction involving with constant phase saturation are a particular case of more common cases. This excessive classification, however, can be avoided considering that constant saturation is a limit of the most representative indices for physical processes (IDD, IDI, IID, DII, DID, and DDI). **Figure A-6** schematically depicts possible saturation directions for an initial saturation combination *S* in a ternary diagram undergoing a waterflood, oilflood, or gasflood process. **Table A-1** lists all possible saturation directions together with the process indices.

Saturation path

As **Figure A-7** depicts, for a fixed saturation direction, e.g., a gasflood process (DDI), the saturation path may be different for each saturation pair. For example, S_1-E and S_2-E paths with constant initial oil saturation experience different saturation paths to achieve the ending saturation combination E in that they start with variable initial water and gas saturations. This represents the impact of initial fluid configuration on fluid displacement and ending fluid configuration at E. Strictly speaking, saturation path addresses the trajectory in which saturation space spanned irrespective of saturation direction (**Oak, 1990**).

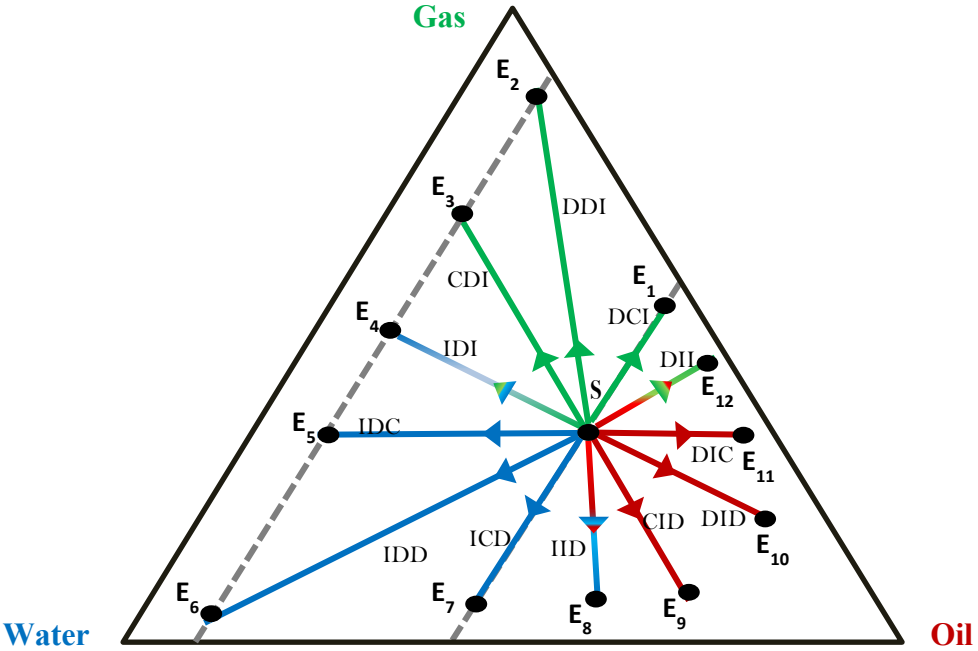

Figure A-6: Schematic of possible saturation directions for different processes starting from (S) and ending to E_1-E_{12}: water flood (blue: E4-E8), oil flood (red: E8-E12), and gas flood (green: E12, E1-E4) processes.

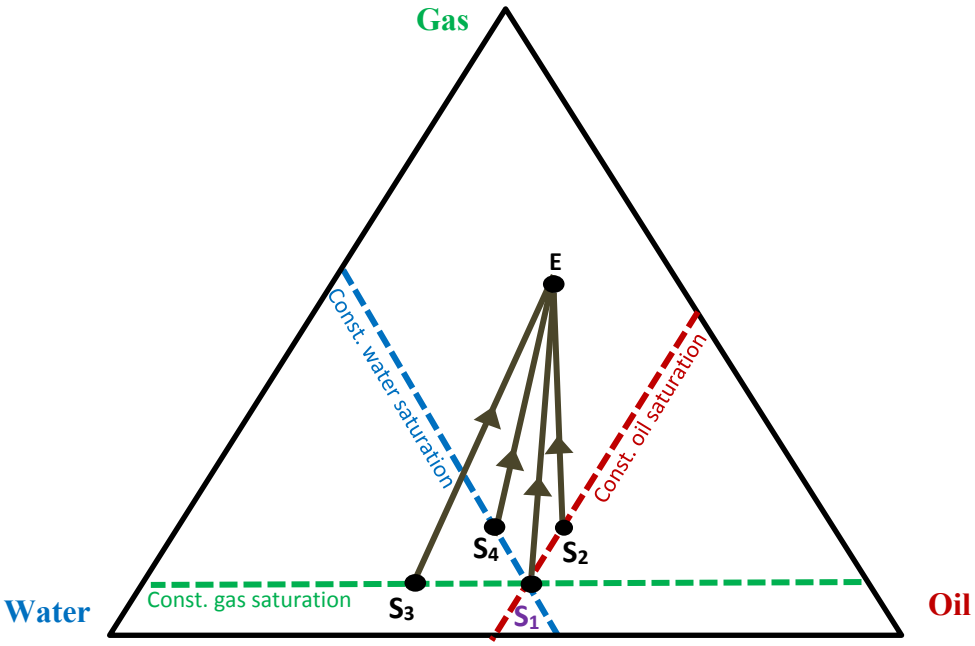

Figure A-7: Schematic of four saturation paths for a fixed saturation direction (DDI: gas flood) from S_1 and three other saturation combinations (i.e., X=2, 3, 4) to ending saturation point (E). Each saturation-path pair S_1-E and S_x-E experiences a unique saturation path. For example, S_1-E and S_3-E have different initial water saturations.

Table A-1: Saturation direction and physical process description

Endpoint	Process index	Physical process
E1	DCI	Gasflood at constant oil saturation
E2	DDI	Gasflood
E3	CDI	Gasflood at constant water saturation
E4	IDI	Gasflood and waterflood
E5	IDC	Waterflood at constant gas saturation
E6	IDD	Waterflood
E7	ICD	Waterflood at constant oil saturation
E8	IID	Waterflood and oil flood
E9	CID	Oilflood at constant water saturation
E10	DID	Oil flood
E11	DIC	Oil flood at constant gas saturation
E12	DII	Oil flood and gasflood

Appendix B: Foam Flow in Porous Media

This appendix discusses the foam functions of generation, transport, coalescence, rheology, and hysteresis in porous media along with reviewing some of the proposed foam models.

Gas mobility is controlled by the foam texture in the flowing part and the gas entrapment in porous media. The increased gas trapping due to the increased capillary pressure difference across the curved lamellae plays a crucial role in the gas mobility reduction. Foam bubble size controls the mobility of foam in porous media (**Hirasaki & Lawson, 1985**). The mechanisms controlling foam texture, or bubble size, are complex. To model these mechanisms, two different approaches have been used in the foam literature. The first option is to use the mechanistic methods which are theory-based models incorporating all the relevant physics regarding foam flow but time-consuming from a simulation point of view. The second option is to use ad-hoc empirical or semi-empirical models which lack parameters such as foam generation, coalescence, and transport. Yet, the latter is relatively easy to implement in the reservoir simulators and is not computationally demanding compared to no foam flow.

FOAM CREATION AND DESTRUCTION IN POROUS MEDIA

The foaming surfactant could be dissolved in water or in gas. The CO_2-in-brine foams are the conventional approach for foam generation and flow in porous media by dissolving surfactant in aqueous phase. This approach suffers from low-performance foam generation and flow: it induces a non-uniform foam quality and the foam stability diminishes far away from the injection area. The CO_2-soluble surfactants, however, are able to generate strong foam (**Xing et al., 2012**). Gas can also be injected along with an aqueous surfactant solution to create in-situ foam referred to low-tension gas flooding (**Farajzadeh et al., 2013**; **Kamal & Mardsen Jr., 1973**; **Lawson & Reisberg, 1980**; **Li et al., 2010**; **Srivastava et al., 2009**; **Wang et al., 2006**).

Three primary mechanisms by which foam is created in the porous media (**Kovscek & Radke, 1994**; **Ransohoff & Radke, 1988**) include snap-off, leave-behind, and lamella division: (**i**) After the gas invasion and expansion out of a pore space, the liquid starts to flow back to the pore and accumulates in that the gas expansion creates a capillary pressure gradient. By achieving enough capillary pressure reduction, the liquid snaps off the gas. (**ii**) By approaching two gas fronts, even with different velocities, to and passing through a liquid pore body, a liquid lens is left behind. In the presence of enough capillary pressure and pressure gradient, the stable lamella form without generating a discontinuous gas phase. (**iii**) The pre-existing mobile lamellae can be subdivided into many at the pore branching point, viz., lamella division.

The relative importance of these mechanisms depends on a critical capillary number. Above this critical parameter, the lamella division and snap-off are the dominant generating mechanism. However, below this value, the dominant mechanism would be leave-behind. An active number of germination sites, depending on pore geometry, fluid property, and capillary number (**Ransohoff & Radke, 1988**), determines the importance of snap-off mechanism. The surfactant properties and concentration does not affect this foam creation mechanism.

The snap-off is the predominant mechanism for foam generation (**Falls et al., 1988**) and is a mechanical process in that it repeatedly occurs in the porous media in one site. Not only does this mechanism create the lamella, but it affects the gas mobility directly through creating the trapped-gas saturation; this behavior is like the oil entrapment. Foam bubbles are thermodynamically unstable due to their high interfacial free energy and eventually are coarsened and destructed separating the liquid and gas phase. Gauglitz et al. (**2002**) and Kam and Rossen (**2003**) suggested that lamella creation mechanism during steady gas-liquid flow is controlled by lamella mobilization and division. They proposed that bubble destruction near the limiting capillary pressure, as will be discussed, is the primary lamella coalescence mechanism.

Chambers and Radke (**1992**) proclaimed two different foam-coalescence mechanisms: capillary suction and gas diffusion. Capillary suction initiates from the DLVO theory (**Derjaguin & Landau, 1941**; **Verwey & Overbeek, 1948**). This theory incorporates intermolecular interactions (i.e., repulsive and attractive forces, affecting the liquid film thickness in the lamella). As a case in point, adsorption of surfactant molecules to the film's gas-liquid surface along with the hydration forces in a small film thickness increase the excess repulsive forces; in contrary, there is attractive van der Waals forces destabilizing the film. To study the macroscopic film stability, this theory applies the Disjoining pressure (Π) which is a function of film thickness. Any negative values of π represent a net repulsive force resisting to the rupture of a film whereas any positive values of π represent a net attractive force causing film rupture. Moreover, the operative film thickness in the porous media is determined by the augmented Young-Laplace equation:

$$P_c = \frac{2\sigma cos\theta}{r} + \Pi(h). \qquad \textbf{Eq. B- 1}$$

The static lamella is stable as long as there are small distributions in capillary pressure. However, above a critical capillary pressure, the coalescence would be catastrophic (**Kovscek & Radke, 1994**).

The second destructive mechanism for existing lamellae pertains to the trapped bubbles. Due to the potential gradient in foam film (i.e., between the concave and convex sides of the film) gas can diffuse into the adjacent bubbles. This gas diffusion between bubbles tends to keep a bubble above a certain size (**Rossen, 1996**). Through the gas diffusion, lamellae may be driven to the pore-throat. If two lamellae reach to the same pore-throat and meet each other, then coalescence occurs.

The third lamella destructive mechanism is Pinch-off (**Myers & Radke, 2000**). When oil presents, if a stable water film, separating the gas bubbles from the oil droplet, does not exist, the

oil globule enters the gas-water interface of the two adjacent gas bubbles. Now, if $\sigma_{gw}^2 + \sigma_{ow}^2 > \sigma_{go}^2$, then the foam lamella pinches off from the oil globule causing the adjacent gas bubbles to join each other (i.e., coalescence happens).

FOAM TEXTURE

The porous medium mold and shape the foam bubbles irrespective of the pre-generated foams or the in-situ foam (**Ettinger & Radke, 1992**). Foam within the porous medium has three different states: Weak foam, intermediate foam, and strong foam corresponding to the low, intermediate, and high-pressure gradient. Strong foam represents a state at which foam is finely textured with a significant reduction in gas mobility or equivalently a large increase in pressure gradient accompanying low-water saturations. Weak foam, on the other hand, is referred to the state at which foam is coarsely textured with a slight reduction is gas mobility (i.e., a slight increase in pressure gradient and high water saturations). The controlling parameter to move among these states is the foam texture (i.e., the number of lamellae per unit volume). The bubble size is near the average pore size in the strong foam in the low-quality region (i.e., low gas volume fraction) (**Alvarez et al., 2001**; **Mamun et al., 2002**). This makes the numerical simulation of strong foam in a low-quality region relatively straightforward. However, the bubble size in the strong foam in the high-quality part changes, significantly, with rock-foam interactions close to the limiting capillary pressure (i.e., the feedback mechanism) (**Kam & Rossen, 2003**). This mechanism behaves like a bumper and mitigates the fluctuations in the capillary pressure so that capillary pressure is maintained near the limiting capillary pressure. The bubble size, accordingly, requires being changed to compensate for variations in the capillary pressure.

FOAM HYSTERESIS

Gas mobility reduction due to foam applications in porous media may exhibit hysteretic behavior due to either relative permeability/capillary pressure or foam generation and flow in porous media

(**Beygi et al., 2015**; **Lotfollahi et al., 2016**). The experimental results show hysteretic behavior in the foam generation due to two general parameters: saturation history and foam parameters. The saturation direction impacts the foam strength: the generated foam in increasing and decreasing gas saturation processes are not identical. Gas trapping is a dynamic process even on the microscopic scale in that the foam is trapped and remobilized continuously in porous media.

Generation experiments are typically conducted by a gradual increase in flow rate (or pressure gradient) at fixed foam quality experiments to generate strong foam, but there are very limited data to reduce injection rate (or pressure gradient) after the foam generation. Kibodeaux (**1997**) applied high-pressure CO_2 and did not find a sudden increase, but a continuous increase in pressure gradient with increasing injection rate, and a hysteresis behavior upon decreasing the injection rate to low values. A coarse foam at the minimum required pressure-gradient jumps to a strong foam experiencing an irreversible process (**Gauglitz et al., 2002**; **Shi, 1996**). The mobility reduction factor exhibited a hysteresis behavior in a cycle of increasing/decreasing surfactant concentration (**Simjoo et al., 2013**). The population balance models capture the abrupt jump in foam generation. Lotfollahi et al. (**2016**) introduced a normalized generation function (bounded between 0 and 1) to the STARS foam model to capture the full spectrum of coarse foam, transient foam, strong foam, and foam hysteresis in porous media. However, the best choice for generation function still remains controversial. The could obtain a good match for the different types of foam generation and foam hysteresis experiments in their paper and data reported by Gauglitz *et al.* (**2002**).

The foam applications involve alternative injection scheme in many places. The hysteresis model then must capture cycle-dependent trapped saturation effect arising from the multicycle process along with the hysteresis in the foam generation.

FOAM TRANSPORT

Foam within the porous media is a non-linear fluid and its viscosity and relative permeability and correlated. Thereby, the foam mobility components (i.e., relative permeability and viscosity) cannot be separately computed and then combined. However, through modeling the foam flow, one needs to consider the parameters affecting both relative permeability and viscosity. Generally, the flowing gas changes the flow resistance and creates an effective gas viscosity. The confined foam bubbles transport as bubble-trains (**Kovscek & Radke, 1994**) behaves like a non-Newtonian fluid.

In the foam flow modeling, the same water relative permeability function is applicable since the liquid phase still flows through a relatively small pore space, where non-wetting phase mainly does not exist (**Bernard & Holm, 1964**; **Huh et al., 1989**; **Kovscek & Radke, 1994**). However, foam affects the steady-state water saturation in that, readily, more pores are filled with non-wetting phase compared to the surfactant-free gas-water flow. In contrary, the gas relative permeability, mainly due to trapped gas reduces the relative permeability could be reduced in the foam flow by 5 to 5000 times compared to no foam flow.

FOAM FLOW MODELING IN POROUS MEDIA

The strength and mobility of foam depend on the foam texture, which, in turn, depends on rock properties, fluid-rock interaction, surfactant properties, liquid and gas flow rates, and the oil properties. The evolution of foam texture, and hence the gas mobility reduction, is directly considered in the foam theoretical models making them a more precise tool to predict the foam flow within the porous media compared to empirical methods. A variety of theoretical models based on the laboratory measurements have been developed since the early 90' including (**i**) the population-based models (**Falls et al., 1988**; **Friedmann et al., 1991**; **Kovscek et al., 1995**), (**ii**) fractional-flow models (**Ashoori et al., 2010**; **Rossen et al., 1999**; **Zhou & Rossen, 1995**), (**iii**)

empirical and semi-empirical models (**Fisher et al., 1990**; **Mohammadi et al., 1993**; **Patzek & Myhill, 1989**), (**iv**) percolation (or network) models (**Rossen & Gauglitz, 1990**), and (**v**) catastrophe models (**Kam, 2008**). The percolation methods need high computational simulation time and in some cases, especially in the transient displacement, it is practically impossible to keep track of all the required modeling parameters within each subtle grid block in the field-scale simulations. The network models, thereby, are not appropriate for full three-dimensional, heterogeneous, and field-scale, reservoir simulations. Among all of these foam models, the population balance is the most mechanistic method explicitly addressing both the foam texture evolving within the porous media and accounting for non-Newtonian gas mobility with respect to bubble population dynamics. Inasmuch as, the complexity and many needed parameters involved in this type of foam modeling bring a shortcoming to this model, many researchers have been trying to simplify this method (**Bertin et al., 1998**; **Chen et al., 2010**; **Friedmann et al., 1991**; **Hatziavramidis et al., 1995**).

Population-balance models

The population-balance methods are the viable mechanistic foam models, accounting for all the pore-level events including the foam generation, coalescence, and transport. These methods differ, mainly, in their representation of both physical and mathematical foam generation and coalescence mechanisms.

The balance-population methods comprise two components: firstly, tackling non-Newtonian gas mobility (i.e., gas relative permeability and effective viscosity in the presence of foam); secondly, incorporating foam into reservoir simulators the same manner that mass, momentum, and energy transports in porous media are modeled (**Kovscek et al., 1995**). The mass conservation equation for the foam, as a component of gas phase, is

(Rate of foam texture modification) + (rate of foam bubbles entrapment) + (foam bubbles convection) = (Net rate of foam generation) + (source-sink foam bubbles)

$$\frac{\partial\left[\emptyset\left(S_f n_f + S_t n_t\right)\right]}{\partial t} + \nabla.\left(u_f n_f\right) = \emptyset S_g\left(k_1\left|v_w\right|\left|v_f\right|^{\frac{1}{3}} - k_{-1}\left|v_f\right| n_f\right) + Q_b,$$

where

$$S_g = S_f + S_t, \quad \textbf{Eq. B- 2}$$

Total gas saturation = flowing gas saturation + trapped gas saturation

$$\bar{u}_f = \frac{\bar{\bar{K}} k_{rf}}{\mu_f}(\nabla\Phi), \text{Darcy velocity}, \quad \textbf{Eq. B- 3}$$

$$\mu_f = \mu_g + \frac{\alpha n_f}{|v_f|^{\frac{1}{3}}}, \text{ effective foam viscosity}, \quad \textbf{Eq. B- 4}$$

$$k_{rf} = k_{rg}^0 S_{fd}^{e_g} = k_{rg}^0\left[X_f(1 - S_{wd})\right]^{e_g}, \text{ foam relative permeability}, \quad \textbf{Eq. B- 5}$$

$$k_{rw} = k_{rw}^0 S_{wd}^{e_w}, \text{ water relative permeability}, \quad \textbf{Eq. B- 6}$$

$$S_{wd} = \frac{S_w - S_{wc}}{1 - S_{wc}}, \text{ normalized water saturation}, \quad \textbf{Eq. B- 7}$$

$$X_t = 1 - X_f = \frac{S_t}{S_g} = X_{t,max}\left[\frac{\beta n_t}{1 + \beta n_t}\right], \text{ trapping fraction}, \quad \textbf{Eq. B- 8}$$

$$v_i = \frac{u_i}{\emptyset S_i}, \text{ phase interstitial velocity}, \quad \textbf{Eq. B- 9}$$

$$k_1 = k_1^0\left[1 - \left(\frac{n_f}{n^*}\right)^{\omega}\right], \text{ the generation rate constant}, \quad \textbf{Eq. B- 10}$$

$$k_{-1} = k_{-1}^0\left(\frac{P_c}{P_c^* - P_c}\right)^2, \text{ the coalescence rate constant}, \quad \textbf{Eq. B- 11}$$

$$P_c^* = P_{c,max}^* \tanh\left(\frac{C_s}{C_s^0}\right), \text{ limiting capillary pressure}. \quad \textbf{Eq. B- 12}$$

where $P_{c,max}^*$ is a limiting value for P_c^* and C_s^0 is a reference surfactant concentration for strong net foam generation. ω is a constant determining the shape of the inverse proportionality of foam-germination sites to the pre-existing gas bubbles. n^* denotes an upper limit for the concentration of foam bubbles that is related to the pore size. $X_{t,max}$ is the maximum fraction of trapped foam, and β is a trapping parameter. Note that If no pre-generated foam is injected or produced within

the simulation, Q_b, foam bubbles number per unit volume per unit time, is practically zero.

Local-equilibrium approximation to the full population-balance models

Chen *et al.* (**2010**) proposed a simplified approximation to the population-balance method for computing number density, or number concentration, of foam bubbles per unit volume of flowing gas, n_f. This model provides an appropriate prediction of field-scale foam applications.

By analyzing the pressure drop results in their experimental work, Ettinger and Radke (**1992**) concluded that foam propagated like a sharp foam front and that local equilibrium is a good approximation. Consequently, Chen *et al.* (**2010**) set the net rate of foam generation in Eq. 2 to zero to equalize the foam generation and coalescence rates. This results in the following equation which must be solved for n_f. Note that if no surfactant presents, the foam texture is set to zero before solving this equation.

$$n_f^{\omega} + \frac{n^{*\omega} k_{-1} |v_f|^{\frac{2}{3}}}{k_1^0 |v_w|} - n^{*\omega} = 0. \qquad \textbf{Eq. B- 13}$$

Bubble-population balance simplifications

Some investigators attempted to simplify the population-balance method. Hatziavramidis *et al.* (**1995**) proposed a model in which the just relative permeability of the weak foam is modified. In the strong foam, the viscosity of the foam is also changed. Bertin *et al.* (**1998**) proposed a bubble population correlation instead of the bacterial balance for the foam.

Hirasaki and Lawson (**1985**) introduced a foam model based on two simultaneous mechanisms affecting mobility of gas in the presence of foam. The reduction of gas relative permeability because of gas trapping following the Falls *et al.* (**1989**) and the increase in gas apparent viscosity due to the resistance of movement of lamellae following the work of Friedmann *et al.* (**1991**). The foam texture modeling, used in the apparent viscosity expression, is based on a modified version of the bubble population correlation (**Bertin et al., 1998**).

Empirical and semi-empirical models

As mentioned above, the consensuses of the foam researchers are that foam does not exist as a bulk phase, foam does not change the water mobility in the porous media, and the foam texture controls the gas mobility. One simple way of including the foam effect, thereby, is through the use of empirical, or semi-empirical, functions to alter gas relative permeability, gas viscosity, or both.

1) Marfoe and Kazemi (**1987**) modified gas viscosity to incorporate foam effect in reservoir simulations. Their model implicitly applies foam bubble size correlation with foamed gas velocity and available flowing water content,

$$\mu_{gf} = \mu_g\left[1 + RC_s(S_w - S_{wc})f(u_g)\right]. \quad \textbf{Eq. B- 14}$$

Here, R and $f(u_g)$ are experimentally fitting parameters.

2) Islam and Farouq Ali (**1990**) expanded the model by Marfoe and Kazemi (**1987**) by adding the detrimental effect of oil in the foam texture along with the effect of absolute permeability and pressure gradient on foam,

$$\mu_{gf} = \mu_g \frac{[1+Df_c(C_s)(S_w-S_{wc})f_k(k)]+f_p(\nabla p)}{1+ES_o^2}. \quad \textbf{Eq. B- 15}$$

The constants D and E and functions f_c, f_k, and f_p are the fitting parameters. Changing the gas relative permeability in the foam flow through the mobility reduction factor (MRF) concept implying that gas relative permeability is reduced according to this parameter depending on foam texture. The general form is to reduce the gas relative permeability based on MRF.

$$k_{rgf}(S_g) = \frac{k_{rgf}(S_g)}{1+MRF}. \quad \textbf{Eq. B- 16}$$

3) Considering a constant MRF. However, the shortcoming of this model, working with an experimentally-fitted constant MRF, is that the forced changes on MRF due to affecting parameters on foam mobility, e.g. gas velocity (or capillary number), surfactant

concentration and presence of oil, are not considered through the simulation.

4) The steady-state, implicit texture foam model in CMG-STARS (**2012**), the MRF is modeled considering surfactant adsorption, partitioning, degradation, and transport through a variety of interpolating parameters as follows:

$$MRF = fmmob\ F_1\ F_2\ F_3\ F_4\ F_5\ F_6. \qquad \textbf{Eq. B- 17}$$

The reference foam mobility reduction factor, fmmob, is achieved at measured values of surfactant concentration, C_s, Capillary number, N_{ca}, above two-time foam generation point capillary number, N_{ca}, fgp, and zero oil saturation. This value usually is 5 to 100 depending on the strength of the foam. F_i parameters control the effect of different parameters on foam texture flow. F_1 is composition contribution. F_2 refers to oil saturation between two low and high oil saturations. F_3 denotes capillary number contribution. F_4 addresses contribution of N_{ca}, f_{gp} with respect to N_{ca}. F_5 is oil mole fraction contribution. And, F_6 is salt contribution.

Lotfollahi et al. (**2016**) combined a normalized generation function with CMG-STARS foam model to cover experimental results thoroughly. It allowed to capture multiple states of foam (coarse and strong) at a specified injection condition as referred to foam hysteresis.

5) Mohammadi *et al.* (1995) introduced another formula for the potential effect of surfactant physical properties and concentration on the foam rheology.

$$MRF = \frac{\nabla p_{foam}}{\nabla p_{no\ foam}} \left(\frac{C_s}{C_s^{max}} \right)^{e_s}. \qquad \textbf{Eq. B- 18}$$

The maximum surfactant concentration for foam effect, C_s^{max}, and e_s are fitting parameters and depend on surfactant properties.

Fixed-P_c^* models

The foam texture depends on capillary pressure (**Khatib et al., 1988**). As gas fractional flow increase, the capillary pressure measured during a foam displacement increases up to a limiting capillary pressure, P_c^*. This increase in capillary pressure makes the lamella (i.e., liquid film surrounding the gas phase in the foam) less stable. Further increase in gas fractional flow results in keeping the capillary pressure at its limiting value while the foam texture starts coarsening. The magnitude of P_c^* depends on surfactant properties and concentration and rock type (**Khatib et al., 1988**). An abrupt transition from a strong foam to no foam at the P_c^*, therefore, results in a sudden change in gas mobility close to the P_c^*. In other words, the system keeps the capillary pressure at its limiting value for a broad range of flow rate and foam quality. Moreover, Capillary pressure is a function of water saturation. The water saturation, therefore, will be kept constant (i.e., at S_w^*). The foam texture will change in the foam flow somehow to maintain the water saturation and capillary pressure at their limiting values. The pressure gradient can be calculated from Darcy's law applied to the water phase having unaffected relative permeability in the presence of foam

$$\nabla p = u_w \frac{\mu_w}{k k_{rw}(S_w^*)} = \frac{u_w}{\lambda_w}. \qquad \textbf{Eq. B- 19}$$

In the absence of significant capillary pressure gradients, ∇p is the same for water and gas. This implies that pressure gradient can be calculated without knowledge of foam texture in advance. The fixed-P_c^* approach, thereby, is simpler than other theoretical approaches in that there is no need to determine foam generation, coalescence, and trapping. This method fits strong foams at the relatively low flow rates and high foam qualities typical of many IOR processes (**Rossen et al., 1999**). However, this model does not apply to transient foam flow (i.e., foam generation period and at the leading edge of an advancing foam) (**Friedmann et al., 1991**; **Patzek & Myhill, 1989**; **Zhou & Rossen, 1995**). For aforementioned foam, the gas mobility at $S_w = S_w^*$ is,

$$\lambda_g = \lambda_w^* \frac{u_g}{u_w} = \lambda_w^* \frac{1-f_w}{f_w}. \qquad \textbf{Eq. B- 20}$$

The transition between low-mobility gas with foam and higher-mobility gas without foam occurs over a narrow range in water saturation close to the S_w^*.

UTCOMP model

Rossen *et al.* (**1999**) proposed this model. It was improved by Cheng *et al.* (**1939**) in the UTCOMP simulator by further assuming that surfactant just dissolves into the water phase and does not alter either the surface tension or the residual saturations.

A foam-free gas relative permeability, k_{rg}^0, is computed

$$\lambda_g = \lambda_w^* \frac{u_g}{u_w} = \lambda_w^* \frac{1-f_w}{f_w}, \qquad \textbf{Eq. B- 21}$$

a) If $S_w < S_w^* - \varepsilon \; or \; C_s < C_s^0 \rightarrow k_{rg} = k_{rg}^0$,

b) If $S_w^* - \varepsilon \leq S_w \leq S_w^* + \varepsilon \; and \; C_s \geq C_s^0 \rightarrow k_{rg}^f = \frac{k_{rg}^0}{1+\frac{(R-1)(S_w - S_w^* + \varepsilon)}{2\varepsilon}}$,

c) If $S_w > S_w^* + \varepsilon \; and \; C_s \geq C_s^0 \rightarrow k_{rg}^f = \frac{k_{rg}^0}{R}$.

Here, $R = R_{ref}\left(\frac{u_g}{u_{g,ref}}\right)^{\sigma-1}$. R_{ref} is the value of R at the reference gas volumetric flux $u_{g,ref}$, and σ is the power-law exponent (i.e., σ=1) depicts Newtonian behavior and σ<1 is a shear-thinning behavior. S_w^* is the saturation at which foam collapses. When ε, a model parameter, approaches zero, the mobility in the high-quality regime is controlled by S_w^*. However, R controls the gas mobility in the low-quality regime.

Fractional flow methods

Foam mobility representation in a reservoir simulator calls for solving foam-transport differential equations. Although the general approach of incorporating complex transport model functions directly into the simulator, e.g. the population-balance methods, is principally applicable, the method of characteristics (MoC) is a simpler alternative. This approach gives promising results

when its associated assumptions are met. Nevertheless, even in the case when not all of the assumptions are qualitatively satisfied, the MoC offers significant insights into process mechanisms (**Rossen et al., 1999**).

The fractional-flow method, a particular case of the method of characteristics, has been a traditional way of modeling immiscible flooding since 1941 (**Rivet et al., 2010**). Although the involved mechanisms in foam flow are both numerous and complex, the fractional-flow methods can be used to mitigate the computational costs associated with the full analytical methods, e.g. percolation methods and population-based models.

Applying the limiting capillary pressure concept (**Khatib et al., 1988**) into the fractional-flow methods greatly simplify the modeling task. The central part of the fractional-flow methods is constructing the time-distance curves independent of the pressure gradient and flow rates. These curves can be constructed either directly from core-flood pressure data or through the tangent line to the fractional flow curves.

The slope of the fractional-flow curve at a specified saturation equals the velocity of a saturation wave at that saturation. Neglecting the dispersion, one can draw a line from the origin to the constructed fractional flow curve at the injected fractional flow to find the chemical shock that separates regions of different surfactant concentration (i.e., rearward waves of higher velocities overtake the forward waves of slower velocities) (**Rivet et al., 2010**).

The major deficiencies of fractional-flow models are the assumption of incompressible fluid, neglecting the interaction between rock and fluid, applying only the steady-state foam flow, and their limitation of one-dimensional modeling. Note also that if P_c^* depends on gas or liquid flow rate (**Friedmann et al., 1991**; **Khatib et al., 1988**), the fixed-P_c^* model would be an approximation method as this condition contradicts the necessary assumption of this model. Moreover, the model applicability may be lessened due to hysteresis and gas trapping mechanisms

affecting the capillary pressure and saturation relationship. The surfactant adsorption can be incorporated into the model as Pope (**1980**) described for fractional-flow theory. Rossen and coworkers (**1995**; **1999**) presented the fractional flow theory for foam flow application. This theory is the basis of other published fractional flow theory models.

Dholkawala et al. (**2007**) proposed a fractional flow theory based on a local equilibrium steady-state foam flow. To find the foam texture, n_f, they equalized their proposed mechanistic in-situ creation and coalescence expression considering the non-linear relationship between injection rates and pressure gradient as follows:

$$r_g = C_g S_w (\nabla p)^m \quad \text{, rate of lamella creation,} \qquad \textbf{Eq. B- 22}$$

$$r_c = C_c n_f \left(\frac{1}{S_w - S_w^*}\right)^n \quad \text{, rate of lamella coalescence,} \qquad \textbf{Eq. B- 23}$$

$$n_f = \frac{C_g}{C_c} (S_w - S_w^*)^n \, S_w (\nabla p)^m \quad \text{, foam texture.} \qquad \textbf{Eq. B- 24}$$

The flow of liquid and gas phase based on Darcy's law is:

$$u_w = \frac{k k_{rw} \nabla p}{\mu_w} \qquad \textbf{Eq. B- 25}$$

$$u_g = \frac{k k_{rg} \nabla p}{\mu_g^f} \qquad \textbf{Eq. B- 26}$$

where k_{rw} and k_{rg} are water and gas relative permeability calculated based on Corey-type function in the absence of foam. Note that effect of foam is just considered in the effective gas viscosity and not included in the relative permeability, because mobility components are inseparable.

$$k_{rj} = k_{rj}^0 \left(\frac{S_j - S_{jr}}{1 - S_{gr} - S_{wr}}\right)^{e_j} \qquad \textbf{Eq. B- 27}$$

The effective gas viscosity follows the non-Newtonian gas viscosity presented by **Eq. B-4**. A simultaneous solving of **Eq. B-** 26 and **Eq. B-** 27 determines the required parameters for constructing the fractional flow curve (i.e., u_g and μ_g^f).

Appendix C: Electrolyte Solution Modeling

This appendix is a compendium of the activity modeling of electrolyte solutions as required for the aqueous compositional relative permeability modeling. We first review the aqueous solutions and its internal potentials. We then address the proposed methods and formulations to model the activity of its components in detail.

Electrolyte solutions

Electrolyte solutions comprising of solutes and solvents are solutions that can conduct electricity. This distinctive feature of electrolyte solution sets it apart from common non-electrolyte solution (**Prausnitz et al., 1999**). A solution of dissolved electrolytes results in the coexistence of ions and undissolved molecules. The electrically charged ions demonstrate that the electrostatic interactions differ in the range and properties from the hard-core interactions as modeled by the classical van der Waals-based formulations.

Commonly used EOS models and the modern liquid models lack the capability of predicting the properties of aqueous solution accurately, at least, when these non-electrolyte EOSs are unassisted (**Prausnitz & Tavares, 2004**). These models have deficiencies to model the phase equilibria of compositions including pure water: the tetrahedral liquid structure of water molecules compared to those of hard-sphere fluids accounts for the unique properties of water. Qualitatively, adding an electrolyte makes modeling of aqueous solution more complicated.

The intricacies of electrolyte system and modeling its activity coefficient compared to the non-electrolyte systems, e.g., elements, compounds, and hydrocarbon mixtures are reviewed in the next section.

Electrolyte interaction potentials

The solution of the dissolved electrolytes in a solvent result in the coexistence of ions and

undissolved molecules. Thorough understanding and modeling of the electrolyte systems require coping with several interaction levels between solutes and solvent(s) due to Coulomb (electrostatic), entropic (repulsive), and discrete quantum (chemical-bonding) forces. The intermolecular (or inter-particle) interactions are noticeable if they surpass the thermal energy ($K_B T$) (**Israelachvili, 2011**). In that the molecules and particle interact in a variety of energy levels, to date no single formulation can report them all. Not only does one require a recipe of approaches to reflect solute-solute, solute-solvent, and solvent-solvent interactions, also each of them involve diverse range of interactions which essentially contrast each other.

The solvent-solvent interactions include permanent dipole and quadrupole moments, and induced-ion dipoles within solvent neutral molecules forming an associated liquid. Further, the solute ions (or its un-dissociated molecules) may interact with solvent molecules. The solute-solvent interaction may also interfere the short-range ion-ion interactions depending on the solvation (or structuring) of solvent molecules process and the formation of the ion-association (i.e., ion-contact, solvation-shell contact, or solvation-shell shared) (**Wright, 2007**).

Molecular moments have a crucial role in electrolyte systems as encountered in subsurface groundwater and hydrocarbon resources for species with small-size or large dipole moment molecules: water molecules have considerable dipole moments (water dipole moments=1.84 > threshold dipole moment of 1.0). Besides, the quadrupole moments are of particular interest to molecules like CO_2 having significant charge concentration at four separate locations per molecule (**Davis, 1996**). The models describing the hydrogen-bonding for an associated liquid may address these interaction levels for both association interactions: self-associating and cross-associating (or solvation). For example, the water-solvent-hydrocarbon system, as encountered in the application of solvents to reduce condensate and water blockage in gas-condensate reservoirs, contains two self-associating compounds: water and alcohol, e.g., methanol and ethanol. The CO_2 sequestration

in aquifer comprises the cross-associating between water and solvated CO_2. As a result, the association interactions must be included in the electrolyte modeling. Nevertheless, to date, there is no versatile model to predictively model the liquid-liquid or vapor-liquid equilibria for cases consisting of alcohol and CO_2 components.

The solute-solute interactions comprise long-range charge-charge Coulombic interactions and short-range interactions between ions and polar molecules, e.g., hard-core repulsion, attraction, and ion-induced dipole interaction. At very high dilute conditions, the only necessary force between ions is large–range force of charge-charge interactions. As the ionic strength increases, however, short-range forces dominate the large-range interionic forces.

For the aqueous electrolyte system, based on temperature, pressure, and solute type and concentration, ions from solvation process associated with the molecules and other charged particles differently. Upon solvation in the aqueous phase, the water molecules may also be polarized by the electrical charges and, thereby, electrolytes complicate their solution by forming a strong (complete) or weak (partial) dissociation. These, further, signifies the complicated task in modeling the behavior of electrically charged species.

Electrolyte activity modeling

There are numerous theoretical, semi-empirical, or empirical methods to model the aqueous phase behavior. From a theoretical perspective, one may categorize the models based on the solvent models, solute structures in solution, or the base theories of electrolyte models.

The electrolyte theoretical models can be developed according to the solvent modeling as primitive or non-primitive models (**Barthel et al., 1998**). The primitive (or continuum-solvent) methods represent electrostatic interactions without considering the ion-solvent interactions. This model subsumes solvent molecules effect implicitly through the significant contribution of solvent in the electrolyte solution (i.e., the dielectric-buffer effect of reducing Coulomb interaction forces

among mixture ions-- also called *dielectric continuum* model). The non-primitive models, however, include the presence of solvent molecular structure explicitly. In other words, the solvent is discrete and modeled as a collection of hard spheres with embedded point dipoles. The primitive-assumption alleviates the mathematical modeling because it does not require theories to relate inter-particle interactions in a solvent to its bulk properties solved. The non-primitive methods, on the other hand, necessiate accurate theories to include long-range effects of the coulomb interaction between ions (**Loehe & Donohue, 1997**).

The solutes give the dissimilar type of structure to the solution as non-electrolyte, weak-electrolyte, and strong-electrolyte for the molecular unit, molecular-ion unit, or ions, respectively. Upon solvation in the aqueous phase, the solvent molecules are polarized by the electrical charges and, thereby, electrolytes complicate their solution by forming a strong or weak dissociation. The former represents electrolytes that completely dissociate to ionic species with no significant amounts of molecular species present. The latter, however, comprises of the molecules partially dissociating to the ions at moderate concentration and the rest of molecules remaining as undissociated and neutral molecule species; in weak dissociation, therefore, the molecules are in equilibrium with the ions derived from them. This complex behavior adds difficulty for the researchers to predictively model the behavior of electrolyte aqueous systems in a broad range of pressure and temperature.

Statistical mechanics connects microscopic level of molecular interactions and macroscopic level of thermodynamic properties. One requires the nature of the constituting particles of the electrolyte system and the inter-particle interactions to feed the statistical mechanics. This established package, in turn, delineates the macroscopic thermodynamic conclusions. From the statistical mechanics' perspective, we may group the electrolyte modeling based on the intended mathematical approach, such as *Poisson-Boltzmann equation*, *integral*

equation theory, or *perturbation theory*. Nevertheless, each of these mathematical methods with varying level of computational cost is applicable to both the aforementioned primitive and non-primitive methods. These theories have attempted to enhance understanding of the aqueous solution. Not only do they not provide rigorous computation methods, but their unaided application still has limitations for some interesting systems for which these models offer the most uncertain guide to understanding. These include, but are not limited to, the system of subsurface resources exhibiting salting-out effect (i.e., weak interaction of an electrolyte with a non-electrolyte other than the solvent, polyelectrolyte system, or electrolyte system constituting of solutes at high concentrations). The semi-empirical models and approximations are, thereby, copious to describe the properties of electrolyte solution (**Rafal et al., 1994**).

Table C-1 represents two sets of the developed electrolyte empirical models based on extensive experimental analysis of diverse electrolyte solutions. On the other hand, these models are tailored to the particular fitting window of temperature, pressure, and composition of electrolytes. The capability of models, therefore, is highly disputed for its application to a broad range of operational conditions.

Table C-1: Two sets of activity models for aqueous electrolyte solutions (empirical/semi-empirical models)

Authors	Activity Model Formulation	Remarks
Meissner and coworkers (**1972a**); (**1972b**); (**1978a**); (**1978b**); (**1980**)	$\log \Gamma_{ij} = \left(z_i \sum_{\substack{m=2k,\\ k>0}} V_{im} I_m log\Gamma^0_{im} + z_j \sum_{\substack{n=2k-1,\\ k>0}} V_{jn} I_n log\Gamma^0_{jn} \right) / [I(z_i + z_j)]$; $V_{ij} = 0.5(Z_i + z_j)^2 / z_i z_j$; $I_j = 0.5 m_j z_j^2$; $I = 0.5 \sum_j m_j z_j^2$ $q_{ij,mix} = (\sum_{m=2k} I_m q^0_{im} + \sum_{n=2k-1} I_n q^0_{nj})/I$ $\Gamma_{ij} = [1 + B(1 + 0.1I)^{q_{ij,mix}} - B]\Gamma^*$; $B = 0.75 - 0.065 q_{ij,mix}$; $\log \Gamma^* = -0.5107\sqrt{I}/(1 + C\sqrt{I})$; $C = 1 + 0.055 q_{ij,mix} \exp(-0.023 I^3)$.	Resemble the *DH* formulation but Meissner correlation is empirical; Defining reduced activity coefficient (Γ) for binary solution; Brønsted (**1922**) proposed that the value of mean activity coefficient of any electrolyte in a mixed solution depends primarily on the interaction of electrolyte cation (anion) with all anions (cations) of the solution. The model is applicable to multicomponent solution; q_{MK}= adjusting parameter independent of temperature and salt type; Γ^0_{ij} and q^0_{ij}: reduced activity coefficient and Meissner parameter of electrolyte *ij* in a pure solution. $a_{MK}$and $b_{MK} = f(T,$ salt type).
Goldberg and coworkers (**1979**); (**1981a**); (**1981b**)	$\ln \gamma_i^m = -\frac{A_G \sqrt{I}}{1 + B_G \sqrt{I}} + \sum_{k=1}^{3} C_{G,k} m^k$; $\ln \gamma_i^m = -A_{G1}\sqrt{I} - A_{G2} I ln(I) + \sum_{i=1}^{n} B_{G,i} m^{(i+1)/2}$	Linear term to add the dynamics of relative permittivity with concentration. They proposed three models (the third model takes $A_{G2} = 0$). The models did not introduce the temperature dependency.

Poisson-Boltzmann-based activity models

Debye and Hückel (**1923**) (DH) derived an expression for the excess Helmholtz energy function for an ideal solution of charged ions. They applied the theory of statistical mechanics for a primitive aqueous solution, made several assumptions, and solved the resulting Poisson-Boltzmann equation. The Poisson equation accounted for an average electrostatic potential of ions considering the distributions of other point-charge ions in solution. The application of a linearized form of the Boltzmann energy of interaction provided the charge density distribution. The *extended* DH models have the following manner for the rational (mole fraction scale) activity coefficient:

$$\ln \gamma_i^* = -\frac{|Z_+ Z_-| A_{DH} \sqrt{I}}{1 + B_{DH} \dot{a}_{DH}^{\alpha_{DH}} \sqrt{I}} + \sum_i C_{i,DH} I^{D_{i,DH}}, \qquad \textbf{Eq. C- 1}$$

where Z_+ and Z_- are the dissociated ions' valences, A_{DH} is a constant depending on the temperature and the solvent, B_{DH} is the DH constants, $C_{i,DH}$ and $D_{i,DH}$ are the model parameters, I expresses ionic strength, and $\alpha_{DH} = 1$ except otherwise described; $\dot{a}_{DH}$ is the distance of the closest approach between two ions (varying between 2.5-11 $A°$) and implies that ions cannot get closer to each other than $\dot{a}_{DH}$ which is a simplified perception of the core hard-sphere repulsion term added to the modified DH theory. The detailed description of the molal activity coefficient modeling from the Debye-Hückel theory is described in Appendix D.

The so-called DH-*limiting-law* (in **Eq. C-** 1, $B_{DH} = C_{i,DH} = 0$) reproduces good approximation of the activity coefficient only for the low range of ionic strengths (I<0.01) due to its inherent major limitations. First, it only takes into account the long-range electrostatic interactions excluding non-ideality due to short-range interactions; second, the point charge assumption of their model is invalid for concentrated solutions. Besides, this assumption is questionable where the size of solvent molecule is comparable to size of the ions; third, although the model keeps the permittivity of the solvent medium constant, this bulk property depends on

temperature, composition, and density of solvent; fourth, the complete dissociation assumption faces difficulties when ions associate with each other and with solvent molecules to form ion-pair or complexes. These infer that electrostatic interaction energy overcomes thermal energy which violates another assumption as made in the DH theory.

The limitations of the DH theory have kept the electrolyte system an unresolved research where various empirical and semi-empirical extension are widely proposed in the literature. One, therefore, must couple this theory with short and intermediate range interactions to thoroughly address the electrolyte solution behavior. The extended DH theory removed the point-charge assumption of the original DH theory and is applicable to a somewhat wider range of concentrations ($I<0.1$ M). This extension allowed for the development of many semi-empirical formulations as reviewed by Zemaitis et al. (**1986**). The proposed models to extend the applicability of the DH theory in the real strong electrolyte solution can be summarized as theoretical models and empirical models represented as an electrolyte EOS (eEOS) or excess GFE. **Table C-2** summarizes some of the extended DH models in chronological order. The predictive capacity of these models spans a diverse range because the number of introduced parameters to include the intermediate/short-range particle interaction or ion-solvent and ion-molecule interaction differ.

Table C-2: Chronological list of some of the DH type activity models for aqueous electrolyte solutions

Model Name	Model Basis	Parameters in Eq. C- 1 or Full Formulation	Remarks
DH (**1923**)	*DH*	Limiting and extended DH law: $C_{i,DH} = 0$; Limiting DH law: $B_{DH}\dot{a}_{DH} = 0$.	Interaction between charged ions; C_{DH} parameter is proportional to the ionic strength and temperature and considerably extends applicability of the DH theory; validity for 1:1 electrolyte up to $I \cong 0.01$ M and for 3:1 electrolytes ≅0.001 M.
Hückel (**1925**)	*DH*	$C_{1,DH}$: constant; $D_{1,DH} = 1$. He justified that adding an I-dependent term represents composition dependency of permittivity	
Bjerrum (**1926**)	*DH*	$\dot{a}_{DH} = \dot{a}_B = \frac{\lvert Z_+ Z_- \rvert e^2}{4\pi\varepsilon_f k_B T}$	A traditional method of Ion-pair treatment to mitigate the DH theory limitations at high ionic interactions. ion-pairing is more plausible at concentrated electrolyte system in that the short-range coulomb interaction increases as does the ion concentration. Stillinger and Lovett (**1968**) conceptually validated and generalized this intuitively developed method. The model states that electrostatic interaction between ions imposes an order to the random thermal motion of the ions to some extent. It is, therefore, possible that some strong interactions make two counter-charge ions to move together on a long-time scale (i.e., the formation of an ion-pair). Bjerrum assumed an arbitrary cut-off for pairing when average electrostatic potential equals $k_B T$. Ions within a distance of $\dot{a}_B$ of each other are associated as ion-pair. Otherwise, the ions are unpaired. The Bjerrum distance varies between 3.5-32 $°A$ for 1-1 to 3-3 electrolytes.
Brüll (**1934**)	*DH*	$A_{DH} = 0.354$; $B_{DH} = 10^8$; $C_{1,DH} = C_{2,DH}$: concentration-independent constants; $D_{1,DH} = 1/2$; $D_{1,DH} = 3/2$.	
Guggenheim (**1935**)	*DH*	$\log \gamma_{\pm}^{m} = -\frac{\alpha\lvert Z_+ Z_- \rvert \sqrt{I}}{1+\sqrt{I}} + \frac{2v_+}{v_+ + v_-}\sum_{á}\beta_{cá}\ m_{á} + \frac{2v_-}{v_+ + v_-}\sum_{ć}\beta_{ća}\ m_{ć}$	Guggenheim hypothesized that individual activity coefficients of ions and mean activity coefficients of electrolytes are equal. Applicable to multicomponent solution, but limited applicability: lack of parameters and the low ionic strength applicability of this method, limited P and T dependency. For single electrolyte, it is reduced form of DH equation with $B_{DH}\dot{a}_{DH} = 1$ and $C_{DH} = 0$. β: tabulated interaction coefficient
Scatchard (**1936**)	*DH+ Gu*	$\alpha_{DH} = 0$; $B_{DH} = 1.5$; $C_{1,DH} = C_s M$ where C_s is adjusting coefficient and M is molality; $D_{1,DH} = 1$. A complex formulation to extend Guggenheim's formulation by introducing a concentration-dependent term into interaction parameters.	

Table C-2 (cont'd): Chronological list of some of the DH type activity models for aqueous electrolyte solutions

Model Name	Model Basis	Parameters in Eq. C- 1 or Full Formulation	Remarks
Davies (**1938**);(**1962**)	*DH+ Gu*	$\alpha_{DH}=0;\ A_{DH}=0.5;\ B_{DH}=1;\ D_{1,DH}=1$ Davies (1938):$C_{1,DH}=0.1\lvert Z_+Z_-\rvert$; Davies (1962): $C_{1,DH}=0.15\lvert Z_+Z_-\rvert$.	The proposed model adds the non-electrostatic short interaction term to DH formulation; it contains **no adjustable parameter** but does not capture ion-association; No temperature dependency (Valid for ~ 298 K); work fairly up to $I \cong 0.1$ M.
Robinson (**1938**)	*DH*	$\alpha_{DH}=0;\ A_{DH}=1.751;\ B_{DH}=2.46;$ $C_{1,DH}=\log(1+0.054M)$; $D_{1,DH}=0;\ C_{2,DH}=-0.2436;\ D_{2,DH}=1.$	This model was formulated for the divalent metals and matched the activity of aqueous solution of 0.05-2 M at 298 K. (No temperature dependency)
Stokes and Robinson (**1948**)	*DH*	$A_{DH}=0.5092;\ B_{DH}=0.3286;\ D_{1,DH}=0;$ $C_{1,DH}=\mathrm{C_{SR}}/\nu\ \log(a_w)\ ;\ D_{2,DH}=0.$ $C_{2,DH}=\log(1+0.0180\times(\nu-\mathrm{C_{SR}})\mathrm{M})$	Considers **salt-in** and **-out** effects; Tested for a large number of aqueous electrolytes; Valid up to M=1 mole/kg.
Guggenheim and Turgeon (**1955**)	*DH+ Br+ SC*	$\ln\gamma_i^*=-\frac{\lvert Z_+Z_-\rvert A_{DH}\sqrt{I}}{1+B_{DH}\sqrt{I}}+\sum_j\theta_{i.j}^{SIT}\,m_j$ $B_{DH}=1.5\ at\ 298\ K$	This formulation is also called Specific ion interaction (**SIT**) model. $\theta_{SIT,i.j}$ is interaction coefficient describing short-range interactions of ions I and j. This parameter is symmetric ($\theta_{i.j}^{SIT}=\theta_{j,i}^{SIT}$). Same-ion interactions are zero. θ_{SIT} can be concentration (or I) dependent.
Freidman (**1962**)	*DH + CT*	$\log\gamma_{\pm}^m=-A_{DH}\lvert Z_+Z_-\rvert\sqrt{I}$ $-\frac{\sum_i(v_iz_i^3)^2}{3v\sum_i(v_iz_i^2)}A_{DH}^2 I\ln I$	Bypassed some of the limitations of *DH* theory by treating coulombs and non-coulomb effects on an equal level. Its coefficients are a function of the charge type of the salt and solvent properties. For symmetrical electrolytes, the second term is zero.
Lietzke and Stoughton (**1962a**); (**1962b**)	*DH*	$\alpha_{DH}=0;$ $C_{1,DH}, C_{2,DH}, C_{3,DH}$ adjustable parameters; $D_{1,DH}=1;\ D_{2,DH}=2;\ D_{3,DH}=3.$	Four adjustable parameters ($B_{DH}, C_{1,DH}, C_{2,DH}, C_{3,DH}$) for any electrolyte are evaluated by the regression from a polynomial osmotic coefficient formulation. Not recommended for electrolytes exhibiting significant association (**Lietzke & Stoughton, 1975**). Nevertheless, many investigators correlated the ionic activity coefficients using this semi-empirical model.
Helgeson and coworkers (**1969**);(**1974**); (**1981**)	*DH*	$C_{1,DH}=\dot{B};$ $D_{1,DH}=1;$	Also called ***B-dot*** equation denoting species-specific parameter. This popular **parameterized** model targets hydrothermal solutions and spans a wide range of temperature (up to 573 K) and for a large number of components. Its formulation can model the ion-pairs in low permittivity and density condition of hydrothermal aquifers. It has widely been applied in industrial application due to its simplicity and straightforward extension to the new system. Its validity, however, is highly questionable for non-NaCl-dominated solutions, for $I \geq 3.$ M (**Bethke, 2007**) or for $T \geq 373$ K (**Møller, 1988**).

Table C-2 (cont'd): Chronological list of some of the DH type activity models for aqueous electrolyte solutions

Model Name	Model Basis	Parameters in Eq. C- 1 or Full Formulation	Remarks
Bromley **(1973)**	*DH + Gu*	$\log\gamma_{\pm}^{m} = 1/\nu\{\nu_C \log\gamma_C + \nu_A \log\gamma_A\}$; $\ln\gamma_x = -A_{DH}Z_x^2\sqrt{I}/(1+\sqrt{I}) + F_x$; $F_x = 0.25\sum_y \dot{B}_{B,xy} m_y (Z_x + Z_y)^2$; $\dot{B}_{B,xy} = B_B + (0.06 + 0.6B_{B,xy})Z_{\pm}/(1+aI)^2$; $B_{B,xy} = B_{B,x} + B_{B,y} + \delta_{B,x}\delta_{B,y}$; $Z_{\pm} = \lvert Z_x Z_y\rvert$ and $a = 1.5/Z_{\pm}$; For single electrolyte solution osmotic coefficient is: $(1-\Phi)/2.303 = 0.333A_{DH}Z_{\pm}\sqrt{I} + F(\sqrt{I}) - 0.5(0.06+0.6B_B)Z_{\pm}G(aI) - 0.5B_B$; $F(X) = 3/X^3[1+X-1/(1+X)-2\ln(1+X)]$; $G(X) = 2/X[(1+2X)/(1+X)^2 - \ln(1+X)/X]$.	Bromley treated a multicomponent solution as a single complex salt. F_x represents ionic interactions of the complex salt; it is applicable to multicomponent solution, given solute specific parameter ($B_{B,CA}$) or its according parameters; For the activity coefficient of an anion (cation): x is the anion (cation) and y are all the cations (anions). B_B *and* δ_B parameters for about 180 electrolytes are given by Bromley at room temperature; the temperature dependent Bromley parameters must be history matched against experimental data for 4 parameters per electrolyte. For osmotic coefficient in a multicomponent mixture, Zemaitis et al. (**1986**) proposed to use Meissner and Kusik eq. (**1978a**). Borge et al. (**1996a** and **1996b**) reported the modified Bromley equation with the B_B parameters in molar scale for more than 80 strong electrolytes. Returns acceptable results up to $I \cong 3$ M
Cruz and Renon **(1978)**; Renon **(1980)**	*DH+B+ NRTL*	$G^{ex} = G^{lr} + G^{B} + G^{sr}$ *lr:* long-range interactions from *DH* theory; *B:* Born contribution to correct for the change of relative permittivity of solvent due to the presence of ions *sr: NRTL*	Contribution from complete and partial dissociations in an undissociated solvent adding different interparticle and intermolecular interactions: ion-ion, ion-molecule, and molecule-molecule by applying the local-composition concept. Four adjustable parameters to represent 15 strong aqueous electrolytes (salts and strong acids) at 298 K and 1 atm up to the highest molalities (76 M).
Bromley-Zemaitis **(1986)**	*DH + Br*	$\log\gamma_{\pm} = \frac{-A\lvert Z_+Z_-\rvert\sqrt{I}}{1+\sqrt{I}} + \frac{(0.06+0.6B)\lvert Z_+Z_-\rvert I}{(1+1.5I/\lvert Z_+Z_-\rvert)^2} + BI + CI^2 + DI^3$ $M = M_1 + M_2T + M_3T^2,\ M = B,C,D$	Also called ***Aqueous***. And enhanced modeling of concentrated electrolyte solutions by adding extra terms to Bromley formulation (**1973**) Returns acceptable results up to $I \cong 30$ M.
Pitzer and Simonson **(1986)**	*DH*	$\ln\gamma_j^m = -z_j^2 A_{DH}\{(2/\rho)\ln(1+\rho I^{0.5}) + I^{0.5}(1-2I/z_j^2)/(1+\rho I^{0.5})\}$; $\rho \cong 2150(d_S/\varepsilon_f T)^{0.5}$.	Evaluates activity coefficient due to coulomb forces of single-charge species *i*; It is also called ***Pitzer-DH*** model. Although ρ relates to a hard-core collision diameter and can be estimated, but in general is an empirical parameter

* ***B***: Born term for mixed solvents and hydration; ***Br***: Brønsted(**1922**); ***CT***: Cluster theory; ***DH***: DH theory by solving Poisson-Boltzmann equation; ***Gu***: Guggenheim (**1935**); ***NRTL***: non-random two-liquid model (**Renon & Prausnitz, 1969**); ***SC***: Scatchard (**1936**); ***SIT***: specific ion interaction theory developed by Brønsted (**1922**) and extended by Scatchard (**1936**) and Guggenheim (**1955**).

Pitzer formulation

The Pitzer formulation (**1973a**) is the extensively accepted model to extend the applicability of the DH theory to higher ionic strengths and multi-salt solutions. As described in **Table C-3**, it is a semi-empirical model based on the virial expansion of the activity coefficients as proposed by Mayer (**1950**). Pitzer and his co-workers provided an alternate form of the DH theory by accounting for hard-core kinetic effects on departure from ideality. They used the energy equation in connection with an approximate distribution function and modified the DH theory. They proposed models both for osmotic and activity coefficient. The latter expresses the activity coefficient as a sum of two terms: modified DH limiting law and an osmotic virial series in electrolyte concentration up to the third virial coefficient. Pitzer mentioned that although they could include fourth or higher order interactions, it is only required for extremely concentrated solutions and, in general, they prefer an alternate method (**Pitzer & Simonson, 1986**). Introducing ternary parameters to the model or otherwise adopting relaxing assumptions, one may extend the Pitzer model to multi-salt solutions. It is notable, however, that the main effect on the activity coefficient of the solution arises from the single-electrolyte parameters and that one may omit the mixed-salt terms without imposing significant error in the estimated properties for the common subsurface petroleum engineering application.

The shortcomings of the Pitzer-type formulation are two folds: one requires to provide an extensive database of several system-specific fitting parameters (for binary and ternary interactions) and for temperature-dependent terms (**Møller, 1988**); and we expect a computationally demanding procedure to compute activity coefficients in the field-scale subsurface applications based on this complex formulation. Nevertheless, in that substantial model parameter dataset is available for an expansive range of electrolytes, the model is versatile in referring thermodynamic properties of the electrolyte solution.

Table C-3: Pitzer formulation as a DH type activity model for the aqueous electrolyte solutions

Model Name	Model Basis	Formulation	Remarks
Pitzer and co-workers **(1973a); (1973b); (1974a); (1974b); (1975); (1976); (1977); (1978a); (1978b); (1978c); (1983)**	*DH* + *M*	$\ln\gamma_Y = z_Y^2 F_P + \sum_{ac=1}^{N_{ac}} m_{ac}\left(2B_{P,Y,ac} + ZC_{P,Y,ac}\right) + \sum_{ca=1}^{N_{ca}} m_{ca}\left(2A_{P,Y,ca} + \sum_{ac=1}^{N_{ac}} m_{ac}\psi_{P,Y,ca,ac}\right) + \sum_{ac=1}^{N_{ac}-1}\sum_{j=ac+1}^{N_{ac}} m_{ac}m_p\psi_{P,ac,j,Y} + \lvert Z_Y\rvert \sum_{ca=1}^{N_{ca}}\sum_{ac=1}^{N_{ac}} m_{ca}m_{ac}C_{P,ca,ac} + \sum_{n=1}^{N_n} m_n(2\lambda_{nY})$; $\Phi - 1 = \frac{2}{\sum_i m_i}[-A_{DH}I^{1.5}/\left(1+b\sqrt{I}\right) + \sum_c\sum_a m_c m_a\left(B^{\Phi}_{P,i,j} + ZC_{P,Y,ac}\right) + \sum_{c<c'}\sum_{c'} m_c m_{c'}\left(A_{P,cc'} + m_a\psi_{P,cc'a}\right) + \sum_{a<a'}\sum_{a'} m_a m_{a'}\left(A_{P,aa'} + m_a\psi_{P,aa'c}\right)]$ $F_P = -\frac{A_{DH}}{3}\left(\frac{I^{0.5}}{1+1.2I^{0.5}} + \frac{2}{1.2}\ln(1+1.2I^{0.5})\right) + S_{P1} + S_{P2} + S_{P3}$; $S_{P1} = \sum_{c=1}^{N_c}\sum_{a=1}^{N_a} m_c m_a \acute{B}_{P,i,j}$; $S_{P2} = \sum_{c=1}^{N_c-1}\sum_{\acute{c}=c+1}^{N_c\varepsilon} m_c m_{\acute{c}}\acute{\Phi}_{P,c,\acute{c}}$; $S_{P3} = \sum_{c=1}^{N_a-1}\sum_{\acute{a}=a+1}^{N_a} m_a m_{\acute{a}}\acute{\Phi}_{P,a,\acute{a}}$; $B^{\Phi}_{P,i,j} = \beta^0_{P,i,j} + \beta^1_{P,i,j}\exp(-\alpha_{P,i,j}\sqrt{I}) + \beta^2_{P,i,j}\exp(-12\sqrt{I})$; $B_{P,i,j} = \beta^0_{P,i,j} + \beta^1_{P,i,j}G\left(\alpha_{P,i,j}\sqrt{I}\right) + \beta^2_{P,i,j}G\left(12\sqrt{I}\right)$; $\acute{B}_{P,i,j} = \beta^1_{P,i,j}\acute{G}\left(\alpha_{P,i,j}\sqrt{I}\right)/I + \beta^2_{P,i,j}\acute{G}\left(12\sqrt{I}\right)/I$; $A_{P,i,j} = \theta_{P,i,j} + E_{P,i,j} + I\acute{E}_{P,i,j}$; $C_{P,i,j} = 0.5\beta^3_{P,i,j}\left\lvert Z_i Z_j\right\rvert^{-0.5}$; $Z = \sum_i \lvert Z_i\rvert m_i$ $G(x) = 2(1-(1+x)e^{-x})/x^2$; $\acute{G}(x) = -2(1-(1+x+x^2/2)e^{-x})/x^2$.	Requires 5 binary interaction parameters between counter-charge ions ($\beta^0_{P,i,j}, \beta^1_{P,i,j}, \beta^2_{P,i,j}, \beta^3_{P,i,j}, \theta_{P,i,j}$) and set of ternary interaction parameters ($\psi_{P,Y,i,j}$). For symmetrical mixing, $E_{P,i,j}$ term disappears and $\Phi_{P,i,j}$ is approximately independent of ionic strength. For cation (anion): Y=specified cation (anion); ac=anion(cation); ca= cation(anion); n=neutral. $E_{P,i,j}$ and $\acute{E}_{P,i,j}$=f(ions charges, I, ε, ρ_s) are due to unsymmetrical mixing effects and are zero for the same charge ions *i* and *j*. For univalent electrolyte:$\alpha_{P,i,j} = 2$, $\beta^2_{P,i,j} = 0$; For 2-2 electrolyte: $\alpha_{P,i,j} = 1.4$. Pitzer parameters for common ions are listed in Harvie et al. (**1984**), Zemaitis et al. (**1986**), Holmes and Mesmer (**1988**) (and references therein), and (**Pitzer, 1991**, **1995**) among others; functional form of temperature-dependent Pitzer parameters are proposed by many investigators including Pitzer (**1991**), Greenberg and Mølle (**1989**), Alai et al. (**2005**), and (**Christov et al., 2007**; **Christov & Møller, 2004**); Some Investigators attempted to reduce the number of Pitzer's equation (**Fürst & Renon, 1982**).

For multicomponent system, at first, one could apply one-electrolyte formulation and upon unsuccessful match of experimental results, add more set of parameters. The source of required parameters in literature are listed in **Table C-3**.

Integral equation functions

The low-concentration chemical models disregard the actual particle sizes and, instead, take into account the particle sizes in the extreme sides of the distance parameter of the charge-charge interaction. The statistical thermodynamics by means of integral equation function not only overcomes this drawback of the Poisson-Boltzmann low-concentration methods, also establishes theoretical basis for modeling of the electrolyte solution. Unlike the DH where the Poisson-Boltzmann equation is solved for the central ion assuming that the ions in the cloud are point-charge sources, the integral equation functions take into account finite-size ions in the cloud. The integral equation yields the spatiotemporal distribution of relation to provide additional condition to solve the integral equation. The closure equation uses either the explicit functional relation between h and c functions $h(\vec{r}_1,\vec{r}_2) = f\big(c(\vec{r}_1,\vec{r}_2)\big)$ or the implicit functional relation between the indirect correlation and the cavity equation through a bridge graph (**Barthel et al., 1998**). Three commonly used closure equations are the hypernetted chain approximation (**Freidman, 1985**), the Percus-Yevick approximation (**1958**), and the mean spherical approximation methods (MSA). The hypernetted chain approximation assumes that the bridge graph is zero and obtains acceptable results for electrolyte solutions at moderate and high concentrations (Molality > 0.1 M). Nevertheless, it is a computationally demanding approach and impractical for the field-scale applications. The Percus-Yevick closure equation is accurate to replicate the repulsive short-range interionic behavior but is limited in predicting the behavior of long-range ionic species. The mean spherical approximation (MSA) is a simplified form of one closure equation obtained for the hard-sphere particles of constant diameter. This model and its variants are computationally expensive

due to the inherent implicitness of its parameters as described in **Table C-4**. The MSA has been adopted with several investigators assuming that it provides more details of the thermodynamic behavior of electrolyte system.

Mean Spherical Approximation

One may generally solve the integral equation function of the MSA for both primitive and non-primitive models (**Simonin et al., 1996**). In the more complex non-primitive formulation, the dielectric constant may freely depend on the temperature and density in multicomponent and multi-solvent mixtures. Based on several introduced approximations, Blum and Wei (**1987**) proposed an analytical approach for the non-primitive MSA closure function. Notwithstanding, it has been a common practice to treat the solvent as a dielectric medium and is modeled implicitly. Blum (**1975**, **1980**) presented the analytical solution to the restricted primitive MSA to solve for interactions of charged hard-spheres with finite size. His work was a step forward representation in the theoretical modeling of the electrolyte solutions. The pair potential is,

$$\Psi_c(r) = \begin{cases} \dfrac{z_i z_j e^2}{\varepsilon_f r} & r < d_{ij} \\ \infty & r > d_{ij} \end{cases}, \qquad \textbf{Eq. C- 2}$$

where d_{ij} is the common diameter of the hard spheres ($d_{ij} = (d_i + d_j)/2$). Blum assumed,

$$\Psi_c(r) = \begin{cases} \varphi_{ij}(\vec{r}) = 0 & r < d_{ij} \\ c_{ij}(\vec{r}) \cong -z_i z_j e^2/(\varepsilon_f kTr) & r > d_{ij} \end{cases}, \qquad \textbf{Eq. C- 3}$$

and solved the pair potential equation. A characteristic screening or shielding length (λ_{MSA}) appears in the solution having a recursive formulation,

$$\lambda_{MSA}^2 = \alpha_B \sum_{i=1}^{n} \rho_j \left(\frac{z_i - \left(\frac{\pi}{2\Delta}\right) d_i^2 P_n}{1 + \lambda_{MSA} d_i} \right)^2, \qquad \textbf{Eq. C- 4}$$

where $\Delta = 1 - \frac{\pi}{6}\sum_i \rho_i d_i^3$. The MSA screening length is related to the Debye screening length through the ion diameter (d_i):

$$\lambda_{DH} \cong 2\lambda_{MSA}(1 + d_i\lambda_{MSA}). \qquad \textbf{Eq. C- 5}$$

The binding MSA method introduces an exponential approximation to correct poor prediction of low-density behavior in spherical-like approximation (**Bernard & Blum, 1996**). This method considers contributions to the ionic interactions especially the hard-core and includes two important effects. It prevents the collapse of the system: based on statistical mechanics, the neutral ionic system form unbounded negative energy that are unstable. It takes into account the ion volume: ions in the Debye-Hückel theory exclude each other. In reality, however, the ions screening cloud is larger than the Debye-Hückel cloud. It includes the ions contact and their and exclusion volume alleviating the problem of negative values of the mean activity logarithm in case of high ionic strength. Nevertheless, the formulation and evaluating the screening parameter of the MSA method is more complicated than the Debye-Hückel theory but researcher have found no virtual difference between the results of the MSA method than Debye-Hückel method. This type of modeling, however, is limited to the electrostatic interactions between spherical ions. One may capture the ion-dipole and diploe-dipole interactions in real solutions with complementary methods.

Table C-4: MSA approach for electrolyte activity modeling

Authors	Model Basis	Activity Model Formulation	Remarks
Waisman and Lebowitz (**1970**)	*RPM*	$\ln\gamma_{\pm}^{m} = \ln\gamma_{\pm}^{ES} + \ln\gamma_{\pm}^{HS} = U^{ES}/NkT - \pi B/2\rho\,(P_n/\Delta)^2$ $\ln\gamma_{\pm}^{ES} = -B\lambda_{MSA}z_j^2/(1+\lambda_{MSA}d_j) - E_1 - E_2 - E_3,$ $E_1 = \pi B z_j d_j P_n/[2\,\Delta(1+\lambda_{MSA}d_j)],$ $E_2 = d_j P_n[\lambda_{MSA}a_j + \pi^2 B d_j^2 P_n/(3\Delta)]/(4\Delta),$ $E_3 = \pi B z_j\left[\sum_i \rho_i d_i^2(2\lambda_{MSA}a_j/4\pi B + 0.5z_i)\right]/6,$ $\ln\gamma_{\pm}^{HS} = C_1 + C_2 + C_3 - C_4 - \ln\Delta,$ $C_1 = d_j^3[\zeta_0 + 3\zeta_1\zeta_2 + 3\zeta_2^3 - \zeta_2^3\zeta_3]/\Delta,$ $C_2 = 3d_j[(d_j\zeta_1 + \zeta_2) + 3d_j\zeta_2^2/(2\Delta)]/\Delta,$ $C_3 = 3(\zeta_2 d_j/(1-\Delta))^2[ln\Delta + \zeta_3/\Delta - \zeta_3^2/(2\Delta^2)],$ $C_4 = (\zeta_2 d_j/(1-\Delta))^3[2ln\Delta + \zeta_3(2-\zeta_3)/\Delta],$ where $B = e^2/(4k_BT\varepsilon_r),$ $P_n = 1/\Omega \times \sum_j \rho d_j z_j/(1+\lambda_{MSA}d_j),$ $\zeta_n = \pi/6 \times \sum_j \rho d_j^n$, Δ= 1-ζ_3, $\lambda_{MSA}^2 = \pi B \sum_j \rho_j[(z_j - \pi d_j^2 P_n/(2\Delta))/(1+\lambda_{MSA}d_j)]^2,$ $\Omega = 1 + \pi/2\Delta \times \sum_j \rho d_j^3/(1+\lambda_{MSA}d_j),$ $a_j = 2\pi B(z_j - \pi d_j^2 P_n/2\Delta)/\lambda_{MSA}(1+\lambda_{MSA}d_j).$	Lebowitz and Percus (**1966**) introduced *MSA*. The *MSA* is a closure approximation equation coupled with the *OZ* equation. The *OZ* integral equation describes the interaction between two particles by applying direct and indirect correlation between any particle pair with the assist of the graph theory. The *MSA* can be solved based on *PM* and *NPM* models. The *PM* models are analytically solved implicitly. Their simplified variants can be solved explicitly; If one adopts NPM-type modeling, no mixing-rule is required; Waisman and Lebowitz (**1972a**;**1972b**) and Wertheim (**1971**) obtained analytical solution of *MSA* using *PT*. Advances in the *MSA* is attributed to the Blum and co-workers; The described *MSA* approach is primitive; Total property (i.e., mean activity coefficient) is sum of *es* and *hs* contribution; The hard-sphere contribution is evaluated from *MCSL* equation; *MSA* accounts for finite-size of individual ions and reduces to DH limiting law as $I \to 0$; *BIMSA* accommodates all associating mechanism (Coulombic, covalent, and solvation) in one association parameter in *MSA* model based on the mass-action law and the WOZ integral equation formalism; λ_{MSA} parameter is solved iteratively and as diameter approaches zero ($d_j \to 0$), $\lambda_{DH} \cong 2\lambda_{MSA}(1 + d_i\lambda_{MSA})$; If ions are of same diameter, $P_n = 0$: $E_1 = E_2 = E_3 = 0$.
Wertheim (**1971**)	*HS-ID*		
Blum and coworkers (**1975**); (**1977**); (**1978**); (**1980**); (**1987**); (**1995**)	*Analytical*		
Simonin and coworkers (**1996**); (**1997**); (**1998**)	*BIMSA*		

BIMSA: Binding-MSA; ***es***: electrostatic contribution; ***hs***: hard-sphere contribution; ***HS-ID***: Hard-sphere with embedded ideal dipoles; ***MCSL***: hard-sphere equation of Mansoori et al. (**1971**); ***MSA***: mean spherical approximation; ***OZ***: Ornstein-Zernike equation (**1914**); ***PDH***: Pitzer-DH model (**Pitzer & Simonson, 1986**); ***PM***: Primitive model; ***NPM***: Non-primitive model in which solvent molecules are resorted; ***PT***: Perturbation theory; ***RPM***: Restricted primitive model in which ions have equal diameters; ***WOZ***: Wertheim-Ornstein-Zernike (**1984**, **1986**).

Perturbation equations

Perturbation theory attacks a property by means of a set of approximation schemes of perturbing that property in terms of a simpler one. As a result, having a precise *a priori* knowledge of the specified property is the keystone of perturbation equation. In case of electrolyte solution, this theory applies a Tylor series expansion of the Helmholtz free energy given the intermolecular pair potential and the reference state radial distribution function. This simplistic approach coupled with the elegant Wertheim theory (**1984**) is the basis of statistical associating fluid theory (SAFT), a widely used non-cubic EOS method in electrolyte modeling in which the contribution to the residual Helmholtz energy is evaluated. The residual Helmholtz energy is due to aggregation of three terms representing contributions from different intermolecular interactions: segment interaction, covalent chain-forming bonds in segments, and site-specific interactions among segments. The SAFT and its variants estimate thermodynamic properties for chain-like molecules in electrolyte solution modeling.

Excess thermodynamic property decomposition

One simple and systematic approach to overcome the drawbacks of pure theoretical molecular electrolyte methods and to complete the electrolyte modeling is to decompose the excess thermodynamic properties. The partial molar excess properties deliver a straightforward method

to obtain activity coefficients, e.g., $\bar{G}_i^{ex} = \left(\frac{\partial N_T G^{ex}}{\partial N_i}\right)_{T,P,N_j \neq i} = RT \ln \gamma_i$. This provides the attribution of unlike interactions among species by linear summation of the contribution of each interaction. For example, the excess GFE of an aqueous solution can be represented by contribution from up to seven terms. A simplified electrolyte model exhibits the excess molar GFE (or molar Helmholtz free energy) by,

$$G^{ex} = G^{LR} + G^{B} + G^{SR}, \qquad \textbf{Eq. C- 6}$$

where G^{LR} denotes the long-range interactions between charged species as represented by either the DH theory or the MSA method; the Born term (G^{B}) evaluates the solvation (or hydration) energy when ions charge (or discharge) the uncharged (or charged) reference system in continuous medium with fixed-permittivity (**Born, 1920**); and G^{SR} points the short-range interactions as denoted by a formulation based on profuse set of classical non-electrolyte thermodynamics, theoretical methods, or empirical formulations. To capture short-range interactions of multicomponent electrolyte solution, several of the relatively successful electrolyte models are established based on the local-composition supposition.

Local composition models

In molecular thermodynamic of liquid solutions, the advent of local-composition concept (**Wilson, 1964**) allowed to contribute the short-range and non-random interactions as opposed to random-mixing behavior in an averaged overall mixture composition. Two successful variants of the local-composition are non-random-two-liquid (NRTL) (**Renon & Prausnitz, 1969**) and universal quasi-chemical (UNIQUAC) (**Abrams & Prausnitz, 1975**) and UNIQUAC Functional group Activity Coefficients (UNIFAC) (**Fredenslund et al., 1975**). This powerful concept and its variants improved modeling of excess Gibbs energy in electrolyte solution substantially. Some of the activity models based on NRTL and UNIQUAC local composition models are listed in **Table C-5.** Yet, they lack predictive potential in subsurface resource modeling as they are limited to low-pressure equilibrium condition. The EOS are perceived to overcome this severe drawback of modern aqueous activity models.

Table C-5: Chronological list of some of activity models for aqueous electrolyte solutions (NRTL- and UNIQUAC-based models)

Model Type	Authors	Model Basis	Excess Gibbs energy	Remarks
eNRTL	Chen and co-workers (**1982**);(**1986**);(**2001**); (**2004**)	*NRTL+PDH+B*	$G^{ex}/RT = G^{ex}_{SR}/RT + G^{ex}_{LR}/RT + \Delta G^{ex}_{B}/RT$; $G^{ex}_{SR}/RT = S_m + S_a + S_c;\ S_m = \sum_m n_m \left(\frac{\sum_j X_j \beta_{jm} \zeta_{jm}}{\sum_k X_k \beta_{km}}\right)$; $S_a = \sum_c z_c n_c \left(\sum_a Y_a \frac{\sum_j X_j \beta_{jc,ac} \zeta_{jc,ac}}{\sum_k X_k \beta_{kc,ac}}\right)$; $S_c = \sum_a z_a n_a \left(\sum_c Y_c \frac{\sum_j X_j \beta_{ja,ca} \zeta_{ja,ca}}{\sum_k X_k \beta_{ka,ca}}\right)$; $\beta_{ij} = \exp(-\alpha_{ij}\zeta_{ij});\ X_j = C_j x_j;\ x_j = n_j / \sum_i n_i$. *j:* m (molecule), c (cation), a (anion); n_j*:* number of segment species j in mixture; C_j: 1 for molecules and z_j for ions species; Indexing is symmetric $\zeta_{ij} \neq \zeta_{ji}$ but for pair-to-pair is symmetric $\beta_{ja,ca} = \beta_{aj,ac}$.	It uses local composition concept of *NRTL* model adapted for electrolyte system (generalization of local ion-solvent interaction) and the extended *DH* (or *PDH*) equation for long-range electrostatic interactions (G^{ex}_{LR}). It uses Born equation to transfer between infinite dilution aqueous solution and infinite dilution mixed solvent solution (ΔG^{ex}_{B}). The local composition interactions are included based on a segment interaction concept. The species of solution are divided into three categories: molecules where electroneutrality is maintained along with ions (anions and cations) where central species follow a like-ion assumption; The model adopts the infinite dilution aqueous solution as reference state of ions and is applicable to multi-solute system; The model parameters are **salt** specific; The non-random factor α_{ij}<0.5. Renon (**1969**) proposed general guideline for selecting α_{ij}; generally, however, it is an adjustable model parameter). Adjustable parameters: 2 local binary interaction parameters per salt. These parameters can be estimated based on a non-linear-programming technique. The model works well up to $I \cong$ 6. M

* ***B***: Born term for mixed solvents and hydration; ***NRTL***: non-random two-liquid model (**Renon & Prausnitz, 1969**)*;* ***PB***: Poisson equation for relating charge density around ion and the electrical potential for a sphere and Boltzmann equation for ion distribution in electrolyte solution; ***PDH***: Pitzer-DH model (**Pitzer & Simonson, 1986**); ***UNIQUAC****:* universal quasi-chemical (**Abrams & Prausnitz, 1975**).

Table C-5 (cont'd): Chronological list of some of activity models for aqueous electrolyte solutions (NRTL- and UNIQUAC-based models)

Model Type	Authors	Model Basis	Excess Gibbs energy	Remarks
eUNIQUAC	Thomsen and co-workers (**1996**); (**1999**); (**2005**); (**2014**)	*UNIQUAC+ PDH*	$G^{ex}/RT = G^{ex}_{SR}/RT + G^{ex}_{LR}/RT,$ $G^{ex}_{LR}/RT = -4w_W M_W A_{UD}[\ln(1+B_{UC}) - B_{UC} + 0.5B^2_{UC}];$ $G^{ex}_{SR}/RT = G^{ex}_{SR,C}/RT + G^{ex}_{SR,R}/RT;$ $G^{ex}_{SR,C}/RT = \sum_i w_i \ln(\digamma_i/w_i) - 5q_i \sum_i w_i q_i \ln(\digamma_i/\aleph_i);$ $G^{ex}_{SR,R}/RT = -\sum_i w_i q_i \ln(\sum_j \aleph_j A_{UR,ji});$ $A_{UR,ji} = \exp[-(u_{ji}-u_{ii})/T];\ u_{ji} = u^0_{ji} + u^t_{ji}T;$ $A_{UD} = f(T');\ B_{UC} = 1.5I^{0.5};\ \digamma_i = w_i r_i/\sum_j w_j r_j;$ $\aleph_i = w_i q_i/\sum_j w_j q_j.$	It is also called extended *UNIQUAC* and applies extended *DH* (or *PDH*) equation for long-range electrostatic interactions contribution to excess Gibbs energy (G^{ex}_{LR}/RT). The model parameters are ion specific. The *UNIQUAC* contribution to the excess Gibbs energy (G^{ex}_{SR}/RT) consists of combinatorial (superscript *C*) and residual (superscript *R*) parts; the model requires two parameters (u^0_{ji} and u^t_{ji}) per binary and two parameters per ion (r_j and q_i); The model works well for I=5 M up to T=573 K.
	Wang and co-workers (**2002**); (**2004**); (**2006**); (**2013**)	*UNIQUAC+ PDH*	$G^{ex}/RT = G^{ex}_{SR}/RT + G^{ex}_{II}/RT + G^{ex}_{LR}/RT$	It applies a second-virial type formulation for specific ion (ion-ion and ion-molecule) interactions. The model parameters are **ion** specific. G^{ex}_{SR}*:* from UNIQUAC, G^{ex}_{LR}*:* from PDH, G^{ex}_{II}*:* specific ion interaction contribution from an ionic-strength dependent symmetrical 2nd virial-coefficient type and pressure dependent expression.

* ***B***: Born term for mixed solvents and hydration; ***NRTL***: non-random two-liquid model (**Renon & Prausnitz, 1969**)*;* ***PB***: Poisson equation for relating charge density around ion and the electrical potential for a sphere and Boltzmann equation for ion distribution in electrolyte solution; ***PDH***: Pitzer-DH model (**Pitzer & Simonson, 1986**); ***UNIQUAC***: universal quasi-chemical (**Abrams & Prausnitz, 1975**).

Aqueous electrolyte EOS (eEOS) models

Local composition models presume a negligible effect of pressure on thermodynamic behavior of aqueous solution. The experimental results, however, do not underpin this assumption (**Hamann, 1984**), at least, due to the elevated dissociation degree of the ion-pairing in the concentrated solutions at the high pressures. As a result, excluding the pressure effect impedes the aqueous activity models to fully describe the behavior of subsurface aquatic resources. To cover this limitation, an EOS can establish an analytical relation between pressure, temperature, and volume of the aqueous electrolyte system spanning the composition space. In general, one can relate the fugacity coefficient from vapor-liquid equilibria to the activity coefficient of electrolyte solutions. These non-ideality parameters are related to unsymmetrical activity coefficient as defined by,

$$\gamma_i^* = \frac{\gamma_i}{\gamma_i^\infty} = \frac{\hat{\varphi}_i}{\hat{\varphi}_i^\infty}, \qquad \textbf{Eq. C- 7}$$

where γ_i and $\hat{\varphi}_i$ stand for fugacity and activity coefficients of component i in a real mixture, respectively, γ_i^∞ denotes activity coefficient at infinite dilution, and $\hat{\varphi}_i^\infty$ is fugacity coefficient of component i at infinite dilution which is calculated based on an ion-free water solution.

In general, eEOS models add correcting terms to a non-electrolyte EOS to include variety of interactions specific to electrolyte solutions. These terms include, at least, long-term electrostatic charge interactions, Born dielectric term, and ion-specific short-range term. The non-electrolyte EOS models include Peng-Robinson EOS (PR) (**Peng & Robinson, 1976**), Soave-Redlich-Kwong EOS (SRK) (**Soave, 1972**), and cubic plus association EOS (CPA) (**Kontogeorgis et al., 1996**) (see **Table C-6**), SAFT (see **Table C-7**), perturbed anisotropic chain theory (PACT) (**Vimalchand & Donohue, 1985**) and Boublik-Mansoori-Carnahan-Starling EOS (BMCS) Boublik (**Boublik, 1970**; **Mansoori et al., 1971**) (see **Table C-8**).

Table C-6: Chronological list of some of the PR-, SRK-, and CPA-based eEOS models

Model	Model Basis		Remarks
	Non-Electrolyte EOS	Other terms	
Simon (**1991**)	*SRK*	*PDH+ B*	The model is based on individual contributions of electrolyte and *NE* components to the mixture Gibbs energy. The effect of an electrolyte on phase equilibria was represented semi-quantitatively. No ionic-association consideration
Fürst and Renon (**1993**)	*SRK*	*MSA*	$A = A^{rep} + A^{sr} + A^{lr}$ *rep*: repulsive-force term; *sr*: short-range term constituting of two parts: the first short-range term (*sr1*) represents the non-electrolyte interactions (from *SRK-EOS*) while the second term (*sr2*) is due to ion-specific short-range interactions (*PBMSA*); *lr*: long-range interactions from PBMSA model; *rep* and *sr1* terms are similar to those of Schwartzentruber (**1989**). No ionic-association was considered; Adjustable parameters: 1-3 binary parameters. The authors applied model to numerous strong electrolyte systems.
Myers et al. (**2002**)	*PR*	*sMSA+ B*	$A = A^{igm} + A^{sr} + A^{B} + A^{lr}$, *sr*: described based on the *PR-EOS* model; *B*: Born contribution due to two processes: 1) initial discharging of ions followed by 2) recharging the ions; *lr*: long-range interactions represented by simplified-*MSA* approach. General eEOS covering broad range of pressure, temperature, and composition without focusing on specific range of conditions or type of electrolytes. Reference state is ideal gas mixture. The model is applicable to ion-hydration. The authors validated the model against 138 aqueous electrolyte solutions. There was a good agreement between the measured and calculated mean activity coefficient.
Vu et al. (**2002**)	*PR*	*xPR*	fugacity coefficient: $\varphi = \varphi^{NE} \times \varphi^{solv} \times \varphi^{lr}$ The solvation and long-range contributions are evaluated based on *xPR* model. The co-volume parameter of non-electrolyte term is the summation of that of non-electrolyte pure component and linear term of mole-fraction average of co-volumes of electrolytes. The attraction parameter of non-electrolyte is evaluated from *xPR* model. Adjustable parameters: size of solvated ions as represented by Stokes diameters for cations and Pauling diameter for anions. The authors applied the model to predict behavior of gas-hydrates produced from water-methanol-salt solutions.
Lin et al. (**2007**)	*PR*	*MSA+ B*	$A^{ex} = A^{sr} + A^{B} + A^{lr}$ *sr*: short-range interactions from *PR-EOS*; *lr*: long-range interactions both from *eMSA* and *iMSA* models; *B*: Born term including ion- charging and –discharging; Adjustable parameters: 3 ion parameters and 1 interaction parameter per ion at room temperature; To evaluate different *eEOS*s, the authors coupled contribution from different models.
Lin et al. (**2007**)	*SRK*	*DH*	$A^{ex} = A^{sr} + A^{lr}$ *sr*: short-range interactions from SRK-EOS; *lr*: long-range interactions from a simplified DH model; In an attempt to evaluate different *eEOSs*, the authors coupled contribution from different models. This model does not capture the ion-charging and ion-discharging processes. Adjustable parameters: 2 ion and 1 interaction parameter per ion at room temperature.

Table C-6 (cont'd): Chronological list of some of the PR-, SRK-, and CPA-based eEOS models

Model	Model Basis		Remarks
	Non-Electrolyte EOS	Other terms	
Lin et al. (**2007**)	*CPA*	*iMSA+ B*	$A^{ex} = A^{sr} + A^{B} + A^{lr}$ *sr*: short-range interactions from *CPA*; *lr*: long-range interactions from *iMSA*; *B*: Born term including ion-charging and –discharging; Adjustable parameters: 3 ion parameters and 1 interaction parameter per ion at room temperature; To evaluate different eEOSs, the authors coupled contribution from different models.
Inchekel et al. (**2008**)	*CPA*	*iMSA+ (B)*	$A = A^{igm} + A^{sr} + A^{assoc} + A^{lr}$ *sr*: short-range attractive term constituting of two parts: the first short-range term (*sr1*) represents the non-electrolyte interactions (from *SRK-EOS*). To evaluate the solvation interactions, the authors applied two approaches: 1) the second term (*sr2*) due to ion-specific short-range interactions (*PBMSA*) ($A^{sr} = A^{SRK} + A^{sr2}$); 2) Born term for variations in solvation characteristics as salt concentration changes ($A^{sr} = A^{SRK} + A^{B,discharge} - A^{B,charge}$); *lr*: long-range interactions from *iMSA*; *assoc:* association term from the *CPA*. Only water is considered as the associating component. Adjustable parameters: three parameters per ion (hard-sphere diameter, energy parameter in SRK-EOS, solvated diameter) and one binary parameter (either solvation parameter or dispersive interaction parameter in SRK-EOS).

****assoc***: association term; ***attr***: attraction term; ***B***: Born term; ***CPA***: cubic plus association EOS (**Kontogeorgis et al., 1996**) a coupled cubic EOS and association parameter from SAFT (CPA reduces to PR/SRK for non-polar (i.e., non-self-associating compounds)); ***disp***: Dispersion term (intermolecular interaction potential from van der Walls forces) due to dispersive potential (*lj* or *sw*) for attraction among hard-sphere molecules in segments; ***ex***: excess Helmholtz free energy; ***hc***: hard-sphere chain term; ***hs***: hard-sphere term; ***igm***: ideal gas mixture; ***iMSA***: implicit (full) *MSA*; ***lj***: Lennard-Jones potential simple model to represent intermolecular interaction potential from van der Waals forces (repulsive and attraction terms) arising at small molecules (Jones,(**1924**)); ***lr***: Long-range electrostatic interactions; ***MSA***: mean spherical approximation; ***nMSA***: non-primitive *MSA*; ***PBMSA***: Planche and Ball's MSA model (**Ball et al., 1985**; **Planche & Renon, 1981**); ***PR***: Peng and Robinson EOS (**Peng & Robinson, 1976**); ***re***: Residual; ***ref***: Reference state or system; ***RPM***: restricted primitive mode; ***SAFT***: Statistical-Associating-Fluid-Theory incorporating the excess Helmholtz energy due to different molecular interactions in an additive manner; ***SRK***: Soave- Redlich-Kwong EOS (**1972**); ***sw***: square-well potential a simplified form of *lj* potential; ***xPR***: extended *PR* (**Péneloux et al., 1989**) by adding residual terms to Helmholtz energy based on a zeroth approximation of the Guggenheim quasi-reticular model (**Guggenheim, 1952**)

Table C-7: Chronological list of some of the SAFT-based eEOS models

Model	Non-Electrolyte EOS + other terms	Remarks
Wu and Prausnitz (**1998**)	*PR+ iMSA+ B*	$A = A^{ref} + A^{assoc} + A^{B} + A^{lr}$ *ref*: normal short-range repulsive interactions and van der Waals attractive among molecules or ions *assoc*.: association due to hydrogen bonding among water molecules from *SAFT*. The model does not capture ion-ion association; *B*: born contribution due to ion formation. It does not account for ion-discharging. *lr*: long-range interactions as represented by *iMSA*. Adjustable parameters: five adjustable parameters for water, one temperature-dependent parameters and one constant parameter for each salt species. The model is applicable to "usual" components in addition to water and NaCl.
Galindo and coworkers (**1999**); (**2003**)	*SAFTvr+ DH (or RPM-MSA)*	$A = A^{id} + A^{ref} + A^{assoc}$ *id*: ideal fluid contribution, *ref*: monomer segments contribution by *SAFTvr* model, *assoc*.: association contribution due to solvent molecules. It does not capture the ion-ion and ion-solvent association. The Born term was not added in the models. The model has one binary interaction parameter per ion-pair and explicitly takes into account the solvent as a dipolar associating fluid with square-well molecules. It is applicable up to 373 K. The model of Patel et al. (**2003**) provided a simple method to model salting-out of nonpolar components. The authors applied the ensemble Monte Carlo simulations to validate theoretical approach.
Sadowski and coworkers (**2005**); (**2008**); (**2009**); (**2013**); (**2014**)	*pcSAFT+ DH*	$A^{ex} = A^{ref} + A^{disp} + A^{assoc} + A^{lr}$ *ref*: the reference hard-chain molecules; *lr*: the contribution due to charging up the system (DH theory); Adjustable parameters: 2 parameters per ion (hydrated ionic diameter and dispersive energy parameter) The model was applied to strong monovalent and bivalent electrolyte system up to 373 K and could reproduce vapor pressure of mixed-salt solution. Held et al. (**2008**) validated their model against 115 electrolyte systems and matched liq. density and mean activity coefficient. Held et al. (**2014**) extended the pcSAFT applicability to modeling weak electrolyte solutions.

Table C-7 (cont'd): Chronological list of some of the SAFT-based eEOS models

Model	Non-Electrolyte EOS + other terms	Remarks
Zhao et al. (**2007**)	*SAFTvr+ nMSA*	$A = A^{id} + A^{ref} + A^{assoc}$ *id*: ideal fluid contribution; *ref*: monomer segments contribution by *SAFTvr* model; *assoc*: association contribution due to solvent molecules. It does not capture the ion-ion and ion-solvent association. The model explicitly adds the solvent as a dipolar associating fluid with square-well molecules. The authors applied ensemble Monte Carlo simulations to validate the theoretical approach.
Herzog et al. (**2010**)	*pcSAFT+ nMSA*	Three non-linear equations are solved to obtain ion-ion, ion-dipole, and dipole-dipole interactions. The ion-dipole term determines the energy of solvation similar to the Born term in primitive-based models. No conversion to other thermodynamic framework is required. Adjustable parameters: ion diameter and association energy (both are salt-specific). The authors validated this model against experimental results for 18 electrolytes in aqueous system up to 343 K.

****assoc.***: association term; ***attr***: attraction term; ***B***: Born term; ***CPA***: cubic plus association EOS (**Kontogeorgis et al., 1996**) a coupled cubic EOS and association parameter from SAFT (CPA reduces to PR/SRK for non-polar (i.e., non-self-associating compounds)); ***disp***: Dispersion term (intermolecular interaction potential from van der Walls forces) due to dispersive potential (*lj* or *sw*) for attraction among hard-sphere molecules in segments; ***ex***: excess Helmholtz free energy; ***hc***: hard-sphere chain term; ***hs***: hard-sphere term; ***igm***: ideal gas mixture; ***iMSA***: implicit (full) *MSA*; ***lj***: Lennard-Jones potential simple model to represent intermolecular interaction potential from van der Waals forces (repulsive and attraction terms) arising at small molecules (**J. E. Jones, 1924**); ***lr***: Long-range electrostatic interactions; ***MSA***: mean spherical approximation; ***nMSA***: non-primitive *MSA*; ***pcSAFT***: Perturbed-chain SAFT is based on a hard-chain fluid as a reference for the 2nd order perturbation theory to develop distribution term for non-spherical molecules (**Gross & Sadowski, 2001**); ***PR***: Peng and Robinson EOS (**1976**); ***re***: Residual; ***ref***: Reference state or system; ***RPM***: restricted primitive mode; ***SAFT***: Statistical-Associating-Fluid-Theory incorporating the excess Helmholtz energy due to different molecular interactions in an additive manner; ***SAFTvr***: *SAFT* variable-range describes the chain molecules formed from hard-core monomers with attractive potentials of variable- range (**Gil-Villegas et al., 1997**); ***SRK***: Soave-Redlich-Kwong EOS (**1972**); ***sw***: square-well potential a simplified form of *lj* potential.

Table C-8: Chronological list of some of the BMCS- and PACT-based eEOS models

Model	Model Basis		Remarks
	Non-Electrolyte EOS	Other terms	
Raatschen et al. (**1987**)	*BMCS*	*PDH* + *Hu* + *B*	$A^{ex} = A^{hs} + A^{attr} + A^{B} + A^{lr}$ *hs*: contribution due to inflation of ideal-gas molecules to hard-spheres as modeled by BMCS model. *attr*: attraction term due to intermolecular forces except for permanent electric charges of ions (*Hu* model). *lr*: *PDH* for dilute electrolyte system + a modified Pitzer equation (**Pitzer, 1973a**) for higher electrolyte concentrations; the model establishes a Helmholtz free energy (H=H (T, V, W)) for mixed solvents. Applicable to supercritical components at high pressures. Validity: T= -10 – 120°C and salinity up to 15 mol%. The model introduces ion-specific parameter but did not investigate several ions.
Pitzer and coworkers (**1989**); (**1993a**); (**1993b**)	*BMCS*	*Pert*	$A = A^{igm} + A^{rep} + A^{dip} + A^{per}$ *rep*: short-range hard-core repulsive interactions due to hard-core effects as modeled by BMCS model. *dip*: dipolar contribution from perturbation theory using Padé approximation (**Rushbrooke et al., 1973**). *per*: perturbation as modeled by a generalized empirical van der Waals attractive term. The authors assumed complete ion-association into ion-pairs. The authors validated the model against NaCl, KCl, and their mixture in an aqueous system
Donohue and coworkers (**1986**); (**1988a**); (**1988b**); (**1991**)	*PACT* + *HP* + *B*		*PACT* for short-range intermolecular interactions, *HP* for long-range Coulombic interactions, and Born term. *PACT* EOS takes into account molecular moments and chemical equilibria and provides acceptable results for pure water properties up to critical point. The model contains one adjustable parameter per anion-cation pair. Although the ionic radii (for both cations and anions) were originally introduced from the Pauling radii, the authors proposed to use the ionic radii as an adjustable parameter. The Jin and Donohue model (**1991**) applied ionic parameters in lieu of electrolyte parameters. Model validity: T= 0 – 100°C, up to 5 M.

* ***attr***: attraction term; ***assoc***: association term; ***attr***: attraction term; ***B***: Born term; ***BMCS***: Boublik-Mansoori extension (**Boublik, 1970**; **Mansoori et al., 1971**) of the Carnahan-Starling EOS for hard spheres; ***dip***: Dipolar contribution; ***ex***: excess Helmholtz free energy; ***hc***: hard-sphere chain term; ***hs***: hard-sphere term; ***HP***: Perturbation expansion for ion-ion interactions based on a restricted primitive perturbation theory (**Henderson & Blum, 1981**); ***Hu***: Helmholtz free energy framework represented by Hu et al. (**1984**; **1985**); ***igm***: ideal gas mixture; ***lr***: Long-range electrolyte interactions; ***MSA***: mean spherical approximation; ***NE:*** non-electrolyte; ***nMSA***: non-primitive *MSA*; ***PACT***: Perturbed-Anisotropic-Chain Theory. This model is non-cubic and transformed to associating *PACT* (*APACT*) by taking into account hydrogen bonding; ***PDH***: Pitzer-DH model (**Pitzer & Simonson, 1986**); ***per***: perturbation; ***Pert***: perturbation theory; ***re***: Residual; ***ref***: Reference state or system; ***sr***: Short-range interaction.

Appendix D: Debye-Hückel Theory

The Debye-Hückel theory (**1923**) is based on a McMillan-Mayer level perspective in the statistical mechanics: stripping away the solvent (water) molecules and, in turn, using a primitive model by considering the main contribution of water in the electrolyte solution to provide dielectric continuum. The Debye-Hückel formulation can be achieved by the classical approach or through the statistical mechanics. We follow the former approach in a same manner as did the Debye and Hückel. They solved the Poisson's equation to relate the charge density (ρ) around ion *i* to the electrical potential (Ψ) for a sphere with radius *r* around ion *i*. From electrostatics the Poisson's equation is,

$$\nabla.\left(\epsilon_f \nabla\Psi_c(r)\right) = -\rho_c(r), \qquad r > \dot{a}_{DH}, \qquad \textbf{Eq. D- 1}$$

where $\Psi_c(r)$ denotes the average electrostatic potential that a test charge experiences at radius r from it center, ϵ_f is effective permittivity the product of relative-permittivity (or dielectric constant) of the solvent (ϵ_r) ($\epsilon_r = 78.30$ for water at 25 ℃) and permittivity at the vacuum (ϵ_0), and ρ_c is the charge density at r from center of charge $z_c e$ and $\dot{a}_{DH}$ denotes the distance of the closest approach between two rigid, hard-spheres, counter-charge ions.

If the size of ions does not differ considerably (i.e., equal-size assumption $\dot{a}_{DH}$ is simply reduced to the diameter of each ion). For any radius less than $\dot{a}_{DH}$, there is no other charge except for the charge at the center and, consequently, the Poisson equation reduces to,

$$\nabla.\left(\epsilon_f \nabla\Psi_c(r)\right) = 0, \qquad 0 < r \leq \dot{a}_{DH}, \qquad \textbf{Eq. D- 2}$$

In the following, we drop the radial distance notation focusing on $r > \dot{a}_{DH}$. For a continuum with constant effective permittivity, the Poisson equation simplifies to,

$$\nabla^2\Psi_c(r) = -\frac{1}{\epsilon_f}\rho_c(r). \qquad \textbf{Eq. D- 3}$$

The charge density per unit volume is defined as,

$$\rho_c(r) = \sum_j z_j e \rho_j \varphi_{jc}(r), \qquad \textbf{Eq. D- 4}$$

where *e* is the electrostatic charge, z_j denotes the charge of species *j*. The number density (ρ_j) is number of ions of species *j* per volume,

$$\rho_j = \frac{N_A n_j}{nV}, \qquad \textbf{Eq. D- 5}$$

where *n* is moles of all ions, n_j is mole number of component *j*, *V* is molar volume, and N_A is Avogadro's number ($N_A = \mathrm{R}/k = 6.23 \times 10^{23}$). In Eq. D- 4, the summation *j* is over all ionic species (anions and cations) situated at radius *r* from the charge center. Considering a strongly simplifying assumption on the density distribution of ions, the radial distribution function (φ_{jc}) can be represented with the Boltzmann probability function,

$$\varphi_{jc}(r) = exp\left(\frac{-1}{kT} E(r)\right), \qquad \textbf{Eq. D- 6}$$

where *k* is the Boltzmann constant (*k*=1.38×10^{-23} *J/K*) and T is temperature in Kelvin. The energy of interaction (*E*) is defined in terms of average electrostatic potential, $E(r) = z_j e \Psi_c(r)$. Combining **Eq. D-** 3 to **Eq. D-** 6 results in the Poisson-Boltzmann equation,

$$\nabla^2 \Psi_c(r) = -\frac{e}{\epsilon_f} \sum_j z_j \rho_j exp\left(\frac{-z_j e \Psi_c(r)}{kT}\right). \qquad \textbf{Eq. D- 7}$$

Generally, solving **Eq. D-** 7 is not trivial. Debye and Hückel expanded the exponential function and linearized the equation,

$$\varphi_{jc}(r) = exp\left(\frac{-z_j e \Psi_c(r)}{kT}\right) = 1 - \frac{z_j e}{kT} \Psi_c(r) + \frac{1}{2}\left(\frac{z_j e}{kT} \Psi_c(r)\right)^2 + \cdots \cong 1 - \frac{z_j e}{kT}. \qquad \textbf{Eq. D- 8}$$

This simplifies the Poisson-Boltzmann equation to,

$$\nabla^2\Psi_c(r) = -\frac{1}{\epsilon_r\epsilon_0}\left[\sum_j z_j e\rho_j - \sum_j z_j e\rho_j \frac{z_j e}{kT}\Psi_c(r)\right], \qquad \textbf{Eq. D- 9}$$

where the first term in the right hand side of **Eq. D-** 9 is equal to zero because of the electro neutrality. This reduces the Poisson-Boltzmann equation to,

$$\nabla^2\Psi_c(r) = -\lambda^2\Psi_c(r), \qquad \textbf{Eq. D- 10}$$

where λ_{DH} as the Debye-Hückel screening length is given by,

$$\lambda_{DH}^2 = \frac{e^2}{kT\epsilon_f}\sum_j z_j^2\rho_j \cong \frac{2d_s N_A^2 e^2}{RT\epsilon_f} I, \qquad \textbf{Eq. D- 11}$$

where d_s is the solvent density which is a good approximation for total density where a dilute solution or small size solutes are considered (total density=$\frac{n_w M_w + \sum n_i M_i}{nV} \cong \frac{n_w M_w}{nV}$). The Debye-Hückel screening length approximates the thickness of the screening layer of the counter-charge ions around a center charge ion. The inverse of the Debye-Hückel screening length is a measure of the electrical double-later thickness (i.e., a first estimate of the distance beyond which Coulomb interactions can be essentially ignored). The Debye length is a solution property and for aqueous solution at 25 ℃ depends on electrolyte concentration:

$$\lambda_{DH}{}^{-1} = \frac{0.429}{Z\sqrt{M}} = \begin{cases} \frac{0.304}{\sqrt{M}} & \text{for 1: 1 symetrical electrolytes,} \\ \frac{0.176}{\sqrt{M}} & \text{for 2: 1 and 1: 2 assymetrical electrolytes,} \\ \frac{0.152}{\sqrt{M}} & \text{for 2: 2 symetrical electrolytes,} \\ \frac{0.124}{\sqrt{M}} & \text{for 1: 3 assymetrical electrolytes.} \end{cases} \qquad \textbf{Eq. D- 12}$$

In the spherical coordinates, the Poisson equation is,

$$\nabla^2\Psi_c = \frac{1}{r^2}\frac{\partial}{\partial r}\left(r^2\frac{\partial\Psi_c}{\partial r}\right) + \frac{1}{r^2\sin\theta}\frac{\partial}{\partial\theta}\left(sin\theta\frac{\partial\Psi_c}{\partial\theta}\right) + \frac{1}{r^2\sin^2\theta}\frac{\partial^2\Psi_c}{\partial\varphi^2}. \quad \textbf{Eq. D- 13}$$

Since the full sphere around ion is considered for the electrolyte system, the symmetric system with respect to φ and θ coordinates prevails (derivatives are zero). As a result,

$$\nabla^2\Psi_c(r) = \frac{d^2\Psi_c(r)}{dr^2} + \frac{2}{r}\frac{d\Psi_c(r)}{dr} = -\lambda_{DH}^2\Psi_c(r). \quad \textbf{Eq. D- 14}$$

The solution of this Helmholtz's type equation using the Laplace transform obtains,

$$\Psi_c(r) = \frac{1}{r}[C_1\, exp(\lambda_{DH}r) + C_2\, exp(-\lambda_{DH}r)]. \quad \textbf{Eq. D- 15}$$

Two boundary condition assist to solve for the C_1 and C_2 constant. The first coefficient is zero because as r→ ∞, a bounded value for the average potential is required; for the second coefficient, considering the point charge assumption without an excluded volume imposes that the Coulomb potential dominates interactional potential. Next, we apply the Gauss's law at the region within $r= \dot{a}_{DH}$ to obtain the second required boundary condition. At the charge surface, the Gauss's law relates outward component of the electrical charge at the closed region with the enclosed charge:

$$\frac{d\Psi_c}{dr} = -\frac{z_c e}{4\pi\varepsilon_f\dot{a}_{DH}^2}. \quad \textbf{Eq. D- 16}$$

Implementing the above condition to **Eq. D-** 15 and dropping the coefficient C_1 returns,

$$\frac{d\Psi_c}{dr} = \frac{d}{dr}\left(\frac{1}{r}C_2\, exp(-\lambda_{DH}r)\right) = -\frac{z_c e}{4\pi\varepsilon_f\dot{a}_{DH}^2}. \quad \textbf{Eq. D- 17}$$

Rearranging for C_2 completes the potential distribution satisfying the boundary conditions for the average electrical potential as,

$$\Psi_c(r) = \frac{z_c e}{4\pi\epsilon_f} \frac{exp(\lambda_{DH}\dot{a}_{DH})}{1+\lambda_{DH}\dot{a}_{DH}} \frac{exp(-\lambda_{DH} r)}{r}. \qquad \textbf{Eq. D- 18}$$

The Debye-Hückel theory implies that potential is diminishes as the radial distance increases from the central charge and is different from the Coulomb potential [$\Psi' = -e^2/(4\pi\epsilon_r\epsilon_0 r^2)$] due to ionic atmosphere around the central charge. Next, we relate the average electrostatic potential to the Helmholtz energy. The differential electrical work (dw_i) required to add one ion with charge dQ_i to electrolyte solution (from r=∞ to r=$\dot{a}_{DH}$) is represented by the product of the electrical potential at the surface and the charge of the ion ($dw_i = \Psi_i dQ_i$). The charge of each ion is $dQ_i = z_i e\omega$ where ω denotes the fraction of final charge due to any ion and varies from zero to one during the charging process.

$$dW_i^{add} = \sum_i \Psi_i dQ_i = \sum_i \left(\frac{z_i e}{4\pi\epsilon_f} \frac{1}{\dot{a}_{DH}(1+\omega\lambda_{DH}\dot{a}_{DH})} \right) z_i e d\omega. \qquad \textbf{Eq. D- 19}$$

In the same manner, the differential electrical work required to remove charge from the ions is represented by,

$$dW_i^{rem} = \sum_i \left(\frac{z_i e}{4\pi\epsilon_f} \frac{1}{\dot{a}_H} \right) z_i e d\omega. \qquad \textbf{Eq. D- 20}$$

The electrical contribution of each atom *i* to the excess chemical potential is the difference between these two work terms integrated over range of zero to one at any time during the charging process ($\mu_i^E = dW_i^{add} - dW_i^{rem}$). It is, also, common to replace individual distance of the closest approach with a common size, resulting in:

$$\mu^E = \frac{z_i^2 e^2 N_A}{4\pi\epsilon_f \dot{a}_{DH}} \int_0^1 \left(\frac{\omega}{(1+\lambda\dot{a})} - \frac{\lambda_{DH}\omega}{\dot{a}_{DH}} \right) d\omega. \qquad \textbf{Eq. D- 21}$$

Solving and further manipulation of **Eq. D-** 21 obtains the chemical potential as,

$$\mu^E = -\frac{z_i^2 e^2 N_A \lambda_{DH}}{8\pi\epsilon_f(1+\lambda_{DH}\dot{a}_{DH})}, \qquad \textbf{Eq. D- 22}$$

The Debye-Hückel theory assumes a dilute enough solution to ignore the chemical contribution to non-ideality of the chemical potential. The rational activity coefficient, therefore, for the Debye-Hückel law is defined as,

$$\ln\gamma^* = \left[\frac{\partial}{\partial n_i}\left(\frac{nG^E}{RT'}\right)\right]_{T',P,n_j j\neq i} = \frac{\mu^E}{RT'}. \qquad \textbf{Eq. D- 23}$$

Replacing in **Eq. D-** 22 completes the molal activity coefficient model from the Debye-Hückel theory (note that $\ln\gamma_i^m = \ln(w_w\gamma_i^*)$ where w_w is the mole fraction of water in aqueous phase).

$$\ln\gamma_i^m = \ln(w_w) - \frac{z_i^2 A_{DHL}\sqrt{I}}{1+B_{DHL}\dot{a}_{DH}\sqrt{I}}, \qquad \textbf{Eq. D- 24}$$

where, $A_{DHL} = \frac{(2d_s)^{\frac{1}{2}}}{8\pi}N_A^2\left(\frac{e^2}{\varepsilon_f RT'}\right)^{3/2}$, and $B_{DHL} = \left(\frac{2e^2N_A^2d_S}{\varepsilon_f RT'}\right)^{1/2}$. A_{DHL} and B_{DHL} are temperature dependent coefficients and at room temperature $A_{DHL} = 0.508$ and $B_{DHL} = 0.328\times10^{10}/m$. **Table D-1** lists the for common ions in subsurface aqueous phase.

Table D-1: The distance of the closest approach of ions (**Garrels & Christ, 1965**)

Ion name	$\dot{a}_{DH}$ (A°)
k^+, Cl^-, Br^-, I^-	3.0
F^-, HS^-, OH^-	3.5
$Na^+, HCO_3^-, SO_4^{2-}, HSO_3^-, CO_3^{2-}, SO_3^{2-}$	4.0-4.5
$a^{2+}, Fe^{2+}, Ni^{2+}, Co^{2+}$	6.0
Mg^{2+}	8.0
H^+, Al^{3+}	9.0

Appendix E: Derivative of UTKR3P Three-Phase Relative Permeability Model

As discussed in Chapter 3, the UTKR3P model is applicable to both black-oil and compositional reservoir simulators. This appendix gives the analytical derivative of UTKR3P model if it is implemented into a fully-implicit or adaptive-implicit based simulator where the numerical derivatives are not preferred. Recall that the UTKR3P formalism is:

$$k_{rj} = k_{rj}^{0} \frac{(1+C_{2j})\bar{S}_j^{C_{1j}}}{1+C_{2j}\bar{S}_j^{C_{1j}\left(1+\frac{1}{C_{2j}}\right)}} \qquad j = \text{phase 1, 2, or 3} \qquad \textbf{Eq. 3-1}$$

where,

$$\bar{S}_j = \frac{S_j^f}{1-\sum_{i=1,i\neq j}^{3} S_{ir}^{3P}}, \qquad \textbf{Eq. 3-2}$$

and,

$$F_j = \frac{S_m^* F_{jm} + S_l^* F_{jl}}{S_m^* + S_l^*}. \qquad \textbf{Eq. 3-3}$$

Here, F_j is a relative permeability parameter. Adopting two arbitrary saturations S_j and S_l as independent variables and S_m as dependent variable, we have:

$$\frac{\partial S_m^*}{\partial S_j} = -1, \frac{\partial S_m^*}{\partial S_l} = -1, \frac{\partial S_l^*}{\partial S_j} = 0, and\ \frac{\partial S_l^*}{\partial S_l} = 1. \qquad \textbf{Eq. E- 1}$$

The derivative of phase relative permeability wrt independent variables is defined by,

$$\frac{\partial k_{rj}}{\partial S_h} = k_{rj} \frac{\partial}{\partial S_h}[\alpha_1 + \alpha_2 + \alpha_3 - \alpha_4], \quad h = j\ and\ l \qquad \textbf{Eq. E- 2}$$

where

$$\alpha_1 = \ln k_{rj}^0,$$

$$\alpha_2 = \ln(1 + C_{2j}),$$

$$\alpha_3 = C_{1j} \ln \bar{S}_j,$$

$$\alpha_4 = \ln\left(1 + C_{2j}\bar{S}_j^{C_{1j}\left(1+\frac{1}{C_{2j}}\right)}\right).$$

Now, we decompose **Eq. E-** 2 based on the partial derivatives as follows:

$$\begin{aligned}
\frac{\partial \alpha_1}{\partial S_h} &= \frac{1}{k_{rj}^0}\frac{dk_{rj}^0}{dS_h}, \\
\frac{\partial \alpha_2}{\partial S_h} &= \frac{1}{1 + C_{2j}}\frac{\partial C_{2j}}{\partial S_h}, \\
\frac{\partial \alpha_3}{\partial S_h} &= \frac{C_{1j}}{\bar{S}_j}\frac{d\bar{S}_j}{dS_h} + \ln(\bar{S}_j)\frac{dC_{1j}}{dS_h}, \\
\frac{\partial \alpha_4}{\partial S_h} &= \frac{1}{1 + \alpha_5}\frac{d\alpha_5}{dS_h},
\end{aligned} \qquad \textbf{Eq. E- 3}$$

where

$$\alpha_5 = C_{2j}\bar{S}_j^{C_{1j}\left(1+\frac{1}{C_{2j}}\right)}.$$

The partial derivative of α_5 gives,

$$\frac{\partial \alpha_5}{\partial S_h} = \frac{1}{C_{2j}}\frac{\partial C_{2j}}{\partial S_h}\left[1 - \frac{C_{1j}\ln \bar{S}_j}{C_{2j}}\right] + \left(1 + \frac{1}{C_{2j}}\right)\left[\frac{\partial C_{1j}}{\partial S_h}\ln \bar{S}_j + \frac{C_{1j}}{\bar{S}_j}\frac{\partial \bar{S}_j}{\partial S_h}\right]. \qquad \textbf{Eq. E- 4}$$

To evaluate the partial derivative of each relative permeability parameter (F_j), we define the following set of dummy parameters, $\partial F_{ji}^h = \frac{\partial F_{ji}}{\partial S_h}, i = m \; and \; l$ where F_{ji} is two-phase relative permeability parameters (i.e., $k_{rji}^0, C_{1ji},$ and C_{2ji}). Then, the partial derivative of F_j with respect to two independent variables (h= j and l) gives,

$$\begin{aligned}
\frac{\partial F_j}{\partial S_j} &= \frac{S_m^*\partial F_{jm}^j + S_l^*\partial F_{jl}^j - F_{jm} + F_j}{S_m^* + S_l^*}, \\
\frac{\partial F_j}{\partial S_l} &= \frac{S_m^*\partial F_{jm}^l + S_l^*\partial F_{jl}^l - F_{jm} + F_{jl}}{S_m^* + S_l^*}.
\end{aligned} \qquad \textbf{Eq. E- 5}$$

The partial derivative of normalized saturation with respect to independent variables are,

$$\frac{\partial \bar{S}_j}{\partial S_h} = \frac{\partial}{\partial S_h}\left[\frac{S_j - S_{jt}}{1 - S_{mr} - S_{lr}}\right], \\ = \frac{1 - \partial S^h_{jt} + \bar{S}_j(\partial S^h_{mr} + \partial S^h_{lr})}{1 - S_{mr} - S_{lr}}, \quad \textbf{Eq. E- 6}$$

where $\partial S^h_{jt}, \partial S^h_{mr}$, and ∂S^h_{lr} are the partial derivatives of parameters with respect to independent variable h.

The partial derivative of residual saturations with respect to independent variables are,

$$\frac{\partial S_{ir}}{\partial S_h} = \frac{\partial}{\partial S_h}\left[S_{ir,2P}\left(1 - b_i S^*_q S^*_w\right)\right], \quad q, w \neq i \; and \; i = j, m, l \\ = \partial S^h_{ir,2P}\left(1 - b_i S^*_q S^*_w\right) - b_i S_{ir,2P}(S^*_q \partial S^{*h}_w + S^*_w \partial S^{*h}_q). \quad \textbf{Eq. E- 7}$$

It results in the following partial derivatives of each residual saturation

$$\therefore \frac{\partial S_{jr}}{\partial S_h} = \partial S^h_{jr,2P}\left(1 - b_j S^*_m S^*_l\right) - b_j S_{jr,2P}\left(S^*_m \partial S^{*h}_l - S^*_l\right), \\ \frac{\partial S_{lr}}{\partial S_h} = \partial S^h_{lr,2P}\left(1 - b_l S^*_m S^*_j\right) - b_l S_{lr,2P}\left(S^*_m \partial S^{*h}_j - S^*_j\right), \quad \textbf{Eq. E- 8} \\ \frac{\partial S_{mr}}{\partial S_h} = \partial S^h_{mr,2P}\left(1 - b_m S^*_j S^*_l\right) - b_m S_{mr,2P}(S^*_j \partial S^{*h}_l - S^*_l \partial S^{*h}_j).$$

where $\partial S^h_{ir,2P}$ is the partial derivative of two-phase residual saturation and is either zero or evaluated based on **Eq. E-** 8 for constant two-phase residual saturations or for the linear saturation-weighted two-phase residual saturations, respectively.

Appendix F: Derivative of UTHYST Three-Phase Hysteresis Model

As discussed in Chapter 4, the UTHYST model is a general multiphase hysteresis model applicable to broad range of multiphase relative permeability and capillary pressure models. This appendix gives the analytical derivative of UTHYST model. Recall that the UTHYST formalism is,

$$S_{jt} = min\left\{S_j, \underbrace{S_{jt}^I + \left(\Delta S_{jt}\right)_n \left(\frac{1 - S_m^I}{1 - S_m^c}\right)^{\alpha_j}}_{\hat{S}_{jt}}\right\}, \qquad \textbf{Eq. 4-1}$$

where phase trapping in the current cycle is calculated by,

$$\left(\Delta S_{jt}\right)_n = \frac{S_j^{max} - S_j}{1 + (L_j)_n \, S_j^{max}}, \qquad \textbf{Eq. 4-2}$$

and Land coefficient is evaluated based on a saturation history dependent parameter as,

$$(L_j)_n = \frac{1}{S_{jr}^M - S_{jt}^I} - \frac{1}{\left(S_j^M\right)_n - S_j^I}, \qquad \textbf{Eq. 4-3}$$

The partial derivative of trapped saturation with respect to independent variables ($S_h = S_j$ and S_l) are,

$$\begin{cases} \dfrac{\partial S_{jt}}{\partial S_h} = \dfrac{\partial \hat{S}_{jt}}{\partial S_h}, & if S_j > S_{jt}, \\ \dfrac{\partial S_{jt}}{\partial S_j} = 1 \text{ and } \dfrac{\partial S_{jt}}{\partial S_l} = 0, & if S_j \le S_{jt}. \end{cases} \qquad \textbf{Eq. F-1}$$

When $S_j > S_{jt}$,

$$\frac{\partial \hat{S}_{jt}}{\partial S_h} = \frac{\partial S_{jt}^I}{\partial S_h} + \left(\frac{1 - S_m^I}{1 - S_m^c}\right)^{\alpha_j} \frac{\partial \left(\Delta S_{jt}\right)_n}{\partial S_h} = \left(\frac{1 - S_m^I}{1 - S_m^c}\right)^{\alpha_j} \frac{\partial \left(\Delta S_{jt}\right)_n}{\partial S_h}. \qquad \textbf{Eq. F-2}$$

The derivative of trapped saturation within cycle *n* with respect to independent variables are,

$$\frac{\partial\left(\Delta S_{jt}\right)_n}{\partial S_l} = 0, \qquad \textbf{Eq. F-3}$$

$$\frac{\partial\left(\Delta S_{jt}\right)_n}{\partial S_j} = -\frac{1 + \frac{\partial\left(L_j\right)_n}{\partial S_j}\left(S_j^{max} - S_j\right)^2}{\left(1 + \left(L_j\right)_n S_j^{max}\right)^2}. \qquad \textbf{Eq. F-4}$$

Since the derivative of Land coefficient in any cycle *n* is zero (a constant value), the derivative of trapped saturation with respect to independent variables are summarized as,

$$\frac{\partial S_{jt}}{\partial S_l} = 0, \qquad \textbf{Eq. F-5}$$

$$\begin{cases} \dfrac{\partial S_{jt}}{\partial S_j} = \dfrac{-1}{\left(1 + \left(L_j\right)_n S_j^{max}\right)^2}, & if S_j > S_{jt}, \\ \dfrac{\partial S_{jt}}{\partial S_j} = 1, & if S_j \le S_{jt}. \end{cases} \qquad \textbf{Eq. F-6}$$

Appendix G: Standard Partial Molal GFE of Electrolyte Solution (HKF-EOS)

In the phenomenological work of developing an electrolyte EOS, Helgeson-Kirkham-Flowers (HKF) (**1981**) made a common proposition that the standard partial molal properties of an aqueous electrolyte solution can be expressed in terms of structural and electrostatic contributions and as a summation of intrinsic and electrostriction terms. The standard state convention for aqueous ions and electrolytes is one of unit activity of the aqueous solute in a hypothetical one molal solution referenced to infinite dilution at any pressure and temperature. For the case of standard partial molal Gibbs free energy ($\bar{G}^0$), we get:

$$\bar{G}_j^0(T,P) = \bar{G}_{j,in}^0 + \Delta\bar{G}_{j,es}^0, \qquad \textbf{Eq. G-1}$$

where $\bar{G}_{j,in}^0$ and $\Delta\bar{G}_{j,es}^0$ denote the intrinsic and electrostatic standard partial molal Gibbs free energies of the j^{th} aqueous ions, respectively. While the former is attributed solely to the ion, the latter contributes to ion-solvent interactions (i.e., structure-independent ion solvation ($\Delta\bar{G}_{j,col}^0$) and electrostatic ion-solvent ($\Delta\bar{G}_{j,sol}^0$)). Combining the non-solvation terms as $\bar{G}_{j,ns}^0 = \bar{G}_{j,in}^0 + \Delta\bar{G}_{j,sol}^0$, one may express $\bar{G}_{j,P,T}^0 = \bar{G}_j^0(P,T)$ as,

$$\bar{G}_{j,P,T}^0 = \bar{G}_{j,ns}^0 + \Delta\bar{G}_{j,es}^0. \qquad \textbf{Eq. G-2}$$

The standard partial molal Gibbs free energy of the i^{th} aqueous electrolyte is expressed as,

$$\bar{G}_{i,P,T}^0 = \sum_j \nu_{j,i}\bar{G}_{j,P,T}^0, \qquad \textbf{Eq. G-3}$$

where $\nu_{j,i}$ represents the stoichiomretric number of moles of j^{th} ion in one mole of i^{th} electrolyte. HKF derived the solvation term from the predicative Born Equation (**Born, 1920**). By further manipulations, HKF obtained the following formulation for the pressure and temperature dependent apparent standard partial molal Gibbs free energy,

$$\Delta\bar{G}_{j,T,P}^0 = \Delta\bar{G}_{f,j}^0 - \bar{S}_{j,P_r,T_r}^0 - C_{H1,j}(Tln(T/T_r) - \Delta T_r \; + \qquad \textbf{Eq. G-4}$$

$$C_{H2,j}(\Delta T_r - \Delta T_{\theta_j} \ln\left(\Delta T_{\theta_j}/\left(\Delta T_{\theta_j} - \Delta T_r\right)\right) +$$

$$\left[\begin{matrix}2\left(a_{H1,j}\Delta T_{\theta_j} + a_{H3,j}T\right)(\Delta P_r) - \\ \left(a_{H2,j}\Delta T_{\theta_j} + a_{H4,j}T\right)(P^2 - P_r^2)\end{matrix}\right]\Big/ 2\Delta T_{\theta_j} -$$

$$\omega_j\left(Z_{P,T} - Z_{P_r,T_r} - Y_{P_r,T_r}\Delta T_r\right),$$

where

$$\Delta T_A = T - T_A,$$
$$Z_{P,T} = -\varepsilon_f^{-1}(T,P),$$
$$Y_{P,T} = \frac{1}{\varepsilon_f}\left(\frac{\partial ln\varepsilon_f}{\partial T}\right)_P.$$

Both relative permittivity (dielectric constant) and density of water are estimated based on a procedure as proposed by Helgeson and Kirkham (**1974**).

Relative permittivity

Solvent (water) relative permittivity is calculated from a fourth degree power function of pressure and density as,

$$\varepsilon_f = \sum_{i=0}^{4}\sum_{j=0}^{4-i} e_{H,ij}T^i\rho^j, \qquad \textbf{Eq. G-5}$$

$$\left(\frac{\partial ln\varepsilon_f}{\partial T}\right)_P = \sum_{i=0}^{4}\sum_{j=0}^{4-i} e_{H,ij}\rho^j T^i(iT^{i-2} - j\alpha_H). \qquad \textbf{Eq. G-6}$$

In **Eq. G-5** and **Eq. G-6**, ρ stands for water density and $e_{H,ij}$ is defined as,

$$e_{H,ij} = \hat{e}_{H,ij} \times 10^{e^*_{H,ij}}, \qquad \textbf{Eq. G-7}$$

where constants $\hat{e}_{H,ij}$ and $e^*_{H,ij}$ are listed in **Table G-1** and **Table G-2**.

Water density

Water density is calculated by applying an iterative method. Based on the differential equation of

Helmholtz free energy we have,

$$dA = -SdT - PdV = -SdT + \frac{P}{\rho^2}d\rho. \qquad \textbf{Eq. G- 8}$$

Helgeson and Kirkham (**1974**) applied the Helmholtz function derived by Keenan et al. (**1969**),

$$\psi = \psi_0 + RT(\ln\rho + \rho Q). \qquad \textbf{Eq. G- 9}$$

where $\psi_0 = f(T)$ and Q term is defined as,

$$Q = x\sum_{j=1}^{7} y_j\, z_j, \qquad \textbf{Eq. G- 10}$$

where

$$x = (\tau - \tau_c),$$
$$y_j = \left(\tau - \tau_{aj}\right)^{j-2},$$
$$z_j = \left(\sum_{i=1}^{8} A_{ij}\left(\rho - \rho_{aj}\right)^{i-1} + e^{-4.8\rho}\sum_{i=9}^{10} A_{ij}\rho^{i-9}\right).$$

In Eq. G- 10**,** $\tau = 1/T$ and $\tau_c = 1.5449$, T denotes temperature in Kelvin, $\tau_{aj} = \tau_c$ for $j = 1$ and $\tau_{aj} = 2.5$ for $j > 1$. **Table G-3** provides the coefficients A_{ij}. Combining Eq. G- 8 and Eq. G- 10 results in,

$$P = \rho^2\left(\frac{\partial A}{\partial\rho}\right)_T = \rho RT\left(1 + \rho Q + \rho^2\left(\frac{\partial Q}{\partial\rho}\right)_T\right), \qquad \textbf{Eq. G- 11}$$

where P denotes pressure in bar and $(\partial Q/\partial\rho)_T$ is evaluated by **Eq. G-** 12. The partial derivative of Q with respect to density at constant pressure in a cumulative format as,

$$\left(\frac{\partial Q}{\partial\rho}\right)_T = x\sum_{j=1}^{7} y_j\left(\frac{\partial z_j}{\partial\rho}\right)_T. \qquad \textbf{Eq. G- 12}$$

Based on the definition of z_j term, one obtains its derivative as,

$$\left(\frac{\partial z_j}{\partial \rho}\right)_T = \sum_{i=1}^{8}(i-1)A_{ij}\left(\rho-\rho_{aj}\right)^{i-2} + e^{-4.8\rho}\left(A_{10j} - 4.8\sum_{i=9}^{10}A_{ij}\rho^{i-9}\right). \qquad \textbf{Eq. G- 13}$$

Table G-4 lists the standard partial molal thermodynamic GFE, enthalpy and entropy of selected aqueous species at the reference pressure and temperature, HKF coefficients (a_{H1}, a_{H2}, a_{H3}, a_{H4}, C_{H1}, and $C_{H2,j}$), Born coefficient ω, and structural temperature parameter (θ_H).

Table G-1: Coefficient $\hat{e}_{H,ij}$ (**Eq. G-7**)

$i\downarrow\ /\ j\rightarrow$	0	1	2	3	4
0	4.391096	-2.33277	4.616621	-4.03643	1.31604
1	-2.18995	1.004984	-1.35651	5.940469	0
2	1.828982	-2.08896	1.604913	0	0
3	1.544887	-6.13942	0	0	0
4	-6.13542	0	0	0	0

Table G-2: Coefficient $e^*_{H,ij}$ (**Eq. G-7**)

$i\downarrow\ /\ j\rightarrow$	0	1	2	3	4
0	2	0	-3	-6	-9
1	2	0	-3	-7	0
2	1	-1	-4	0	0
3	2	-2	0	0	0
4	1	0	0	0	0

Table G-3: Coefficient $A_{H,ij}$ in term z_j (**Eq. G-** 10)

$i\downarrow\ /\ j\rightarrow$	1	2	3	4	5	6	7
1	29.49294	-5.19859	6.833535	-0.15641	-6.39724	-3.96614	-0.69049
2	-132.139	7.779182	-26.1498	-0.72546	26.40928	15.45306	2.740742
3	274.6463	-33.3019	65.3264	-9.27343	-47.7404	-29.1425	-5.10281
4	-360.938	-16.2546	-26.182	4.312584	56.32313	29.5688	3.963609
5	342.1843	-177.311					
6	-244.5	127.4874					
7	155.1854	137.4615					
8	5.972849	155.9784					
9	-410.308	337.3118	-137.466	6.787498	136.8732	79.84797	13.04125
10	-416.059	-209.889	-733.968	10.40172	645.8188	399.1757	71.53135

Table G-4: Conventional Standard partial molal thermodynamic properties of selected aqueous species at 25℃

Species	$\Delta\bar{G}^0_{f,j}$ (kJ/mol)	$\Delta\bar{H}^0_{f,j}$ (kJ/mol)	$\bar{S} \times 10^2$ (kJ/mol/K)	$C_{H1} \times 10^2$ (kJ/mol/K)	$C_{H2} \times 10^3$ (kJ/mol/K)	$a_{H1} \times 10^4$ (kJ/mol/bar)	$a_{H2} \times 10^8$ (kJ/mol/bar^2)	$a_{H3} \times 10^5$ (kJ/mol/bar)	$a_{H4} \times 10^9$ (kJ/mol/bar)^2	$\omega \times 10^1$ (kJ/mol)	θ (K)
Ag^+	77.15	105.82	7.33	8.40	-5.53	0.84	31.40	-1.30	16.33	9.04	264.90
Al^{3+}	-489.73	-531.76	-30.81	27.33	-33.03	-29.43	-3.77	-13.40	90.85	120.21	229.60
Au^+	163.29	201.70	11.10	6.71	-10.43	17.17	12.56	-6.28	46.89	7.54	245.60
Au^{3+}	433.75	414.13	-21.44	18.73	-32.95	-29.52	-3.77	-13.40	90.85	100.51	229.60
Ba^{2+}	-561.11	-538.01	0.96	14.33	-26.97	-4.65	43.50	-9.58	66.53	41.24	245.02
Br^-	-104.11	-121.58	8.29	2.69	-31.46	37.43	-70.18	-27.80	179.61	58.02	206.75
Ca^{2+}	-553.31	-543.46	-5.65	15.02	-13.86	-14.96	47.74	-0.52	7.40	51.77	266.14
Cl^-	-131.38	-167.19	5.69	-2.03	-8.55	24.12	-29.14	-4.48	43.40	60.96	246.02
Cs^+	-291.90	-258.21	13.31	12.54	-39.30	28.05	-18.46	-17.94	117.48	4.08	217.04
Cu^+	50.03	71.73	4.06	11.36	-4.69	-9.21	35.59	-0.42	10.89	14.03	271.40
Cu^{2+}	65.53	65.73	-9.71	16.63	-18.21	-22.19	23.03	-2.93	26.38	61.83	257.00
F^-	-281.87	-335.58	-1.34	0.37	-4.42	3.44	4.68	-0.09	1.31	74.82	272.42
Fe^{2+}	-78.92	-89.19	-13.77	14.79	-17.04	-19.68	26.80	-2.09	21.35	61.02	260.80
Fe^{3+}	-4.61	-48.57	-31.61	27.64	-37.18	-30.52	-8.79	-16.33	108.86	113.15	223.90
H^+	0.00	0.00	0.00	0.00	0.00	0.00	0.00	0.00	0.00	0.00	0.00
$HCO3^-$	-587.33	-690.39	9.84	6.45	-12.56	33.02	-37.36	-11.22	60.08	55.66	236.87
Hg^{2+}	164.76	170.27	-3.35	18.34	-15.53	-15.49	31.82	-1.05	14.65	48.20	267.90
HS^-	12.06	-17.66	6.28	-1.03	-9.50	27.26	-29.22	-5.41	41.16	59.08	252.19
I^-	-51.97	-56.94	10.68	0.57	-28.54	58.45	-120.08	-70.60	437.90	54.15	186.51
K^+	-282.93	-252.34	10.13	7.73	-12.25	13.01	3.12	-8.15	60.73	8.07	234.19
Li^+	-292.85	-278.64	1.13	11.43	-5.17	0.17	15.16	-0.18	9.34	20.36	253.94
Mg^{2+}	-455.11	-467.09	-13.82	16.34	-11.16	-17.46	58.98	-0.03	2.95	64.36	270.56
Mn^{2+}	-228.18	-220.74	-7.37	19.09	-14.95	-13.82	34.75	-0.63	12.14	58.64	267.50
Na^+	-262.19	-240.46	5.86	14.95	-26.32	8.01	-20.03	-23.56	153.07	13.84	215.17
$NH4^+$	-79.51	-133.35	11.14	14.25	-16.04	23.24	-25.46	-12.08	81.81	7.50	225.29
$NO3^-$	-111.41	-207.37	14.70	16.01	-74.19	52.08	-134.23	-76.52	445.23	47.29	185.29
OH^-	-157.44	-230.18	-1.09	10.35	-25.99	2.16	-0.42	-8.31	45.35	72.21	253.52
Pb^{2+}	-24.04	0.92	1.76	23.16	-15.20	-12.14	32.66	-0.84	13.40	45.17	267.80
$SO4^{--}$	-745.05	-910.21	1.88	0.56	-19.65	24.39	18.66	-2.72	29.83	133.38	263.03
Sr^{2+}	-559.82	-546.20	-3.27	14.23	-13.02	-14.43	54.75	-0.58	3.78	47.57	268.97
Zn^{2+}	-147.92	-153.49	-10.97	18.12	-15.91	-17.17	31.40	-1.30	16.33	61.02	266.20

Appendix H: Standard Partial Molar GFE of Electrolyte Solution (Approximation Method)

In this appendix, we review the approximation method to calculate the standard molar GFE of electrolytes. This alternative option (compare to the described method in **Appendix G**) is applicable when for some components the reference data is not provided by the HKF tables or when the approximation method suffices. Based on the definition of GFE of component *i* in a mixture and assuming a constant partial molar enthalpy ($\bar{H}_i = -T^2(\partial(\bar{G}_i/T)/\partial T)_{P,n_j\, j\neq i}$) and partial molar volume ($\bar{V}_i = (\partial \bar{G}_i/\partial T)_{T,n_j\, j\neq i}$) over the field operation conditions, one may obtain molar GFE at elevated pressure and temperature from the reference condition (**Sandler, 2006**),

$$\bar{G}^0_{iw}(T,P) = \bar{G}^{ref}_{iw} + \bar{V}^{\infty,T_{ref}}_{iw}\,(P - P^{ref}) + \bar{H}^{ref}_{iw}(1 - T/T^{ref}), \qquad \textbf{Eq. H-1}$$

$$\underline{G}^0_W(T,P) = \underline{G}^{ref}_W + \underline{V}^{0,T_{ref}}_W\,(P - P^{ref}) + \underline{H}^{ref}_W(1 - T/T^{ref}), \qquad \textbf{Eq. H-2}$$

where reference properties for water component and electrolytes are from pure water state and an ideal hypothetical unit molality solution, respectively. The reference GFE and enthalpy (kJ/mole) for some common species in aqueous system are listed in **Table H-1**.

Table H-1: Reference GFE and enthalpy (kJ/mol) for some solutes in aqueous system based on an ideal hypothetical unit molality at T=25℃ and P=1 atm (**Rossini et al., 1952**)

Substance	$\bar{G}_w^{ref}$	$\bar{H}_w^{ref}$	Substance	$\bar{G}_w^{ref}$	$\bar{H}_w^{ref}$	Substance	$\bar{G}_w^{ref}$	$\bar{H}_w^{ref}$
Aluminum			CO_3^{2-}	-528.1	-676.26	$ClO3^-$	-2.59	-98.32
Al^{3+}	-481.16	-524.67	CH_2O_2	-356.06	-410.03	**Fluorine**		
Barium			H_2CO_3	-623.42	-698.73	F-	-276.48	-329.11
Ba^{2+}	-560.66	-538.36	CH_3OH	-175.23	-245.89	HF	-294.6	-329.11
$BaHCO3^+$	-1147.71	-1229.47	CH_4ON_2	-203.84	-319.24	HF_2^-	-575.3	-642.66
$BaCO_3$	-1088.68		**Calcium**			**Iron**		
$BaOH^+$	-717.95	-768.3	Ca^{2+}	-553.04	-542.96	Fe^{2+}	-84.94	-87.86
$Ba(OH)_2$	-875.29	-998.22	$CaHCO_3^+$	-1140.1	-1234.07	$Fe(OH)^{2+}$	-233.93	-282
$BaBr_2$	-766.09	-780.19	$CaCO_3$	-1081.15	-1219.22	$Fe(OH)_2^+$	-444.34	
$BaCl_2$	-822.99	-873.28	$CaOH^+$	-710.34	-772.9	$FeCl^{2+}$	-150.21	-179.49
BaI_2	-664.00	-650.24	$Ca(OH)_2$	-867.64	-1002.82	FeO_2H^-	-379.07	
$BaSO_4$	-1302.48	-1445.86	$CaCl_2$	-815.38	-877.89	**Hydrogen**		
$Ba(NO_3)_2$	-781.57	-951.48	CaF_2	-1106	-1201.18	H_2	0	0
$Ba(CHO_2)_2$	-1734.69	0	$CaBr_2$	-758.68	-784.79	OH^-	-157.3	-229.94
Bromine			$CaSO_4$	-1295.03	-654.84	H^+	0	0
Br^-	-102.82	-120.92	$Ca(NO_3)_2$	-774.04	-1450.47			
HBrO	-83.26	0	$Ca(HCO_3)_2$	-1727.16	-956.09			
Carbon			**Chlorine**					
HCO_3^-	-587.06	-691.11	Cl-	-131.17	-167.46			
CO_2	-386.23	-412.92	HClO	-79.96	-116.44			

Table H-1 (cont'd): Reference GFE and enthalpy (kJ/mol) for some solutes in aqueous system based on an ideal hypothetical unit molality at T=25℃ and P=1 atm (**Rossini et al., 1952**)

Substance	$\overline{G}_w^{ref}$	$\overline{H}_w^{ref}$	Substance	$\overline{G}_w^{ref}$	$\overline{H}_w^{ref}$	Substance	$\overline{G}_w^{ref}$	$\overline{H}_w^{ref}$
Magnesium			**Potassium**			$Sr(NO_3)_2$	-777.39	-958.22
Mg^{2+}	-456.01	-461.96	KCl	-413.45	-418.65	$Sr(HCO_3)_2$	-1731.34	-1927.57
$MgHCO_3^+$	-1043.07	-1153.07	$KClO_3$	-284.89	-349.53	**Sodium**		
$MgCO_3$	-984.12	-1138.22	$KClO_4$	-293.05	-382.63	Na^+	-261.87	-239.66
$MgOH^+$	-613.31	-691.90	KBr	-385.1	-372.12	$NaHCO_3$	-848.93	-930.77
$MgCl_2$	-718.35	-796.88	$KBrO_3$	-236.81	-291.21	$NaCO_3^-$	-789.98	-915.92
$MgBr_2$	-661.66	-703.79	KI	-333.95	-307.15	NaOH	-419.17	-469.6
MgI_2	-559.36	-573.84	KIO_3	-417.98	-481.16	NaF	-540.99	-568.77
$MgSO_4$	-1198.00	-1369.47	KNO_3	-392.79	-457.78	NaCl	-393.04	-407.11
Nitrogen			**Silicon**			$NaClO_3$	-264.47	-337.98
NH_4HCO_3	-666.55	-823.91	H_4SiO_4	-1256.46		$NaClO_4$	-272.63	-371.08
$(NH_4)_2CO_3$	-687.10	-941.86	**Strontium**			NaBr	-364.69	-360.58
NH_4^+	-79.50	-132.80	Sr^{2+}	-557.31	-545.51	Na_2SO_4	-1265.74	-1386.83
HNO_3	-110.50	-206.57	$SrHCO_3^+$	-1144.37	-1236.62	$NaNO_3$	-372.38	-446.23
$H_2N_2O_2^-$	75.310	-39.33	$SrCO_3$	-1085.41	-1221.77	**Sulfur**		
NH_3	-26.65	-80.83	$SrOH^+$	-714.61	-775.45	S^{2-}	83.68	41.84
NH_4OH	-263.8	-366.69	$Sr(OH)_2$	-871.11	-1005.37	SO_3^{2-}	-497.06	-624.25
K^+	-282.28	-251.21	$SrCl_2$	-818.81	-880.44	SO_4^{2-}	-741.99	-907.51
KOH	-439.58	-481.16	$SrBr_2$	-761.91	-787.43	HS^-	12.59	-179.49
			$SrSO_4$	-1298.3	-1453.44	H_2S	-27.36	-39.33

Appendix I: Ideal Gas Heat Capacity and Entropy

Petroleum Technical Data Book (**Daubert & Danner, 1997**) provides a comprehensive list of compounds ideal-gas heat capacity and entropy. Ignoring the enthalpy coefficient at $T = 0°R$, we apply an adjusted formulation as follows,

$$c_P \left(\frac{Btu}{lb\,°R}\right) = A + BT + CT^2 + DT^3 + ET^4, \quad \textbf{Eq. I-1}$$

$$S \left(\frac{Btu}{lb\,°R}\right) = Aln(T) + BT + \frac{C}{2}T^2 + \frac{D}{3}T^3 + \frac{E}{4}T^4, \quad \textbf{Eq. I-2}$$

where T is in $°R$ and $A - E$ are compounds coefficients as listed in the API data book and are generally valid for the range of reservoir applications as list below. **Table I-1** lists the required coefficients in **Eq. I-1** and **Eq. I-2**.

Table I-1: Coefficients for ideal gas heat capacity and entropy

Compound	A	$B \times 10^3$	$C \times 10^6$	$D \times 10^{10}$	$E \times 10^{14}$
water	0.447642	-0.0438	0.09149	-0.2265	0.13861
nitrogen	0.254098	-0.0332	0.04591	-0.124	0.075835
carbon dioxide	0.158843	-0.0674	0.44432	-3.8648	10.36916
hydrogen sulfide	0.237448	-0.0465	0.11644	-0.4531	0.574205
methane	0.538285	-0.4228	1.01783	-4.6573	6.94806
ethane	0.264612	-0.0491	0.87421	-5.1241	9.06741
propane	0.160304	0.25217	0.54429	-3.6757	6.77425
butane	0.099687	0.5331	0.16222	-1.7171	3.3479
iso-butane	0.099070	0.47747	0.27478	-2.3762	4.548225
pentane	0.111829	0.45703	0.25899	-2.1786	4.09225
iso-pentane	0.015946	0.7649	-0.0827	-0.5721	1.478385
neo-pentane	0.181771	0.37382	0.27648	-1.9029	3.301505
hexane	0.089705	0.5307	0.17335	-1.8088	3.512985
n-heptane	0.023136	0.52183	0.19034	-1.9388	3.77732
n-octane	0.077802	0.55873	0.15609	-1.8525	3.753675
n-nonane	0.061466	0.59148	0.15234	-2.0148	4.24315
n-decane	0.203437	-0.0708	1.22204	-9.2308	21.496
n-undecane	0.199863	-0.0593	1.20848	-9.1658	21.35355
n-dodecane	0.196878	-0.0496	1.19716	-9.1115	21.23456
n-tridecane	0.330217	-0.6419	2.10363	-14.884	34.26801
n-tetradecane	0.192186	-0.0345	1.17939	-9.0265	21.04813
n-pentadecane	0.190048	0.02648	1.16737	-8.9447	20.82175
n-hexadecane	0.188657	-0.0231	1.16602	-8.9625	20.9079
n-heptadecane	0.187198	-0.0184	1.16048	-8.936	20.84961
n-octadecane	0.185900	-0.0142	1.15556	-8.9123	20.79776
n-nonadecane	0.184737	-0.0105	1.15115	-8.8912	20.75129

Table I-1 (cont'd): Coefficients for ideal gas heat capacity and entropy

Compound	A	$B \times 10^3$	$C \times 10^6$	$D \times 10^{10}$	$E \times 10^{14}$
n-eicosane	0.183696	-0.0071	1.14722	-8.8724	20.7102
cyclopentane	-0.210728	1.09897	-0.3816	0.59556	-0.2499
cyclohexane	-0.180876	1.01601	-0.2307	-0.1841	1.02623
n-propylcyclohexane	-0.139692	1.09021	-0.374	0.48768	0.03033
n-butylcyclohexane	-0.104640	1.00314	-0.2957	0.17801	0.47974
n-pentylcyclohexane	-0.130846	1.09162	-0.391	0.58549	-0.13053
n-hexylcyclohexane	-0.113195	1.06168	-0.3805	0.61193	-0.26626
n-heptylcyclohexane	-0.136637	1.14093	-0.4661	0.9788	-0.81525
n-octylcyclohexane	-0.078811	1.0023	-0.3525	0.57393	-0.26132
n-nonylcyclohexane	-0.080179	0.9812	-0.3067	0.3117	0.17338
n-decylcyclohexane	-0.093692	1.03244	-0.3668	0.5845	-0.25117
benzene	-0.185637	1.06455	-0.5469	1.46756	-1.60024
toluene	-0.053111	0.69122	-0.1309	-0.3942	1.344565
methanol	0.256237	-0.0555	0.49608	-2.6713	4.411425
ethanol	0.103480	0.41145	0.12423	-1.3448	2.65031
n-propanol	0.075054	0.48939	0.07584	-1.1811	2.42624
n-butanol	0.037725	0.61935	-0.025	-0.837	1.99496
phenol	-0.070346	0.7818	-0.3251	0.55557	-0.16568
ethyl methyl ether	0.132270	0.41925	0.09014	-1.0094	1.8541

Appendix J: UTKR3P and UTHYST Models in IPARS Simulator

IPARS OVERVIEW

The Implicit Parallel Accurate Reservoir Simulator (IPARS) framework provides a general research simulator suitable for the purpose of examining several physics and mathematical approaches (**Wheeler, 2002**). In this dissertation, we implemented the developed models into the compositional element of the general framework.

In this appendix, we describe the updates implemented in IPARS reservoir simulator for the implementation of the three-phase UTKR3P and UTHYST models. We also describe the required input parameters and an input data file. The updated files for the implementation of these models include frame36c.siz, idata.df, prop.df, owell.df, rock.dh, xarydat.dh, xarray.df, xisdat.df, xprop.df, xstdout.df, xstep.df, and xutil.df.

UTKR3P MODEL

The three-phase UTKR3P model is a parameterized relative permeability model. It required an update on the input format of fluid petrophysical properties. Here, we updated the rock.dh and prop.df files to read the relevant relative permeability parameters. The user can define relative permeability parameters based on the designated rock types (*NXROCKS*). The logical *UTKR3PF* keyword in the input file turns the UTKR3P model on.

The input two-phase relative permeability parameters have a general format of (*X(j,i,rt)*). Here, *X* denotes the relative permeability parameter, *j* and *i* are the experimental property of phase *j* when flows with phase *i*, and *RT* represents the rock type. *X* parameters include endpoint relative permeabilities (*PRL*), first and second curvatures (*C1L* and *C2L*), and phase residual saturations (*SRL*). The general phase properties include critical saturations (*SC(j,rt)*) and b parameter in residual saturation formulation (*b(j,rt)*).

In general, three-phase relative permeability parameters are evaluated based on a linear saturation-weighted interpolation scheme between two-phase properties (see **Eq. 3-3**). The user can override this approach for any specified parameter and phase (i.e., keeping the parameter(s) constant during the simulation). Here, an appropriate *IX3P (IPR3P, IC13P, IC23P, ISR3P)* keyword and value must be added. The *IX3P* value is a three-digit integer where class of one, ten, and hundred represent water, oil, and gas phases, respectively. The *X3P* keyword followed by three real values are required for any designated parameter by the *IX3P* keyword. For example, *IC13P=101* followed by *C13P=3.0 0.0 5.0* assigns a constant first curvature of water and gas relative permeability curves during the simulation. If the relative permeability flag is turned on (*OUT_RELP= TRUE*) the relative permeability parameters and values are printed out to the fort.30 output file (use *IKRPRTSIZE, IKRPRTIDIM, IKRPRTJDIM,* and *IKRPRTKDIM*).

For example, **Table J-1** lists the relative permeability data for a set of general three phases (PH1, PH2, and PH3). Here, PH2 end-point relative permeability and PH1 1st curvature remain constant during the simulation. The relative permeability outputs of elements (1,1,1) and (15,4,5) for three phases are printed out.

The ROCK FLUID PROP section of IPARS input file includes the following keywords:

```
NXROCKS = 1      ROCK1(,,) =1      MODEREL(1) = 7    UTKR3PF= TRUE
C1L(1,2,1) = 3.00  C1L(1,3,1) = 3.00  C1L(2,1,1)= 4.00  C1L(2,3,1) = 4.00   C1L(3,1,1) = 5.00   C1L(3,2,1)= 5.00
C2L(,,)      = 0.0    C2L(3,1,1)=1.0     C2L(3,2,1)=1.5
PRL(1,2,1) = 0.4   PRL(1,3,1)= 0.5    PRL(2,1,1)=0.6    PRL(2,3,1) = 0.6    PRL(3,1,1)= 1.0     PRL(3,2,1)=1.0
SRL(1,2,1) = 0.10  SRL(1,3,1)= 0.14   SRL(2,1,1)=0.20   SRL(2,3,1) = 0.15   SRL(3,1,1)= 0.30    SRL(3,2,1)=0.25
BSR(,) = 0.0          SCJ(,) = 0.0
IC13P(,1)=1          C1L3P(,1) = 0.   0.   5.            IPR3P(,1)=010       PRL3P(,1) = 0.6
OUT_RELP=TRUE
IKRPRTSIZE=6
IKRPRTIDIM() = 1        1        1        15       15       15
IKRPRTJDIM() = 1        1        1        4        4        4
IKRPRTKDIM()= 1         1        1        5        5        5
IKRPRTPH()    = 1       2        3        1        2        3
```

UTHYST MODEL

The three-phase UTHYST model is turned on by UTHYSTF flag. Each rock type requires specific set of hysteresis parameters. The hysteresis model may be applied to any specified phase by the IHYSTPH keyword. Phase input parameters include α parameter (HYSTA) and Land coefficient (CLAND). The saturation tolerance value (ε_h or SATTOLHYST) is general for all phases showing a hysteretic behavior. The hysteresis related parameters are printed out to the fort.35 output file. The following lines of an IPARS deck file assign the hysteresis to gas phase (PH3) where $\alpha_3 = 1.0$, L=3.0, and $\varepsilon_h = 0.001$.

UTHYSTF=TRUE SATTOLHYST = 0.001
IHYSTPH(,1) = 0 0 1
HYSTA(,1) = 0. 0. 1.0
CLAND(,1) = 0. 0. 3.0

Table J-1: Relative permeability parameters (IPARS sample case study)

Two-phase relative permeability data	**Value**
Residual saturation of PH1 ($\boldsymbol{S^L_{1r2}, S^L_{1r3}}$)	0.10,0.14
Residual saturation of PH2 ($\boldsymbol{S^L_{2r1}, S^L_{2r3}}$)	0.20,0.15
Residual saturation of PH3 ($\boldsymbol{S^L_{3r1}, S^L_{3r2}}$)	0.30,0.25
End-point relative permeability for PH1 ($\boldsymbol{k^{0L}_{r12}, k^{0L}_{r13}}$)	0.4,0.5
End-point relative permeability for PH2 ($\boldsymbol{k^{0L}_{r21} = k^{0L}_{r23}}$)	0.6
End-point relative permeability for PH3 ($\boldsymbol{k^{0L}_{r31} = k^{0L}_{r32}}$)	1.0
1st curvature of relative permeability for PH1 ($\boldsymbol{C^L_{112} = C^L_{113}}$)	3.0
1st curvature of relative permeability for PH2 ($\boldsymbol{C^L_{121} = C^L_{123}}$)	4.0
1st curvature of relative permeability for PH3 ($\boldsymbol{C^L_{131} = C^L_{132}}$)	5.0
2nd curvature of relative permeability for PH1 ($\boldsymbol{C^L_{212} = C^L_{213}}$)	0.0
2nd curvature of relative permeability for PH2 ($\boldsymbol{C^L_{221} = C^L_{223}}$)	0.0
2nd curvature of relative permeability for PH3 ($\boldsymbol{C^L_{231}, C^L_{232}}$)	1.0, 1.5
Two- and three-phase constant parameters	**Value**
1st curvature of relative permeability for PH3 ($\boldsymbol{C^{L3P}_{131}}$)	5.0
End-point relative permeability for PH2 ($\boldsymbol{k^{03P}_{r2}}$)	0.6
General phase parameters *	**Value**
b_i parameter in **Eq. 3-4**	0.0
Critical saturation ($\boldsymbol{S_{ci}}$)	0.0

***** i denotes all phases (PH1, PH2, and PH3)

Appendix K: UTKR3P and UTHYST Models in UT-DOECO2 Simulator

UT-DOECO2 OVERVIEW

The UT-DOECO2 reservoir simulator is an isothermal, three-dimensional, compositional gasflood simulator. The solution scheme is IMPEC (implicit pressure/explicit concentration). It applies a three-phase hydrocarbon flash using Peng-Robinson EOS. The gridding options are Cartesian and unstructured/corner point type. A geomechanical module developed and implemented. shows an overall flowchart of the UT-DOECO2 simulator.

RELATIVE PERMEABILITY MODELING

The user manual of the DOECO2 simulator provides the detailed description of the required keywords for the UTKR3P and UTHYST models (**Delshad et al., 2014**). Here, we review the general updates in the DOECO2 code for the relative permeability and hysteresis modeling. **Table K-1** summarizes the revised relative permeability models and the hysteresis options in the UT-DOECO2 code.

Table K-1: Relative permeability and hysteresis options in UT-DOECO2 simulator

				Hysteresis Models[1]			
Model	**IPEM**	**ICAP[2]**	**Composition Dependent**	**IHYSTPH =1[3]**	**IHYSTPH =2[4]**	**IHYSTPH =3 [5]**	**IHYSTPH =4 [6]**
Baker	1	0 or 1	NO	NO	NO	NO	NO
Modified Stone II	2	0 or 1	NO	NO	NO	NO	NO
Corey	3	0 or 1	NO	YES	YES	YES	NO
Modified Corey[7]	4	0 or 1	NO	YES	YES	YES	NO
Stone I	5	0 or 1	NO	NO	NO	NO	NO
Jerauld	6	NO[8]	NO[9]	YES	NO	NO	NO
UTKR3P	7	0 or 2	YES[7]	YES	YES	YES	YES
Lookup Table	8	N.A.	N.A.	N.A.	N.A.	N.A.	N.A.

1) No hysteresis for all phases (IHYST=0) and No Hysteresis for specific phase IHYSTPH(j)=0

2) ICAP=0: NO capillary or trapping number Effect, ICAP=1: Capillary Number Dependency, ICAP=2: Trapping Number Dependency

3) Carlson hysteresis model for intermediate- and non- wetting phases (**1981**)

4) Hysteresis model to add the effect of trapped gas on oil residual situation (**Fayers & Matthews, 1984**).

5) Larsen and Skauge model for water as wetting phase and gas as non-wetting phase (**1998**)

6) UTHYST model (**Beygi et al., 2013**)

7) Calculating three-phase relative permeabilities in CO_2 floods based on an extension of the Corey model (**Dria et al., 1993**)

8) Original model has capillary number dependency. However, it is not implemented into DOECO2

9) Original model has composition consistency based on Parachor-weighted molar density. However, it is not implemented into the UT-DOECO2 simulator.

HYSTERESIS MODELING

The hysteresis options can be applied to any relative permeability model. From the available multiphase relative permeability models in the DOECO2, however, the hysteresis is applied to only three relative permeability models: The Corey and its modified revision, the Jerauld model, and the UTKR3P models (see **Table K-2**). Among different hysteresis models, we selected two

two-phase hysteresis models (general Carlson model (**1981**)) and the Fayers and Matthew model (**1984**) for oleic phase) and two three-phase hysteresis models including Larsen and Skauge model (**1998**) for the aqueous and gaseous phases and the general UTHYST model (**Beygi et al., 2013**).

Table K-2: Multiphase relative permeability models for hysteresis modeling in UT-DOECO2 simulator

Relative permeability index (IPERM)	**3**	**4**	**6**	**7**
Relative permeability model	Corey model (**Corey et al., 1956**)	Modified Corey model (**Dria et al., 1993**)	Jerauld model (**Jerauld, 1997b**)	UTKR3P model (**Beygi et al., 2013**)

Note that the hysteresis model for each phase is an input parameter. Table K-3 provides a detailed guide to selecting the hysteresis model for each phase according to the specified process and wettability condition. It also summarizes the hysteresis models and their phase applicability for different phases along with the relative permeability model to which the models were implemented. Note that the user requires to input hysteresis model for each phase. Otherwise, the code stops working with an error message. **Table K-4** provides the detailed guide to select hysteresis model for each phase according to the desired process and wettability condition.

Table K-3: Hysteresis models and phase applicability in UT-DOECO2 simulator

Hysteresis Models	IHYSTPH	Applicability			IPERM (*)	Comment
		Water	Oil	Gas		
Default Hysteresis in UTKR3P (**Beygi et al., 2013**)	-1	YES	YES	YES	7	Inherent hysteresis model (saturation path dependency in UTKR3P model is applied)
No Hysteresis	0	YES	YES	YES	ALL	No hysteresis is applied
Carlson (**1981**)	1	YES	YES	YES	3, 4, 6, and 7 (**)	Intermediate- and Non-wetting phases hysteresis
Fayers and Matthew (**1984**)	2	NO	YES	NO	7	Oleic phase hysteresis when hysteresis is also applied to gaseous phase
Larsen and Skauge (**1998**)	3	YES	NO	YES	3, 4, and 7	Water as wetting phase and gas as non-wetting phase
UTHYST (**Beygi et al., 2013**)	4	YES	YES	YES	7	Intermediate- and non-wetting hysteresis

(*****) IPERM to which the hysteresis model is applied.

(******) For the Jerauld's relative permeability model, the Carlson hysteresis model (IHYST=1) is applied just to the gaseous phase

Table K-4: Hysteresis models and applicability based on wettability in UT-DOECO2 simulator

Hysteretic Phase	Hysteresis Model* (Water/Oil/Gas)	Phase Wettability**			Comment
		Water	Oil	Gas	
Gas	001, 003, 004	W / I	W / I	N	
Oil	010, 040	W	I		2-Phase water-oil
Water	100	I	W		2-Phase water-oil
Gas + Water	101, 104, 401, 403, 404	I	W	N	No Hysteresis for wetting phase
Gas + Oil	021, 023, 024	W	I	N	No Hysteresis for wetting phase
Water + Oil + Gas (1)	311, 313, 314, 321, 323, 324, 341, 343, 344	W	I	N	Only IHYST=3 applies hysteresis to water as wetting phase
Water + Oil + Gas (2)	121, 123, 124, 421,423,424	I	W	N	Only IHYST=2 applies hysteresis to oil as wetting phase

* Three-digit (XYZ) index represents hysteresis model X, Y, and Z for water, oil, and gas phases respectively.

** W= Wetting , I= Intermediate-wet, N= Non-wetting.

Appendix L: Low-Tension Gas Flood Modeling

We present a new framework for the four-phase compositional/chemical simulator to model gas/chemical EOR processes including low-tension-gas flooding and foam. The four phases that may flow simultaneously are (1) aqueous, (2) oil, (3) gas and (4) microemulsion phases. In this formulation, a hydrocarbon compositional model is coupled with microemulsion phase behavior. **Table L-1** summarizes the component type and the phases in which each component is allowed in this code. The following section describes the modeling of the hybrid chemical-gas process including robust three-phase relative permeability and hysteresis models for better modeling of the situations encountered in this cyclic process: multiphase flow at low-saturation region, compositional effects due to the mass transfer among the phases, phase appearance/disappearance, and the saturation-history dependency of the relative permeability.

Table L-1: Component and phase allocation in UT-DOECO2 simulator

		Phase			
		Aqueous	**Oleic**	**Gaseous**	**Microemulsion**
Component	**Water**	X			X
	Polymer	X			X
	Hydrocarbon		X	X	X
	Non-condensable gases	X	X	X	X
	Surfactant				X

The following sections give an overview of the low-tension gas flooding in the UT-DOECO2.

Surfactant phase behavior

The microemulsion phase behavior is based on Winsor (**1954**) and Pope and Nelson (**1978**). The formulation of the binodal curve using Hand's rule (**Hand, 1939**) is assumed the same in all phase environments. Hand's rule is based on the empirical observation that equilibrium phase

concentration ratios are straight lines on a log-log scale. The binodal curve is computed from,

$$\frac{C_{3l}}{C_{2l}} = A\left(\frac{C_{3l}}{C_{1l}}\right)^{B}, \qquad \textbf{Eq. L-1}$$

Here *l* denotes phases and *A* and *B* are empirical parameters. For a symmetric binodal curve *B* = -1 (i.e., the current formulation used). Phase concentrations are calculated explicitly in terms of oil concentration C_{2l} (recalling $\sum_{k=1}^{3} C_{kl} = 1$). The microemulsion phase is designated as phase one, which is the aqueous phase.

While the microemulsion/excess-oil IFT decreases drastically as brine salinity increases, the microemulsion/excess-brine IFT increases drastically as brine salinity increases. The salinity at the crossover point of these two IFTs is called the optimum salinity. At the optimum salinity, the same amount of water and oil are dissolved in the microemulsion phase (surfactant-rich phase - in this code aqueous phase). For intermediate salinities less than or equal to the optimum salinity, parameter A in binodal curve formulation is calculated as follow:

$$A = (A_0 - A_1)\left(1 - \frac{C_{SE}}{C_{SEOP}}\right) + A_1, \quad for\ C_{SE} \le C_{SEOP}, \qquad \textbf{Eq. L-2}$$

where C_{SE} is the salt concentration in the aqueous phase and C_{SEOP} is the optimum salinity. $A_{s=0,\,1}$ is the parameter related to the maximum height of the binodal curve ($C_{3max,s}$) and is defines as,

$$A_s = \left(\frac{2C_{3max,s}}{1-2C_{3max,s}}\right)^2, \qquad \textbf{Eq. L-3}$$

where s=0, 1 represents the zero and optimum salinities, respectively.

In a brine/oil/surfactant mixture, the phase behavior is a function of C_{SE} among other factors such as co-solvent concentration, temperature, pressure, and solution gas. The microemulsion phase behavior is characterized as Type I (oil solubilized in the aqueous phase) when C_{SE} is equal or less than the lower effective salinity (C_{SEL}) and two phases are in equilibrium:

the oleic phase which is essentially pure and the microemulsion phase containing water, salt, surfactant, and the solubilized oil. This phase behavior environment is called Type I as well because the tie lines have the negative slope on a conventional ternary diagram. In Type I or Type II(+) environment phase (water solubilized in oil) the tie lines have a positive slope and C_{SE} is equal or greater than the upper effective salinity (C_{SEU}). In this case, also there are two phases in equilibrium: microemulsion and excess aqueous phase. The microemulsion phase contains a surfactant, oil and the solubilized water, and the aqueous phase which is essentially pure. For intermediate salinity $C_{SEL} \leq C_{SE} \leq C_{SEU}$, there are three phases in equilibrium depending on the component composition, oleic, microemulsion, and aqueous phase. This environment is called Type III (middle phase in equilibrium with excess oil and water phases) and has a Type I and a Type II (+) lobe on a ternary diagram. The implementation is currently considered for Type I surfactant phase behavior in the UT-DOECO2 simulator. The following two parameters are evaluated to obtain surfactant-rich microemulsion phase composition:

$$R_{31} = \frac{C_3}{C_1}, \qquad \textbf{Eq. L-4}$$

$$R_{32} = \frac{A}{R_{31}}, \qquad \textbf{Eq. L-5}$$

where C_1 and C_3 are total volume concentration of water and surfactant, respectively. The microemulsion-phase concentrations are calculated as follows:

$$C_{i3} = \begin{cases} R_{32} \times (R_{31} + R_{31} \times R_{32} + R_{32})^{-1} & i = 1 \\ 1 - (1 + R_{31})C_{13} & i = 2 \\ 1 - C_{13} - C_{23} & i = 3 \end{cases} \qquad \textbf{Eq. L-6}$$

Surfactant Retention

Surfactant loss due to adsorption and phase trapping is an important parameter in the chemical-EOR projects. A Langmuir-type isotherm is used to describe the surfactant adsorption onto solid

mineral surfaces. The model takes into account the salinity and surfactant concentration with reversibility options. The salinity for surfactant adsorption is defined as a linear summation of monovalent cation and effective divalent cations.

Interfacial tension

Two models are implemented to calculate the interfacial tension between (IFT) microemulsion and oil phases: modified Healy and Reed (**1974**) (**Hirasaki, 1981**) and Huh (**1979**). The interfacial tension depends on solubilization parameter. In these models, a constant oil-water interfacial tension is considered and in the absence of a surfactant or in the case of low surfactant concentration (i.e., below the Critical micelle concentration (CMC)), the IFT reduces to water-oil IFT.

Microemulsion viscosity

Microemulsion viscosity is modeled in terms of pure component viscosities and the concentrations of oil, water, and surfactant in the microemulsion phase:

$$\mu_1 = C_{11}\mu_w e^{\alpha_{v1}(C_{21}+C_{31})} + C_{21}\mu_o e^{\alpha_{v2}(C_{11}+C_{31})} + C_{31}\alpha_{v3} e^{(\alpha_{v4}C_{11}+\alpha v_5 C_{21})}, \quad \textbf{Eq. L-7}$$

where C_{i1} denotes the concentration of component i in the aqueous phase and the α_v parameters are determined by matching laboratory microemulsion viscosities at several compositions. In the absence of surfactant and polymer, water and oil phase viscosities reduce to pure water and oil viscosities (μ_w, μ_o). When polymer is present, μ_w is replaced by μ_P.

Hydrocarbon dissolution

At surfactant concentrations higher than CMC the hydrocarbon solubilizes in the microemulsion phase. The mass transfer of hydrocarbon components to the microemulsion phase is a function of the salinity, surfactant molecule, temperature etc. Oil dissolved in the aqueous phase can be either in equilibrium with the oil concentration in the oleic phase or with the limited mass transfer. The

equilibrium K-values, defined as the ratio of each component concentration in the aqueous phase to that in the oleic phase are specified and sorted as a function of surfactant concentration. The kinetic mass transfer rate can be further added for the limited mass transfer option.

Surfactant mixing rule

Typically, a mixture of surfactants is used during the low-tension-gas flood: a low interfacial tension surfactant and a foaming surfactant. The former reduces the IFT to ultra-low values and, thereby, the residual oil saturation is decreased. The latter provides the essential gas mobility/conformance control. In reality, all the surfactants have both IFT and foaming to different degrees and are rarely independent. Antón *et al.* (**2008**) discuss mixing rules to estimate microemulsion phase behavior when more than one surfactant is present. The impact of mixing two surfactants also needs to be evaluated on foaming properties (**Andrianov et al., 2012**).

For the *ideal* mixture of two surfactants, a nonlinear mixing rule is applied to model the changes in optimal salinity as a function of surfactants concentration (**Salager et al., 1979a**).

$$lnC^*_{SEOP} = x_1 lnC_{SEOP_1} + x_2 lnC_{SEOP_2}. \qquad \textbf{Eq. L-8}$$

Here, C^*_{SEOP}, C_{SEOP_1} and C_{SEOP_2} are the optimum salinities for the mixture of surfactants, surfactant 1 and surfactant 2, respectively. x_1 and x_2 are mole fractions for surfactants 1 and 2. The optimum solubilization ratio follows a linear mixing rule as (**Mohammadi et al., 2009**),

$$ln\sigma^*_s = x_1 ln\sigma_{s_1} + x_2 ln\sigma_{s_2}, \qquad \textbf{Eq. L-9}$$

where σ^*_s, σ_{s_1}, and σ_{s_2} are the optimum solubilization ratio of the mixture, surfactant 1, and surfactant 2, respectively.

Oil composition effect on microemulsion phase behavior

Key surfactant properties depend on crude oil composition (**Baran et al., 1994**; **Salager et al., 1979a**; **Salager et al., 1979b**). The crude oil composition effect is introduced by the equivalent alkane carbon number (EACN) concept. The surfactant phase behavior parameters, e.g. optimum salinity, solubilization parameter, and width of Winsor Type III salinity are estimated using the following linear formulations,

$$Ln\ C_{SEOP} = S_{se}(EACN - E_{min}), \quad \textbf{Eq. L-10}$$

$$\sigma_s = S_{R,S}EACN + b_{\sigma,S}, \quad \textbf{Eq. L-11}$$

$$\frac{C_{SEU} - C_{SEL}}{C_{SEOP}} = S_{ds}EACN + b_{ds}, \quad \textbf{Eq. L-12}$$

Here S_{se}, E_{min}, $S_{\sigma,S}$, $b_{\sigma,S}$, S_{ds}, and b_{ds} are constants and dynamically calculated based upon a linear EACN-interpolation scheme between the two experimentally matched sets of surfactant phase behavior parameters for the same surfactant but having different EACNs. When the effect of EACN on the surfactant phase behavior is considered, A_S in the Hand's rule formulation is evaluated as follows:

$$A_s = {\sigma_S}^{-2}. \quad \textbf{Eq. L-13}$$

In this study, the EACN of a given crude oil corresponds to the lipophilicity of the crude oil (i.e., the salinity at the transition from Winsor Type I to II environment): the number of carbon atoms of an alkane exhibiting a hydrophobicity equivalent to the crude oil. EACN for an oil mixture with provided components and composition is estimated using Cash *et al.* (**1977**) linear mixture formulation,

$$EACN = \sum_{i=1}^{N_c} x_i ACN_i, \quad \textbf{Eq. L- 14}$$

where N_c is the number of components in the mixture, x_i is the mole fraction of component *i* and

ACN_i is the alkane carbon number of the hydrocarbon component i.

Foam

The implicit texture UT-foam model (**Rossen et al., 1999**) and local-equilibrium population-balance foam model (**Chen et al., 2010**) were incorporated in the DOECO2 simulator (see **Appendix B**). The UT-foam model gives a steep increase in the gas mobility as water saturation decreases in the immediate vicinity of the limiting water saturation (S_w^*) and a constant reduction in the gas mobility for a larger value of water saturation. The model allows for non-Newtonian behavior in the low-quality regime: the mobility reduction factor is a power-law function of gas superficial velocity.

In foam model of Chen *et al*. (**2010**), lamella-generation rate is taken as a power-law expression, proportional to the magnitude of the interstitial velocity of surfactant solution and 1/3 power of the interstitial gas velocity. The model employs a capillary-pressure-dependent kinetic expression for lamella coalescence (to reflect the limiting capillary pressure) and a term to represent the trapped fraction of foam. This model uses the shear-thinning expression of Hirasaki and Lawson (**1985**) for the effective gas viscosity.

In the presence of microemulsion phase, most of the surfactant remains in this phase. The results of pipette foaming test by Srivastava (**2010**) showed Type I and Type III microemulsion phases form a significant foam, but foam does not form in Type II. Foam in Type I is more stable compared to Type III due to lower salinity and lower amount of solubilized oil in the microemulsion phase. Foam does not generate in excess aqueous phases from Type III and Type II due to surfactant partitioning into microemulsion phase. As a result, when microemulsion phase is present, the aqueous phase properties such as saturation, velocity, and capillary pressure will be replaced with their corresponding values for the microemulsion phase (**Delshad et al., 2014**; **Naderi Beni et al., 2013**).

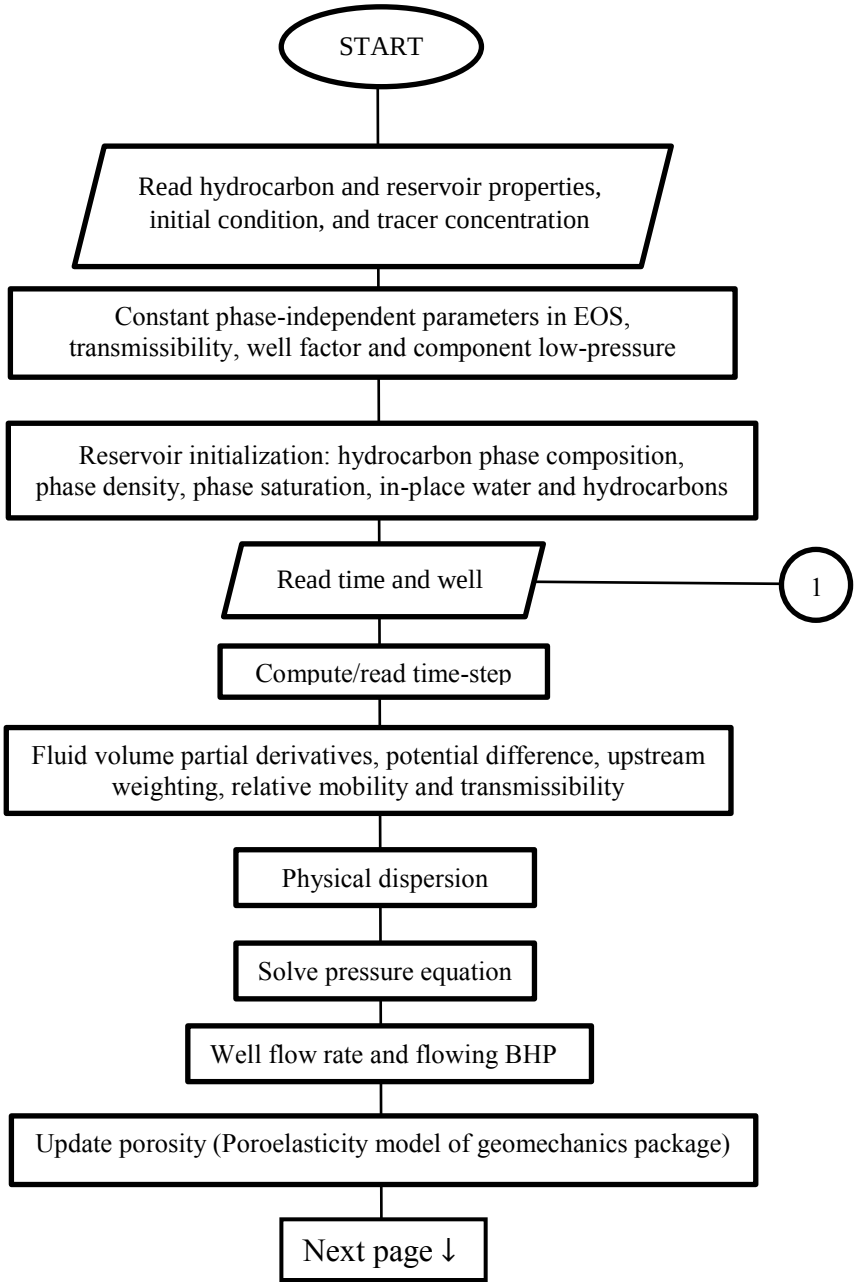

Figure L-1: Summary flowchart of UT-DOECO2 simulator

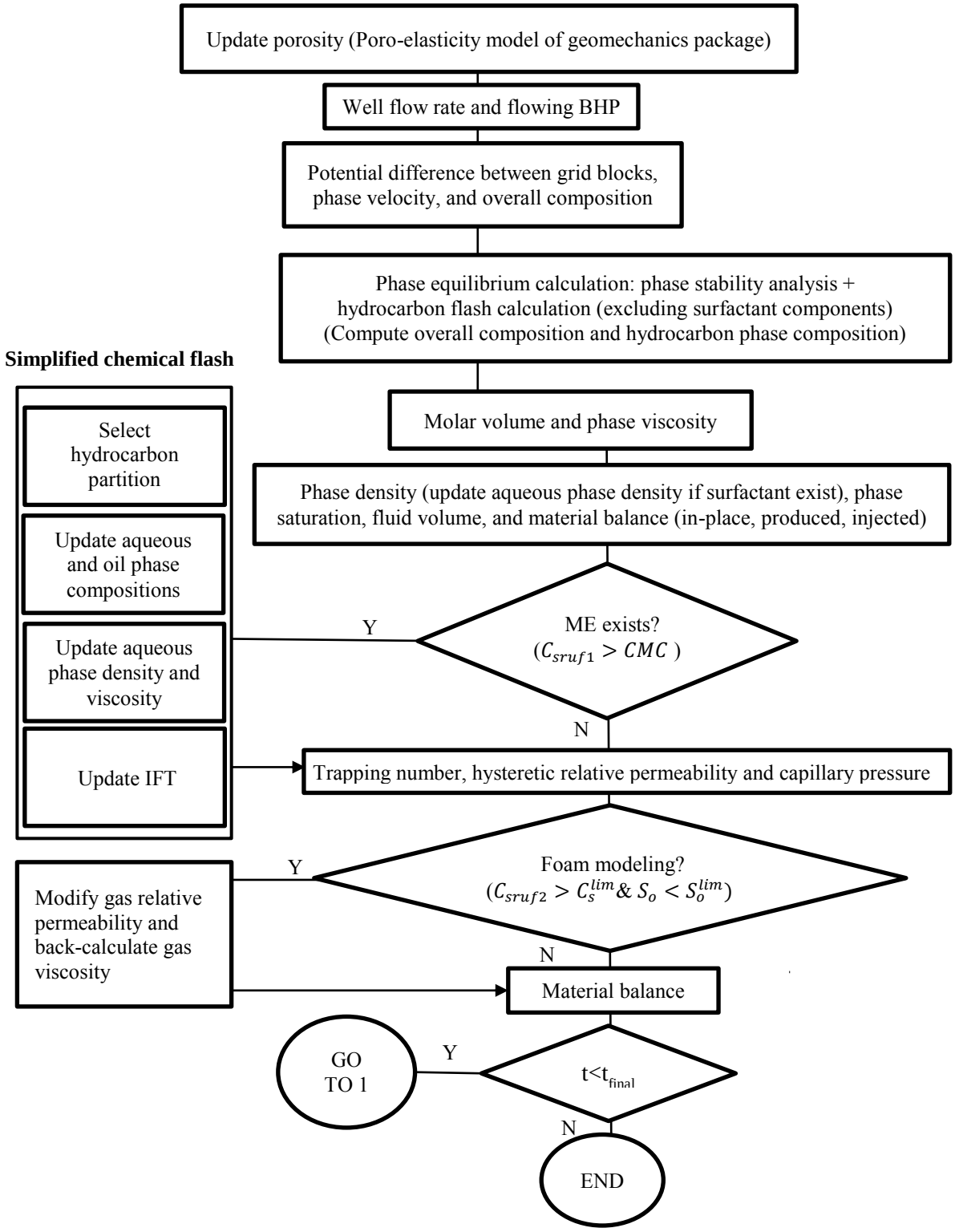

Figure L-1 (cont'd): Summary flowchart of UT-DOECO2 simulator

Glossary

All units are expressed in terms of fundamental quantities, mass M, mole N, length L, time T, and temperature Θ.

a	=	Constant in general initial-trapped saturation formulation
A_{DH}	=	Debye-Hückel general constant
A_{DHL}	=	Debye-Hückel limiting slope, $M^{1/2}N^{-1/2}$
$A_{H,ij}$	=	Coefficient in HKF formulation for solvent density calculation in aqueous solution
a_w	=	A wettability-dependent constant
$\dot{a}_B$	=	Bjerrum distance
$\dot{a}_{DH}$	=	Distance of the closest approach between two ions in Debye-Hückel theory, L
b	=	Free parameter in three-phase residual saturation formulation
B_{DHL}	=	Debye-Hückel limiting parameter, $M^{1/2}N^{-1/2}L^{-1}$
C_1 and C_2	=	Relative permeability curvature parameters
C_S	=	Spreading coefficient, MT^{-2}
C_{SEL} and C_{SEU}	=	Lower and upper effective salinity limit, ML^{-3}
C_{SEOP}	=	Optimum effective salinity, ML^{-3}
d	=	Constant in general initial-trapped saturation formulation
D	=	Depth, L
(also)	=	Debye (unit of electric dipole moment) = $3.3356 \times 10^{-30}\ C\ m,\ M^{1/2}T^{-1}L^{5/2}$
e	=	Electronic charge = $1.60210 \times 10^{-19} C$, $M^{1/2}T^{-1}L^{3/2}$
$\hat{e}_{H,ij}$ and $e^*_{H,ij}$	=	Coefficients in HKF formulation for solvent relative permittivity calculation in aqueous solution
E	=	Electric field, $M^{1/2}T^{-1}L^{-1/2}$
f_h	=	Dimensionless oil-like parameters based on Parachor-weighted molar density
g	=	Gravitational constant, Lt^{-2}
$\overline{G}$	=	Partial molar Gibbs free energy, ML^2t^{-2}
I	=	Ionic strength, $N\ M^{-1}$
$\vec{k}$	=	Permeability tensor, L^2
k_B	=	Boltzmann constant =$1.3807 \times 10^{-23}\ J/K$, $M\ L^2T^{-2}\Theta^{-1}$
k_r^0	=	End-point relative permeability
k_r	=	Relative permeability
L	=	Land coefficient
m	=	Molality, $N\ M^{-1}$
n_{HH}	=	Constant parameter impacting oil-isoperm curvature
N_A	=	Avogadro number =$6.0220 \times 10^{23}\ /mol$, N^{-1}
N_T	=	Trapping number
P	=	Pressure, $ML^{-1}t^{-2}$
P_c	=	Capillary pressure, $ML^{-1}t^{-2}$
r	=	Radial position coordinate, L
q	=	Charge, $M^{1/2}T^{-1}L^{3/2}$
R	=	Molar gas constant $= N_A k_B = 8.314 J/K/mol$, $M\ L^2T^{-2}\Theta^{-1}N^{-1}$
R_H	=	Mean hydraulic radius of the pores occupied by a particular phase, L
S	=	Saturation, L^3/L^3
S^*	=	Effective or reduced saturation, L^3/L^3

$\bar{S}$	=	Normalized saturation
S_m^I	=	saturation of conjugate phase (m) at the start of the current cycle
S_r^*	=	Residual saturation corrected for compositional changes, L^3/L^3
T	=	Trapping model parameter
(also)	=	Temperature, Θ
ΔS_t	=	Trapped saturation in current cycle, L^3/L^3
α	=	Conjugate-phase reduction factor in UTHYST model
α_{LS}	=	Permeability reduction factor in three-phase hysteresis model of Larsen and Skauge
β	=	Constant in trapped saturation equation
α_{Al} and β_{Al}	=	Fitting parameters of zero-oil-isoperm curvature
α_S and β_S	=	Contact angle dependent coefficient
β_F	=	Constant to change the curvature of residual oil saturation
ε_0	=	Permittivity of free space = $8.8542 \times 10^{-12} C^2 J^{-1} m^{-1}$, $M^{1/2} T^{-1} L^{1/2} N^{-1}$
ε_f	=	Effective permittivity= $\varepsilon_0 \varepsilon_r$ Faraday/m, $M^{1/2} T^{-1} L^{1/2} N^{-1}$
ε_h	=	Saturation toleration factor (SATTOLHYST), L^3/L^3
ε_r	=	Relative permittivity (Dielectric constant) of the solvent
ε	=	Pore size distribution factor in Land's imbibition relative permeability equation
θ	=	Trapping coefficient
λ	=	Empirical constant in the Killough's parametric interpolation method
(also)	=	Mobility, $M^{-1} L^3 T$
λ_{DH}	=	Debye screening length, L^{-1}
λ_{MSA}	=	MSA screening length, L^{-1}
μ	=	Viscosity, $ML^{-1}T^{-1}$
ξ	=	Molar density, NL^{-3}
ρ	=	Density, ML^{-3}
σ	=	Interfacial tension, Mt^{-2}
τ	=	Trapping model parameter
(also)	=	Fisher (decay) exponent in trapped cluster morphology formulation
Φ	=	Phase potential, $ML^{-1}T^{-2}$
ψ	=	Electrical potential, $M^{1/2} L^{1/2} T^{-1}$
ς	=	Angular variable indicating balance of gas and water saturation $\varsigma = S_g/1 - S_{wc} - S_o$
$\mathfrak{f}$	=	Fractal dimension of the porous medium
∞	=	In bulk solution out of the electrolyte system
$\mathfrak{G}$ and $\mathfrak{C}$	=	Local binary quantity in eNRTL model
$\aleph$	=	Surface area fraction of each component in UNIQUAC model
$\mathfrak{z}$	=	Volume fraction in UNIQUAC model

Subscripts and superscripts:

$2P$ and $3P$	=	Two- and three-phase
c	=	critical saturation (minimum attainable saturation in multi-phase flow)
calc	=	Calculated
comp	=	Compositional effects
cr	=	Critical non-wetting saturation corresponding to the point where maximum trapped saturation is first reached
Dec	=	Decreasing saturation process
expr	=	Experimentally measured parameter
f	=	Flowing saturation
h	=	Hysteresis

I	=	Start of cycle in UTHYST model
Inc	=	Increasing saturation process
int	=	Intermediate
irj	=	Phase i residual saturation to phase j
L	=	Total liquid
n	=	Cycle number
ocw	=	Value to oil at connate water saturation
PD	=	Primary decreasing
PI	=	Primary increasing
r	=	Residual
t	=	Trapped
wir	=	Value at irreducible water saturation
wh	=	Water-hydrocarbon

Abbreviation and acronyms:

$1D/2D/3D$	=	One/two/three dimensional
B	=	Billion
bbl	=	Barrel of oil or oil equivalent
BHP	=	Bottom-hole pressure
$BOPD$	=	Barrel of oil per day
$CCUS$	=	Carbon capture, utilization, and storage
EOS	=	Equation of state
$eEOS$	=	Electrolyte EOS
$FWAG$	=	Foam assisted water-alternate-gas injection scheme
GFE	=	Gibbs free energy
$K\ or\ M$	=	Thousand
LHS	=	Left hand side
MM	=	Million
MoC	=	Method of characteristic
PDF	=	Probability distribution function
ppm	=	Part per million
PV	=	Pore volume
Rb	=	Reservoir barrel
REV	=	Representative elementary volume
RHS	=	Right hand side
ROZ	=	Residual oil zone
SAG	=	Surfactant-alternate-gas injection scheme
$SCAL$	=	Specific core analysis
$Scfd$	=	Standard cubic feet per day
STB	=	Stock-tank barrel
TDS	=	Total dissolved solids
Tpd	=	Metric ton per day
TZ	=	Transition zone
VAR	=	Vertical aspect ratio
WAG	=	Water-alternate-gas injection scheme

Bibliography

Abdallah, W., Buckley, J. S., Carnegie, A., Edwards, J., Herold, B., Fordham, E., . . . Ziauddin, M. (2007). Fundamentals of wettability. *Oilfield Review, 19*(2), 44-61.

Abrams, D. S., & Prausnitz, J. M. (1975). Statistical Thermodynamics of Liquid Mixtures: A New Expression for the Excess Gibbs Energy of Partly or Completely Miscible Systems. *AIChE Journal, 21*(1), 116-128.

Adamson, A. W. (1960). *Physical Chemistry of Surfaces*. New York: Interscience Publishers Inc.

Ahmadloo, F., Asghari, K., & Yadali Jamaloei, B. (2009). *Experimental and Theoretical Studies of Three-Phase Relative Permeability.* Paper presented at the Paper SPE 124538 presented at the SPE Annual Technical and Exhibition, New Orleans, LA.

Aissaoui, A. (1983). Etude théorique et expérimentale de l'hystérésis des pressions capillaries et des perméabilitiés relatives en vue du stockage *PhD Thesis*. Paris: Ecole des Mines de Paris.

Akbarabadi, M., & Piri, M. (2013). Relative Permeability Hysteresis and Capillary Trapping Characteristics of Supercritical CO_2/Brine Systems: An Experimental Study at Reservoir Conditions. *Advances in Water Resources, 52*, 19-206.

Al-Harrasi, A. S., Al-Maamari, R. S., & Masalmeh, S. K. (2012). *Laboratory Investigation of Low Salinity Waterflooding for Carbonate Reservoirs*. Paper presented at the International Petroleum Exhibition & Conference, Abu Dhabi.

Al-Kharusi, A. S., & Blunt, M. J. (2007). Network Extraction from Sandstone and Carbonate Pore Space Images. *Journal of Petrol. Science and Eng., 56*, 219-231.

Al-Mansoori, S. K., Iglauer, S., Pentland, C. H., & Blunt, M. J. (2009). Three-phase measurements of oil and gas trapping in sand packs. *Advances in Water Resources, 32*, 1535-1542.

Al-Menhali, A. S., & Krevor, S. (2016). Capillary Trapping of CO_2 in Oil Reservoirs: Observations in a Mixed-Wet Carbonate Rock. *Environ. Sci. Technol., 50*(5), 2727-2734.

Al-Shalabi, E. W. (2014). *Modeling the Effect of Injecting Low Salinity Water on Oil Recovery from Carbonate Reservoirs.* (Ph.D. dissertation), The University of Texas at Austin, Austin, Texas.

Al Mansoori, S. K., Iglauer, S., Pentland, C. H., & Blunt, M. J. (2009). Three-Phase Measurements of Oil and Gas Trapping in Sand Packs. *Advances in Water Resources, 32*, 1535-1542.

Alai, M., Sutton, M., & Carroll, S. (2005). Evaporative Evolution of a Na–Cl–NO_3–K–Ca–SO_4–Mg–Si brine at 95°C: Experiments and Modeling Relevant to Yucca Mountain, Nevada. *Geochemical Transactions, 6*(2), 31-45.

Alemań, M. A. (1986). Personal communication with Baker, L.E. as noted in Paper SPE/DOE 17369.

Alemań, M. A., & Slattery, J. C. (1988). Estimation of Three-Phase Relative Permeabilities. *Transport in Porous Media, 3*, 111-132.

Alizadeh, A. H., & Piri, M. (2014). The Effect of SaturationHiistory on Three-Phase Relative Permeability: An Experimental Study. *Water Resources Research, 50*, 1636-1664.

Alvarez, J., Rivas, H., & Rossen, W. R. (2001). Unified Model for Steady-State Foam Behavior at High and Low Foam Qualities. *SPE Journal, 6*(3), 325-333. doi:10.2118/74141-PA

Amaechi, B., Iglauer, S., Pentland, C. H., Bijeljic, B., & Blunt, M. J. (2014). An Experimental Study of Three-Phase Trapping in Sand Packs. *Transp. Porous Med., 103*(3), 421-436.

Anderko, A., & Pitzer, K. S. (1993a). Equation-of-State Representation of Phase Equilibria and Volumetric Properties of the System NaCl-H2O above 573 K. *Geochimica et Cosmochimica Acta, 57*, 1657-1680.

Anderko, A., & Pitzer, K. S. (1993b). Phase equilibria and volumetric properties of the systems KCl-H2O and NaCI-KCl-H2O above 573 K: Equation of state representation. *Galchvnka PI Cosmochirnicu, 57*, 4885-4897.

Andrianov, A., Farajzadeh, R., Mahamoodi Nick, M., Talanana, M., & Zitha, P. L. J. (2012). Immiscible Foam for Enhancing Oil Recovery: Bulk and Porous Media Experiments. *Ind. Eng. Chem. Res, 51*(5), 2214-2226.

Antón, R. E., Andérez, J. M., Bracho, C., Vejar, F., & Salager, J. L. (2008). Practical Surfactant Mixing Rules Based on the Attainment of Microemulsion–Oil–Water Three-Phase Behavior Systems. *Adv. Polym. Sci., 218*, 83-113.

Arbogast, T., Pencheva, G., Wheeler, M. F., & Yotov, I. (2007). A multiscale Mortar Mixed Finite Element Method. *Multiscale Model. Simul., 6*, 319-346.

Arche, G. E. (1950). Introduction to Petrophysics of Reservoir Rocks. *Am. Assoc. Pet. Geol. Bull., 34*(5), 943-961.

Arns, C. H., Bauget, F., Limaye, A., Sakellariou, A., Senden, T. J., Sheppard, A. P., . . . Øren, P.-E. (2005). Pore-Scale Characterization of Carbonates using X-ray Microtomography. *SPE Journal, 10*(4), 475-484.

Arns, C. H., Knackstedt, M. A., Pinczewski, V., & Garboczi, E. J. (2002). Computation of Linear Elastic Properties from Microtomographic Images: Methodology and Agreement Between Theory and Experiments. *Geophysics, 67*(5), 1396-1405.

Arns, J.-Y., Robins, V., Sheppard, A. P., Sok, R. M., Pinczewski, W. V., & Knackstedt, M. A. (2004). Effect of Pore Network Topology on relative Permeability. *Transport in Porous Media, 55*, 21-46.

Ashoori, E., van der Heijden, T., & Rossen, W. R. (2010). Fractional-Flow Theory of Foam Displacements With Oil. doi:10.2118/121579-PA

Aziz, K., & Settari, A. (1979). *Petroleum Reservoir Simulation*. London: Applied Science Publisher.

Bachu, S., Gunter, W. D., & Perkins, E. H. (1994). Aquifer disposal of CO_2: Hydrodynamic and mineral trapping. *Energy Conversion and Management, 35*(4), 269-279. doi:http://dx.doi.org/10.1016/0196-8904(94)90060-4

Badalassi, V. E., Ceniceros, H. D., & Banerjee, S. (2003). Computation of Multiphase Systems with Phase Field Models. *Journal of Computational Physics, 190*(1), 371-397.

Baker, L. E. (1987). *Review of Three-Phase Relative Permeability Literature: Data and Correlation Methods*. Retrieved from Tulsa, OK:

Baker, L. E. (1988). Three-Phase Relative Permeability Correlations. Tulsa, OK, OK: Society of Petroleum Engineers.

Baker, L. E. (1993). Three-Phase Relative Permeability of Water-Wet, Intermediate-Wet and Oil-Wet Sandstone. Retrieved from

Baker, L. E. (1995). *Three-Phase Relative Permeability of Water-Wet, Intermediate-Wet and Oil-Wet Sandstone*. Retrieved from London:

Bakke, S., & Øren, P.-E. (1997). 3-D Pore-Scale Modelling of Sandstones and Flow Simulations in the Pore Networks. *SPE Journal*.

Balbinski, E. F., Fishlock, T. P., Goodyear, S. G., & Jones, P. I. R. (1999). Key Characteristics of Three-Phase Oil Relative Permeability Formulations for Improved Oil Recovery Predictions. *Journal of Petroleum Geoscience, 5*, 339-346.

Balhoff, M. T., Thomas, S. G., & Wheeler, M. F. (2008). Mortar Coupling and Upscaling of Pore-Scale Models. *Comput. Geosci., 12*, 15-27.

Ball, F.-X., Planche, H., Furst, W., & Renon, H. (1985). Representation of Deviation from Ideality in Concentrated Aqueous Solutions of Electrolytes Using a Mean Spherical Approximation Molecular Model. *AIChE Journal, 31*, 1233.

Baran, J. R. J., Pope, G. A., Wade, W. H., Weerasooriya, V., & Yapa, A. (1994). Microemulsion formation with Mixed Chlorinated Hydrocarbon Liquids. *Journal of Colloid and Interface Science, 168*(1), 67-72.

Bartell, F. E., & Osterhof, H. J. (1927). Determination of the Wetability of a Solid by a Liquid. *Ind. Eng. Chem., 19*(11), 1277-1280.

Barthel, J. M. G., Krienke, H., & Kunz, W. (1998). *Physical Chemistry of Electrolyte Solutinos, Modern Aspects*. New York: Springer.

Basan, P. B., Lowden, B. D., Whattler, P. R., & Attard, J. (1997). Pore-Size Data in Petrophysics: a Perspective on the Measurement of Pore Geometry. *The Geological Society, Special Publications, 122*, 47-67.

Batychy, J. P., & McCaffery, F. G. (1978). *Low Interfacial Tension Displacement Studies*. Paper presented at the Annual Technical Meeting, Calgary, Alberta.

Bear, J. (1972). *Dynamics of Fluids in Porous Media*. Amsterdam, The Netherlands: Elsevier Publishing Company.

Bear, J., & Bachmat, Y. (1990). *Introduction to Modeling of Transport Phenomena in Porous Media*. The Netherlands: Kluwer Academic Publishers.

Beattie, C. I., Boberg, T. C., & McNab, G. S. (1991). Reservoir Simulation of Cyclic Steam Stimulation in the Cold Lake Oil Sands. *SPE Res Eng, 6*(2), 200-206.

Berg, S., Ott, H., Klapp, S. A., Schwing, A., Neiteler, R., Brussee, N., . . . Stampanoni, M. (2013). *Real-time 3D Imaging of Haines Jumps in Porous Media Flow*. Paper presented at the Proceedings of the National Academy of Sciences of the United States of America.

Bernard, G. G., & Holm, L. W. (1964). Effect of Foam on Permeability of Porous Media to Gas. doi:10.2118/983-PA

Bernard, O., & Blum, L. (1996). Binding Mean Spherical Approximation for Pairing Ions: An Exponential Approximation and Thermodynamics. *J. Phys. Chem., 104*, 4746-4756.

Bertin, H. J., Quintard, M. Y., & Castanier, L. M. (1998). *Modeling Transient Foam Flow in Porous Media Using a Bubble Population Correlation*.

Bethke, C. M. (2007). *Geochemical and Biogeochmeical Reaction Modeling*. New York: Cambridge University Press.

Beygi, M. R., Delshad, M., Pudugramam, V. S., Pope, G. A., & Wheeler, M. F. (2013). A New Approach to Model Hysteresis and Its Impact on CO2-EOR Processes with Mobility Control Strategies.

Beygi, M. R., Delshad, M., Pudugramam, V. S., Pope, G. A., & Wheeler, M. F. (2015). Novel Three-Phase Compositional Relative Permeability and Three-Phase Hysteresis Models. *SPE Journal, 20*(1), 21-34.

Bikerman, J. J. (1973). *Foams* (Vol. 10).

Bjerrum, N. K. (1926). Dan. Vidensk. *Mat. -fys. Medd., 7*(9).

Blanchard, O. I., & Summers, L. H. (1986). *Hysteresis and the European Unemployment Problem*. Retrieved from http://www.nber.org/books/fisc86-1

Blom, S. M. P., Hagoort, J., & Soetekouw, D. P. N. (2000). relative Permeaiblity at Near-Critical Conditions. *SPE Journal, 5*(2), 172-181.

Blum, L. (1975). Mean Spherical Model for Asymmetric Electrolytes: I. Method of solution. *Molecular Physics, 30*(5), 1529-1535.

Blum, L. (1978). Solution of the Mean Spherical Approximation for Hard Ions and Dipoles of Arbitrary Size. *Journal of Statistical Physics, 18*(5), 451-474.

Blum, L. (1980). Primitive Electrolytes in the Mean Spherical Approximation. *Theoretical Chemistry: Advances and Perspectives, 5*, 1-66.

Blum, L., & Bernard, O. (1995). The General Solution of the Binding Mean Spherical Approximation for Pairing Ions. *Journal of Statistical Physics, 79*(3/4), 569-583.

Blum, L., & HØye, J. S. (1977). Mean Spherical Model for Asymmetric Electrolytes. 2. Thermodynamic Properties and the Pair Correlation Function. *J. Phys. Chem., 81*(13), 1311-1316.

Blum, L., & Wei, D. (1987). Analytical Solution of the Mean Spherical Approximation for an Arbitrary Mixture of Ions in a Dipolar Solvent. *Journal of Chemical Physics, 87*, 555-565.

Blunt, M. J. (2000). An Empirical Model for Three-Phase Relative Permeability. *SPE J., 5*(4), 435-445.

Blunt, M. J. (2001). Flow in Porous Media-Pore-Network Models and Multiphase Flow. *Current Opinion in Colloid & Interface Science, 6*, 197-207.

Blunt, M. J., Bijeljic, B., Dong, H., Gharbi, O., Iglauer, S., Mostaghimi, P., . . . Pentland, C. (2013). Pore-Scale Imaging and Modelling. *Advances in Water Resources, 51*, 197-216.

Blunt, M. J., Jackson, M. D., Piri, M., & Valvatne, P. H. (2002). Detailed Physics, Predictive Capabilities and Macroscopic Consequences for Pore-Network Models of Multiphase Flow. *Advances in Water Resources, 25*(8-12), 1069-1089.

Blunt, M. J., & Scher, H. (1995). Pore-Level Modeling of Wetting. *Physical Review E, 52*(6), 6387-6403.

Borge, G., Castano, R., Carril, M. P., Cobillon, M. S., & Madariaga, J. M. (1996a). Development of a Modified Bromley's Methodology (MBM) for the Estimation of Ionic Media Effects on Solution Equilibria. Part 1. Calculation of the Interaction Parameters in the Molar and Molal Scales at 25 C. *Fluid Phase Equilibria, 121*, 85-98.

Borge, G., Castano, R., Carril, M. P., Cobillon, M. S., & Madariaga, J. M. (1996b). Development of a Modified Bromley's Methodology (MBM) for the Estimation of Ionic Media Effects

on Solution Equilibria. Part 2. Correlation of of the Molar and Molal Interactions Parameters with Charge and Crystal Radii of the Ions. *Fluid Phase Equilibria, 121*, 99-109.

Born, M. (1920). Volumen und Hydratationswärme der Ionen. *Zeitschrift für Physik*, 45-49.

Boublik, T. (1970). Hard-Sphere Equation of State. *J. Chem. Phys., 53*, 471-472.

Bowen, R. M. (1982). Compressible Porous Media Models by Use of the Theory of Mixtures. *Int. J. Engng. Sci., 20*(6), 697-735.

Bradford, S. A., Abriola, L. M., & Leij, F. J. (1997). Wettability Effects on Two- and Three- Fluid Relative Permeabilities. *J. of Contaminant Hydrology, 28*, 171-191.

Bradley, D. J., & Pitzer, K. S. (1983). Thermodynamics of Electrolytes. XII. Dielectric Properties of Water and Debye-Hückel Parameters to 350 C and 1 kbar. *Journal of Physical Chemistry, 83*, 1599-1603.

Braun, E. M., & Holland, R. F. (1995). Relative Permeability Hysteresis: Laboratory Measurements and a Conceptual Model. *SPE Res Eng, 10*(3). doi:10.2118/28615-PA

Bromley, L. A. (1973). Thermodynamic Properties of Strong Electrolyte in Aqueous Solutions. *AIChE Journal, 19*(2), 313-320.

Brønsted, J. N. (1922). Studies on Solubility IV. The Principle of the Specific Interaction of Ions. *J. Am. Chem. Soc., 44*, 877-898.

Brooks, R. H., & Corey, A. T. (1966). Properties of Porous Media Affecting Fluid Flow. *J. Irrigation and Drainage, No. IR-2*, 61-88.

Brown, R. J. S., & Fatt, I. (1956). Measurements of Fractional Wettability of Oil Field Rocks by the Nuclear Magnetic Relaxation Method. *Trans. AIME, 207*, 262-264.

Brownell, L. E., & Katz, D. L. (1947). Flow of Fluids Through Porous Media, Part II, Simultaneous Flow of Two Homogeneous Phases. *Chemical Engineering Process, 43*, 601-612.

Brüll, L. (1934). Gazz. *Chim. Ital., 64*, 261-278, 607-624.

Bryant, S. L., & Blunt, M. J. (1994). Prediction of Relative Permeability in Simple Porous Media. *Physc. Rev., 46*(4), 2004-2011.

Bryant, S. L., King, P. R., & Mellor, D. W. (1993a). Network Model Evaluation of Permeability and Spatial Correlation in a Real Random Sphere Packing. *Transport in Porous Media, 11*(1), 53-70.

Bryant, S. L., Mellor, D. W., & Cade, C. A. (1993b). Physically Representative Network Models of Transport in Porous Media. *AIChE Journal, 39*(3), 387-396.

Burdine, N. T. (1953). Relative Permeability Calculations from Pore-Size Distribution Data. *Petroleum Transactions, AIME*, 71-78.

Cameretti, L. F., & Sadowski, G. (2005). Modeling of Aqueous Electrolyte Solutions with Perturbed-Chain Statistical Associated Fluid Theory. *Ind. Eng. Chem. Res., 44*, 3355-3362.

Carlson, F. M. (1981). Simulation of Relative Permeability Hysteresis to the Non-Wetting Phase *Paper SPE 10157 presented at SPE Annual Technical Conference and Exhibition*. San Antonio, TX.

Cash, L., Cayias, J. L., Fournier, G., McAllister, D., Schartz, T., Schechter, R. S., & Wade, W. H. (1977). Application of Low Interfacial Tension Scaling Rules to Binary Hydrocarbon Mixtures. *Journal of Collid & Interface Science*(59), 39-44.

Chatzis, I. (1980). *A Network Approach to Analyze and Model Capillary and Transport Phenomena in Porous Media*. Retrieved from Waterloo, ON.:

Chatzis, I., & Dullien, F. A. L. (1985). The modeling of Mercury Porosimetry and the Relative Permeability of Mercury in Sandstones using Percolation Theory. *INt. Chem. Eng., 25*(1), 47-66.

Chatzis, I., Morrow, N. R., & Lim, H. T. (1983). Magnitude and Detailed Structure of Residual Oil. *SPEJ*, 311-326.

Chavent, G. (2009). A Fully Equivalent Global Pressure Formulation for Three-Phase Compressible Flow. *Appl. Anal., 88*, 1527-1541.

Chavent, G., Roupert, R. d. C., & Schäfer, G. (2008). *A Fully Equivalent Global Pressure Formulation for Three-Phase Compressible Flows.* Paper presented at the Conference Scaling'Up 08, Dubrovnik.

Chen, C., C,, Britt, H. I., Boston, J. F., & Evans, L. B. (1982). Local Composition Model for Excess Gibbs Energy of Electrolyte Systems. *AIChE Journal, 28*, 588.

Chen, C. C., Bokis, C. P., & Mathias, P. M. (2001). A Segment-Based Excess Gibbs Energy Model for Aqueous Organic Electrolyte Systems. *AIChE Journal, 47*, 2593.

Chen, C. C., & Evans, L. B. (1986). A Local Composition Model for the Excess Gibbs Energy of Aqueous electrolyte Systems. *AIChE Journal, 32*, 444.

Chen, C. C., & Song, Y. (2004). Generalized Electrolyte-NRTL Model for Mixed-Solvent Electrolyte Systems. *AIChE Journal, 50*(8), 1928-1941.

Chen, Q., Gerritsen, G., M., & Kovscek, A. R. (2010a). Modeling Foam Displacement With the Local-Equilibrium Approximation: Theory and Experimental Verification. *SPE Journal, 15*(1), 171-183.

Chen, S., & Doolen, G. D. (1998). Lattice Boltzmann Method for Fluid Flows. *Annual Review of Fluid Mechanics, 30*(1).

Chilingar, G. V., & T.F., Y. (1983). Some notes on wettability and relative. *Energy Sources, 7*(1), 67-75.

Christensen, J. R., Stenby, E. H., & Skauge, A. (2001). Review of WAG Field Experience. *SPE Res. Eval & Eng., 4*(2), 97-106. doi:10.2118/71203-PA

Christov, C., Dickson, A. G., & Møller, N. (2007). Thermodynamic Modeling of Aqueous Aluminum Chemistry and Solid-Liquid Equilibria to High Solution Concentration and Temperature. I. The acidic H-Al-Na-K-Cl-H2O system from 0 to 100 C. *Journal of Solution Chemistry, 36*, 1495-1523.

Christov, C., & Møller, N. (2004). Chemical Equilibrium Model of Solution Behavior and Solubility in the H-Na-K-OH-Cl-HSO4-SO4-H2O System to High Concentration and Temperature. *Geochimica et Cosmochimica Acta, 68*, 1309-1331.

Cissokho, M., Boussour, S., Cordier, P., Bertin, H., & Hamon, G. (2009). *Low salinity Oil Recovery on Clayey Sandstone: Experimental Study*. Paper presented at the International Symposium of the Society of Core Analysts, Noordwijk, The Netherlands.

Coker, D. A., Torquato, S., & Dunsmuir, J. H. (1996). Morphology and Physical Properties of Fontainebleau Sandstone via a Tomographic Analysis. *Journal of Geophys. Res. Solid., 101*, 17497-17506.

Coles, M. E., Hazlett, R. D., Spanne, P., Soll, W. E., & Muegge, E. L. (1998). Pore Level Imaging of Fluid Rransport using Synchrotron X-ray Microtomography. *Journal of Petroleum Science and Engineering, 19*, 55-63.

Computer Modeling Group. (2012). *STARS. Thermal & Advanced Processes Reservoir Simulator*. Retrieved from Calgary, Canada.

Corey, A. T., Rathjens, C. H., Henderson, J. H., & Wyllie, M. R. J. (1956). Three-Phase Relative Permeability. *J. Pet Tech, 8*(11), 63-65.

Craig, F. F. (1971). *The Reservoir Engineering Aspects of Waterflooding. Monograph Series 3*. Dallas, Texas, USA: SPE

Crowell, D. C., Dean, G. W., & Loomis, A. G. (1966). *Efficiency of Gas Displacement from a Water-Drive Reservoir*. Retrieved from

Cruz, J.-L., & Renon, H. (1978). A New Thermodynamic Representation of Binary Electrolyte Solutions Nonideality in the Whole Range of Concentrations. *AIChE Journal, 24*(5), 817-830.

Dang, C. T. Q., Nghiem, L. X., Chen, Z. J., & Nguyen, Q. P. (2013). *Modeling Low Salinity Waterflooding: Ion Exchange, Geochemistry and Wettability Alteration*.

Daubert, T. E., & Danner, R. P. (1997). *API Technical Data Book-- Petroleum Refining*. Washington, DC: American Petroleum Institute (API).

Davies, C. W. (1938). The Extent of Dissociation of Salts in Water. Part VIII. An Equation for the Mean Ionic Activity Coefficient of an Electrolyte in Water, and a Revision of the Dissociation Constants of Some Sulphates. *Journal of Chemical Society*, 2093-2298.

Davies, C. W. (1962). *Ion Associatio*. Butterworths, Washington, D.C.

Davis, H. T. (1996). *Statistical Mechanics of Phases, Interfaces, and Thin Films*. New York: VCH Publishers Inc.

De Gennes, P. G., Brochard-Wyart, F., & Quéré, D. (2004). *Capillarity and wetting phenomena*. New York: Springer.

De Prisco, G., Toelke, J., & Dernaika, M. R. (2012). Computation of Relative Permeability functions in 3D Digital Rocks by a Fractioal Flow Approach Using the Lattice Boltzmann Method. Aberdeen, Scotland, UK: paper prepared for presentation at the International Symposium of the Society of Core.

Debenedetti, D. G., & Stillinger, F. H. (2001). Review Article Supercooled Liquids and the Glass Transition. *Nature, 410*, 259-267.

Debye, P., & Hückel, E. (1923). Zur Theorie der Elektrolyte. I. Gefrierpunktserniedrigung und Verwandte Erscheinungen (On the Theory of Electrolytes I. Freezing Point Depression and Related Phenomena. *Physikalische Zeitschrift, 24*(9), 185-206.

Dehghanpour, H. (2011). *Measurement and Modeling of Three-Phase Oil Relative Permeability*. Retrieved from

Delshad, M., Delshad, M., Pope, G. A., & Lake, L. W. (1987). Two- and Three-Phase Relative Permeabilities of Micellar Fluids. *SPE Formation Evaluation, 2*(3), 327-337. doi:10.2118/13581-PA

Delshad, M., Lenhard, R. J., Oostrom, M., & Pope, G. A. (2003). A Mixed-Wet Hysteretic Relative Permeability and Capillary Pressure Model for Reservoir Simulations. *SPE Res Eng*, 329-334.

Delshad, M., & Pope, G. A. (1989). Comparison of Three-Phase Oil Relative Permeability Models. *Transport in Porous Media, 4*(1), 59-83.

Delshad, M., Wheeler, M. F., & Kong, X. (2010). *A Critical Assessment of CO_2 Injection Strategies in Saline Aquifers*. Paper presented at the SPE Western Regional Meeting, Anaheim, California, USA.

Delshad, M., Wheeler, M. F., Sepehrnoori, K., & Pope, G. A. (2014). *Development of an Advanced Simulator to Model Mobility Control and Geomechanics during CO_2 Floods*. Retrieved from http://www.osti.gov/scitech/servlets/purl/1130970/

Demianov, A., & Dinariev, O. E., N. (2011). Density Functional Modelling in Multiphase Compositional Hydrodynamics. *The Canadian Journal of Chemical Engineering, 89*, 206-226.

Derjaguin, B., & Landau, L. (1941). Theory of the Stability of Strongly Charged Lyophobic Sols and of the Adhesion of Strongly Charged Particles in Solutions of Electrolytes. *Acta Physico Chemica, URSS, 14*, 633.

Dernaika, M. R., Basioni, M. A., Dawoud, A. M., Kalam, M. Z., & Skjæveland, S. M. (2013). Variations in Bounding and Scanning Relative Permeability Curves With Different Carbonate Rock Type. *SPE J.*, *16*(03), 265-280. doi:10.2118/162265-PA

di Chariara Roupert, R., Chavent, G., & Schäfer, G. (2010). Three-Phase Compressible Flow in Porous Media: Total Differential Compatible Interpolation of Relative Permeabilities. *Journal of Computational Physics*, *229*, 4762-4780.

DiCarlo, D. A., Sahni, A., & Blunt, M. J. (2000). Three-Phase Relative Permeability of Water-Wet, Oil-Wet, and Mixed-Wet Sandpacks. *SPE J., 5*(1), 82-91.

Dietricht, J. K., & Bonder, P. L. (1976). *Three-Phase Oil Relative Permeability Models.* Paper presented at the SPE Annual Fall Technical Conference and Exhibition, New Orleans, LA.

Dijkstra, H. A., & Weijer, W. (2005). Stability of the Global Ocean Circulation: Basic Bifurcation Diagrams. *Journal of Physical Oceanography, 35*, 933-948.

Dixit, A. B., McDougall, S. R., Sorbie, K. S., & Buckley, J. S. (1999a). Pore-Scale Modeling of Wettability Effects and Their Influence on Oil Recovery. *SPE Res. Eval. Eng., 32*(1), 1-12.

Donaldson, E. C., & Dean, G. W. (1966). *Two- and Three- Phase Relative Permeability Studies*. Retrieved from

Dong, H., Touati, M., & Blunt, M. (2007). Pore Network Modeling: Analysis of Pore Size Distribution of Arabian Core Samples: Society of Petroleum Engineers.

Dreyer, W., Jamnik, J., Guhlke, C., Huth, R. M., J., & Gaberšček, M. (2010). The thermodynamic Origin of Hysteresis in Insertion Batteries. *Nature Materials, 9*, 448-453.

Dria, D. E., Pope, G. A., & Sepehrnoori, K. (1993). Three-Phase Gas/Oil/Brine Relative Permeabilities Measured under CO_2 Flooding Conditions. *SPE Res Eng, 8*(2), 143-150.

Dullien, F. A. L. (1992). *Porous Media: Fluid Transport and Pore Structure*. San Diego, California: Academic Press, Inc.

Dullien, F. A. L., El-Sayed, M. S., & Batra, V. K. (1977). Rate of Capillary Rise in Porous Media with Nonuniform Pores. *Journal of Colloid and Interface Science, 60*(3), 497-506.

Dullien, F. A. L., Zarcone, C., Macdonald, I. F., Collins, A., & Bochard, D. E. (1989). The Effects of Surface Roughness on the Capillary Pressure Curves and the Heights of Capillary Rise in Glass Bead Packs. *J. Coll. Int. Sci., 127*(2), 362-373.

Egermann, P., Vizika, O., Kallet, L., Requin, C., & Sonier, F. (2000). *Hysteresis in Three-Phase Flow: Experiments, Modelling and Reservoir Simulations.* Paper presented at the Paper presented at the IEA Workshop and Symposium on Enhanced Oil Recovery, Edinburgh, Scotland.

Element, D. J., Masters, J. H. K., Sargent, N. C., Jayasekera, A. J., & Goodyear, S. G. (2003). *Assessment of Three-Phase Relative Permeability Models Using Laboratory Hysteresis Data.* Paper presented at the Paper SPE 84903 presented at the SPE International Improved Oil Recovery Conference in Asia Pacific, Kuala Lumpur, Malaysia.

Eleri, O. O., , G., A., Skauge, A., & Larsen, J. A. (1995). Calculation of Three-Phase Relative Permeabilities from Displacement Experiments *paper SCA1995-09 presented at the International Symposium of the Society of the Core Analysis*.

Enick, R. M., Olsen, D. K., Ammer, J. R., & Schuller, W. (2012). *Mobility and Conformance Control for CO_2 EOR via Thickeners, Foams, and Gels -- A Literature Review of 40 Years of Research and Pilot Tests*.

Eral, H. B., M. 't Mannetje, D. J. C., & Oh, J. M. (2013). Contact Angle Hysteresis: a Review of Fundamentals and Applications. *Colloid Polym. Sci., 291*, 247-260. doi:10.1007/s00396-012-2796-6

Ettinger, R. A., & Radke, C. J. (1992). Influence of Texture on Steady Foam Flow in Berea Sandstone. *SPE Reservoir Engineering, 7*(1), 83-90.

Falls, A. H., G.J., H., T.W., P., D.A., G., D.D., M., & T., R. (1988). Development of a Mechanistic Foam Simulator: The Population Balance and Generation by Snap-Off. *SPE Res. Eng., 3*(3), 884-892.

Farajzadeh, R., Ameri, A., Faber, M. J., van Batenburg, D. W., Boersma, D. M., & Bruining, J. (2013). Effect of Continuous, Trapped, and Flowing Gas on Performance of Alkaline Surfactant Polymer (ASP) Flooding. *Ind. Eng. Chem. Res., 52*(38), 13839-13848.

Fatt, I. (1956). The Network Model of Porous Media. *Trans. AIME, 207*, 144-181.

Fayers, F. J., Foakes, A. P., Lin, C. Y., & Puckett, D. A. (2000). *An Improved Three-Phase Flow Model Incorporating Compositional Variance.* Paper presented at the Paper SPE 59313 presented at the SPE/DOE Improved Oil Recovery Symposium, Tulsa, OK.

Fayers, F. J., & Matthews, J. D. (1984). Evaluation of Normalized Stone's Methods for Estimating Three Phase Relative Permeabilities. *SPE J., 242*(2), 224-232.

Fenwick, D. H., & Blunt, M. J. (1988). Network Modeling of Three-Phase Flow in Porous Media. *SPE Journal*, 86-97.

Fincham, A. E., & Ferreol, B. (1998). *History Matching of Laboratory Coreflooding Experiments.* Paper presented at the SPE 50576, The Hague.

Firoozabadi, A., & Ramey, J., H.J. (1988). Surface Tension of Water-Hydrocarbon Systems at Reservoir Conditions. *Journal of Canadian Pet. Tech., 27*(3), 41-48.

Fisher, A. W., Foulser, R. W. S., & Goodyear, S. G. (1990). *Mathematical Modeling of Foam Flooding*.

Flannery, B. P., Deckman, H. W., & Roberge, W. G., D'Amico K.L. (1987). Three-Dimensional X-ray Microtomography. *Science, 237*, 1439-1444.

Flett, M., Gurton, R., & Taggart, I. (2004). *The Function of Gas-Water Relative Permeability Hysteresis in the Sequestration of Carbon Dioxide in Saline Formations*. Paper presented at the SPE Asia Pacific Oil and Gas Conference and Exhibition, Perth, Australia.

Fredenslund, A., Jones, R. L., & Prausnitz, J. M. (1975). Group-Contribution Estimation of Activity Coefficients in Nonideal Liquid Mixtures. *AIChE Journal, 21*, 1086.

Freidman, H. L. (1985). *A Course in Statistical Mechanics*. Englewood Cliffs: Prentice-Hall.

Fried, A. (1961). *The Foam-Drive Process for Increasing the Recovery of Oil*. Retrieved from San Francisco:

Friedman, H. L. (1962). *Ionic Solution Theory*. London: Interscience Publishers.

Friedmann, F., Chen, W. H., & Gauglitz, P. A. (1991). Experimental and Simulation Study of High-Temperature Foam Displacement in Porous Media. *6*(1), 37-45. doi:10.2118/17357-PA

Fürst, W. l., & Renon, H. (1982). Effect of the Various Parameters in the Application of Pitzer's Model to Solid-Liquid Equilibrium. Preliminary Study for Strong 1-1 Electrolytes. *Ind. Eng. Chem. Process Des. Dev., 21*, 396-400.

Fürst, W. l., & Renon, H. (1993). Representation of Excess Properties of Electrolyte Solutions Using a New Equation of State. *AIChE Journal, 39*, 335-343.

Galindo, A., Gil-Villegas, A., Jackson, G., & Burgess, A. N. (1999). SAFT-VRE: Phase Behavior of Electrolyte Solutions with the Statistical Associating Fluid Theory for Potentials of Variable Range. *J. Phys. Chem. B, 103*, 10272-10281.

Ganis, B., Kumar, K., Pencheva, G., Wheeler, M. F., & Yotov, I. (2014). A Global Jacobian Method for Mortar Discretizations of a Fully Implicit Two-Phase Flow Model. *Multiscale Modeling & Simulation, 12*(4), 1401-1423.

Garrels, R. M., & Christ, C. L. (1965). *Solutions, Minerals, and Equilibria*. New York: Harper and Row.

Gauglitz, P. A., Friedmann, F., Kam, S. I., & Rossen, W. R. (2002). Foam Generation in Homogeneous Porous Media. *Chemical Engineering Science, 57*(19), 4037-4052.

Geffen, T. M., Owens, W. W., Parrish, D. R., & Morse, R. A. (1951). Experimental Investigation of Factors Affecting Laboratory Relative PErmeability Measurements. *Petro.l Trans. AIME, 192*, 99-110.

Geffen, T. M., Parrish, D. R., Haynes, G. W., & Morse, R. A. (1952). Efficicency of Gas Displacement from Porous Media by Liquid Flooding. *Trans AIME, 195*, 29-38.

Georgiadis, A., Berg, S., Makurat, A., Maitland, G., & Ott, H. (2013). Pore-Scale Micro-Computed-Tomography Imaging: Nonwetting-Phase Cluster-Size Distribution During Drainage and Imbibition. *Physical Review E, 88*(033002), 1-9.

Ghomian, Y. (2008). *Reservoir Simulation Studies for Coupled CO_2 Sequestration and Enhanced Oil Recovery*. (Ph.D. dissertation), The University of Texas at Austin, Austin, Texas.

Gibbs, J. W. (1875-1878). *Influences of Surfaces of Discontinuity uopn the Equilibrium of Heterogeneous Masses. Theory of Capillarity.* (Vol. 1). Woodbridge: OX Bow Press.

Gil-Villegas, A., Galindo, A., Whitehead, P. J., Mills, S. J., Jackson, G., & Burgess, A. N. (1997). Statistical Associating Fluid Theory for Chain Molecules with Attractive Potentials of Variable Range. *Journal of Chem. Phys., 106*, 4168-4186.

Goldberg, R. N. (1979). Evaluated Activity and Osmotic Coefficients for Aqueous Solutions: Bi-Univalent Compounds of Lead, Copper, Manganese, and Uranium. *Journal Physc. Chem. Ref. Data, 8*(4), 1005-1050.

Goldberg, R. N. (1981a). Evaluated Activity and Osmotic Coefficients for Aqueous Solutions: Univalent Compounds of Zinc, Camium, and Ethylene Bis (Trimethylammonium) Chloride and Lodide. *Journal Physc. Chem. Ref. Data, 10*(1), 1-55.

Goldberg, R. N. (1981b). Evaluated Activity and Osmotic Coefficients for Aqueous Solutions: Thirty-Six UniBivalent Electrolytes. *Journal Physc. Chem. Ref. Data, 10*(3), 671-764.

Gouet-Kaplan, M., Tartakovsky, A., & Berkowitz, B. (2009). Simulation of the Interplay Between Resident and Infiltrating Water in Partially Saturated Porous Media. *Water Resources Research*.

Gray, W. G., & Miller, C. T. (2005). Thermodynamically Constrained Averaging Theory Approach for Modeling Flow and Transport Phenomena in Porous Medium Systems: 1. Motivation and Overview. *Advances in Water Resources, 28*, 161-180.

Green, D. W., & Willhite, G. P. (1998). *Enhanced Oil Recovery*. Dallas: Society of Petroleum Engineers.

Greenberg, J., & Møller, N. (1989). The Prediction of Mineral Solubilities in Natural Waters - a Chemical Equilibrium Model for the Na-K-Ca-Cl-SO_4-H_2O System to High Concentration from 0 to 250 C. *Geochimica et Cosmochimica Acta, 53*, 2503-2518.

Griffin, R. A., & Jurinak, J. J. (1973). Estimation of Activity Coefficients from the Electrical Conductivity of Natural Aquatic Systems and Soil Extracts. *Soil Sci., 116*, 26-30.

Gross, J., & Sadowski, G. (2001). Perturbed-Chain SAFT: an Equation of State Based on a Perturbation Theory for Chain Molecules. *Ind. Eng. Chem. Res., 40*, 1244-1260.

Grunau, D., Chen, S., & Egger, K. (1993). A lattice Boltzmann Model for Multi-Phase Fluid. *Physics of Fluids A, 5*, 2557.

Guckert, L. G. (1968). *Gamma-Ray Absorption Method of Measuring Gas Saturation and its AppLication to Three-Phase Relative Permeability Studies*. Retrieved from

Guggenheim, E. A. (1935). L. The Specific Thermodynamic Properties of Aqueous Solutions of Strong Electrolytes. *The London, Edinburgh, and Dublin Philosophical, 19*(127), 588-643.

Guggenheim, E. A. (1940). The Thermodynamics of Interfaces in Systems of Several Components. *Trans. Faraday Soc., 35*, 397-412.

Guggenheim, E. A. (1952). *The Theory of Equilibrium Properties for some Simple Classes of Mixtures, Solutions and Alloys*. Oxford: Clarendon Press.

Guggenheim, E. A., & Turgeon, J. C. (1955). Specific Interaction of Ions. *Trans. Faraday Soc., 511*, 747-761.

Gunstensen, A. K., & Rothman, D. H. (1993). Lattice-Boltzmann Studies of Immiscible Two-Phase Flow Through Porous Media. *Journal of Geophysical Research: Solid Earth, 98*, 6431-6441.

Gupta, R., Smith, G. G., Hu, L., Willingham, T., Lo Cascio, M., Shyeh, J. J., & Harris, C. R. (2011). *Enhanced Waterflood for Carbonate Reservoirs - Impact of Injection Water Composition*. Paper presented at the SPE Middle East Oil and Gas Show and Conference, Manama, Bahrain.

Hagoort, J. (1990). Oil Recovery by Gravity Drainage. *20*(3), 139-150. doi:10.2118/7424-PA

Haines, W. B. (1930). Studies in the Physical Properties of Soil. V. the Hysteresis Effect in Capillary Properties, and the Modes of Moisture Distribution Associated Therewith. *The Journal of Agricultural Science, 20*(1), 97-116.

Hamann, S. D. (1984). Influence of Pressure on Activity Coefficients of Electrolytes in Solution. *Journal of Chem. Soc., Faraday Trans. 1,, 80*, 2541-2548.

Hammond, P. S. (2012). A Dynamic Pore Network Model for Oil Displacement byWettability-Altering Surfactant Solution. *Transp. Porous Med., 92*, 789-817.

Hand, D. B. (1939). The Distribution of a Consolute Liquid between Two Immiscible Liquids. *J. of Physics and Chem., 1961-2000*, 34.

Harouaka, A., Trentham, B., & Melzer, S. (2014). Permian Basin Production Proves ROZ Viability. *Oil & Gas Journal*, 78.

Harvie, C. E., Møller, N., & Weare, J. H. (1984). The Prediction of Mineral Solubilities in Natural Waters: The Na-K-Mg-Ca-H-$ClSO_4$-OH-HCO_3-CO_3-CrH_2O System to High Ionic Strengths at 25°C. *Geochimica et Cosmochimica Acta, 48*, 723-751.

Hassanizadeh, S. M., & Gray, W. G. (1990). Mechanics and Thermodynamics of Multiphase Flow in Porous Media Including Interphase Boundaries. *Advances in Water Resources, 13*(4), 169-186.

Hatziavramidis, D. T., Alameddine, B. R., Weinstein, H. G., Djabbarah, N. F., & Revay, J. M. (1995). *A Mechanistic Foam Model for Simulation of Steamfoam Field Applications*.

Hawkins, J. T., & Bouchard, A. J. (1989). Reservoir Engineering Applications of Capillary Pressure and Relative Permeability Hysteresis *Conference Paper Number 8909*: Society of Sore Analysis.

Hazlett, R. D. (1995). Simulation of Capillary-Dominated Displacements in Microtomographic Images of Reservoir Rocks. *Trans. Porous Med., 20*(1-2), 21-35.

Healy, R. N., & Reed, R. L. (1974). Physiochemical Aspects of Microemulsion Flooding. *SPE Journal, 14*, 491-501.

Held, C., Cameretti, L. F., & Sadowski, G. (2008). Modeling Aqueous Electrolyte Solutions Part 1. Fully Dissociated Electrolytes. *Fluid Phase Equilibria, 270*, 87-96.

Held, C., Reschke, T., Mohammad, S., Luza, A., & Sadowski, G. (2014). ePC-SAFT revised. *Chemical Engineering Research and Design, 92*, 2884-2897.

Held, C., & Sadowski, G. (2009). Modeling Aqueous Electrolyte Solutions. Part 2. Weak Electrolytes. *Fluid Phase Equilibria, 279*(2), 141-148.

Helgeson, H. C. (1969). Thermodynamics of Hydrothermal Systems at Elevated Temperatures and Pressures. *American Journal of Science, 267*(7), 729-804.

Helgeson, H. C., & Kirkham, D. H. (1974). Theoretical Prediction of the Thermodynamic Behavior of Aqueous Electrolytes at High Pressure and Temperatures: I. Summary of the Thermodynamic/Electrostatic Properties of the Solvent. *American Journal of Science, 274*, 1089-1198.

Helgeson, H. C., Kirkham, D. H., & Flowers, G. C. (1981). Theoretical Prediction of the Thermodynamic Behavior of Aqueous Electrolytea at High Pressures and Temperatures: IV. Calculation of Activity Coefficients, Osmotic Coefficients, and Apparent Molal and Standard and Relative Partial Molal Properties to 600°C. *American Journal of Science, 281*, 1249-1516.

Helland, J. O., & Jettestuen, E. (2014). *Numerical Simulation of Capillary-Controlled Three-Phase Displacements on 3D Images*. Paper presented at the paper SCA2014-030 presented at the International Symposium of the Society of Core Analysts, Avignon, France.

Henderson, D., & Blum, L. (1981). Perturbation Theory, The Mean Spherical Approximation, and The Electrical Double Layer. *Canadian Journal of Chemistry, 59*, 1903-1905.

Hernández-Lemus, E., Nicasio-Collazo, L. A., & Castañeda-Priego, R. (2012). Hysteresis in Pressure-Driven DNA Denaturation. *PLoS ONE, 7*(4), e33789.

Herring, A. L., Harpera, E. J., Anderssona, L. S., A., Bayc, B. K., & Wildenschilda, D. (2013). Effect of Fluid Topology on Residual Nonwetting Phase Trapping: Implications for Geologic CO_2 Sequestration. *Advances in Water Resources, 62*(part A), 47-58.

Herzog, S., Gross, J., & Arlt, W. (2010). Equation of State for Aqueous Electrolyte Systems Based on the Semirestricted Non-Primitive Mean Spherical Approximation. *Fluid Phase Equilibria, 297*(1), 23-33.

Hingerl, F. F., Wagner, T., Kulik, D. A., Thomsen, K., & Driesner, T. (2014). A New Aqueous Activity Model for Geothermal Brines in the System Na-K-Ca-Mg-H-Cl-SO_4-H_2O from 25 to 300 °C. *Chemical Geology, 381*, 78-93.

Hiorth, A., Cathles, M. L., & Madland, M. V. (2010). The Impact of Pore Water Chemistry on Carbonate Surface Charge and Oil Wettability. *Transp Porous Med., 85*, 1-21.

Hirasaki, G. J. (1981). Application of the Theory of Multicomponent, Multiphase Displacement to Three-Component, Two-phase Surfactant Flooding. *Soc. Pet. Eng. J.*, 191-204.

Hirasaki, G. J., & Lawson, J. B. (1985). Mechanisms of Foam Flow in Porous Media: Apparent Viscosity in Smooth Capillaries. *SPE Journal, 25*(2), 176-190. doi:10.2118/12129-PA

Hirt, C. W., & Nichols, B. D. (1981). Volume of fluid (VOF) Method for the Dynamics of Free Boundaries. *Journal of Computational Physics, 39*(1), 201-225.

Holmes, H. F., & Mesmer, R. E. (1988). Isopiestic Studies of Aqueous Solutions at Elevated Temperatures. VIII. The alkali-Metal Sulfates. *J. Chem. Thermodynamics, 18*, 263-275.

Holmgren, C. R., & Morse, R. A. (1951). Effect of Free Gas Saturation on Oil Recovery by Waterflooding. *Petroleum Trans. AIME, 192*, 135.

Holtz, M. H. (2002). Residual Gas Saturation to Aquifer Influx: A Calculation Method for 3-D Computer Reservoir Model Construction: Society of Petroleum Engineers.

Honarpour, M., Cullick, A. S., Saad, N., & Humphreys, N. V. (1995). Effect of Rock Heterogeneity on Relative Permeability: Implications for Scale-up. *JPT*. doi:10.2118/29311-PA

Honarpour, M., & Saad, N. (1994). *Influence of Small-Scale Rock Laminations on Core Plug Oil/Water Relative Permeability and Capillary Pressure*.

Honarpour, M., Koederitz, L., & Harvey, A. H. (1986). *Relative Permeability of Petroleum Reservoirs*. Boca Raton, Florida: CRC Press, Inc.

Hu, Y., Liidecke, D., & J.M., P. (1984). Molecular Thermodynamics of Fluid Mixtures Containing Molecules Differing in Size and Potential Energy. *Fluid Phase Equilibria, 17*, 217-241.

Hu, Y., Xu, Y. N., & Prausnitz, J. M. (1985). Molecular thermodynamics of gas solubility. *Fluid Phase Equilibria, 23*, 15-40.

Huang, B., Bates, M., & Zhuang, X. (2009). Super-Resolution Fluorescence Microscopy. *Annual Review of Biochemistry, 78*.

Hückel, E. (1925). Zur Theorie konzentrierterer wässeriger Lösungen starker Elektrolyte. *Physikalische Zeitschrift, 26*, 93-147.

Huh, C. (1979). Interfacial Tension and Solubilizing Ability of a Microemulsion Phase that Coexists with Oil and Brine. *J. Colloid Interface Sci., 71*, 408-428.

Huh, D. G., Cochrane, T. D., & Kovarik, F. S. (1989). The Effect of Microscopic Heterogeneity on CO_2-Foam Mobility: Part 1--Mechanistic Study. doi:10.2118/17359-PA

Hui, M. H., & Blunt, m. J. (2000). *Pore-Scale Modleing of Three-Phase flow and the Effects of wettability.* Paper presented at the SPE 59309. Proceedings of the SPE/DOE Improved Oil Recovery Symposium, Tulsa.

Hummel, R. E. (1985). *Electronic Properties of Materials: An Introduction for Engineers*. Berlin: Springer-Verlag Berlin Heidelberg GmbH.

Humphry, K. J., Suijkerbuijk, B. M. J. M., van der Linde, H. A., Pieterse, S. G. J., & Masalmeh, S. K. (2013). *Impact of Wettability on Residual Oil Saturation and Capillary Desaturation Curves.* Paper presented at the International Symposium of the Society of Core Analysts, Napa Valley, California, USA.

Hunter, R. J. (2001). *Foundations of Colloid Science 2nd Edition*. New York: Oxford University Press.

Hustad, O. S. (2002). A Fully Coupled Three-Phase Model for Capillary Pressure and Relative Permeability for Implicit Compositional Reservoir Simulation. *SPE J., 7*(1), 59-69.

Hustad, O. S., & Browning, D. J. (2010). A Fully Coupled Three-Phase Model for Capillary Pressure and Relative Permeability for Implicit Compositional Reservoir Simulation. *SPE J.*, 1009-1025.

Hustad, O. S., & Hansen, A.-G. (1996). *A Consistent Formulation for Three-Phase Relative Permeability and Phase Pressure Based on Three Sets of Two-Phase Data.* Paper presented at the Paper in book RUTH, A Norwegian Research Program on Improved Oil Recovery, Program Summary, Norwegian Petroleum Directorate, Stavanger.

Hustad, O. S., & Holt, T. (1992). *Gravity Stable Displacement of Oil by Hydrocarbon after Waterflooding.* Paper presented at the Paper SPE 24116 presented at the SPE/DOE Symposium on Enhanced Oil Recovery, Tulsa, OK.

Idowu, N. A., & Blunt, M. J. (2010). Pore-Scale Modelling of Rate Effects in Waterflooding. *Transp. Porous Med., 83*(1), 151-169.

Iglauer, S. (2011). Dissolution trapping of Carbon Dioxide in reservoir Formation Brine- A Carbon Storage Mechanism. In h. Nakajima (Ed.), *Mass Transfer- Advanced Aspects*. Rijeka, Croatia: InTech.

Iglauer, S., Fernø, M. A., Shearing, P., & Blunt, M. J. (2012). Comparison of Residual Oil Cluster Size Distribution, Morphology and Saturation in Oil-wet and Water-wet Sandstone. *Journal of Colloid and Interface Science, 375*(1), 187-192. doi:http://dx.doi.org/10.1016/j.jcis.2012.02.025

Iglauer, S., Paluszny, A., & Blunt, M. J. (2013). Simultaneous Oil Recovery and Residual Gas Storage: A Pore-Level Analysis using in situ X-Ray Micro-Tomography. *Fuel*, *103*, 905-914.

Iglauer, S., Rahman, T., Sarmadivaleh, M., Al-Hinai, A., Fernø, M. A., & Lebedev, M. (2016). Influence of Wettability on Residual Gas Trapping and Enhanced Oil Recovery in Three-Phase Flow: A Pore-Scale Analysis by Use of Microcomputed Tomography. *SPE Journal*. doi:10.2118/179727-PA

Ikonomou, G. D., & Donohue, M. D. (1986). Thermodynamics of Hydrogen-Bonded Molecules: The Associated Perturbed Anisotropic Chain Theory. *AIChE Journal, 32*(10), 1716-1725.

Inamuro, T., Konishi, N., & Ogino, F. (2000). A Galilean Invariant Model of the Lattice Boltzmann Method for Multiphase Fluid Flows Using Free Energy Approach. *Computer Physics Communications, 129*, 32-45.

Inchekel, R., de Hamptinee, J.-C., & Fürst, W. (2008). The Simultaneous Representation of Dielectric Constant, Volume and Activity Coefficients Using an Electrolyte Equation of State. *Fluid Phase Equilibria, 271*, 19-27.

Irwin, D. D., & Batycky, J. P. (1997). The Successive Displacement Process: Oil Recovery During Blowdown. *SPE Reservoir Engineering*.

Islam, M. R., & Farouq-Ali, S. M. (1990). Numerical Simulation of Foam Flow in Porous Media. *J. Can. Pet. Tech.*

Israelachvili, J. N. (2011). *Intermolecular and Surface Forces*. Waltham, MA: Academic Press, Elsevier.

Jackson, M. D., Valvatne, P. H., & Blunt, M. J. (2005). Prediction of Wettability Variation Within an Oil/Water Transition Zone and Its Impact on Production. *SPE Journal*, 184-195.

Jacqmin, D. (1999). Calculation of Two-Phase Navier–Stokes Flows Using Phase-Field Modeling. *Journal of Computational Physics, 155*(1), 96-127.

Jarrell, P. M., Fox, C. E., Stein, M. H., & Webb, S. L. (2002). *Practical Aspects of CO_2 flooding* (Vol. 22). Richardson, TX: SPE.

Jerauld, G. R. (1997a). Prudhoe Bay Gas/Oil Relative Permeability. *SPE Res Eng, 12*(1), 66-73.

Jerauld, G. R. (1997b). General Three-Phase Relative Permeability Model for Prudhoe Bay. *SPE Res Eng, 12*(4), 255-263.

Jerauld, G. R., & Rathmell, J. J. (1997c). Wettability and Relative Permeability of Prudhoe Bay: As Case Study in Mixed-Wet Reservoirs. *SPE Res. Eng.*, 58-65.

Jerauld, G. R., & Salter, S. J. (1990). The Effect of Pore-Structure on Hysteresis in Relative Permeability and Capillary Pressure: Pore-Level Modeling. *Transport in Porous Media, 5*, 103-151.

Jerauld, G. R., Webb, K. J., Lin, C.-Y., & Seccombe, J. C. (2008). Modeling Low-Salinity Waterflooding. *SPE Res. Eval. Eng., 11*(6), 1000-1012. doi:10.2118/102239-PA

Jiang, F., & Tsuji, T. (2014). Changes in Pore Geometry and Relative Permeability Caused by Carbonate Precipitation in Porous Media. *Physical Review E, 90*(5), 053306.

Jiang, Z., van Dijke, M. I. J., Sorbie, K. S., & Couples, G. D. (2013). Representation of Multiscale Heterogeneity via Multiscale Pore Networks. *Water Resources Research, 49*, 5734-5449.

Jin, G., & Donohue, M. D. (1988a). An Equation of State for Electrolyte Solutions. 1. Aqueous Systems Containing Strong Electrolytes. *Industrial & Engineering Chemistry Research, 27*(6), 1073-1084.

Jin, G., & Donhue, M. D. (1988b). An Equation of State for Electrolyte Solutions. 2. Single Volatile Weak Electrolytes in Water. *Industrial & Engineering Chemistry Research, 27*(9), 1737-1743.

Jin, G., & Donohue, M. D. (1991). An Equation of State for Electrolyte Solutions. 3. Aqueous Slutions Containing Multiple Salts. *Industrial & Engineering Chemistry Research, 30*(1), 240-248.

Jin, M. (1995). *A Study of Non-Aqueous Phase Liquid Characterization and Surfactant Remediation.* (Ph.D. dissertation), The University of Texas at Austin, Austin, Texas.

Joekar-Niasar, V., & Hassanizadeh, M. (2012). Uniqueness of Specific Interfacial Area–Capillary Pressure–Saturation Relationship Under Non-Equilibrium Conditions in Two-Phase Porous Media Flow. *Transp. Porous Med., 94*, 465–486.

Joekar-Niasar, V., Hassanizadeh, S. M., & Dahle, H. K. (2010). Non-Equilibrium Effects in Capillarity and Interfacial Area in Two-Phase Flow: Dynamic Pore-Network Modelling. *J. Fluid Mech., 655*, 38-71.

Johnson, E. F., Bossler, D. P., & Neumann, V. O. (1959). Calculation of Relative Permeability from Displacement Experiments. *Trans. AIME., 216*, 370-372.

Jones, A., Doyle, J., Jacobsen, T., & Kjønsvik, D. (1995). Which Sub-Seismic Heterogeneities Influence Waterflood Performance? A Case Study of a Low Net-to-Gross Fluvial Reservoir. *Geological Society, London, Special Publications, 84*(1), 5-18. doi:10.1144/gsl.sp.1995.084.01.02

Jones, D. R., Perttunen, C. D., & Stuckman, B. E. (1993). Lipschitzian Optimization without the Lipschitz Constant. *Journal of Optimization Theory and Applications, 79*(1), 157-181. doi:10.1007/BF00941892

Jones, J. E. (1924). On the Determination of Molecular Fields. II. From the Equation of State of a Gas. *106*(738), 463.

Kalaydjian, F. (1987). A macroscopic description of multiphase flow in porous media involving spacetime evolution of fluid/fluid interface. *Transport in Porous Media, 2*(6), 537-552. doi:10.1007/bf00192154

Kalaydjian, F., Vizika, O., Moulu, J.-C., & Munkerud, P. K. (1995). The Role of Wettability and Spreading in Gas Injection Processes under Secondary Conditions, 63-71.

Kam, S. I. (2008). Improved Mechanistic Foam Simulation with Foam Catastrophe Theory. *Colloids and Surfaces A: Physicochem. Eng. Aspects, 318*, 62-77.

Kam, S. I., & Rossen, W. R. (2003). A Model for Foam Generation in Homogeneous Porous Media. *SPE Journal, 8*(4), 417-425. doi:10.2118/87334-PA

Kamal, M., & Mardsen Jr., S. S. (1973). *Displacement of a Micellar Slug Foam in Unconsolidated Porous Media.* Paper presented at the Paper SPE 4584 presented at the Fall Meeting of the Society of Petroleum Engineers of AIME, Las Vegas, Nevada.

Kazemi Nia Korrani, A. (2014). *Mechanistic Modeling of Low Salinity Water Injection.* (Ph.D. dissertation), The University of Texas at Austin, Austin, Texas.

Kazempour, M., Manrique, E. J., Alvarado, V., Zhang, J., & Lantz, M. (2013). Role of Active Clays on Alkaline–Surfactant–Polymer Formulation Performance in Sandstone Formations. *Fuel, 104*, 593-606.

Keenan, J. H., Keyes, F. G., Hill, P. G., & Moore, J. G. (1969). *Steam Tables*. New York: John Wiley and Sons, Inc.

Ketcham, R. A., & Carlson, W. D. (2001). Acquisition, Optimization and Interpretation of X-ray Computed Tomographic Imagery: Applications to the Geosciences. *Computers & Geosciences, 27*(4), 381-400.

Khan, S. A. (1992). *An Expert System to Aid in Compositional Simulation of Miscible Gas Flooding.* (Ph.D. dissertation), The University of Texas at Austin, Austin, Texas.

Khan, S. A., Pope, G. A., & Sepehrnoori, K. (1992). *Fluid Characterization of Three-Phase CO_2/Oil Mixtures*. Paper presented at the SPE/DOE Enhanced Oil Recovery Symposium, Tulsa, Oklahoma.

Khatib, Z. I., Hirasaki, G. J., & Falls, A. H. (1988). Effects of Capillary Pressure on Coalescence and Phase Mobilities in Forms Flowing Through Porous Media. *SPE Res. Eng., 3*(3), 919-926.

Kianinejad, A., Chen, X., & DiCarlo, D. A. (2015). The effect of saturation path on three-phase relative permeability. *Water Resour. Res., 51*, 9141–9164.

Kianinejad, A., Chen, X., & DiCarlo, D. A. (2016). Modeling Relative Permeability Variations in Three-Phase Space: Society of Petroleum Engineers.

Kibodeaux, K. R. (1997). *Experimental and Theoretical Studies of Foam Mechanisms in Enhanced Oil Recovery and Matrix Acidization Applications.* (Ph.D. dissertation), The University of Texas at Austin, Austin, Texas.

Killins, C. R., Nielsen, R. F., & Calhoun, J. C., Jr. (1953). Capillary Desaturation and Imbibition in Rocks. *Producers Monthly, 18*(2), 30-39.

Killough, J. E. (1976). Reservoir Simulation with History-Dependent Saturation Functions. *SPE J., 16*(1), 37-48.

Kirkwood, G. J., & Buff, F. P. (1951). The Statistical Mechanical Theory of Solutions. I *Journal of Chemical Physics, 19*, 774-777.

Kirkwood, G. J., & Oppenheim, I. (1961). *Chemical Thermodynamics*. New York: McGraw-Hill.

Kjosavik, A., Ringen, J. K., & Skjæveland, S. M. (2002). Relative Permeability Correlation for Mixed-Wet Reservoirs. *SPE Journal, 7*(1), 49-58. doi:10.2118/77328-PA

Kleppe, J., Delaplace, P., Lenormand, R., Hamon, G., & Chaput, E. (1997). *Representation of Capillary Pressure Hysteresis in Reservoir Simulation.* Paper presented at the Paper SPE

38899 presented at the SPE Annual Technical Conference and Exhibition, San Antonio, TX.
Knight, R. (1991). Hysteresis in the Electrical Resistivity of Partially Saturated Sandstones. *Geophysics, 56*(12), 2139-2147.
Kokal, S., & Maini, B. (1990). An Improved Model for Estimating Three-Phase Oil-Water-Gas Relative Permeabilities from Two-Phase Oil-Water and Oil-Gas Phase. *JCPT, 29*(2), 105-113.
Kontogeorgis, G. M., Voutsas, E. C., & Tassios, D. P. (1996). An Equation of State for Associating Fluids. *Industrial & Engineering Chemistry Research, 35*(11), 4310-4318.
Kovscek, A. R., Patzek, T. W., & Radke, C. J. (1995). A Mechanistic Population Balance Model for Transient and Steady-State Foam Flow in Boise Sandstone. *Chem. Eng. Science, 50*(23), 3783-3799.
Kovscek, A. R., & Radke, C. J. (1994). *Fundamentals of Foam Transport in Porous Media, in L. Schramm (ed.), Foams: Fundamentals and Applications in the Petroleum Industry*. Paper presented at the ACS Symposium Series No. 242, Washington D.C.
Kovscek, A. R., Wong, H., & Radke, C. J. (1993). A Pore-Level Scenario for the Development of Mixed Wettability in Oil Reservoirs. *AIChE J., 39*(6), 1072-1085.
Kralik, J. G., Manak, L. J., Jerauld, G. R., & Spence, A. P. (2000). Effect of Trapped Gas on Relative Permeability and Residual Oil Saturation in an Oil-Wet Sandstone: Society of Petroleum Engineers.
Kulkarni, R., Watson, A. T., Nortdtvedt, J. E., & Sylte, A. (1998). Two-Phase Flow in Porous Media: Property Identification and Model Validation. *Fluid Mechanics and Transport Phenomena, AIChe Journal, 44*(11), 2337-2350.
Kumar, A., Noh, M., Pope, G. A., Sepehrnoori, K., Bryant, S., & Lake, L. W. (2004). Reservoir Simulation of CO_2 Storage in Deep Saline Aquifers. *SPE J.* doi:10.2118/89343-MS
Kusik, C. L., & Meissner, H. P. (1978b). Electrolyte Activity Coefficients in Inorganic Processing. *AIChE Symposium Series 173*, 14-20.
Kuuskraa, V. A., Van Leeuwen, T., & Wellace, M. (2011). *Improving Domestic Energy Security and Lowering CO_2 Emissions with "Next Generation" CO_2-Enhanced Oil Recovery (CO_2-EOR)*. Retrieved from
Kyte, J. R., Stanflift, R. J. J., Stephan, S. C. J., & Rapoport, L. A. (1956). Mechanism of Waterflooding in the Presence of Free Gas. *Pet. Trans. AIME, 207*, 215-221.
Lager, A., Webb, K. J., & Black, C. J. J. (2007). *Impact of Brine Chemistry on Oil Recovery*. Paper presented at the Paper A24 presented at the 14th EAGE Symposium on Improved Oil Recovery, Cairo.
Lager, A., Webb, K. J., Black, C. J. J., Singleton, M., & Sorbie, K. S. (2008a). Low Salinity Oil Recovery--An Experimental Investigation. *Petrophysics, 49*(1), 28.
Lager, A., Webb, K. J., Black, C. J. J., Singleton, M., & Sorbie, K. S. (2008b). *LoSal Enhanced Oil Recovery: Evidence of Enhanced Oil Recovery at the Reservoir Scale*.
Lake, L. W., Russell, T. J., Rossen, W. R., & Pope, G. A. (2014). *Fundumental of Enhanced Oil Recovery*. Richardson, TX: Society of Petroleum Engineers.

Land, C. S. (1968). Calculation of Imbibition Relative Permeability for Two- and Three- Phase Flow from Rock Properties. *SPE J., 8*(2), 149-156.

Land, C. S. (1971). Comparison of Calculated with Experimental Imbibition Relative Permeability. *SPE J., 11*(4), 419-425.

Langelier, W. F. (1936). The Analytical Control of Anti-Corrosion Water Treatment. *J. Am. Water Wks. Assoc, 28*, 1500.

Larsen, J. A., & Skauge, A. (1998). Methodology for Numerical Simulation with Cycle-Dependent Relative Permeabilities. *SPE J.*, 163-173.

Larson, R. G., Scriven, L. E., & Davis, H. T. (1981). Percolation Theory of Two-Phase Flow in Porous Media. *Chern. Eng. Sci., 36*, 57-73.

Lawson, J. B., & Reisberg, J. (1980). Alternate Slugs of Gas and Dilute Surfactant For Mobility Control During Chemical Flooding *Lawson, J. B. and Reisberg, J. 1980. Alternate Slugs of Gas and Dilute Surfactant For Mobility Control During Chemical Flooding. Paper Paper SPE 8839 presented at SPE/DOE Enhanced Oil Recovery Symposium*. Tulsa, Oklahoma.

Lebowitz, J. L., & Percus, J. K. (1966). Mean Syherical Model for Lattice Gases with Extended Hard Cores and Continuum Fluids. *Physcial Review, 144*(1), 251-258.

Lee, D. T., & Schachter, B. J. (1980). Two Algorithms for Constructing a Delaunay Triangulation. *International Journal of Computer and Information Sciences, 9*(3).

Lee, S. Y., Webb, K. J., Collins, I., Lager, A., Clarke, S., O'Sullivan, M., . . . Wang, X. (2010). *Low Salinity Oil Recovery: Increasing Understanding of the Underlying Mechanisms*.

Lerdahl, T. R., Øren, P.-E., & Bakke, S. (2000). A Predictive Network Model for Three-Phase Flow in Porous Media.

Leverett, M. C., & Lewis, W. B. (1941). Steady Flow of Gas-Oil-Water Mixtures Through Unconsolidated Sands. *Trans., AIME, 142*, 107-116.

Lewis, G. N., & Randall, M. (1921). The Activity Coefficient of Strong Electrolytes. *Journal of American Chemistry Society, 43*, 1112-1154.

Li, R. F., Yan, W., Liu, S., Hirasaki, G. J., & Miller, C. A. (2010). Foam Mobility Control for Surfactant Enhanced Oil Recovery. *SPE Journal, 15*(04), 928-942.

Lietzke, M. H., & Stoughton, R. W. (1962a). Thermodynamic Investigation of Aqueous Electrolytes to 275°C. *Journal of Chemical Education, 39*(5), 230-235.

Lietzke, M. H., & Stoughton, R. W. (1962b). The Calculation of Activity Coefficients from Osmotic Coefficient Data. *Journal of Physical Chemistry, 66*(3), 508-509.

Lietzke, M. H., & Stoughton, R. W. (1975). Extension of a Two-Structure Model for Electrolyte Solutions to Aqueous Mixed Electrolyte Systems. *Journal of Inorganic and Nuclear Chemistry, 37*(12), 2503-2506.

Lin, Y., Thomsen, k., & de Hemptinne, J.-C. (2007). Multicomponent Equations of State for Electrolytes. *AIChE Journal, 53*(4), 989-1005.

Lindquist, W. B., Venkatarangan, A., Dunsmuir, J., & Wong, T. F. (2000). Pore and Throar Size Distributions Measured from Synchrotron X-ray Tomographic Images of Fontainbleau Sandstones. *J. Geophys. Res., 105B*, 21508.

Liu, H., Valocchi, A. J., & Kang, Q. (2012). Three-Dimensional Lattice Boltzmann Model for Immiscible Two-Phase Flow Simulations. *Physical Review E, 85*, 046309:046301-046314.

Loehe, J. R., & Donohue, M. D. (1997). Recent Advances in Modeling Thermodynamic Properties o f Aqueous Strong Electrolyte Systems. *AIChE Journal*, 180-195.

Lomeland, F., Ebeltoft, E., & Thomas, W. H. (2005). *A New Versatile Relative Permeability Correlation.* Paper presented at the Paper SCA 2005-32, International Symposium of the Society of Core Analysts, Toronto, Canada.

Longeron, D. G., Argaud, M. J., & Feraud, J. P. (1989). Effect of Overburden Pressure and the Nature and Microscopic Distribution of Fluids on Electrical Properties of Rock Sample. *SPE Formation Evaluation, 4*, 194-202.

Lorenz, C. D., & Ziff, R. M. (1998). Precise Determination of the Bond Percolation Thresholds and Finite-Size Scaling Corrections for the sc, fcc, and bcc Lattices. *Physical Review E, 57*(6), 230-236. doi:10.1103/PhysRevE.52.6387

Lotfollahi, M., Kim, I., Beygi, M. R., Worthen, A. J., Huh, C., Johnston, K. P., . . . DiCarlo, D. A. (2016). Foam Generation Hysteresis in Porous Media: Experiments and New Insights. *Transport in Porous Media*, 1-17. doi:10.1007/s11242-016-0796-6

Lotfollahi, M., Varavei, A., Delshad, M., Farajzadeh, R., & Pope, G. A. (2015). Development of a Hybrid Black-Oil/Surfactant Enhanced Oil Recovery Reservoir Simulator. *Journal of Petroleum Science and Engineering*.

Ma, T. D., & Youngren, G. K. (1994). Performance of Immiscible Water-Alternate-Gas (WAG) Injection at Kuparuk River Unit, North Slope, Alaska. *Pa*.

MacAllister, D. J., Miller, K. C., Graham, S. K., & Yang, C. T. (1993). Application of X-Ray CT Scanning to Determine Gas/Water Relative Permeabilities. *SPE Formation Evaluation, 8*(3), 184-188.

Maini, B. B., Nicola, F., Goldman, J., & Sarma, H. K. (1990). Measurement and Estimation of Three-Phase Relative Permeability. *Petroleum Recovery Institute*.

Maloney, D., & Brinkmeyer, A. (1992). *Three-Phase Permeabilities and Other Characteristics of 260-mD Fired Berea* (report no.: NIPER-581 (DE92001036)). Retrieved from Bartlesville, Ok:

Maloney, D., Honarpour, M., & Brinkmeyer, A. D. (1990). *The Effects of Rock Characteristics on Relative Permeability*. Retrieved from Bartlesville, OK:

Mamun, C. K., Rong, J. G., Kam, S. I., Liljestrand, H. M., & Rossen, W. R. (2002). *Extending Foam Technology from Improved Oil Recovery to Environmental Remediation*.

Mani, V., & Mohanty, K. K. (1998). Pore-Level Network Modeling of Three-Phase Capillary Pressure and Relative Permeability. *SPE Journal, 3*(3), 238-248.

Mansoori, G. A., Carnahan, N. F., Starling, K. E., & Leland, T. W. (1971). Equilibrium Thermodynamic Properties of the Mixture of Hard Spheres. *J. Chem. Phys., 54*, 1523-1525.

Marfoe, C. H., Kazemi, H., & Ramirez, W. F. (1987). *Numerical Simulation of Foam Flow in Porous Media*.

Marle, C. M. (1981). *Multiphase Flow in Porous Media*: Gulf Publishing Co.

Marle, C. M. (1982). On Macroscopic Equations Governing Multiphase Flow with Diffusion and Chemical Reactions in Porous Media. *International Journal of Engineering Science, 20*(5), 643-662. doi:10.1016/0020-7225(82)90118-5

Marmur, A., & Bittoun, E. (2009). When Wenzel and Cassie are Right: Reconciling Local and Global Considerations. *Langmuir, 25*(3), 1277-1281. doi:10.1021/La802667b

Masalmeh, S. K. (2001). *Experimental Measurements of Capillary Pressure and relative Permeability Hysteresis*. Paper presented at the Paper SCA 2001-23 presented at the International Symposium of the Society of Core Analysts, Edinburgh.

Masalmeh, S. K., Abu-Shiekah, I. M., & Jing, X. (2007). Improved Characterization and Modeling of Capillary Transition Zones in Carbonate Reservoirs. *10*(2). doi:10.2118/109094-PA

Masalmeh, S. K., & Wei, L. (2010). *Impact of Relative Permeability Hysteresis, IFT dependent and Three Phase Models on the Performance of Gas Based EOR Processes*. Paper presented at the Abu Dhabi International Petroleum Exhibition and Conference, Abu Dhabi, UAE.

Matheron, G. (1965). *Les variables régionalisées et leur estimation une application de la théorie des fonctions aléatoires aux sciences de la nature*. Paris: Masson.

Mayer, M. G. (1950). Nuclear Configurations in the Spin-Orbit Coupling Model. i. empirical evidence. *Physical Review, 78*(1), 16.

McCoy, R. L., Hartsock, J. H., & Dobson, R. J. (1981). Preliminary Results of the Wells-of-Opportunity Geopressured-Geothermal Testing Program: SPE-8958.

McGuire, P. L., Chatham, J. R., Paskvan, F. K., Sommer, D. M., & Carini, F. H. (2005). *Low Salinity Oil Recovery: An Exciting New EOR Opportunity for Alaska's North Slope*. Paper presented at the SPE Western Regional Meeting, Irvine, California.

McKay, B. A. (1974). *Laboratory Studies of Gas Displacement from Sandstone Reservoirs Having Strong Water Drive*. Retrieved from Canberra:

Meakin, P., & Tartakovsky, A. M. (2009). Modeling and Simulation of Pore-Scale Multiphase Fluid Flow and Reactive Transport in Fractured and Porous media. *Rev. Geophys., 47*, 2008RG000263: 000261-000247.

Mehmani, Y., & Balhoff, M. (2014). Bridging from Pore to Continuum: AHybrid Mortar Domain Decomposition Framework for Subsurface Flow and Storage. *Multiscale Model. Simul., 12*(2), 667-693.

Meissner, H. P. (1980). *Prediction of Activity Coefficicents of Strong Electrolytes in Aqueous Systems.* Paper presented at the Thermodynamics of Aqueous Systems with Industrial Applications.

Meissner, H. P., & Kusik, C. L. (1972b). Activity Coefficients of Strong Electrolytes in Multicomponent Aqueous Solution. *AIChE Journal, 18*, 294-298.

Meissner, H. P., & Kusik, C. L. (1978a). *Electrolyte Activity Coefficicents in Inorganic Processing.* Paper presented at the AIChE Symposium Series 173.

Meissner, H. P., & Tester, J. W. (1972a). Activity Coefficients of Strong Electrolytes in Aqueous Solution. *Industrial Engineering Chemical Process Design Development, 11*(1), 128-133.

Mikelic, A., Wheeler, M. F., & Wick, T. (2015). Phase-Field Modeling of a Fluid-Driven Fracture in a Poroelastic Medium. *Computational Geosciences, 19*(6), 1171-1195.

Moctezuma, A., Bekri, S., & Laroche, C. (2003). A Dual Network Model for Relative Permeability of Bimodal Rocks Application in a Vuggy Carbonate *paper presented at the International Symposium of the Society of Core*. Pau, France.

Mohammadi, H., Delshad, M., & Pope, G. A. (2009). Mechanistic Modeling of Alkaline/ Surfactant/ Polymer Floods. *SPE Res. Eval. & Eng., 12*(04), 518-527.

Mohammadi, S. S., Coombe, D. A., & Stevenson, V. M. (1993). Test of steam-foam process for mobility control in South-Casper Creek reservoir. *J. Can. Pet. Technol., 32*(10), 49-54.

Mohanty, K. K., Masino, W. H., Jr., Ma, T. D., & Nash, L. J. (1995). Role of Three-Hydrocarbon-Phase Flow in a Gas Displacement Process. *SPE Res Eng, 10*(3). doi:10.2118/24115-PA

Mohanty, K. K., & Miller, A. E. (1991). Factors Influencing Unsteady Relative Permeability of a Mixed-Wet Reservoir Rock. *SPE Form. Eval., 6*(3), 349-358.

Mohanty, K. K., & Salter, S. J. (1982). Multiphase Flow in Porous Media: II. Pore-Level Modeling: Society of Petroleum Engineers.

Møller, N. (1988). The Prediction of Mineral Solubilities in Natural Waters: A Chemical Equilibrium Model for the Na-Ca-Cl-SO4-H2O system, to High Temperature and Concentration. *Geochimica et Cosmochimica Acta, 52*, 821-837.

Moncorgé, A., Patacchini, L., & de Loubens, R. (2012). Multi-Phase, Multi-Component Simulation Framework for Advanced Recovery Mechanisms *Paper SPE 161615 presented at the Abu Dhabi International Petroleum Exhibition and Conference*. Abu Dhabi, UAE.

Moore, T. F., & Slobod, R. C. (1955). *Displacement of Oil by Water–Effect of Wettability, Rate, and Viscosity on Recovery*. Paper presented at the Paper SPE 502-G presented at the SPE Annual Fall Meeting.

Morgan, G. T., & Gordon, D. T. (1970). Influence of Pore Geometry on Water-Oil Relative Permeability. *Journal of Petroleum Technology*, 1199-1208.

Morrow, N., & Buckley, J. (2011). Improved Oil Recovery by Low-Salinity Waterflooding. *Journal of Petroleum Technology, 63*(5), 106-112.

Morrow, N. R. (1970). Physics and Thermodynamics of Capillary Action in Porous Media. *Ind. Reg. Chem., 62*(6), 32-56.

Morrow, N. R. (1975). The Effects of Surface Roughness on Contact Angle with Special Reference to Petorleum Recovery. *J. Can. Pet. Tech., 14*, 42-54.

Morrow, N. R. (1990). Wettability and its efects on oil recovery. *J. Pet. Technol, 42*, 1476-1484.

Moulu, J.-C., Vizika, O., Egermann, P., & Kalaydjian, F. (1999). *A New Three-Phase Relative Permeability Model for Various Wettability Conditions.* Paper presented at the Paper SPE 56477 presented at the Annual Technical Conference and Exhibition, Houston, TX.

Moulu, J.-C., Vizika, O., Kalaydjian, F., & Duquerroix, J.-P. (1997). *A New Model for Three-Phase Relative Permeabilities Baaed on a Fractal Representation of the Porous Medium.* Paper presented at the Paper SPE 38891 presented at Annual Technical Conference and Exhibition, San Antonio, TX.

Mualem, Y. (1976). A New Model of Predicting the Hydraulic Conductivity of Unsaturated Porous Medium. *Water Resources Reseach, 12*(3), 513-522.

Myers, J., Sandler, S., & Wood, R. H. (2002). An Equation of State for Electrolyte Solutions Covering Wide Ranges of Temperature, Pressure, and Composition. *Ind. Eng. Chem. Res., 41*, 3282-3297.

Myers, T. J., & Radke, C. J. (2000). Transient Foam Displacement in the Presence of Residual Oil: Experiment and Simulation Using a Population-Balance Model. *Industrial & Engineering Chemistry Research, 39*(8), 2725-2741.

Naar, J., & Wygal, R. J. (1961). Three-Phase Imbibition Relative Permeability. *SPE J., 12*, 254-258.

Naar, J., Wygal, R. J., & Henderson, J. H. (1962). Imbibition Relative Permeability in Unconsolidated Porous Media. *SPE Journal, 2*(1), 13-17. doi:10.2118/213-PA

Naderi Beni, A., Varavei, A., Delshad, M., & Farajzadeh, R. (2013). Modeling Gas Solubility in Water for Foam Propagation in Porous Media *Society of Petroleum Engineers. doi:10.2118/163579-MS*.

Nann, A., Held, C., & Sadowski, G. (2013). Liquid−Liquid Equilibria of 1‑Butanol/Water/IL Systems. *Industrial & Engineering Chemistry Research, 52*, 18472–18481.

Naraghi, M. E., Spikes, K., & Srinivasan, S. (2016). *3-D Reconstruction of Porous Media From a 2-D Section and Comparisons of Transport and Elastic Properties.* Paper presented at the Society of Petroleum Engineers.

Natarajan, D., Verma, N. K., Abdul Salam, T., Al-Sammak, I., Koronfol, S., Dernaika, M., & Teh, W. J. (2014). *Computation of Relative Permeability Curves in Middle Eastern Carbonates Using Digital Rock Physics*. Paper presented at the International Petroleum Technology Conference.

Nguyen, V. H., Sheppard, A. P., Knackstedt, M. A., & Pinczewski, W. V. (2005). The Effects of Displacement Rate and Wettability on Imbibition Relative Permeabilities: Society of Petroleum Engineers.

Niessner, J., Berg, S., & Hassanizadeh, S. M. (2011). Comparison of Two-Phase Darcy's Law with a Thermodynamically Consistent Approach. *Transport in Porous Media, 88*, 133-148. doi:10.1007/s11242-011-9730-0

Niessner, J., & Hassanizadeh, S. M. (2009). Modeling Kinetic Interphase Mass Transfer for Two-Phase Flow in Porous Media Including Fluid-Fluid Interfacial Area. *Transp Porous Med., 80*(2), 329-344.

Nordbotten, J. M., Celia, M. A., Dahle, H. K., & Hassanizadeh, S. M. (2008). On the Definition of Macroscale Pressure for Multiphase Flow in Porous Media. *Water Resources Research, 44*(6), 1-8.

Oak, M. J. (1989). *Two- and Three-Phase Relative Permeability of Water-Wet Berea Sandstone* (Report no.: F89-P-74). Retrieved from Tulsa, OK:

Oak, M. J. (1990). *Three-Phase Relative Permeability of Water-Wet Berea Sandstone*, Tulsa, Ok.

Oak, M. J. (1991). *Three-Phase Relative Permeability of Intermediate-Wet Berea Sandstone.* Paper presented at the Paper SPE 22599 presented at SPE Annual Technical Conference and Exhibition, Dallas, TX.

Oak, M. J. (1992). *Three-Phase Relative Permeability of Oil-Wet Rock* (Report no.: F92-P-24). Retrieved from Tulsa, OK:

Oelkers, E. H., Helgeson, H. C., Shock, E. L., Sverjensky, D. A., Johnson, J. W., & Pokrovskii, V. A. (1995). Summary of the Apparent Standard Partial Molal Gibbs Free Energies of Formation of Aqueous Species, Minerals, and Gases at Pressures 1 to 5000 Bars and Temperatures of 25 to 1000 C. *Journal of Phys. Chem. Ref. Data, 24*(4), 1401-1560.

Omekeh, A. V., Friis, H. A., Fjelde, I., & Evje, S. (2012). *Modeling of Ion-Exchange and Solubility in Low Salinity Water Flooding. Society of Petroleum Engineers*.

Øren, P.-E., & Bakke, S. (2002). Process Based Reconstruction of Sandstones and Prediction of Transport Properties. *Transport in Porous Media, 46*(2-3), 311-343.

Øren, P.-E., Bakke, S., & Arntzen, O. J. (1998). Extending Predictive Capabilities to Network Models. *SPE Journal, 3*(4), 324-336.

Øren, P.-E., Billiotte, J., & Pinczowski, W. V. (1992). Mobilization of Waterflood Residual Oil by Gas Injection for Water-Wet Conditions. *SPE Formation Eval.*, 70-78.

Øren, P.-E., & Pinczewski, W. V. (1994). Effect of Wettability and Spreading on Recovery of Waterflooding Residual Oil by Immiscible Gasflooding. *SPE Formation Eval.*, 149-156.

Øren, P.-E., & Pinczewski, W. V. (1995). Fluid Distributions and Pore-Scale Displacement Mechanisms in Drainage Dominated Three-Phase Flow. *Transport in Porous Media, 20*, 105-133.

Ornstein, L. S., & Zernike, F. (1914). Accidental Deviations of Density and Opalescence at the Critical Point of a Single Substance. *Proc. Acad. Sci. Amsterdam, 17*, 793-806.

Osher, S., & Fedkiw, R. P. (2001). Level Set Methods: an Overview and Some Recent Results. *Journal of Computational Physics, 169*, 463-502.

Osoba, J. S., Richardson, J. G., Kerver, J. K., Hafford, J. A., & Blair, P. M. (1951). Laboratory Measurements of Relative Permeability. *Trans., AIME, 192*, 46-56.

Owens, W. W., & Archer, D. L. (1971). The Effect of Rock Wettability on Oil-Water Relative Permeability. *JPT*, 873.

Paricaud, P., Galindo, A., & Jackson, G. (2002). Recent advances in the Use of the SAFT Approach in Describing Electrolytes, Interfaces, Liquid Crystals and Polymers. *Fluid Phase Equilibria, 194-197*, 87-96.

Parker, J. C., & Lenhard, R. J. (1987). A Model for Hysteretic Constitutive Relations Governing Multiphase Flow `Saturation-Pressure Relations. *Water Resource Research, 23*(12).

Parkhurst, D. L., & Appelo, C. A. J. (2013). Description of input and examples for PHREEQC version 3—A computer program for speciation, batch-reaction, one-dimensional transport, and inverse geochemical calculations *U.S. Geological Survey Techniques and Methods* (pp. 497).

Parmeswar, R., & Maerefat, N. L. (1986). *A Comparison of Methods for the Representation of Three-Phase Relative Permeability Data*.

Parmeswar, R., Maerefat, N. L., & Brinkmeyer, A. (1988). *Preliminary Results on the Effect of Fluid Viscosity on Three-Phase Relative Permeability*. Retrieved from Bartlesville, OK:

Patel, B. H., Paricaud, P., Galindo, A., & Matiland, G. C. (2003). Prediction of the Salting-Out Effect of Strong Electrolytes on Water + Alkane Solutions. *Ind. Eng. Chem. Res., 42*, 3809-3823.

Paterson, A., Robin, M., Fermigier, M., Jenffer, P., & Hulin, J. P. (1998). Effect of Density and Spatial Distribution of Wettability Heterogeneities on Contact Angle. *J. Pet. Sci. Eng., 20*, 127-132.

Pathak, P., Davis, H. T., & Scriven, L. E. (1982). Dependence of Residual Nonwetting Liquid on Pore Topology: Society of Petroleum Engineers.

Patzek, T. W. (2001). Verification of a Complete Pore Network Simulator of Drainage and Imbibition. *SPE Journal*, 144-156.

Patzek, T. W., & Myhill, N. A. (1989). *Simulation of the Bishop Steam Foam Pilot*. Paper presented at the Paper SPE 18786 presented at SPE California Regional Meeting, Bakersfield, CA, USA.

Payatakes, A. C., Ng, K. M., & Flumerfelt, R. W. (1980). Oil Ganglion Dynamics During Immiscible Displacement: Model Formulation. *AIChE J., 26*, 430-443.

Pejic, D., & Maini, B. (2003). *Three-Phase Relative Permeability of Petroleum Reservoirs.* Paper presented at the Paper SPE 81021 presented at the SPE Latin American and Caribbean Petroleum Engineering Conference, Port-of-Spain, Trinidad, West Indies.

Péneloux, A., Abdoul, W., & Rauzy, E. (1989). Excess Functions and Equations of State. *Fluid Phase Equilibria, 47*, 115-132.

Peng, D. Y., & Robinson, D. B. (1976). A New Two-Constant Equation of State. *Industrial and Engineering Chemistry: Fundamentals, 15*, 59-64.

Pennell, K. D., Pope, G. A., & Abriola, L. M. (1996). Influence of Viscous and Buoyancy Foces on the Mobilization of Residual Tetrachloroethylene during Surfactant Flushing. *Environmental Science and Technology, 30*(4), 1328-1335.

Pentland, C. H., Iglauer, S., Gharbi, O., Okada, K., & Suekane, T. (2012). *The influence of Pore Space Geometry on the Entrapment of Carbon Dioxide by Capilary Forces.* Paper presented at the Paper SPE 158516 presented at the SPE Asia Pcific Oil and Gas Conference and Exhibition, Perth, Australia.

Percus, J. K., & Yevick, G. J. (1958). Analysis of Classical Statistical Mechanics by Means of Collective Coordinates. *Physical Review, 110*(1), 1-13.

Perry, P. H., & Chilton, C. H. (1973). *Chemical Engineer's Handbook* (5th ed.): McGraw-Hill.

Peters, E. J. (2012). *Advanced Petrophysics*. Austin: Greenleaf Book Group.

Petersen Jr, E. B., Lohne, A., Vatne, K. O., Helland, J. O., Virnovsky, G., & Øren, P.-E. (2008). *Relative Permeabilities for Two- and Three-Phase Flow Processes Relevant to the Depressurization of the Statfjord Field*. Paper presented at the Paper SCA2008-23,International Symposium of the society of Core Analysis, Abu Dhabi, UAE.

Peveraro, R., & Thomas, E. C. (2010). *Effective Porosity: A Defensible Definition for shaly Sands*. Paper presented at the SPWLA 51st Annual Logging Symposium.

Pilotti, M. (2000). Reconstruction of Clastic Porous Media. *Trans. Porous Media, 41*(3), 359-364.

Piri, M., & Blunt, M. J. (2005). Three-Dimensional Mixed-Wet Random Pore-Scale Network Modeling of Two- and Three-Phase Flow in Porous Media. I. Model Description. *Physical Review E, 71*(2), 026301:026301-026330.

Pitzer, K. S. (1973a). Thermodynamics of Electrolytes. I. Theoretical Basis and General Equations. *J. Phys. Chem., 77*, 268–277.

Pitzer, K. S. (1975). Thermodynamics of Electrolytes. V. Effects of Higher-Order Electrostatic Terms. *Journal ofSolution Chemistry, 4*(3), 249-265.
Pitzer, K. S. (1991). *Activity Coefficients in Electrolyte Solutions, 2d Edition*: CRC Press Inc.
Pitzer, K. S. (1995). *Thermodynamics*. New York: McGraw-Hill.
Pitzer, K. S., & Kim, J. J. (1974b). Thermodynamics of Electrolytes. IV. Activity and Osmotic Coefficients for Mixed Electrolytes. *journal of the American Chemical Society, 96*, 5701-5707.
Pitzer, K. S., & Mayorga, G. (1973b). Thermodynamics of Electrolytes. II. Activity and Osmotic Coefficients for Strong electrolytes with One or Both Ion Univalent. *Journal of Physical Chemistry, 77*(19), 2300-2308.
Pitzer, K. S., & Mayorga, G. (1974a). Thermodynamics of Electrolytes. III. Activity and Osmotic Coefficicients for 2-2 Electrolytes. *Journal of Solution Chemistry, 3*(7), 539-546.
Pitzer, K. S., Peterson, J. R., & Silvester, L. F. (1978a). Thermodynamics of Electrolytes. IX. Rare Earth Chlorides, Nitrates, and Perchlorates. *Journal of Solution Chemistry, 7*, 45-56.
Pitzer, K. S., Roy, R. N., & Silvester, L. F. (1977). Thermodynamics of Electrolytes. VII. Sulfuric Acid. *Journal of American Chemical Society, 99*, 4930.
Pitzer, K. S., & Silvester, L. F. (1976). Thermodynamics of Electrolytes. VI. Waek Electrolytes Including H3PO4. *Journal of Solution Chemistry, 5*, 269.
Pitzer, K. S., & Silvester, L. F. (1978c). Thermodynamics of Electrolytes. XI. Properties of 3:2, 4:2, and other High-Valence Types. *Journal of Physical Chemistry, 82*, 1239.
Pitzer, K. S., & Simonson, J. M. (1986). Thermodynamics of Multicomponent, Miscible, Ionic Systems: Theory and Equations. *Journal of Physical Chemistry, 90*, 3005-3009.
Pitzer, K. S., & Tanger, J. C. (1989). Critical Exponents for the Coexistence Curves for NaCl-H2O near the Critical Temperature of H2O. *Chem. Phys. Lett., 156*(4), 418.
Planche, H., & Renon, H. (1981). Mean Spherical Approximation Applied to a Simple but Nonprimitive Model of Interaction for Electrolyte Solutions and Polar Substances. *Journal of Phys. Chem, 85*, 3924.
Plohr, B., Marchesin, D., Bedrikovetsky, P., Altoé F°, J. E., & de Souza, A. J. (2002). *Hysteresis in Three-Phase Porous Media Flow*. Paper presented at the 8th European Conference on the Mathematics of Oil Recovery, Freiberg, Germany.
Pope, G. A., & Nelson, R. C. (1978). A Chemical Flooding Compositional Simulator. *SPE Journal, 18*, 339-354.
Pope, G. A., Wu, W., Narayanaswamy, G., Delshad, M., Sharma, M. M., & Wang, P. (2000). Modeling Relative Permeability Effects in Gas-Condensate Reservoirs. *SPE Res Eng, 3*(2), 171-178.
Prausnitz, J. M., Lichtenthaler, R. N., & Gomes de Azevedo, E. (1999). *Molecular Thermodynamics of Fluid-Phase Equilibria*. Upper Saddle River, New Jersey: Prentice-Hall International Series.
Prausnitz, J. M., & Tavares, F. W. (2004). Thermodynamics of Fluid-Phase Equilibria for Standard Chemical Engineering Operations. *AIChE Journal*, 739-761.
Prodanovic, M., & Bryant, S. L. (2006). A Level Set Method for Determining Critical Curvatures for Drainage and Imbibition. *Journal of Colloid and Interface Science, 304*, 442-458.

Pruess, K., & García, J. (2002). Multiphase Flow Dynamics during CO_2 Disposal into Saline Aquifers. *Environmental Geology, 42*(2), 282-295. doi:10.1007/s00254-001-0498-3

Pruess, K., Xu, T., Apps, J., & Garcia, J. (2003). Numerical Modeling of Aquifer Disposal of CO_2. *SPE J., 8*(1), 49-60. doi:10.2118/83695-PA

Pu, H., Xie, X., Yin, P., & Morrow, N. R. (2008). *Application of Coalbed Methane Water to Oil Recovery from Tensleep Sandstone by Low Salinity Waterflooding*.

Puglisi, G., & Truskinovsky, L. (2002). Rate Independent Hysteresis in a Bi-Stable Chain. *Journal of the Mechanics and Physics of Solids, 50*, 165-187.

Raatschen, W., Harvey, A., & Prausnitz, J. M. (1987). Equation of State for Solutions of electrolytes in Mixed Solvents. *Fluid Phase Equilibria, 38*, 19-38.

Raeini, A. Q., Bijeljic, B., & Blunt, M. J. (2014). Numerical Modelling of Sub-pore Scale Events in Two-Phase Flow Through Porous Media. *Transp. Porous Med., 101*, 191-213.

Raeini, A. Q., Blunt, M. J., & Bijeljic, B. (2012). Modelling Two-Phase Flow in Porous Media at the Pore Scale Using the Volume-of-Fluid Method. *Journal of Computational Physics, 231*, 5653-5668.

Rafal, M., Berthold, J. W., Scrivner, N. C., & Grise, S. L. (1994). Models for electrolyte Solutions *Models for Thermodynamic and Phase-Equilibria Calculations*. New York: Marcel Decker.

Ramstad, T., Idowu, N., Nardi, C., & Øren, P.-E. (2012). Relative Permeability Calculations from Two-Phase Flow Simulations Directly on Digital Images of Porous Rocks. *Transp Porous Med., 94*, 487-504. doi:10.1007/s11242-011-9877-8

Ransohoff, T. C., & Radke, C. J. (1988). Mechanisms of Foam Generation in Glassbead Packs. *SPE Res Eng, 3*(2), 573-585.

Reid, R. C., Prausnitz, J. M., & Poling, B. E. (1987). *The Properties of Gases and Liquids* (Fourth ed.). New York: McGraw-Hill.

Reid, S. (1956). *The Flow of Three Immiscible Fluids in Porous Media*. Retrieved from UK:

Renon, H. (1980). *Concentrated Solutions of Electrolytes.* Paper presented at the 2nd International Conference on Phase Equilibria and Fluid Properties in the Chemical Industry, Berlin.

Renon, H., & Prausnitz, J. M. (1969). Estimation of Parameter for the NRTL Equation for Excess Gibbs Energies for Strongly Nonideal Liquid Mixtures. *Industrial & Engineering Chemistry Process Design and Development, 8*(3), 413-419.

RezaeiDoust, A., Puntervold, T., Strand, S., & Austad, T. (2009). Smart Water as Wettability Modifier in Carbonate and Sandstone: A Discussion of Similarities/Differences in the Chemical Mechanisms. *Energy Fuels, 23*, 4479-4485. doi:10.1021/ef900185q

Righi, E. F., Royo, J., Gentil, P., Castelo, R., Del Monte, A., & Bosco, S. (2004). *Experimental Study of Tertiary Immiscible WAG Injection*. Paper presented at the SPE/DOE Symposium on Improved Oil Recovery, Tulsa, Oklahoma.

Rivet, S. M., Lake, L. W., & Pope, G. A. (2010). *A Coreflood Investigation of Low-Salinity Enhanced Oil Recovery*.

Robinson, R. A. (1938). The Activity Coefficient of Cobalt Chloride in Aqueous Solution at 25 C. *Trans. Faraday Soc., 34*, 1142-1143.

Robinson, R. L., & Slattery, J. C. (1994). Estimation of Three-Phase Relative Permeability. *Transport in Porous Media, 16*, 263-287.

Rossen, W. R. (1996). Foams in Enhanced Oil Recovery. In R. K. Prud'homme & S. Khan (Eds.), *Foams: Theory, Measurements and Applications*. New York: Marcel Dekker.

Rossen, W. R., & Gauglitz, P. A. (1990). Percolation Theory of Creation and Mobilization of Foams in Porous Media. *AIChE Journal, 36*(8), 1176-1188.

Rossen, W. R., Zeilinger, S. C., Shi, J. X., & Lim, M. T. (1999). Simplified Mechanistic Simulation of Foam Processes in Porous Media. *4*(3). doi:10.2118/57678-PA

Rossini, F. D., Wagman, D. D., & Evans, W. H. (1952). *Selected Values of Chemical Thermodynamic Properties.*: US Government Printing Office Washington, DC.

Rowlinson, J. S., & Widom, B. (1989). *Molecular Theory of Capillarity*. Oxford: Clarendon Press.

Rushbrooke, G. S., Stell, G., & Hoye, J. S. (1973). Theory of polar fluids: I. Dipolar hard spheres. *Molecular Physics, 26*, 1199-1215.

Saadatpoor, E. (2012). *Local Capillary Trapping in Geological Carbon Storage.* (Ph.D. dissertation), The University of Texas at austin, Austin, Texas.

Saber, N. (2011). *Phase Behaviour Prediction for Ill-Defined Hydrocarbon Mixtures.* (Ph.D. dissertation), University of Alberta, Edmonton, Alberta.

Sahni, A., Burger, J., & Blunt, M. J. (1998). Measurement of Three-Phase Relative Permeability During Gravity Drainage Using CT: Society of Petroleum Engineers.

Salager, J. L., Bourrel, M., Schechter, R. S., & W.H, W. (1979a). Mixing rules for Optimum Phase Behavior Formulations of Surfactant/Oil/Water Systems. *SPE Journal, 19*(5), 271-278.

Salager, J. L., Morgan, J. C., Schechter, R. S., W.H., W., & Vasquez, E. (1979b). Optimum Formulation of Surfactant/Water/Oil Systems for Minimum Interfacial Tension and Phase Behavior. *SPE Journal, 19*(2), 107-115.

Salathiel, R. A. (1973). Oil Recovery by Surface Film Drainage in Mixed-Wettability Rocks. *JPT*, 1216.

Sandler, S. I. (2006). *Chemical, Biochemical, and Engineering Thermodynamics*. Hoboken, NJ: John Wiley & Sons, Inc.

Saraf, D. N., Batycky, J. P., Jackson, C. H., & Fisher, D. B. (1982). An Experimental Investigation of Three-Phase Flow of Water-Oil- Gas Mixtures Through Water-Wet Sandstones: Society of Petroleum Engineers.

Saraf, D. N., & Fatt, I. (1967). Three-Phase Relative Permeability Measurement Using a Nuclear Magnetic Resonance Technique for Estimating Fluid Saturation. *SPE Journal, 7*, 235-242.

Sarem, A. M. (1966). Three-Phase Relative Permeability Measurements by Unsteady-State Method. *SPE Journal*, September.

Scardovelli, R., & Zaleski, S. (1999). Direct Numerical Simulation of Free-Surface and Interfacial Flow. *Ann. Rev. Fluid Mech., 31*, 567-603.

Scatchard, G. (1936). Concentated Solutions of Strong Electrolytes. *Chemical Review, 19*(3), 309-327.

Scheven, U. M. (2005). Quantitative Nuclear Magnetic Resonance Measurements of Preasymptotic Dispersion in Flow Through Porous Media. *Physics of Fluids, 17*(11), 117107.

Schneider, F. N., & Owens, W. W. (1970). Sandstone and Carbonate Two- and Three-Phase Relative Permeability Characteristics. *SPE J., 3*, 75-84.

Schoof, C. (2007). Ice Sheet Grounding Line Dynamics: Steady States, Stability, and Hysteresis. *Journal of Geophysical Research, 112*, 1-19.

Schulte, W. M. (2005). *Challenges and Strategy for Increased Oil Recovery*. Paper presented at the International Petroleum Technology Conference, Doha, Qatar.

Schwartzentruber, J., Renon, H., & Watanasiri, S. (1989). Development of a New Equation of State for Phase Equilibrium Calculations. *Fluid Phase Equilibria, 52*, 127.

Seccombe, J. C., Lager, A., Webb, K. J., Jerauld, G. R., & Fueg, E. S. (2010). *LoSal™ EOR Field Evaluation*. Paper presented at the Paper SPE 113480 presented at the SPE/DOE Symposium on Improved Oil Recovery, Tulsa, OK.

Shafer, J. L., Braun, E. M., Wood III, A. C., & Wooten, J. M. (1990). *Obtaining Relative Permeability Data Using a Combination of Steady-State and Unsteady-State Corefloods*. Paper presented at the Fourth Annual Technical Conference of the Society of Core Analysis, Dallas, Texas.

Shahverdi, H., Jamiolahmady, M., Sohrabi, M., Ireland, S., Fatemi, S. M., & Rabertson, G. (2011). Evaluation of Three-Phase Relative Permeability Models for WAG Injection Using Water-Wet and Mixed-Wet Core Flood Experiments: Society of Petroleum Engineers.

Shahverdi, H., & Sohrabi, M. (2012, April 14-18). Three-Phase Relative Permeability and Hysteresis Model for Simulation of Water Alternate Gas (WAG) Injection.

Shan, X., & Chen, H. (1994). Simulation of Nonideal Gases and Gas-Liquid Phase Transitions by the Lattice Boltzmann Equation. *Phys. Rev. E, 49*(4), 2941-2948.

Sharma, M. M., & Filoco, P. R. (2000). Effect of Brine Salinity and Crude-Oil Properties on Oil Recovery and Residual Saturations. *SPE Journal, 5*(3), 293-300. doi:10.2118/65402-PA

Shi, J.-X. (1996). *Simulation and Experimental Studies of Foam for Enhanced Oil Recovery.* (Ph.D. dissertation), The University of Texas at Austin, Austin, Texas.

Silvester, L. F., & Pitzer, K. S. (1978b). Thermodynamics of Electrolytes. X. Enthalpy and the Effect of Temperature on the Activity Coefficients. *Journal of Solution Chemistry, 7*, 327.

Simjoo, M., Dong, Y., Andrianov, A., Talanana, M., & Zitha, P. L. J. (2013). Novel Insight Into Foam Mobility Control. *SPE Journal*, 416-427.

Simon, H.-G., Kistenmacher, H., Prausnitz, J. M., & Vortmeyer, D. (1991). An Equation of State for Systems Containing Electrolytes and Nonelectrolytes. *Chem. Eng. Process., 29*, 139-146.

Simonin, J.-P. (1997). Real Ionic Solutions in the Mean Spherical Approximation. 2. Pure Strong Electrolytes up to Very High Concentrations, and Mixtures, in the Primitive Model. *Journal of Phys. Chem., 101*, 4313-4320.

Simonin, J.-P., Bernard, O., & Blum, L. (1998). Real Ionic Solutions in the Mean Spherical Approximation. 3. Osmotic and Activity Coefficients for Associating Electrolytes in the Primitive Model. *Journal of Phys. Chem., 102*, 4411-4417.

Simonin, J.-P., Blum, L., & Turq, P. (1996). Real Ionic Solutions in the Mean Spherical Approximation. 1. Simple Salts in the Primitive Model. *J. Phys. Chem., 100*, 7704-7709.

Singh, M., Mani, V., Honarpour, M., & Mohanty, K. K. (2001). Comparison of viscous and gravity dominated gas–oil relative permeabilities. *Journal of Petroleum Science and Engineering, 30*(2), 67-81. doi:http://dx.doi.org/10.1016/S0920-4105(01)00101-2

Skauge, A., Haskjold, G., Thorsen, T., & Aarra, M. (1997). *Accuracy of Gas–Oil Relative Permeability from Two-Phase Flow Experiments*. Paper presented at the SCA 9707. International Symposium of the Society of Core Analysts, Calgary, Canada.

Skauge, A., & Larsen, J. A. (1994). Three-phase Relative Permeabilities and Trapped Gas Measurements Related to WAG Processes *SCA 9421*: Society of Core Analysis.

Skauge, A., & Ottesen, B. (2002). *A Summary of Experimentally Derived Relative Permeability and Residual Saturation on North Sea Reservoir Cores.* Paper presented at the SCA2002-12.

Skjæveland, S. M., & Kleppe, J. (1992). *Recent Advances in Improved Oil Recovery Methods for North Sea Sandstone Reservoirs*. Retrieved from

Skjæveland, S. M., Siqveland, L. M., Kjosavik, A., Thomas, W. L. H., & Virnovsky, G. A. (2000). Capillary Pressure Correlation for Mixed-Wet Reservoirs. *SPE Res. Eval & Eng., 3*(1), 60-67. doi:10.2118/60900-PA

Skrettingland, K., Holt, T., Tweheyo, M. T., & Skjevrak, I. (2010). *Snorre Low Salinity Water Injection—Core Flooding Experiments And Single Well Field Pilot*. Paper presented at the Paper SPE 129877 presented at the SPE/DOE Improved Oil Recovery Symposium, Tulsa, OK.

Snell, R. W. (1962). Three-Phase Relative Permeability in an Unconsolidated Sand. *J. Inst. Pet.*, 80-88.

Soave, G. (1972). Equilibrium Constants from a Modified Redlich-Kwong Equation of State. *Chemical Engineering Science, 27*, 1197-1203.

Sorop, T. G., Shehadeh, K. M., Suijkerbuijk, B. M. J. M., van der Linder, H. A., Mahani, H., Brussee, N. J., . . . Coorn, A. (2015). Relative Permeability Measurements to Quantify the Low Salinity Flooding effect at Field Scale *presented at the Abu Dhabi International Petroleum Exhibition and Conference*. Abu Dhabi, UAE: SPE-177856.

Spiteri, E. J., & Juanes, R. (2006). Impact of Relative Permeability Hysteresis on the Numerical Simulation of WAG Injection. *Journal of Petroleum Science and Engineering, 50*(2), 115-139.

Spiteri, E. J., Juanes, R., Blunt, M. J., & Orr, F. M. J. (2008). A New Model of Trapping and Relative Permeability Hysteresis for All Wettability Characteristics. *SPE J., 13*(3), 277-288.

Srivastava, M. (2010). *Foam Assisted Low Interfacial Tension Enhanced Oil Recovery.* (Ph.D. dissertation), The University of Texas at Austin, Austin, Texas.

Srivastava, M., Zhang, J., Nguyen, Q. P., & Pope, G. A. (2009). A Systematic Study of Alkali Surfactant Gas Injection as an Enhanced Oil Recovery Technique. Louis, New Orleans, USA: Paper SPE 124752 presented at the SPE Annual Technical Conference and Exhibition.

Standing, M. B. (1975). *Notes on Relative Permeability Relationships*. Retrieved from NTH, Norway:

Stegemeier, G. L. (1977). *Mechanisms of Entrapment and Mobilization of Oil in Porous Media.* Paper presented at the AlChE Symposium on Improved Oil Recovery by Surfactant and Polymer Flooding, Kansas City.

Stillinger, F. H. J., & Lovett, R. (1968). Ion-Pair Theory of Concentrated Electrolytes. I. Basic Concepts. *Journal of Chemical Physics, 48*(9), 3858-3868.

Stokes, R. H., & Robinson, R. A. (1948). Ionic Hydration and Activity in Electrolyte Solutions. *journal of the American Chemical Society, 70*, 1870-1878.

Stone, H. L. (1970). Probability Model for Estimating Three-Phase Relative Permeability. *JPT, 22*(2), 218-241.

Stone, H. L. (1973). Estimation of Three-Phase Relative Permeability and Residual Oil Data. *Journal of Canadian Pet. Tech., 12*(4), 53-61.

Suicmez, V. S., Piri, M., & Blunt, M. J. (2008). Effects of Wettability and Pore-Level Displacement on Hydrocarbon Trapping. *Advances in Water Resources, 31*(3), 503-512. doi**:**http://dx.doi.org/10.1016/j.advwatres.2007.11.003

Survey: Miscible CO_2 continues to eclipse steam in US EOR production. (2014). (pp. TECHNOLOGY; Pg. 78).

Sussman, M., Smereka, P., & Osher, S. (1994). A Level Set Approach for Computing Solutions to Incompressible Two-Phase Flow. *Journal of Computational Physics, 114*(1), 146-159.

Sutton, R. P. (2009). *An Improved Model for Water-Hydrocarbon Surface Tension at Reservoir Conditions*. Paper presented at the SPE Annual Technical Conference and Exhibition,, New Orleans.

Suzanne, K., Hamon, G., Billiotte, J., & Trocme, V. (2003). *Experimental Relationships between Residual Gas Saturation and Initial Gas Saturation in Heterogeneous Sandstone Reservoirs.* Paper presented at the Paper SPE 84038 presented at the SPE Annual Technical Conference and Exhibition, Denver, Colorado.

Tang, G.-Q., & Firoozabadi, A. (2000). *Relative Permeability Modification in Gas-Liquid Systems Through Wettability Alteration to Intermediate Gas-Wetting*.

Tang, G.-Q., & Morrow, N. R. (1999). Influence of Brine Composition and Fines Migration on Crude Oil/Brine/Rock Interactions and Oil Recovery. *J. Pet. Sci. Eng., 24*, 99-111.

Tartakovsky, A., & Meakin, P. (2005). Modeling of Surface Tension and Contact Angles with Smoothed Particle Hydrodynamics. *Physical Review E, 72*, 026301: 026301-026309.

Thomsen, K. (2005). Modeling Electrolyte Solutinos with the Extended Universal Quasichemical (UNIQUAC) Model. *Pure Appl. Chem., 77*(3), 531-542.

Thomsen, K., P., R., & Gani, R. (1996). Correlation and Prediction of Thermal Properties and Phase Behaviour for a Class of Aqueous Electrolyte Systems. *Chemical Engineering Science, 51*(14), 3675–3683.

Thomsen, K., & Rasmussen, P. (1999). Modeling of Vapor–Liquid–Solid Equilibrium in Gas–Aqueous Electrolyte Systems. *Chemical Engineering Science, 54*(12), 1787–1802.

Thyne, G., & Pubudu, G. (2011). *Evaluation of Low-Salinity Waterflooding for 51 Fields in Wyoming*. Paper presented at the International Symposium of the Society of Core Analysts, Austin, TX.

Toselli, A., & Widlund, O. (2005). *Domain Decomposition Methods- Algorithms and Theory* (Vol. 34). Heidelberg, Germany: Springer-Verlag.

Trangenstein, J. A. (1987). Customized Minimization Techniques for Phase Equilibrium Computations in Reservoir Simulation. *Chem. Eng. Sci., 42*(12), 2847-2863.

Treiber, L. E., & Owens, W. W. (1972). A Laboratory Evaluation of the Wettability of Fifty Oil-Producing Reservoirs. *SPEJ*, 531-540.

Trouillaud, A., Patacchini, L., de Loubens, R., & Moncorge, A. (2014). Simulation of Surfactant Flooding in the Presence of Dissolved and Free Gas Accounting for the Dynamic Effect of Pressure and Oil Composition on Microemulsion Phase Behavior *Paper SPE 169148 presented at the SPE Improved Oil Recovery Symposium, Tulsa, Oklahoma, 12-16 April*. Tulsa, Oklahoma, USA.

Tryggvason, G., Bunner, B., Esmaeeli, A., Juric, D., Al-Rawahi, N., Tauber, W., . . . Jan, Y.-J. (2001). A Front Tracking Method for the Computations of Multiphase Flow. *Journal of Computational Physics, 169*(2), 708-759.

U.S. Field Production of Crude Oil. (2016). from U.S. Energy Information Administration (EIA)

Ubbink, O., & Issa, R. I. (1999). A Method for Capturing Sharp Fluid Interfaces on Arbitrary Meshes. *Journal of Computational Physics, 153*(1), 26-50.

van Dijke, M. I. J., McDougall, S. R., & Sorbie, K. S. (2001). Three-Phase Capillary Pressure and Relative Permeability Relationships in Mixed-Wet Systems. *Transport in Porous Media, 44*, 1-32.

van Dijke, M. I. J., & Sorbie, K. S. (2002). The Relation between Interfacial Tensions and Wettability in Three-Phase Systems: Consequences for Pore Occupancy and Relative Permeability. *Journal of Petroleum Science and Engineering, 33*, 39-48.

van Dijke, M. I. J., Sorbie, K. S., Sohrabi, M., & Danesh, A. (2006). Simulation of WAG floods in an Oil-Wet Micromodel using a 2-D Pore-Scale Network Model. *Journal of Pet. Sci. Eng., 52*(1-4), 71-86.

van Genuchtenm, M. Th. (1980). A closed form equation for predicting the hydraulic conductivity of unsaturated soils. Soil Sci. Soc. Am. J., 44: 892-898.

van Spronsen, E. (1982). *Three-Phase Relative Permeability Measurements Using the Centrifuge Method*. Paper presented at the Third Joint Symposium on Enhanced Oil Recovery of the SPE, Tulsa, OK.

Venkatraman, A., Lake, L. W., & Johns, R. T. (2014). Gibbs Free Energy Minimization for Prediction of Solubility of Acid Gases in Water. *Industrial & Engineering Chemistry Research, 53*, 6157-6168.

Verwey, E. J. W., & Overbeek, J. T. G. (1948). *Theory of the stability of lyophobic colloids,* . Amesterdam: Elsevier.

Vimalchand, P., & Donohue, M. D. (1985). Thermodynamics of Quadrupolar Molecules: The Perturbed-Anisotropic-Chain Theory. *Ind. Eng. Chem. Fundam., 24*(2), 246.

Vizika, O. (1993). *Effect of the Spreading Coefficient on the Efficiency of Oil Recovery with Gravity Drainage.* Paper presented at the Symposium of Oil Recovery, 205th National Meeting of ACS, Denver, CO.

Vizika, O., & Lombard, J.-M. (1996). Wettability and Spreading: Two Key Parameters in Oil Recovery with Three-Phase Gravity Drainage. *SPE Res Eng, 11*, 54-60.

Vu, V. Q., Suchaux, P. D., & Fürst, W. (2002). Use of a Predictive Electrolyte equation of state for the Calculation of the Gas Hydrate Formation Temperature in the case of Systems with Methanol and Salts. *Fluid Phase Equilibria, 194-197*, 361-370.

Wagner, A. J. (2008). *A Practical Introduction to the Lattice Boltzmann Method*. Retrieved from Fargo:

Waisman, E., & Lebowitz, J. L. (1970). Exact Solution of an Integral Equation for Structure of a Primitive Model of Electrolytes. *Journal of Chemical Physics, 52*, 4307.

Waisman, E., & Lebowitz, J. L. (1972a). Mean Spherical Model Integral Equation for Charged Hard Spheres. I. Method of Solution. *J. Chem. Phys., 56*, 3086-3093.

Waisman, E., & Lebowitz, J. L. (1972b). Mean Spherical Model Integral Equation for Charged Hard Spheres. II. Results. *J. Chem. Phys, 56*, 3093-3099.

Wales, D. J. (2010). Energy landscapes: Some New Horizons. *Curr. Opin. Struct. Biol.,, 20*, 3-10.

Wang, F. H. L., Braun, E. M., Kuzan, J. D., Djabbarah, N. F., Honarpour, M., Chiasson, C., & Milligan, B. (2008). *Application of Unique Methodology and Laboratory Capability for Evaluation of Hydrocarbon Recovery Processes*.

Wang, P., Anderko, A., Springer, R. D., & Young, R. D. (2006). Modeling Phase equilibria and Speciation in Mixed-Solvent Electrolyte Systems: II. Liquid–Liquid Equilibria and Properties of Associating Electrolyte Solutions. *Journal of Molecular Liquids, 125*(1), 37-44.

Wang, P., Anderko, A., & Young, R. D. (2002). A Speciation-Based Model for Mixed-Solvent Elecelectrolyte Systems. *Fluid Phase Equilibria, 203*(1), 141–176.

Wang, P., Kosinski, J. J., Lencka, M. M., Anderko, A., & Springer, R. D. (2013). Thermodynamic Modeling of Boric Acid and Selected Metal Borate Systems. *Pure and Applied Chemistry, 85*(11).

Wang, P., Springer, R. D., Anderko, A., & Young, R. D. (2004). Modeling Phase Equilibria and Speciation in Mixed-Solvent Electrolyte Systems. *Fluid Phase Equilibria, 222*, 11–17.

Wardlaw, N. C. (1982). The Effect of Geometry, Wettability, Viscosity and Interfacial Tension on Trapping in Single Pore-Throat Pairs. *Journal of Canadian Petroleum Technology*, 21-27.

Wardlaw, N. C., & Cassan, J. P. (1978). Estimation of recovery Efficiency by Visual Observation of Pore Systems in Reservoir Rocks. *Bulletin of Canadian Petroleum Geology, 26*(4), 572-686.

Webb, K. J., Black, C. J. J., & Al-Ajeel, H. (2004). *Low Salinity Oil Recovery - Log-Inject-Log*.

Webb, K. J., Black, C. J. J., & Edmonds, I. J. (2005). *Low salinity oil recovery–The role of reservoir condition corefloods*. Paper presented at the IOR-2005, 13th European Symposium on Improved Oil Recovery.

Weifeng, L., Zubo, Z., Qingjie, L., Desheng, M., & Kangyun, W. (2012). Measurement of Three-Phase Relative Permeabilities of Various Saturating Histories and Wettability Conditions *Paper SCA2012-43 presented at the International Symposium of the society of Core Analysis* Aberdeen, Scotland, UK.

Wertheim, M. S. (1971). Exact Solution of the Mean Spherical Model for fluids of Hard Spheres with Permanent Electric Dipole Moments. *Journal of Chem. Phys., 55*, 4291-4298.

Wertheim, M. S. (1984). Fluids with Highly Directional Attractive Forces. I. Statistical Thermodynamics. *Journal of Statistical Physics, 35*(1-2), 19-34.

Wertheim, M. S. (1986). Fluids of Dimerizing Hard Spheres, and Fluid Mixtures of Hard Spheres and Dispheres. *Journal of Chem. Phys., 85*(5), 2929-2936.

Wheeler, J., et al. (2002). IPARS User's Manual. Austin, Texas: Center for Subsurface Modeling, ICES, The University of Texas at Austin.

Wildenschild, D., & Sheppard, A. P. (2013). X-ray Imaging and Analysis Techniques for Quantifying Pore-Scale Structure and Processes in Subsurface Porous Medium Systems. *Adv. Water Resources, 51*, 217-246.

Wilson, G. M. (1964). Vapor-Liquid Equilibrium. XI. A New Expression for the Excess Free Energy of Mixing. *J. Am. Chem. Soc., 86*(2), 127-113.

Winsor, P. A. (1954). Solvent Properties of Amphiphilic Compounds. *Butterworths*.

Wolf-Gladrow, D. A. (2000). *Lattice-Gas Cellular Automata and Lattice-Boltzmann Models*. Berlin: Springer.

Wright, M. R. (2007). *An Introduction to Aqueous Electrolyte Solutions*. West Sussex: John Wiley & Sons Ltd.

Wu, J., & Prausnitz, J. M. (1998). Phase Equilibria for Systems Containing Hydrocarbons, Water, and Salt: An Extended Peng-Robinson Equation of State. *Ind. Eng. Chem. Res., 37*, 1634-1643.

Wyckoff, R. D., & Botset, H. G. (1936). The Flow of Gas- Liquid Mixtures Through Unconsolidated Sands. *Journal of Applied Physics, 7*(9), 325-345. doi:doi:http://dx.doi.org/10.1063/1.1745402

Wyllie, M. R. J., & Gardner, G. H. F. (1958). The Generalized Kozeny-Carman Equation. Its Application to Problems of Multi-Phase Flow in Porous Media. *World Oil, 146*, 121.

Xing, D., Wei, B., McLendon, W. J., Enick, R. M., McNulty, S., Trickett, K., . . . Soong, Y. (2012). CO_2-Soluble, Nonionic, Water-Soluble Surfactants That Stabilize CO_2-in-Brine Foams. *17*(4), 1172-1185. doi:10.2118/129907-PA

Yang, S.-Y., Hirasaki, G. J., Basu, S., & Vaidya, R. (1999). Mechanisms for Contact Angle Hysteresis and Advancing Contact Angles. *J. Pet. Sci. Eng., 24*, 63-73.

Yildiz, H. O., Valat, M., & Morrow, N. R. (1999). Effect of Brine Composition on Wettability and Oil Recovery of a Prudhoe Bay Crude Oil. *JCPT, 38*(1), 26-31.

Yousef, A. A., Al-Saleh, S., Al-Kaabi, A., & Al-Jwafi, M. (2010). *Laboratory Investigation of Novel Oil Recovery Method for Carbonate Reservoirs*. Paper presented at the Canadian Unconventional Resources & International Petroleum Conference, Calgary, Alberta.

Yousef, A. A., Liu, J., Blanchard, G., Al-Saleh, S., Al-Zahrani, T., Al-Zahrani, R., . . . Al-Mulhim, N. (2012). *SmartWater Flooding: Industry's First Field Test in Carbonate Reservoirs*. Paper presented at the SPE Annual Technical Conference and Exhibition, San Antonio, TX.

Yuan, C., & Pope, G. A. (2012). A New Method to Model Relative Permeability in Compositional Simulators to Avoid Discontinuous Changes Caused by Phase Identification Problems. *SPE J., 12*, 1221-1230.

Yuan, H. H. (1981). The Influence of Pore Coordination on Petrophysical Parameters: Society of Petroleum Engineers.

Zeinijahromi, A., Ahmetgareev, V., Ibatullin, R., & Bedrikovetsky, P. (2015). Sensitivity Study of Low Salinity Water Injection in Zichebashskoe Oilfield. *Journal of Petroleum and Gas Engineering, 6*(1), 10-21. doi:10.5897/JPGE 2014.0212

Zemaitis, J. F. J., Clark, D. M., Rafal, M., & N.C., S. (1986). *Handbook of Aqueous Electrolyte Thermodynamics*. New York: American Institute of Chemical Engineers.

Zhao, H., dos Ramos, M. C., & McCabe, C. (2007). Development of an Equation of State for Electrolyte Solutions by Combining the Statistical Associating Fluid Theory and the Mean Spherical Approximation for the Non-primitive Model. *Journal of Chem. Phys., 126*, 224503-224501-244503-224514.

Zhao, H. Q., & MacDonald, I. F. (1993). 1993, An Unbiased and Efficient Procedure for 3-D Connectivity Measurement as Applied to Porous Media. *J. Microscopy, 172*, 157-162.

Zhou, D., & Blunt, M. J. (1997). Effect of Spreading Coefficient on the Distribution of Light Non-Aqueous Phase Liquid in the Subsurface. *J. Contaminant Hydrology, 25*, 1-19.

Zhou, Z., & Rossen, W. R. (1995). Applying Fractional-Flow Theory to Foam Processes at the "Limiting Capillary Pressure&quot. *SPE Adv. Technolgy, 3*(1). doi:10.2118/24180-PA

Zhuang, P., Blackburn, M. N., & Peterson, C. B. (1996). Characterization of the Denaturation and Renaturation of Human Plasma Vitronectin. I. Biophysical Characterization of Protein Unfolding and Multimerization. *The Journal of biological chemistry, 271*(24), 14323-14332.

Zuckerman, D. M., Fisher, M. E., & Lee, B. P. (1997). Critique of Primitive Model Electrolyte Theories. *Physical Review E., 56*(6), 6569-6580.

Zuo, L., & Benson, S. M. (2014). Process-Dependent Residual Trapping of CO_2 in Sandstone. *Geophysical Research Letters, 41*(8), 2820-2826.